Pasquale Cavaliere *Editor*

Cold-Spray Coatings

Recent Trends and Future Perspectives

Springer

Cold-Spray Coatings

Pasquale Cavaliere
Editor

Cold-Spray Coatings

Recent Trends and Future Perspectives

Springer

Editor
Pasquale Cavaliere
Department of Innovation Engineering
University of Salento
Lecce, Italy

ISBN 978-3-319-67182-6 ISBN 978-3-319-67183-3 (eBook)
https://doi.org/10.1007/978-3-319-67183-3

Library of Congress Control Number: 2017955840

Printed on acid-free paper

This Springer imprint is published by Springer Nature
The registered company is Springer International Publishing AG
The registered company address is: Gewerbestrasse 11, 6330 Cham, Switzerland

Preface

Cold spray is a recently developed coating technology mainly aimed at the protection and repair of components employed in important industry sectors. These sectors include: aerospace, automotive, transportation, die casting, petrochemical plants, mineral and metal processing, electronics, marine, and ceramics and glass manufacturing. The thickness of cold spray coating almost has no limitation for most metals and metal matrix composites. Considering this fact, cold spray has been successfully applied as an additive manufacturing technology to fabricate individual components and restore damaged ones in recent years. This development shines a new light on the conventional additive manufacturing technologies and significantly broadens application fields of cold spray. Cold spray additive manufacturing as a new member of additive manufacturing family has great potentials to fabricate components with rotational structures, e.g., cylinder walls and flanges. It also allows production of net-shape structures or complex-geometry structures by the aid of well-designed masks or molds.

Cold spray belongs to the family of thermal spray methods, but differs from other techniques in that it is a solid-state process, wherein the sprayed particles are deposited through supersonic-velocity impact with the substrate at temperatures far below the melting point of the sprayed material. Adhesion occurring in the solid state lends distinctive features to cold spray deposits and makes cold spray appropriate for depositing both traditional and advanced materials on several substrate material types, including in temperature-sensitive applications. Cold spray is also suitable for forming coatings of oxygen-sensitive materials such as aluminum, copper, and titanium. In addition, because the feedstock powder is neither heated nor melted in the process, it can be reused in future coating cycles. Cold spray is very well suited for restoring damaged metal parts and apparatus in industry. The addition of coatings to parts comprising the original material of manufacture is a significant means of improving the equipment performance, without the expense of producing a new part production (i.e., cost-saving selection) or increasing environmental waste.

Conventional thermal spray processes often entail grain growth, chemical reactions, cracks, evaporation, thermal residual stresses, thermal shrinkage, phase

transformation, and oxidation; these are absent in cold spray. Because cold spray uses relatively low gas temperatures, it is also operationally safer. Another advantage is the ability to coat substrates of <1 mm in thickness without substrate damage. Furthermore, the process can produce well-bonded thick coatings or multilayer coatings, because coatings are produced with compressive stresses. With high kinetic energy and low gas temperatures, cold spray can provide coatings with wrought microstructures and low porosities. Moreover, because the spray trace is relatively small (1–25 mm^2), cold spray allows the high efficiency deposition of precise coatings, although the deposition efficiency does vary with the types of powder being sprayed.

Scientists continue to develop cold spray technology to fulfill the needs of high-performance applications. This book outlines current knowledge in cold spray by reviewing the major fundamentals of the cold spray process and its features, applications, and bonding mechanisms in brief. It also provides an overview of recent and emerging developments in the process and the potential of this technology. Despite cold spray being still an emerging technology, investigations and applications have been widely reported in previous works, attracting great attentions from both scientific and industrial communities. Existing works mainly focused on applications, product properties, processing parameters optimization, spray strategy, and robot control. So far, a systematic summarization and review on these topics is still lacking. In this book, the different aspects of this emerging technology are addressed in the context of technology, materials, and applications.

My special acknowledgments to the passion and cooperation of all the authors and reviewers who made possible the realization of the book and the reduction of the publication time with their hard work and prompt responses.

My special thanks to the professionalism of the editorial office assistants. Finally, I would like to dedicate the work to Iole, always close to me.

Lecce, Italy Pasquale Cavaliere

Contents

Part I
Cold Spray Fundamentals

Chapter 1
Fundamentals of Cold Spray Processing: Evolution and Future Perspectives

Bandar AlMangour

1.1 Introduction

1.1.1 Motivations and Outline of the Chapter

Metal coatings can be deposited by multiple thermal spraying techniques, such as high-velocity oxygen fuel (HVOF) and plasma spraying. In these spraying processes, the feedstock powders can melt significantly (Sampath et al. 2004). This can generate coatings with high residual stresses, crack formation, material oxidation, and phase transformation, all of which can influence the physical, electrochemical, and mechanical properties of the coatings (Sampath et al. 2004). A recently introduced spraying technique called cold-gas dynamic spraying, or simply cold spraying (CS), was initially developed at the Institute of Theoretical and Applied Mechanics in Russia (Dykhuizen and Smith 1998; Irissou et al. 2007). In this process, particles with micrometer-scale sizes are accelerated by a relatively low-temperature gas jet to a high velocity, accumulating into dense coatings on impact (Grujicic et al. 2004a; Van Steenkiste and Smith 2004; Marx et al. 2006).

In contrast to thermal spraying technologies, powder melting is infrequent in CS, because kinetic energy provides the major driving force for powder consolidation and adhesion to the substrate via metallurgical bonding (Gärtner et al. 2006a). The relatively low processing temperatures increase the possibility of retaining the microstructures and properties of the feedstock materials (Irissou et al. 2008). CS belongs to the family of thermal spray methods but differs from other techniques in being a solid-state process, wherein the sprayed particles are deposited through

B. AlMangour (✉)
School of Engineering and Applied Sciences, Harvard University, Cambridge, MA 02138, USA
e-mail: balmangour@seas.harvard.edu; balmangour@gmail.com

P. Cavaliere (ed.), *Cold-Spray Coatings*,
https://doi.org/10.1007/978-3-319-67183-3_1

supersonic velocity impact with the substrate at temperatures far below the melting point of the sprayed material. Adhesion occurring in the solid state lends distinctive features to CS deposits and makes CS appropriate for depositing both traditional and advanced materials on several substrate material types, including in temperature-sensitive applications (Champagne 2007).

Successful bonding in CS is associated with the degree of particle deformation during impact and increases in temperature at the particle–particle and particle–substrate interfaces (Assadi et al. 2003). In other words, increased plastic flow by adiabatic shear instability is necessary for bonding (Assadi et al. 2003; Schmidt et al. 2006). The adhesion of the powder to the substrate depends on whether it exceeds a critical velocity, which varies among powders (Gilmore et al. 1999). The critical velocity in CS is generally a function of material properties (Stoltenhoff et al. 2002).

Since its discovery, CS has undergone much development; current CS technology is utilized in an expanding range of industries for many applications, mainly in surface restoration, as well as the wear-resistant and corrosion-resistant repair of metals and alloys. Several international organizations continue to develop the CS technology to fulfill the needs of high-performance applications. This chapter outlines current knowledge in CS by reviewing the fundamentals of the CS process and its features, applications, and bonding mechanisms in brief, and also provides an overview of recent and emerging developments in the process and the future potential of this technology. The different aspects of CS are addressed in the context of the essential parameters affecting deposition behavior. The merits, limitations, and applications of the process are also described.

1.1.2 Historical Background

The cold gas dynamic spray process was initially invented and patented by Dr. Anatolii Papyrin and his colleagues at the Institute of Theoretical and Applied Mechanics at Novosibirsk, Russia, in the mid-1980s (Alkhimov et al. 1990). The researchers were conducting experiments in a wind tunnel subjected to a supersonic two-phase flow of gas and solid metallic particles, studying the effects of the particles on the flow structure and the interaction of the two-phase flow with a body (Alkhimov et al. 1990). They observed that, under specific conditions, fine particles injected in the flow stream were deposited on the leading edges of the model bodies. As the particle velocity was increased, the effect of impact transformed from the erosion of the substrate to the rapid accumulation of a coating (Alkhimov et al. 1990; Champagne 2007). The scientists realized the potential of this phenomenon as a new alternative coating procedure and developed a spray coating machine based on the principle. They successfully deposited many different metals, alloys, and composites onto multiple substrate materials, demonstrating the suitability of CS for numerous uses (Alkhimov et al. 1990; Champagne 2007).

1.2 General Process Overview

The CS process is an advanced coating technique in which solid powder particles (1–100 μm in diameter) are accelerated to speeds reaching 1500 m/s by a supersonic gas jet. The powder particles undergo significant deformation on impact with the substrate, thereby forming a coating. The quality of the coating depends on the powder and substrate types, as well as the processing parameters, such as the gas pressure and type, gas temperature, standoff distance, and particle velocity (Champagne 2007).

As shown in Fig. 1.1, CS appears very simple. First, a high-pressure gas supply of nitrogen, helium, or a mixture of these is compressed to 1.0–4.0 MPa and flowed through the system in two different paths. The first path passes through the powder feeder in order to transport the particles to the gun. A typical CS gun is equipped with a converging/diverging de Laval-type nozzle, which permits the gas and particles to reach supersonic velocities (Papyrin et al. 2006; Maev and Leshchynsky 2008). The second path travels through an electric gas heater and is preheated to temperatures of 100–800 °C (Maev and Leshchynsky 2008). This provides an additional increase to the gas velocity and, consequently, increases the particle velocity. The two paths converge near the nozzle entrance (Maev and Leshchynsky 2008). Finally, the feedstock powders reach supersonic velocities, exit the gun nozzle, and collide with the substrate to form a coating (Maev and Leshchynsky 2008). Although the inlet gas is preheated to high temperatures, the particles remain solid in state because the time of contact between the high-temperature gas and particles is relatively short; the gas temperature is also often much lower than the melting point of the powder. In addition, the temperature of the gas is decreased significantly with the expansion of the divergent section of the gun nozzle (Papyrin et al. 2006).

Although the principle of CS is simple, controlling the process is very difficult owing to the many processing parameters. The type of gas, gas pressure and temperature, powder shape and size, nozzle design, standoff distance, traverse speed, and velocity of the particles all strongly affect the properties of the coating.

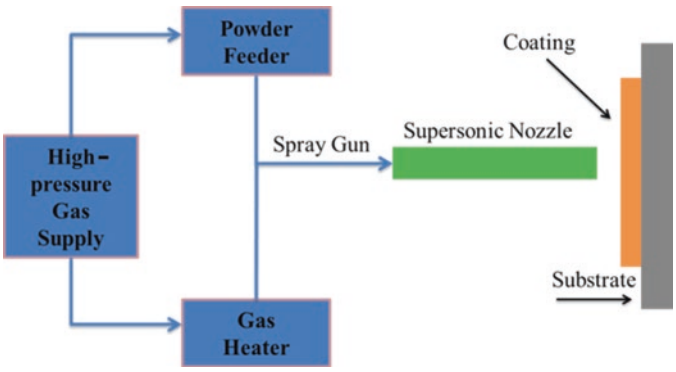

Fig. 1.1 Schematic of the CS process

1.3 Advantages and Limitations of CS

As illustrated in Fig. 1.2, the main differences between CS and other thermal spray processes are the gas temperature and particle velocity. CS utilizes high particle velocities instead of high gas temperatures to form coatings, which has many advantages. CS is suitable for forming coatings of temperature-sensitive materials (Champagne 2007; Irissou et al. 2008), as well as oxygen-sensitive materials such as aluminum, copper, and titanium. In addition, because the feedstock powder is neither heated nor melted in the process, it can be reused in future coating cycles (Champagne 2007). CS is very well suited for restoring damaged metal parts and apparatus in industrial paraphernalia. The addition of coatings to parts comprising the original material of manufacture is an efficient means of improving the equipment performance, without the expense of producing a new part (i.e., cost saving selection) or increasing environmental waste.

Conventional thermal spray processes often entail grain growth, chemical reactions, cracks, evaporation, thermal residual stresses, thermal shrinkage, phase transformation, and oxidation; these are absent in CS (Papyrin et al. 2006). Because CS uses relatively low gas temperatures, it is operationally safer regarding thermal radiation and metal vapors (Champagne 2007). Another advantage is the ability to coat substrates of <1 mm in thickness without substrate damage. Furthermore, the process can produce well-bonded thick coatings or multilayer coatings, because coatings are produced with compressive stresses (Champagne 2007). With high kinetic energy and low gas temperatures, CS can provide coatings with wrought microstructures and low porosities (Champagne 2007). Moreover, because the spray trace is relatively small (1–25 mm^2), CS allows the high-efficiency deposition of precise coatings (Ghelichi and Guagliano 2009), although the deposition efficiency does vary with the types of powder being sprayed.

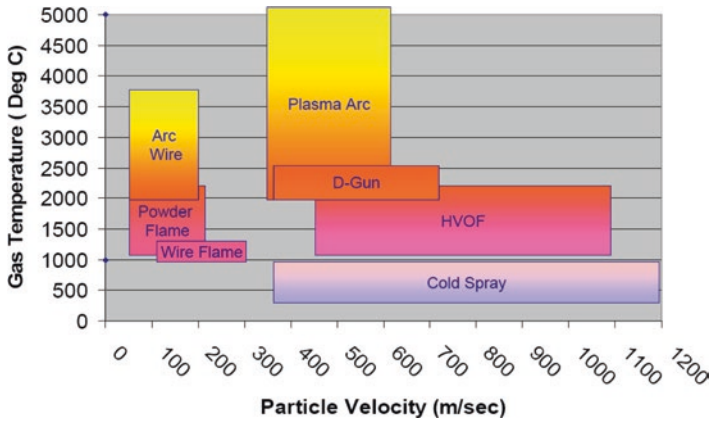

Fig. 1.2 Comparison of CS and thermal spray processing parameters (Champagne 2007)—*D-Gun* detonation gun spraying, *HVOF* high-velocity oxygen fuel

CS, however, does have limitations. One disadvantage that may occur while spraying is nozzle blockage, especially during longer spraying processes; this causes different deposition rates over time and affects the coating properties (Irissou et al. 2008). While CS can utilize a wide range of dissimilar feedstocks and substrates, it is limited to relatively ductile metal powders or hard metals mixed with ductile metals; the technique cannot deposit hard single-species particles such as ceramics (Grujicic et al. 2003). This is because the particles must undergo plastic deformation for interparticle bonding to occur. Similarly, spraying onto ceramic substrates is difficult, with low coating–substrate interfacial bond strength. Furthermore, processing gas consumption is high relative to that in thermal spray processes, typically on the order of 1–2 m^3/min (Gärtner et al. 2006a). Indeed, when helium gas is required to maximize the particle velocity, the high cost of this nonrenewable resource becomes a concern.

The smallness of the spray trace, while allowing precise coverage, combined with the short standoff distance causes difficulties in coating large-surface-area substrates. In addition, CS creates as-sprayed coatings with very poor ductility because the structure is very hard and interparticle bonds can be relatively weak (Borchers et al. 2005; Sundararajan et al. 2009). Finally, the quality and microstructure of the powder must be considered. Because the process is relatively low temperature, the compositional aspects of the as-sprayed coatings are equivalent to those of the feedstock, but the microstructure becomes work hardened and recrystallization may occur at particle–particle interfaces (Kim et al. 2005a; Zou et al. 2009). The chemical composition of the feedstock is retained, including its impurities, which then appear in the coating. Accordingly, the powder production stage should be optimized before attempting to produce coatings.

1.4 Applications of CS

Numerous studies have claimed that CS provides coatings with superior corrosion, wear resistance, and mechanical integrity in the as-sprayed condition (Yandouzi et al. 2007). These coatings can be used in many sectors, including the aerospace, automotive, transportation, die casting, petrochemical, mineral and metal processing, electronics, marine, and ceramics and glass manufacturing industries (Marx et al. 2006; Champagne 2007). Table 1.1 shows the potential applications of CS in different industrial sectors.

1.5 Bonding Mechanisms and Powder Consolidation in CS

1.5.1 Bonding Mechanisms

Although many numerical simulations and experimental investigations have been performed to understand the bonding mechanism in CS, it remains poorly understood (Maev and Leshchynsky 2008). Currently, the most likely bonding mechanism

Table 1.1 CS coating materials and applications in different industrial sectors

Application	Coating materials	Industry sector
Corrosion resistance	Al and Ni alloys, Ti, Ta	Aerospace Oil and gas Petrochemical Power generation
Pb-free bearings	Al, Cu alloys	Automotive Motorsport Aerospace
Wear-resistant coatings	WC–Co	Oil and gas
Bio-inert devices	Ti	Medical

in CS is associated with adiabatic shear instability (ASI), as proposed by Assadi et al. (2003). In this mechanism, the particle–particle or particle–substrate interfacial areas experience severe localized shear deformation during impact, which disrupts the thin oxide surface films on the particles, permitting strong particle–substrate contact (Assadi et al. 2003; Schmidt et al. 2006). This phenomenon, combined with the high compressive stresses developed on collision of the particles with the substrate, is necessary for bonding (Assadi et al. 2003; Grujicic et al. 2004a; Schmidt et al. 2006). In other words, the material loses shear strength and undergoes severe deformation such that the deformation mechanism changes from plastic to viscous flow (Assadi et al. 2003; Grujicic et al. 2003). This facilitates the formation of metallurgical bonds (i.e., atomic bonds) of the particles to the substrate, as well as between particles. However, all of the analyses supporting this proposal are based on numerical simulations (Assadi et al. 2003; Grujicic et al. 2003, 2004a), which sometimes deviate from experimental tests.

Bae et al. (2008) have suggested the existence of a thermal boost-up zone (TBZ), which indicates a specific transitional temperature point (i.e., a sharp increase in temperature) before the start of ASI. TBZs are caused by unstable plastic deformation when the rate of thermal softening exceeds the rate of work hardening (Bae et al. 2008). However, in another study performed by the same authors (Bae et al. 2009), in which a simulation of a titanium particle colliding with a titanium substrate was performed, it was shown that the TBZ was not required for successful bonding. Therefore, although ASI is a likely bonding mechanism for CS, successful particle–particle or particle–substrate bonding does not necessarily require the existence of ASI.

Hussain et al. (2009) proposed another bonding mechanism known as mechanical interlocking after cold spraying copper particles onto aluminum substrates. They suggested that the impaction of the copper particles on the aluminum substrate caused lips to form in the aluminum substrate, which partially enveloped the copper particles (Hussain et al. 2009). This created a mechanical interlock between the substrate and impacting particles, as shown in Fig. 1.3.

The powder can adhere to the substrate during CS with high bond strength. Van Steenkiste et al. (2002) suggested that the formation of the coating occurs in four main stages, as demonstrated in Fig. 1.4. First, the substrate is cratered and the first

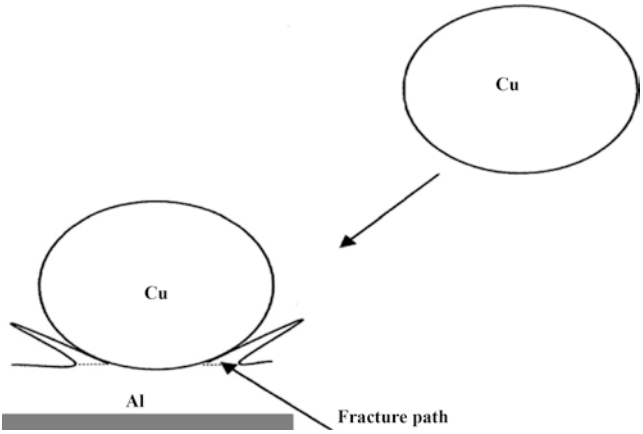

Fig. 1.3 Schematic of jet formation on an aluminum substrate by an approaching Cu particle. The jet is trapped in the copper coating by the incoming copper particles. During bond strength testing, fracture occurs in the aluminum jet, indicated by the *dotted line*. Here, copper and aluminum are examples for the sake of illustration; other metallic species show the same behaviors (Hussain et al. 2009)

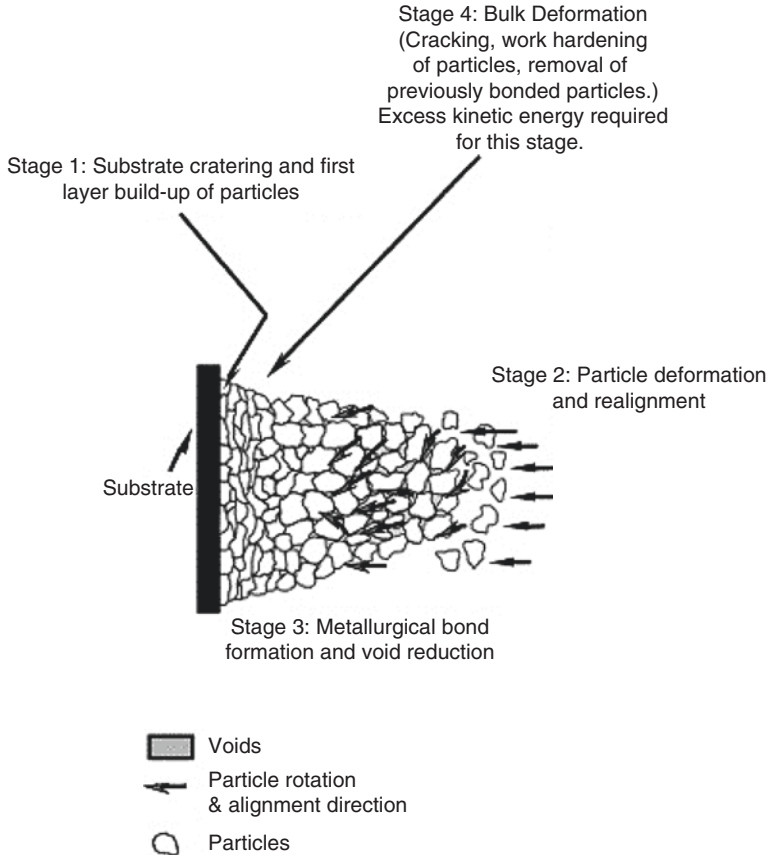

Fig. 1.4 Stages of coating formation in CS (Van Steenkiste et al. 2002)

monolayer of particles is formed. The challenge in this stage relies on particle and substrate conditions, such as roughness, hardness, and temperature (Ghelichi and Guagliano 2009). Next, the approaching particles are deformed, rotated, and readjusted. Then, particle–particle metallurgical bonds form in increasing numbers, creating a thick and hard coating. Finally, as the coating continues to accumulate, the constant shot peening (compressive stress) causes further plastic deformation and work hardening. At a given impact velocity, some of these stages may occur simultaneously (Van Steenkiste et al. 2002).

1.5.2 Cold Sprayability of Materials

The ease with which a metal can be processed by CS, i.e., the cold sprayability, depends largely on the plastic deformation mechanisms of the metal. The deformation mechanisms are usually determined by dislocation motion and interactions, which are dictated mainly by the crystal structure (Amodeo and Ghoniem 1990). Therefore, feedstock powders can be classified according to crystal structure, since similar structures have similar mechanical properties. The most popular group is face-centered cubic (FCC) metals, such as aluminum, copper, nickel, and 316L stainless steel. Metals like tungsten, tantalum, molybdenum, and chromium are body-centered cubic (BCC). Zinc, cobalt, and titanium are hexagonally close packed (HCP). In general, metals with the FCC lattice have the highest number of slip systems, which provide them with the greatest deformability (Borchers et al. 2004; Vlcek et al. 2005). Because metals with HCP and BCC structures have fewer slip systems, they tend to have lower plasticity, making them less suitable for CS processing. More extreme processing parameters must be selected for materials with high resistances to deformation or high melting temperatures (Vlcek et al. 2005).

1.6 Important Factors in CS

1.6.1 Deposition Efficiency

Deposition efficiency (DE) can be simply defined as the weight of particles successfully adhered to the substrate (m_s = final weight of the substrate − initial substrate weight) divided by the total weight of the initial feedstock particles (M_p). Mathematically, the deposition efficiency can be expressed as (Papyrin et al. 2006):

$$\mathrm{DE} = \frac{m_s}{M_p} \times 100 \tag{1.1}$$

In order to improve adhesion, sand blasting is commonly used. However, this method has drawbacks, mainly from the contamination of the substrate by sand-blasted particles (Ghelichi and Guagliano 2009). Particle adhesion depends on many factors,

including the contact surface area, plastic deformation, yield stress, processing parameters (mainly the temperature and pressure of the gas), and the particle and substrate temperatures (Ghelichi and Guagliano 2009). In fact, the DE increases as the particle velocity significantly exceeds the critical velocity (Gilmore et al. 1999; Gärtner et al. 2006a; Fukanuma et al. 2006), as explained in the following.

1.6.2 Critical Velocity

The critical velocity V_{crit} is defined as the minimum particle velocity necessary for a material to adhere to the substrate (Papyrin et al. 2006). As demonstrated in Fig. 1.5, if the particle velocity is lower than V_{crit}, then either the particle makes impact and bounces back from the substrate or the particle hits the substrate and causes surface abrasion. However, if the particle velocity reaches or exceeds V_{crit}, then particle adhesion occurs. The value of V_{crit} depends on many factors, such as the material types of the substrate and feedstock powder, processing parameters, particle size, and substrate surface properties, like roughness (Gärtner et al. 2006a).

Assadi et al. (2003) used simulation modeling methods to predict V_{crit}. The critical velocity is associated with ASI, and the simulation results are summarized into the following equation:

$$V_{crit} = 667 - 0.014\,\rho + 0.08\,\left(T_m - T_{Ref}\right) + 10^{-7}\sigma_{\text{uts}} - 0.4\left(T_i - T_{Ref}\right) \tag{1.2}$$

where ρ is the particle density, T_m is the melting temperature, T_{Ref} is the reference temperature at which the ultimate tensile strength is determined, σ_{uts} is the ultimate tensile strength, and T_{i} is the initial particle temperature.

Schmidt et al. (2006) developed another correlation for predicting V_{crit}:

$$V_{\text{Crit}} = \sqrt{\left[4F_{\text{I}}\sigma_{\text{uts}}\left(1 - \frac{T_{\text{i}} - T_{\text{Ref}}}{T_{\text{m}} - T_{\text{Ref}}}\right)\rho_{\text{p}}^{-1}\right] + F_2 c_{\text{p}}\left(T_{\text{m}} - T_{\text{i}}\right)} \tag{1.3}$$

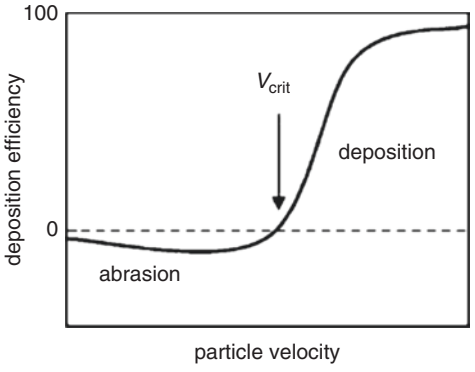

Fig. 1.5 The effect of particle velocity on DE in CS (Gärtner et al. 2006a)

where σ_{uts} is the ultimate tensile strength, T_i is the initial particle temperature, T_{Ref} is the reference temperature at which the ultimate tensile strength is determined, T_m is the melting point of the particle, ρ_p is the density of the particle, c_p is the particle-specific heat capacity, and F_1 and F_2 are constants representing material-dependent calibration factors.

Figure 1.6 compares the calculated V_{crit} using Eqs. 1.2 and 1.3 with the experimental results of spray experiments and impact tests. The work by Assadi and his colleagues did not consider the size of particles as a significant factor in determining V_{crit} (Schmidt et al. 2006). In fact, smaller-size particles usually contain higher proportions of oxides, which hinder bonding (Blazynski 1983; Van Steenkiste and Smith 2004). Therefore, the prediction is much better using Eq. 1.3, especially when using tin and tantalum, which have significantly different properties than copper.

If the particle velocity greatly exceeds V_{crit}, this causes not only a higher DE, as illustrated in Fig. 1.5, but also a lower porosity (Kim et al. 2005b; Gärtner et al. 2006a). It is important to produce coatings with low porosities, as porosity influences the mechanical, electrical, and thermal properties of CS coatings (Li et al. 2006a; Sudharshan Phani et al. 2007). For example, a low-porosity coating generally exhibits higher hardness and better corrosion resistance compared to a more porous coating of the same material. The porosity level in CS coatings depends mainly on the feedstock material and processing parameters (Klinkov et al. 2005; Sudharshan Phani et al. 2007). However, it is possible to reduce the porosity of the as-sprayed coating using post-heat treatments (Li et al. 2006a; Novoselova et al. 2006; Sudharshan Phani et al. 2007; Sundararajan et al. 2009; Zahiri et al. 2009;

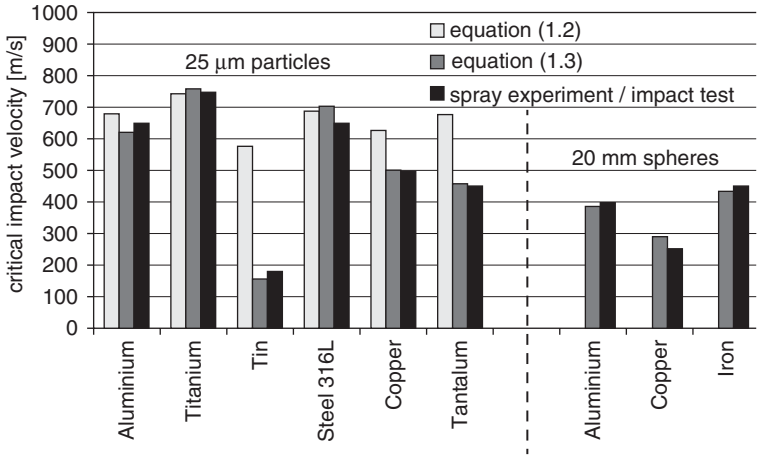

Fig. 1.6 Comparison of calculated critical velocity with experimental results of spray experiments and impact tests (Schmidt et al. 2006)

AL-Mangour et al. 2013; AL-Mangour et al. 2014). In addition, mechanical properties can be attained that approach bulk values for the coating material after post-CS heat treatment (Sudharshan Phani et al. 2007).

1.6.3 Gas Temperature and Pressure

Researchers have investigated the effects of different processing parameters on coating quality. Gas temperature and gas pressure have been studied the most extensively because they affect the particle impact velocity strongly (Gärtner et al. 2006a; Maev and Leshchynsky 2008; Wong et al. 2011; Meng et al. 2011). The typical gas used in CS is nitrogen, helium, or a mixture of the two (Borchers et al. 2008; Wong et al. 2011). Previous investigations have confirmed that higher particle impact velocities, generated by higher gas temperatures, produce coatings with higher DE and quality, as determined by lower porosity and higher strength (Stoltenhoff et al. 2002; Gärtner et al. 2006a, b; Borchers et al. 2008; Meng et al. 2011; Wong et al. 2011). High gas temperature is beneficial because it intensifies plastic deformation by promoting dislocation motion, recovery, and recrystallization (Gärtner et al. 2006b; Borchers et al. 2008; Meng et al. 2011).

For a given gas type and pressure, in order to obtain higher particle impact velocities, the gas temperature must be increased (Stoltenhoff et al. 2002; Meng et al. 2011). However, technical problems are associated with increased gas temperature, such as the sensitivity of the CS gun nozzle to high temperatures (i.e., material limitations), oxidation, and nitridation (Champagne 2007). On the other hand, it has been shown CS processing with helium gas produces a much higher particle impact velocity than that with nitrogen gas at the same temperature and pressure (Gilmore et al. 1999; Stoltenhoff et al. 2002; Li and Li 2003; Borchers et al. 2008; AL-Mangour et al. 2014), leading to a lower porosity. However, nitrogen is usually preferred because of the high cost of helium. Therefore, the challenge is to optimize the CS processing parameters to produce high-quality coatings using nitrogen gas.

The gas velocity υ can be calculated using the equation below (Grujicic et al. 2004b):

$$\upsilon = \sqrt{\gamma RT / M_w} \tag{1.4}$$

where γ is the ratio of the constant-pressure- and the constant-volume-specific heats, which is approximately 1.66 for monoatomic gases (e.g., helium) and 1.4 for diatomic gases (e.g., nitrogen and oxygen). R is the gas constant (8314 J/kmol·K), T is the gas temperature, and M_w is the molecular weight of the gas. According to Eq. 1.4, increasing the temperature increases the velocity when all other parameters are constant. More interestingly, the critical velocity seems to decrease with increasing gas temperature, which may be because of thermal softening of the particles (Gärtner et al. 2006a; Lee et al. 2007). Most existing reports on the effect of gas temperature are based on numerical simulations (Sakaki and Shimizu 2001, Li et al. 2006b, Katanoda et al. 2007, Yin et al. 2010, Chuanshao et al. 2011,); therefore, further experimental analysis should be performed to establish better understanding.

1.7 Enhancements to the CS Process

With the development of the CS process, numerous studies have been undertaken for process enhancement. Current enhanced CS processes include kinetic metallization (KM), pulsed gas dynamic spraying (PGDS), and vacuum CS (VCS) (Moridi et al. 2014).

KM (Fig. 1.7) differs from other forms of CS in that it uses a convergent barrel nozzle under choked flow conditions to achieve a velocity of Mach 1 (Moridi et al. 2014). To compensate for friction, the nozzle is also slightly diverged from a straight path. To accelerate gas velocity, other CS processes use de Laval nozzles. Coatings made with KM have demonstrated stronger particle–particle and particle–substrate bonds (Wang et al. 2010).

Multiple patents exist for KM processes globally. One example, by Inovati (2016), uses a special design comprising a set of friction-aided spouts for depositing the particles, where metallic particles carried in low-pressure helium or nitrogen gas (70–130 psi) within the nozzle can reach a maximum speed of 1000 m/s. The amount of inert carrier gas used in the acceleration of particles by KM is greatly reduced compared to those in supersonic methods for the same purposes (Irissou et al. 2008). The major deviation of KM from other CS processes is the lower kinetic energy of particle impact involved. This is achieved by slightly increasing the temperature of the powder particles used, allowing easy plastic deformation.

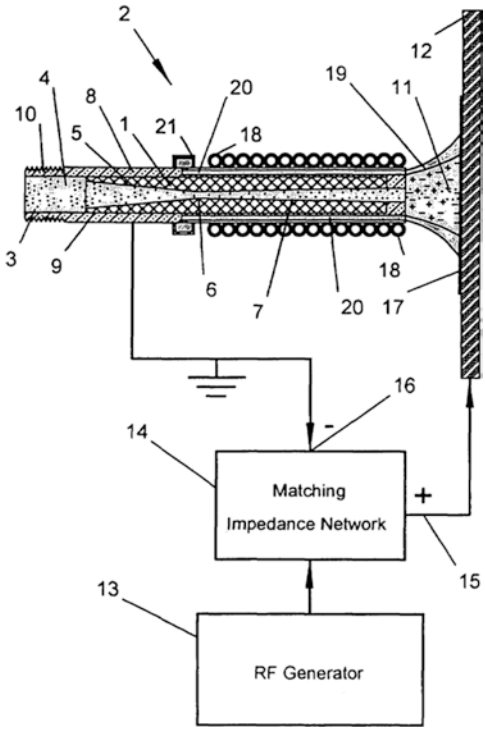

Fig. 1.7 KM schematic (Tapphorn and Gabel 2007)

PGDS (Fig. 1.8) warms the feedstock particles to a transitional temperature higher than the temperatures encountered in conventional CS processes (Jodoin et al. 2007). Moreover, it promotes elevation in plastic deformation while maintaining the impact speed. The process also utilizes non-motionless pressure effects to produce concurrently higher pressure at the exit point, as opposed to conventional CS processes, which use perpetual fixed-flow exits (Yin et al. 2016). Unlike the case of CS, it is possible to accomplish elevated particle impact temperatures with PGDS owing to the gas compression that causes the propelling flow. Thus, it is expected that PGDS could permit particles to reach elevated impact speeds and intermediate impact temperatures, which could lead to relatively lower critical speeds than those in CS, thus improving the plastic deformation upon impact with the underlying substrate at a constant impact velocity.

VCS (Fig. 1.9) takes place in a vacuum cistern. The substrate is placed opposite to a spurt with a spray gun at one end within the vacuum chamber; the spray gun deposits the metal particles. Here, the metallic powdered particles in the vacuum chamber are accelerated to a high velocity so that, at the point of impact with the substrate, they undergo deformation on the active surface of the substrate and create strong bonds. VCS technology is preferred for the coating of thin films. The vacuum tank allows for recovery of gases and collection of oversprays (Muehlberger 2004). VCS differs from other CS systems in allowing for the deposition of nanoscale particles. The most recent form of VCS is referred to as the aerosol deposition method (Akedo et al. 2008). Detailed information on the patent can be found elsewhere (Muehlberger 2004).

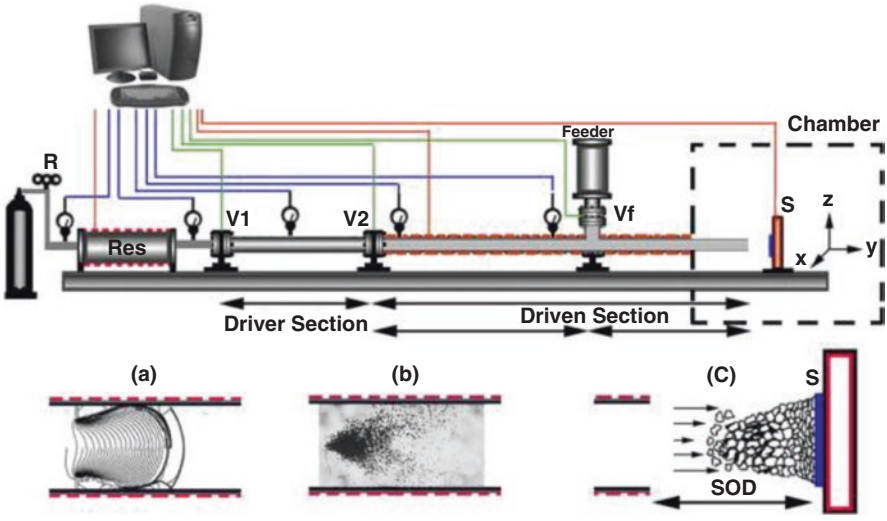

Fig. 1.8 Schematic of the PGDS technique (**a**–**c**) represents shockwave generation, particles flowing under compressed gas, and coating buildup, respectively, which occur during one pulse (Jodoin et al. 2007)

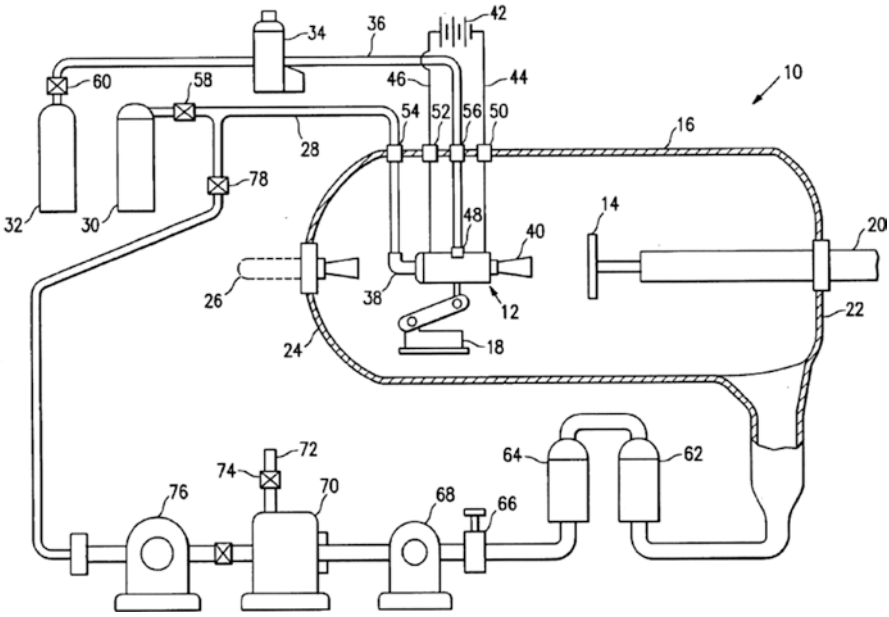

Fig. 1.9 VCS setup (Muehlberger 2004)

A recent application of VCS was in hydroxyapatite (HA) coatings utilized in the biomedical sector (Choudhuri et al. 2009). The VCS-deposited HA nanosheets showed significant deformation. The structures were thick with investigations revealing the formation of dense deposits of nanosheets. The study showed that the application of graphene nanosheets (GN) significantly improved the fracture strength and exhibited better HA coatings that covered fractures with deposits. VCS to achieve a composite with GN and HA (Fig. 1.10) with thin film coatings was suggested for use in regenerating tough tissues (Liu et al. 2014).

1.8 Recent Developments in Cold Spray Technology

1.8.1 Shockwave-Induced Spraying

The development of shockwave-induced spraying (SISP) is among the latest advancements in material deposition. The method enables the solid-state deposition of materials beyond typical CS, with elevated deposition rates and efficiencies. It is anticipated that SISP will become a favored solid-state spraying process for applications requiring high productivity at low cost. Other possible advances include the development of smaller, more portable, low-pressure CS units for field use and other applications.

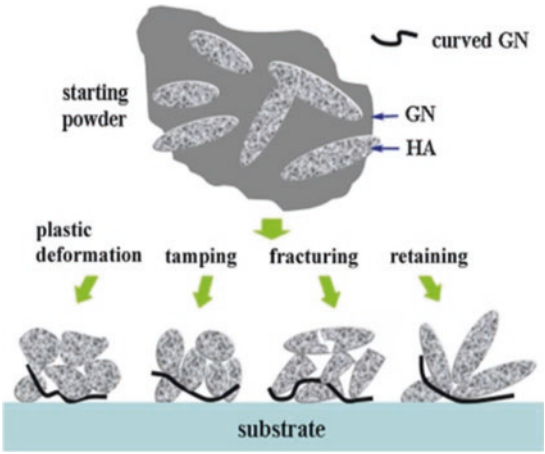

Fig. 1.10 Schematic demonstrating the formation mechanisms of the HA–GN nanocomposite coating (Liu et al. 2014)

SISP involves the production of streams of shockwaves using a regulator that rapidly opens and closes to allow a flow of inert gas under high pressure. The generated stream of shockwaves passes through a straight outlet, compressing the gas already in the nozzle. This creates an intensely heated pulse at supersonic speed, with a frequency of ~10–30 Hz. This pulse travels through the powder particles, heating them below their thermal deformation point and accelerating them as they are carried toward the outlet. Conventional CS processing, meanwhile, requires diverging–converging outlets (which lead to a higher exit pressure), which SISP does not (Karimi et al. 2011).

SISP works such that the less supersonic system dictates the rate of the gas flow as well as the number of generated pulse streams; however, heating of the powdered particles is due to the compression produced by the shockwaves. The SISP system allows the gas in the nozzle to cool as it expands toward the diverging de Laval outlet. The critical velocity of the powdered particles is reduced, allowing bonding of the solid caused by movement of heated particles through the nozzle. SISP utilizes both kinetic and thermal energy from the solid particles, promoting excellent deposition of solid-state particles on numerous materials. The greatest benefit of this system is its minimization of energy consumption, thus reducing operation costs in terms of energy, as compared to CS (Karimi et al. 2011).

1.8.2 Nozzle Design

Improvements in the nozzle design have promoted relatively higher deposition velocities as well as the capability to deposit bigger particles (Lupoi and O'Neill 2011). This has greatly improved the operating ability by elevating the spray location, although it limits the prevailing angle of the nozzle divergence to sustain a stable gas flow. Nozzle modifications are made by attaching pneumatic channels to the individual gas and powdered mixture feed channels and the corresponding

common pre-chamber. Fluid dynamic models were employed to design nozzles with substantially elevated particle velocities, creating denser coatings and higher deposition efficiency. Augmentation of the length of the nozzle has been demonstrated to significantly affect the particle velocity. For instance, by increasing the length of the central nozzle from 82 mm to 211 mm with nitrogen as the carrier gas, the computed velocity of a 12 μm copper particle is increased from 553 m/s to 742 m/s (Schleef et al. 2014): a 33% increase. The materials also limit the practical length of existing nozzles (Klinkov et al. 2005). Supplementary nozzle advancements entail the utilization of modern nozzle designs, such as convergent barrels, to enhance powder flow via the nozzle and design optimization to minimize gas flow friction via the nozzle (Li et al. 2006b). An increase in the gas temperature typically causes a proportional increase in the gas velocity; nozzle design can be improved by including gas heating (Lupoi 2014).

An experimental setup used to estimate the efficient nozzle design geometry values for a CS process is depicted in Fig. 1.11. A_i and A_e denote the cross-sectional areas of the inlet and outlet, respectively; L_c and L_d are the lengths of the converging and diverging nozzle sections, respectively; A^* represents the cross-sectional area of the nozzle throat (Meyer and Lupoi 2015) (Table 1.2).

The depositional efficiency tests from the three experiments show that the CS process attains maximum depositional efficiency with nozzle dimensions corresponding to those of N3, as shown in Table 1.3.

Thus, the nozzle designed mainly improved the coating process. The relatively elevated particle speed from the advanced plunger design promoted a greater covering density, thereby improving the mechanical properties (Champagne and Helfritch 2016). CS nozzle design also helps increase operation capability by maintaining the stability of gas flow.

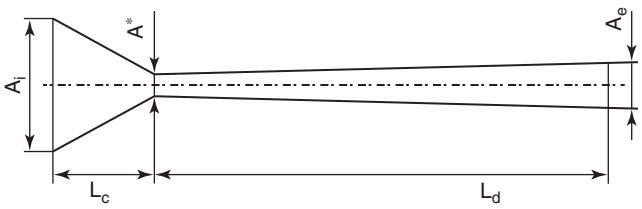

Fig. 1.11 CS nozzle geometry (Meyer and Lupoi 2015)

Table 1.2 Geometrical details of the nozzles *N1*, *N2*, and *N3*

Nozzle	A_i [mm^2]	L_c [mm]	A^* [mm^2]	L_d [mm]	A_c [mm^2]
*N*1	314	30	3.1	180	28.3
*N*2	44.2	15.5	5.7	190	47.8
*N*3	314	20	5.7	190	47.8

Meyer and Lupoi (2015)

Table 1.3 Depositional efficiency comparison

Nozzle	DE [%]
*N*1	16.3
*N*2	32.5
*N*3	33.5

Lupoi (2014)

1.9 CS Process Advancements and Applications

CS processes have led to the emergence of sprayed composite materials. CS allows the fabrication of tungsten/copper composites among the best materials for the production of heat sinks owing to their high heat conductivities and very low coefficients of thermal expansion. Previously, infiltration methods were used to produce such composites; this was costly because of the high temperatures used and the products suffered from low deposition and densification. CS processes are less expensive in producing composites with end qualities superior to those of composites created by the infiltration method (Kang and Kang 2003).

Another recent promising work is the metallization of low-weight and high-strength carbon fiber composites, which are promising for the aerospace industry. Traditional manufacturing processes are difficult to apply in forming coatings of fiber composite materials because they are time-consuming, labor-intensive, and expensive; however, the metallization of carbon fiber-reinforced polymer (CFRP) composites helps increase the conductivity of the fuselage in aerospace engineering. CS processes have helped to solve problems of oxidation and weight increases in CFRP structures. Through the CS process, sprayed conductive metal particles remain in the solid state, forming a thin layer of non-oxidized conductive metal (Archambault et al. 2016) (Fig. 1.12).

In the biomedical field, AL-Mangour et al. (2013) proposed the use of Co–Cr and stainless steel alloy mixtures for medical implants. Co–Cr is more resistant to corrosion than stainless steel but is also more difficult to manufacture and more expensive. CS allows cheap and easy improvement of stainless steel in terms of corrosion resistance and strength by combining it with Co–Cr. This could ultimately lead to new biomaterials in the future.

CS is also used to increase the resistance to dry sliding wear of Ni–WC composite materials. According to experimental results, the inclusion of WC particles through CS stabilized the coefficient of friction and decreased the rate of wear. These effects are attributed to the creation of a cohesive and stable mechanically mixed layer on the top of the Ni–WC coating wear track (Alidokht et al. 2016).

Magnesium alloys also have high strength-to-weight ratios, making them suitable candidates for use in the transport industry. However, they are highly susceptible to wear and corrosion. CS processing could allow the use of such alloys because it produces composites with stronger bonds and greater resistance to wear and corrosion. According to Wang et al. (2010), the addition of Al_2O_3 to coatings has been shown to increase the strength of Mg–Al bonds, thereby strengthening the fabricated alloys.

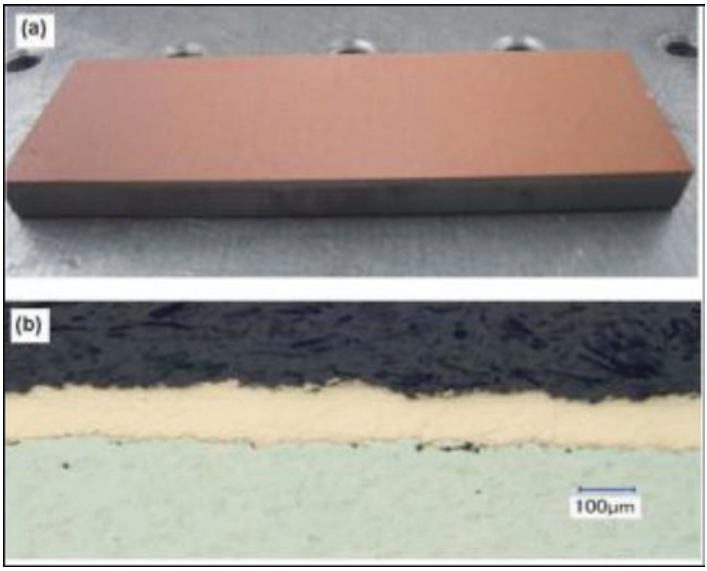

Fig. 1.12 Typical copper coating on Invar substrate obtained by CS process: (**a**) plane view and (**b**) cross-sectional image, revealing the quality of the deposited metallic layer (Archambault et al. 2016)

CS can also be applied to additive manufacturing, which assembles an object as a whole rather than through the creation of component parts that are joined together. Research has shown that CS can create three-dimensional shapes of varying geometries. Robotic control can help to direct the nozzle to follow the contours of the desired shape. Several layers of metal are continuously deposited to achieve the desired thickness. Machining is performed on the resulting object to achieve the desired finish (Champagne et al. 2010). Recent research (Champagne and Helfritch 2016) suggested that additive manufacturing would be the most commercially viable option for the application of CS processes, if further advancements occur to refine CS deposits.

With the evolution of technology, it is expected that the applicability of CS will expand to more advanced fields such as those involving wind energy, photovoltaic energy, architecture, and medicine. For instance, in photovoltaic applications, the technology can be applied for the fabrication of intricate conductive designs in solar cells. Wind power production might be able to utilize CS to improve surface performance in elements manufactured from complex polymer–matrix composites. The future of CS depends on its potential to deposit advanced materials onto a wide range of substrates with the least thermal cost and penalty. These factors will define the opportunities and future directions of CS.

References

Akedo J, Nakano S, Jaehyuk P, Ashida K (2008) The aerosol deposition method. Synthes Engl Ed 1:121–130. https://doi.org/10.5571/syntheng.1.121

Alidokht SA, Manimunda P, Vo P, Yue S, Chromik RR (2016) Cold spray deposition of a Ni-WC composite coating and its dry sliding wear behavior. Surf Coat Technol 308:424–434. https://doi.org/10.1016/j.surfcoat.2016.09.089

Alkhimov A, Kosarev V, Papyrin A (1990) A method of cold gas-dynamic spraying. Dokl Akad Nauk SSSR 315:1062–1065

AL-Mangour B, Mongrain R, Irissou E, Yue S (2013) Improving the strength and corrosion resistance of 316L stainless steel for biomedical applications using cold spray. Surf Coat Techn 216:297–307. https://doi.org/10.1016/j.surfcoat.2012.11.061

AL-Mangour B, Vo P, Mongrain R, Irissou E, Yue S (2014) Effect of heat treatment on the microstructure and mechanical properties of stainless steel 316L coatings produced by cold spray for biomedical applications. J Therm Spray Technol 23:641–652. https://doi.org/10.1007/s11666-013-0053-2

Amodeo RJ, Ghoniem NM (1990) Dislocation dynamics. I. A proposed methodology for deformation micromechanics. Phys Rev B 41:6958–6967. https://doi.org/10.1103/PhysRevB.41.6958

Archambault G, Jodoin B, Gaydos S, Yandouzi M (2016) Metallization of carbon fiber reinforced polymer composite by cold spray and lay-up molding processes. Surf Coat Technol 300:78–86. https://doi.org/10.1016/j.surfcoat.2016.05.008

Assadi H, Gärtner F, Stoltenhoff T, Kreye H (2003) Bonding mechanism in cold gas spraying. Acta Mater 51:4379–4394. https://doi.org/10.1016/S1359-6454(03)00274-X

Bae G, Xiong Y, Kumar S, Kang K, Lee C (2008) General aspects of interface bonding in kinetic sprayed coatings. Acta Mater 56:4858–4868. https://doi.org/10.1016/j.actamat.2008.06.003

Bae G, Kumar S, Yoon S, Kang K, Na H, Kim H-J, Lee C (2009) Bonding features and associated mechanisms in kinetic sprayed titanium coatings. Acta Mater 57:5654–5666. https://doi.org/10.1016/j.actamat.2009.07.061

Blazynski T (1983) Explosive welding, forming and compaction. Applied Science Publishers, London

Borchers C, Gärtner F, Stoltenhoff T, Kreye H (2004) Microstructural bonding features of cold sprayed face centered cubic metals. J Appl Phys 96:4288. https://doi.org/10.1063/1.1789278

Borchers C, Gärtner F, Stoltenhoff T, Kreye H (2005) Formation of persistent dislocation loops by ultra-high strain-rate deformation during cold spraying. Acta Mater 53:2991–3000. https://doi.org/10.1016/j.actamat.2005.02.048

Borchers C, Schmidt T, Gärtner F, Kreye H (2008) High strain rate deformation microstructures of stainless steel 316L by cold spraying and explosive powder compaction. Appl Phys A: Mater Sci Proc 90:517–526. https://doi.org/10.1007/s00339-007-4314-0

Champagne VK (2007) The cold spray materials deposition process: fundamentals and applications. CRC Press. Cambridge, England

Champagne V, Helfritch D (2016) The unique abilities of cold spray deposition. Int Mater Rev 61:437–455. https://doi.org/10.1080/09506608.2016.1194948

Champagne V, Helfritch D, Wienhold E, Dehaven J (2010) The development of nickel-aluminum reactive material by cold spray process. Army Research Laboratory Technical Report ARL-TR-5189

Choudhuri A, Mohanty P, Karthikeyan J (2009) Bio-ceramic composite coatings by cold spray technology. Proc Int Thermal Spray Conf, Japan Association for Earthquake Engineering

Chuanshao L, Song C, Jianxin Z (2011) Numerical simulation of gas-particle two phase flow in aluminum-oxide ceramics powder spraying process. Consumer Electron Comm Netw (CECNet), 2011 Int Conf 16–18 April 2011. 4216–4218. doi:https://doi.org/10.1109/CECNET.2011.5768755

Dykhuizen RC, Smith MF (1998) Gas dynamic principles of cold spray. J Therm Spray Technol 7:205–212. https://doi.org/10.1361/105996398770350945

Fukanuma H, Ohno N, Sun B, Huang R (2006) In-flight particle velocity measurements with DPV-2000 in cold spray. Surf Coat Technol 201:1935–1941. https://doi.org/10.1016/j.surfcoat.2006.04.035

Gärtner F, Stoltenhoff T, Schmidt T, Kreye H (2006a) The cold spray process and its potential for industrial applications. J Therm Spray Technol 15:223–232. https://doi.org/10.1361/105996306X108110

Gärtner F, Stoltenhoff T, Voyer J, Kreye H, Riekehr S, Koçak M (2006b) Mechanical properties of cold-sprayed and thermally sprayed copper coatings. Surf Coat Technol 200:6770–6782. https://doi.org/10.1016/j.surfcoat.2005.10.007

Ghelichi R, Guagliano M (2009) Coating by the cold spray process: a state of the art. Fratt Integr Strutt 8:30–44. https://doi.org/10.3221/IGF-ESIS.08.03

Gilmore DL, Dykhuizen RC, Neiser RA, Smith MF, Roemer TJ (1999) Particle velocity and deposition efficiency in the cold spray process. J Therm Spray Technol 8:576–582. https://doi.org/10.1361/105996399770350278

Grujicic M, Saylor JR, Beasley DE, DeRosset WS, Helfritch D (2003) Computational analysis of the interfacial bonding between feed-powder particles and the substrate in the cold-gas dynamic-spray process. Appl Surf Sci 219:211–227. https://doi.org/10.1016/S0169-4332(03)00643-3

Grujicic M, Zhao CL, DeRosset WS, Helfritch D (2004a) Adiabatic shear instability based mechanism for particles/substrate bonding in the cold-gas dynamic-spray process. Mater Des 25:681–688. https://doi.org/10.1016/j.matdes.2004.03.008

Grujicic M, Zhao CL, Tong C, DeRosset WS, Helfritch D (2004b) Analysis of the impact velocity of powder particles in the cold-gas dynamic-spray process. Mater Sci Eng A 368:222–230. https://doi.org/10.1016/j.msea.2003.10.312

Hussain T, McCartney DG, Shipway PH, Zhang D (2009) Bonding mechanisms in cold spraying: the contributions of metallurgical and mechanical components. J Therm Spray Technol 18:364–379. https://doi.org/10.1007/s11666-009-9298-1

Inovati (2016) Kinetic metallization: coatings once thought impossible. Inovati Innovative Technology Inc. http://www.inovati.com. Accessed 8 Apr 2017

Irissou E, Legoux J-G, Arsenault B, Moreau C (2007) Investigation of al-Al_2O_3 cold spray coating formation and properties. J Therm Spray Technol 16:661–668. https://doi.org/10.1007/s11666-007-9086-8

Irissou E, Legoux J-G, Ryabinin AN, Jodoin B, Moreau C (2008) Review on cold spray process and technology: part I—intellectual property. J Therm Spray Technol 17:495–516. https://doi.org/10.1007/s11666-008-9203-3

Jodoin B, Richer P, Bérubé G, Ajdelsztajn L, Erdi-Betchi A, Yandouzi M (2007) Pulsed-gas dynamic spraying: process analysis, development and selected coating examples. Surf Coat Technol 201:7544–7551. https://doi.org/10.1016/j.surfcoat.2007.02.033

Kang H-K, Kang SB (2003) Tungsten/copper composite deposits produced by a cold spray. Scr Mater 49:1169–1174. https://doi.org/10.1016/j.scriptamat.2003.08.023

Karimi M, Jodoin B, Rankin G (2011) Shock-wave-induced spraying: modeling and physics of a new spray process. J Therm Spray Technol 20:866–881. https://doi.org/10.1007/s11666-011-9622-4

Katanoda H, Fukuhara M, Iino N (2007) Numerical study of combination parameters for particle impact velocity and temperature in cold spray. J Therm Spray Technol 16:627–633. https://doi.org/10.1007/s11666-007-9087-7

Kim H-J, Lee C-H, Hwang S-Y (2005a) Fabrication of WC–co coatings by cold spray deposition. Surf Coat Technol 191:335–340. https://doi.org/10.1016/j.surfcoat.2004.04.058

Kim H-J, Lee C-H, Hwang S-Y (2005b) Superhard nano WC–12%co coating by cold spray deposition. Mater Sci Eng A 391:243–248. https://doi.org/10.1016/j.msea.2004.08.082

Klinkov SV, Kosarev VF, Rein M (2005) Cold spray deposition: significance of particle impact phenomena. Aerosp Sci Technol 9:582–591. https://doi.org/10.1016/j.ast.2005.03.005

Lee J, Shin S, Kim H, Lee C (2007) Effect of gas temperature on critical velocity and deposition characteristics in kinetic spraying. Appl Surf Sci 253:3512–3520. https://doi.org/10.1016/j.apsusc.2006.07.061

Li C-J, Li W-Y (2003) Deposition characteristics of titanium coating in cold spraying. Surf Coat Technol 167:278–283. https://doi.org/10.1016/S0257-8972(02)00919-2

Li W-Y, Li C-J, Liao H (2006a) Effect of annealing treatment on the microstructure and properties of cold-sprayed Cu coating. J Therm Spray Technol 15:206–211. https://doi.org/10.1361/105996306X108066

Li W-Y, Liao H, Wang H-T, Li C-J, Zhang G, Coddet C (2006b) Optimal design of a convergent-barrel cold spray nozzle by numerical method. Appl Surf Sci 253:708–713. https://doi.org/10.1016/j.apsusc.2005.12.157

Liu Y, Huang J, Li H (2014) Nanostructural characteristics of vacuum cold-sprayed hydroxyapatite/graphene-nanosheet coatings for biomedical applications. J Therm Spray Technol 23:1149–1156. https://doi.org/10.1007/s11666-014-0069-2

Lupoi R (2014) Current design and performance of cold spray nozzles: experimental and numerical observations on deposition efficiency and particle velocity. Surf Eng 30:316–322. https://doi.org/10.1179/1743294413Y.0000000214

Lupoi R, O'Neill W (2011) Powder stream characteristics in cold spray nozzles. Surf Coat Technol 206:1069–1076. https://doi.org/10.1016/j.surfcoat.2011.07.061

Maev RG, Leshchynsky V (2008) Introduction to low pressure gas dynamic spray: physics & technology. Weinheim (Germany), Wiley-VCH 234

Marx S, Paul A, Köhler A, Hüttl G (2006) Cold spraying: innovative layers for new applications. J Therm Spray Technol 15:177–183. https://doi.org/10.1361/105996306X107977

Meng X, Zhang J, Zhao J, Liang Y, Zhang Y (2011) Influence of gas temperature on microstructure and properties of cold spray 304SS coating. J Mater Sci Technol 27:809–815. https://doi.org/10.1016/S1005-0302(11)60147-3

Meyer M, Lupoi R (2015) An analysis of the particulate flow in cold spray nozzles. Mech Sci 6:127–136. https://doi.org/10.5194/ms-6-127-2015

Moridi A, Hassani-Gangaraj SM, Guagliano M, Dao M (2014) Cold spray coating: review of material systems and future perspectives. Surf Eng 30:369–395. https://doi.org/10.1179/1743294414Y.0000000270

Muehlberger E (2004) Method and apparatus for low pressure cold spraying. US Patent 6759085 B2, 6 Jul 2004

Novoselova T, Fox P, Morgan R, O'Neill W (2006) Experimental study of titanium/aluminium deposits produced by cold gas dynamic spray. Surf Coat Technol 200:2775–2783. https://doi.org/10.1016/j.surfcoat.2004.10.133

Papyrin A, Kosarev V, Klinkov S, Alkhimov A, Fomin V (2006) Cold spray technology. Elsevier. Amsterdam, The Netherland

Sakaki K, Shimizu Y (2001) Effect of the increase in the entrance convergent section length of the gun nozzle on the high-velocity oxygen fuel and cold spray process. J Therm Spray Technol 10:487–496. https://doi.org/10.1361/105996301770349268

Sampath S, Jiang XY, Matejicek J, Prchlik L, Kulkarni A, Vaidya A (2004) Role of thermal spray processing method on the microstructure, residual stress and properties of coatings: an integrated study for Ni–5 wt.%Al bond coats. Mater Sci Eng A 364:216–231. https://doi.org/10.1016/j.msea.2003.08.023

Schleef S, Jaggi M, Löwe H, Schneebeli M (2014) An improved machine to produce nature-identical snow in the laboratory. J Glaciol 60:94–102. https://doi.org/10.3189/2014JoG13J118

Schmidt T, Gärtner F, Assadi H, Kreye H (2006) Development of a generalized parameter window for cold spray deposition. Acta Mater 54:729–742. https://doi.org/10.1016/j.actamat.2005.10.005

Stoltenhoff T, Kreye H, Richter HJ (2002) An analysis of the cold spray process and its coatings. J Therm Spray Technol 11:542–550. https://doi.org/10.1361/105996302770348682

Sudharshan Phani P, Srinivasa Rao D, Joshi SV, Sundararajan G (2007) Effect of process parameters and heat treatments on properties of cold sprayed copper coatings. J Therm Spray Technol 16:425–434. https://doi.org/10.1007/s11666-007-9048-1

Sundararajan G, Sudharshan Phani P, Jyothirmayi A, Gundakaram RC (2009) The influence of heat treatment on the microstructural, mechanical and corrosion behaviour of cold sprayed SS 316L coatings. J Mater Sci 44:2320–2326. https://doi.org/10.1007/s10853-008-3200-2

Tapphorn RM, Gabel H (2007) System and process for solid-state deposition and consolidation of high velocity powder particles using thermal plastic deformation. US Patent 6915964 B2, 12 Jul 2005

Van Steenkiste T, Smith J (2004) Evaluation of coatings produced via kinetic and cold spray processes. J Therm Spray Technol 13:274–282. https://doi.org/10.1361/10599630419427

Van Steenkiste TH, Smith JR, Teets RE (2002) Aluminum coatings via kinetic spray with relatively large powder particles. Surf Coat Technol 154:237–252. https://doi.org/10.1016/S0257-8972(02)00018-X

Vlcek J, Gimeno L, Huber H, Lugscheider E (2005) A systematic approach to material eligibility for the cold-spray process. J Therm Spray Technol 14:125–133. https://doi.org/10.1361/10599630522738

Wang Q, Spencer K, Birbilis N, Zhang M-X (2010) The influence of ceramic particles on bond strength of cold spray composite coatings on AZ91 alloy substrate. Surf Coat Technol 205:50–56. https://doi.org/10.1016/j.surfcoat.2010.06.008

Wong W, Irissou E, Ryabinin AN, Legoux J-G, Yue S (2011) Influence of helium and nitrogen gases on the properties of cold gas dynamic sprayed pure titanium coatings. J Therm Spray Technol 20:213–226. https://doi.org/10.1007/s11666-010-9568-y

Yandouzi M, Sansoucy E, Ajdelsztajn L, Jodoin B (2007) WC-based cermet coatings produced by cold gas dynamic and pulsed gas dynamic spraying processes. Surf Coat Technol 202:382–390. https://doi.org/10.1016/j.surfcoat.2007.05.095

Yin S, Wang X-F, Li W-Y, Xu B-P (2010) Numerical study on the effect of substrate angle on particle impact velocity and normal velocity component in cold gas dynamic spraying based on CFD. J Therm Spray Technol 19:1155–1162. https://doi.org/10.1007/s11666-010-9510-3

Yin S, Meyer M, Li W, Liao H, Lupoi R (2016) Gas flow, particle acceleration, and heat transfer in cold spray: a review. J Therm Spray Technol 25:874–896. https://doi.org/10.1007/s11666-016-0406-8

Zahiri SH, Antonio CI, Jahedi M (2009) Elimination of porosity in directly fabricated titanium via cold gas dynamic spraying. J Mater Process Technol 209:922–929. https://doi.org/10.1016/j.jmatprotec.2008.03.005

Zou Y, Qin Q, Irissou E, Legoux J-G, Yue S, Szpunar JA (2009) Dynamic recrystallization in the particle/particle interfacial region of cold-sprayed nickel coating: electron backscatter diffraction characterization. Scr Mater 61:899–902. https://doi.org/10.1016/j.scriptamat.2009.07.020

Chapter 2
Cold Spray Applications

Victor K. Champagne Jr, Victor K. Champagne III, and Christian Widener

2.1 Introduction

Cold spray has revolutionized field repair of components and has had a profound effect on reducing sustainment costs in the aerospace industry, and similar savings can also be realized in several other important industry sectors including the petrochemical and nuclear power industries. According to a GAO report, the Department of Defense (DOD) spends between $10 and 20 billion annually on corrosion prevention and mitigation, and CS has been used to improve corrosion resistance and reduce the amount of maintenance required by military and contract personnel for the US Department of Defense (DOD) and for industry. A recent study commissioned by the National Association of Corrosion Engineers (NACE) suggests that the national corrosion bill has an annual value exceeding $270 billion. The aerospace industry has experienced significant corrosion and wear problems with certain aerospace materials, especially magnesium alloys that are used to fabricate aircraft components. The most severe of these are associated with large and expensive transmission and gearbox housings for rotorcraft, which have to be removed prematurely from service because of corrosion and/or wear. Additionally, since these parts are produced from castings, there is a need to repair defects associated with the sand casting process, during production, such as open porosity and

V.K. Champagne Jr (✉)
US Army Research Laboratory, ATTN: RDRL-WMM-D,
BLDG 4600, Amherst, MA 01003, USA
e-mail: Victor.k.champagne.civ@mail.mil

V.K. Champagne III (✉)
University of Massachusetts, 48 Noble Street, Dudley, MA 01571, USA
e-mail: vchampagne@umass.edu

C. Widener
South Dakota School of Mines and Technology,
501 E St Joseph Street, Rapid City, SD 57701, USA
e-mail: Christian.Widener@sdsmt.edu

P. Cavaliere (ed.), *Cold-Spray Coatings*,
https://doi.org/10.1007/978-3-319-67183-3_2

shrinkage that would otherwise render the parts unusable. Many of the parts cannot be reclaimed because there is no existing technology that can be used for dimensional restoration. This application represents a major aerospace cold spray application that will serve as an exemplary example of cold spray transition and implementation.

2.2 Aerospace Applications

2.2.1 Cold Spray Implementation

The aerospace industry is conservative in regard to adopting new technologies and rightfully so. If a new technology has not been adequately tested and evaluated for a specific application, the consequences could be catastrophic, resulting in the loss of human lives and expensive aircraft. Traditionally, this process takes upward of 20 years because of the vast amount of testing and verification required. A significant investment must be made and prescribed qualification protocol adhered to with a concerted effort from different support groups, including research, engineering, manufacturing, quality control, inspection, logistics, and acquisition. The process to qualify a cold spray repair involves extensive testing and evaluation of test coupons, as well as subscale or full-scale components and/or assemblies, some of which require flight testing for flight safety critical components. Ultimately, the process progresses to feasibility assessment and finally demonstration and validation, before it can be applied to production and/or field use.

2.2.2 Consideration of Cold Spray for Magnesium Repair

The deposition of aluminum and aluminum alloys, deposited by cold spray, is now becoming an accepted practice to provide dimensional restoration and a degree of corrosion protection to magnesium components. It is known that the addition of aluminum to magnesium promotes the formation of better passive films than unalloyed magnesium. Therefore, it is not surprising that the application of cold sprayed aluminum to magnesium and magnesium alloys constitutes a method to inhibit corrosion in aqueous media. The protective capability of pure aluminum cold sprayed on magnesium has been demonstrated by others (Zheng et al. 2006; McCune and Ricketts 2004; Gärtner et al. 2006; Balani et al. 2005). In all cases, the corrosion potentials of cold sprayed magnesium coupons approached those of commercially pure aluminum. Such polarization behaviors are promising since there is no galvanic protection strategy that is reasonable for magnesium given magnesium's strong thermodynamic potential for oxidation.

In galvanic corrosion, only small areas surrounding the dissimilar interface require protection, for which cold spray represents an innovative alternative to the use of washers and insulating bushings.

2.2.3 Replacement and Sustainment Costs

The US DoD reportedly spends millions of dollars to mitigate magnesium corrosion in their various aircraft fleets (Champagne 2007). Many expensive magnesium components are decommissioned because the lack of an appropriate repair technique to provide dimensional restoration after corrosion has been removed (Champagne 2007). The Army and Navy helicopter fleet is comprised of thousands of aircraft, each having numerous components manufactured from magnesium alloys, generally consisting of transmission and gearbox housings. In addition to helicopters, magnesium alloy gearboxes are used extensively in fixed-wing aircraft for the military and are currently designed into the Joint Strike Fighter (JSF). Add to this the thousands of commercial aircraft around the world, and it is easy to visualize the magnitude of the problem and that thousands of magnesium components currently in service are adversely affected. The cost of each component can be several hundred thousand dollars. A Sikorsky Aircraft Corporation 2009 trade study showed that the annual cost for the UH-60 main gearbox corrosion of about 600 helicopters is over US$17 million. In 2001, the Fleet Readiness Center, NC, conducted an extensive review of the cost of corrosion on the main transmission of one type of helicopter and reported that from 1991 to 2000, the total estimated cost for both unscheduled maintenance and module replacement was about $41 million. Most of the corrosion occurs at attachment points where a dissimilar metal is in contact with the coated magnesium component. This includes flanges, mounting pads, tie rods, lugs, and mounting bolts.

2.2.4 Cold Spray Repair for Magnesium Aerospace Parts

Many of the corrosion problems associated with magnesium helicopter components occur at the contact points between inserts and mating parts, where ferrous metals are located, creating galvanic couples (Vlcek et al. 2005). In addition, magnesium (Mg) alloys are also very susceptible to surface damage due to impact, which occurs frequently during manufacture and/or overhaul and repair. Scratches from improper handling or tool marks can result in preferential corrosion sites. The Department of Defense and the aerospace industry have expended much effort over the last two decades to develop specific surface treatments to prevent corrosion, to increase surface hardness, and to combat impact damage for magnesium alloys in order to prolong equipment service life; however, the means to provide dimensional restoration

to large areas on components where deep corrosion has occurred remains a challenge (Champagne et al. 2008).

For original equipment manufacturers (OEMs), the standard practice is to hard anodize the surface using a process designated Dow 17, followed by an application of a phenolic resin (one version is designated "Rockhard"). For non-mating surfaces, multiple coats of chromate epoxy polyamide primer followed by multiple coats of epoxy paint are applied. For mating surfaces, no primer or paint is used, but other types of sealant compounds are applied. In repair/overhaul facilities, the standard practice is to use a chromate conversion coating, MIL-M-3171, followed by the Rockhard and the chromate primer and paint for non-mating surfaces and a sealant compound for mating surfaces. It has been demonstrated that cold spray can be incorporated as a repair technique for dimensional restoration of worn and/or corroded parts in combination with the standard surface treatments and can be used without these surface treatments.

Figure 2.1 is a photograph of the UH-60 helicopter showing the areas most susceptible to corrosion on various transmission parts. Because of the localized nature of the corrosion, surface treatments intended to mitigate the problem would only have to be applied in these specific areas. A combination of galvanic and crevice corrosion is the primary corrosion mechanism for Mg alloy gearboxes. Water and salt spray tend to accumulate in the recessed holes around the bolts, and galvanic corrosion occurs between the cadmium (Cd)-plated bolt head and the surrounding Mg alloy, as well as between the shank of the bolt and the ID of the hole. In addition, gearboxes usually have Cd-plated steel studs and bushings press fitted into

Fig. 2.1 Corrosion-prone areas on UH-60 Black Hawk transmission components

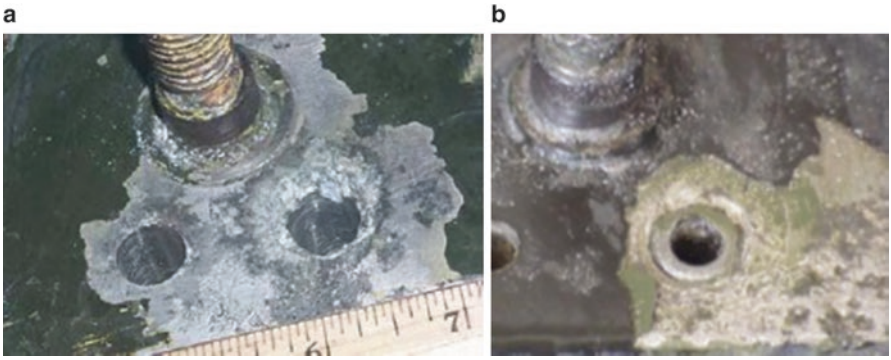

Fig. 2.2 Corrosion around a stud and hole (**a**) and around an insert (**b**) on a helicopter magnesium gearbox housing (Courtesy Robert Kestler, FRC-E)

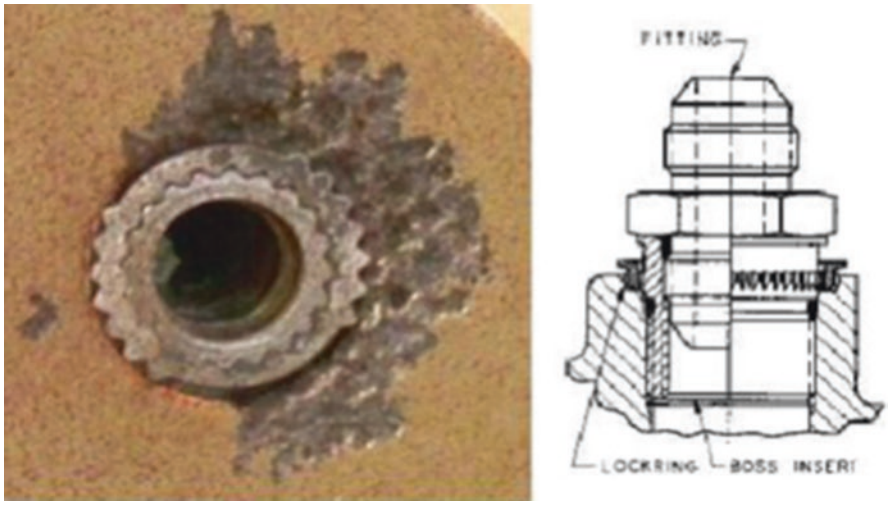

Fig. 2.3 Rosan insert. *Left* – shows corrosion around insert on a helicopter magnesium gearbox housing. *Right* – cross section of insert with fitting (Courtesy Robert Kestler, FRC-E)

them, and galvanic corrosion occurs around these areas (Fig. 2.2). In particular, Rosan inserts are frequently used to hold bushings, fittings, and threaded fasteners into housings (Fig. 2.3). These fittings are designed to be press fitted into the housing, where their teeth bite into the Mg alloy and create a high degree of plastic deformation. Any coating or surface treatment that is applied to the Mg at repair facilities must be able to withstand the insertion. When corrosion becomes excessive, material is removed and an Al shim is glued in place of the missing Mg alloy. These shims can be as thick as 0.100 inches and cannot carry load, thereby weakening the structure. Because of the localized nature of the corrosion, surface treatments intended to mitigate the problem would only have to be applied in these specific

areas. In summary, the susceptibility of magnesium components to corrosion and damage, even with the most current surface protection schemes, is still very significant as shown by the very high repair/overhaul and maintenance costs.

2.2.5 Selection Methodology for Cold Spray Aluminum Alloys

It had been determined through extensive testing and evaluation by several major US aerospace manufacturers and the DoD that the deposition of aluminum and certain aluminum alloys followed by the phenolic resin and a sealant would have the highest probability of success in reducing corrosion and impact damage for magnesium aerospace components. The technical challenge was to identify a method to deposit the aluminum alloys onto the magnesium and meet all service requirements for bond strength and corrosion resistance without sacrificing the structural integrity of the substrate. The processing of production parts as well as field repair capability was an important attribute in the selection of a viable process. Initially, a review of the current state of the art was conducted and critiqued before cold spray was down selected as the technology of choice for this application.

2.2.6 Technical Approach

The critical tasks associated with the qualification of the cold spray coatings on magnesium components were established in a document known as the Materials Joint Test Protocol (JTP) developed by representatives of the DOD, original equipment manufacturers (OEMs), industry, and academia. The quantitative and qualitative performance objectives required to qualify cold spray to repair magnesium aerospace components are provided in Table 2.1, which also contains a summary of the test results for a "nonstructural" repair for 6061 Al cold spray deposited onto ZE41A-T5 Mg. The final performance objectives were set by the Naval Air Command (NAVAIR) and ARL with input from industry, including the Sikorsky Aircraft Corporation, as part of an Environmental Security Technology Certification Program (ESTCP), No. WP-0620, titled "Supersonic Particle Deposition for Repair of Magnesium Aircraft Components," which has been established as an aerospace industry standard. The program extended from 2005 to 2011 and culminated with the qualification of the cold spray process for use on the UH-60 Black Hawk, in collaboration with the Sikorsky Aircraft Corporation, and the establishment of the first dedicated cold spray repair facility at the Navy Fleet Readiness Center (FRC East), Cherry Point, North Carolina. This program served as an international benchmark for the adaptation of cold spray for the aerospace industry. The cold spray process is now viewed as the best possible method for depositing the aluminum alloys to provide dimensional restoration to magnesium components and significantly improving performance and reducing life-cycle costs. The quantitative performance objectives are

Table 2.1 Performance objectives and test results

Performance objective	Data requirements	Success criteria	Results
Quantitative performance objectives			
Deposition rate	Coating thickness measurement to an accuracy of ±0.0005 in.	Ability to deposit coatings at a rate of at least 0.005″ per hour with coating quality such that they pass the acceptance criteria specified in the JTP	Passed deposition rates were magnitudes higher
Coating thickness uniformity	Coating thickness measurement to an accuracy of ±0.0005 in.	*Cold spray* coating thickness shall be uniform within ±20% for deposition onto various surfaces that simulate Mg alloy components	Passed uniform, no waviness
Microstructure	Examined with optical microscopy	A uniform microstructure, especially for alloy coatings, must be achieved	Passed uniform
Hardness	American Society for Testing and Materials (ASTM) E384-10e2	Vickers microhardness of as-deposited coatings shall be no less than 50 VHN	Passed 105 VHN
Fatigue	R. R. Moore high-speed rotating-beam machine	No debit as compared to baseline non-coated specimens as specified in the JTP	Passed No debit, credit for 7075Al substrates
Stress/strain testing Ductility	Tensile testing ASTM E8	Monotonic stress/strain testing shall be conducted in a standard tensile tester. This will evaluate strain tolerance	Passed 50ksi, UTS; 42ksi,YS; 7%, EL
Residual stress	X-ray diffraction (XRD)	Applied coating must be in either a compressive or neutral stress state	Passed 13ksi compression
Adhesion in tension	ASTM C633	Coating must meet or exceed 8.0 ksi	Passed >10,000 psi
Shear adhesion	MIL-SPEC MIL-J-24445A	Coating must meet or exceed 8.0 ksi	Passed Up to 35,000 psi
Rosan insert	Sikorsky test	*Rosan* insert must be capable of being inserted into a hole containing a cold spray coating without delamination, cracking, or spalling	Passed coating remained intact
Impact test	ASTM D5420	Coating is examined for after a weight is dropped at prescribed height	Passed no spalling

(continued)

Table 2.1 (continued)

Performance objective	Data requirements	Success criteria	Results
Fretting fatigue	Conducted by the UTRC Epsilon Technology Corp. System	No debit as compared to baseline non-coated specimens as specified in the JTP	Passed coating system dependent
Salt spray corrosion	ASTM B117	Minimum of 336-h exposure without penetration of salt spray through coating to the substrate as described in the JTP	Passed >7000 h
Cyclic corrosion	General Motors (GM) 9540 specification	Minimum of 500-h exposure without penetration of salt spray through coating to the substrate as described in the JTP	Passed >500 h
Qualitative performance objectives			
Appearance	Visual inspection	Coatings are continuous, smooth, adherent, uniform in appearance, free from blisters, pits, nodules, and other apparent defects	Passed Uniform coating, no defects
Porosity	Examined with optical microscopy	Porosity of *cold spray* coatings should be less than 2%	Passed <1%
Machinability	Visual examination	Coating deposited on a rod is machined on a lathe and chip formation is characterized	Passed Chip comparable to wrought material
Beach corrosion	Conducted by Navy at Cape Canaveral, FL	No observable penetration or pitting through the coating and into the magnesium	Passed No pitting
Galvanic corrosion	ASTM G71-81	No defined criteria. Used for comparison to high-velocity oxygen fuel (HVOF) Al-12 Si baseline specimen	Passed
Crevice corrosion	ASTM G78	No observable corrosion product	Passed

based on the Joint Test Protocol (JTP). The JTP was designed to define the upper and lower technical capabilities of the cold spray repair process. Results from the program are contained in reference Champagne et al. (2008), and it is not the intent to duplicate data already presented but to point out highlights associated with the discussion material as it pertains to this chapter. Table 2.1 summarizes the test results. It is not possible within the context of this chapter to explain and discuss all of the test methods and accompanying results. However, it is essential in order to appreciate the tremendous potential that the cold spray technique has for the repair of aerospace parts that some of the more important tests are presented in some level of detail.

2.2.7 Triple Lug Adhesion Test

The triple lug shear test method was used as an additional means to better quantify coating adhesion. Triple lug procedure methodology is prescribed in military specification, MIL-J-24445A. A mechanical drawing of the test coupons is provided as Fig. 2.4. A coating with a thickness of greater than 0.125 inches is deposited onto the specimen. Three lugs are machined from the coating. The lugs are sheared from the test specimen using a compressive load frame setup as shown in Fig. 2.5. Only one lug is sheared from the specimen at a time. Failure stress is reported based on the load at failure and the surface area of the lug. Control specimens milled from single pieces of cast magnesium were included in the matrix to establish a baseline. All of the 6061 He coatings showed very high adhesion on the magnesium alloys. The average adhesive strength of the 6061 He coating, deposited onto ZE41A-T5, actually exceeded the average strength of the baseline ZE41A-T5 samples. Correspondingly, most of the twelve 6061 lugs on the ZE41A-T5 broke off by fracturing material well beneath the coating/substrate interface at strength levels as high as 35,000 psi. This serves as substantial proof that structural repair is possible with the 6061 He CS coating since the weakest point is no longer at the coating interface but within the Mg substrate.

2.2.8 Tensile Testing of Bulk CS Material

The 6061 helium tensile specimens were machined from a sprayed block of CS 6061 as described in Table 2.2. The CS was deposited using the same parameters as for all other 6061 samples in this study. The substrate was a 4 x 4-inch piece of

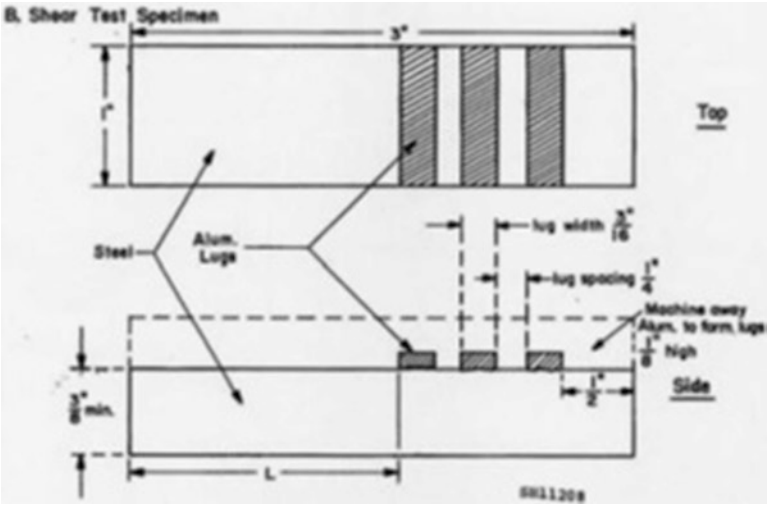

Fig. 2.4 Schematic of the triple lug test specimen

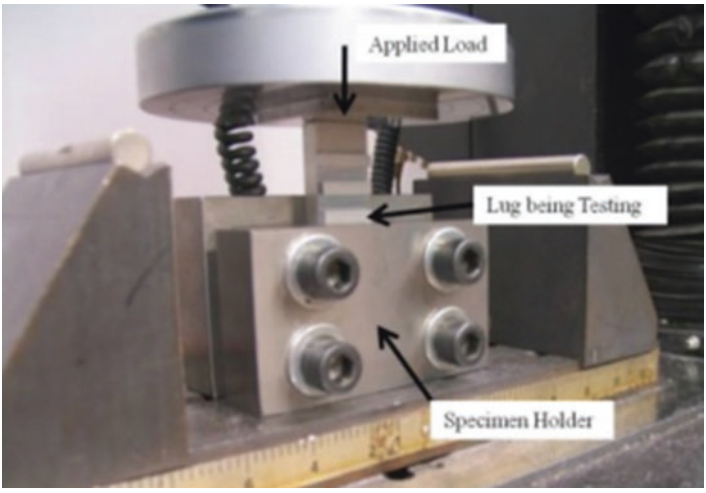

Fig. 2.5 Triple lug test fixture and apparatus

Table 2.2 6061 helium tensile test specimen dimensions (inches)

Block width	4
Block length	4
Block thickness	0.6
Number of tensile specimens	6
Tensile specimen width	0.25
Tensile specimen length	0.125

3/8-inch-thick-wrought 6061-T6. After deposition, the substrate was milled away from the deposit. This resulted in a single piece of 6061 cold spray with an approximate thickness of 0.6 inches. Six tensile bars were then machined to the dimensions specified in Table 2.2. In addition to ultimate tensile strength (UTS), the elastic modulus, yield strength (YS), and percent elongation at failure were characterized for the 6061 helium depositions. This additional mechanical data was deemed important to determine the load-bearing capability of the CS coatings. The purpose of tensile testing is to determine the tensile strength, yield, modulus, and other tensile material properties of the substrate/coating combinations, as well as the contribution of the coating to the strength of the substrate. Tensile test results were used to guide fatigue testing. The test was carried out in accordance with American Society for Testing and Materials (ASTM) E8, using a strain rate of 0.05″/min at room temperature and approximately 50% relative humidity. The results are shown in Table 2.3.

The results listed in Table 2.3 clearly indicate the potential for cold spray 6061 Al as a "structural" material that can be considered for use on other substrate materials than ZE41A-T5 Mg. The ultimate tensile strength (UTS) of the as-cold sprayed 6061 AL was as high as 50ksi with a corresponding yield strength (YS) of 42ksi and % elongation (EL) of 3%. A post-processing procedure of feedstock 6061 Al powder has been developed and can yield CS material with minimum UTS of 45ksi, YS of 38ksi, and as much as 7% EL. Table 2.4 lists the mechanical properties of other common aerospace

Table 2.3 Tensile test results for CS 6061 Al

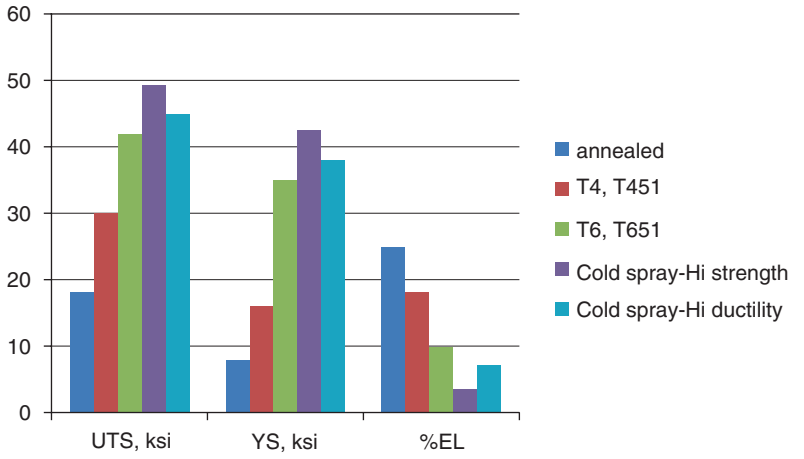

Table 2.4 Mechanical properties of cold spray aluminum aerospace alloys

Alloy	Parameters		Specimen ID	HRB	%IACS	UTS MPa (ksi)	%El
	Press.	Temp					
6061	20 bar	400°C	CS-12-275	31.0	44.03	239 (34.6)	7
6061	25 bar	450°C	CS-13-096	40.4	41.5	310 (45.0)	5
2024	25 bar	400°C	CS-14-150	64.6	30.18	392 (56.8)	5.8
2024	30 bar	500°C	CS-14-152	57.3	31.96	346 (50.2)	10.9
7075	25 bar	400°C	CS-14-128	65.2	31.08	387 (56.2)	6.9
7075	25 bar	400°C	CS-14-120	50.1	35.92	326 (47.3)	11.8
7075	30 bar	500°C	CS-14-125	62.7	31.11	394 (57.2)	11.5
5056	20 bar	500°C	CS-14-101	63	26.25	406 (58.9)	15.4
5056	30 bar	500°C	CS-14-102	62	26.64	400 (58.0)	22.7

aluminum alloys varying process parameters. The development of high-strength CS aluminum alloys with high ductility has been a major accomplishment for the implementation of cold spray for "structural" material repair and for additive manufacturing.

2.2.9 Microstructural Analysis

Optical and electron microscopy were used to characterize the coating/substrate interface and to evaluate the integrity of the deposit. The density, bond line integrity, microstructure, and inherent material features of the coating were characterized. Acceptable nonstructural repair processing windows for the 6061 helium coating were developed as contained in Table 2.4. One of the relationships studied with this coating was between pressure, adhesion, and microstructure. Results for bond bars deposited at three different pressures were investigated. The pressures were increased in 5 bar increments starting from "a" to "b" to "c." The adhesive strength improves with increasing pressure. The highest pressure samples exhibited only glue failure. Additionally, the highest pressure samples exhibited glue failure at deposition rates exceeding 9 mils per pass. Figure 2.6 shows optical micrographs, of

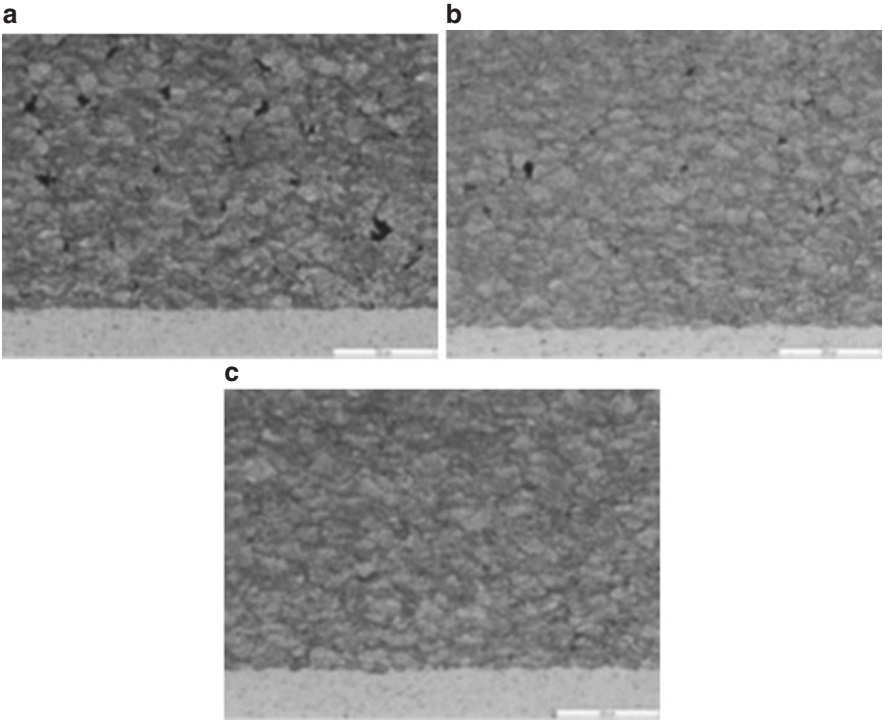

Fig. 2.6 Etched optical micrographs of 6061 CS coatings sprayed with a He carrier gas at consecutively higher pressures. Note the increase in density at the highest pressure (far right)

three different 6061 He coatings. The samples were etched with Kroll's reagent to reveal splat boundaries. Porosity was observed to decrease with increasing pressure, while the temperature was held constant. These results indicate that a direct relationship between particle velocity and porosity exists in this processing regime. As with the CP-Al N2 and the CP-Al He coatings, the preliminary unscribed B117 salt spray coatings deposited by ARL exceeded 7000 h of total exposure with no pinhole defects. Testing was stopped prior to observing any failures. This serves to substantiate that the cold spray coating is dense with no interconnected porosity that extends to the surface. In fact, the porosity levels were <0.2%. The microstructure of the as-cold sprayed 6061 AL was uniform and consisted primarily of the aluminum matrix, the α-Al(CrMnFe)Si phase at the particle boundaries, and the Mg_2Si phase adjacent to the α-phase (Fig. 2.7) (Gavras et al. n.d.). These observations are in agreement with those by Belsito et al. (Belsito et al. n.d.).

2.2.10 Specification Development

ARL recognized the need to standardize the cold spray process to facilitate widespread adaptation of the technology and to mitigate the potential misuse of the newly developed repair process for magnesium. The specific concern was the practice of using low-pressure/low-temperature portable cold spray systems to repair structural areas on magnesium components. Therefore, two actions were taken; one was to introduce a general cold spray process specification that could be utilized by the DOD and private industry, throughout the nation, as well as internationally, and the

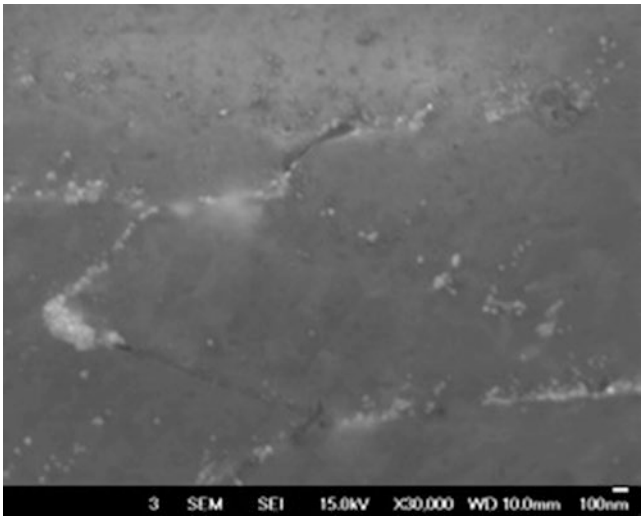

Fig. 2.7 SEM of cold sprayed 6061 Al consisting of α-Al(CrMnFe)Si, 0.25%, and Mg_2Si, 1.68% (Gavras et al. n.d.)

second, to provide the means to educate the user community about cold spray. In 2008, the Defense Standardization Program (DSP) Office granted approval of the first military specification developed by ARL, MIL-STD-3021, which is a manufacturing process standard, entitled "Materials Deposition, Cold Spray." The procedures covered by this standard are intended to ensure that cold spray coating operations, either manual or automated, meet prescribed requirements. ARL also introduced another specification on 12 May 2014 that covers requirements intended for use in the procurement of powders that will be used to produce coatings utilizing the cold spray material deposition process, entitled "Material Powders Utilized for Cold Spray," MIL-DTL-32495. These documents are necessary to standardize the feedstock and the cold spray process in order to facilitate implementation across major industries.

2.2.11 Transition of Cold Spray for Aerospace

Various research and development programs concluded that the material characteristics of cold spray aluminum alloys, especially 6061-Al, would be the best candidate for meeting the prescribed performance requirements while enabling the dimensional restoration for magnesium. However, recent developments have resulted in the introduction of other aluminum alloys suitable for cold spray including alloy 2024, 7075, 5056, and 5083. The cold spray process was chosen as the best possible method for depositing the aluminum coatings and would be viewed as part of an overall strategy of replacement of the chromate processes such as Dow 17 and MIL-M-3171 currently in use today, eliminating environmental and worker safety issues, while significantly improving performance and reducing life-cycle costs. The cold spray process has now been incorporated into production and has been modified for field repair, across the USA and abroad, and has emerged as a feasible economic alternative over competing technologies.

2.2.12 Other Cold Spray Applications

The cold spray process has matured from an emerging technology to a viable alternative to thermal spray for selected applications (Papyrin 2001). Research and development efforts of Champagne have shown cold spray to be a promising cost-effective and environmentally acceptable technology to impart surface protection and restore dimensional tolerances to magnesium, aluminum, and titanium alloy components on helicopters and fixed-wing aircraft (Champagne 2007; Champagne et al. 2008). Corrosion of magnesium helicopter gearboxes is a major issue both for the DOD and the commercial aircraft industry. The use of cold spray coatings may be a means to reduce subsequent corrosion damage in gearboxes, especially if it can be combined with improved protection systems, such as Tagnite coatings. Cold spray repairs offer improved performance and permit the reclamation of properties as well as dimensional restoration, and since replacements would be less frequent,

it would also reduce logistics cost, since fewer gearboxes would be required in the field and fewer would have to be shipped back and forth between depots and operating bases. There is significant potential for cost reduction by decreasing the number of condemnations and improving operational readiness and safety.

M. Barbosa et al. have presented research showing that cold spray could be used to produce a dense pure titanium coating onto aluminum 7075 substrates, with thickness greater than 300 μm with no deleterious microstructural changes (Barbosa et al. n.d.). It was concluded that the cold spray process could be optimized to produce superior coatings to conventional thermal spray techniques, economically and at higher deposition rates, making it ideal for aerospace applications.

Stoltenhoff and Zimmermann showed the potential of cold spray as a repair technology using three different precipitation hardened aluminum alloys, AA2224, AA6061, and AA7075, for use on CH-53 helicopter landing gear shock struts and C-160 aircraft propeller blades (Stoltenhoff and Zimmermann n.d.). One of these aerospace applications had already been transferred to production and the other was in the approval process. The fatigue properties of the coating/substrate system were identified as key evaluation criteria for acceptance, and as previously stated, the cold spray coatings produced at optimized conditions do not adversely affect the component properties (Stoltenhoff and Zimmermann n.d.). In fact, an improvement of the fatigue resistance was observed for several coated samples, most likely the result of the beneficial compressive stresses induced as a result of the cold spray process in the coating which helps to avoid crack formation and propagation. The authors note that when service conditions are taken into account, including single events that cause superficial damages like impacts of foreign bodies or defects from tool marks during overhaul and maintenance (Stoltenhoff and Zimmermann n.d.).

Dr. Kumar from the International Advanced Research Centre for Powder Metallurgy and New Materials (ARCI), Hyderabad, India, has reported using the cold spray process on a variety of applications to repair gas turbine components including 6061 aluminum fan casings susceptible to damage where high thermal processes, such as welding, could not be tolerated. Another application was the titanium compressor case isogrid fabrication, where titanium cold spray was used to build up areas to minimize starting stock material and machining waste. This same approach was also successful on other parts using other materials including copper, aluminum, and zinc as well as for other parts including diffusers, combustors, turbines, and exhaust nozzles. Kumar also reported success in the repair of aluminum and magnesium aerospace components such as the S-70 Seahawk and for C-160 Transall propeller blade repair (Kumar and Chavan n.d.).

2.2.13 B-1 FEB Panel Repair

A common problem on military aircraft is wear due to chafing around fastener holes on skin panels. This chafing results in skin panels that exceed fit tolerances at the fastener locations. The South Dakota School of Mines and Technology (SDSM&T)

Repair, Refurbish, and Return to Service (R3S) Applied Research Center and the Army Research Lab (ARL) Cold Spray Center in cooperation with H. F. Webster Engineering Services developed a repair process for a B-1 Bomber Left Upper Aft forward equipment bay (FEB) panel that experienced chafing damage in service around the fastener holes, resulting in an out-of-tolerance fit for the panel. The FEB panel is secured to the airframe with 100° tapered flat head Tridair fasteners (Fig. 2.8). The fasteners are designed to be installed flush with the panel for laminar airflow over the skin surface. In service, the chamfer wears causing the fastener holes to become elongated, rendering the panels unserviceable (Fig. 2.9). The panel is fabricated from 2024-T6 aluminum. The repair utilized an aluminum alloy powder compatible to the substrate material and was cold sprayed normal to the chamfered surface of the panel. Load transfer, fatigue, and tensile tests were accomplished,

Fig. 2.8 Forward equipment bay (FEB) panels on the B-1 Bomber repaired 2012

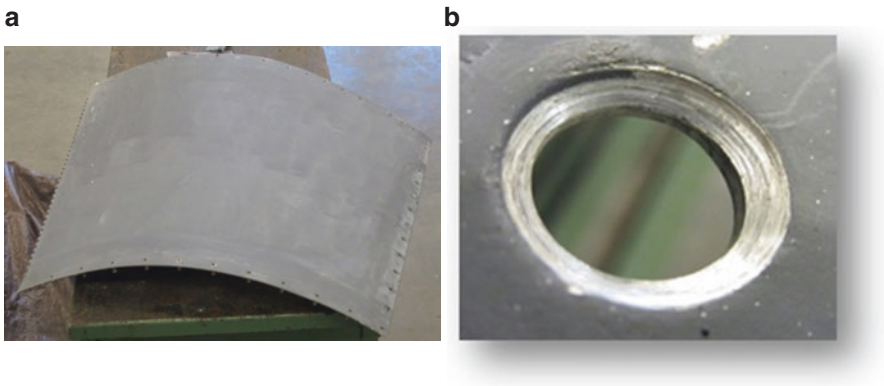

Fig. 2.9 A single FEB panel and close-up of wear around fastener holes

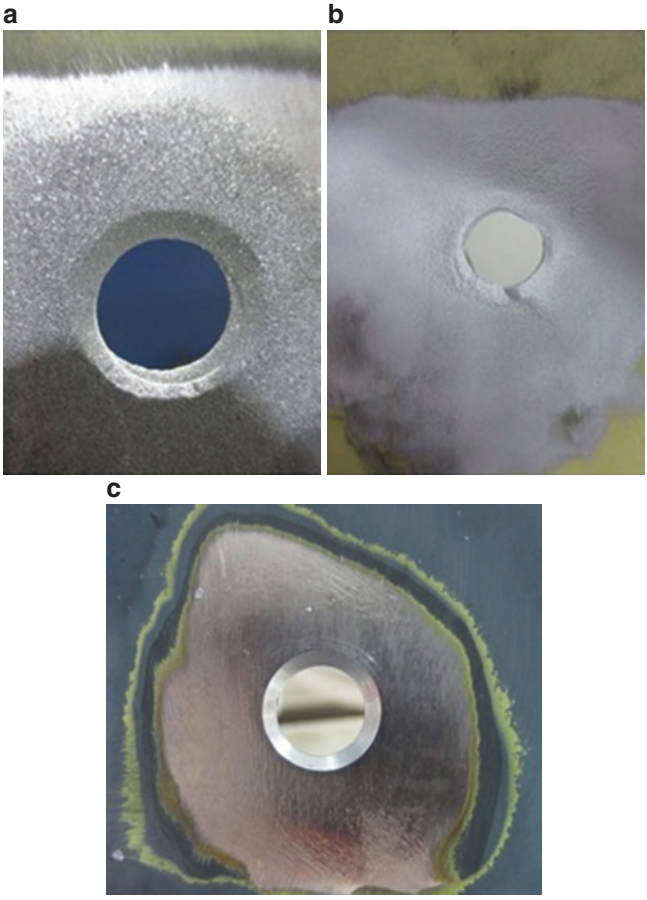

Fig. 2.10 (**a**) Fastener hole grit blasted prior to cold spray, (**b**) after cold spray repair, and (**c**) after final machining with all original dimensions restored

along with three-lug shear testing and metallography to characterize and qualify the repair. The results demonstrated the capability of cold spray to provide a permanent repair for this application, restoring the full capability of the panel (Fig. 2.10a–c). Cold spray technology has been proven to provide a low-cost solution to repair FEB panels and is nonstructural but offers a superior solution than polymer-based repairs. Temperature measurements taken on the surface of the aluminum FEB panel never exceeded 100 °C, thereby mitigating any concern about overaging the 2024 T-6 aluminum substrate.

The benefits of the FEB panel repair include the following: (1) minimal amounts of material are added and no parent material is removed, (2) the cold spray material is "locked in place" under compression, (3) the cold spray material can match the CTE (coefficient of thermal expansion) of the panel, (4) the repair can be accomplished multiple times without affecting the substrate (does not overheat or overage

the Al panel), and (5) the FEB panel can be quickly repaired and reinstalled on the same aircraft, minimizing down time.

Based on Mil-HDBK-5H guidelines (Section 2.2.13), calculated bearing load depends on straight section thickness (Fig. 2.11). Utilizing the data contained in Table 2.5 and the equations below, the measured panel thickness of 0.147 in. leads to a max load of 3369 lbs:

$$P = \text{Fbry} \times (t - h) \times d \quad h = \tan(40^{\circ}) \times (cd - d)$$

The mechanical test results revealed that the CS coupons prepared to simulate the fastener hole repair met or exceeded the required bearing loads for the parent material and fastener type for this application (Fig. 2.12). Even when tested to failure (greater than 1.5 × bearing yield), the cold spray material did not separate from the panel (Fig. 2.13). The test coupons were sprayed using a high-pressure cold spray system, and the coupons were tested at 40 in.-lbs torque and 10 load torque cycles 2600 lbs and 3400 lbs (two coupons were tested at each load).

The first panel was repaired and installed on a B-1B for flight testing in August 2012 and is still in service today. Further applications of this technology can be

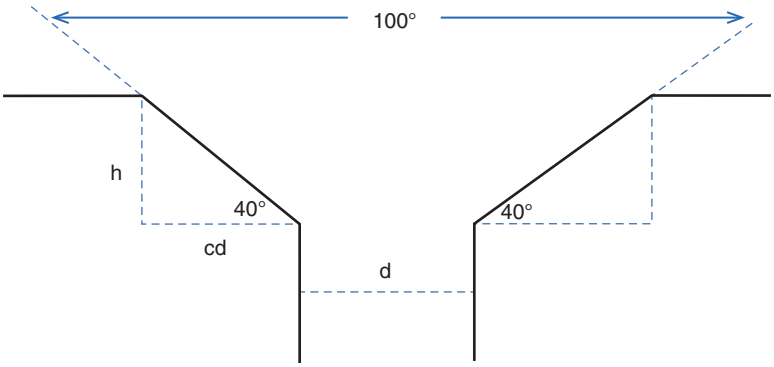

Fig. 2.11 Schematic of the countersink used to calculate the bearing load

Table 2.5 Data used to calculate bearing load of fastener

t=0.030-in. bearing surface

Edge Distance	e	1.25	in
Hole Diameter	D	0.375	in
e/D	3.333333		
Bearing Yield Stress	Fbry	95000	psi
Hole Diameter	d	0.375	in
Countersink Diameter	cd	0.635	in
Thickness	t	0.137	in
Countersink Depth	h	0.107	in
Load	P	995	lbs

t=0.073-in. bearing surface

Edge Distance	e	1.25	in
Hole Diameter	D	0.375	in
e/D	3.333333		
Bearing Yield Stress	Fbry	95000	psi
Hole Diameter	d	0.375	in
Thickness	t	0.125	in
Countersink Depth	h	0.052	in
Load	P	2585	lbs

t=0.095-in. bearing surface

Edge Distance	e	1.25	in
Hole Diameter	D	0.375	in
e/D	3.333333		
Bearing Yield Stress	Fbry	95000	psi
Hole Diameter	d	0.375	in
Thickness	t	0.147	in
Countersink Depth	h	0.052	in
Load	P	3369	lbs

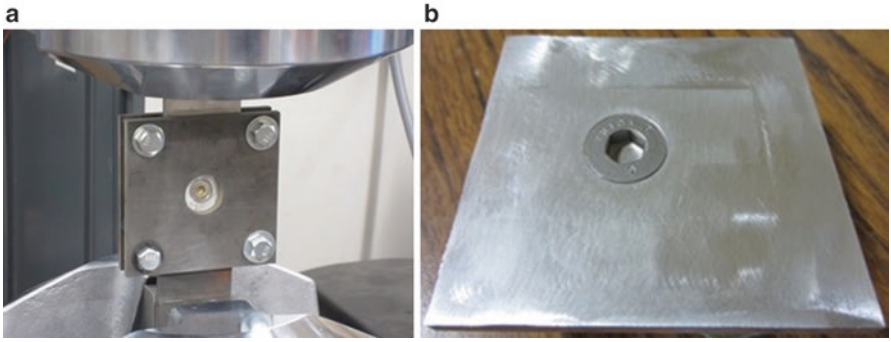

Fig. 2.12 Test coupon with a fastener installed into a hole repaired by cold spray and inserted into a test fixture designed to test the cold spray repair simulating an actual FEB panel

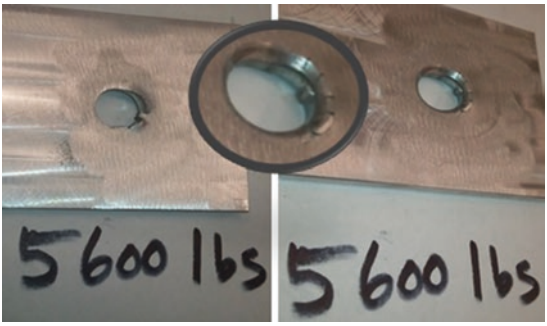

Fig. 2.13 Fasteners pulled to failure yet the CS material does not separate from the substrate

applied to all major design series (MDS) aircraft and are an example of infusing new technologies into current DOD maintenance processes to reduce sustainment cost while maintaining the viability of older weapon systems.

2.2.14 Hydraulic Line Repair

Chafing of titanium hydraulic tubing, Haynes AMS 4944 (Ti3Al2.5 V), as a result of vibration and abrasive action is a major maintenance problem on the B-1B aircraft in terms of maintenance man hours (Fig. 2.14). A technological solution that reduces the frequency of hydraulic tubing chafing would have broad applicability across the DOD and could be incorporated for use on similar commercial components. Cold spray preventative maintenance of hydraulic lines has been proven to be fairly simple and effective from both an economic and technical standpoint. A feasibility study was accomplished in 2009 which demonstrated the effectiveness of the cold spray process in preventing hydraulic tube chafing by the application of a CP-titanium coating providing a wear surface in areas known to experience chafing problems. This preventative measure can be performed during programmed depot maintenance (PDM) or

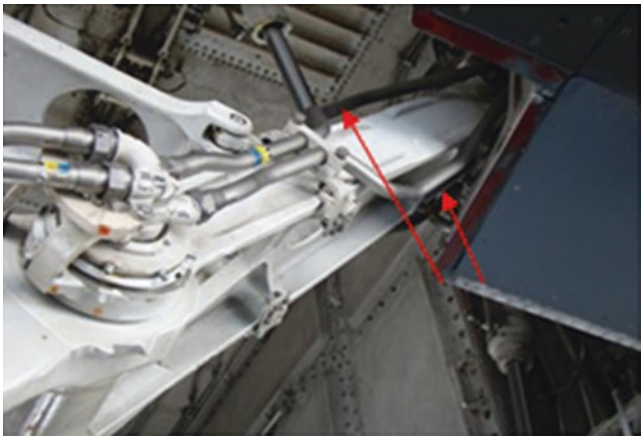

Fig. 2.14 Wheel well titanium hydraulic lines that chafe during flight

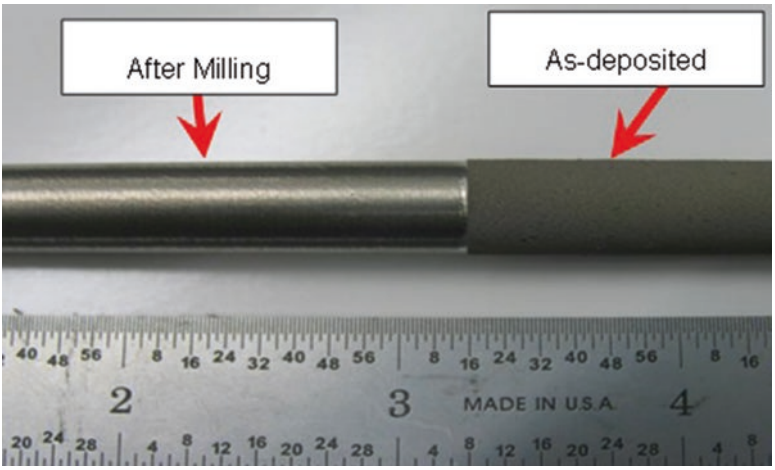

Fig. 2.15 As-sprayed CP-Ti (*right*) and after machining (*left*)

during the high-velocity maintenance (HVM) process to prevent or reduce occurrences of hydraulic tubing chafing in the field. A characterization study was accomplished which showed that a titanium (Ti) coating could be successfully applied to titanium tubing providing an additional "sacrificial" wear surface (Fig. 2.15). The study showed that the Ti coating had adequate deposition efficiency (~70%), bond strength (> 12ksi), density (~99%), and hardness (93HRB). Additionally, the cold spray deposit was subjected to burst testing >16,000 psi and complete optical and electron microscopy (Fig. 2.16) of the microstructure, bond line integrity, and porosity (<1%). An operational wear test was also accomplished to verify the results of the initial feasibility study. The test involved two B-1 aircraft. They had two previously identified hydraulic lines (per aircraft) that have a high incidence of chafing.

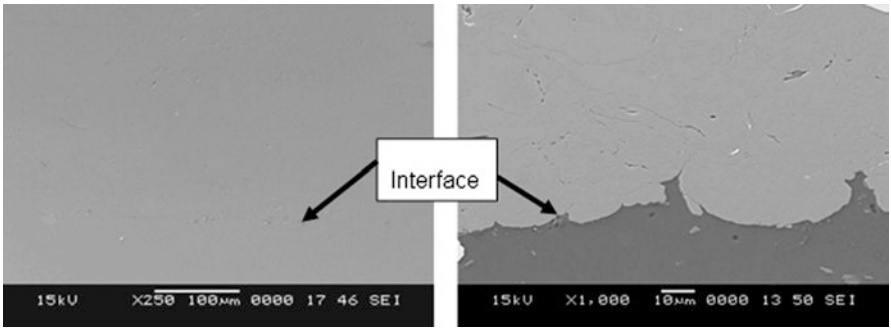

Fig. 2.16 Scanning electron microscopy of the interface between the cold spray CP-Ti coating and the Ti3Al2.5 V hydraulic line showing high density and mechanical mixing

The hydraulic lines were sprayed with CP-Ti to prevent the chafing of main landing gear wheel well (behind the follow-up door) and wing spoiler actuator.

Once the coated lines were installed, an operational wear test was conducted for approximately 5 months. The test involved performing weekly dimensional measurements of the cold spray coating to determine the effectiveness of the coating, as it related to chafing prevention. The coating was applied to a B-1 nose landing gear (NLG) accumulator hydraulic line, was installed, and has been flown for 5 years with no adverse effects and no observed chafing beyond limits and has several thousand flight hours to date.

Since the conclusion of the wear test, proposed logistical and maintenance processes to implement the new process were developed, including the research and development of different coating materials and application parameters based on the outcome of the wear test. The different coating materials will account for varying wear mechanisms on different hydraulic tubing applications. Finally, an indicator layer/mechanism would be developed so that maintenance personnel can identify when the sacrificial layer has been worn through.

2.2.15 AH-64 Apache Mast Support Repair

Corrosion and mechanical damage has rendered a number of AH-64 mast supports non-serviceable for continued use on the AH-64 Apache helicopter (Fig. 2.17). The US Army Research Laboratory developed a portable cold spray repair that has been shown to have superior performance in the qualification tests conducted, is inexpensive, can be incorporated into production, and has been modified for field repair, making it a feasible alternative over competing technologies. The goal of this effort was to repair both the corrosion and mechanical damage by blending and machining damaged areas and rebuilding lost material using cold spray with aluminum powder and finish blending and machining to the original dimensions (Fig. 2.18). The mast support is fabricated from aluminum alloy 7149, and therefore protective finishes such as

Fig. 2.17 AH-64, Apache helicopter mast support

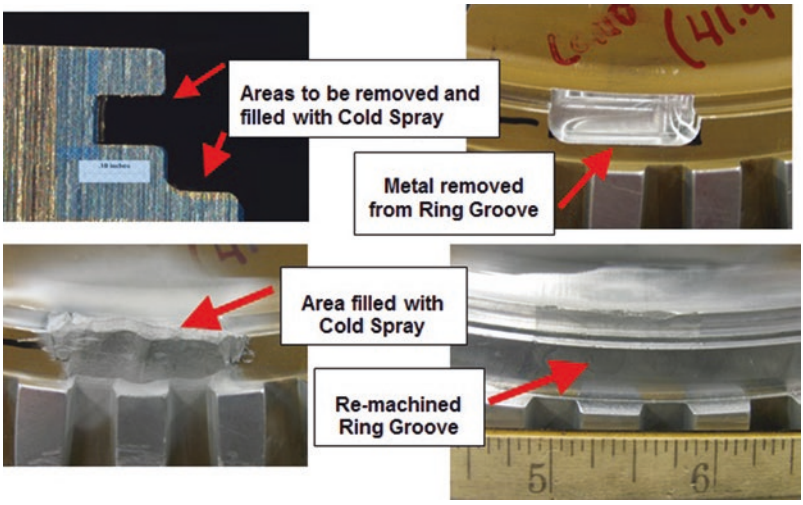

Fig. 2.18 Step-by-step process to repair the snap ring groove of the AH-64 by cold spray

a conversion coating, primer, and topcoat may be applied to the repaired areas after the cold spray coating. While it is possible to perform a remediation without rebuilding lost material, the number of times this type of repair could be performed would be limited. With use of cold spray to rebuild lost material, the component could be remediated as many times as necessary until its safe life has been reached.

2.2.16 Navy Valve Actuator Repair

In this application, cold spray is being used to repair corrosion damage to a part made from 6061 aluminum, which suffered from both exfoliation and pitting corrosion, as seen in Fig. 2.19. It is generally believed that exfoliation corrosion is

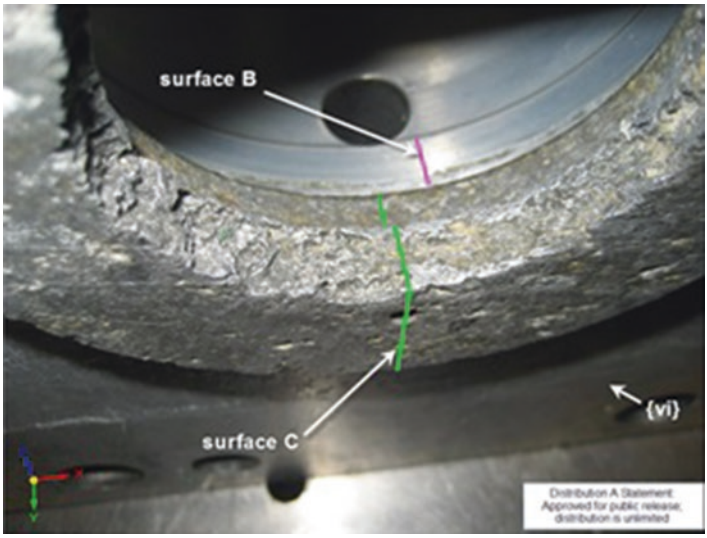

Fig. 2.19 Close-up photo of seawater corrosion damage on the outboard portion and sealing surfaces on the valve actuator internal bore

intergranular in nature and propagates due to a galvanic interaction between the precipitates and the matrix. When the precipitates are noble and concentrated at the grain boundaries, then the attack occurs at the solute depleted regions around the precipitates and propagates rapidly into the material along those boundaries (Robinson and Jackson 1999). Pitting corrosion is another common form of attack observed in 6061 aluminum components, particularly in a seawater environment (Aylor and Moran 1986).

TIG, MIG, and laser cladding of aluminum could be possible options for repair of the aluminum actuator. These methods would be able to produce strengths and porosities that would meet or exceed the requirements for the repair of the aluminum actuator in coupon-type test samples. However, limited space, tight tolerances, and numerous finished part features adjoining to the repair locations make these options unattractive. The internal bore with the critical mating surfaces has an internal diameter less than 102 mm (4 in.). This makes it impractical to fit a MIG or TIG welder into the internal bore. Laser cladding of internal bore surfaces is a new and growing technique. It has been proven to be effective at cladding the internal diameter of steel bores with nickel. However, at this time, all commercial process operations are being run without an inert atmosphere which would be required for optimal properties in aluminum cladding.

The actuator was repaired using a VRC Gen III high-pressure cold spray system (VRC Metal Systems, Rapid City, SD, USA), as shown in Fig. 2.20. 6061 Al coatings were produced via cold spray from commercially available gas-atomized 6061 Al powder (Valimet, Stockton, CA, USA), −325 mesh, deposited on a 6061 aluminum alloy substrate. Helium was used as the process gas to achieve high impact

Fig. 2.20 VRC Gen III Hybrid cold spray system

velocities between incident particles. The pressure and temperature of helium were maintained at 34.5 bar and 500 °C at the heater exit, respectively. Deposition took place using a nozzle standoff distance of 20 mm (0.79 in.), 45° deposition angle, medium powder feed rate of approximately 10 g/min, and a nozzle traveling speed of 250 mm/s. Finally, total deposition thicknesses ranged from 2 mm to 8 mm (.049″ to .318″). Prior to repair of the aluminum actuator, proof of concept testing was required to ensure that cold spray could achieve the level of properties needed for the repair. A mock-up, tensile testing, ASTM C633 bond testing, and porosity testing were all required prior to the repair of the aluminum actuator. Due to the high level of risk, all the tests would need to be passed before the repair of the aluminum actuator would be authorized.

The Navy valve actuator was successfully repaired using high-pressure cold spray deposition (Fig. 2.21). The repair process development has shown the potential for even more challenging future applications as the strength of the cold spray deposited material was found to be in excess of 200 MPa as deposited. It is felt that through further development, even higher strengths will be achievable using high-pressure cold spray systems. This repair is now being offered commercially by MOOG, which demonstrates a full technology transition pathway from a university R&D laboratory in partnership with an equipment supplier to design and provide the necessary hardware for the repair and an industrial service provider to fulfill

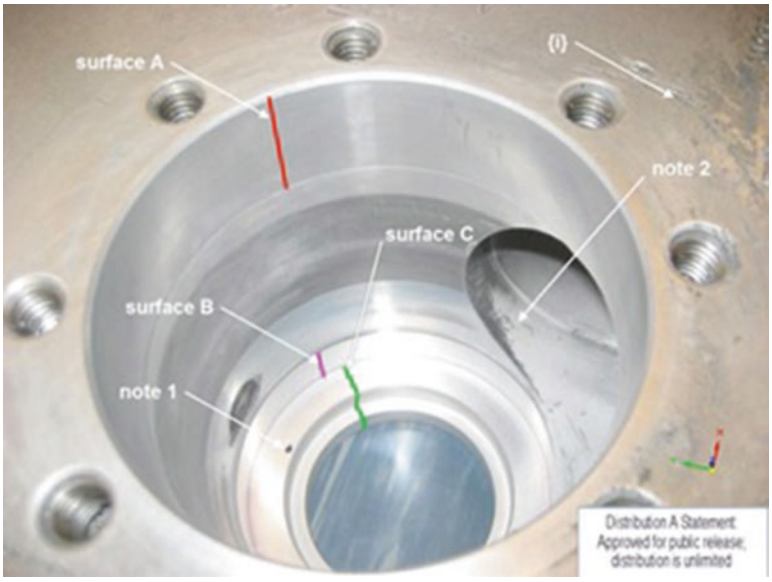

Fig. 2.21 Photo of the final machining performed on the repaired actuator, which was successfully returned to service

future repair needs. The actuator has been in service for over 2 years. This repair is expected to both provide a generous return on investment as a repair process and to increase system availability by providing an alternative to the long lead times of new purchased parts.

2.3 Joining Dissimilar Materials

The ability to join lightweight dissimilar materials is important in order to produce hybrid structures and components for a variety of engineering applications in the automotive and aerospace industries (Kah et al. 2014). The joining of dissimilar materials by the use of cold spray can be accomplished for certain combinations of materials (Champagne et al. 2016). It is not the intent of this section to list all of the potential combinations but to point out the fact that it is possible to capitalize on the exceptional bond strength achieved between various materials when cold sprayed and incorporate its use to form a suitable joint. Cold spray can be used alone or in conjunction with other techniques to join dissimilar materials. The ability to join aluminum to magnesium has been investigated by numerous researchers using a variety of techniques but with limited success. It is a challenge from a metallurgical perspective due to the formation of brittle intermetallic compounds (IMCs), and the resultant joints have been poor or lacked sufficient structural integrity for practical use (Champagne et al. n.d.). The joining of magnesium to aluminum will illustrate the potential of cold spray to be used in this fashion for certain applications.

The ability to join Al and Mg also represents a significant challenge for many industries, including automotive, petrochemical, and aerospace industries, and success would enable significant weight savings to be realized and subsequent energy efficiency in the automobile industry and the requirement for chemical plants and cryogenic applications (Walsh 2000; Bernard et al. 2001). Dissimilar welding of aluminum (Al) and magnesium (Mg) alloys would achieve weight reduction and high efficiency of production by a substitution of Mg alloys for Al alloys (Avedesian and Baker 1999; Mordike and Ebert 2001). Magnesium is an engineering material of choice for such applications as transmission housings because of its low density, high stiffness, and high specific strength (Musfirah and Jaharah 2012). The military and industry have numerous applications in aerospace, munitions, and vehicles that require the joining of dissimilar materials. Reduction in weight and improvement in performance are important in the design and manufacture of armored military vehicles, and therefore, a solution to this problem is important to enable the use of dissimilar material joints. The ability to provide structural repair of expensive gearbox housings that have experienced corrosion or wear during use would save millions of dollars a year for the military and commercial aircraft industry in replacement costs for new parts.

Shear, hardness, and tensile testing were conducted to determine bond integrity at the dissimilar metal joint. Electron and optical microscopy were performed to analyze the interface and microstructure.

2.3.1 ARL "Glueless" Bond Strength Test

The "glueless" bond strength test method was developed to evaluate the bond strength of cold spray deposits on a substrate. The traditional test method used throughout the aerospace industry has been ASTM C633, titled "Standard Test Method for Adhesion or Cohesion Strength of Thermal Spray Coatings." This test procedure prescribes that a cold spray coating/deposit be applied to a 25.4-mm (1 inch) diameter substrate bar onto which a mating bar of the same diameter is glued to the top of the cold spray deposit. This approach offers a quick evaluation of adhesion strength of thin deposits but limits the value of the ultimate tensile strength (UTS) that can be measured to approximately 69–90 MPa (10–13 ksi), which corresponds to the strength of the glue. However, high-pressure cold spray material far exceeds these strength values, and test results have been typically reported as glue failures with tensile strength values of the cold spray deposit designated as "greater than 69 MPa." Since cold spray has advanced and now can achieve bond strength values much greater than 69–90 MPa (10–13 ksi), a test method for accurate and precise measurement at these strength levels was required. Therefore, to investigate the actual bond strength of cold spray deposits, a means of evaluating bond strength without using glue was developed at ARL. The test specimen and accompanying fixture were designed to uniformly pull the cold spray coating/deposit normal to the substrate interface in uniaxial tension with failure occurring in a 12.7-mm (0.5 in.) diameter section. A diagram of the specimen is shown in Fig. 2.22. The spray

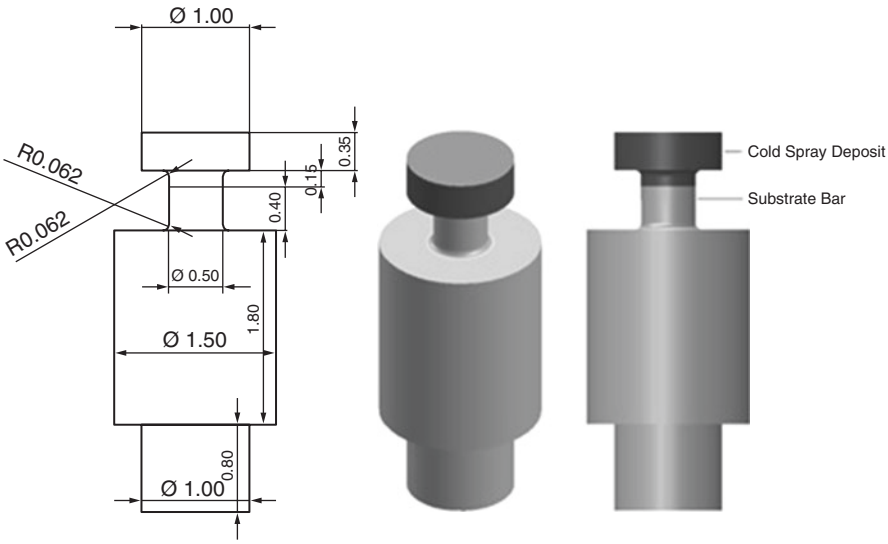

Fig. 2.22 "Glueless" bond strength test specimen mechanical drawing (dimensions in inches)

conditions/parameters were optimized prior to this effort. The specimens were sprayed using a robotic arm to manipulate the cold spray applicator, and the substrate bars were placed in a circular array rotated using a single-axis rotary turntable. A spiral raster path pattern was utilized in order to reduce processing time and overspray. The robot was used to move the gun slowly across the specimens resulting in a spiral pattern to deposit each layer. The rotational speed and robot transverse were adjusted such that the relative velocity was equal to that of a typical raster cold spray pattern. The samples can be viewed in Fig. 2.23a, b before and after spraying. The as-sprayed specimens were machined to the required dimensions to form a cap and neck geometry. During testing, the specimen is secured in a two-plate fixture designed as shown in Fig. 2.24. The bottom section of the specimen and the overhead clamp are threaded to 25.4 X 305 mm (1 X 12 inch) for attachment to the load frame. The samples are pulled in tension using an Instron Model 1125 tension load frame. The test is carried out using a strain rate of 1.27 mm/min (0.05 in./min) at room temperature and approximately 50% relative humidity.

2.3.2 ARL "Glueless" Bond Strength Test Results

The bond strength test results for a series of 6061 Al cold spray deposits on ZE41A-T5 Mg were obtained, and the average maximum load was 2106 ± 50 kg (4644 lbf ±110 lbf). These values correspond to an average ultimate tensile strength (UTS) of 163 ± 3.8 MPa (23.7 ± 0.6 ksi). Values as high as 184 MPa (26.7 ksi) with a corresponding load of 2379 kg (5246.7 lbs) were recorded. These values are

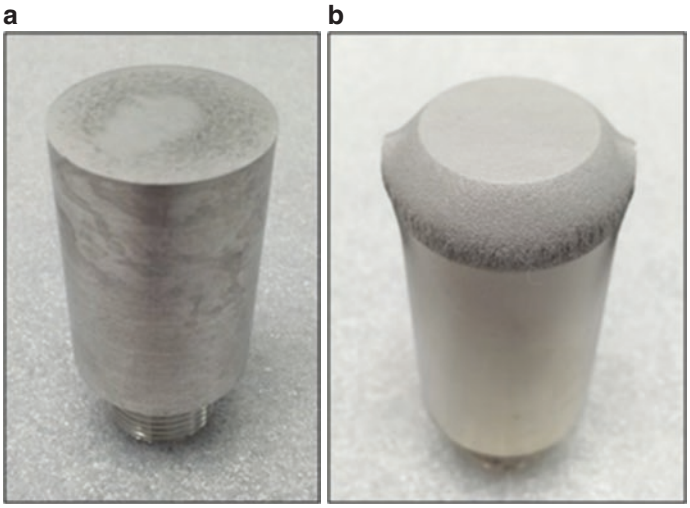

Fig. 2.23 Uncoated ZE41A Mg "glueless" bond strength test bar (**a**) and after spraying (**b**)

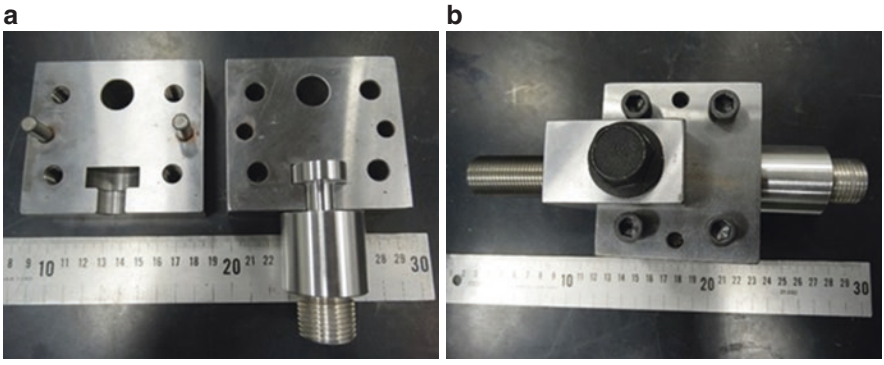

Fig. 2.24 "Glueless" bond strength test specimen fixture (**a**) and after being secured (**b**)

commensurate with those reported by Champagne III et al. in their investigation of joining cast ZE41A Mg to wrought 6061 Al by the CS process and friction stir welding (Champagne et al. 2016). They reported UTS values ranging from 130 to 164 MPa, but it is important to note that when 5056 Al was used as the cold spray particulate material, the values of UTS increased and ranged from 181 to 198 MPa. Published values of the UTS of ZE41A-T5 Mg are 205 MPa (MatWeb's searchable database of material properties n.d.). Failure stress is reported based on the load at failure and the cross-sectional surface area at the failure point. A representative tested sample is shown in Fig. 2.10 with the failure shown at the deposit–substrate interface. The failure site varies from that of the shear test samples which was anticipated since the area of highest stress is at the interface within the tensile samples, while it is slightly subsurface for the shear test samples. Ultimate tensile strengths for adhesion of cold sprayed 6061 aluminum are reported well beyond the previous

measurement limits using the ASTM C633 adhesion test. With testing capabilities no longer bound by the properties of the adhesive, the glueless bond test methodology can be transferred to a wide variety of cold spray deposit materials and substrates in the assessment for structural repair applications.

2.3.3 Hardness Testing

Hardness was measured on standard metallographic specimens. The hardness was recorded over an average of a minimum of five evenly spaced indentations in accordance with ASTM E 384. Vickers hardness testing was performed using a 500-g load. The ZE41A-T5 Mg substrate had an average hardness value of 68 HV, while that of the cold spray 6061 Al was 105 HV.

2.3.4 Optical and Electron Microscopy

Metallographic samples were taken to evaluate the microstructural features of the dissimilar metal joint between the 6061 Al cold spray deposit and the ZE41A-T5 Mg. Cross sections of the welded joint were taken utilizing a Leco cutoff saw, and 1-in. diameter metallographic samples were mounted in Bakelite and prepared incorporating a series of grinding steps starting at 180 grit and finishing with 2400 grit. Final polishing was accomplished using 3-um diamond paste followed by 0.25-um diamond paste and completed using a 0.05-um colloidal silica suspension. The important aspects of the evaluation were that, as anticipated, no evidence of a heat-affected zone (HAZ) was observed since the cold spray process is accomplished below any phase transformation temperatures and well below the melting point of both materials being joined. The magnesium alloy ZE41A is a casting alloy having a combination of lightweight, stiffness, and high strength and is currently used in the military and commercial aerospace industry for applications as high as 250 °C for transmission housings. The major alloying elements are Zn and Zr, as well as the rare earth element cerium. This alloy has a thermally stable microstructure consisting of an α-Mg matrix, Mg eutectics, and various primary and secondary phases containing rare earth elements (Kasprzak et al. 2015). The ZE41A Mg cast alloy used in this study was heat treated to the T-5 condition, which is an artificially aged condition, and the microstructure consists of α-Mg and β-Mg-Zn-RE according to Riddle et al. (Riddle et al. 2004).

2.4 Discussion

The materials, cast ZE41A-T5 Mg and 6061 Al, were chosen in this study because of their widespread applicability across several sectors of the aerospace and automotive industries. As previously discussed, the ability to join magnesium and

aluminum has been attempted using various welding and joining processes to a limited degree. Many of the resultant joints have been poor or lacked sufficient structural integrity to be considered for applications, demanding high loads. Electron microscopy showed the absence of a coarse intermetallic layer of Mg2Al3 and Mg17Al12 being formed at the dissimilar metal interface, and values of shear and tensile strength were obtained that were equal to or close to those of the weakest material being joined (Mg) when employing the cold spray process. The high mechanical properties obtained in this study can be attributed to the high-strength bond achieved by the cold spray process and warrant further discussion. Since the temperature of the gas stream is below the melting point of the particulate material during cold spray, the resultant consolidated material is formed in the solid state which made it feasible for joining low-melting temperature alloys, such as magnesium and aluminum. Since the adhesion of the impacted particles to the substrate, as well as the cohesion of the subsequent layers of CS deposit, was accomplished in the solid state, the cold spray joints were shown to maintain the microstructure, grain size, and elemental composition of the starting feedstock powder. The formation of a heat-affected zone (HAZ) was avoided, as well as deleterious tensile stresses that would occur during thermal contraction, associated with most welding techniques. Most importantly, the formation of Mg2Al3 and Mg17Al12 IMCs was avoided. The CS process involves the acceleration of micron-sized particles which undergoes tremendous plastic deformation. Upon impact, the plastic deformation disrupts and breaks down surface oxide layers on both the powder and substrate leading to a metallurgical bond, as well as mechanical interlocking, as was evidenced in the data presented. The magnitude of the bond strength is directly related to the optimization of the CS process parameters, condition of the feedstock powder, and surface preparation (Kasprzak et al. 2015). Since the feedstock powder is deposited in the solid state, the microstructure is retained after deposition with the exception of dynamic recrystallization due to high strain levels. The CS process is conducive to materials that can undergo high levels of strain with low energy input, but also work hardens sufficiently to obtain the desired strength. Localized temperature increases and strain concentration play a major role in the high-speed deformation of the aluminum particles upon impact causing adiabatic shear. Approximately 90% of the work of plastic deformation is converted to heat, and the flow stress of most metals is sensitive to temperature and decreasing as temperature increases. During impact of the solid feedstock powder particles, the oxide layers on both the powder and the substrate surface are disrupted and partially removed along with other impurities at the particle/substrate interface causing the exposure of highly reactive un-oxidized metal and subsequent metallic bonding between particle and substrate material (Riddle et al. 2004). The feedstock powder forms an adherent metallurgical bond with the substrate as a result of the severe plastic deformation during particle impact (Maev et al. 2006; Villafuerte 2015). The predominate bonding mechanism of the cold spray joint can be attributed to adiabatic shear, in combination with mechanical interlocking (Maev and Leshchynsky 2016). These attributes of the CS process were found to contribute to the exceptional strengths obtained from the dissimilar metal joint.

2.5 Conclusions

- CS did not result in the formation of an intermetallic layer at the dissimilar metal interface between cast ZE41A-T5 Mg and cold spray 6061 Al as confirmed by optical and electron microscopy. This is because the process is performed well above the melting temperature and the cold spray feedstock powder is consolidated in the solid state.
- Triple lug shear and tension testing results showed that CS is able to produce structural joints between dissimilar metals (ZE41A-T5 Mg and 6061 Al), with a bond strength equal to or superior to that of the substrate when tested in shear and uniaxial tension.
- Hardness testing has shown that the cold spray 6061 Al was 105 HV, while that of the cast ZE41A-T5 Mg had an average hardness value of 68 HV.
- This data suggests that CS can be used to form a dissimilar metal joint between ZE41A-T5 Mg and 6061 Al and be considered for structural repair.

References

Avedesian MM, Baker H (1999) ASM specialty handbook, magnesium and magnesium alloys. ASM International, Materials Park

Aylor DM, Moran PJ (1986) Pitting corrosion behavior of 6061 Aluminum alloy foils in sea water. J Electrochem Soc 133(5):949–951

Balani K, Laha T, Agarwal A, Karthikeyan J, Munroe N (2005) Effect of carrier gases on microstructural and electrochemical behavior of cold sprayed 1100 Aluminum coating. Surf Coating Tech 195(2–3):272–279

Barbosa M et al (n.d.) Cold spray deposition of titanium onto aluminium alloys. DIA MUNDIAL DOS MATERIAIS 2009, Menção Honrosa ORDEM DOS ENGENHEIROS

Belsito D, McNally B, Bassett L, Champagne V, Sisson R (n.d.) Proceedings of MS&T 2013 conference

Bernard SM, Samet JM, Grambsch A, Ebi KL, Romieu I (2001) The potential impacts of climate variability and change on air pollution related health effects in the United States. Environ Health Perspect 109:199–209

Champagne V (ed) (2007) The cold spray materials deposition process. Woodhead Publishing/CRC Press, Cambridge, p 327

Champagne VK, Leyman PF, Helfritch DJ (2008) Magnesium repair by cold spray. ARL technical report ARL-TR-4438. May, 34 p

Champagne III et al (2016, January) Joining of cast ZE41A-Mg to wrought 6061 Al by the cold spray process and friction stir welding. J Therm Spray Technol 25(1):143–159

Champagne V Jr, Kaplowitz D, Champagne III VK, Howe C, West MK, McNallie B, Rokni M (n.d.) Dissimilar metal joining and structural repair of ZE41A-T5 cast magnesium by the cold spray (CS) process, materials and manufacturing processes. https://doi.org/10.1080/10426914.2016.1257137

Gärtner F, Stoltenhoff T, Schmidt T, Kreye H (2006) The cold spray process and its potential for industrial applications. J Thermal Spray Technology 15(2):223–232

Gavras AG, Lados DA, Champagne VK, Singh D (n.d.) Small fatigue crack growth mechanisms and interfacial stability in cold-spray 6061 aluminum alloys. Worcester Polytechnic Institute Internal Report

Kah P, Suoranta R, Martikainen J, Magnus C (2014) Techniques for joining dissimilar materials: metals and polymers. Rev Adv Mater Sci 36:152–164

Kasprzak W et al (2015) Correlating hardness retention and phase transformations of Al and Mg cast alloys for aerospace applications. J Mater Eng Perform 24(3)

Kumar S, Chavan NM (n.d.) Cold spray coating technology: activities at ARCI. Briefing, International Advanced Research Centre for powder Metallurgy and New Materials (ARCI) Hyderabad

Maev R, Leshchynsky V (eds) (2016) *Cold gas dynamic spray*. CRC Press/Taylor and Francis Publishing, Boca Raton

Maev R, Leshchynsky V, Papyrin A (2006) Structure formation of Ni-based composite coatings during low pressure gas dynamic spraying. Proceedings of the 2006 ITSC, ASM, Seattle

MatWeb's searchable database of material properties. (n.d.) http://www.matweb.com/

McCune R, Ricketts M (2004) "Selective galvanizing by cold spray processing" in "cold spray 2004". ASM International – TSS, Akron

Mordike BL, Ebert T (2001) Magnesium: properties – applications – potential. Mater Sci Eng A 302(1):37–45

Musfirah AH, Jaharah AG (2012) Magnesium and aluminum alloys in automotive industry. J Appl Sci Res 8(9):4865–4875. ISSN 1819–544X

Papyrin A (2001) Cold spray technology. Adv Mater Process 159:49–51

Riddle Y, Barber L, Makhlouf, M (2004) Characterization of Mg alloy solidification and As-cast microstructure. Magnesium Technol TMS 203–208

Robinson M, Jackson N (1999) The influence of grain structure and intergranular corrosion rate on exfoliation and stress corrosion cracking of high strength Al-Cu-Mg alloys. Corros Sci 41(5):1013–1028

Stoltenhoff T, Zimmermann F (n.d.) LOXPlate® coatings for aluminum aerospace components exposed to high dynamic stresses. Praxair Surface Technologies GmbH, Ratingen

Villafuerte J (ed) (2015) Modern cold spray, materials, process, and applications, vol 56. Springer International Publishing, Cham. https://doi.org/10.1007/978-3-319-16772-5

Vlcek J, Gimeno L, Huber H, Lugscheider E (2005) A systematic approach to material eligibility for the cold spray process. J Therm Spray Technol 14:125–133

Walsh MP (2000) Motor vehicle pollution control. Platin Met Rev 44:22–30

Zheng W, Derushie C, Lo J, Essadigi E (2006) Corrosion protection of joining areas in magnesium die cast and sheet products. Mater Sci Forum 546–549:523–528

Chapter 3
Coeval Cold Spray Additive Manufacturing Variances and Innovative Contributions

Rija Nirina Raoelison

3.1 Introduction: Flexibility of Cold Spraying Today Towards a Larger Taxonomy

Known as a breakthrough technology, the cold spray method is a distinctive technique that enables the production of functional parts by a self-consolidation of solid powders using high-speed collision. Tremendous attention has been given to cold spraying (CS), even more today with the dissemination of the additive manufacturing method. Since nearly 20 years, this process has strikingly emerged among thermal spray processes due to its ability to work at low temperature that prevents thereby adverse events generated at high temperature. This major advantage has decisively transformed the capabilities of thermal spraying and made cold spraying a viable cold and solid state additive structural or material manufacturing method for various materials including metals, ceramics and polymers but also advanced materials such as nanomaterials and composites. Industries and scientific community found great potentials from cold spray additive manufacturing and still explore its potentials, so that innovative technological solutions always arise along R&D actions through decades. Today, there are several R&D cold spray installations worldwide, e.g. in America, Australia, Asia, Europe, and Russia (Schwenk, 2012), and the cold spray technology knows a growing market (Krömer and Werner, 2012) with substantial developments of functional coatings or bulk components to fulfil new needs or to create advanced performances (Moridi et al. 2014; Assadi et al. 2016; Grigoriev et al. 2015; Marx et al. 2006).

Along the development of cold spraying, the technical dimension, and particularly in terms of manufacturing method, has always been a major genesis of progresses and novelties. Albeit the cold spray additive manufacturing consists of a

R.N. Raoelison (✉)
Laboratoire Interdisciplinaire Carnot de Bourgogne – Site UTBM, UMR 6303 CNRS, Université de Bourgogne Franche-Comté UTBM F-90010 Belfort, France
e-mail: rija-nirina.raoelison@utbm.fr

P. Cavaliere (ed.), *Cold-Spray Coatings*,
https://doi.org/10.1007/978-3-319-67183-3_3

single principle, i.e. a supersonic gas flow through a nozzle to generate high-speed collision of solid particles, some distinctive methods have been developed. Basically, a major depiction relies on the level of both pressure and temperature of the compressed gas that generates the supersonic flow. The current status of cold spraying suggests a wide range of working gas pressure from a few μPa up to some MPa and a gas temperature setting in between 20 and 800 °C typically. This flexibility yields method variants with distinctive features and specific contributions. The cold spray deposition capability has long been experienced at high gas pressures with the possibility to preheat the gas below 1000 °C. Those conditions have been widely applied since they can produce high deposition efficiency and facilitate the deposition conditions. In the literature, the term high-pressure cold spraying (HPCS) is generally considered to specify the deposition conditions using such gas setting, but no conventional definition of pressure range has been clearly fixed. The notion of high pressure mainly relies on the experienced conditions or on the capacity of CS installations. The experimental literature of CS provides numerous cases of suitable gas setting. The gas preheating lies in between 20 °C and 800 °C for the solid state deposition to prevail, and the HPCS deposition generally uses a gas pressure up to 5 MPa, though there is no theoretical upper delimitation. The downer pressure of HPCS is not also fixed neither by theoretical considerations nor by standard convention but by an innovative use of the cold spray method, subjectively. Indeed, a compact design of CS system was recently developed to allow an in situ use of cold spraying without displacing the workpiece. Restoration and repair represent typical applications. Such CS system is a portable device with a typical maximum working pressure of about 1 MPa for a safe use. This is a low-pressure condition, and the term low-pressure cold spraying (LPCS) has been enacted in this respect. The gas preheating is also limited for current commercialized LPCS devices like DYMET 423 or CenterLine-SST LCPS. The highest working temperature is roughly 600 °C. Due to those limitations, LPCS is less efficient than HPCS in terms of kinematic capability. HPCS enables providing high gas velocities that facilitate the selection of particle granulometry. HPCS covers a large particle size range of 5 μm–100 μm for a successful deposition (Raoelison et al. 2016), whereas LPCS requires small-sized particles to reach the velocity threshold for the deposit bonding to occur. Furthermore, the suitable particles' size range becomes more reduced since fine particles involve deposition difficulties due to a bad flowability or a self-agglomeration even a clogging, particularly when they are exposed to a heated gas (Raoelison et al. 2016). The cold spray manufacturing of small powders becomes efficient under vacuum deposition condition. Subatmospheric pressure is generally employed and a non-heated gas eases the deposition of fine and ultra-fine powders. This method variance has been endorsed for submicron, even nanosized particles, and can be termed as very-low-pressure cold spraying (VLPCS). A taxonomy of the cold spray method variances is depicted in Fig. 3.1 in terms of gas working conditions or using other discriminative factors, viz. suitable particle size and deposit thickness. Pragmatically, VLPCS can produce a thin coating of some nanometres against some dozen micrometres for LPCS and HPCS, but HPCS also enables the fabrication of bulk component and no thickness limitation was particularly specified. Figure 3.2 provides a non-exhaustive example of cold spray realizations that

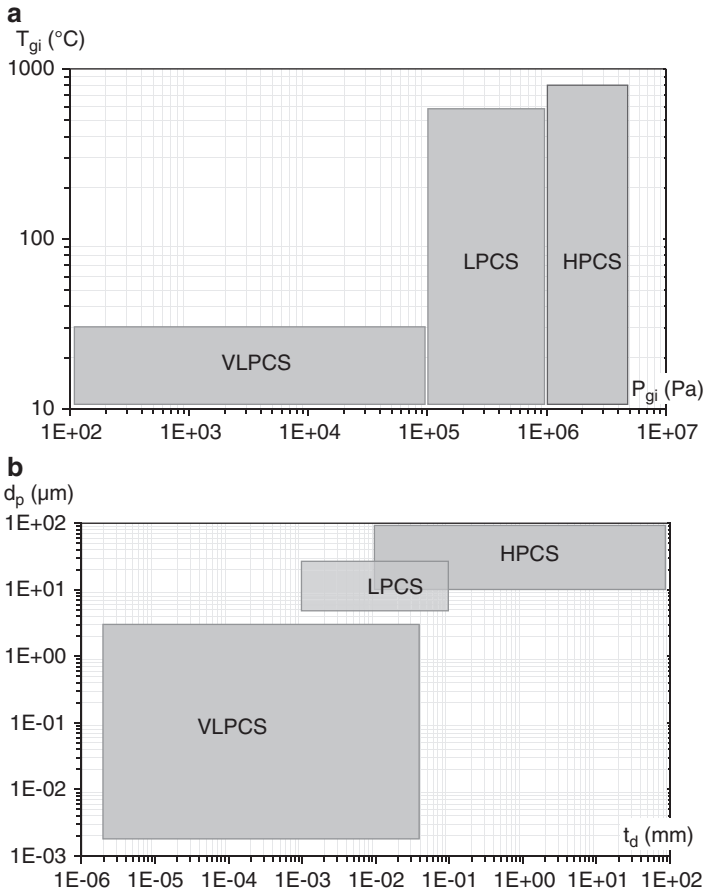

Fig. 3.1 Taxonomy of current cold spray method variances depicted by a diagram working gas pressure-working gas temperature (**a**) or a diagram particle diameter-deposit thickness (**b**)

shows a representative dimension variance of manufactured deposit. For instance, thin-film coating was obtained by VLPCS using submicron-sized powders (Chun and Ahn 2011). Figure 3.2b shows a typical HPCS bulk component with a large size of some centimetres (Dean et al. 2013).

With these deposition variants and their achievements, the cold spray method has known some years of milestones and new perspectives of material and processing technology. The past decade was a particular period which has brought substantial adaptability of cold spraying. Recent developments have evidenced further scalability of this deposition method towards a lager taxonomy. A new peculiar variance uses a series of impulse spray that produces the same kinematic performance as for continuous spray-based method, but a major difference lies in the thermal features of the spray. Unlike the previous cold spray variances that involve a gas expansion and then a cooling to cause a supersonic flow, the impulse spray method, which denotes pulse gas dynamic spraying (PGDS), allows to heat the gas spray through

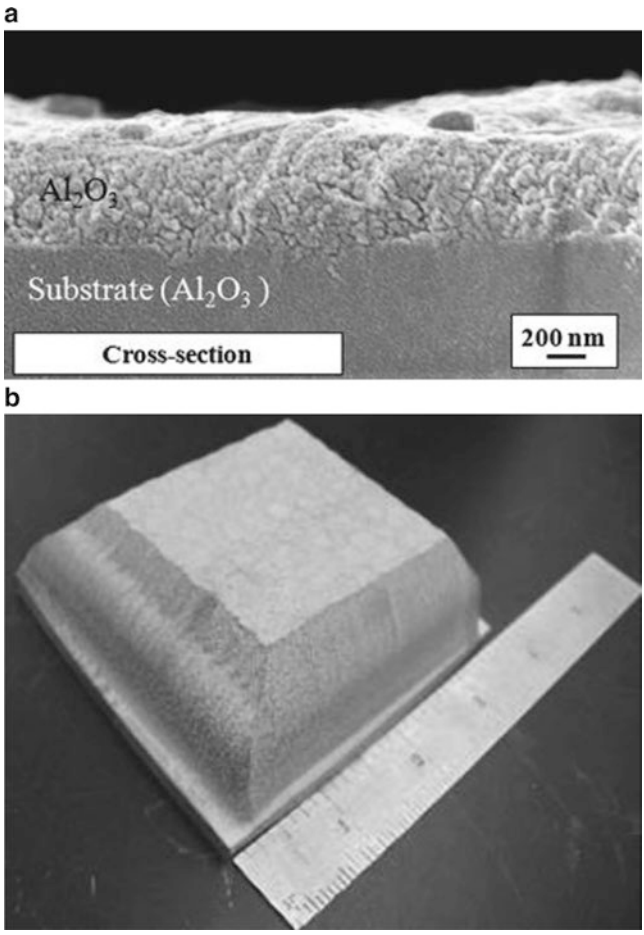

Fig. 3.2 Typical variances of deposit size in CS (**a**) thin coating obtained by VLPCS (Chun and Ahn 2011) and (**b**) bulk HPCS Ni-Al component for energetic application (Dean et al. 2013)

the nozzle while it generates the supersonic motion of the particles (Jodoin et al. 2007; Yandouzi et al. 2007, 2009; Sansoucy et al. 2008). This circumstance offers a sort of thermal tailoring which can have a positive effect on the deposition capability. The literature of cold spraying also encompasses another variance of thermal control using an assisted method that directly acts on the particles. In this respect, a laser-assisted cold spray (LACS) deposition has been endorsed for which the term cold spray refers to the usual continuous spray-based method (Kulmala and Vuoristo 2008; Bray et al. 2009; Ahn et al. 2012). A laser beam heats the particles and/or the substrate, and the heating spot moves synchronously with the nozzle displacement. The LACS method belongs to a hybrid variant of cold spraying that currently emerges. The hybridization of cold spraying is becoming a new added value among modern use. The cold spray method has also been combined with a focused ion

beam cutting. This novelty represents a new research and development investigations and will certainly be a major element of future innovation.

Together, these explorations of the cold spray manufacturing capabilities highlight great possibilities which seem to conceal substantial potentials towards further perspectives in the field of material and processing technology. This chapter addresses a review of those coeval cold spray additive manufacturing variances and their innovative contributions. The next sections report a brief chronology of cold spraying and the generic modern deposition method as it stands nowadays (Sect. 3.2), a concise survey of material capabilities (Sect. 3.3) and an overview of pragmatic deposit possibilities (Sect. 3.4). The distinctive variances of cold spray deposition depicted on Fig. 3.1 will be presented in stand-alone sections: Sect. 3.3 for the low-pressure cold spray method bringing new benefits, Sect. 3.5 for the very low-pressure cold spray manufacturing for the development of advanced technological solutions and Sect. 3.9 for the pulse gas dynamic process providing an alternative thermal control of the gas spray. This chapter also addresses an overview of hybrid combinations based on the cold spray technology, including a novel hybrid variant for 3D submicron architecturation (Sect. 3.6) and laser-assisted cold spray method that enables the deposition improvement or enhances the deposit features (Sect. 3.7). The last section will restitute concluding remarks about those capabilities of cold spraying today.

3.2 Historical Review of the Cold Spray Technology Up to the Generic Modern Method

The development of the cold spray technology has led to several inventions patented for over a century and mostly since a couple of decades, but according to a chronological review, three key milestones can be identified: the finding of Thurston in the 1900s, the invention of Rocheville in 1958 and the Russian developments of the 1990s. 'I am not aware that metal particles have ever been thrown upon or against a metal plate for the purpose of driving the said metal particles with such force as to cause them to be incorporated with the body of said metal and form a coating by impact or impingement' issued Thurston in its patent published in 1902 (Thurston 1900) describing a method of particle deposition onto a substrate (Fig. 3.3) that became a great technological breakthrough a century later. This method consists of a hopper providing metal powders that fall into a funnel-shaped chamber having a nozzle tip. Thurston used a blast air supplied by a pneumatic pressure and a pipe to drive the powders from the exhaust cone of the chamber onto a substrate. It was mentioned that the collision produces an embedment of the (metal) powders into the (metal) substrate forming thereby a permanent coating for some experienced combinations including copper or aluminium powders and iron or steel substrate. However, the powder size was not specified and the embedment seems to require a substrate heating. The method as it was patented seems to meet kinematic limitations, but Thurston has indicated the possibility of using a different source of propellant gas such as superheated steam or any high-pressure gas. Using a non-heated gas, such

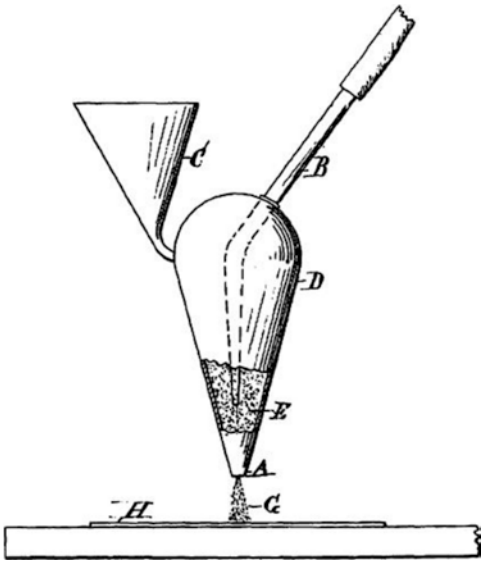

Fig. 3.3 Primary CS method (Thurston 1900). *C* is a hopper providing powders in the chamber *D*. Blast air supply driven by the pipe *B* forces the powders through the nozzle *A*. The powders spray *G* collides onto the substrate *H* to form a deposit

method would limit the particle velocity at roughly 300 m/s (Irissou et al. 2008). Thurston presented this deposition method as a surface coating process covering a wide range of metals.

Thereafter, a better specification of both condition and method for cold spray deposition appeared with a major technological advance due to an invention patented by Rocheville available by the 1960s (Charles 1958). The patent describes a system for spraying powders that employs a convergent-divergent nozzle. The nozzle is flexible, i.e. can be handled by an operator or can be a stationary component combined with a moving substrate. Rocheville has underlined a capability of supersonic blast air and thus supersonic velocities of propelled fine powders. Uniform, thin and cohesive metallic coatings were produced over the surface of various substrates such as aluminium, magnesium, lead or other materials (Charles 1958). Historically, the use of micro-sized powders was first mentioned and the working gas pressure level was first specified. The invention of Rocheville has already adopted the principle of two distinct streams, viz. high pressure and low pressure known nowadays as main gas supply and secondary gas supply, respectively, fed into the nozzle to generate a propellant gas flow through a convergent-divergent section and to drive the powders to be sprayed onto the substrate, respectively. A pressurization at about 10Bar is indicated for the air main supply, and the secondary source has a typical pressure of 0.6–1Bar with a low mass flow rate with respect to the main high-pressure flow. A first modernization of the cold spray method can be attributed to this Rocheville's invention since it has introduced the enactment of fundamental features of cold spraying and particularly the principle of gas expansion to produce a confined supersonic propellant flow. The genuine difference relies on the nozzle architecture that suggests a hierarchical separate feeding of the main gas and the powder supply. The powders are fed ahead the convergent-divergent exhaust, and then the supersonic air acts as a blast current driving the powders onto

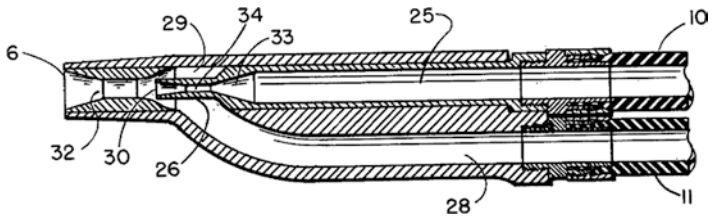

Fig. 3.4 Nozzle system invented by Rocheville to reach supersonic velocities (Charles 1958). *25* is the convergent-divergent part *25* connected to a high-pressure line *10*. *28* is the secondary duct providing powders connected to a low-pressure line *11*. The powders are fed into the chamber *32* which is the continuation of the divergent section *26*

the substrate through a passage that forms a continuation of the divergent section of the convergent-divergent part (Fig. 3.4). Thereby, the gas stream and powder stream are mixed outside the convergent-divergent part of the hierarchical nozzle, whereas for modern nozzles, together those streams are fed into a single convergent-divergent line. The powders are directly injected into the nozzle to be accelerated by the supersonic propellant gas through the divergent section and then to be directly sprayed on a substrate in front of the nozzle's exit. This deposition condition characterizes the Russian's innovations of the 1990s that bore the generic modern method of cold spraying as it stands today. The development of cold spraying in the 1980s at the Institute of Theoretical and Applied Mechanics of the Russian Academy of Sciences (ITAM-RAS) in Novosibirsk was a result of an experimental discovery, while Russian researchers have investigated the behaviour of a two-phase flow (case of gas dynamics mixed with solid particles used as tracers) crossing through an obstacle. Adhesion of the solid particles onto the surface of the immersed obstacle was observed. This circumstance has been explored as a potential and viable coating technology denoted cold gas dynamic spraying (CGDS) by the ITAM-RAS. Substantial progresses have been achieved. High velocities up to 1200 m/s have been reached for 1–50 μm sized particles that produce thereby a continuous deposit formation. New patents appeared from these Russian pioneering contributions since 1986 in Russia, 1994 in the USA and 1996 in Europe (Alkhimov et al. 1990; Papyrin et al. 2007; Irissou et al. 2008). The cold spray method has known a growing interest with a modernization that enables a precise setting of the gas working parameters, a good control of the nozzle motion and a safe use. The CGDS process can be considered as a HPCS variance since high-pressure and high-temperature gas conditions have long been experienced along the development of this method. For the sake of consistency, this categorization is enacted in this manuscript to disentangle the contributions of the cold spray manufacturing across all variant deposition methods.

Today, computer-controlled CS installations are available and marketed for R&D works or industrial purposes. A typical architecture of such modern cold spray system is presented in Fig. 3.8. It is mainly composed of a gas supply, a powder feedstock, a system of data acquisition and control, a control console, a gas heated unit and a de Laval nozzle which can be equipped with a prechamber and an induction heating system to heat the gas prior to entering the nozzle. The workstation includes a spray component (nozzle + guidance unit) with a controlled motion using

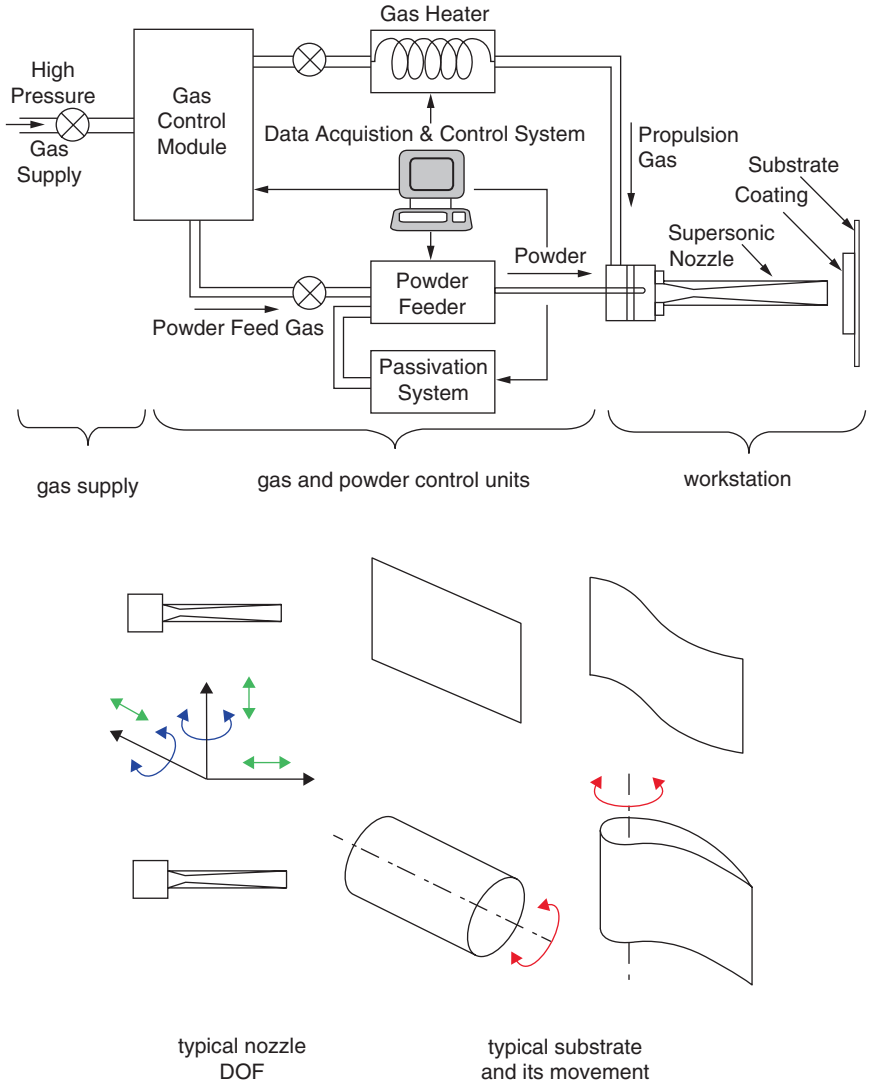

Fig. 3.5 Typical architecture of modern CS system (Papyrin 2006). Typical nozzle DOF and substrate shape with the movement of the support component in the working area

a robot arm, and also a substrate support system which can also be moved or fixed in the working area. The motionless substrate usually concerns flat or incurved surfaces to coat, whereas moving substrate deals with axisymmetric workpieces or revolution components for which a rotating motion is used. The combination of the spray component motion and the substrate system motion allows for building and shaping the deposit or even producing 3D asymmetric complex shapes. Such flexibility can generate new cold spray technology events in the field of metallic additive prototyping applications (Fig. 3.5).

3.3 A Concise Survey of Material Possibility for Cold Spraying Today

The CGDS process has gained benefits from the theoretical and experimental knowledges in the field of two-phase flow developed by Russian researchers of ITAM-RAS. It was specified that successful depositions were performed for various powder natures, viz. metal, alloy and mechanical metal/alloy mixture, and for diversified substrates in terms of shape and material nature (Alkhimov et al. 1990; Papyrin et al. 2007). In addition, thick coatings can be generated, whereas in some decades ago, the deposit thickness was limited to about 2 μm using the system of Rocheville, and a few material cases alone were experienced. The cold spray method was initially performed on metals, but today it is suitable for a wider range of materials (Table 3.1). Since the 2000s, CGDS has known an important diversification of feasibility studies that clearly demonstrates a great versatility in terms of processable materials.

Metals and alloys still represent a ubiquitous working case but with more diversifications. They have the major advantage to be easily processable in addition to the various functionalizations they offer. The last decade was also a period of ceramics and MCrAlY success for CGDS. Oxide-based- and ceramic-based phase are now part of the cold spray additive manufacturing possibilities. Furthermore, metal mixtures also remain a predominant trend of CGDS materials since they couple experimental deposition facility and advanced functionalization of metal matrix composites (MMCs). Metals provide a broad range of properties that can be combined via a CGDS deposition using specific powder mixtures to meet or to create performances. But CGDS MMCs include also metal matrix mixed with ceramic reinforcements (Al_2O_3, SiC, B_4C, WC, TiN). In both MMC cases, the cold spray process is less restrictive in terms of thermal coefficient expansion (TCE) compatibility due the low-temperature deposition that can prevent thermomechanical strain or stress mismatch. Table 3.2 represents various material pairs producing MMCs by cold spraying. Successful mixtures are metal/metal, metal/oxide, metal/carbide, metal/nitride and metal/ceramic.

Table 3.1 Successful enacted materials along the development of cold spraying

Materials enacted in cold spraying	Chronological evolution						
	1999	2003	2005	2006	2007	2008 …	Nowadays
Metals and alloys							
Composites (MMCs)							
Ceramics							
Oxides							
Nanomaterials							
WC cermets							
Intermetallics (IMCs)							
Amorphous metals							
Polymers							
Energetic materials							
MCrAlY systems							

Table 3.2 Variance of MMCs produced by CGDS

Phase	CTE (10^{-6} /°C^{-})	*Materials*	Successful material combinations for CGDS MMC deposits										
Ceramic reinforcement	8–9	Al_2O_3				●		●	●	●			
	5–6	B_4C				●			●				
	–	*CuO*				●							
	4–5	*SiC*				●		●				●	
	9–10	*TiN*				●		●					
	5	*WC*							●				
Functional metals	23	*Al*		●				●			●	●	
	16	*Cu*				●							●
	12	*Fe*				●							
	13	*Ni*	●			●							
	8.5	*Ti*			●	●							
	30	*Zn*				●							
Metal matrix			*Sn*	*Zn*	*Mg*	*Al*	*Ag*	*Cu*	*Ni*	*SS*	*Fe*	*Ti*	*W*
Melting point (°C)			230	420	650	660	960	1080	1455	1500	1530	1660	3420
CTE (10^{-6} /°C)			23	30	25	23	19	16	13	15–17	12	8.5	4.5

Table 3.3 Functional improvement based on nanocrystalline powders and CS deposition

Nanocrystalline	Functional improvements	References
Al	Fatigue strength improvement	Ghelichi et al. (2014)
Al	Significant hardness increase	Ajdelsztajn et al. (2005)
Al-Mg	Significant hardness increase	Richer et al. (2006)
Al_xNi_y	Faster and higher reactivity	Bacciochini et al. (2012)
Cu	Wear resistance improvement	Liu et al. (2012)
Ni	Significant hardness increase	Ajdelsztajn et al. (2006a)
NiCrAlY	Stable oxidation resistance at high temperature	Zhang et al. (2008)
WC-Co	Significant hardness increase	Yandouzi et al. (2007)

Note that the cold spray method includes new material events as well. Amorphous materials and nanofeatured materials also rank among recent innovative material trends in CGDS, with a growing interest. For amorphous materials such as bulk metallic glasses (BMGs), the cold spray additive manufacturing can become an alternative process of bulk component fabrication since such materials are brittle and highly resistant to be easily formable without any assisted thermomechanical softening that also can change the primary amorphous structure. With cold spraying, the additive deposition directly forms and shapes a part, while the initial structure is retained due to the low-temperature deposition. Likewise, the cold spray method is generally compatible with other thermally sensitive materials including polymer, intermetallics, energetics materials and nanocrystalline metals, for which the cold deposition also prevents structural transformations or thermally activated phenomena. This is why cold spraying became more and more attractive in such situations, since a decade, and particularly for nanocrystalline metals. The possibility to retain the nanocrystallinity is crucial for those materials to preserve their intrinsic properties. Against standard crystalline metals, they increase the hardness, the fatigue resistance and the wear resistance (Ajdelsztajn et al. 2005, 2006a, b; Richer et al. 2006; Yandouzi et al. 2007; Li et al. 2007; Hall et al. 2008; Zhang et al. 2011; Liu et al. 2012; Ghelichi et al. 2014), improve the reactivity of energetic compounds or foster a stable oxidation resistance at high temperature (Zhang et al. 2008; Bacciochini et al. 2012) (Table 3.3). Using nanocrystalline powders, CGDS can thus produce such performance for a surface functionalization as well as for a bulk component. With the constant development of material systems based on nanofeatures, the development of nanotechnological solutions will remain a future research direction for the CGDS technology.

3.4 Overview of Technological Solutions Generated by the Generic Modern CGDS

Numerous technological solutions derived from the compatibility of CGDS with various materials including both coeval and advanced materials. This versatility of CGDS has enabled a broad possibility of functionalization (Table 3.4), and

Table 3.4 Overview of CS technological solutions and typical application sectors

Functional properties of CGDS deposits	Investigated materials for CS deposits																Typical application sectors
	Metals and alloys	Metal/ polymer	MMCs: M/ceramic	MMCs: M/M	Inter-metallics (IMCs)	Oxides	Cera-mics	WC cermets	MMCs/ cermets	MAlCer	MCrAlY	Stellites	Carbides	Polymers	Thermites	Nano-materials	
Corrosion resistant	●	●	●	●	●				●	●	●	●	●			●	Aerospace, automotive, electronics, defence, petrochemical, oil industry, energy
Oxidation resistant	●	●		●	●	●			●	●	●						
Erosion (electric, by cavitation,) resistant	●		●					●				●	●			●	Aerospace, naval, electrical applications
High specific strength	●	●	●		●		●									●	Various industrial sectors
Wear resistant	●		●	●	●	●	●	●	●							●	Automotive, aerospace, machining, arts
Abrasive	●							●				●				●	Various industrial sectors
Antifriction (sliding components)	●			●								●					Various industrial sectors, civil engineering
Specific bonding layer	●									●	●						Various industrial sectors

Restoration	●		●														Aerospace, defence, petrochemical
Bulk material	●													●		●	Various industrial sectors
Biocompatibility	●					●								●		●	Biomedical (surgical implants)
Antibacterial	●	●				●								●			Biomedical
Conductive/ insulation (electrical, thermal)	●		●	●		●	●			●						●	Electronic, aerospace, energetic
Photovoltaic performance	●		●			●										●	Energy generation industry
Photocatalytic performance	●					●										●	Energy generation industry
Energetic materials	●				●	●									●		Energy generation industry, energetic

meaningful contributions can be attributed to combined materials producing MMC deposits albeit metals have long been exploited since the primary feasibility studies. Among CGDS functional metals, copper, aluminium and silver confer a suitable matrix for high effective conduction (electrical or thermal) performance. Zinc, aluminium and stainless steel as well as oxide-based systems have been used as protective coating against the chemical atmospheric corrosion of ferrous alloys and magnesium alloys. A CGDS deposition of superalloy material can also produce corrosion-resistant coatings subjected to a strongly heated and aggressive media. Ti-based and Ni-based superalloys are typical CGDS deposits explored for surface multi-functionalization including a protection against erosion or oxidation under severe conditions and a longevity conferred by their good thermomechanical resistance of Ti and Ni at high-temperature exposure. Typical applications are diesel combustion chamber, turbines engines, aircraft engine component and so on in the motor vehicle industry, the power engineering sector and the aerospace applications. Those examples do not restitute all of the technological solutions developed from metal powders, but they illustrate the great potentials of CGDS using such powders for specific and modern functionalization.

MMC CGDS coatings enable the combination of various material performances and found a broad application. Hard materials are generally combined with metals (easily processable in cold spraying) to produce a wear-resistant coating. Typical successful hard powders are oxide, carbide, nitride and ceramics. Those ceramic/metal coatings can resist high-temperature mechanical loading while fostering an increased durability for a variety of applications such as cutting tools, grinding tools, spacecraft shielding, high-temperature turbine blades, combustion chamber, etc. However, with the flexibility of material combination in cold spraying, the performances created by CGDS metal matrix composites are manifold and also multifunctional, for instance, a good wear behaviour and an increased fatigue strength, a high thermal conductivity combined with an increased creep resistance, a double function of great creep and corrosion resistance at high temperatures, a coupled high electrical conductivity and mechanical resistance, a combination of structural thermomechanical longevity-weight-lightness and so forth coupling several performances of electrical, mechanical, thermal, magnetic and chemical properties depending on the specific requirements. The capability range of CGDS MMCs is certainly wider than this non-comprehensive performance survey, and both current and future investigations will bring additional accomplishments.

Among the CGDS current innovative trends, there is the use of nanomaterials to develop optimized functions or highly performant MMCs. Carbon nanotubes (CNTs) have recently become a CGDS material, investigated for their unequalled properties: high thermal conductivity up to 3000 Wm^{-1} K^{-1}, very high strength up to 63Gpa, high stiffness of about 1TPa and very low coefficient of thermal expansion at both low and high temperatures (~0.5 10^{-6} K^{-1} below 500 K, ~4 10^{-6} K^{-1} at 1600 K) (Bakshi et al. 2008; Cho et al. 2012; Pialago et al. 2013). CGDS MMC-CNT mixtures have been explored for thermal management materials for new generation of electronic devices offering a better longevity and high thermal efficiency. Tribology needs exploit CNT-based coatings such as CNT/Cu and CNT/Al MMCs

(Bakshi et al. 2008; Cho et al. 2012; Pialago et al. 2013) to combine high thermal stability and high mechanical performances. Otherwise, recent CDGS applications have also been extended to biomedical field with the development of biocompatible coating. A few composites (HA/Ti and HA/PEEK) have been investigated to promote the consolidation of implant onto bones through a good biocompatibility (Zhou and Mohanty 2012; Lee et al. 2013). The low-temperature deposition during cold spraying can prevent undesirable thermally activated changes and particularly the oxidation of the titanium or the deterioration of the hydroxyapatite bioactivity.

Together, those technological solutions reflect the real CGDS capabilities towards more possibilities for various applications. They are numerous to be completely reviewed, but Table 3.4 addresses however a typical depiction that gives an overview of the cold spray pragmatic contributions.

3.5 Low-Pressure Cold Spray Deposition with New Possibilities and Benefits

Although the cold spray additive manufacturing has already experienced a substantial material diversity, a recent technological prowess related to a material issue has been achieved. This concerns especially the case of deposit/substrate hybridation. Generally, the material dissimilarity between the feedstock powder and the substrate involves an intrinsic incompatibility, whereas the surface functionalization technology increasingly introduces such a combination challenge. Note that outside technological domain, there is also a specific interest given to this new trend of combination in the field of art and aesthetic. Artistic practice painting on various panel natures (glass, rusty sheets of iron, copper plate) using different feedstock powders (copper, lead, zinc and aluminium) as paintwork has been explored (Petri Vuoristo 2015). Regarding the aesthetic application, the LPCS deposition is exploited for the metallic decoration of wine glass (Petri Vuoristo 2015).

In the literature of cold spraying, the ‘hybrid deposit/substrate assembly’ is the current generation of technological breakthrough with numerous combination achievements as follows: oxide/ceramic (Fan et al. 2007; Yang et al. 2011; Chun et al. 2014), oxide/polymer (Burlacov et al. 2007; Chun et al. 2008a, b), metal/polymer (Zhang et al. 2005; Lupoi and O’Neill 2010; King et al. 2013; Gardon et al. 2013), metal/PMCs (Robitaille et al. 2009; Lupoi and O’Neill 2010; Zhou et al. 2011), polymer/metal (Xu and Hutchings 2006; Alhulaifi et al. 2012), metal/ceramic (Zhang et al. 2005; King et al. 2010; Jung et al. 2010; Kim et al. 2013), ceramic/metal (Chun et al. 2008a, b; Wang et al. 2010; Seo et al. 2012) and cermet/metal (Yandouzi et al. 2007; Ang et al. 2011; Dosta et al. 2013; Couto et al. 2013; Ji et al. 2013). Due to the powder/substrate dissimilarity in terms of mechanical behaviour and/or thermal sensitivity, the major difficulty for that hybridation fulfilment relies on the adhesion capability without destroying the substrate during the collision or overheating the gas during the deposition. Either way, bonding and deposit

Table 3.5 Hybrid deposit/substrate combinations produced by LPCS

Hybrid nature	Hybrid coating/substrate combinations	References
Oxide/ceramic	WO_3/Si Al-Al_2O_3(10–90)/Si Al-SiC(10–90)/Si	Lee et al. (2004a) Lee et al. (2005) Lee et al. (2004b)
Oxide/polymer	TiO_2/ PEEK, PES, PET, PFVD, PPSU, PSU	Burlacov et al. (2007)
Metal/polymer	Cu, Sn/epoxy, PVC Cu/ABS, PC	Ganesan et al. (2013) Lupoi and O'Neill (2010)
Metal/PMCs	Al/CFR-PEEK Cu/CFRP Zn/CFR-epoxy	Zhou et al. (2011) Lupoi and O'Neill (2010) Robitaille et al. (2009)
Polymer/metal	PE/Al PPA/Al	Alhulaifi et al. (2012) Xu and Hutchings (2006)
Metal/ceramic	Al/PZT Cu/glass, Si	King et al. (2010) Kim et al. (2013)
Ceramic/metal	SiC/Inconel	Seo et al. (2012)
Else	HA/PEEK HA_Ag-PEEK/glass	Lee et al. (2013) Sanpo et al. (2008)

consolidation easily fail because of unsuitable gas working conditions. The review of successful depositions rather recommends a low pressure, mostly below about 12–15Bar, and a low temperature working. The LCPS condition is conclusive for a variety of experienced hybrid natures (Table 3.5). For instance, a working gas set to 6–8Bar and 280 °C produces a SiC/Inconel adhesion (Seo et al. 2012) as well as a formation of a copper 300 μm thick onto a ceramic substrate (Kim et al. 2013). For polymer metallization, a gas pressure of 10Bar is appropriate with a preheating below 500 °C typically which can prevent undesirable thermal effects of the substrate surface exposed to the impinging gas flow. Soft metals having low melting temperature such as tin and zinc are also found to be suitable for LPCS (Lupoi and O'Neill 2010; Zhou et al. 2011; Ganesan et al. 2012, 2013). Used as an intermediate bonding layer, they enable the obtainment of thick metal coating on a polymer substrate (Ganesan et al. 2012, 2013). For carbon or glass fibre-reinforced composite substrate, a low-impact energy prevents a structural degradation and a soft metallic particle is also conclusive, e.g. tin and aluminium for GFRCs and CFR-PEEK substrate, respectively (Lupoi and O'Neill 2010; Zhou et al. 2011; Ganesan et al. 2012, 2013). In the reverse situation, i.e. for a polymer/metal hybridation of the deposit/substrate assembly, a good deposit formation was obtained using a propellant gas set to 275 °C and 5Bar, which is quite similar to those previous gas working conditions (Alhulaifi et al. 2012).

At present, the cold spray technology has gained new benefits with the recent launch of compact LPCS system, designed to be portable and easy to handle. This method has quickly matured to be cogently used in restoration and repair. LPCS deposition has been extensively employed for structural, dimensional or functional repair of various metallic components regardless their size, with the possibility of on-site repair. Thereby, the LPCS system brings a refurbishment solution that can substantially contribute to the current and future ecological challenges. The LPCS

repair is an efficient eco-friendly option for the purpose of recycling which can help to avoid the ecological impacts related to a new manufacturing and particularly the eco-impacts related to the raw material extraction, the energy consumptions during the transformation processes, the logistics and the end-of-life management of the manufactured component. Furthermore, LPCS restoration is also recommended for economic arguments (Christian Widener et al. 2012; Neil Matthews 2012; Ed Malison 2013; Christian Widener 2014; Roman Gr. Maev et al. 2014) such as the opportunity of cost saving and decreased commissioning lead time. A typical application and meaningful gain can be found in aerospace sector which has recently adopted the LPCS repair. For instance, the LPCS repair of the corroded surfaces of helicopter modules allows for a cost saving up to 50% (Neil Matthews 2012) or to completely rehabilitate functional holes of high-speed airplane fasteners that gives an increased longevity of the B1-bomber US engine. The LPCS repair produces both restored dimensions and restored structural performance that pass several validation tests and thus confers a life extension (Christian Widener et al. 2012). Specific repair and control procedures (MIL-STD-3021) have been performed in the US Department of Defense to suggest a sort of standard use of the LPCS repair in this sector (Champagne and Helfritch 2015). In automotive sector, interests given to the LPCS repair have resulted in a full refurbishment of a big-sized cast magnesium-based structure (Roman Gr. Maev et al. 2014). Those pragmatic benefits reward the efforts to exploit the full potential of LPCS. But the LPCS repair also found a crucial application regarding the dimension compensation of large or costly structure machined with inaccurate dimensions. The LPCS on-site restoration of the functional dimension prevents superfluous wastes, saving thereby meaningful costs. A bad machining remains a prominent manufacturing risk, especially in the case of tight tolerance combined with a large surface of machine. Such circumstance was met for some machined block engines having a final dimension 0.46 mm under the accurate tolerance. A LPCS deposition then enables a dimensional compensation for an accurate rectification in accordance with the true functional dimension (Roman Gr. Maev et al. 2014). Likewise, LPCS has been similarly used to rehabilitate a body in white damaged by a surface embossment (Roman Gr. Maev et al. 2014). Note that LPCS restoration covers other application fields such as art sector. In this respect, typical successful completion is the in situ restoration of antique metallic sculptures using a compact low-pressure CS system (Kashirin et al. 2017). With those typical examples, the benefits of LPCS are very persuasive. However, the LPCS method generally fails to reach high deposition efficiency (DE), this being a main limitation to go through. The DE is weak, about 10% even lower when working with a 6Bar compressed air (Ning et al. 2007; Ogawa et al. 2008; Raoelison et al. 2016). For an affordable employment of LPCS, i.e. using air or nitrogen as propellant gas, the DE remains low and does not generally exceed 40% despite various improvement combinations including gas, nozzle and particle features (Ning et al. 2007; Irissou et al. 2007; Melendez and McDonald 2013; Raoelison et al. 2016). Thus, in terms of high-volume powder consumption, LCPS can become less cost-efficient so that the conditions of optimum deposition efficiency need to be identified to encourage an economically viable use of this method.

3.6 Very-Low-Pressure Cold Spraying and Advanced Technological Solutions

The VLPCS method has received a particular interest for the additive manufacturing of fine powders from a few microns down to some nanometres (~5 μm–20 nm). Typically, the working pressure is in the range of 0.1–20 kPa (Chun et al. 2008b), and the deposition operates within a vacuum chamber under a condition of non-preheated propellant gas. In the literature, the term nanoparticle deposition system (NPDS) has been communicated to specify the CS apparatus for such purpose. This deposition method is also called vacuum cold spraying (VCS). Pragmatically, this method is of relevance to the fabrication of nanoporous media or thin solid coatings (Fan et al. 2006a; Yang et al. 2007, 2012; Jung et al. 2010; Wang et al. 2012), especially since nowadays, while porous materials have become an innovative material, whereas in the past, dense materials free of pores and cavities have long been developed to ensure a good structural integrity. Henceforth, the manufacturing of a micron and submicron porous structure has received increasing attention (Table 3.6). Energy absorption (Wang et al. 2013), storage capabilities (Xia et al. 2013), removal or cleaning functions (Lefebvre et al. 2008), osseointegration improvement of surgical implants (Ryan et al. 2006), conduction properties (Luan et al. 2012) and catalytic performances (Fan et al. 2006b) are some of the newly advanced technological solutions conferred by a fine porosity. The vacuum spraying method has mostly been applied to the elaboration of nanoporous TiO_2 coating for dye-sensitized solar cells (DSSCs) whose performance is directly affected by the nanoporous structure. Harnessed for photovoltaic and photocatalytic properties, the nanopores within the TiO_2 coating can be obtained by a direct deposition of nanopowders that forms nanopores between unbonded surfaces during the coating formation. The vacuum

Table 3.6 Submicron porous features and functional performances developed by VLPCS

Powder	Porous feature	Functional property or performance	References
$TiO_{2\ ns}$[a]	Unimodal nanopores (~19 nm)	Photocatalysis for water purification, photovoltage for DSSCs and ECI[b] of 5%	Yang et al. (2007, 2012)
$TiO_{2\ np}$[c]	Bimodal nanopores (10 nm,50 nm)	Better photoelectron production increasing the photovoltage capability of DSSCs	Fan et al. (2006a), Yang et al. (2012)
TiO_2-PEG	Large nanopores	Better photocatalytic activity of solar cell and energy conversion efficiency of ~7%	Yang et al. (2007)
TiN_{ns}[d]	Pore size of 2–8 nm, porosity > 50%	Combination of high electrical resistivity with high fracture toughness	Wang et al. (2012)

[a]Nanosized TiO_2 powders (25 nm)
[b]ECI: energy conversion efficiency
[c]Nanoporous TiO_2 prepared by a TiO_2-PEG mixture + a PEG removal process
[d]Nanosized TiN powders (20 nm)

deposition without any gas heating ensures suitable kinematics for the successful impingement and adhesion of such fine particles. The cold deposition combined with high-impact pressure enables the direct consolidation of the TiO_2 nanostructure as well as the self-assembling with the glass anode. Against conventional manufacturing based on sintering method that generally uses an enclosure thermally controlled system, VLPCS can work on large surfaces to be covered by a continuous coating. In addition, VLPCS deposition of TiO_2 nanoparticles provides some attractive benefits such as the manufacturing cost (Fan et al. 2007) and the nanoporous structuration (Yang et al. 2007, 2012; Sova et al. 2013). VLPCS nanoporous TiO_2 coating also promotes reactant transports required for treatment purification efficiency (Yang et al. 2007). Furthermore, the low-temperature deposition allows to overcome the restrictions of thermal effect. For instance, a TiO_2 coating was performed on metal and polymer substrates without any thermally activated deterioration (Chun et al. 2008a, b). Otherwise, the nanoporous structure produced by VLPCS of nanosized powders has also been explored for other performances. In Wang et al. (2012), 20 nm sized TiN particles were deposited to generate a 70 µm thick porous coating with nanopore size and proportion of about 2–8 nm and 58–67%, respectively. The nanoporous deposit combines high electrical resistivity, high fracture toughness and low microhardness (Wang et al. 2012).

Instead of a direct deposition of nanosized particles, some studies have preferred a preparation of nanoarchitectured powders which consist of agglomerated TiO_2 nanoparticles mixed with a removable PEG phase. The TiO_2-PEG mixture is elaborated by a rotatory evaporation process and then crushed into fine agglomerates (0.5–3 µm) used as primary powders (Fan et al. 2006a). Nanoporous powders can be generated by removing the PEG phase using a selective removal process. Chemical and sintering treatment can consolidate the nanoparticle cohesion to keep the nanoporous structure. A direct deposition of such nanoporous powders allows for producing bimodal-sized nanopores with an increased photovoltage capacity compared to conventional unimodal distributed nanoporosity produced by the direct deposition of nanopowders (Yang et al. 2012). Note however that the PEG removal can also be a post annealing step. In this circumstance, the primary TiO_2-PEG powders are deposited, and the TiO_2-PEG coating is thermally treated to keep the TiO_2 media alone (Fan et al. 2006a; Yang et al. 2007). Compared to the results given by the direct deposition of TiO_2 nanoparticles, the spraying condition being the same, this approach confers large nanopores with an increased photocatalytic activity (Fan et al. 2006a). Otherwise, the post annealing removal approach provides also a better overall energy conversion efficiency against the direct deposition of nanoporous powders (Fan et al. 2006a). Today, a porous photocatalytic TiO_2 coating with a thickness of some dozen µm can be produced by VLPCS. The nanopores increase the production of photoelectrons and thus contribute to a better conversion efficiency which can reach up to 7.1% (Fan et al. 2006a, 2007; Yang et al. 2012), against 5% for a more dense TiO_2 coating obtained by a VLPCS direct deposition of TiO_2 nanopowders. To be competitive, the VLPCS-coated DSSCs should go through the efficiency of about 10% provided by the current commercialized DSSCs. Improvement efforts in that direction have

highlighted real issues related to the sensitivity of the photovoltaic solar cell performance to some process parameters. The powder preparation as well as the coating post-treatment (Fan et al. 2006a, c; Yang et al. 2012), the vacuum pressure level (Fan et al. 2007) and the propellant gas flow (Yang et al. 2011) appear to have major effects. Their optimization will contribute for a better process proficiency despite the significant achievements of VLPCS.

A further application of VLPCS is the fabrication of electrical heating ceramic-based coating, electrically conductive and having a good oxidation resistance at high temperature (Wang et al. 2011). VLPCS thin SiC-$MoSi_2$ deposit was performed to meet such requirements. A 10 µm thick dense stacking was produced. There is a three-fold decrease in electrical conduction while increasing the propellant gas flow rate until a critical value. But a deep understanding of the interactions between process parameters, structural features and functional intrinsic performance should be investigated to provide further insight into ways of improving the deposition procedure and thus to endorse the VLPCS method as a viable manufacturing technology.

In a series of recent studies, the VLPCS deposition of nanoparticles at room temperature has been presented as a potential coating process without thermal damage (Chun et al. 2008a, b, c, 2012, 2014; Jung et al. 2010; Chun and Ahn 2011). Developments have resulted in significant achievements in terms of material possibilities and coating/substrate combinations as follows: Al_2O_3/Al_2O_3 (Chun and Ahn 2011), (Sn, Al_2O_3, TiO_2)/(Si, Al_2O_3) (Chun et al. 2014), TiO_2/(SS, Sn, Cu, Al, PMMA, PET) (Chun et al. 2008a, b) and Ni/Si (Jung et al. 2010). Foremost, this method can produce a thin micrometric layer (Jung et al. 2010), a nanometric film (Chun et al. 2008a; Chun and Ahn 2011) or multilayered thin deposits made of various combinations of stacked materials such as Sn/Al_2O_3/Sn onto a silicon wafer, TiO_2/Al_2O_3/Sn onto a silicon wafer or TiO_2/Al_2O_3 onto a sapphire substrate (Chun et al. 2014). A typical multilayer stack is illustrated in Fig. 3.6. However, the sensitivity of the deposition requires some cautions such as a short standoff distance, a careful motion control and a specific nozzle (Jung et al. 2010).

3.7 Novel Hybrid Variant of CS Manufacturing for Submicron 3D Architecturation

To date, the advent of nanotechnology marks a new age of technological progress. The manufacturing technology has recently included the microscale working and is also evolving towards the nanofabrication. A recent study reported an overview of 3D nanoscale manufacturing processes while noting common specific difficulties: a limitation due to process difficulties such as manufacturing accuracy, effect of processing conditions, geometrical constraints and materials availability (Ahn et al. 2011). The additive manufacturing technology is a new approach which has recently been investigated to go through such restrictions with the merits to be a more rapid manufacturing method, able to a 3D architecturation and working at low temperature, regarding particularly the VLPCS process (Ahn et al. 2011). For this purpose,

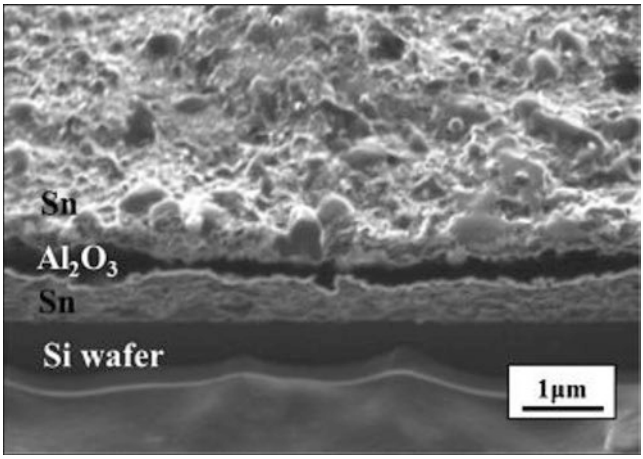

Fig. 3.6 VLPCS multilayered thin stacks using various materials (Chun et al. 2014)

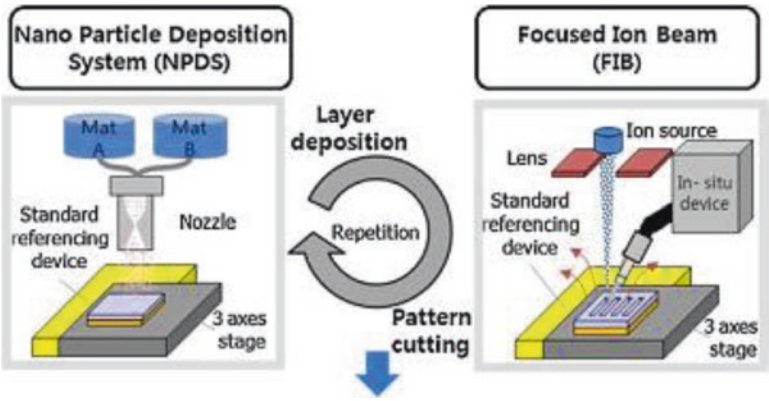

Fig. 3.7 Novel nanoscale hybrid manufacturing method for a 3D nanoarchitecturation (Ahn et al. 2011)

outstanding works have been conducted at the School of Mechanical and Aerospace and Institute of Advanced Machinery and Design of the Korean Seoul National University. Korean researchers have greatly developed the VLPCS deposition of nanopowders. The additive manufacturing of multilayered nanothick materials as presented in the previous section (Fig. 3.6) has already been a major milestone in the field of nanofabrication. They have combined this capability with a nanosubtractive process to perform a nanoscale 3D manufacturing method that relies on a sequential deposition-cutting process (Ahn et al. 2011). The VLPCS process, denoting NPDS, produces the deposit layer, and an in situ focused ion beam (FIB) process shapes the 3D architecturation (Fig. 3.7). The repetition of the layer deposition and a pattern cutting spatially tailored thus produces the 3D nanostructured and nanoshaped workpiece.

Ahn et al. underline various advantages of this hybrid manufacturing process, the NDPS method providing a non-heated processing, the use and combination of several materials, a high deposition rate and the dry working condition without needs of post-processing, neither binder use nor solutions requirements (Ahn et al. 2011). The FIB method enables a direct subtractive shaping, an incredible precision due to a fine resolution in the range of nm, a room temperature working condition and a large solid material scalability. Together, those benefits give a 3D submicron structure by a fast fabrication without undesirable chemical or thermally activated reactions and with a great flexibility in terms of material possibility in addition to a good repeatability.

By means of the hybrid NDPS-FIB method, Ahn et al. have performed some fiddly feasibilities. A typical substantial technical achievement is the multilayer structuration combining thin deposition and fine texturation as illustrated in Fig. 3.8. A FIB texturation creates a micro hole across a thin Sn layer deposited onto a Si wafer. The cold spray deposition of Al_2O_3 nanoparticles generates a new media filling the pocket and covering the Sn layer. On the Al_2O_3 layer, a Sn deposit was produced again, and those successive operations can be repeatedly reiterated to manufacture multilayered, multimaterial and finely architectured stacks.

In Fig. 3.9, further capabilities based on the FIB cutting possibilities are demonstrated. With a rectangular shape cutting, a multilayer stack is transformed into a rectangular block that emerges from the primary substrate (Fig. 3.9a). Each layer of

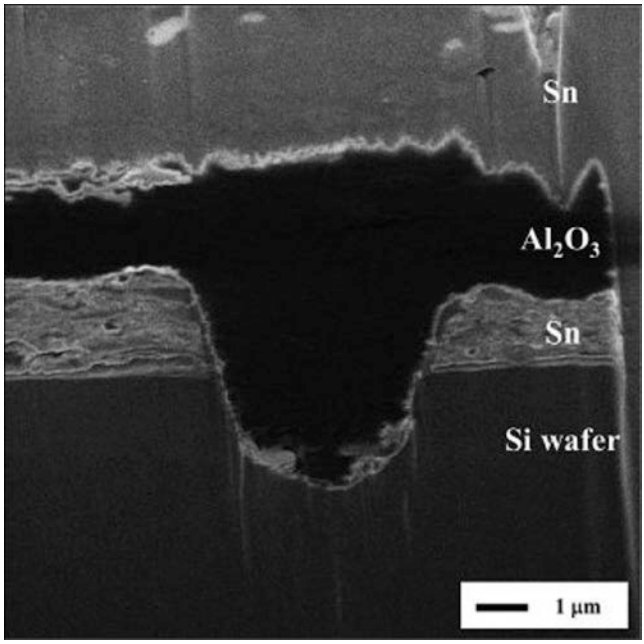

Fig. 3.8 Multilayer and multimaterial structuration of thin films combining thin deposition and fine texturation (Ahn et al. 2011)

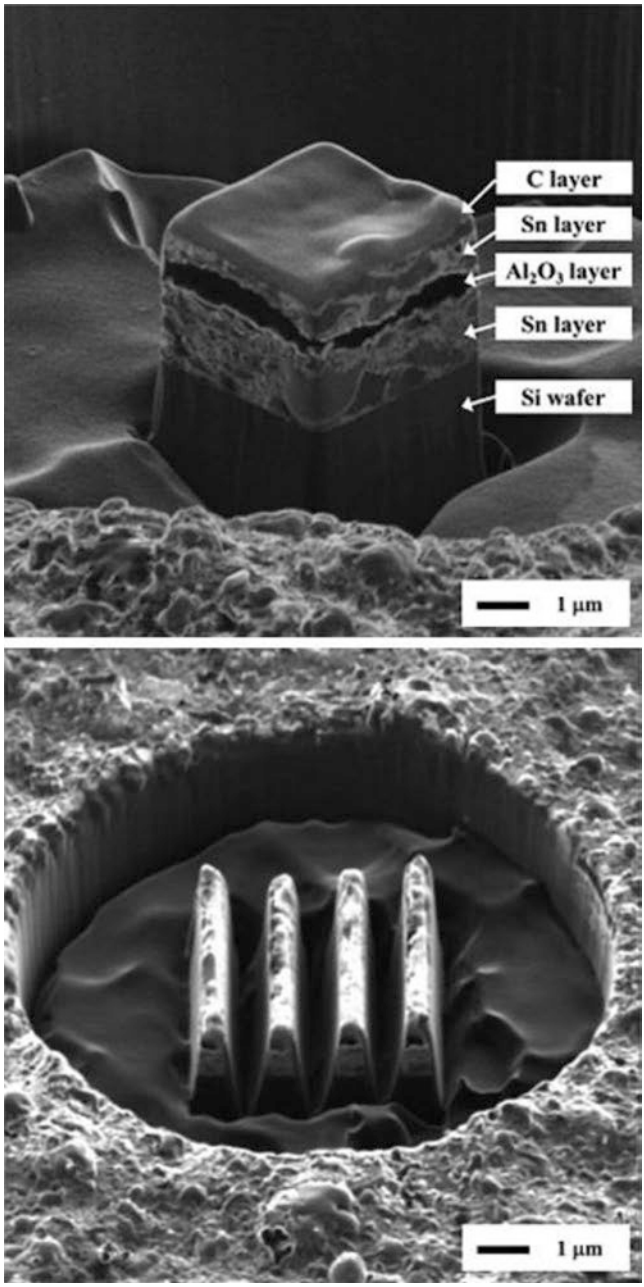

Fig. 3.9 Multilayered, multimaterial and fine 3D architecturation using hybrid NDPS-FIB deposition-shaping method (Ahn et al. 2011)

the 3D block is evidenced as well as each face and each edge. The sharpness of the 3D structuration clearly appears although some apparent heterogeneity of layer thickness can be observed. The authors attributed this nonuniformity to the granulometry of the powder feedstock that has a sparse distribution (Ahn et al. 2011). Figure 3.9b presents another 3D architecturation that also exhibits a clear sharpness and more complex shaping using circular cutting prior to a line shape cutting. A submicron profile made of a periodic line pattern is fabricated. Thereby, the hybrid NDPS-FIB method is shown as a process for patterning multilayered thin films. Those achievements make the cold spray-based method an encouraging technology for 3D submicron manufacturing including the possibility of material structuration at this same scale level. A further better control of the cutting beam during the FIB step will bring new perspectives with probably more novelties. This aspect drives the future R&D actions towards more added values (Ahn et al. 2011).

3.8 Laser-Assisted Cold Spraying Method to Generate Positive Thermal Effect

The cold spray method was substantially exploited for the various specific advantages offered by the low-temperature deposition as outlined through the previous sections. However, despite the prominent technological contributions, the major benefit of the cold gas dynamic spray, i.e. the cold gas state due the gas expansion throughout the de Laval nozzle which is required to generate the supersonic velocities, can also be a main weakness. The CS method can suffer from kinematic limitations which raise issues of deposition efficiency, particularly regarding either LPCS and VLPCS methods or also HPCS of difficult material combinations. The improvement of the deposition efficiency can be as challenging as developing novel viable applications. In the literature of cold spraying, the use of an assisted laser heating has been considered to gain positive thermal effects that improve the deposition capability or enable increased deposit features (Kulmala and Vuoristo 2008; Bray et al. 2009; Ahn et al. 2012; Christoulis et al. 2012; Olakanmi et al. 2013; Yao et al. 2015; Olakanmi 2016). The laser system is a moving heat source which interacts with the particles and/or the substrate to facilitate the deposit formation by thermomechanical softening which promotes the interfacial bonding during the deposition. Thereby, laser-assisted cold spraying (LaCS) increases the processability condition of difficult deposition circumstances. The heating laser beam is synchronously tailored with the nozzle motion, and three major distinctive variances have been adopted depending on how the laser beam is positioned with respect to the powder beam of the nozzle. Christoulis et al. (2010, 2012) use the laser beam to preheat the substrate and each deposited layer while fixing a spatial offset in between the laser spot and the powders beam (Fig. 3.10a). The conjugated scanning (Fig. 3.10b) evolves in a single direction to produce a continuous and regular heating over the top surface of the substrate or the deposited layer (Fig. 3.10b). The preheating time

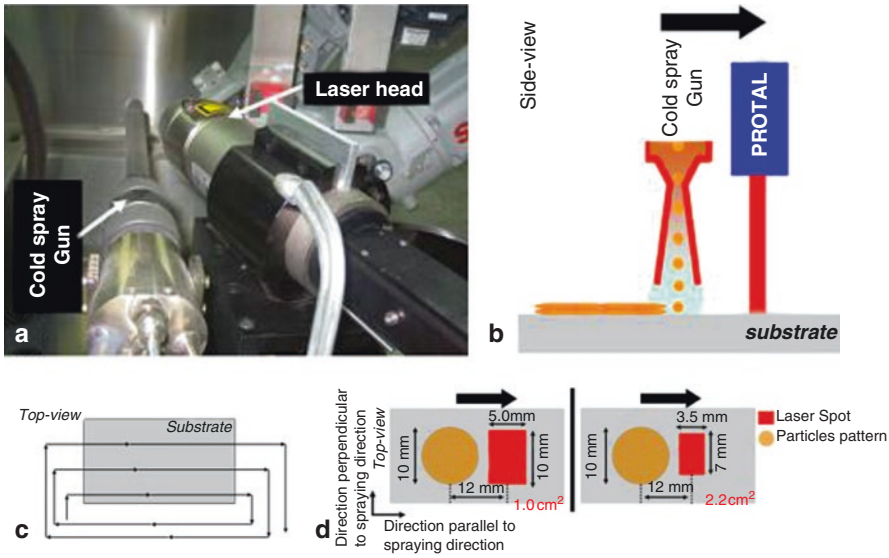

Fig. 3.10 LaCS system enacted as a preheating + deposition processing (**a**) based on a spatial offset between the laser beam and the nozzle jet (**b**), using a single-direction scanning principle (**c**) and laser suitable spot size setting via the input energy (**d**) (Christoulis et al. 2010)

laps are in the range of some milliseconds before the particles collide onto the preheated zone. The laser spot is tailored via the laser input energy to be matched with the particle spot size to cover the deposition zone along the preheating pattern (Fig. 3.10d). Against usual cold spray manufacturing that generally needs a stand-alone surface preparation prior to the deposition operation, this LaCS variance is also presented as a single-step process, combining those two stages of usual CS, and enables producing coatings with a better densification and structural consolidation (Christoulis et al. 2012). In addition to the preheating function, the laser beam can also produce an ablation to clean the substrate surface (Christoulis et al. 2010). The treatment of the substrate under such conditions fosters a coating thickening suggesting thereby a better deposition efficiency, as found during a HPCS deposition of Al powders onto a stainless steel substrate (Christoulis et al. 2010, 2012).

The other variance of hybrid LaCS rather generates a simultaneous heating of both particles and substrate by a concentric disposition of both laser heating spot and particles jet spot ahead the substrate (Kulmala and Vuoristo 2008; Bray et al. 2009; Yao et al. 2015) or by a coaxial disposition of both laser beam and nozzle (Ahn et al. 2012). The hybrid concentric LaCS variant has been enacted for HPCS (Bray et al. 2009; Yao et al. 2015) as well as for LPCS (Kulmala and Vuoristo 2008) using a simple oblique disposition of the laser beam as illustrated in Fig. 3.11. There is no particular recommendation about the inclination angle despite the possibility

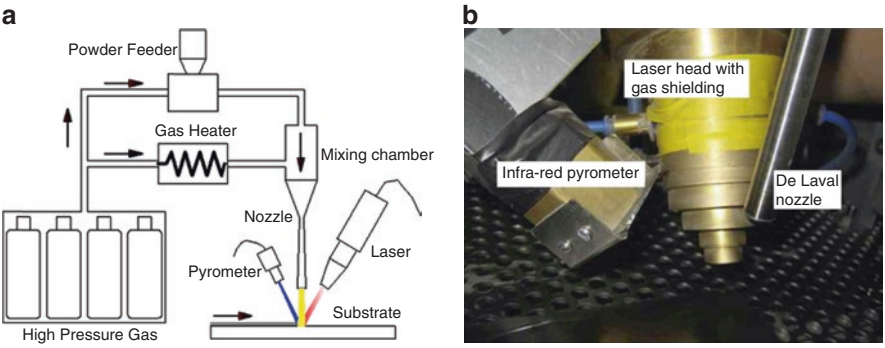

Fig. 3.11 Hybrid concentric LaCS variant method: (**a**) typical set-up architecture (Yao et al. 2015) and (**b**) experimental layout (Bray et al. 2009)

of non-uniform coating formation due to an asymmetric heating, as found using a disposition at 30° to the normal of the substrate surface (Yao et al. 2015). Some studies adopted an angle of 15° without any specific argument (Kulmala and Vuoristo 2008; Olakanmi et al. 2013), but however the expected results are obtained. In (Kulmala and Vuoristo 2008), the hybrid concentric LaCS is applied to LPCS to increase the deposition efficiency since the fact of poor DE is a major problem of LPCS. Indeed the working pressure ranges in between 6 and 12 bar on commercialized portable CS systems, and the gas heating does not exceed 600 °C roughly for the sake of longevity of the set-up components; the DE is thus weak, typically, in the range of 10% if using a 6 Bar standard pressure and air as propellant gas (Ning et al. 2007; Juha Lagerbom et al. 2007; Ogawa et al. 2008). Despite some prospective improvement factors including a long preheating of the powder feedstock (Ning et al. 2007), the use of irregular-shaped particles (Ning et al. 2007; Juha Lagerbom et al. 2007), the combination of metallic particle with ceramics (Juha Lagerbom et al. 2007; Irissou et al. 2007; Melendez and McDonald 2013) and the DE of LPCS remains weak, about 30% even combining some of those factors (Ning et al. 2007; Juha Lagerbom et al. 2007). High DE would be achievable using helium as propellant gas (Raoelison et al. 2016), but this makes the LPCS less attractive due to economic arguments. More affordable, nitrogen gas is generally preferred instead or air which is a free gas. The LaLPCS hybridation becomes an available alternative to remedy the situation of weak deposition efficiency. Results evidenced by Kulmala et al. are consistent with this tendency. LaLPCS depositions of copper-based coating and nickel-based coating onto grid-blasted low-carbon steel were performed using a 6 Bar compressed air, preheated at about 450 °C for the copper powders and 650 °C for the nickel powders, with the laser beam covering the powder beam spot but being less large in the scanning direction (Kulmala and Vuoristo 2008). Against a LPCS deposition, LaLPCS increases up to twofold the coating thickness with the laser local heating (up to 800 °C), and produces also a full densification of the copper

coating. Otherwise, the selective concentric laser heating can make HPCS economically viable. In (Bray et al. 2009), albeit the laser beam (spot size of 4 mm) heats the centre of the powder beam alone (spot size of 8 mm), a highly dense titanium coating is generated using unheated nitrogen gas, compressed at 30Bar. Yao et al. use the LaHPCS method, with a 30Bar nitrogen gas preheated at 550 °C and a focused laser heating up to 1000 °C, to produce diamond/Ni coating with a strong interfacial bonding and having appreciable features including a dense microstructure and non-transformed phases, those benefits providing together increased tribological performances (Yao et al. 2015). In Olakanmi et al. (2013), LaHPCS created corrosion-resistant Al-Si coating with a good structural integrity, while a 5 mm spot sized laser beam enhanced also the deposition efficiency.

The coaxial LaCS is a singular innovation of the LaCS approach, especially as this hybridation has been remarkably extended to the CS working of nanosized powders that requires vacuum condition deposition and micronozzle (Chun et al. 2008b; Jung et al. 2010). The coaxial disposition of the laser beam within the micronozzle is made of an optical device (Fig. 3.12a) driving the laser source from a beam expander to the substrate through the nozzle throat (Fig. 3.12b). Denoted as laser-assisted nanoparticle deposition system (LaNDPS), this tricky coupled architecture has the particular capability to heat the particles before and during the collision onto the substrate, while this latter is also simultaneously heated by the coaxial laser spot. Deposition of TiO_2 nanoparticles onto FTO-glass and ITO-PET substrates was performed to fabricate DSSCs. The coaxial laser heating enhanced the nanoparticles intercohesion and self-consolidation within a coating, thick up to 14 μm and free of physically and thermally activated damages, while keeping the

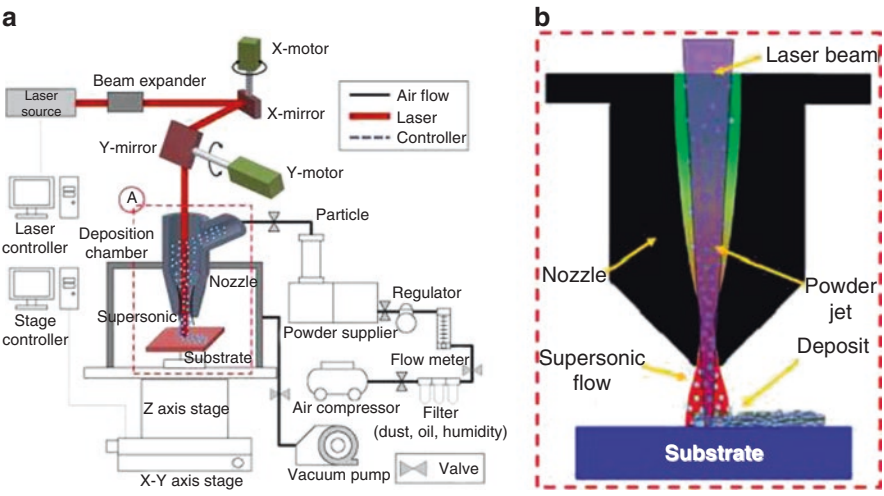

Fig. 3.12 Hybrid coaxial LACS variant method applied to vacuum deposition of nanosized powders (Ahn et al. 2012): LaNDPS set-up architecture (**a**) and coaxially disposition of both laser beam and powder beam (**b**)

primary anatase nature of TiO_2 particles (Ahn et al. 2012). Against NDPS coating (i.e. without laser assistance), LaNDPS coatings exhibit improved mechanical features such as the increase of elastic modulus and hardness from 1.7GPa to 5GPa and 0.22GPa to 0.31GPa, respectively (Fig. 3.13). Furthermore, the LaNDPS deposition contributes for better photovoltaic efficiencies (Ahn et al. 2012). Together, all these LaCS achievements are currently limited, but they are representative of the positive thermal effects expected with the laser assistance coupled with the cold spray deposition.

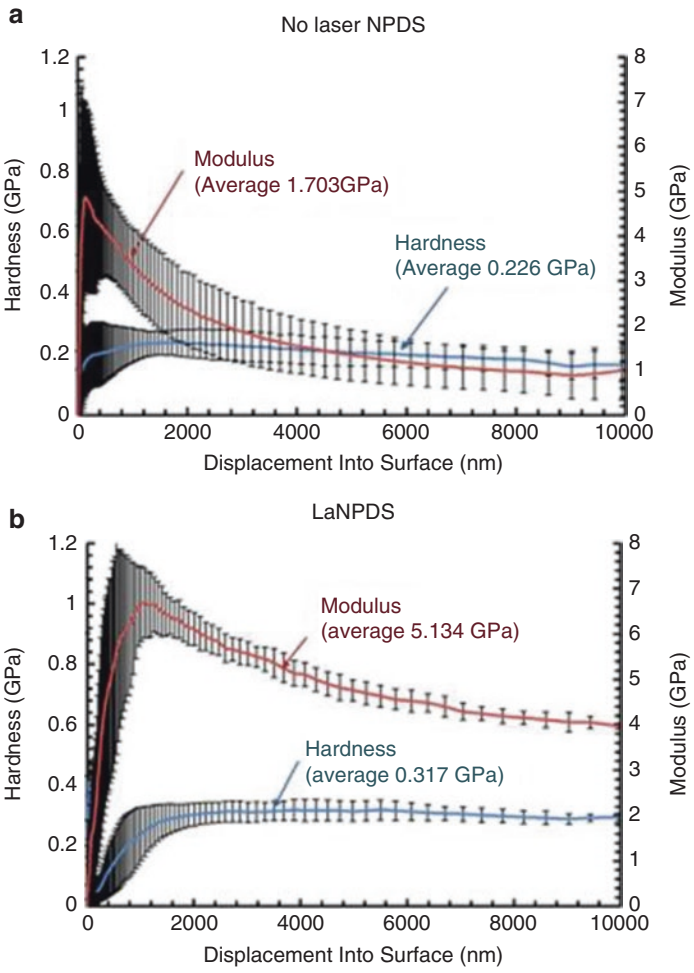

Fig. 3.13 Benefits of laser assistance for TiO_2 coating on ITO-PET substrate produced by LaNDPS, case without laser heating (**a**) and increased elastic modulus and hardness due to the laser heating (**b**) (Ahn et al. 2012)

3.9 Pulse Gas-Dynamic Spraying Providing High Kinematic and High-Temperature Deposition

PGDS is a new variance of the cold spray method. The particle kinematic is not governed by an expanding gas flow, but, instead, a development and propagation of compression waves produced by a cyclic shock impulse are used to accelerate the particles at high velocity, in the same range than in the usual cold spraying. The main benefit of this method relies on the circumstance of gas heating towards the nozzle exit, whereas in the usual cold spraying, the gas temperature decreases due to the expansion of the gas throughout the divergent section of the de Laval nozzle. In PDGS, the nozzle exhaust zone experiences a temperature increase due to compression waves. Figure 3.14 describes the architecture of a PGDS system. A tubular wave guide with a uniform cross section, which is the spray gun, is axially connected to a shock wave generator and receives particle inflows from a powder feedstock through a radial connection. The particles are accelerated by shock wave propagation within the quiescent inert gas in the spray gun and then collide onto a substrate at the gun exit. The shock wave generator consists in a cyclic pressure impulse using an intermittent activation of valves connected to a prechamber containing a compressed gas. Thereby, the short duration of admission of the high pressurized gas generates compression waves that develop shock waves inside the spray gun. The synchronization between the gas impulse and the powders admission is monitored by a computer, and the cyclic automation ensures a periodic deposition of particle flow to form a coating onto the substrate. The cycle is reactivated once the atmospheric pressure has been reached inside the gun (Jodoin et al. 2007). Researchers at the University of Ottawa Cold Spray Laboratory have been working extensively on this innovative cold spray method (Jodoin et al. 2007). It was demonstrated that the PGDS deposition covers the material benefits of usual cold

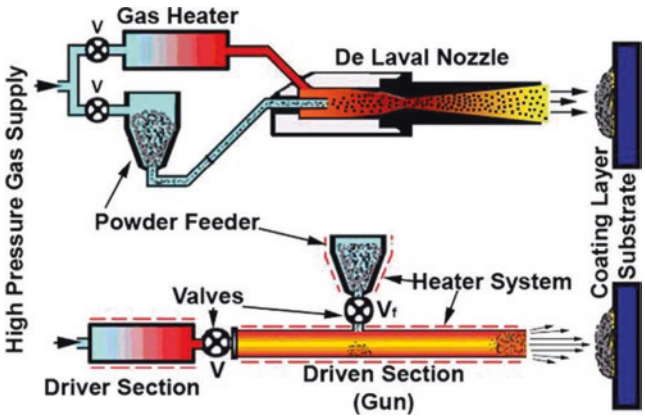

Fig. 3.14 Typical architecture of PGDS system compared with CGDS (Yandouzi et al. 2007)

spraying, and furthermore, PGDS enables more capabilities due to the combination of supersonic velocities with the circumstance of gas heating through the gun section. The PGDS can produce thick and dense coatings for several materials including metals, composites, nanocrystalline powder, amorphous compounds and cermets (Jodoin et al. 2007; Yandouzi et al. 2007; Sansoucy et al. 2008; Yandouzi et al. 2009). In addition, against CS, PGDS allows also for an increase of adhesion strength (Yandouzi et al. 2009), a better homogenization of composite coatings (Yandouzi et al. 2009), an improvement of coating property such as the hardness (Yandouzi et al. 2007) and a thickening of coatings made of hard powders (Jodoin et al. 2007).

According to a phenomenological characterization of the PGDS process Fan et al. 2007, both velocity and temperature within the exhaust zone of the gun increase with the pressure and the temperature of the gas in the shock wave generator. An effect of the pulsed gas nature was also found, and the speed of sound within the pulsed gas would be a major factor of kinematic efficiency. However, the better proficiency of the process can require a further identification of the different physical interactions that prevail. The simultaneous or asynchronous occurrence of the expansion of the pulsed gas, the mixing with the initially quiescent gas inside the gun, the compressive wave development and the shock wave propagation, depending on the property variances between those two gases, represent typical important factors to be further depicted for a better understanding of both kinematic and thermal aspects of PGDS. Otherwise, the response time of the pulse valve limits the efficiency of the shock wave generation. The development of valves with a very fast full opening and compatible servo-system will strongly contribute to the optimization of the PGDS process.

3.10 Concluding Remarks on the Capabilities of the Cold Spray Technology Today

Discovered in the 1900s, the cold spray additive manufacturing method has been developed over a century through three key milestones: the finding of Thurston in the 1900s, the invention of Rocheville in 1958 and the Russian developments of the 1990s. Thurston produced a permanent coating due to an embedment of metal powders into a metal substrate by means of blast air supplied by a pneumatic pressure. Rocheville introduced the enactment of the de Laval nozzle integrated in a system of two distinct stream lines, viz. a high-pressure line generating a supersonic gas flow through the de Laval nozzle and a stand-alone low-pressure line feeding the powders ahead the convergent-divergent line exhaust. Then, the supersonic gas acts as a blast current spreading the powders onto the substrate. Later, Russian developments adopted a principle of mixed two-phase flow (gas + particles) within the de Laval nozzle to achieve substantial progresses including high velocities up to 1200 m/s for 1–50 μm sized particles, deposition of continuous coating, various patents and process expertise. Denoted cold gas dynamic spraying (CGDS) by the

Institute of Theoretical and Applied Mechanics of the Russian Academy of Sciences (ITAM-RAS) in Novosibirsk, the cold spray additive manufacturing has known several decades of improvements and innovations with a continuous development due to great potentials revealed along the exploration of the capabilities of this manufacturing technology. Since the 2000s, CGDS has known an important diversification of feasibility studies that clearly demonstrates a great flexibility in terms of processable materials. Metals and alloys, oxides, ceramics, polymers and advanced materials such as amorphous metals, intermetallics (IMCs) and nanofeatured materials form a wide range of CGDS material possibility that includes also the composite case for which successful mixtures are metal/metal, metal/oxide, metal/carbide, metal/nitride, metal/ceramic and metal/advanced materials, all of that providing various surface functionalizations and deposit performances. With nanocrystalline metals, the cold spray method enables functional improvements, e.g. fatigue strength improvement, significant hardness increase, faster and higher energetic reactivity and stable oxidation resistance at high temperature.

At present, the cold spray additive manufacturing encompasses a substantial material diversity, and notable achievements have been also realized in terms of deposit/substrate hybridation whereas in conventional thermal spraying, such a hybridation suffers from material incompatibilities. In the literature of cold spraying, combinations of dissimilar material appear with various developments of surface functionalization which rather recommend a low-pressure and low-temperature gas condition mostly below about 12–15Bar, to obtain successful depositions. The low-pressure cold spray method (LPCS) is conclusive for a variety of experienced hybrid natures including oxide/ceramic, oxide/polymer, metal/polymer, metal/PMCs, polymer/metal, metal/ceramic, ceramic/metal and cermet/metal. To date, LPCS becomes also a viable restoration and repair process, using compact LPCS system, portable and easy to handle. This modern use facilitates in situ or on-site repairs of various metallic workpieces, can be applied on large-scale structures and offers the possibility of structural, dimensional or functional repair and/or restoration. These benefits make the LPCS method an efficient eco-friendly option for the purpose of recycling in addition to economic advantage. Otherwise, the LPCS deposition extends beyond technological functionalization since it currently covers art and aesthetic applications such as the metallic decoration of wine glass and artistic metallic painting on various panel natures (glass, rusty sheets of iron, copper plate) using various metals as paintwork (copper, lead, zinc and aluminium).

In cold spraying, micron-sized powders have long been used to fabricate deposits, except for recent investigations that consider primary small-sized powders. Fine and ultra-fine powders become suitable for cold spraying under vacuum deposition conditions, i.e. using subatmospheric and non-heated gas condition. This method variance has been endorsed for submicron even nanosized particles (5 μm–20 nm) and can be termed as very low-pressure cold spraying (VLPCS), capable of producing thin and very thin coatings. Thin micrometric layer, nanometric film or multilayered thin deposits made of various combinations of stacked materials such as $Sn/Al_2O_3/Sn$ onto a silicon wafer, $TiO_2/Al_2O_3/Sn$ onto a silicon wafer or TiO_2/Al_2O_3 onto a sapphire substrate represent typical prowess of VLPCS. Besides, such achievements reveal the

possibility of layer-by-layer material hybridation giving a hierarchical hybrid stack. But hybridation of deposit/substrate without thermal damage, using nanoparticles, is also a further potential application of VLPCS. Successful combinations are Al_2O_3/Al_2O_3 (Chun and Ahn 2011), (Sn, Al_2O_3, TiO_2)/(Si, Al_2O_3), TiO_2/(SS, Sn, Cu, Al, PMMA, PET) and Ni/Si. In a series of studies, the nanoparticle deposition by VLPCS is dedicated to the elaboration of nanoporous architecture for catalytic performances, removal or cleaning functions, conduction properties and energy absorption or for multifunctionalized coating combining some of those performances. Much effort has been done to manufacture nanoporous TiO_2 coating for photovoltaic and photocatalytic properties of dye-sensitized solar cells (DSSCs). The cold deposition combined with high-impact pressure enables the consolidation of TiO_2 nanostructure as well as the self-assembling with glass anode. The VLPCS enabled three variants of nanopores for TiO_2 coating, each of which providing specific functional property or performance such as photocatalysis for water purification, photovoltage for solar cell with an energy efficiency of 5% produced by unimodal nanopores, better photoelectron production increasing the photovoltage capability of solar cell produced by bimodal nanopores and better photocatalytic activity of solar cell with an energy conversion efficiency of ~7% produced by large nanopores. A typical multiple function of nanoporous coating is the combination of high electrical resistivity with high fracture toughness generated by a nanoporous TiN coating.

Furthermore, the hybridation of the cold spray additive manufacturing with some other processes brings novel contributions. Combined with a focused ion beam (FIB) cutting, the capability of the VLPCS deposition also evolves towards the domain of nanofabrication given the possibility to manufacture nano-multilayered coating by VLPCS and the possibility of direct subtractive shaping with high accuracy enabled by the FIB cutting. Three-dimensional fiddly nanostructured and nanoshaped workpieces have been performed to demonstrate technological achievements such as the patterning of multilayered thin films to create 3D micron and submicron architectures. Moreover, a distinctive innovative hybridation of VLPCS is the disposition of the nanoparticle deposition system (NDPS) with a laser assistance. A coaxial disposition of both laser beam and nozzle heats both nanoparticles and substrate during the deposition. The laser-assisted NDPS (LaNDPS) method produced a better consolidated TiO_2 coating without structural changes of the primary anatase TiO_2 powders, with increased mechanical features and conferring improved photovoltaic efficiencies. However, the literature of the laser-assisted cold spray (LaCS) hydridation includes other variants that rely on a conjugate scanning of the nozzle, non-coaxial to the laser beam. Used as a local preheating during a short step of some milliseconds before the nozzle passes through the preheated zone, or used as a simultaneous heating of the particles beam and the substrate ahead the collision zone, the non-coaxial nozzle/laser beam variance generates positive thermal effects. This hybrid LaCS method facilitates the processability condition of difficult deposition circumstances, improves the deposition efficiency for low-pressure cold spraying, enables better densification, or increases deposit features such as tribological performances of diamond/Ni coating or structural integrity of corrosion-resistant Al-Si coating. Note that in terms of thermal capability

improvement, the cold spray method has known a recent variant that combines high kinematics and high-temperature conditions by means of impulse pressurized gas. Denoted pulse gas dynamic spraying (PGDS), this variance keeps the kinematic advantages of usual cold spraying while offering also benefits of particle heating within the spraying gun exhaust. PGDS can improve the material capability of cold spraying and can generate various added values such as an increase of adhesion strength, a better homogenization of composite coatings, an improvement of coating property such as the hardness and a thickening of hard material-based coatings. In addition, PGDS can produce thick and dense coatings for several materials including metals, composites, nanocrystalline powder, amorphous compounds and cermets.

Together, all these achievements reveal a great flexibility of the cold spray additive manufacturing in terms of material possibilities, deposition methods and technological solutions. Albeit they are not certainly fully comprehensive and will certainly evolve towards additional future findings, those contributions highlight substantial capabilities. Current trends are numerous due to the versatility of this method, and this chapter addressed a technological survey which provided a large depiction of the potentials of cold spraying as it stands today.

References

Ahn SH, Chun DM, Kim CS (2011) Nanoscale hybrid manufacturing process by nano particle deposition system (NPDS) and focused ion beam (FIB). CIRP Ann – Manuf Technol 60:583–586. https://doi.org/10.1016/j.cirp.2011.03.071

Ahn S-H, Choi J-O, Kim C-S et al (2012) Laser-assisted nano particle deposition system and its application for dye sensitized solar cell fabrication. CIRP Ann – Manuf Technol 61:575–578. https://doi.org/10.1016/j.cirp.2012.03.094

Ajdelsztajn L, Schoenung JM, Jodoin B, Kim GE (2005) Cold spray deposition of nanocrystalline aluminum alloys. Metall Mater Trans A 36:657–666. https://doi.org/10.1007/s11661-005-0182-4

Ajdelsztajn L, Jodoin B, Schoenung JM (2006a) Synthesis and mechanical properties of nanocrystalline Ni coatings produced by cold gas dynamic spraying. Surf Coat Technol 201:1166–1172. https://doi.org/10.1016/j.surfcoat.2006.01.037

Ajdelsztajn L, Zúñiga A, Jodoin B, Lavernia EJ (2006b) Cold-spray processing of a Nanocrystalline al-cu-mg-Fe-Ni alloy with Sc. J Therm Spray Technol 15:184–190. https://doi.org/10.1361/105996306X107995

Alhulaifi AS, Buck GA, Arbegast WJ (2012) Numerical and experimental investigation of cold spray gas dynamic effects for polymer coating. J Therm Spray Technol 21:852–862. https://doi.org/10.1007/s11666-012-9743-4

Alkhimov AP, Papyrin AN, Kosarev VF, Nesterovich NI, Shushpanov MM, Papyrin AN (1990) Gas-dynamic spraying method for applying a coating. https://www.google.com/patents/US5302414. Accessed 14 Oct 2016

Ang ASM, Berndt CC, Cheang P (2011) Deposition effects of WC particle size on cold sprayed WC–co coatings. Surf Coat Technol 205:3260–3267. https://doi.org/10.1016/j.surfcoat.2010.11.045

Assadi H, Kreye H, Gärtner F, Klassen T (2016) Cold spraying – A materials perspective, Acta Mater. https://doi.org/10.1016/j.actamat.2016.06.034

Bacciochini A, Radulescu MI, Charron-Tousignant Y et al (2012) Enhanced reactivity of mechanically-activated nano-scale gasless reactive materials consolidated by coldspray. Surf Coat Technol 206:4343–4348. https://doi.org/10.1016/j.surfcoat.2012.02.024

Bakshi SR, Singh V, Balani K et al (2008) Carbon nanotube reinforced aluminum composite coating via cold spraying. Surf Coat Technol 202:5162–5169. https://doi.org/10.1016/j.surfcoat.2008.05.042

Bray M, Cockburn A, O'Neill W (2009) The laser-assisted cold spray process and deposit characterisation. Surf Coat Technol 203:2851–2857. https://doi.org/10.1016/j.surfcoat.2009.02.135

Burlacov I, Jirkovský J, Kavan L et al (2007) Cold gas dynamic spraying (CGDS) of TiO2 (anatase) powders onto poly(sulfone) substrates: microstructural characterisation and photocatalytic efficiency. J Photochem Photobiol Chem 187:285–292. https://doi.org/10.1016/j.jphotochem.2006.10.023

Champagne V, Helfritch D (2015) Critical assessment 11: structural repairs by cold spray. Mater Sci Technol 31:627–634. https://doi.org/10.1179/1743284714Y.0000000723

Charles R (1958) Device for treating the surface of a workpiece. https://www.google.com/patents/US3100724. Accessed 14 Oct 2016

Cho S, Takagi K, Kwon H et al (2012) Multi-walled carbon nanotube-reinforced copper nanocomposite coating fabricated by low-pressure cold spray process. Surf Coat Technol 206:3488–3494. https://doi.org/10.1016/j.surfcoat.2012.02.021

Christian Widener (2014) Repair and Refurbishment Lessons Learned Using Cold Spray. CSAT workshop 2014. http://www.coldsprayteam.com/pastCSATworkshops.html. Accessed 9 Sept 2017

Christian Widener, Rob Hrabe, Brian James, Victor Champagne (2012) B1 Bomber-FEB Panel Repair by CS. CSAT workshop 2012. http://www.coldsprayteam.com/pastCSATworkshops.html. Accessed 9 Sept 2017

Christoulis DK, Guetta S, Irissou E et al (2010) Cold-spraying coupled to Nano-pulsed Nd-YaG laser surface pre-treatment. J Therm Spray Technol 19:1062–1073. https://doi.org/10.1007/s11666-010-9500-5

Christoulis DK, Jeandin M, Irissou E, Legoux J-G, Knapp W (2012) Laser-Assisted Cold Spray (LACS). InTech. http://www.intechopen.com/books/nd-yag-laser/laser-assisted-cold-spray-lacs. Accessed 8 Nov 2016

Chun D-M, Ahn S-H (2011) Deposition mechanism of dry sprayed ceramic particles at room temperature using a nano-particle deposition system. Acta Mater 59:2693–2703. https://doi.org/10.1016/j.actamat.2011.01.007

Chun DM, Kim MH, Lee JC, Ahn SH (2008a) TiO2 coating on metal and polymer substrates by nano-particle deposition system (NPDS). CIRP Ann – Manuf Technol 57:551–554. https://doi.org/10.1016/j.cirp.2008.03.111

Chun D-M, Kim M-H, Lee J-C, Ahn S-H (2008b) A Nano-particle deposition system for ceramic and metal coating at room temperature and low vacuum conditions. Int J Precis Eng Manuf 9:51–53

Chun D-M, Kim M-H, Lee J-C, Ahn S-H (2008) Nano particle deposition system (NPDS) for ceramic and metal coating at room temperature and low vacuum condition. IEEE:383–386. doi:https://doi.org/10.1109/ICSMA.2008.4505557

Chun D-M, Choi J-O, Lee CS et al (2012) Nano-particle deposition system (NPDS): low energy solvent-free dry spray process for direct patterning of metals and ceramics at room temperature. Int J Precis Eng Manuf 13:1107–1112. https://doi.org/10.1007/s12541-012-0145-9

Chun D-M, Kim C-S, Choi J-O et al (2014) Multilayer deposition of ceramic and metal at room temperature using nanoparticle deposition system (NPDS) and planarization process. Int J Adv Manuf Technol 72:41–46. https://doi.org/10.1007/s00170-013-5327-9

Couto M, Dosta S, Torrell M et al (2013) Cold spray deposition of WC–17 and 12Co cermets onto aluminum. Surf Coat Technol 235:54–61. https://doi.org/10.1016/j.surfcoat.2013.07.011

Dean SW, Potter JK, Yetter RA et al (2013) Energetic intermetallic materials formed by cold spray. Intermetallics 43:121–130. https://doi.org/10.1016/j.intermet.2013.07.019

Dosta S, Couto M, Guilemany JM (2013) Cold spray deposition of a WC-25Co cermet onto Al7075-T6 and carbon steel substrates. Acta Mater 61:643–652. https://doi.org/10.1016/j.actamat.2012.10.011

Ed Malison (2013) Practical Application of SST equipment, powders and knowledge. CSAT workshop 2013. http://www.coldsprayteam.com/pastCSATworkshops.html. Accessed 9 Sept 2017

Fan S-Q, Yang G-J, Li C-J et al (2006a) Characterization of microstructure of Nano-TiO2 coating deposited by vacuum cold spraying. J Therm Spray Technol 15:513–517. https://doi.org/10.1361/105996306X146901

Fan S-Q, Li C-J, Li C-X et al (2006b) Preliminary study of performance of dye-sensitized solar cell of Nano-TiO2 coating deposited by vacuum cold spraying. Mater Trans 47:1703–1709. https://doi.org/10.2320/matertrans.47.1703

Fan S-Q, Li C-J, Li C-X et al (2006c) Preliminary study of performance of dye-sensitized solar cell of Nano-TiO2 coating deposited by vacuum cold spraying. Mater Trans JIM 47:1703–1709. https://doi.org/10.2320/matertrans.47.1703

Fan S-Q, Li C-J, Yang G-J, Zhang L-Z, Gao J-C, Xi Y-X (2007) Fabrication of nano-TiO2 coating for dye-sensitized solar cell by vacuum cold spraying at room temperature. J Therm Spray Technol 16:893–897. https://doi.org/10.1007/s11666-007-9090-z

Ganesan A, Affi J, Yamada M, Fukumoto M (2012) Bonding behavior studies of cold sprayed copper coating on the PVC polymer substrate. Surf Coat Technol 207:262–269. https://doi.org/10.1016/j.surfcoat.2012.06.086

Ganesan A, Yamada M, Fukumoto M (2013) Cold spray coating deposition mechanism on the thermoplastic and thermosetting polymer substrates. J Therm Spray Technol 22:1275–1282. https://doi.org/10.1007/s11666-013-9984-x

Gardon M, Latorre A, Torrell M et al (2013) Cold gas spray titanium coatings onto a biocompatible polymer. Mater Lett 106:97–99. https://doi.org/10.1016/j.matlet.2013.04.115

Ghelichi R, Bagherifard S, Mac Donald D et al (2014) Fatigue strength of al alloy cold sprayed with nanocrystalline powders. Int J Fatigue 65:51–57. https://doi.org/10.1016/j.ijfatigue.2013.09.001

Grigoriev S, Okunkova A, Sova A, Bertrand P, Smurov I (2015) Cold spraying: From process fundamentals towards advanced applications. Surf Coat Technol 268:77–84. https://doi.org/10.1016/j.surfcoat.2014.09.060

Hall AC, Brewer LN, Roemer TJ (2008) Preparation of aluminum coatings containing homogenous Nanocrystalline microstructures using the cold spray process. J Therm Spray Technol 17:352–359. https://doi.org/10.1007/s11666-008-9180-6

Irissou E, Legoux J-G, Arsenault B, Moreau C (2007) Investigation of al-Al2O3 cold spray coating formation and properties. J Therm Spray Technol 16:661–668. https://doi.org/10.1007/s11666-007-9086-8

Irissou E, Legoux J-G, Ryabinin AN et al (2008) Review on cold spray process and technology: part I – intellectual property. J Therm Spray Technol 17:495–516. https://doi.org/10.1007/s11666-008-9203-3

Ji G-C, Wang H-T, Chen X et al (2013) Characterization of cold-sprayed multimodal WC-12Co coating. Surf Coat Technol 235:536–543. https://doi.org/10.1016/j.surfcoat.2013.08.021

Jodoin B, Richer P, Bérubé G et al (2007) Pulsed-gas dynamic spraying: process analysis, development and selected coating examples. Surf Coat Technol 201:7544–7551. https://doi.org/10.1016/j.surfcoat.2007.02.033

Juha Lagerbom, Heli Koivuluoto, Jussi Larjo, et al (2007) Comparison of coatings prepared by two different cold spray processes

Jung K, Song W, Chun D-M et al (2010) Nickel line patterning using silicon supersonic micronozzle integrated with a nanoparticle deposition system. Jpn J Appl Phys 49.:05EC09. https://doi.org/10.1143/JJAP.49.05EC09

Kashirin A, Klyuev O, Buzdygar T, Shkodkin A (n.d.) Modern applications of the low pressure cold spray. http://dymet.info/en/app.html. Accessed 9 Sept 2017

Kim D-Y, Park J-J, Lee J-G et al (2013) Cold spray deposition of copper electrodes on silicon and glass substrates. J Therm Spray Technol 22:1092–1102. https://doi.org/10.1007/s11666-013-9953-4

King PC, Zahiri S, Jahedi M, Friend J (2010) Aluminium coating of lead zirconate titanate – a study of cold spray variables. Surf Coat Technol 205:2016–2022. https://doi.org/10.1016/j.surfcoat.2010.08.084

King PC, Poole AJ, Horne S et al (2013) Embedment of copper particles into polymers by cold spray. Surf Coat Technol 216:60–67. https://doi.org/10.1016/j.surfcoat.2012.11.023
Krömer W (2012) Overview of the global thermal spray market and trends in Europe. Weld Cut:377
Kulmala M, Vuoristo P (2008) Influence of process conditions in laser-assisted low-pressure cold spraying. Surf Coat Technol 202:4503–4508. https://doi.org/10.1016/j.surfcoat.2008.04.034
Lee HY, Yu YH, Lee YC et al (2004a) Interfacial studies between cold-sprayed WO3, Y2O3 films and Si substrate. Appl Surf Sci 227:244–249. https://doi.org/10.1016/j.apsusc.2003.11.073
Lee HY, Yu YH, Lee YC et al (2004b) Cold spray of SiC and Al2O3 with soft metal incorporation: a technical contribution. J Therm Spray Technol 13:184–189. https://doi.org/10.1361/10599630419355
Lee HY, Jung SH, Lee SY et al (2005) Correlation between Al2O3 particles and interface of al–Al2O3 coatings by cold spray. Appl Surf Sci 252:1891–1898. https://doi.org/10.1016/j.apsusc.2005.03.148
Lee JH, Jang HL, Lee KM et al (2013) In vitro and in vivo evaluation of the bioactivity of hydroxyapatite-coated polyetheretherketone biocomposites created by cold spray technology. Acta Biomater 9:6177–6187. https://doi.org/10.1016/j.actbio.2012.11.030
Lefebvre L-P, Banhart J, Dunand DC (2008) Porous metals and metallic foams: current status and recent developments. Adv Eng Mater 10:775–787. https://doi.org/10.1002/adem.200800241
Li C-J, Yang G-J, Gao P-H et al (2007) Characterization of nanostructured WC-co deposited by cold spraying. J Therm Spray Technol 16:1011–1020. https://doi.org/10.1007/s11666-007-9096-6
Liu J, Zhou X, Zheng X et al (2012) Tribological behavior of cold-sprayed nanocrystalline and conventional copper coatings. Appl Surf Sci 258:7490–7496. https://doi.org/10.1016/j.apsusc.2012.04.070
Luan Y, Xue Y-W, Shi Z-G (2012) Synthesis of hierarchically macro/meso/microporous carbon spheres and its application in fast rechargeable electric double layer capacitor. Mater Lett 88:30–32. https://doi.org/10.1016/j.matlet.2012.08.046
Lupoi R, O'Neill W (2010) Deposition of metallic coatings on polymer surfaces using cold spray. Surf Coat Technol 205:2167–2173. https://doi.org/10.1016/j.surfcoat.2010.08.128
Marx S, Paul A, Köhler A, Hüttl G (2006) Cold spraying: innovative layers for new applications. J Therm Spray Technol 15:177–183. https://doi.org/10.1361/105996306X107977
Melendez NM, McDonald AG (2013) Development of WC-based metal matrix composite coatings using low-pressure cold gas dynamic spraying. Surf Coat Technol 214:101–109. https://doi.org/10.1016/j.surfcoat.2012.11.010
Moridi A, Hassani-Gangaraj SM, Guagliano M, Dao M (2014) Cold spray coating: review of material systems and future perspect. Surf Eng 36:369–395
Neil Matthews (2012) Cold Spray Applications for the Australian Defence Department
Ning X-J, Jang J-H, Kim H-J (2007) The effects of powder properties on in-flight particle velocity and deposition process during low pressure cold spray process. Appl Surf Sci 253:7449–7455. https://doi.org/10.1016/j.apsusc.2007.03.031
Ogawa K, Ito K, Ichimura K et al (2008) Characterization of low-pressure cold-sprayed aluminum coatings. J Therm Spray Technol 17:728–735. https://doi.org/10.1007/s11666-008-9254-5
Olakanmi EO (2016) Optimization of the quality characteristics of laser-assisted cold-sprayed (LACS) aluminum coatings with Taguchi Design of Experiments (DOE). Mater Manuf Process 31:1490–1499. https://doi.org/10.1080/10426914.2014.984306
Olakanmi EO, Tlotleng M, Meacock C et al (2013) Deposition mechanism and microstructure of laser-assisted cold-sprayed (LACS) al-12 wt.%Si coatings: effects of laser power. JOM 65:776–783. https://doi.org/10.1007/s11837-013-0611-6
Papyrin AN (2006) Cold spray: state of the art and applications. ENISE, St-Etienne
Papyrin A, Kosarev V, Klinkov S et al (2007) Chapter 1 – discovery of the cold spray phenomenon and its basic features. In: Cold spray technology. Elsevier, Oxford, pp 1–32
Petri Vuoristo (2015) CGS Low Pressure Case Studies on Industrial Sectors
Pialago EJT, Kwon OK, Park CW (2013) Nucleate boiling heat transfer of R134a on cold sprayed CNT–cu composite coatings. Appl Therm Eng 56:112–119. https://doi.org/10.1016/j.applthermaleng.2013.03.046

Raoelison RN, Aubignat E, Planche M-P et al (2016) Low pressure cold spraying under 6 bar pressure deposition: exploration of high deposition efficiency solutions using a mathematical modelling. Surf Coat Technol 302:47–55. https://doi.org/10.1016/j.surfcoat.2016.05.068

Richer P, Jodoin B, Ajdelsztajn L, Lavernia EJ (2006) Substrate roughness and thickness effects on cold spray Nanocrystalline al-mg coatings. J Therm Spray Technol 15:246–254. https://doi.org/10.1361/105996306X108174

Robitaille F, Yandouzi M, Hind S, Jodoin B (2009) Metallic coating of aerospace carbon/epoxy composites by the pulsed gas dynamic spraying process. Surf Coat Technol 203:2954–2960. https://doi.org/10.1016/j.surfcoat.2009.03.011

Roman Gr. Maev, Emil Strumban, Volf Leshchinskiy, Dmitry Dzhurinskiy (2014) Repair applications of the LPCS process

Ryan G, Pandit A, Apatsidis DP (2006) Fabrication methods of porous metals for use in orthopaedic applications. Biomaterials 27:2651–2670. https://doi.org/10.1016/j.biomaterials.2005.12.002

Sanpo N, Tan ML, Cheang P, Khor KA (2008) Antibacterial property of cold-sprayed HA-ag/PEEK coating. J Therm Spray Technol 18:10–15. https://doi.org/10.1007/s11666-008-9283-0

Sansoucy E, Marcoux P, Ajdelsztajn L, Jodoin B (2008) Properties of SiC-reinforced aluminum alloy coatings produced by the cold gas dynamic spraying process. Surf Coat Technol 202:3988–3996. https://doi.org/10.1016/j.surfcoat.2008.02.017

Schwenk A (2012) Integration of the kinetic-systems into the sulzer-product portfolio. Erding, Schweiz

Seo D, Sayar M, Ogawa K (2012) SiO2 and MoSi2 formation on Inconel 625 surface via SiC coating deposited by cold spray. Surf Coat Technol 206:2851–2858. https://doi.org/10.1016/j.surfcoat.2011.12.010

Sova A, Klinkov S, Kosarev V et al (2013) Preliminary study on deposition of aluminium and copper powders by cold spray micronozzle using helium. Surf Coat Technol 220:98–101. https://doi.org/10.1016/j.surfcoat.2012.09.036

Thurston SH (1900) Method of impacting one metal upon another

Wang F, Zhang D, Zheng S, Qi B (2010) Characteristic of cold sprayed catalytic coating for hydrogen production through fuel reforming. Int J Hydrog Energy 35:8206–8215. https://doi.org/10.1016/j.ijhydene.2009.12.087

Wang Y-Y, Liu Y, Li C-J et al (2011) Investigation on the electrical properties of vacuum cold sprayed SiC-MoSi2 coatings at elevated temperatures. J Therm Spray Technol 20:892–897. https://doi.org/10.1007/s11666-011-9635-z

Wang Y-Y, Liu Y, Li C-J et al (2012) Electrical and mechanical properties of nano-structured TiN coatings deposited by vacuum cold spray. Vacuum 86:953–959. https://doi.org/10.1016/j.vacuum.2011.06.026

Wang W, Burgueño R, Hong J-W, Lee I (2013) Nano-deposition on 3-D open-cell aluminum foam materials for improved energy absorption capacity. Mater Sci Eng A 572:75–82. https://doi.org/10.1016/j.msea.2013.02.032

Xia K, Gao Q, Jiang J, Wang H (2013) An unusual method to prepare a highly microporous carbon for hydrogen storage application. Mater Lett 100:227–229. https://doi.org/10.1016/j.matlet.2013.03.026

Xu Y, Hutchings IM (2006) Cold spray deposition of thermoplastic powder. Surf Coat Technol 201:3044–3050. https://doi.org/10.1016/j.surfcoat.2006.06.016

Yandouzi M, Sansoucy E, Ajdelsztajn L, Jodoin B (2007) WC-based cermet coatings produced by cold gas dynamic and pulsed gas dynamic spraying processes. Surf Coat Technol 202:382–390. https://doi.org/10.1016/j.surfcoat.2007.05.095

Yandouzi M, Richer P, Jodoin B (2009) SiC particulate reinforced al–12Si alloy composite coatings produced by the pulsed gas dynamic spray process: microstructure and properties. Surf Coat Technol 203:3260–3270. https://doi.org/10.1016/j.surfcoat.2009.04.001

Yang G-J, Li C-J, Fan S-Q et al (2007) Influence of annealing on Photocatalytic performance and adhesion of vacuum cold-sprayed nanostructured TiO2 coating. J Therm Spray Technol 16:873–880. https://doi.org/10.1007/s11666-007-9109-5

Yang G-J, Li C-J, Liao K-X et al (2011) Influence of gas flow during vacuum cold spraying of nano-porous TiO2 film by using strengthened nanostructured powder on performance of dye-sensitized solar cell. Thin Solid Films 519:4709–4713. https://doi.org/10.1016/j.tsf.2011.01.021

Yang G-J, Liao K-X, Li C-J et al (2012) Formation of pore structure and its influence on the mass transport property of vacuum cold sprayed TiO2 coatings using strengthened nanostructured powder. J Therm Spray Technol 21:505–513. https://doi.org/10.1007/s11666-012-9741-6

Yao J, Yang L, Li B, Li Z (2015) Beneficial effects of laser irradiation on the deposition process of diamond/Ni60 composite coating with cold spray. Appl Surf Sci 330:300–308. https://doi.org/10.1016/j.apsusc.2015.01.029

Zhang D, Shipway PH, McCartney DG (2005) Cold gas dynamic spraying of aluminum: the role of substrate characteristics in deposit formation. J Therm Spray Technol 14:109–116. https://doi.org/10.1361/10599630522666

Zhang Q, Li C-J, Li C-X et al (2008) Study of oxidation behavior of nanostructured NiCrAlY bond coatings deposited by cold spraying. Surf Coat Technol 202:3378–3384. https://doi.org/10.1016/j.surfcoat.2007.12.028

Zhang YY, Wu XK, Cui H, Zhang JS (2011) Cold-spray processing of a high density Nanocrystalline aluminum alloy 2009 coating using a mixture of as-atomized and as-Cryomilled powders. J Therm Spray Technol 20:1125–1132. https://doi.org/10.1007/s11666-011-9652-y

Zhou X, Mohanty P (2012) Electrochemical behavior of cold sprayed hydroxyapatite/titanium composite in hanks' solution. Electrochim Acta 65:134–140. https://doi.org/10.1016/j.electacta.2012.01.018

Zhou XL, Chen AF, Liu JC et al (2011) Preparation of metallic coatings on polymer matrix composites by cold spray. Surf Coat Technol 206:132–136. https://doi.org/10.1016/j.surfcoat.2011.07.005

Chapter 4
Low-Pressure Cold Spray (LPCS)

Roman Gr. Maev and Volf Leshchynsky

4.1 Basics of Low-Pressure Cold Spray (LPCS) Technology

4.1.1 High-Pressure Cold Spraying (HPCS) Versus Low-Pressure Cold Spraying (LPCS)

Cold spraying technologies being used in industry may be splitted up to HPCS (max. Gas pressure ≈40 bar) and LPCS (max. Gas pressure ≈9 bar). The temperatures of the propellant gas are in the range of 20–650 °C. The compressed air, nitrogen and helium gases are usually used. The main advantages of LPCS technology are relatively low cost of both spraying process and the portable spray systems being applied. Moreover, the LPCS system portability, using compressed air as the propellant gas allows to apply the technology on-site and infield (Maev and Leshchynsky 2015).

In the LPCS process, powder particles impinge upon substrate with lower velocity than that of HPCS particles. So, the LPCS particle kinetic energy differs considerably from that of HPCS. Additionally, particle velocities depend on the particle size, density and morphology. In both cold spraying processes, a coating formation consists of two stages: particle-substrate interactions and particle-particle interactions. At the first stage, bonding between the particles and the substrate is achieved. The particle-particle interactions result in a coating formation at the second stage. Development of post-processing technology for CS coating is of great importance to achieve the required coating properties. The general classification of cold spraying and post-processing steps is shown on Fig. 4.1.

A particle consolidation due to CS process is known to be achieved when particle velocity is equal or more than certain critical velocity which depends on material properties and structure (Assadi et al. 2003). Additionally, particle surface oxide

R.Gr. Maev • V. Leshchynsky (✉)
Institute for Diagnostic Imaging Research, University of Windsor, Windsor, Canada
e-mail: maev@uwindsor.ca; leshynsk@uwindsor.ca

P. Cavaliere (ed.), *Cold-Spray Coatings*,
https://doi.org/10.1007/978-3-319-67183-3_4

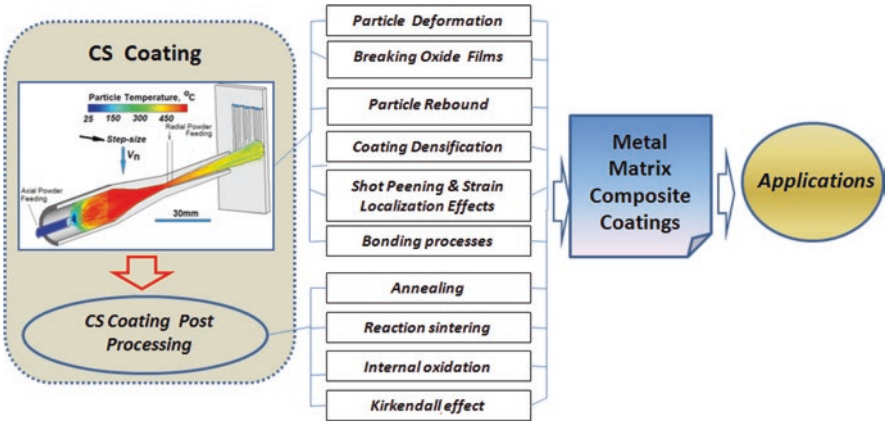

Fig. 4.1 Classification of the main structure formation processes of CS coatings

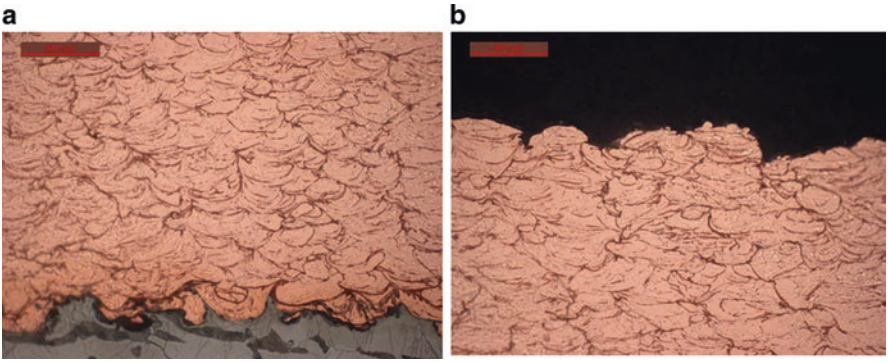

Fig. 4.2 Microstructure of HPCS copper coating on the steel substrate (cross-section): (**a**) area of interface; (**b**) top layer of the coating. Etched with $FeCl_3$-HCl-H_2O solution

films affect the critical velocity. M. Yu et al. 2013 have shown that increase of oxygen film thickness on the particle surface raises the critical velocity that results in higher velocity needed for successful bonding. In cold spraying, several processes such as particle deformation, particle rebound, breaking oxide films, strain localization and coating densification lead to coating formation. So, analysis of microstructure will specify the differences between HPCS and LPCS processes.

HPCS process is known to ensure high particle velocities that allow to achieve the adiabatic shear band formation and bonding at the interface (Papyrin et al. 2006). The microstructures of HPCS copper coating (Fig. 4.2) clearly demonstrate parachute shape of the copper particles deposited at particle velocity of 900–1000 m/s that reveals about strain rates in the range of 10^7–10^9 sec^{-1}. Such a high-velocity particle impact allows to achieve the near full density of the surface layer (Fig. 4.2b).

Contrary, the LPCS coatings formed by particles' impact at velocities 300–550 m/s show relatively uniform deformation of the particles without high-velocity strain localization features such as jet formation at the particle surface (Fig. 4.3).

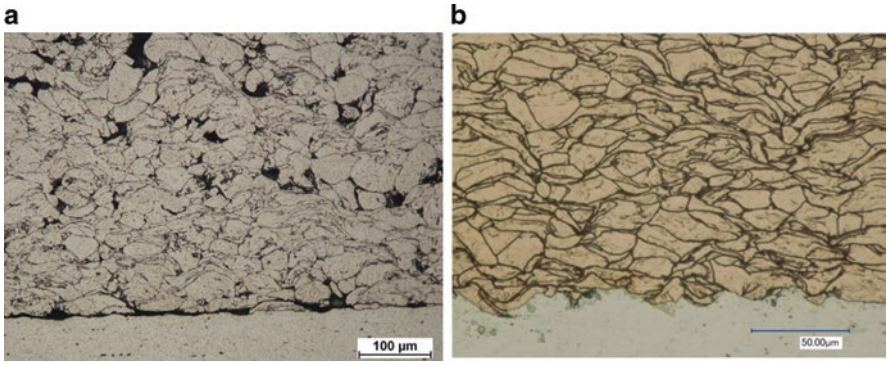

Fig. 4.3 Microstructure of LPCS aluminium (**a**) and copper (**b**) coatings on the aluminium substrate (cross-section). Al coating is etched with HF-HNO_3-HCl-H_2O solution, and copper coating is etched with $FeCl_3$-HCl-H_2O solution

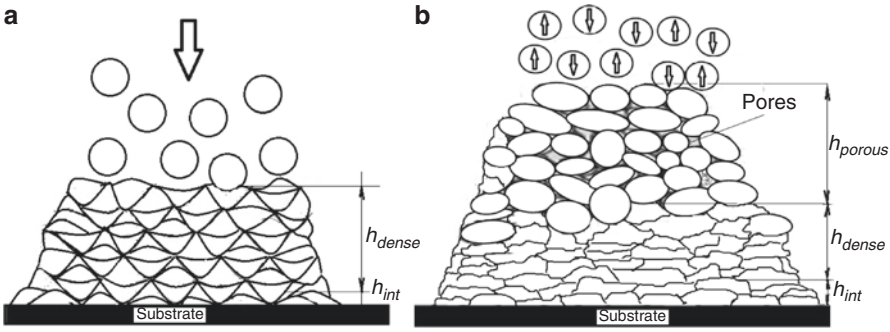

Fig. 4.4 Coating formation at high-pressure (**a**) and low-pressure (**b**) cold spraying

The shape of consolidated particles is flattened both for Al coating (Fig. 4.3a) and Cu coating (Fig. 4.3b). Comparison of microstructures of Figs. 4.2b and 4.3b demonstrates that interparticle boundaries of LPCS coating are etched at higher extent than that of HPCS coating. It reveals about weaker bonding of the particles as compared with that of HPCS coating because the LPCS particle velocity is lower than critical.

For this reason, the bonding mechanism due to adiabatic shear band formation cannot be realized at low LPCS process, and the deposition efficiency of LPCS process is considerably lower than that of HPCS. Nevertheless, it is obvious, LPCS allows to achieve the particle consolidation due to another deformation mechanism of interparticle bonding.

The main features of both HPCS and LPCS structure formation processes shown on Fig. 4.4 are the following:

1. The HPCS coating microstructure may be shared by interface and coating core zones (Fig. 4.4a), while LPCS coating microstructure has got the porous top layer as shown on Fig. 4.4b.

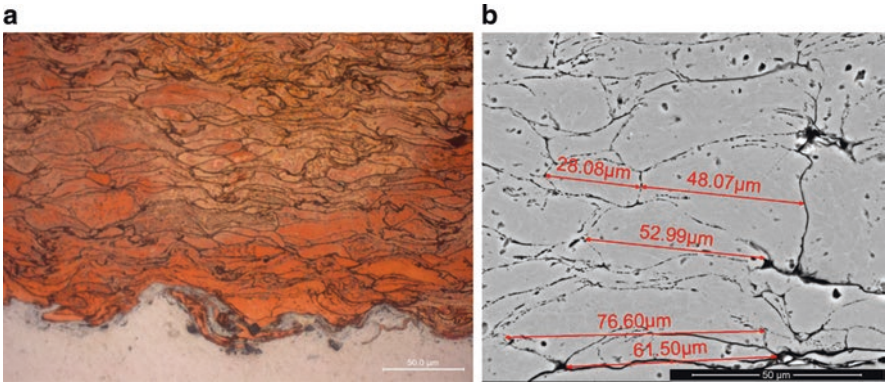

Fig. 4.5 Vortexes formation at the copper coating – aluminium substrate interface during LPCS process (**a**) – and microstructure of LPCS aluminium coating made of 45 μm particles (**b**)

2. The HPCS consolidated particles have the parachute-like shape with jet formation at the particle-particle interface, while the most of LPCS consolidated particles are only flattened. The flattening ratio of particles consolidated by HPCS is lower than that of LPCS particles. So LPCS results in more uniform distribution of strains in the particle.
3. The coating-substrate interface of HPCS coating is characterized by severe deformation of the particles and substrate surface resulting in vortexes formation as shown on Fig. 4.2a. Similar effect is described in works of Papyrin 2001; Champagne 2007; Hussain et al. 2009. However, it is possible to achieve the similar regime at LPCS process as shown on Fig. 4.5a for LPCS deposition of copper onto aluminium substrate. In the both cases, severe deformation of both the impinged particles and substrate occur that results in high values of adhesion strength (Maev and Leshchynsky 2015).
4. The presence of the LPCS coating porous top layer with thickness $\boldsymbol{h_{porous}}$ (Fig. 4.4b) reveals about relatively low kinetic energy of primary particles forming this top layer that does not allow to accomplish its effective densification. For this reason, the particle strains are not high (Fig. 4.3a). However, additional densification and particle deformation are caused by a bombardment of the top layer by following particles which are rebounded from the surface. The relatively low deposition efficiency of the LPCS process reveals about occurrence of shot peening effect which results in formation of near full dense layer $\boldsymbol{h_{dense}}$ of the coating and intensive particle deformation (Fig. 4.4b).
5. A strain localization of particle plastic flow by adiabatic shear band formation due to the particle impingement with the substrate at strain rates 10^7–10^9 s^{-1} is proven to be a general mechanism of particle bonding and, consequently, coating formation during HPCS process (Champagne 2007; Assadi et al. 2003; Papyrin 2006; Champagne and Helfritch 2015). Contrary, LPCS process with strain rates

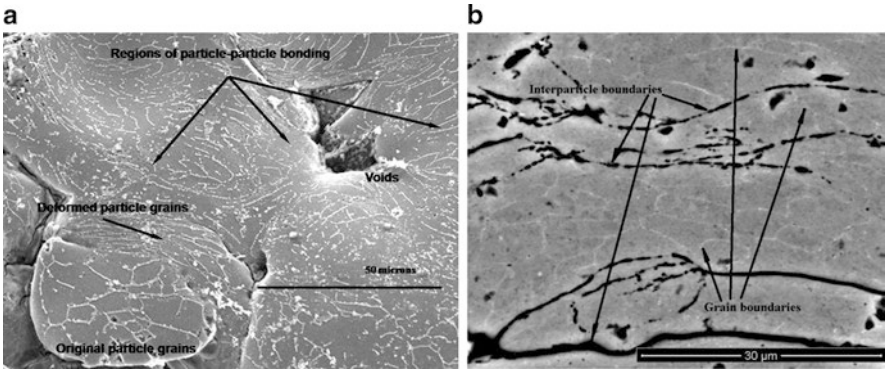

Fig. 4.6 SEM of aluminium HPCS coating made of 50 μm particles (Steenkiste et al. 2015) (**a**) and aluminium LPCS coatings made of 45 μm particles (**b**)

10^4–10^7 s^{-1} cannot achieve the conditions of adiabatic shear band formation at the particle-substrate and particle-particle interface. That is why particle consolidation process at LPCS differs from that of HPCS. These features are shown on Fig. 4.6. The microstructure of HPCS coating consists of the regions of particle-particle boundaries containing severely deformed grains and areas of adiabatic shear bands (Fig. 4.6a). Contrary, the microstructure of LPCS coating consists of flattened particles which contain the uniformly deformed grains without any indications of strain localization.

6. The particle deformation during the LPCS process consists of two stages: (i) the particle strain during the particle impact and (ii) the particle strain due to shot peening of the coated layer. For this reason, the flattening ratio of the consolidated particles is more than that of HPCS coatings (Fig. 4.6a, b). Comparison of the consolidated particle flattening ratio with grain distortion (Figs. 4.5b and 4.6b) demonstrates relatively low uniform strains of the grains. That is why breaking oxide films on the particle surface and metallurgical bonding at the particle-substrate and particle-particle interface might not be achieved. Nevertheless, the adhesion and bonding strength of the LPCS coatings are near to those of HPCS coatings perhaps due to shot peening effect.

Fig. 4.6a depicts the microstructure of aluminium coating made of large particles (greater than 50 microns) after electropolishing. The grain boundaries are clearly seen. Areas of interparticle bonding are shown by arrows. The strains which have occurred between particles result in distortion of the grain structure. For example, the particle in the lower left side of the picture shows internal plastic flow of the grain boundaries at the impact site; however, the original grain structure was preserved in locations removed from the impact area (Van Steenkiste et al. 2015).

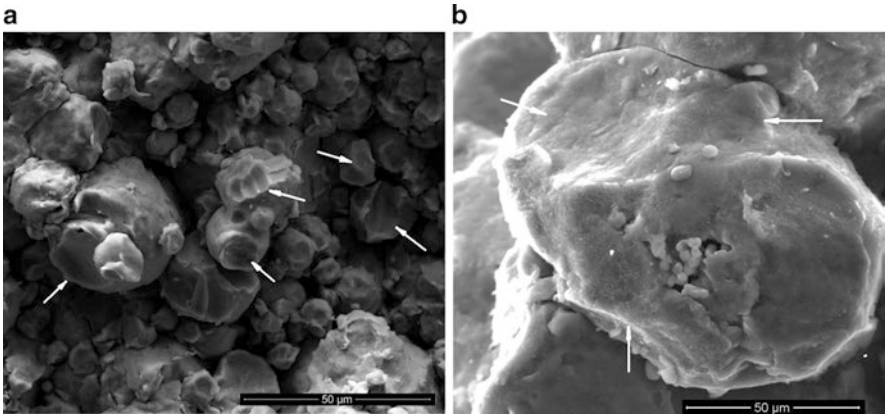

Fig. 4.7 SEM images of the surface topography of LPCS stainless steel coating (**a**) and Al-alloy coating (**b**). (**a**) AISI 304 powder with particle size of 25 µm; Al – Al13%Si powder mixture, particle size-45 µm

4.1.2 Bonding Mechanisms

In the region where GDS processes are realized, particles impact and bond with the surface for specifically defined particle velocities. Many authors (Papyrin 2001; Alkhimov et al. 2000; Stoltenhoff et al. 2002) consider cold spray phenomenon to be strictly governed by the interaction of particles with the substrate. However, there is a distinct lack of literature describing and evaluating collective particle behaviour in LPCS. As discussed in the previous section, the interaction of incoming particles with the substrate at LPCS particle velocities (below critical velocity threshold) can result in particles that rebound from (rather than adhere to) the surface (deposition efficiency in the range of 30–50%). Thus, in order to fully understand the LPCS process, then, it is necessary to characterize the effect of preliminary particles' impacts that does not result in material adhesion. Klinkov (2005) suggests that these impacts lead to breaking consolidated particles' oxide film and, consequently, the activation of the surface. Succeeding particles impinging on an activated surface area are then more likely to bond to the substrate. The surface topography images shown on Fig. 4.7 demonstrate indications of adhered particle surface damage by following impinging particles rebounded from the surface. The severe surface deformation in some areas (white arrows) is clearly seen, and damage of oxide film is obvious in this case. At present time, however, proper characterization of this surface activation with respect to, for example, the nature and quantity of preliminary impacts is difficult at best. For this reason, its physical mechanism is not fully understood yet and needs to be further studied.

As described earlier (Champagne 2007; Assadi et al. 2003; Papyrin 2006), in HPCS, high particle velocities are obtained through accelerating an expanding gas stream to velocities in the range of 500–1200 m/s by means of a converging-diverging de Laval-type nozzle. In this process, the gas is heated only to increase the

particle velocity and to increase particle deformation upon impact. Thus, powder layers form as a result of the kinetic energy of the particles as they hit the substrate, the bonding of particles in HPS as a result of extensive plastic deformation and related phenomena at the interface. In general, for the particle to be bonded, its kinetic energy must be transformed into heat and strain energy within both the particle and substrate. For this reason, inelastic collision processes which involve the plastic deformation of the particle and substrate are the main phenomenon causing particle consolidation. Such plastic deformation can be roughly approximated by the flattening of spherical incident particles into a plate-like structure having aspect ratios between 3:1 and 5:1 (Van Steenkiste et al. 2002). In order for sufficient plastic deformation to take place, the contact stress at the interface must exceed the yield stress of the particle. Thus, the powders that are typically employed in most CS processes consist of metals with relatively high ductility. Hence, the fundamental theories of plasticity provide the scientific basis for particle impact analysis.

LPCS bonding process is characterized by the following effects: (i) breaking oxide film by preliminary particles impacts that do not result in material adhesion, (ii) impact particle consolidation at certain conditions and (iii) further densification, deformation and consolidation of particle aggregates due to shot peening effect.

4.1.3 Temperature Effects: LPCS Localization Processes

As shown before, although many coatings (i.e. pure metals, alloys, polymers, composites and bulk metallic glasses) have been obtained, the bonding mechanisms of coatings are not precisely known. A prevalent opinion is that bonding of CS coatings depends on the localization processes due to occurrence of adiabatic shear instability at the impact interface.

There are three primary flow localization processes. In the first (a typical strain-hardening material under nonadiabatic conditions), the shear stress increases due to strain hardening. For this case, material softening at certain temperature needs to be taken into account. In the second, the plastic strain energy that is dissipated as heat under adiabatic conditions, resulting in a temperature increase, in turn causing material softening whose effect overwhelms that of strain hardening. It is during this stage that the development of flow heterogeneity may be observed, indicating the onset of a weak instability process (Molinari 1997). The third type of plastic flow is characterized by the marked development of strain localization, resulting in the formation of an adiabatic shear band that eventually propagates along the circumference of the specimen. The fluctuations in stress, strain, temperature or microstructure and the inherent instability of strain softening can give rise to plastic flow (shear) localization (Grujicic et al. 2004). Thus, shearing and heating (and subsequent softening) become highly localized, while the material strain and heating in surrounding regions remain negligible. This, in turn, causes the flow stress to rapidly decrease (“localization”).

In current high-pressure CS, technology is of fundamental importance to create a very high-speed gas that can accelerate the injected powders to velocities exceeding the critical velocity (about 500–800 m/s) at which adiabatic shear band formation occurs. The critical gas velocity that must be achieved in CS is material dependant, being affected by particle size and density, elastic-plastic properties and structure. The low-pressure air CS system possesses the particle velocities in the range of 300–500 m/s that result in lack of adiabatic shear band formation effect and, consequently, low deposition efficiency of Al and Cu spraying and impossibility of stainless steel and other alloy deposition. However, adiabatic shear band strain localization may not be limited to the interface. Adiabatic shear bands may also occur in bulk particles (Walter 1992) as well as in powder granular media (Hu and Molinari 2004). Additionally, strain localization effects due to a particle volume temperature gradient need to be taken into account. The lack of strain localization analysis – particularly with respect to its influence on the structure of the formed coatings – limits our present understanding and further development of the low-pressure CS process. The present chapter is targeted at providing insight into low-pressure CS particle consolidation processes where the particle significant gradients in both temperature and strain rate occur.

4.1.3.1 Experimental Procedure

The low-pressure CS process was used for depositing Cu and stainless steel coatings on low-carbon steel substrates. Commercially available Cu and AISI 904 powder, with particles ranging in size from 5 to 100 μm, has been used. The particles were accelerated to a high velocity by injecting them into a stream of high-pressure carrier gas which is subsequently expanded to supersonic velocity through a converging-diverging de Laval nozzle. After exiting the nozzle, the particles are impacted onto a substrate, where the solid particles deform and create a bond with the substrate. As the process continues, particles continue to impact and form bonds with the previously consolidated material resulting in a uniform deposit with relatively little porosity and high bond strength. The low-carbon steel substrates were grit blasted (blasting air pressure 0.75 MPa, standoff distance 150 mm and traverse speed 20–40 mm/s) with alumina (mesh 36) to remove the scale layer formed due to hot rolling process used to produce the substrate material. Commercially available low oxygen Cu powder (Tafa, Inc., Concord, NH and USA) and AISI 904 powder with an average diameter about 45 μm were used. To form a coating, the following CS parameters were utilized with Tessonics low-pressure CS machine: propellant gas, air; gas pressure, 9–10 bar; and gas temperature, 400–800 °C. Optical light microscopy Leica DMI5000 M with a digital camera DFS 320 R2 was used for metallographic characterization.

4.1.3.2 Results and Discussion

Localization Versus Particle Temperature and Velocity

The idealized representative structure of the particle with radius R_p impinged with substrate during CS will contain the particle walls of thickness $w/2$ and particle core. The particle wall structure differs from that of the particle core because of strain localization effects. Thus, it may be assumed that the walls form a topologically continuous skeleton structure within which isolated islands of the particle core are encapsulated, similar to Estrin et al. 1998. If the surfaces of the deformed particles are the spheres of radius $R_{d.}$, diameter of the deformed particle is $2R_f$, and its height is – $2h_x$,

$$2R_d = \frac{R_f^2 + R_x^2}{h_x} \tag{4.1}$$

The volume fraction of interparticle walls may be defined as

$$f = \frac{\left(S_d \cdot w/2\right) \cdot 2}{4/3\pi R_p^3} \tag{4.2}$$

Here S_d is the surface area of spherical segment with radius R_d and height h_x: $S_d = 2\pi R_d h_x$. R_d may be defined on the base of an incompressibility rule that means volumes of the particle before and after deformation are equal.

Analysis of localization phenomenon may be made on the base of cylindrical samples impact with Taylor method described by (Gust 1982 and Eakins and Thadhani 2006). The rod-on-rigid-anvil impact experiment firstly performed by Taylor in 1948 remains a popular method of investigating the mechanical response of a material to dynamic loading. In the original configuration, a cylindrically shaped specimen is impacted against a rigid anvil at velocities sufficient to induce plastic deformation without failure, where strain rates in the range of 10^3–10^6 s^{-1} are typical (Eakins and Thadhani 2006). By comparing the shape and localization area fraction of the finally deformed and initial specimens for a given impact velocity, estimates of the strain localization effect may be made. Geometry of the localization area is defined on the base of impact experiment results (Gust 1982) (see Fig. 4.8.).

One can note that strain localization volume depends on impact temperature. Increase of the temperature results in raise of the localization volume probably due to lower yield stress at higher temperature. The effect of temperature on the distortion of the AISI 4340 samples cylindrical surface $\varepsilon_r = \Delta r/r_0$ is demonstrated on Fig. 4.9 (Gust 1982 experimental results).

The results reveal that raise of temperature up to 715°K does not change the localization parameter. However, the further temperature increase results in enhancement of localization effect.

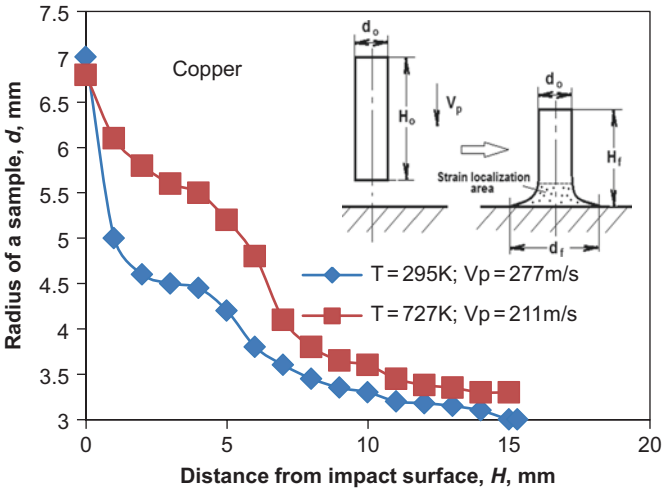

Fig. 4.8 Geometry of localization area due to impact at ambient temperature and 727 °K (the *curves* are calculated using Gust 1982 experimental results for Copper)

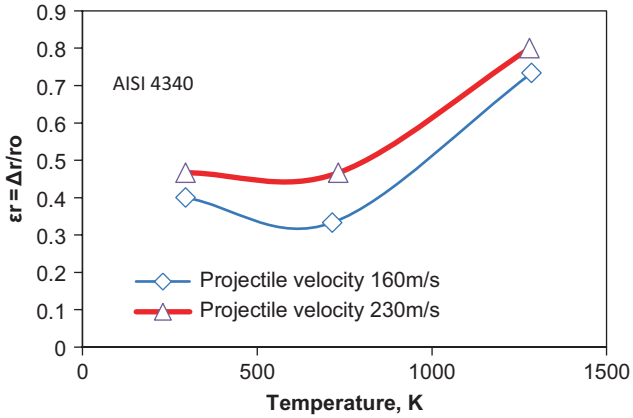

Fig. 4.9 Effect of temperature on the distortion of the AISI 4340 sample cylindrical surface

The influence of impact velocity on the strain localization area ***f*** at compression of Al and Cu cylinders is shown on Fig. 4.10.

The increase of impact speed leads to enlargement of localized strain volume fraction for both Al and Cu samples in the range of 100–400 m/s. The further increase of particle velocities above critical velocity threshold results in change of deformation mechanism at the interface due to adiabatic shear band development (Assadi et al. 2003, 2016; Schmidt et al. 2006). So, it looks like LPCS process allows to realize preferably the low-impact velocity localization mechanism.

One of the main specific features of LPCS is known as radial particle injection into divergent part of de Laval nozzle (Fig. 4.1). The propellant gas is heated up to tempera-

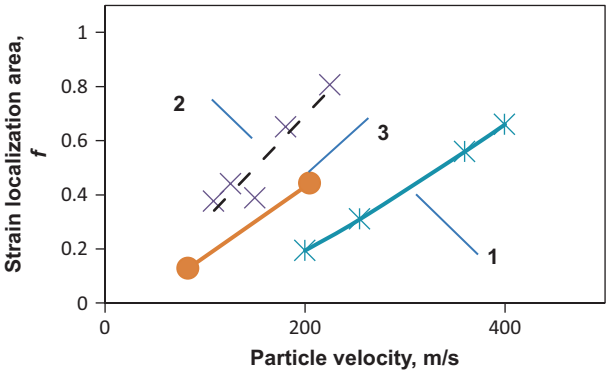

Fig. 4.10 The strain localization area fraction *f* vs. particle velocity. *1* – Gust 1982 experimental results of Al cylinders impact deformation; *2* – Gust 1982 experimental results of Cu cylinders impact deformation; *3* – Eakins and Thadhani 2006 experimental results of Cu cylinders impact deformation

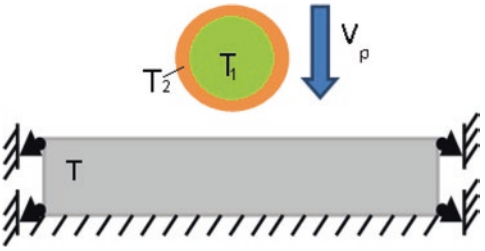

Fig. 4.11 The schematic diagram of impact model with boundary conditions

tures 300–500 °C, and particles injected are heated during acceleration. The temperature distribution through the particle is function of a material thermal conductivity, particle acceleration time and surface temperature. The rough evaluation of the particle temperature gradient shows that it is possible to apply an assumption of the two-layer temperature distribution for numerical simulation of particle deformation process.

Numerical Simulation

To study the stainless steel particle deformation during deposition with the CS process, a dynamic simulation of impact of the AISI 316 L particle imaging upon the carbon steel substrate was run, using commercial Ls-Dyna multi-material *arbitrary Lagrangian-Eulerian* method (Ls-Dyna 2013). A 2-D FEM analysis was performed for 50 μm particle size configurations. Figure 4.11 shows the scheme of the simulated model. The bottom surface of the simulated substrate was fixed, and additionally the horizontal movements of the substrate in two perpendicular directions were limited by fixing the substrate sides. For 50 μm AISI 316 L particles impinging upon the substrate at the impact velocity V_p = 400 m/s.

Flow stress of both materials was defined using Johnson-Cook model which is described by the following equation:

$$\sigma = \left(A + B\varepsilon^{n}\right)\left(1 + C\ln\dot{\varepsilon}^{*}\right)\left(1 - T^{*\mathrm{m}}\right) \tag{4.3}$$

where σ is the (Von Mises) flow stress, A is the yield stress at reference temperature and reference strain rate, B is the coefficient of strain hardening, n is the strain hardening exponent, ε is the plastic strain, $\dot{\varepsilon}^{*} = \dot{\varepsilon} / \dot{\varepsilon}_{0}$ is the dimensionless strain rate with $\dot{\varepsilon}$ being the strain rate and $\dot{\varepsilon}_{0}$ the reference strain rate and T^{*} is the homologous temperature and expressed as:

$$T^{*} = \frac{T - T_{ref}}{T_{\mathrm{m}} - T_{ref}}$$

A, B, C, m and n are Johnson-Cook constants which were taken from (Assadi et al. 2003).

Figure 4.5 a, b demonstrates the equivalent strain distribution in the particles during impact of particle with temperature gradient. It can be seen from the images in Fig. 4.11a that the strain of the surface layer with initial temperature 282 C is about $\varepsilon_i = 1.1$, while the strain of similar surface layer with initial temperature of 550 C (Fig. 4.11b) is in the range of $\varepsilon_i = 2.1$–3.2. Thus, the preliminary modelling results reveal about intensifying localization effect due to impact deformation of the particles with temperature gradient. It is interesting to note that the temperature distribution for both cases (Figs. 4.12. and 4.13.a, b) is similar in spite of difference of initial temperatures of both particle core and shell.

The numerical simulation results of stainless steel particle impact demonstrate that increase of particle initial temperature gradient allows to achieve high equivalent strains at the interface at the relatively low particle velocities without adiabatic shear band formation effect. Validation of this assumption may be made by microstructure analysis of CS coatings deposited by LPCS.

Comparison of CS-deposited copper and stainless steel coating microstructures is shown on Figs. 4.2, 4.3 and 4.14. It is clearly seen on Fig. 4.2a that high-pressure CS deposition leads to mushroom shape and jetting of the most particles that reveals about adiabatic shear band formation at the particle-particle interface as shown in (Assadi et al. 2003, 2016; Maev and Leshchynsky 2015). Contrary, microstructure of copper coatings made with low-pressure CS demonstrates preferably elliptical shape of particles. Looks like adiabatic shear band localization mechanisms are not developed in the last case because the particle velocity is lower than critical velocity defined by Assadi et al. 2003. Nevertheless, one can see the high density of low-pressure CS copper coatings that reveals about occurrence of severe deformation of the copper particles with another mechanism. Based on numerical simulation results of Cu particle deformation (not shown here), one can assume that temperature gradient particle deformation mechanism may result in relatively high strains of the particle shell (up to $\varepsilon_i > 3.5$) that lead to coating intensive densification and consolidation.

Similar hypothesis of LPCS coating structure formation may be used for stainless steel coatings. Microstructure presented on Fig. 4.14.a shows deformed particles

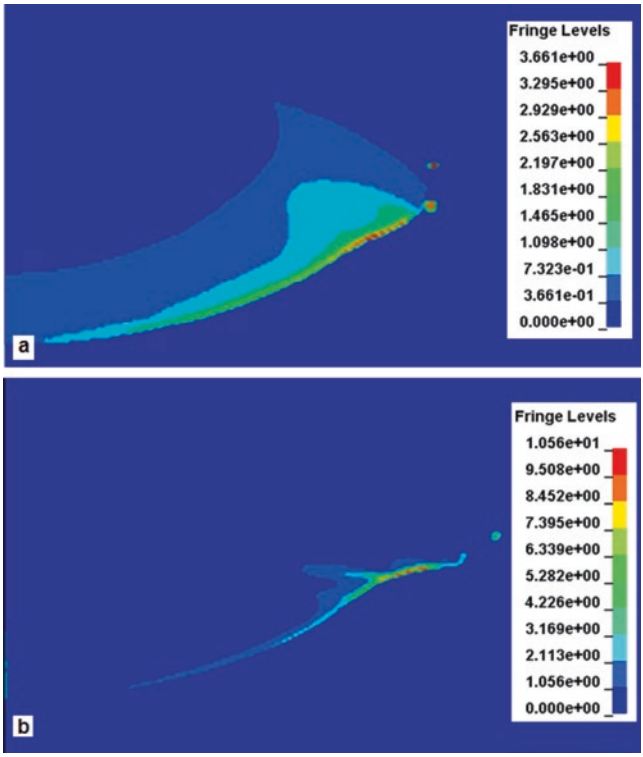

Fig. 4.12 Numerical simulation results of the impact with the carbon steel substrate. Equivalent strain distribution at 50 μm particle impact with 400 m/s. (**a**) Particle shell-5um, core T = 25 C, shell T = 282 C, impact time −0.08us; (**b**) particle shell-5um, core T = 110C, shell T = 550C, impact time −0.08us

without essential features of adiabatic shear band localization. The total strain of separate particles is high. However, some of the particles are not severely deformed. A distortion of grains in the deformed particle allows to approximately estimate a strain distribution through the particle. It is clearly seen (circles on Fig. 4.14.b) that the severe deformation of grains is observed in the particle surface layers that reveals about strain localization in these areas. The higher temperature of the particle surface layer (see Fig. 4.13.) leads to decrease the steel flow stress that results in strain localization during the particle impact. Contrary, the particle core with lower temperature does not deform intensively. So, this effect seems to be an evidence of presence of strain localization processes at the particle-particle interface due to deformation of the particles with the temperature gradient.

One can note that some recrystallized grains are observed in the structure (white arrows on Fig. 4.8.b). It is difficult to define the origin of recrystallization, and this effect will be further studied in the ongoing work.

The effect of strain localization due to low-pressure cold spraying deformation of particles with temperature gradient is defined by (i) analysis of impact

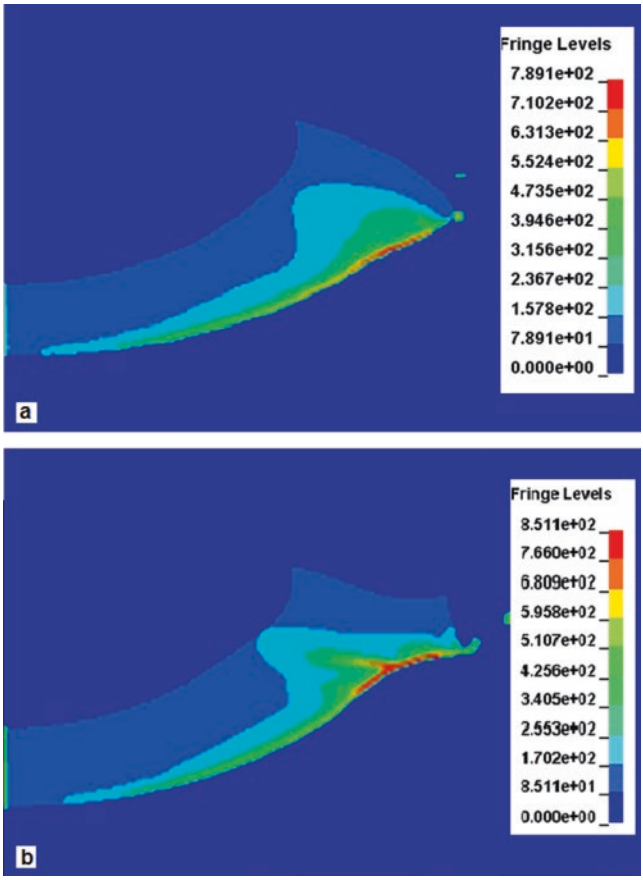

Fig. 4.13 Numerical simulation results of the impact with the carbon steel substrate. Temperature distribution at 50 μm particle impact with 400 m/s. (**a**) Particle shell−5 um, core $T = 25$ C, shell $T = 282$ C, impact time −0.08 us; (**b**) particle shell-5um, core $T = 110$ C, shell $T = 550$ C, impact time −0.08 us

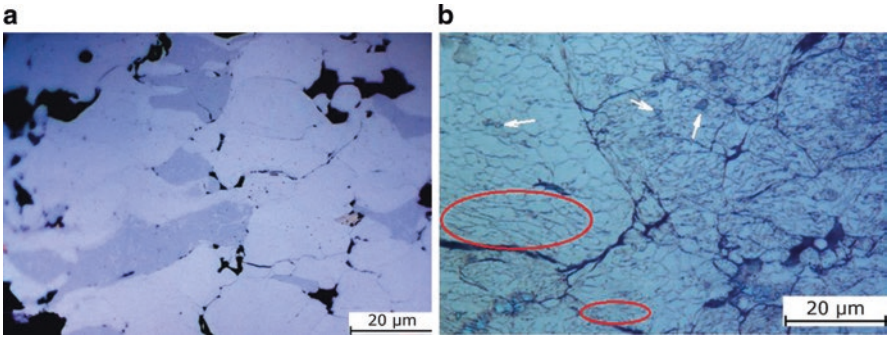

Fig. 4.14 Microstructure of stainless steel (AISI 904) coating made by low-pressure CS. Propellant gas-air, $T = 800$C. (**a**) unetched; (**b**) after etching with Glyceregia

compression, (ii) numerical simulation and (iii) analysis of the deposited Cu and stainless steel microstructure.

It is found influence of particle thermal gradient on the parameters of localization at axial compression with strain rates of 10^{-3}–10^{-7} s^{-1}, localization areas in the stainless steel particles after deposition. The temperature gradient of the particles to be sprayed was achieved due to particle radial injection and short time of the particle acceleration in the divergent part of the de Laval nozzle.

4.1.4 Composite Coatings

While relatively wide dissemination of the HPCS technology occurs during the last decade, the application of LPCS process which is being applied for deposition of soft metals and metal matrix composites (Maev and Leshchynsky 2007) is not widespread. The advanced material science needs the new composite materials which consist of a soft matrix and hardening phases such as carbides, intermetallics, etc. The deposition of these composite materials by LPCS and structure formation processes during following processing steps have not been deeply described and developed yet. As shown on Fig. 4.1, the main goal of technology is to analyze the specific features of CS and post-processing of composite coatings obtained by deposition of powder mixtures or separate layers of the soft and hard materials and to define their influence on composite structure and properties.

The properties of composite materials depend on their phase composition and structure of various phases. For this reason, it seems to be reasonable to organize the cold-sprayed material structure by following heat treatment. Such a combined technology opens the new opportunities to control the phase composition, dislocation and grain structure of materials. In this case, the new possibilities to obtain various phase composition and properties of materials are opened. This combined technology looks to be extremely reasonable in the case of LPCS build-up process because of its simplicity, portability and ability to be applied in industrial environment. That is why from application point of view, development of the combined LPCS – heat treatment technology is very important for composite materials (coatings) obtained by CS.

The main processes controlling CS coating structure formation during annealing (Fig. 4.1) are the following:

(i) Recrystallization, phase transformation during coating annealing
(ii) Reaction sintering processes with some compounds and intermetallic phases formation
(iii) Internal oxidation processes

Some specific effects such as Kirkendall effect, pores and cracks initiation and growth have to be taken into account.

Advanced surface engineering offers many possibilities to modify the properties of surfaces to achieve the better exploitation performance using various surface treatments, deposition of thin layers or processing of thick surface coatings as shown by Holmberg and Matthews 2009. Thin coatings, like physical vapour deposition (PVD) and chemical vapour deposition (CVD) coatings, are excellent in many tribological applications, and they are being used largely today. However, they may be helpless, in particular, in harsh, high-load and high-temperature conditions due to both material and structural limitations originating from their tiny thickness, which is typically in the range of 1–3 μm and even less. The use of thick composite coatings is another solution to tailor surface properties of the component. As shown in Chap.1, the typical processing methods for thick coatings are thermal spraying and laser powder cladding. These methods offer a flexible route to produce the composite structured, rather thick coatings, in a typical thickness range of 150 μm…3 mm, on a substrate material selected according to other criteria, like price, extent of alloying elements and other additives, mechanical strength and low weight (Davis 2004). CS technology opens the wide possibilities to produce the thick metal and composite coatings in the wider thickness range (100 μm…10 mm) with high dimensional accuracy due to coating formation at the relatively low temperatures.

In general, a composition, structure and surface characteristic determine the properties of materials. The surface properties of various components have a strong influence on their behaviour. In most of cases, the component surface is exposed by a combination of various factors such as mechanical, tribological, thermal, corrosion, etc. These factors can cause degradation of material properties or even its damage. Coating can reduce the environmental effects in many cases (Fig. 4.15.).

Over the last decades, a myriad of hybrid coating materials suitable for thick coatings – mainly mixtures and composites of ceramics, metals and polymers – has been

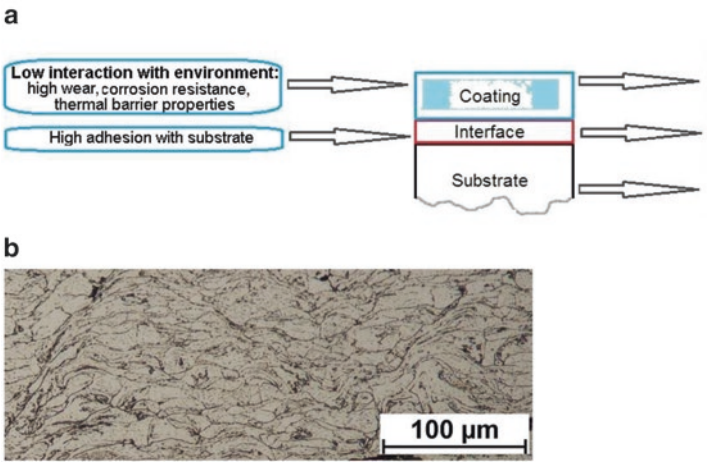

Fig. 4.15 Functions of the coatings. (**a**) The main possible functions of the coating and interface; (**b**) an example of the LPCS Al coating structure on the A2024 substrate

developed. Entirely new possibilities for developing high-performance materials have opened up in the 2000s, with the development of new manufacturing methods, wide spread adoption of nanotechnology and more in-depth understanding through new process diagnostics and higher modelling capacity (Holmberg et al. 2014). Particle-reinforced composite materials consisting of a metal matrix and hard dispersed particles offer a potential solution for increased wear resistance demands. An improvement in wear properties is often counterbalanced by the deterioration of other properties, such as impact resistance or corrosion resistance. It is important to tailor and optimize the material for the particular application, taking all the requirements into consideration.

Thick composite coatings, such as the LPCS coatings, need to be characterized and classified in terms of their complex composite microstructure, including interparticle boundaries, grains, pores, phases, etc. Figure 4.16 shows a general LPCS coating characterization based on its microstructure. It is seen that the composite coatings need to be made of powder mixtures. Deposition of the powder mixtures is one of the main advantages of LPCS technology (Maev and Leshchynsky 2007). These second phases are incorporated during deposition process or created later within the coating using post-processing treatment.

Dispersion phases in the coatings can influence the coating properties and as a rule improves them. The combination of the coating matrix (base material) and dispersion phases results in significant change of the properties, and so careful selection of this combination is very important (Steinhauser and Wielage 1997). Mainly, various compounds in the form of particles or, in small amounts, short fibres are used as the reinforcement phase.

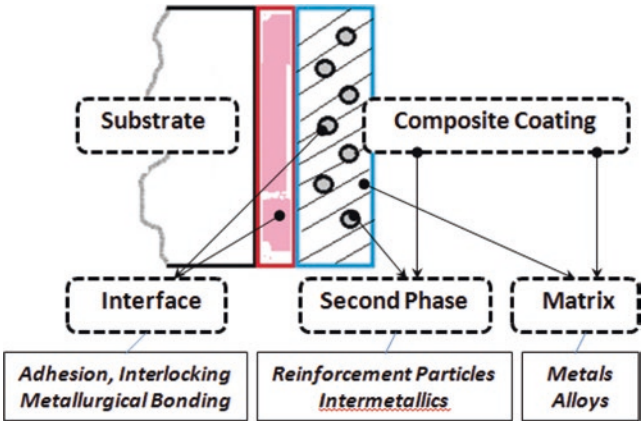

Fig. 4.16 Microstructure schematic depiction of LPCS metal matrix composite (MMC) coating

4.2 LPCS Applications

As shown by Pawlowski 2008, advanced thermal spray technologies such as HVOF, wire arc or flame spraying, plasma spraying and detonation spraying are widely used within the automotive industry, among many others. As an example, according to Barbezat (2006), a large portion of engine and transmission components are coated using various processes. While some of these applications have already reached maturity, many others are relatively new, representing an important market for the future of spraying technologies and, in particular, CS. The range of materials that may be coated, as well as the quality of CS deposits, depends to a large extent on the particle velocities that may be attained, as well as the mechanical characteristics of both the particles and substrate. From this viewpoint, it is beneficial to compare the capabilities of HPCS and LPCS processes in the context of their industrial applications. As discussed by Villafuerte (2005), the application of helium as a processing gas for HPCS provides the highest possible supersonic flow velocities. This technology, then, is capable of successfully depositing the widest range of materials in an oxygen-free environment. Unfortunately, helium is both relatively expensive and requires the use of special gas-handling and recovery/recycling equipment. Nitrogen, on the other hand, is considerably less expensive while being equally capable of providing an oxygen-free environment. The supersonic velocities obtained with nitrogen, however, are lower than with helium, limiting the range of coatings that can be produced. Air in fact offers the least expensive alternative but has the narrowest range of known applications, being generally limited to those processes that are not extremely sensitive to the presence of oxygen at low temperatures. The recent work of (Li et al. 2017) demonstrates that in the most of cases the HPCS material contains poorly bonded splats which could exceed 20% of the total volume of the coating. So, application of combined CS and coating heat treatment/sintering technology is important to achieve the desired coating properties.

In the case of LPCS with using air as a propellant gas, the particle velocities are in the range of 300–500 m/sec which is only sufficient for the successful bonding of soft metals such as Zn, Al and Sn. It has been shown in previous chapter that uniform and localized plastic deformation at the particle-substrate and particle-particle interface is necessary to achieve the proper bonding. For this reason, successfully cold-sprayed powders and substrates consist primarily of metals with relatively high plasticity. Nevertheless, as discussed by Maev and Leshchynsky 2007, there exist clear-cut distinctions between the behaviour of single and collective particle groups when impacting a surface. It is for this reason that it is indeed possible to successfully spray various powder mixtures onto both metallic and ceramic substrates alike. In fact, the presence of a metal-ceramic powder mixture allows sufficient particle deformation to take place at particle velocities that are significantly lower than that required for the bonding of pure metals. Therefore, the range of materials that can be successfully sprayed by LPCS may be expanded to include not only pure metals such as Al, Zn, Cu, Fe, Ni and Ti but also composites such as Al-Al_2O_3, Al-B_4C, Al-Zn-Al_2O_3, Cu-Pb-Sn Cu-W, Cu-Zn-TiC and Ni-SiC, among others. In order to

emphasize the benefits of LPCS, some specific applications are described in the sections to follow.

4.2.1 Repair Applications of LPCS Technology

Various surface engineering technologies such as laser cladding, HVOF and plasma spraying are presently used to repair aerospace, automotive, marine, rail or other such components where excessive wear has occurred. Here, CS processes are utilized to reduce residual material stresses without perturbing the nanostructure of the build-up layer with excessively high temperatures. Also, these techniques are beneficial for repairing irreplaceable, high-value or over-machined components. The ultimate application of CS, however, is to build components up from nothing; this may be accomplished using a laser cladding system and a 3D-CAD drawing of the component. It is for this reason that CS is emerging as a special technique for rapid prototyping (RP). Indeed, the combination of CS with RP is an interesting approach to repair technology which offers an alternative to traditional tool builders, remanufacturers and repair industries. For example, a LPCS build-up process may be readily implemented into the industrial workplace by means of a portable LPCS machine (Fig. 4.17a), providing a cost cutting repair technology that may be employed to

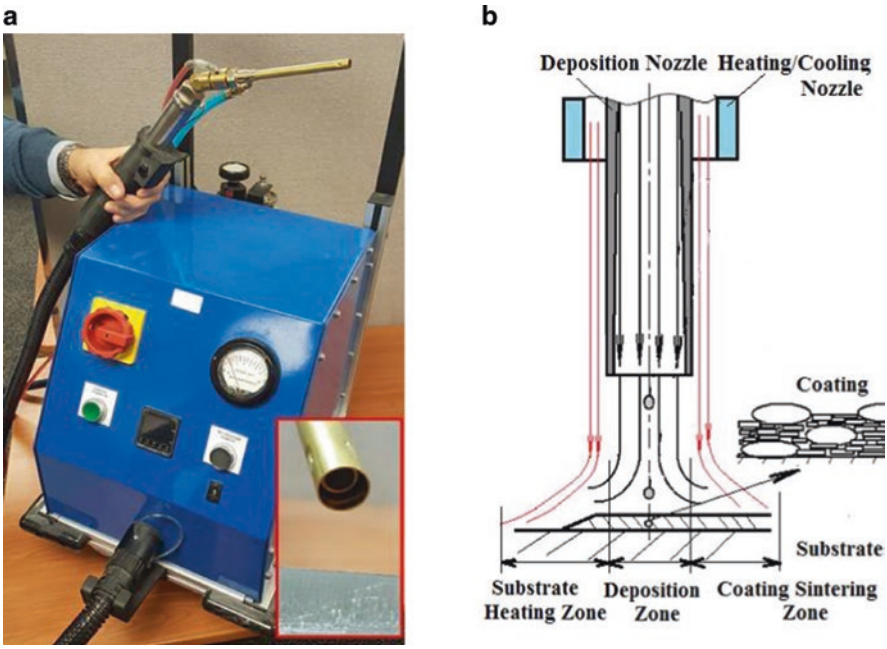

Fig. 4.17 Double-flow cold spray portable machine in accordance with Maev et al. 2017 (**a**) and schematics of the composite coating deposition (**b**)

increase the wear resistance of mechanical components, in casting repair and sealing and car body shape restorations. The repair of aluminium structures by LPCS techniques is also of particular interest in reclamation applications. Instead of replacing an entire structure, it is sufficient in many cases to simply employ a surface coating. Hence, tremendous savings may be realized through the application of LPCS techniques.

For further development to take place with respect to improving the wear resistance of mechanical components, it is necessary to efficiently choose composite coatings for LPCS that bring about the desired mechanical properties. Because of their versatility, then, metal-ceramic composite coatings are of great interest. For example, the incorporation of metal and ceramic particles within various alloys acts to increase their load-bearing capacity (Straffelini et al. 2004). This technology provides new opportunity for the employment of Al-, Ni- and Cu-based metal matrix composites (MMC) in applications where sliding resistance is of concern.

Since cold spray does not require heat, like common repair processes such as welding, it allows the repaired part to be restored close to its original shape. Authors are exploring double-flow LPCS-3D printing as an alternate way to restore various metal art works. The unique capabilities of the LPCS process include (i) corrosion protection, (ii) leakage sealing and (iii) material build-up. The indicated capabilities enable the application of the LPCS process in such diverse areas as:

(i) Oil and gas offshore platform and pipeline repair and maintenance
(ii) Municipal electrical and water supply services
(iii) Vehicle, aircraft and yacht body repair and maintenance
(iv) Cultural heritage objects restoration

The Double-Flow Cold Spray Machine

While the details of LPCS technology were described elsewhere (Maev and Leshchynsky 2007), the double-flow cold spray machine (Fig. 4.17) is developed to overcome the well-known drawbacks of LPCS technology described in p. 1. The main features of new machine design are the following:

(i) Presence of the air cooling envelope which allows to cool/heat the nozzle and substrate during deposition process. It ensures to control the temperature regime at the deposition field.
(ii) Opportunity to couple the cold spray gun with the shot peening gun (Maev et al. 2017) in order to additionally densify and severely deform the deposited coating at various temperatures.
(iii) Opportunity to make layered coating in a single pass deposition.

The use of double-flow LPCS technology insures the particle deformation both during impact and following densification at the controlled temperatures allows to deposit a variety of powders, including **metals or metal-ceramic mixtures. The composite coatings** can be formed.

It is important to emphasize that the compressed nitrogen pressure was kept constant at 0.6 MPa, which is quite low, compared to other cold spray methods (usually in the range of 2–5 MPa) (Assadi et al. 2003 and Van Steenkiste et al.

1999). Due to the fact that special high-pressure pumps are no longer needed, this feature makes CS with powder radial injection technology much more suitable for industrial environments. Additionally, nitrogen consumption is lower than in typical cold spray systems, requiring only about 0.2–0.3 m^3/min (as compared to typical rates of 1.3 m^3/min) (Van Steenkiste et al. 1999). The particle velocities at the exit plane of the supersonic nozzle, as measured by a laser Doppler velocimeter, were in the range of 550 m/s. The powder feeding rate was varied in the range of 0.5–1.5 g/s, while the standoff distance from the exit of the nozzle to the substrate was held constant at 15 mm. Commercially available aluminium, nickel and copper powders (−50 microns), TiC powder (−45 microns), Zinc powder (5–10 microns) and Tungsten powder (3–10 microns) were used as the base materials.

Repair of Damaged Aluminium Panels

Repair of damaged aluminium panels is quite difficult and needs lots of labour hours. LPCS allows for quick and economically reasonable repair of the dented aluminium body panels. Areas with high demand for aluminium body panel repair include (i) airplane repair and maintenance, (ii) helicopter repair and maintenance, (iii) yacht repair and maintenance and car repair and maintenance.

Figure 4.18 depicts the Al coating height dependences on distance from the centre of dent. The dent geometry was measured as well. The coating of microstructure is shown on Fig. 4.19. The results reveal that the LPCS technology allows to obtain the dense coating with good adhesion strength on A2024 substrate. Previously similar results were obtained for repair of steel body in white as shown on Fig. 4.20 (Maev and Leshchynsky 2007).

Sculpture Restoration

Works of art are subject to a variety of disfiguring influences, many caused by environmental effects, changes in temperature and humidity in particular, as well as

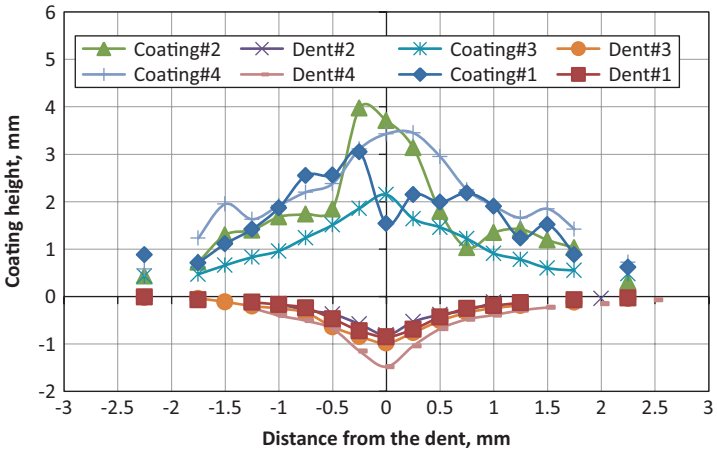

Fig. 4.18 Geometry of LPCS-deposited Al layers on the dents of A2024 aluminium alloy panels

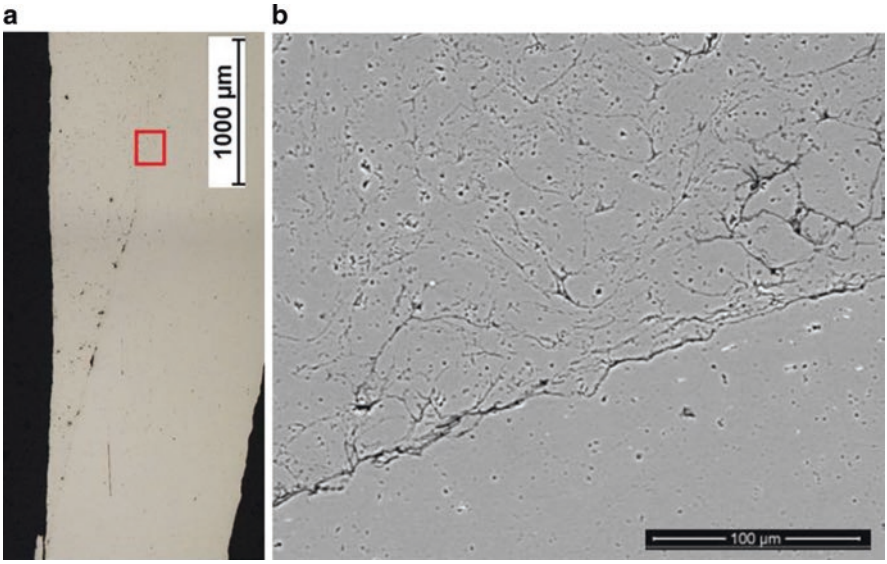

Fig. 4.19 Microstructures of A2024 dent repair by LPCS aluminium coating after grinding. (**a**) Al coating in the dent field (no etched); (**b**) Al coating in the square area (**a**) (etchning with HF-HNO_3-HCl-H_2O solution)

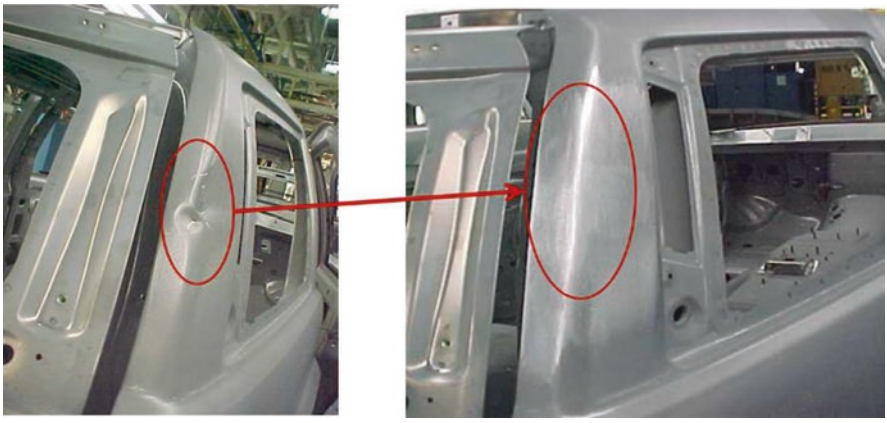

Fig. 4.20 In-field dent repair of Chrysler vehicle by LPCS in the car assembling plant (Maev and Leshchynsky 2007)

damage from pollution. Metal art conservation and art sculpture restoration are the preservation by slowing or stopping altogether the processes that lead to the damage to works of art, as well as the restoration of those objects.

Metal monuments and works of art are among the largest material groups for cultural heritage objects. Iron, copper, titanium, aluminium and their various alloys play an important role as original core materials among a very wide assortment of

alloys used by artists in the past. Original metalwork and sculpture sustain a variety of damage over its lifetime. Most metals corrode on contact with water, acids, salts, oils, aggressive metal polishes and other chemicals. The type of corrosion depends on the composition of the base metal. Additionally, original cast surface and subsurface defects such as cracks, pores and other defects can accelerate the corrosion damage. Among the other possibilities is physical damage due to various kinds of impacts or mishandling of metal items. Accidental damage, material degradation and dirt deposition are the most common types of deterioration. Apart from physical damage, the most typical type of deterioration seen in metal artefacts is the result of chemical changes due to interaction with chemicals spread in the environment. Alteration and corrosion processes on buried archaeological artefacts are quite different to those exposed to atmospheric degradation (Schmitt et al. 2009). Thus, the restoration technology should be flexible and allow for restoring metal objects from any of the forms of damage detailed above.

The LPCS technology gives capability of in situ material deposition from tens of microns to centimetres, varying the composition and characteristics of the formed coatings and imparting such properties as near full coating density, high adhesion strength and corrosion resistance of the formed coatings. The relatively low temperature and carefully controlled deposition rate without significant heating of the substrate are the main specific features of the LPCS technology, which allow its wide usage as the precision restoration procedure of various metal works of art. Therefore, the implementation of the proposed cold spray process for restoration of metal works of art can make the process of restoring metal works of art considerably more efficient and economically attractive. Especially important is the application of the LPCS technology in the field of cost sensitive cultural heritage objects, allowing the maintenance and in-field repair/restoration and corrosion protection of metal sculptures and monuments.

An example of LPCS restoration technology application is shown on Fig. 4.21 which demonstrates the restoration of the bronze statue of General Gordon located at the Gordon School in Wokingham. The right legs on the camel were severely corroded due to water ingress corroding the steel reinforcing structure in the legs. The right front leg#2 (Fig. 4.21b) was removed and shipped to Canada to be restored using the LPCS process. On completion, the leg was returned to the UK and welded back onto the camel. The completed restoration with in-field restoration of the leg#2 is shown on Fig. 4.21d.

4.2.2 Corrosion Protection of Aluminium Alloys

Since aluminium and magnesium alloys are very important in aerospace and automotive manufacturing, a number of studies have been conducted on the applicability of cold spray coatings to corrosion protection of such alloys (DeForce et al. 2007; Lee et al. 2005; Spencer et al. 2009; Tao et al. 2009; Gray and Luan 2002). Deposition of corrosion-protective coating on aluminium and magnesium alloys by

Fig. 4.21 Restoration of Gordon Camel bronze sculpture (UK). (**a**) Monument general view; (**b**) leg#1 after LPCS and patination; (**c**) leg#1 after cold spraying; (**d**) leg#2 after in-field LPCS and grinding

the LPCS technique presents a special interest due to the possibility of applying the coatings in field conditions and in repair shops (Koivuluoto et al. 2008; Yandouzi et al. 2014; Champagne et al. 2015). Two examples demonstrating effectiveness of cold spray-deposited coatings for corrosion protection of high-strength aluminium (AA2024) and magnesium (AZ31) alloys are given below.

High-Strength Aluminium Alloys

High-strength aluminium alloys, such as AA2024, containing copper as primary alloying element are used for structural applications in aircraft industry due to their good fatigue resistance and high-strength/weight ratio (Heinz et al. 2000; Nakai and Rto 2000).

However, it is also known that the copper-rich aluminium alloys are prone to corrosion (Nie 2014). In chloride solution such types of localized corrosion as pitting, galvanic corrosion and intergranular corrosion, including exfoliation corrosion, have been observed (Boag et al. 2010: Boag et al. 2011; Hughes et al. 2011). The localized corrosion of high-strength aluminium components can lead to their sudden failures and results in considerable loses. In order to protect high-strength aluminium parts from localized and other types of corrosion, protective coatings have to be used (ASM Handbook 2003).

A systematic study of the dependence between Al-Al203-Zn powder spray composition and the corrosion-protective properties of the LPCS-deposited coatings on high-strength AA2024-T3 Alclad substrates was performed by (Dzhurinskiy et al. 2012). The following precursor materials were used for the LPCS process-based coating deposition: Al metal powder (designation CP1), Zn metal powder and alumina Al_20_3 powder. The powder compositions were varied: (i) 75%Al + 25%Al_2O_3 – CP2; (ii) 50%Al + 50%Al_2O_3 – CP3; (iii) 30%Al + 50%Al_2O_3 + 20%Zn – CP4; and (iv) 35%Al + 40%Al_2O_3 + 25%Zn (in volume %) – CP5.

The corrosion resistance of the protective coatings was evaluated using the open circuit potential and potentiodynamic polarization techniques (Ahmad 2006). The samples were placed in 1 M sodium chloride solution at room temperate and subjected to the accelerated corrosion test according to ASTM B117. The corrosion rate (CR) was calculated in accordance to ASTM G102.

Open Circuit Potential (OCP) Monitoring

The evolution of the OPS for samples immersed in chloride solution is shown in Fig. 4.22a. As can be seen, an abrupt decrease in OCP takes place around a 15-min mark, indicating that the tendency to corrode is increased. This initial fall is ascribed to the destruction of a virgin aluminium oxide film formed during the cold mill rolling process. The OCP of the Alclad sample gets stabilized at 730 mV/SCE. The corrosion behaviour of the examined cold-sprayed coatings depends on the powder feedstock composition. The OCP of the cold-sprayed coating made of pure aluminium (CP1) does not depend on immersion time in the sodium chloride media. That reveals the presence of a relatively stable protective oxide film on the coating surface similar to that described in the paper of Rojas and Rodil 2012. The as-sprayed CP2 and CP3 coatings exhibit the slight change of the OCP towards to the negative value during immersion time, and the potential stabilizes at −762 mV/SCE

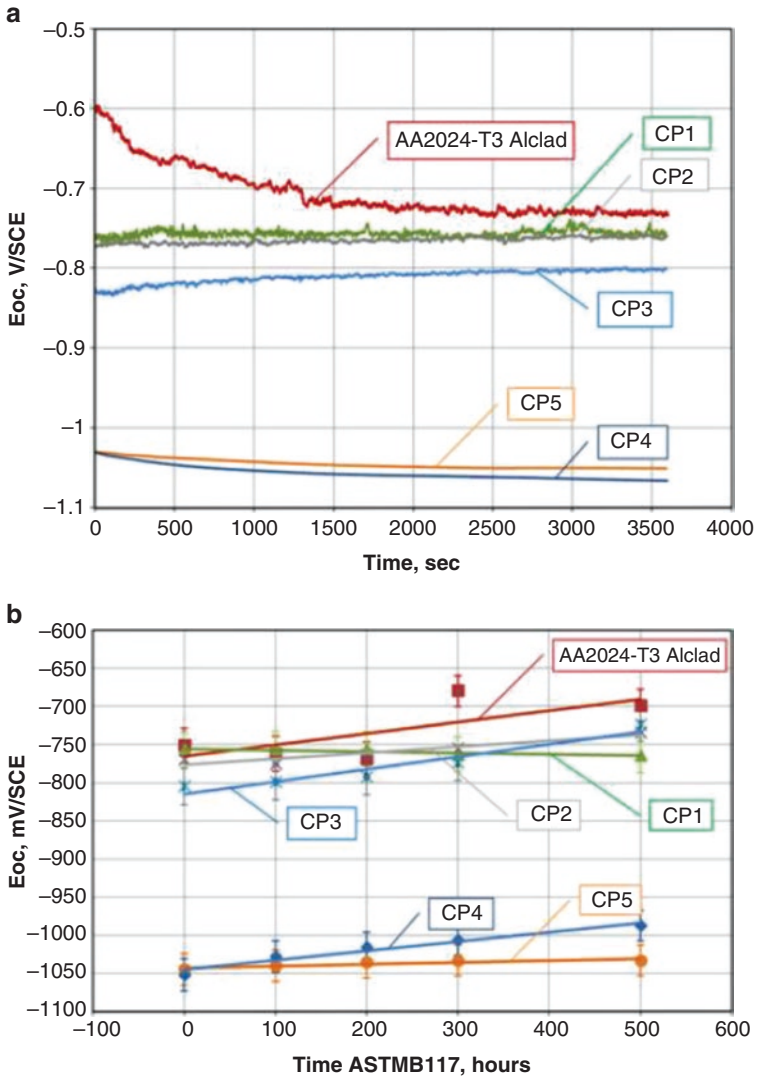

Fig. 4.22 Evolution of the open circuit potential (E_{OC}) for the investigated samples: (**a**) E_{OC} as a function of immersion time in corrosive media; (**b**) E_{OC} as a function (linear regression) of accelerated salt fog corrosion test

for CP2 and −801 mV/SCE for CP3, respectively, whereas the Al-Zn-Al_2O_3 coatings exhibit the decrease of the potential up to −1050 mV/SCE. It should be noticed that the higher is the volume % of Zn in the sprayed powder composition, the more negative OCP potential is observed, which can be linked to the sacrificial behaviour of Zn as it was demonstrated in (Baker et al. 2000; Guzman et al. 2000).

The OCP oscillation behaviour that displays itself as data noise is another characteristic feature of the potential monitoring. The observed oscillation is usually attributed either to the initiation of pitting or to the passive film breakdown. The parameters of the oscillation depend on the surface roughness and electrochemical reaction kinetics (Tao et al. 2010). As can be seen in Fig. 4.1a, the amplitude of the OCP oscillation for the Alclad substrate (surface roughness Ra = 0.6 μm) is approximately 8 mV. The amplitude of the OCP oscillation for the Al coating (surface roughness Ra = 12.5 μm) is about 2 mV. That may indicate that the Al coating is dissolving more uniform as compared with AA2024-T3 Alclad substrate surface.

The kinetics of the corrosion process may be evaluated in terms of the dependence of the OCP on the corrosion time (Winston 2011). The experimental data of the OCP variation with time $E_{corr} = f(t)$ is approximated by linear functions as shown in Fig. 4.22b. It can be seen that the OCP of pure Al coating (CP1) remains stable during the entire test time, while the Al-Al_2O_3 coatings (CP2 and CP3) become more noble due to permanent oxidation in a corrosion environment which results in a growth of the dense oxide film. The behaviour of Al-Zn-Al_2O_3 coatings (CP4 and CP5) differs from other coating behaviours due to the sacrificial effect of Zn and results in higher corrosion rate due to providing sacrificial corrosion protection to AA2024-T3 Alclad substrate.

Potentiodynamic Polarization Measurements

The potentiodynamic DC polarization testing was conducted to gain detailed understanding of the coating corrosion properties (Chang and Park 2010). The potentiodynamic polarization curves of uncoated AA2024-T3 Alclad substrate and as-sprayed CP1, CP2 and CP3 coating layers are presented in Fig. 4.23a. It can be seen that the corrosion potential E_{corr} is decreasing with an increase of alumina content in the CP1, CP2 and CP3 coatings. The corrosion potential is about 720 mV/SCE for the AA2024-T3 Alclad, whereas for the CP1 coating is −738 mV/SCE which is in agreement with (Guillaumin and Mankowski 1999; DeForce et al. 2007). For the CP2 and CP3 coating layers in as-sprayed condition, the corrosion potential becomes about −1080 mV/SCE.

The polarization curves of the examined composite coatings CP2 and CP3, depicted in Fig. 4.23a, exhibit two breakdown potentials: the more active E_{b1} is close to −1080 mV/SCE, and the nobler E_{b2} is close to −760 mV/SCE, where the region between E_{b1} and E_{b2} is a passivity area in which the current density remains practically constant. Each of these breakdown potentials presents a threshold of the anodic current density sharp growth. According to (Maitra and English 1981; Smulko et al. 2007) the breakdown potential, E_{b2} corresponds to the dissolution potential of an Al matrix, whereas E_{b1} is associated with the dissolution of the aluminium along the boundaries between aluminium and alumina particles. Thereby, the corrosion protection efficiency was different with an increase of ceramic particles content in the coatings.

The kinetics of the corrosion potential evolution during an accelerated corrosion test are shown in Fig. 4.23b as a function of the emersion time. The obtained results show two types of corrosion potential behaviour with time $E_{corr} = f(t)$: (i) E_{corr} increases with time and (ii) E_{corr} decreases with time. This reveals two coating corrosion mechanisms: noble for CP1, CP2,and CP3 (associated with the growth of

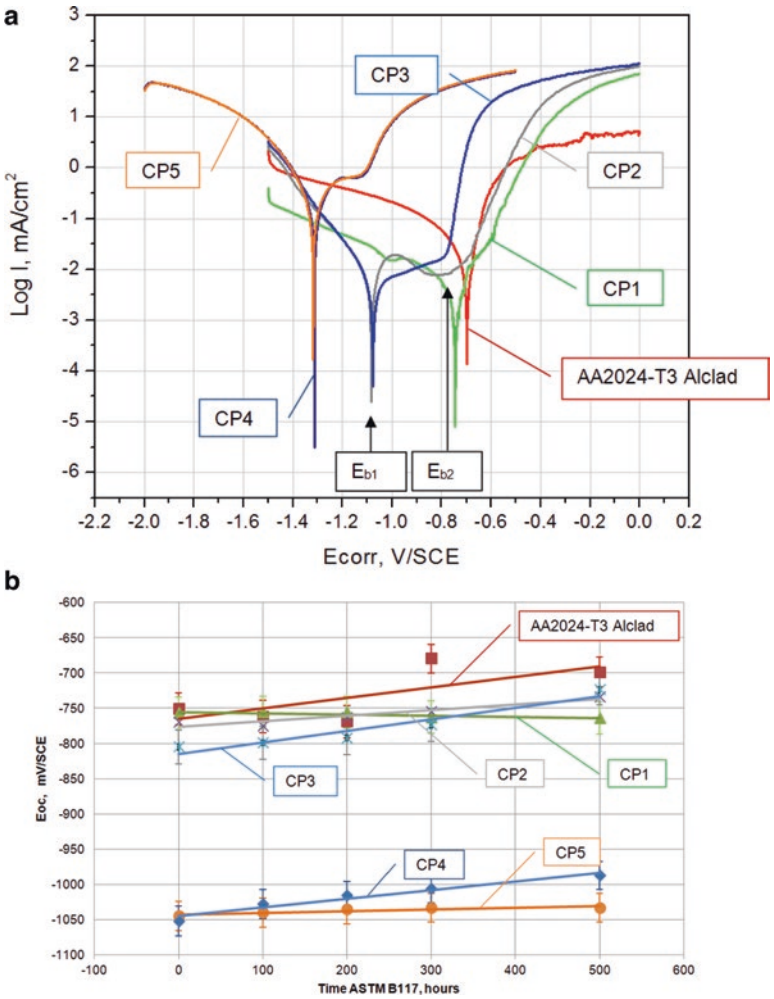

Fig. 4.23 Evolution of the corrosion potential (E_{corr}) for the investigated samples: (**a**) Potentiodynamic DC polarization curves before corrosion test; (**b**) E_{corr} as a function (linear regression) of accelerated salt fog corrosion test

oxide film) and sacrificial for CP4 and CP5 (associated with the dissolution of the coating layer due to the presence of Zn).

The behaviour of corrosion current (I_{corr}) is shown in Fig. 4.24. The I_{corr} is poised at 0.2 μA/cm^2 for the AA2024-T3 Alclad substrate and at 0.8 μA/cm^2 for the CP1 coating. Contrary, the I_{corr} dependence of the CP2 and CP3 coatings decreases from 1.3 to 1.05 μA/cm^2 and from 0.9 to 0.3 μA/cm^2, respectively. Thus, the experimental results show that LPCS-deposited Al powder coating layers have the best corrosion protection properties as compared to other composite coatings studier in this work. Also, the results of DC polarization measurements are in agreement with the OCP measurements, where it was demonstrated that the potential depends on the content of Al_2O_3 within the coating.

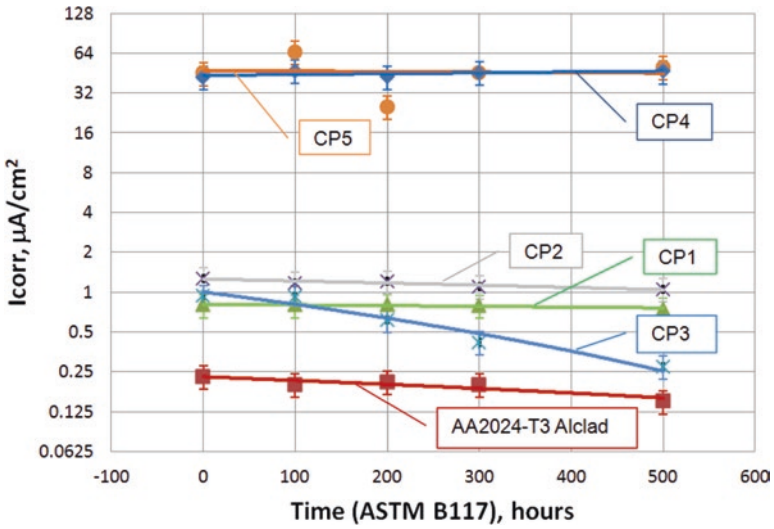

Fig. 4.24 Evolution of the corrosion current (I_{corr}) as a function (linear regression) of accelerated salt fog corrosion test

Al-Zn-Al_2O_3 coatings exhibit significantly higher I_{corr} values than those of AA2024-T3 Alclad substrate (46 µA/cm² for CP4 and 50 µA/cm² for CP5). The E_{corr} of CP4 and CP5 coatings is significantly lower than that of Alclad substrate, which reveals an active dissolution of the Al-Zn-Al_2O_3 composite. This behaviour confirms that the CP4 and CP5 coatings are providing a sacrificial corrosion protection mechanism. A comparison of the corrosion behaviour of LPCS-deposited Al-Al_2O_3 and Al-Zn-Al_2O_3 composite coatings shows that the formation of the new interfaces may significantly change the corrosion mechanism from a noble to sacrificial corrosion protection (Covac et al. 2010).

The corrosion rate (CR) calculation results depicted in Fig. 4.25 reveal that all LPCS-deposited Al-Al_2O_3 coatings have approximately the same CR. This data may be explained by the fact that galvanic corrosion between Al_2O_3 and Al particles is unlikely to take place because the resistivity of alumina is greater than 10^{14} Ω cm (DeForce et al. 2007; Orazem et al. 2006). The higher corrosion rates of the Al-Zn-Al_2O_3 coatings (CP4, CP5) may be explained by the action of both the Cl^- ions in the NaCl solution and the galvanic coupling effect between the noble Al and the much more active Zn particles resulting in the formation of $Zn_5(OH)_8Cl_2{\cdot}H_2O$ and ZnO corrosion products (Li et al. 2010). It is important to note that the presented CR values should be considered as corrosion rate estimations only.

The analysis of the LPCS-deposited coatings passivation behaviour is based on an evaluation of the coating morphology. The coating surface was examined using scanning electron microscopy (SEM), and the chemical composition of the coating layers surface was determined by energy dispersive X-ray spectroscopy (EDX). The images depicted in Fig. 4.26 show that the coating morphology is quite different for the as-sprayed coatings. An increase of the reinforcing ceramic phase in the coating leads to an increase of the coating roughness, thereby increasing the number of sites

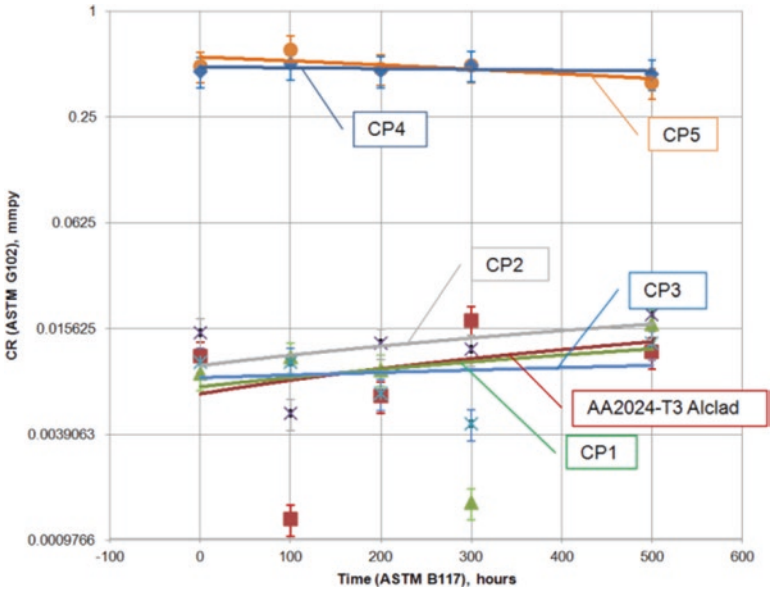

Fig. 4.25 Evolution of corrosion rate as a function (linear regression) of accelerated salt fog corrosion test environment

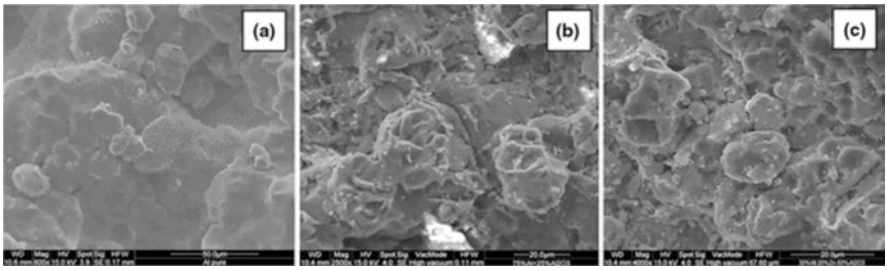

Fig. 4.26 SEM images of the coating layers topography: (**a**) Al feedstock powder coating (CP1), (**b**) 75%Al-25%Al_2O_3 feedstock powder coating (CP2) and 30%Al-20%Zn-50%Al_2O_3 feedstock powder coating (CP3)

where corrosion attack can be initiated. It was reported (Li and Li 2006; Motzet and Pollmann 1999; Fenker et al. 2014) that the coating morphology plays a critical role in corrosion propagation over the sprayed surface, where the higher coating roughness corresponds to lower pitting potential. That has been confirmed by the OCP measurement results shown in Fig. 4.22. The observed amplitude of the OCP oscillations is decreasing with the coating roughness increase.

Micrographs of the LPCS-deposited coating surfaces after 500 h immersion in the corrosion environment in accordance with ASTM B117 are shown in Fig. 4.27. The CP1, CP2 and CP3 coating look like having a similar homogeneously dense

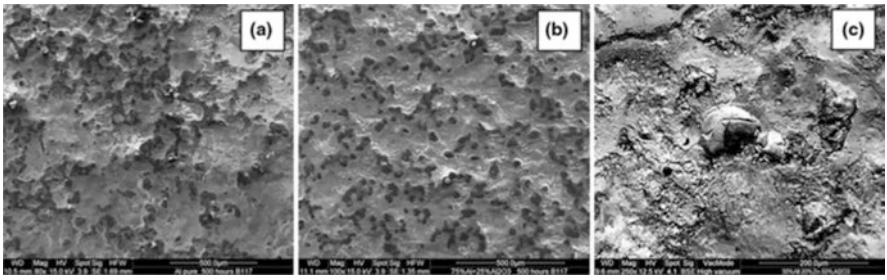

Fig. 4.27 SEM images of the coating layers topography after immersion in corrosive environment for 500 h (ASTM B117): (**a**) Al feedstock powder coating (CP1), (**b**) 75%Al-25%Al_2O_3 feedstock powder coating (CP2) and 30%Al-20%Zn-50%Al_2O_3 feedstock powder coating (CP3)

scale formed on the surface. However, image analysis revealed that the fraction of the surface area occupied by white rust increases with an increase of alumina content, to approximately 55% for CP1 and 65% for CP2, respectively.

The granular oxide scale around the aluminium particle can be seen at higher magnification. Figure 4.28b shows the region of CP1 coating where aluminium phase islands (dark grey) are found. EDX analysis confirmed that dark grey areas on the image are associated with aluminium, whereas white grey areas correspond to tetrahydroxoaluminate oxide layers. The significant increase of the oxygen content is believed to be associated with the formation of $Al_2O_3{\cdot}2H_2O$. According to (Takahashi et al. 2010; Pourbaix 1975; Hong and Nagumo 1997; Sasaki and Burstein 1996), in chloride solution aluminium ionizes rapidly to the Al^{3+} ion, which in its turn also rapidly hydrolyses: $Al^{3+} + 3Cl^- \rightarrow AlCl_3$ and $2AlCl_3 + 6H_2O \rightarrow 2Al(OH)3 + 6HCl)$ that is transformed slowly to $Al(OH)_3$ and finally to $Al_2O_3{\cdot}2H_2O$, which plays an important role in the passivation of aluminium. Figure 4.28a shows the needle crystal nucleation of the aluminium oxide. Fine-grain lamellas have a leaf-like structure with leaves the size of about tens of nanometers. Such needle structure of $Al_2O_3{\cdot}2H_2O$ is known to be typical for aluminium oxide nucleation and its crystal growing (Tian et al. 2009; Hwang et al. 2010).

The following conclusions can be drawn based on the material laid out:

- LPCS process offers unique opportunities to uniformly spray dense composite corrosion-resisting coatings. The use of a portable LPCS machines allows to apply the process in both the field and the industrial environment conditions.
- Electrochemical methods (e.g. polarization measurements, electrochemical impedance spectroscopy, open circuit potential, etc.) can be effectively used for the corrosion behaviour evaluation of LPCS-formed protective coatings.
- The results of the accelerated corrosion test demonstrate that the Al6022 high-strength Al alloy can be moat effectively protected by LPCS-deposited Al coating. In case of a composite Al-Zn-Al_2O_3 coating, the protection properties are gradually degraded via the sacrificial mechanism of the formed Al-Zn galvanic couples.

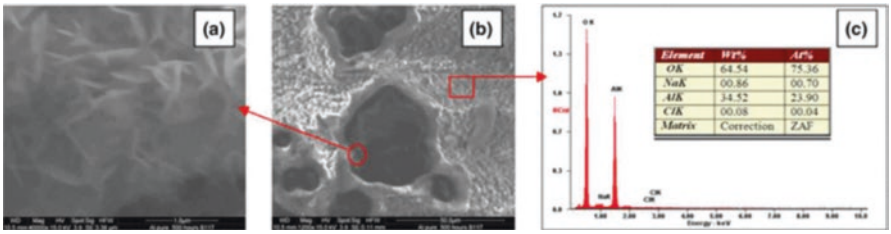

Fig. 4.28 Magnified SEM images of the coating layers topography: (**a**) Al_2O_3 nucleation around Al particle, (**b**) dense passivation layer on the coating surface after 500 h of salt fog environment and (**c**) EDX analysis of the corroded passivation layer composition

4.2.3 Utilization of LPCS Intermetallic Thermal Barrier Coatings for Low Heat Rejection Diesel Engines

Stringent requirements in the automotive industry continuously lead to the reduction of the overall vehicle weight and fuel consumption, which requires broad utilization of lightweight components, and particularly in engine applications. On the other hand, technological enhancements in engine thermal efficiency require from engine components the ability to operate under higher temperatures and peak loads. The use of TBCs can lead to the temperature reduction as much as 200 °C at the piston crown of an engine, thus improving the durability of engine components as well as enhancing the fuel efficiency (Balaji and Maridurai 2016). However, conventional ceramic-based TBC, such as YSZ, has poor reliability due to their inherent ceramic brittle behaviour, thus making the coating lifetime span very limited. With this regard, the application of hybrid structures of aluminium alloys and TBC has a promising potential (Harach and Vecchio 2001; Jindal et al. 2006). However, producing a reliable interface between aluminium alloy and ceramic TBC represents a challenge because of large difference in CTE between TBC and aluminium substrate. As an alternative solution to this problem, new CS methods are being developed providing strong coating interface and TBC with low thermal conductivity at the same time. However, the deposition of conventional Zr-based TBC by means of CS is restricted because of the lack of ZrO_2 ceramics ductility. Therefore, other types of powder materials need to be selected for CS processing, which in combination with the subsequent sintering can replace the conventional ZrO_2 ceramic TBC.

Intermetallic compounds are of the considerable interest because of their high-temperature strength, low density and high creep resistance. However, application of intermetallics has been limited due to their highly brittle behaviour at ambient temperature. Whereas intermetallics are complemented with ductile metallic phase, together they offer a good combination of strength and toughness. Based on this idea, a new class of structural material known as metal-intermetallic laminate (MIL) composites was developed by Harach and Vecchio 2001. That includes MIL composites, based on the combination of Fe-Al, Ti–Al_3Ti and Ni–Al_3Ni, that have been attained recently by means of reactive foil sintering (Balaji and T. Maridurai 2016;

Luo and Acoff 2004). However, there were no reports on their application as TBC yet. Another approach to deliver reliable and durable TBC was undertaken by researchers (Shin et al. 2007; Bobzin et al. 2017) and resulted in producing of nano-amophous metal-based TBC (MBTBC) that have been deposited by high-frequency induction plasma spraying (IPS) of iron-based nanostructured powders. The thermal conductivity of the obtained MBTBC was found to be as low as 1.22 W/mK, which is comparable to Zr-based ceramics; however, their thermal stability was still an issue. As the next step in the obtaining of durable and effective TBC, the multilayer intermetallic coatings were proposed as the further development of MIL and MBTBC technologies. Their formation became feasible by using a combination of both spray and reactive sintering technology, adapted to obtain the specific coating properties after each processing step.

The first step in obtaining of multilayer intermetallic coatings is the metal powder deposition delivered by CS (Maev and Leshchynsky 2015). It is a rapidly developing coating technology in which metal powder particles in the range of 10 to 150 μm are fed into a supersonic gas stream and accelerated to a high velocity by the drag effect; then, they are projected on a substrate in the raw solid-state, unlike IPS where severe oxidation of metal particles occurs during deposition. Authors (Maev et al. 2011) have developed the low-pressure cold spray technology, which was followed by post-processing sintering to produce the multilayer thermal barrier coatings (Fig. 4.29a, b) based on commercially available Al-, stainless steel-, Ni- and Co-based powders. The material selection was based on the intermetallics properties studied by Terada et al. 1995. The study suggests that the number of the potentially interesting intermetallics suitable for thermal barrier applications is limited to aluminides of Fe, Ni and Co with the least complex B2-type crystal structure and thermal conductivities in the range of 10 ~ 20 W/mK. So, the goal of the experiment was to obtain these types of intermetallics in the cold-sprayed layers of aluminium and metal alloy powders during consequent sintering. As a result of the sintering treatment (at the temperatures of 500, 550, 575, 600 and 625 °C for 4 h), the intermetallic layers were formed around metal powder particles, and their diffusion zones were varying in thickness depending on the annealing temperature and time exposure (Jalilvand et al. 2013).

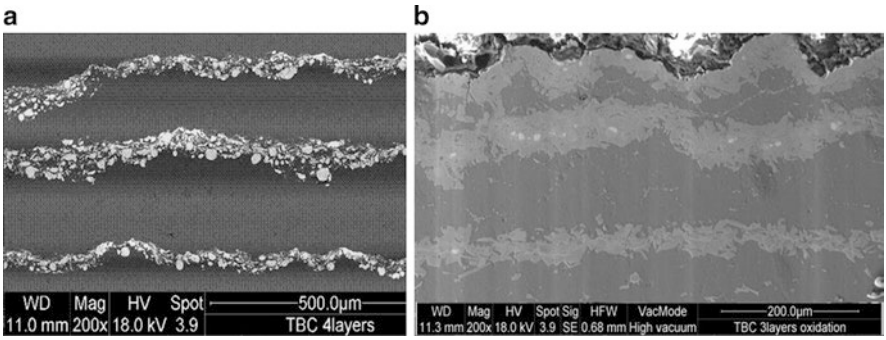

Fig. 4.29 SEM images of Al – SHS 717 layered coating after CS deposition (**a**) and layered coating after reaction sintering (**b**)

At the present time the study of the intermetallics formation by reaction synthesis of SHS717, AMS-4777, A-4783 and aluminium alloy powders has not been reported yet. Since the selected metal powders have complex compositions, the influence of their alloying elements on the growth of intermetallics is currently unknown. In the present work the synthesized intermetallics have been studied using SEM, EDS and XRD. The thermo-physical properties of the obtained TBC were evaluated to determine the thermal conductivity and CTE. The mechanical properties of the obtained intermetallic layers were evaluated by the dynamic microhardness tester and adhesion peel test. The results obtained from the different specimens were compared and then analyzed to explain the different reaction mechanisms that control the growth of the intermetallic layers.

Materials Selection

As mentioned above, to produce the multilayer intermetallic TBC, two main technological steps are required, i.e. cold spraying and consequent sintering (annealing). The current approach for the attaining of intermetallic materials is essentially based on the initial identification of binary intermetallic compounds such as Fe, Ni and Co aluminides exposing high thermo-mechanical properties.

The proposed composite TBC multilayered structure comprises of a bond layer to match CTE of a substrate and an insulation layer that actually prevents heat transfer. The volume fractions of two mentioned phases can be controlled by thickness of deposited layers to obtain the smooth thermo-mechanical properties transition from largest CTE to lowest thermal conductivity. This approach has been utilized to tailor intermetallic TBC composition to provide the best match to the material of the substrate. For the aluminium piston made from aluminium alloy A13, the best bond coat selection is pure aluminium powder. The aluminium bond layer also serves as Al atoms source for synthesizing aluminides in the Fe-, Ni- or Co-based layers during the annealing. The composition of intermetallic layers needs to be selected based on the thermal conductivity of aluminides they form. However, the number of potentially interesting compounds for thermal barrier applications is limited. Each of these binary compounds has individual crystal symmetry, and if it is complex, the compound is not able to retain its phase stability and therefore its thermomechanical properties at elevated temperatures. For that reason the aluminides of Fe, Ni and Co with the least complex B2-type crystal structures were selected for the experiment, provided that their target thermal conductivities are going to be in the range of ~10 W/mK (Terada et al. 1995; Massalski 1986).

The data (Terada et al. 1995) reveal that an increase of aluminium content in the range of 40–55 at % results in a significant change of the thermal conductivity of Ni- and Co-based intermetallics reaching a sharp maximum at 50% (NiAl and CoAl compounds). However, the thermal conductivities in the range of ~10 W/mK condition can be achieved by controlling constituent's concentrations and volume fractions through CS processing parameters.

Based on previous results (Maev et al. 2011), the following powder materials are chosen for study: (i) SHS-717 (Fe-25Cr-8Mo-10 W-5Mn-5B-2C-2Si) stainless steel powder from NanoSteel Company, (ii) AMS-4777 (Ni-7Cr-3B-5Si), A-4783 (Co-20Cr-18Ni-5 W-1B-8Si) metal alloy powders from Carpenter Technology

Table 4.1 Chemical composition of the powders

Powder Material	Chemistry, wt (%)										
	Iron	Al	Cr	Mo	W	C	Mn	Si	B	Ni	Co
SHS717	Balance	–	20	5.0	10.0	2.0	5.0	2.0	<5.0		
AMS4777	3.0	–	7.0	–	–	–	–	4.1	3.0	Balance	–
A4783	–	–	19.0	–	4.0	0.4	–	8.0	0.8	17.0	Balance
Al	–	Balance	–	–	–	–	–	–	–		

Corporation Al-101 and (iii) pure aluminium powder, supplied by Atlantic Equipment Engineers Ltd., served bifold purposes as a bond coat for metal powder layers as well as a base reagent during the post-processing to synthesize intermetallics. The mean particle size of all powders is in the range of 45 μm. Chemical composition of powder materials used is shown in Table 4.1.

Coating Formation: Cold Spraying

The spray experiments were carried out using robotic spraying system. The powders were supplied by a powder hopper and were injected into the divergent portion of the nozzle near the throat area by means of vacuum developed by an accelerated stream of compressed air passing through the nozzle. The injected particles were accelerated in the high-velocity air stream and projected onto aluminium substrate. To increase the air velocity and ultimately the particle velocity, the compressed air was preheated to 300 °C for spraying of aluminium and to 400 °C for spraying of metal alloy powders. The pressure and temperature of the compressed air were monitored by a pressure gauge and a thermocouple positioned inside the gun. The gun was installed on a gantry robot to scan the air-powder jet over the substrate surface. The compressed air pressure was kept constant at 0.5 MPa. The gun transverse speed for metal alloy powders spraying was about 30 mm/s, while for aluminium powder it was about 70 mm/s. The powder feeding rate was varied in the range of 0.5 ~ 1.5 g/s, while the standoff distance, measured from the exit of the nozzle to the substrate, was held constant at 10 mm. Up to six layers of aluminium powder with the thickness of 100…125 μm were interlayed with embedded into them Fe, Ni and Co alloy powder particles, and the average penetration depth was about 50 μm.

As it was outlined above, the most efficient design for TBC consisting of heterogeneous materials is the layered structure. The number of layers is determined by the specific requirements for the piston crown temperature reduction as well as the coating deposition technological capabilities. Since CS processing doesn't thermally affect both powder and substrate, the residual stresses induced by this process allow deposition of thicker coatings compare to conventional thermal spray YSZ TBC, which is about of 0.3 mm. However, considering the ultimate TBC composition that was designated as intermetallic aluminides, the prevailing volume fraction of aluminium was supposed to be supplied to ensure lowest thermal conductivity of TBC after annealing. This requirement is valid for all aluminium alloying elements of Fe, Ni and Co accordingly to Terada et al. 1995. Considering the mesh size of the sup-

plied powders #325, which corresponds to the particle size of ~45 μm, the aluminium layer thickness was chosen to be ~100 μm. This thickness is believed to be sufficient for the aluminium layer to provide a substrate for stainless steel, Ni or Co alloy particles penetration into the aluminium bed and to ensure a sufficient diffusion of Al while converting into aluminides during the annealing. During CS stainless steel, Ni or Co alloy deposition, each aluminium layer was compacted by absorbing metal particles while retaining its initial thickness and providing pure aluminium interlayer between stainless steel, Ni or Co alloy layers to supplement plenty of aluminium during the annealing. The total thickness of final TBC was set to 1 mm, which is three times larger than YSZ TBC. The TBC deposited by CS totally contained ten layers: five stainless steel layers and five aluminium inter-layers (Fig. 4.30).

Coating Formation: Intermetallic Synthesis Examination

The second stage in the coating formation process was heat treatment which allowed for the alloying of aluminium and stainless steel components and the formation of intermetallic phases by means of solid-state diffusion since the temperature was kept below the melting point of aluminium (660 °C). The coating annealing was made in the Carbolite tube furnace in nitrogen atmosphere at temperatures of 550–600 °C over a period of 3 h. After sintering, the samples were mounted in epoxy resin, sectioned perpendicular to the surface of the coating, polished using standard metallographic technique and examined by optical microscopy and SEM with EDS. Optical light microscopy Leica DMI5000 M with a digital camera DFS 320 R2 was used for metallographic characterization. SEM and EDS examinations were made by microscope FEI, including EDS X-ray microanalyzer manufactured by EDAX. The thicknesses of intermetallic layers and the sizes of SHS-717, AMS-4777 and A-4783 stand-alone particles were measured for different sintering conditions. The diffusion zones around stand-alone particles can be identified; however, determination of the thickness of the diffused intermetallic phases in particulate materials has some difficulties as compared to the classical diffusion kinetics experiments, where the thickness of the transform layers is easy to define.

In this study we consider the embedded stainless steel, Ni and Co alloy particle diameter as the base for the diffusion layer determination. As stated above, the maximum particle size of SHS-717, AMS-4777 and A-4783 powders was about 45 μm,

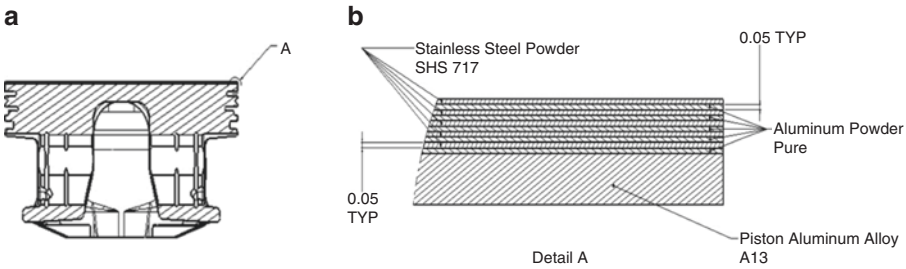

Fig. 4.30 The piston (**a**) and schematics of the piston multilayer TBC (**b**)

and according to the classification of mesh size #325, 80% of the spherical particles have this size. Due to indefinite location of the particles relatively to the cross-section plane in the metallographic specimen, only separate particles are sectioned at the diametrical plane (Fig. 4.31a).

It is safe to assume that the largest raw particles of size ~45 μm will be transformed into the largest intermetallic particles. So, based on this assumption we may define the largest intermetallic areas as the diffusion zones of the large particles, and the task of the microstructure analysis will be to define the thicknesses and phase compositions of intermetallic layers around those particles like shown on (Fig. 4.31b). XRD measurements were made using diffractometer D5000 and Siemens AG, with copper as the X-ray source ($\lambda = K\alpha\ Cu = 0.154178$ nm).

The coating thermo-physical properties were measured by a laser flash method which is a standard testing technique to measure a material's thermal diffusivity. It was utilized with Netzsch LFA-447 light flash analyzer with accordance to ASTM E1461-01. In this instrument a high-performance Xenon flash lamp takes the place of the laser, which is usually employed for this proven technique.

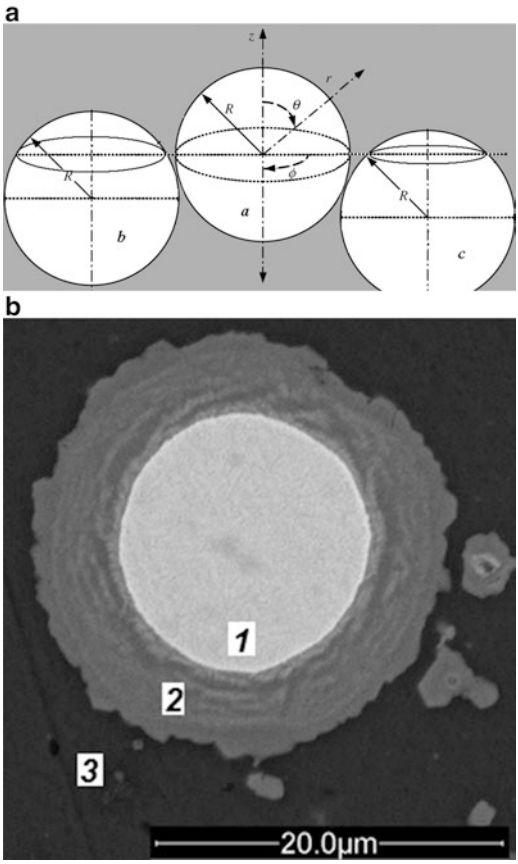

Fig. 4.31 (**a**) Location of the section plane of stainless steel particles in the specimen: only the middle particle *a* is sectioned at the diametrical plane, other particles *b* and *c* expose smaller than diameter cuts. (**b**) SEM image of the largest particle cross-section after sintering SHS-717 multilayer coating at 575 °C

The thermal expansion coefficients (CTE) of multilayer TBC were determined using the Orton Dilatometer Model 1000D before and after annealing. The multilayer TBC samples of 2 mm thickness were prepared for the length of 1 in. each and then placed in a dilatometer. Each sample was heated to 775 K with the rate of 5 K per minute. The sample length measurements were recorded automatically for every 10 K increment during the heating cycle by a linear variable displacement transducer. A fully automated tensile testing system, Zwick/Roell Z150, was employed to evaluate the coating adhesion strength in accordance with the widely used tensile adhesion test standard ASTM-C633. In this test the coated sample in the shape of a cylinder d 25.4 mm × 25.4 mm long is glued to an uncoated similar counterpart which was just grit blasted and then tested with the universal testing machine. The adhesive used in the adhesion test was the F-1000 adhesive film from Cytec Industries Inc. cured for 1 h at 450 K and 50 N of pressure. The value of the tensile load, in which the separation of the coated/uncoated parts occur, is registered and transformed in an adhesion value or the bond strength by calculating the load/area relation.

Coating Structure Characterization

As shown above, the thermo-physical properties of the layered composites are the function of the intermetallic composition, its layer thickness, structure and cohering ductile matrix. In this research, these intermetallics are produced by reactive diffusion in alternatively stacked layers of two different metals. The intermetallic layers on the particles interface grow as a result of the annealing with the predetermined temperature and time. Therefore, the kinetics of the diffusion process is the key feature in controlling the properties of the synthesizing TBC. Based on the assumption that intermetallic layer thickness exhibits the direct proportion with growth kinetics, the average thickness of the aluminide layer around the embedded particles may be used to calculate the kinetic parameters for the diffusion between the stainless steel embedded particles and aluminium matrix (Jindal et al. 2006). However, the annealing that was performed at temperature of 625 °C resulted in the fast inception of self-propagating high-temperature synthesis (SHS) of all specimens. A formation of the melted zones which resulted in warping of the specimens, dissociation of the stainless steel, Ni and Co alloy layers, their thorough mixing with the aluminium matrix and homogeneous precipitation of the intermetallic phases is clearly seen on Fig. 4.32. Since SHS observed at 625 °C resulted in complete particle melting, the measurement of the aluminide layer thicknesses around the embedded particles was performed on specimens annealed at temperatures 500, 550, 575 and 600 °C (Fig. 4.34a, b, and c).

The results of measurements are shown on Fig. 4.34 as the aluminide layers thickness dependence on the holding time. The measurement results of all specimens reveal regular gradual trends of aluminide thickness growth on temperature and time due to a solid-state diffusion process. While the aluminide thickness on the stainless steel particles grows gradually at the temperature range 500–600 °C, AMS4777 and A4783 particles exhibit SHS reactions with aluminium matrix already at the temperatures close to ~600 °C. This transition from solid-state diffusion to SHS reaction is seen on graphs of Fig. 4.34b, c. The above analysis of reac-

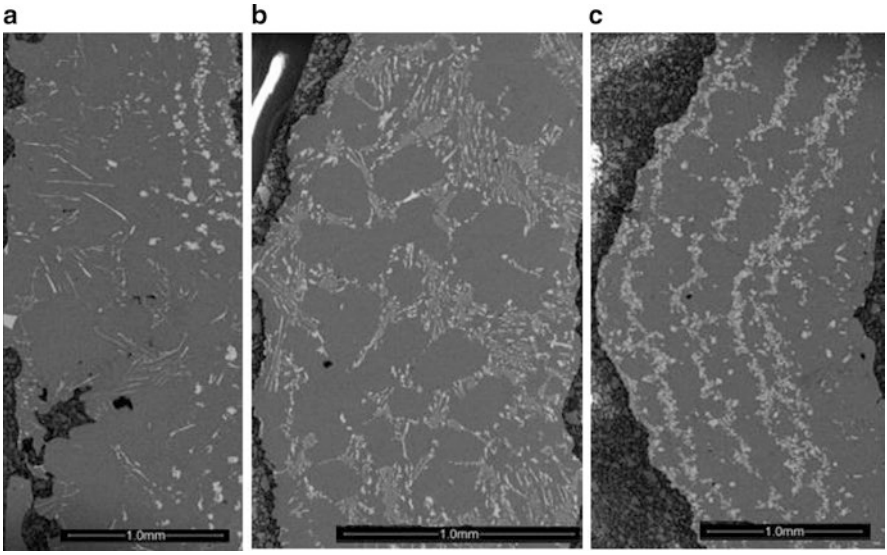

Fig. 4.32 SEM images of TBCs annealed at 625 °C: (**a**) SHS-717 multilayer coating; (**b**) AMS-4777 multilayer coating; (**c**) A-4783 multilayer coating

tion kinetics of Al-Fe intermetallic compounds shows the possibility for controlled solid-state intermetallic synthesis of separate SHS-717 Fe alloy particles at the temperatures of ~550–600 °C. AMS-4777 Ni alloy particles and A-4783 Co-Ni-Cr alloy particles exhibit the similar behaviour at narrower temperature range of ~550–575 °C. The SHS reactions take place at higher temperatures which result in increase of the intermetallic layer thickness around the particles. However, a lot of cracks and voids are generated in this case because of sharp increase of the reaction temperature due to the highly exothermic nature of SHS reactions.

Reaction synthesis of intermetallics leads to a complex phase formation that takes place through multiple reaction stages, therefore SEM and EDS were performed throughout multiple particles in different coating zones to define certain zone chemical composition, and XRD analysis is made in order to determine the prevailing phases. SEM analysis of the SHS-717 particles embedded into Al matrix and sintered at the temperature of 550 °C during 3 h showed that the reaction layer consists of various phases (Fig. 4.30). EDS spectra of the SHS-717 particle exhibit the Al content of ~11 wt% in the bright core and Al content of ~63% in the grey phase that in accordance with binary phase diagram (Massalski 1986) reveals two stages of reactions: formation of FeAl, Fe_3Al and further formation of Fe_2Al_5. The small debris particles, formed due to the particle fracture during spraying, consist predominately of Fe_2Al_5-based phase due to the prevailing Al content surrounding them. The complex chemical composition of the SHS-717 particles results in high content of Mo, Cr and Si mostly in the FeAl phase; however, the content of these elements in

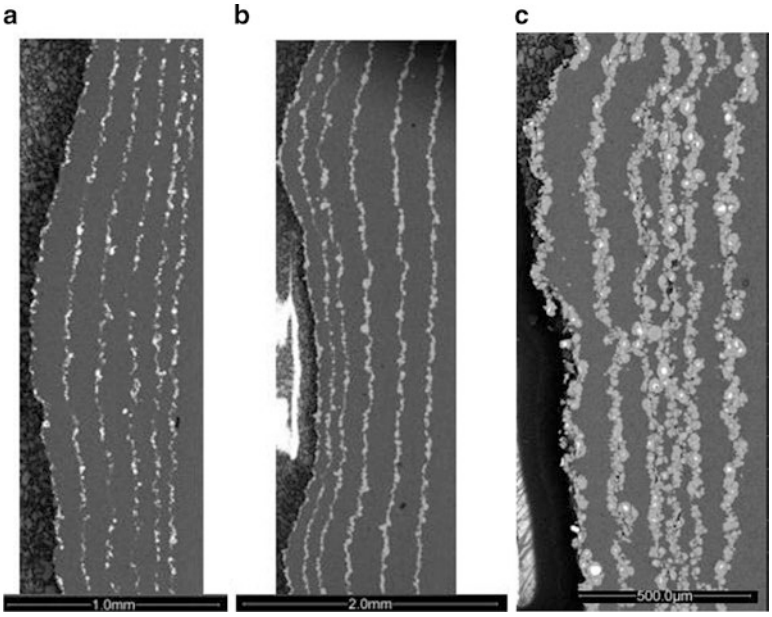

Fig. 4.33 SEM images of TBCs annealed at 550 °C: (**a**) SHS-717 multilayer coating; (**b**) AMS-4777 multilayer coating; (**c**) A-4783 multilayer coating

the Fe_2Al_5 grey phase is lower. The coatings' phase composition is shown in Table 4.2. The results of XRD analysis demonstrate formation of intermetallics at all examined annealing temperatures. The main phases of SHS 717 particles (complex iron carbides and nitrides) disappear at the annealing at 575–600 °C, while chromium carbide is Cr23C6 stable similar to results of Shin et al. 2007 (Fig. 4.33).

Reaction diffusion processes taking place during sintering of AMS-4777 – Al composite coating have their own specific features with the formation of intermediate phases during the diffusion of Al into the Ni-Fe-Si-Cr-B particles. The SEM images of the Ni-based particles after sintering at 550 °C during 3 h depicted on Fig. 4.34d show the presence of two phases, i.e. grey and dark, within AMS4777 particle. The whole particle contains the dark phase as well. The main constituent phases of the original AMS4777 powder are Ni-based phases and complex borides (see Table 4.2). As-sprayed coating phase composition is similar to that of powder that is in agreement with results described in the paper (Luo and Acoff 2004). The sintering reactions result in some borides decomposition and formation of the intermetallic compounds under the prevailing phase of pure Al and aluminides Al_3Ni and AlN. Formation of Al-Co-Ni intermetallics during sintering of A4783 – Al composite coating at 550 °C during 3 h is shown on Fig. 4.35. The reaction diffusion proceeds with a mechanism similar to that of SHS-717-Al composite (Fig. 4.31). The particles have a core (area #1) with the content of Al is about ~23 wt% (Fig. 4.35). High content of Ni and Cr leads to the formation of complex Al-Co-Ni-Cr phases. The further diffusion of Al results in the formation of phase with the high Al content

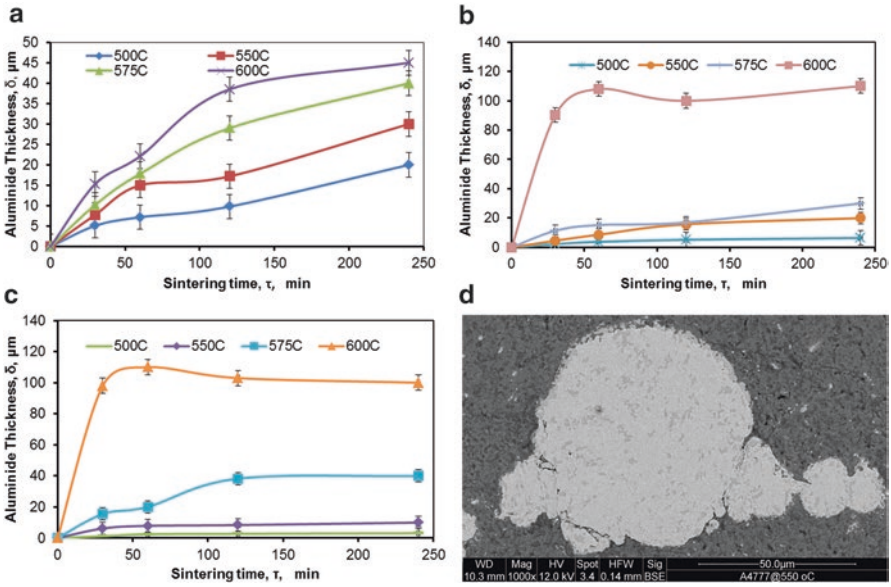

Fig. 4.34 Dependences of aluminide intermetallic layers grow on time for (**a**) SHS-717 particles embedded into aluminium matrix; (**b**) AMS-4777 particles embedded into aluminium matrix; (**c**) A-4783 particles embedded into aluminium matrix. (**d**) SEM image of AMS4777-Al composite phases after sintering at 550 °C: two distinct phases within one particle

Table 4.2 XRD analysis results

	Based material	As-sprayed	Annealing temperature (°C)			
			500	550	575	600
1	SHS-717-Al	Fe2Al5, Fe, Al, Fe23(C,B)6, Cr23C6	Fe2Al5, Fe, Al, Fe23(C,B)6, Cr23C6	Fe2Al5, FeAl, Fe, Al, Fe23(C,B)6, Cr23C6	Fe3Al, Fe2Al5, FeAl, Fe, Al, Cr23C6	Fe2Al5, FeAl, Fe, Al, Cr23C6
2	AMS-4777	Al, Ni, M23B6, CrB	Al, Ni, M23B6, CrB	Al, Ni, M23B6, CrB	Al3Ni, Ni, Al, M23B6, CrB	Al3Ni, AlNi, M23B6, Ni, Al
3	A-4783	Al, Co CoNiCr σ-phase	Al, Co, CoNiCr σ-phase	Al, Co, CoNiCr σ-phase	Al5Co2, Co,Al, CoNiCr σ-phase	Al5Co2,AlCo Co,Al

of ~60 wt%. Assuming the phases similar to those of binary Al-Co diagram (Massalski 1986), two fields of phases on Fig. 4.35 may be defined as the unreacted core (area # 1) and fully sintered intermetallic area # 2 corresponding to the AlCo and Al_5Co_2. XRD analysis results reveal about presence of CoNiCr σ-phase which was characterized by Zhanpeng 1981. This phase is not described in detail in the literature, and it is seen that SHS reactions (at the temperature of 600 °C) result in its disappearing.

a

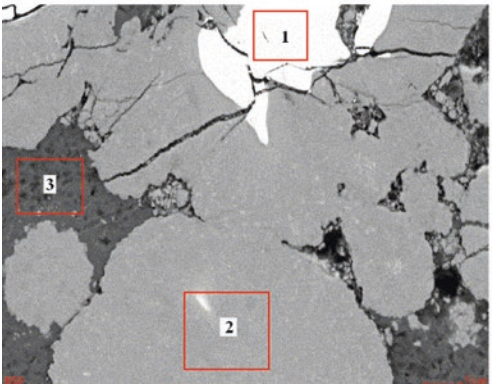

b

Area of Definition	Chemical composition , wt%						
	Al	Co	Ni	Cr	Si	O	C
Area 1	23.13	33.48	13.5	14.2	8.23	3.46	3.96
Area 2	60.83	16.63	6.92	6.02	3.47	2.44	3.7

Fig. 4.35 SEM image (**a**) and EDS analysis (**b**) of A-4783 – Al phases after sintering at 550 °C

Thermal Conductivity, Thermal Expansion Coefficient and Adhesion Strength

Light flash analyzer Netzsch LFA-447 was used as a standard testing method to measure the material's thermal diffusivity with accordance to ASTM E1461–01 and then converted to thermal conductivity using the following equation:

$$k(T) = \propto (T)^{*} Cp(T)^{*} \rho$$

where:

$k(T)$ – thermal conductivity at constant temperature T
$\alpha(T)$ – thermal diffusivity determined by light flash analyzer
Cp – material specific heat
ρ – material density

In order to determine the intermetallic thermal conductivities evolution with the change of the environment temperature, the samples annealed at 575 °C during 3 h were tested at the different temperatures. The dependence of their thermal conductivities from the ambient temperatures is shown on Fig. 4.36a.

The comparison of the intermetallics thermal conductivities shown on Fig. 4.36a indicates good thermal barrier properties of SHS-717 – Al intermetallic phases achieved because of their complex structure. Due to this effect, the thermal conductivities of these phases are evaluated to be similar to quasi-crystals observed on metal-based thermal barrier coatings (MTBC) (Shin et al. 2007). The thermal conductivities of AMS-4777 – Al and A-4783 – Al layers (both ~10–20 W/mK) are believed to be associated with the formation of intermetallics and Ni-Co solid solution inclusions as shown in Table 4.2 and Figs. 4.34 and 4.35. The effect of alloying elements on multilayer TBC thermal conductivity and its variations appear to be due to disordering of the coating layers by the doped intermetallic phases.

The thermal expansion coefficients (CTE) of multilayer TBC annealed at 575 °C were determined using the Orton Dilatometer Model 1000D at different temperature exposures. The temperature dependence of the thermal expansion coefficients are shown on Fig. 4.36b. The analysis of thermal expansion coefficient curves of the examined multilayer coatings reveals about gradual increase of CTE with the rising temperature. It is well known that the thermal expansion is a complicated function of thermal and elastic properties of the individual components. The values of CTE for the annealed intermetallic layers and aluminium matrix slightly differ. However, due to the small thicknesses of both intermetallic and aluminium layers, with ~50 μm and 100 μm, correspondently, the stresses generated between the TBC layers due to the difference in CTE are expected to be significantly less than in other types of either MIL or MBTBC.

The adhesion tests were performed on the samples with SHS-717 – Al multilayer coatings which seem to be the most suitable for engine applications because they possess the lowest thermal conductivity. The specimens for adhesion tests were annealed at different temperatures during 3 h. Comparison of the SHS-717 – Al coating adhesive strength shown in Fig. 4.37a illustrates the effect of the intermetallic phase's formation during reactive solid-state sintering. While as-sprayed Al coating exhibits an adhesive strength of ~37 MPa, the further penetration of the SHS-717 formed intermetallic layers results in an increase of the adhesive strength up to ~40–44 MPa possibly due to the additional plastic deformation of the ductile aluminium layer. Moreover,

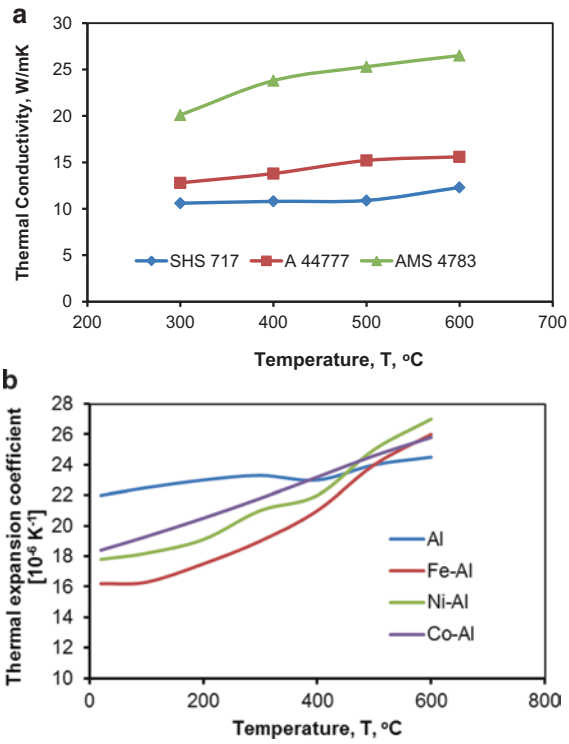

Fig. 4.36 Thermal conductivities of the intermetallic layers in TBC made from SHS717, AMS4777 and A4783 alloys (**a**). Thermal expansion coefficients of the intermetallic and aluminium layers of TBC made from SHS717, AMS4777 and A4783 alloys (**b**)

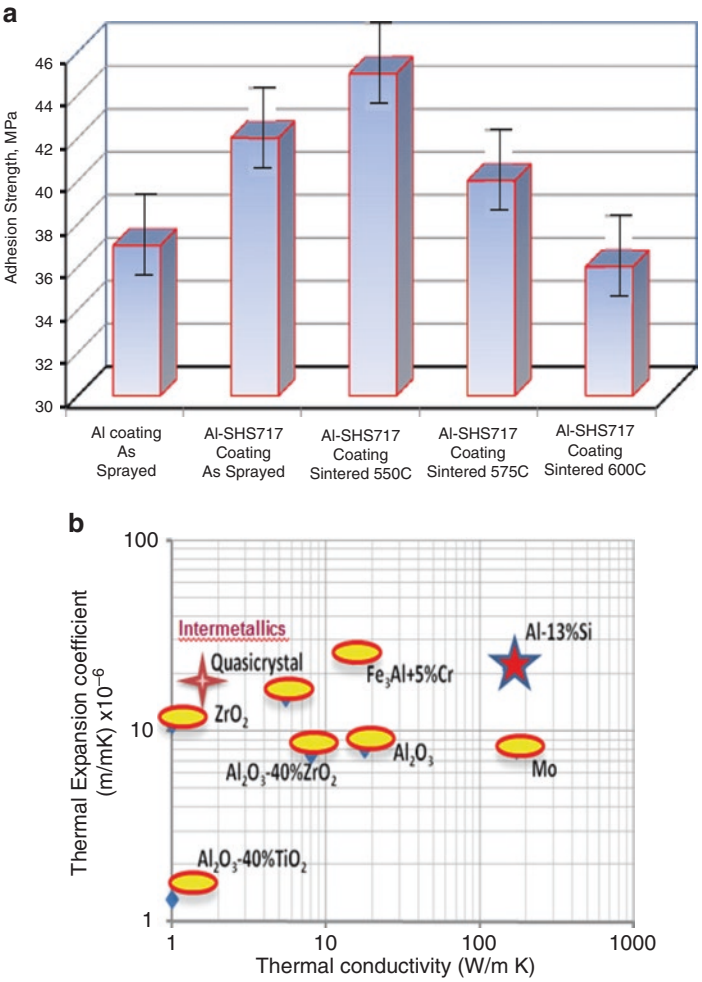

Fig. 4.37 Adhesive strength of SHS-717 coatings at various conditions (**a**); diagram for TBC materials thermal expansion coefficient vs. thermal conductivity (**b**)

solid-state sintering at temperatures of ~500–550 °C leads to an additional increase of the adhesive strength. That might be possible due to the diffusion reactions between SHS-717 particles and aluminium matrix at the temperatures of ~500–550 °C, which result in more interparticle bonding because of the higher rate of the aluminium diffusion during the reaction synthesis.

The concept of the multilayer intermetallic thermal barrier coatings synthesis demonstrated the feasibility to combine two technologies – cold spraying and consequent annealing – in order to produce the composite coating with synthesized layers of intermetallics serving as thermal insulators. The aluminium layers between intermetallics perform the multiple functions including:

– Bonding between the intermetallic layers to provide coating integrity

– Source of aluminium for synthesizing of aluminides in intermetallic layers
– Matching the coefficient of thermal expansion (CTE) to the Al coating substrate shown on Fig. 4.37b
– Plastic matrix in the composite absorbing thermal and mechanical stresses, thus improving coating durability

Summarizing the data illustrated above, Fig. 4.37b indicates that besides matching the CTE of aluminium, multilayer intermetallic coatings have a great potential to reduce the coating thermal conductivity down to today's industry leaders such zirconium oxides, aluminium oxides and YSZ.

Based on presented results, the following conclusions may be made:

1. The multilayer Al-SHS 717 cold-sprayed coatings with the layer thickness of 40–50 μm each can be tailored to provide required thermal insulation properties as sprayed.
2. Sintering of the composite Al-SHS 717 coating results in the layers interface reactions and consequent intermetallic formation which enhances the thermal barrier coating properties.
3. Thermal expansion coefficient of multilayer Al-SHS 717 intermetallic TBCs is similar to those of Al-13% Si alloy.
4. The thermal conductivity of multilayer Al-SHS 717 intermetallic TBC is similar to those reported for LHR diesel engine with yttria-stabilized zirconia (YSZ).

References

Ahmad Z (2006) Principles of corrosion engineering and corrosion control. Butterworth-Heinemann, p 187

Alkhimov AP, Gudilov AI, Kosarev VF, Nesterovich NI (2000) Specific features of microparticle deformation upon impact on a rigid barrier. J Appl Mech Tech Phys 41(1):188–192

ASM Handbook (2003) Corrosion: fundamentals, testing, and protection, vol 13A. ASM International, New York, pp 1779–1793

Assadi H, Gartner F, Stoltenhoff T, Kreye H (2003) Bonding mechanism in cold spraying. Acta Mater 51:4379–4394

Assadi H, Kreye H, Gartner F, Klassen T (2016) Cold spraying – a materials perspective. Acta Mater 116:382–407

Baker MA, Gissler W, Klose S, Trampert M, Weber F (2000) Morphologies and corrosion properties of PVD Zn-Al coatings. Surf Coat Technol 125:207

Balaji D, Maridurai T (2016) Experimental investigation on engine performance and emission in diesel engine by aluminum-titanium thermal barrier coating. Int J Chem Sci 14(1):152–160

Boag A, Taylor RJ, Muster TH, Goodman N, Hughes AE (2010) Stable pit formation on AA2024-T3 in a NaCl environment. Corros Sci 52(1):90–103

Boag A, Hughes AE, Glenn AM, Muster TN (2011) Corrosion of AA2024-T3 part I. Localized corrosion of isolated IM particles. Corros Sci 53(1):17–26

Bobzin K, Öte M, Königstein T (2017) Investigation of amorphous/nanocrystalline iron-based thermal barrier coatings. J Therm Spray Tech. https://doi.org/10.1007/s11666-016-0520-7

Barbezat G (2006) Application of thermal spraying in the automobile industry. Surf Coat Technol 201:2028–2031

Champagne VK (2007) The cold spray materials deposition process: fundamentals and applications. Woodhead Publishing Limited, Cambridge, pp 230–312

Champagne V, Helfritch D (2015) Critical assessment 11: structural repairs by cold spray. Mater Sci Technol 31(6):627–634
Chang BY, Park SM (2010) Electrochemical impedance spectroscopy. Annu Rev Anal Chem 3:207–229
Covac C, Alaux TJ, Marrow E, Covekar A, Legat M (2010) Correlations of electrochemical noise, acoustic emission and complementary monitoring techniques during intergranular stress-corrosion cracking of austenitic stainless steel. Corros Sci 52(6):2015–2025
Davis JR (ed) (2004) Handbook of thermal spray technology. ASM International, Ohio, pp 220–225
DeForce B, Eden T, Potter J, Champagne V, Leyman P, Helfritch D (2007) Application of aluminum coatings for the corrosion protection of magnesium by cold spray. Proceedings of TRI service corrosion conference, Denver, USA
Dzhurinskiy D, Maeva E, Ev L, Maev RG (2012) Corrosion protection of light alloys using low pressure cold spray. J Therm Spray Tech 2(12):304–313
Eakins DE Thadhani NN (2006) Instrumented Taylor anvil-on-rod impact tests for validating applicability of standard strength models to transient deformation states, J Appl Phys 100:073503: doi: https://doi.org/10.1063/1.2354326
Estrin Y, Toth LS, Molinari A, Brechet Y (1998) A dislocation based model for all hardenibg stages in large strain deformation. Acta Mater 46(15):5509–5522
Fenker M, Balzer M, Kappl H (2014) Corrosion protection with hard coatings on steel: past approaches and current research efforts. Surf Coat Technol 257:182–205
Gray JE, Luan B (2002) Protective coatings on magnesium and its alloys — a critical review. J Alloys Compd 336(1–2):88–113
Grujicic M, Zhao CL, DeRosset WS, Helfritch D (2004) Adiabatic shear instability based mechanism for particles/substrate bonding in the cold-gas dynamic-spray process. Mater Des 25:681–688
Guillaumin V, Mankowski G (1999) Corrosion protection with aluminum coatings on steel. Corros Sci 41:421–438
Gust WH (1982) High impact deformation of metal cylinders at elevated temperatures. J Appl Phys 53(5):3566–3575
Guzman MA, Gissler W, Klose S, De Rossi S (2000) Vapour deposited Zn-Cr alloy coatings for enhanced manufacturing and corrosion resistance of steel sheets. Surf Coat Technol 125:218–227
Harach DJ, Vecchio KS (2001) Microstructure evolution in metal-intermetallic laminate (MIL) composites synthesized by reactive foil sintering in air. Metall Mater Trans A 32A:1493–1505
Heinz A, Haszler A, Keidel C, Bendictus R, Mille WS (2000) Recent development in aluminium alloys for aerospace applications. Mater Sci Eng 280(1):102–107
Holmberg K, Matthews A. (2009) Coatings tribology: properties, mechanisms, techniques and applications in surface engineering. Elsevier tribology and interface engineering series no. 56.2nd ed. Amsterdam, The Netherlands: Elsevier
Holmberg K, Laukkanen A, Ghabchi A, Rombouts M, Turunen E, Waudby R, Suhonen T, Valtonen K, Sarlin E (2014) Computational modelling based wear resistance analysis of thick composite coatings. Tribol Int 72:13–30
Hong T, Nagumo M (1997) Effect of surface roughness on early stages of pitting corrosion of type 301 stainless steel. Corros Sci 39:665
Hu N, Molinari JF (2004) Shear bands in dense metallic granular materials. J Mech Phys Solids 52:499–531
Hughes AE, Boag A, Glenn AM, Muster TN, Ryan C, Luo C, Thompson GE (2011) Corrosion of AA2024-T3 part II co-operative corrosion. Corros Sci 53(1):27–39
Hussain T, McCartney DG, Shipway PH, Zhang D (2009) Bonding mechanisms in cold spraying: the contributions of metallurgical and mechanical components. J Therm Spray Technol 18(3):364–379
Hwang IJ, Hwang DY, Kim YM, Yoo B, Shin DH (2010) Formation of uniform passive oxide layers on high Si content Al alloy by plasma electrolytic oxidation. Alloys J Compd 504:527–530

Jalilvand V, Omidvar H, Shakeri HR, Rahimipour MR (2013) Microstructural evolution during transient liquid phase bonding of Inconel 738LC using AMS 4777 filler alloy. Mater Charact 75:20–28
Jindal V, Srivastava VC, Das A, Ghosh RN (2006) Reactive diffusion in the roll bonded iron–aluminum system. Mater Lett 60:1758–1761
Klinkov SV, Kosarev VF, Rein M (2005) Cold spray deposition: significance of particle impact phenomena. Aerosp Sci Technol 9(7):582–591
Koivuluoto H, Lagerbom J, Kylmalahti M, Vuoristo P (2008) Microstructure and mechanical properties of low-pressure cold-sprayed (LPCS) coatings. J Therm Spray Technol 17(5–6):721–727
Lee H, Jung SH, Lee SY, Ho Y, Kyung Y, Ko H (2005) Fundamental study of cold gas dynamic spray process. Appl Surf Sci 252:1891–1898
Li W, Li DY (2006) Influence of surface morphology on corrosion and electronic behavior. Acta Mater 54:445–452
Li H, Li X, Sun M, Wang H, Huang G (2010) Corrosion resistance of cold-sprayed Zn-50Al coatings in seawater. J Chin Soc Corros Prot 30:62–66
Li Q, Lu H, Cui J, Kuma V, An M, Li DY (2017) Produce mirror-shining surface of electrogalvanized steel with significantly elevated scratch resistance through combined nanoelectrodeposition and passivation treatment. Wear 376-377:1707–1712
Ls-Dyna keyword user's manual (2013) Vol I. LSTC
Luo J-G, Acoff VL (2004) Using cold roll bonding and annealing to process Ti/al multi-layered composites from elemental foils. Mater Sci Eng A Struct Mater 379(1–2):164–172
Maev RG, Leshchynsky V (2007) Introduction to low pressure gas dynamic spray. John Willey and Son – VCH, Manheim, p 207
Maev RG, Leshchynsky V (2015) Cold gas dynamic spray. CRC Press, Boca Raton, 334p
Maev R Gr, Leshchinsky E, Maeva E (2011) New cold spray based technique of FeAl intermetallic compound coating synthesis. In: Proceeding of ITSC 2011 Conference, Hamburg, Germany
Maev R Gr, Leshchynsky V, Strumban E., Ziganshin D., Belenkov R., Dzhurinskiy D. (2017) Apparatus and method for cold spray coating processing. US Patent Application, US2017/0121825
Maitra S, English GC (1981) Mechanism of localized corrosion of 7075 alloy plate. Metall Trans A 12:535
Massalski TB (1986) Binary alloy phase diagrams. ASM International, Metals Park, p 112
Molinari A (1997) Collective behaviour and spacing of adiabatic shear bands. J Mech Phys Solids 45(9):1551–1575
Motzet H, Pollmann H (1999) Synthesis and characterization of sulfite-containing AFM phases in the system CaO-Al2O3-SO2-H2O. Cem Concr Res 29:1005–1011
Nakai M, Rto T (2000) New aspect of development of high strength aluminum alloys for aerospace applications. Mater Sci Eng 285(1–2):62–68
Nie JF (2014) Physical metallurgy of light alloys. Elsevier, Physical Mettalurgy, pp 2009–2156
Orazem ME, Pebere N, Tribollet B (2006) Enhanced graphical representation of electrochemical impedance data. J Electrochem Soc 153(4):B129–B136
Papyrin A (2001) Cold spray technology. Adv Mater Process 159(9):49–51
Papyrin A, Kosarev V, Klinkov S, Alkhimov A (2006) Cold spray technology. Elsevier, London pp 125–210
Pawlowski L (2008) The science and engineering of thermal spray coatings. John Wiley & Sons, England, pp 220–590
Pourbaix M (1975) Atlas of electrochemical equilibria in aqueous solutions. NACE, Houston
Rojas PN, Rodil SE (2012) Corrosion behaviour of amorphous niobium oxide coatings. Int J Electrochem Sci 7:1443–1458
Sasaki GT, Burstein G (1996) The generation of surface roughness during slurry erosion-corrosion and its effect on the pitting potential. Corros Sci 38:2111–2124
Schmidt T, Gartner F, Kreye H (2006) New developments in cold spray based on higher gas and particle temperatures. Therm Spray Technol 15:488–494

Schmitt G, Schütze M, Hays G (2009) Global needs for knowledge dissemination, research and development in materials deterioration and corrosion control. World Corrosion Organization (WCO), New York

Shin D-II, Gitzhofer F, Moreau C (2007) Thermal property evolution of metal based thermal barrier coatings with heat treatments. J Mater Sci 42:5915–5923

Smulko JM, Darowicki K, Zieliñski A (2007) On electrochemical noise analysis for monitoring of uniform corrosion rate. IEEE Trans Instrum Meas 56(5):2018–2023

Spencer K, Fabijanic DM, Zhang M-X (2009) The use of al–Al2O3 cold spray coatings to improve the surface properties of magnesium alloys. Surf Coat Technol 204:336–344

Steinhauser S, Wielage B (1997) Composite coatings: manufacture, properties, and applications. Surf Eng 13(4):289–294

Straffelini G, Pellizzari M, Molinari A (2004) Influence of load and temperature on the dry sliding behaviour of Al-based metal-matrix-composites against friction material. Wear 256(7-8):754–763

Stoltenhoff T, Kreye H, Richter HJ (2002) An analysis of the cold spray process and its coatings. J Therm Spray Technol 11(4):542–550

Tian W, Wang Y, Zhang T, Yang Y (2009) Sliding wear and electrochemical corrosion behavior of plasma sprayed nanocomposite Al2O3-13%TiO2 coatings. Mater Chem Phys 118:37–45

Takahashi H, Sakairi M, Kikuchi T (2010) Three-dimensional microstructure fabrication with aluminum anodizing, laser irradiation, and electrodeposition. Mod Asp Electrochem 46:59–174

Tao Y, Xiong T, Sun C, Kong L, Cui X, Li T (2010) Microstructure and corrosion performance of a cold sprayed aluminium coating on AZ91D magnesium alloy. Corros Sci 52:3191–3197

Terada Y, Ohkubo K, Nakagawa K, Mohri T, Suzuki T (1995) Thermal conductivity of B-2 aluminides and titanides. Intermetallics 3:347–355

Van Steenkiste TH, Smith JR, Teets RE, Moleski JJ, Gorkiewicz DW, Tison RP, Marantz DR, Kowalsky KA, Riggs WL, Zajchowski PH, Pilsner B, McCune RC, Barnett KJ (1999) Kinetic spray coatings. Surf Coat Technol 111(1):62–71

Van Steenkiste TH, Smith JR, Teets RE, Moleski JJ, Gorkiewicz DW (2000) Kinetic spray coating method and apparatus. US Patent 6:139–913

Van Steenkiste TH, Smith JR, Teets RE (2002) Aluminum coatings via kinetic spray with relatively large powder particles. Surf Coat Technol 154(2-3):237–252

Van Steenkiste TH, Kowalsky K, Berghorn C (2015) Particle velocity and particle temperature parameter effects on coating formation. In: Maev R, Leshchynsky V (eds) Book cold gas dynamic spray. CRC Press, pp 220–235

Villafuerte J (2005) Cold spray: a new technology. Weld J 84(5):24–29

Walter JW (1992) Numerical experiments on adiabatic shear band formation in one dimension. Int J Plast 8:657–693

Winston R (ed) (2011) Uhlig's corrosion handbook, 3rd edn. Wiley, Oxford, London, p 1296

Yandouzi M, Gaydos S, Guo D, Ghelichi R, Jodoin B (2014) Aircraft skin restoration and evaluation. J Therm Spray Tech 23(8):1281–1290

Yu M, Li W, Guo X, Liao H (2013) Impacting behavior of large oxidized copper particles in cold spraying. J Therm Spray Technol 22:433–440

Zhanpeng J (1981) A study of the range of stability of sigma phase in some ternary systems. Scand J Metall 10:279–287

Chapter 5
Structure–Properties Relations in High-Pressure Cold-Sprayed Deposits

M. Reza Rokni, Steven R. Nutt, Christian A. Widener, Grant A. Crawford, and Victor K. Champagne

5.1 Introduction

5.1.1 Overview of Cold Spray

CS is a deposition/consolidation process in which powder particles (typically 5–50 μm) are accelerated to speeds of 300–1400 m/s by a high-pressure carrier gas as the gas expands in the divergent section of a de Laval nozzle (Gärtner et al. 2006a, b; Assadi et al. 2003; Schmidt et al. 2006; Papyrin et al. 2007; Champagne 2007). To achieve greater gas flow velocities in the nozzle, the compressed gas is often preheated; sometimes as high as 1100 °C is used but is typically in the range of 40–70% of the particle melting temperature. Because the contact time of spray particles with the hot gas is relatively short and the gas is rapidly cooling as it expands in the diverging section of the nozzle, the temperature of the particles remains substantially below the initial gas preheat temperature. Hence, the deposition can be easily controlled to occur below the melting temperature of the feedstock powder material, producing deposits from particles that remain in the solid state. Because of this, CS deposits are essentially free of thermally induced defects

M.R. Rokni (✉) • S.R. Nutt
M.C. Gill Composites Center, Department of Chemical Engineering and Materials Science, University of Southern California, Los Angeles, CA, USA
e-mail: Rokni@USC.edu; Nutt@usc.edu

C.A. Widener • G.A. Crawford
Department of Materials & Metallurgical Engineering, South Dakota School of Mines & Technology, Rapid City, SD, USA
e-mail: Christian.Widener@sdsmt.edu; Grant.crawford@sdsmt.edu

V.K. Champagne
U.S. Army Research Laboratory, Weapons and Materials Research Directorate, Aberdeen, Proving Ground, MD, USA
e-mail: victor.k.champagne.civ@mail.mil

P. Cavaliere (ed.), *Cold-Spray Coatings*,
https://doi.org/10.1007/978-3-319-67183-3_5

commonly observed in traditional thermal spray deposits, such as oxidation, evaporation, gas release, shrinkage porosity, and thermally induced residual stresses (Champagne 2007; Alkhimov et al. 1994; Grujicic et al. 2004a; Grujicic et al. 2003). Because of these advantages over other spray deposition processes, CS has generated a great deal of interest within the manufacturing community for repair, advanced coatings, and additive manufacturing applications.

5.1.2 Comparison of High-Pressure to Low-Pressure CS

CS processes are generally divided into two categories – high-pressure cold spray (HPCS) and low-pressure cold spray (LPCS) – each has advantages and limitations and should be viewed as complementary. In reality, pressure is simply a process variable in a continuum across a very large process window, but the distinction comes from common equipment design variations that arise as a result of dealing with only lower pressures or primarily high pressures. The distinctions between the two CS processes can be summarized as follows:

1. In the HPCS process, the solid powder feedstock particles mix with the carrier gas in the pre-chamber zone. They are then fed into the gas stream, upstream of the converging section of the nozzle, as shown in Fig. 5.1(a). However, in LPCS process, powder particles are introduced downstream of the throat section of the nozzle, perpendicular to the diverging part of the nozzle, and accelerated toward the substrate, as shown in Fig. 5.1.
2. In LPCS, the carrier gas is heated only in the spray gun, while in the HPCS process, gas is preheated in a separate heating unit as well as in the spray gun (Fig. 5.1).
3. The amount of powder that can be fed per unit time increases with increased gas flows and thus can be greater in the HPCS process. Typical spraying parameters used in these two CS processes are summarized in Table 5.1. The main differences relate to process gas, pressure level, and electrical power used.
4. For HPCS, a high-pressure powder feeder operated at a pressure near or greater than the main gas stream must be used to allow mixing of the main gas and powder feed line. High-pressure powder feeders are also usually larger and more costly than the feeders needed for low-pressure use.

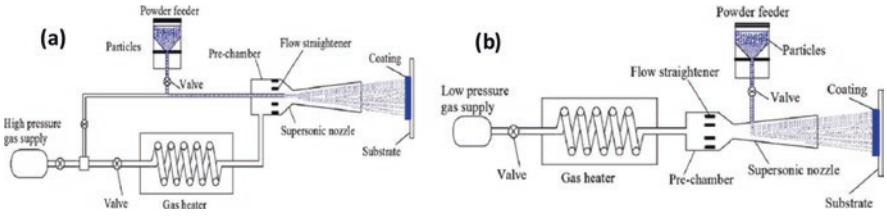

Fig. 5.1 Schematic presentation of CS processes: (**a**) HPCS (Grujicic et al. 2004a) and (**b**) LPCS (Maev and Leshchynsky 1998)

Table 5.1 Typical spraying parameters used in CS processes

Spraying parameter	HPCS	LPCS
Process gas	N2, He, mixture	Compressed air
Pressure (bar)	7–40	6–10
Preheating temperature	RT-1000	RT-650
Gas flow rate (m^3/min)	0.85–2.5 (N2), max. 4.2 (He)	0.3–0.4
Powder feed rate (kg/h)	4.5–13.5	0.3–3
Spraying distance (mm)	10–50	5–15
Electrical power (kW)	17–47	3.3
Particle size (μm)	5–50	5–30

5. A major challenge associated with all cold spray processes is nozzle clogging, which can become more severe as particle velocity and temperature are increased. To overcome the problem, a blended powder can be used, in which larger or harder particles are added to the first particle population as well as using various clogging-resistant nozzle materials (Champagne 2007; Smith 2007; Karthikeyan 2007).
6. Another common issue for both processes is erosive wear of the nozzle throat. This wear can affect the nozzle operation and lead to variations in operating conditions and deposit quality. This problem becomes more severe when hard particles are sprayed if wear-resistant materials such as sintered tungsten carbide are not used for the nozzle.
7. LPCS generally requires less costly equipment because the pressures are lower. However, the nozzle design in LPCS is restricted to a lower range of expansion Mach number (usually <3), and the inlet pressure is also restricted (normally 1.7 MPa) to ensure that atmospheric pressure is sufficient to supply powders to the nozzle. As a result, lower particle velocities can be reached through the downstream powder feeding technique.
8. The primary advantages of the HPCS over LPCS are the larger material selection and higher quality of the deposits, although the investment costs for HPCS equipment are greater than those for LPCS. In addition, the HPCS can be more efficient, with greater gas flow and powder feed rates.

5.1.3 Relationship Between Coating Microstructure and Mechanical Properties

Microstructural characterization and finite element analysis (FEA) show that the powder particles experience high strains (up to 10) and high strain rates (up to 10^9/s) during CS (Rokni et al. 2015a, b; Champagne et al. 2017), yielding densities similar to those of wrought materials. Studies have demonstrated that CS can be used to produce dense deposits of a wide range of materials, including aluminum (Al) and its alloys, copper (Cu), nickel (Ni) and its alloys, 316 L, and Ti-6Al-4 V, on

dissimilar substrates, including glass (Song et al. 2013) and polymers (Kruger and Ullrich 2011). Metal matrix composites (MMCs) and free forms with custom-graded properties can also be deposited by CS (Debiccari et al. 2011; Yu et al., 2013; Ko et al. 2013).

A much wider range of materials can be deposited by HPCS systems compared to LPCSs. This is because HPCS systems generate substantially higher particle impact velocities and thereby increase the extent of severe plastic deformation (SPD) at the interface with the substrate and with adjoining particles (Ozdemir et al. 2016; Rokni et al. 2014d, e). The formation of the deposit depends strongly on the high strain rate deformation via particle impacts, and thus the effects of material and process parameters on particle deformation are of critical importance.

The microstructural phenomena that occur in CS deposits can result in significant changes and variations in the local mechanical properties at the micron and submicron level. These changes can have adverse or beneficial effects on the performance characteristics of the deposit. Thus, to design and create a deposit with specific mechanical properties, an understanding of the various impact-induced microstructural phenomena is required. In this chapter, the various changes and the relationships between the microstructural evolution and mechanical properties that arise in CS deposits are reviewed. Where possible, recommendations are provided to indicate how to utilize available mechanisms to obtain desired microstructures and mechanical properties. The chapter is intended as a reference for researchers studying phenomena occurring during HPCS and for industrial practitioners seeking to apply the process in engineering applications.

5.2 Microstructure of CS Feedstock Powder and Deposition

Early investigations revealed that CS deposits retained feedstock microstructures (Gärtner et al. 2006a, b; Assadi et al. 2003; Schmidt et al. 2006; Papyrin et al. 2007; Champagne 2007). However, in recent years, microstructural features such as high dislocation density (Rokni et al. 2015a, b; Champagne et al. 2017; Ozdemir et al. 2016; Rokni et al. 2014a. b; Schmidt et al. 2009; Borchers et al. 2005; Borchers et al. 2003), ultrafine grain (UFG) structures (Rokni et al. 2014a; Rokni et al. 2014b; kim et al. 2009; Bae et al. 2010b; Moy et al. 2010; Zou et al. 2009; Li and Li 2003), phase transformation (Li et al. 2007; Richer et al. 2008; Li et al. 2011), and localized amorphous phases (Li et al. 2005; Xiong et al. 2008, Luo et al. 2011; Wang et al. 2009) have been observed. In this section, the mechanisms of evolution of these microstructural features in feedstock powders, as well as in CS deposits, are reviewed with respect to grain structure, dynamic restoration phenomena (recrystallization and recovery), precipitation, phase transformation, and amorphization. Understanding more clearly the relationships between the feedstock microstructure and CS deposit microstructures is critical to control product microstructure and optimize properties and performance of the deposit.

5.2.1 Microstructure of Feedstock Powder

The first step toward developing a clear understanding of CS microstructure is understanding the original feedstock powder microstructure. Here, salient microstructural features of gas-atomized powder are reported. Gas-atomized powder is the most common type of powder used in the CS industry today, and the vast majority of CS deposits are generated from this type of powder.

5.2.1.1 SEM Observations

The appearance of a typical gas-atomized powder is shown in Fig. 5.2 captured by scanning electron microscopy (SEM) (Rokni et al. 2014). Figure 5.2a shows that the powder particle size distribution can be slightly bimodal, consisting of a mixture of larger and smaller particles. Note that small particles below 5 μm tend to agglomerate around larger ones during solidification, creating irregular shapes of the powder agglomerates. Figure 5.2b shows a typical gas-atomized powder particle ~20 μm in diameter. The ~1–4 μm grain structure manifests as recessed grooves, along with smaller particles attached to the surface.

Figure 5.3a shows backscattered electron (BSE) images of typical gas-atomized powders, designated as type I (Rokni et al. 2014d). Type I particles exhibit a cellular structure often observed in metals solidified from the melt (Rokni et al. 2015a, Champagne et al. 2017; Rokni et al. 2014d, e). Cellular microstructure has been attributed to multiple causes, including (1) high cooling rate and rapid solidification (Wang et al. 2009), (2) pre-solidified microdroplets and dendrite fragments (Lavernia 1989), and (3) thermal equilibration and partial remelting of solid particles (Annavarapu and Doherty 1993). Note that the BSE image in Fig. 5.3a shows strong z-contrast (atomic number contrast), associated with composition variation at the grain boundaries (GBs) resulting from solute segregation during solidification. Solute segregation has been widely observed in gas-atomized powders (Rokni et al. 2015a; Ajdelsztajn et al. 2006a, b, c; Berube et al. 2012; Zhang and Zhang 2011;

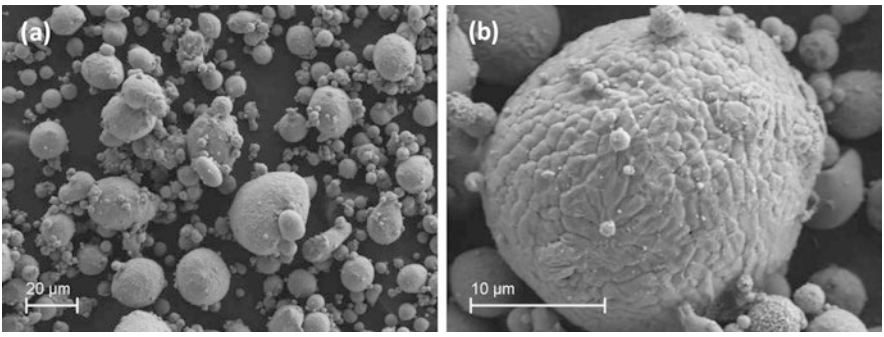

Fig. 5.2 SEM images of gas-atomized powder showing (**a**) powder morphology, (**b**) surface structure (Rokni et al. 2014d)

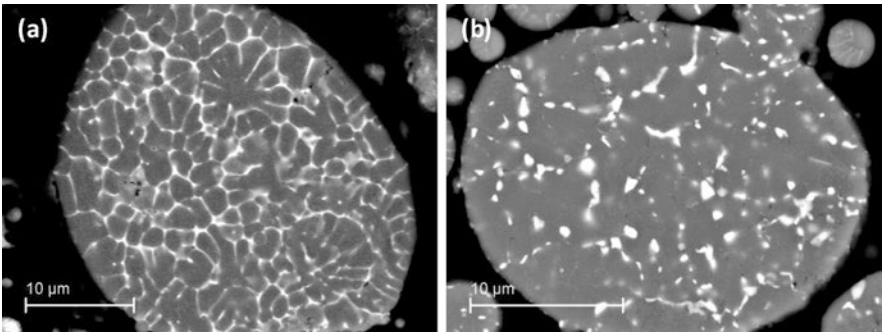

Fig. 5.3 SEM micrographs of a typical gas-atomized showing cross section of (**a**) type I particle showing internal grain structure and GB solute segregation and (**b**) type II particle with GB precipitates (Rokni et al. 2014d)

Trivedi et al. 2003). However, type II particles are also found in some of the gas-atomized powders within the same batch, as shown in Fig. 5.3b (Rokni et al. 2014d). The difference between the two types lies in the internal grain and GB structure. In contrast, type II particles exhibit coarser grains with more extensive GB precipitation compared to type I. Type II particles may experience slower cooling rates during atomization, affording sufficient time for GB solutes to precipitate. Several researchers (Ajdelsztajn et al. 2006a; Berube et al. 2012; Trivedi et al. 2003) have argued that type I microstructure is observed primarily in smaller particles while type II is typical of larger particles.

Note that not all powder batches feature both particle types. If the feedstock powder is a precipitate-hardened alloy, both particle types are prevalent throughout the powder batch in ratios of ~3:1, type I to type II (Rokni et al. 2014d). On the other hand, if the spraying powder is not a precipitate-hardened alloy, then type II is normally absent. Differences in powder microstructures may or may not be significant for achieving a given coating property, but it is important to consider that microstructural variations in the powder will also be present in the CS deposit.

5.2.1.2 In-Depth Characterization

Electron backscattered diffraction (EBSD) and transmission electron microscopy (TEM) have been used to characterize the internal grain structure of powder particles (Zou et al. 2009, 2010). A typical interior grain structure of a gas-atomized Al7075 particle is shown in Fig. 5.4a (Rokni et al. 2014d). The interior grain structure resembles the surface grain structure shown previously (Fig. 5.2b). The grain structure is not uniform, featuring both asymmetrical grain shapes and micron-size grains.

Using EBSD (Fig. 5.4a), it was confirmed that the grains in feedstock powders are also not fully relaxed, and internal stress is present in the powders (Rokni et al. 2014d). The particles show regions with high and low densities of low-angle grain boundaries (white lines in Fig. 5.4(a)), which presents evidence of dislocation sub-

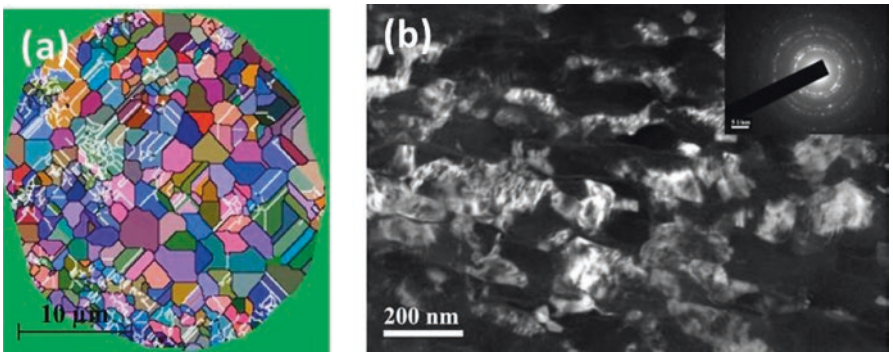

Fig. 5.4 (**a**) EBSD and (**b**) TEM images showing the presence of dislocation structures and LAGBs (*white lines* (**a**) in a gas-atomized 7075 Al powder). The inserted SADP is from the same region as in (**b**) (Rokni et al. 2014d)

structure existing in the as-received powder. The presence of dislocation structures was confirmed by TEM observations, shown in Fig. 5.4(b). This image shows that the starting powder particles contain a moderate density of dislocations and dislocation substructure. Many grains exhibit complex diffraction contrast, and the inserted selected area diffraction pattern (SADP), collected from the entire area in Fig. 5.4(b), shows several spots which are elongated.

5.2.2 Microstructure Characteristics of CS Deposits

5.2.2.1 General Features

Light microscopy (LM) and SEM have been used to investigate the morphology of deformed particles in as-deposited CS materials (Xiong et al. 2008; Balani et al. 2005; Koivuluoto et al. 2007; Koivuluoto et al. 2008; Kairet et al. 2007; Stoltenhoff et al. 2006; Jodoin et al. 2006; Bae et al. 2010a). In these studies, the CS deposits are dense, and the porosity is typically negligible (<1%), as shown in Fig. 5.5. The images also reveal the presence of prior particle boundaries (PPBs), a common feature of powder metallurgical (P/M) structures (Upadhyaya 1997; Berbon et al. 2001). Each particle experiences sufficient plastic deformation to conform to the underlying deposited layer, resulting in a dense deposit.

CS deposits often exhibit heterogeneous deformation within deposited particles. One of the earliest microstructural characterization studies of CS Al deposits showed a microstructure comprised of both highly deformed and more lightly deformed regions that corresponded to peripheral and interior regions of particles, respectively (Morgan et al. 2004). As shown in Fig. 5.5c, the level of deformation varies with radial position within the PPBs, with peripheral regions showing extensive deformation and interior regions showing less extensive deformation. SEM observations showed that intense shear localization causes reshaping of spherical

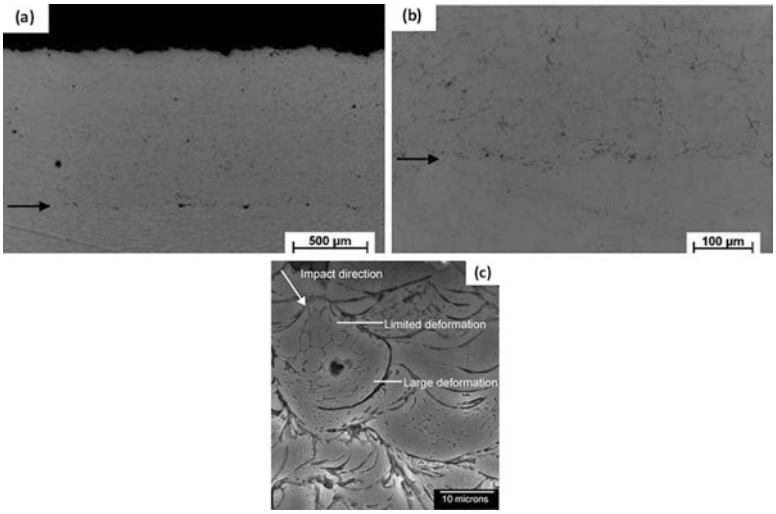

Fig. 5.5 LM (**a**) and SEM (**b**) images of CS Cu microstructure (Koivuluoto et al. 2008) and (**c**) deformation of grain structure within the particle at the leading edge (Morgan et al. 2004)

particles into long thin splats at particle–particle interfaces. However, slight changes to the aspect ratio (width/height) of the particle were observed in the particle interiors (limited deformation regions). This heterogeneous deformation leads to bimodal grain structures in CS deposits. Similar microstructural features have also been reported for other CS deposits (Schmidt et al. 2008; Borchers et al. 2005; Borchers et al. 2003; Zou et al. 2009, 2010; Morgan et al. 2004).

The general features of the microstructure at the scale of the splat/particle, described above, raise questions about what occurs at a finer scale during the buildup process. The corresponding phenomena govern the final (mechanical and physical) properties of the deposit and are described in the following sections.

5.2.2.2 Fine-Scale Microstructure

Details of the grain structures within the two regions described in the previous section have been revealed using EBSD (Rokni et al. 2014b, d; Zou et al. 2009; Morgan et al. 2004; AL-Mangour et al. 2013, 2014; Sundararajan et al. 2009). For example, Zou et al. (2009) reported inhomogeneous deformation during CS of Ni and Cu, observing a mixture of UFGs and elongated grains of different sizes in the microstructure (Fig. 5.6(a)). Rokni et al. (2014b, c, d, 2015b) reported similar features in different CS Al alloys. As shown in Fig. 5.6b, particle–particle interactions caused the formation of UFGs (dashed circle) in peripheral regions of highly deformed particles in CS 6061 Al deposits (Rokni et al. 2014b). A third region, where the degree of plastic deformation is not as great as in UFG regions, was also observed

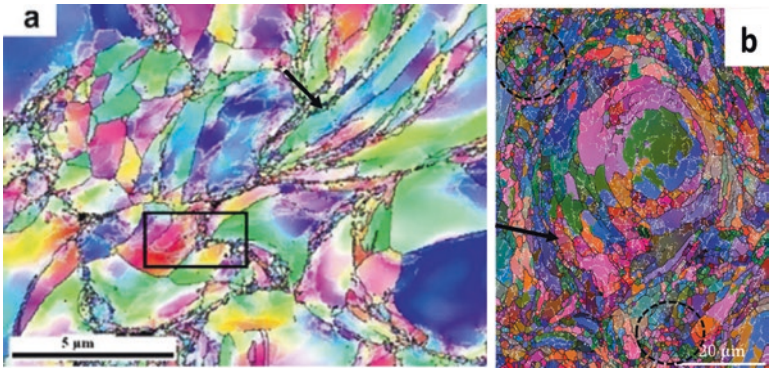

Fig. 5.6 EBSD characterization of (**a**) Ni (Zou et al. 2009) and (**b**) 6061 Al deposits (Rokni et al. 2014b)

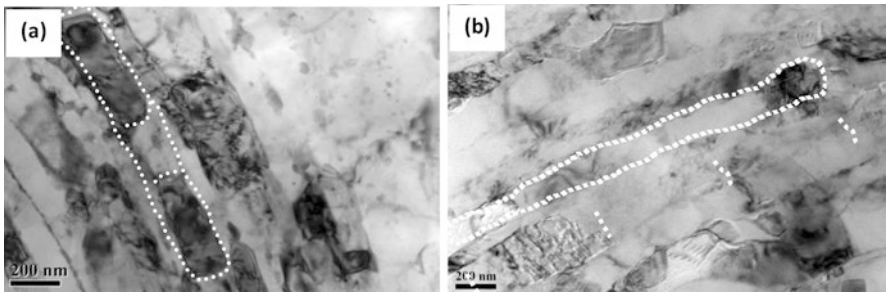

Fig. 5.7 TEM micrograph of CS (**a**) 7075 and (**b**) 6061 showing pancake structures with interconnecting LAGBs; dashed lines show ladder-like structure (Rokni et al. 2014b)

in the CS deposit, and these are aptly termed "pancake structure" (black arrows in Fig. 5.6). The flattened, elongated grains reflect extensive shear deformation but do not qualify as fine grained (Champagne et al. 2017; Rokni et al. 2014b, d, 2015b).

The evolution of microstructure within CS deposits, and particularly the pancake grain structures, has also been revealed by TEM (Fig. 5.7). The mechanism by which such pancake grain structures form has been attributed to adiabatic shear instability (ASI) on particle surfaces during high-velocity impact (Assadi et al. 2003; Schmidt et al. 2006; Rokni et al. 2014b, 2015b; Schmidt et al. 2009; Zou et al. 2009, 2010; Bae et al. 2009; Goldbaum et al. 2012). Crystallographic slip on a dominant slip system propagates through multiple- or cross-slip events, producing the distinctive grain shape (Humphreys and Hatherly 2004). Indeed, nearly identical grain shapes are also observed in adiabatic shear bands produced by dynamic loading (Zhang and Zhang 2011; Hansen and Jensen 1999; Hansen 2001; McQueen and Mecking 1987; Sellars 1987). The white dashed lines in Fig. 5.7 outline the pancake grains and highlight partitioning into a "ladder-like" structure with low-angle grain boundaries (LAGBs) comprising transverse rungs.

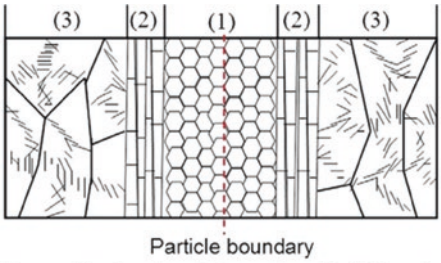

(1) Recrystallized equiaxed fine grains with high angle grain boundaries
(2) Directional ribbon structure subgrains with low angle grain boundaries
(3) Deformed grains with high density dislocation cells/walls

Fig. 5.8 Schematic illustration of the microstructure at interparticle boundaries in CS deposits (Lee and Kim 2015)

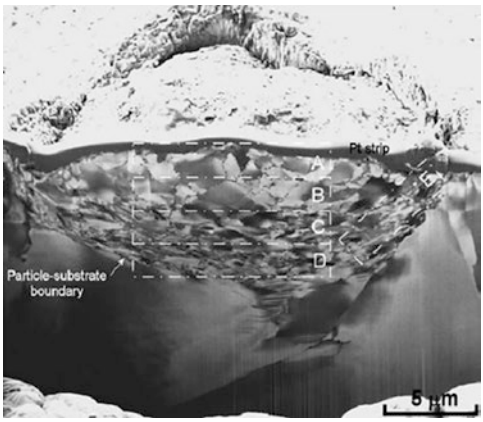

Fig. 5.9 FIB image of the CS copper particle cross section and areas chosen for analysis of grain deformation (King et al. 2009)

Lee and Kim (2015) illustrated the typical microstructure between two CS deposited particles in Fig. 5.8, showing the features common in different CS deposits. The illustration assumes that particles experience sufficient plastic deformation to form equiaxed UFGs at the particle–particle interface (region 1). Pancake grains divided by transverse LAGBs constitute ladder-like structures that appear next to the UFGs (region 2). Adjacent to the pancake grains, moderately deformed particle interiors with dislocation walls and/or cells formed in these regions (region 3).

Polished sections through individual CS particles provided further insights into the distribution of plastic flow and the evolution of grain structure. King et al. (2009) used focused ion beam (FIB) to the section through a single CS Cu particle, shown in Fig. 5.9. There was a general tendency for increasing deformation with increasing subsurface depth (below the top surface of the particle), with the maximum deformation occurring near the particle–substrate interface.

Various other features associated with heavy deformation have been revealed in CS metallic microstructures via TEM, including dislocation cell structures and dislocation loops (Rokni et al. 2014a, c; Li et al. 2007). The significant dislocation density in CS deposits is consistent with SPD at high strain rates during processing.

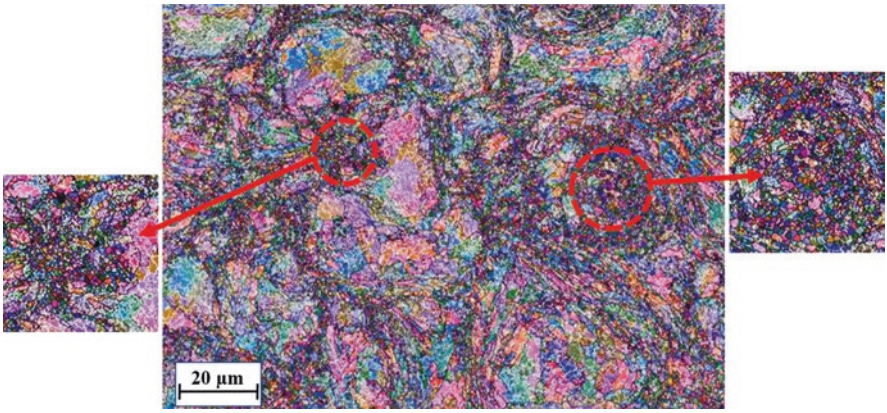

Fig. 5.10 EBSD pattern from the 7075 Al CS deposit indicating the LAGB distribution. The magnified images show the *yellow dashed circles* pointing to less LAGBs in these areas (Rokni et al. 2014d)

Compared with a typical dislocation density of ~10^{12} m^{-2} in annealed alloys, the density can be increased up to 10^{16} m^{-2} for cold-sprayed cBN/NiCrAl nanocomposites (Luo and Li 2012).

5.2.2.3 Formation Mechanisms of the UFG Structures

The appearance of the typical UFG structures resulting from CS is shown in Fig. 5.10, which shows an EBSD orientation map of a CS 7075 Al deposit showing the complexity of grain structure. Note that some particles experience sufficient deformation and heat during impact to completely recrystallize, producing UFG structures (dashed circles). There are few LAGBs in the UFG regions compared to surrounding areas. Enlargements of these regions are shown in Fig. 5.10. The peculiar grain structure has been cited as evidence for the occurrence of continuous dynamic recrystallization (CDRX) and conversion of the LAGBs to HAGBs. Indeed, dynamic recrystallization via CDRX has been reported during deposition of other metals and alloys (Rokni et al. 2014b, d; Zou et al. 2009; Yin et al. 2015).

Geometric dynamic recrystallization (GDRX) has also been proposed as a mechanism for the formation of UFG structures in high stacking-fault energy (SFE) alloys, particularly Al alloys, deformed under large strains at high temperatures (˃200 °C) (Humphreys and Hatherly 2004; Rokni et al. 2011, 2012, 2014b, d; Blum et al. 1996; Kassner and Barrabes 2005; Luo et al. 2014). Pinching off and annihilation of HAGBs occur as the original grains thin to about a few times the subgrain diameter (Blum et al. 1996; Kassner and Barrabes 2005). The GB annihilation is due to the presence of warm or hot high-strain deformation that can result in serrated boundaries, presumably in association with dynamic recovery (DRV) (Blum et al. 1996). Highly localized deformation at PPBs, produced by CS processing,

may thin the grains (observed in Fig. 5.9) to the dimensions of the subgrain diameters, producing UFG structures. As such, the occurrence of GDRX in regions with pancake grain structures can transform these regions into UFG structures, as described elsewhere (Rokni et al. 2014b, d).

A mechanism known as rotational dynamic recrystallization (DRX) has also been proposed (Trivedi et al. 2003) as a possible cause for DRX adjacent to interface regions in CS deposits. In the case of rotational DRX, strain-free grains are created in another way. The sequence of rotational DRX is shown in Fig. 5.11. This mechanism, which was originally reported by Zou et al. (2009), has been explained by Lee and Kim (2015).

Static recovery (SRV) and static recrystallization (SRX) can be assisted by the residual heat of plastic deformation occurring in subsequently impacted particles (Lee and Kim 2015; Hansen et al. 2008; Bae et al. 2010a, b). When SRV and SRX occur, the microstructure alteration occurs in the highly strained areas. As shown schematically in Fig. 5.12, both static-recovered and static-recrystallized microstructures appear in a CS Al deposit. However, because SRV and SRX are competitive phenomena, most stored strain energy is consumed first by SRV, and if the strain energy is sufficient to activate recrystallization, SRX will consume the remainder of the stored energy, generating recrystallized grains (Lee and Kim 2015; Hansen et al. 2008). Note that in high SFE materials such as Al, the activation energy required for SRV is less for SRX, and the dislocation glide and climb are active. Therefore, most of the stored strain energy is relieved through SRV (Humphreys and Hatherly 2004; Vandermeer and Hansen 2008; McQueen 2002; Hu 1963; Hasegawa et al. 1982).

The extent and distribution of UFGs, or simply the degree of recrystallization, depend on the material properties of the feedstock powder. Differences in SFEs, activation energies for recrystallization, and thermal conductivities can affect the extent of recrystallization. For example, Zou et al. (2009, 2010) reported less

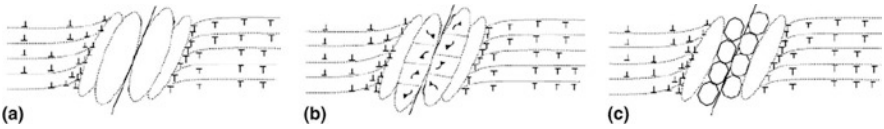

Fig. 5.11 Sequence of rotational DRX: (**a**) formation of elongated subgrains due to an accumulation of dislocations, (**b**) breakup of elongated subgrains, and (**c**) the rotation of the broken subgrains (Zou et al. 2009)

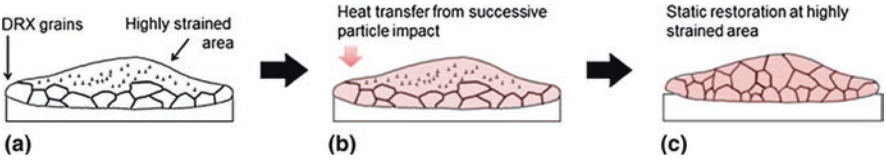

Fig. 5.12 The sequence of microstructural change via SRV and SRX during the kinetic spray: (**a**) microstructural state after the deposition stage, (**b**) additional heating by subsequent particle impact, and (**c**) microstructural change via SRV and SRX (Hansen et al. 2008)

uniform recrystallization for Ni compared to Cu, and Bae et al. (2010b) observed that in the case of poor thermal conductors such as Ti, SRV and SRX can be much more extensive due to local retention of transient thermal energy. Figure 5.13 shows grain refinement has transformed about half of the splat (by volume) into UFGs through recrystallization, primarily SRX.

In cases where the feedstock powder is nanocrystalline (NC), the NC structure is often retained after CS, as observed in a CS Al–Mg alloy (Rokni et al. 2014e; Ajdelsztajn et al. 2006b). There have been reports of dynamic amorphization in Al–Al, Ni–Al (AL-Mangour et al. 2014), Al–Cu (Guetta et al. 2009), Cu–Ni (Xiong et al. 2011), Al–Mg (Wang et al. 2014; Ko et al. 2014), and Fe–Al (Ko et al. 2015; Yoon et al. 2009) systems over thicknesses of up to tens of nanometers. In the case of metallic glasses, CS can result in partial devitrification of the initially amorphous phase (Yoon et al. 2009). A wide range of examples of amorphization and DRX in CS deposits have been reported (Zou et al. 2009; Lee and Kim 2015; Guetta et al. 2009; Ko et al. 2015; Zahiri et al. 2009b).

5.2.3 *Effect of Post-CS Heat Treatment*

Although the CS process involves SPD of the powder particles, the plastic strain experienced by particles is nonuniform, and thus the microstructure of the deposited material is also nonuniform. However, heat treatment (HT) can change and homogenize the microstructure of CS deposits and generate different microstructural features throughout the specimen. As a result, HTs have important implications for microstructural homogeneity and optimization of mechanical properties in CS deposits.

Figure 5.14 shows typical cross-sectional views of stainless steel (SS) 316 L as-deposited and heat-treated coatings produced using N_2 as propellant gas (Bandar et al. 2014). In the as-deposited condition (Fig. 5.14a), particles have high aspect ratios, and the deposit contains some porosity and triple-junction voids due presumably to incomplete bonding of particle–particle interfaces. A decrease in porosity

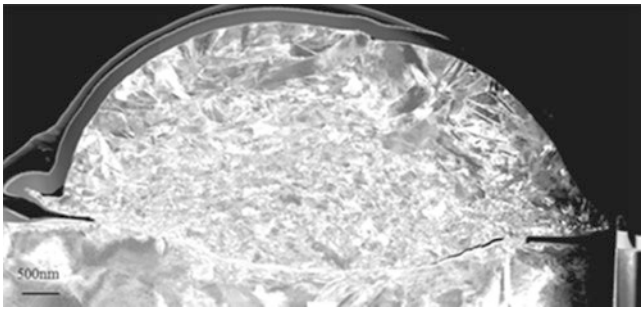

Fig. 5.13 Dark-field TEM image of a thin foil of a Ti cold-deposited splat onto a Ti–6Al–4 V substrate (King et al. 2009)

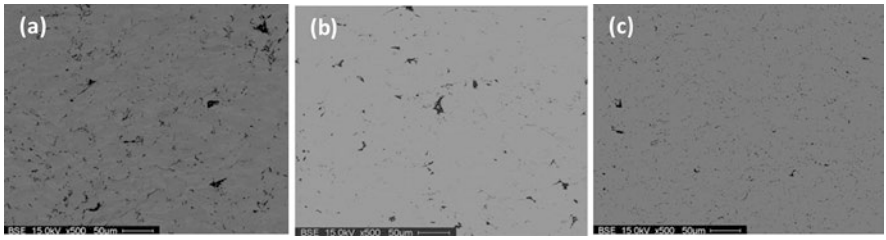

Fig. 5.14 SEM microstructures of CS SS 316 L coating deposited by N_2 as process gas in the (**a**) as-coated condition, (**b**) after HT at 400 °C, and (**c**) after HT at 1100 °C (AL-Mangour et al. 2014)

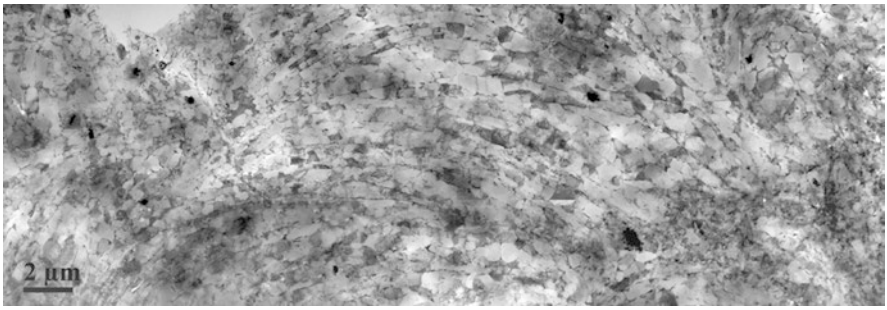

Fig. 5.15 TEM image obtained from the CS 7075 deposition after annealing at 450 °C for 45 min (Rokni et al. 2015a)

was obtained in the deposit after annealing at 400 °C, as shown in Fig. 5.14b. Also, the splat-shaped particles are now replaced with more equiaxed grains. There is a marked decline in porosity after annealing at 1100 °C (Fig. 5.14c). The decrease in porosity with increasing annealing temperature in the N_2-deposited coatings was explained using microstructural sintering models. The fine porosity observed in the CS deposit after annealing was also attributed to incomplete "sintering" at interparticle interfaces.

Figure 5.15 shows a montage of TEM images from a CS 7075 Al deposit after annealing (Rokni et al. 2015a). The annealing process provides some additional thermal driving force for SRV and SRX, releasing much of the stored energy. The grains are equiaxed with well-defined, straight GBs, unlike the inhomogeneous microstructure observed in the pre-annealed deposit (Fig. 5.10). Furthermore, many of the grains are free of dislocations (limited diffraction contrast), and residual stress has been relieved through the annealing process. In these cases, the grains appear dislocation-free because the slip distance across the UFG grains is small enough that dislocations can rapidly glide across the grain during the course of annealing and be absorbed into the opposite GB without major interactions with each other (Rokni et al. 2014e). This mechanism has also been reported to play an important role in other SPD materials, such as cryomilled UFG Al extrusions (Hayes et al. 2004; Romanov 1995; Eckert 1995).

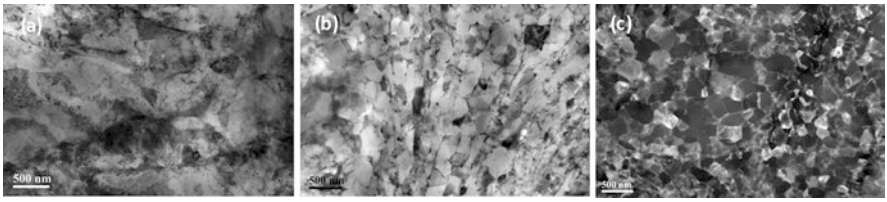

Fig. 5.16 TEM images obtained from different regions in CS 7075 deposit after annealing to 450 °C, (**a**) particle interiors, (**b**) particle interfaces with the pancake structures, and (**c**) particle interfaces with UFG structure (Rokni et al. 2015a)

As described before, the microstructure characteristics of CS deposits contain three distinct regions – particle interiors, particle interfaces with UFG structure, and particle interiors with pancake grain structure. The microstructure in these three regions after annealing can be compared to the pre-annealed deposit. It was also observed that interior regions of 7075 Al CS particles did not significantly change after annealing (Fig. 5.16a) (Rokni et al. 2015a). This retention of grain structure has been attributed to the presence of fine age-hardening precipitates within grains and their effect in restricting GB migration (Rokni et al. 2017a, b; Shin et al. 2000). However, as shown in Fig. 5.16b, peripheral regions of particles with pancake grain structures exhibit recrystallization during annealing and develop a UFG structure (Figs. 5.16b). Peripheral regions of particles that were originally characterized by UFG structures prior to annealing are also relatively unaffected by annealing (Fig. 5.16c). Although subtle, these regions show a slight reduction in overall dislocation density, increased GB definition, and evidence of modest recrystallization.

In all reports of CS deposits and associated microstructures, negligible post-annealing grain growth has been consistently reported. Resistance to grain growth in CS deposits has been attributed to extensive solute segregation at GBs in the deposits (Rokni et al. 2015b, 2017a, b; Zou et al. 2009; Berube et al. 2012; Trivedi et al. 2003; Shin et al. 2000). The segregation can lead to nucleation of GB precipitates during annealing and restrict GB migration. Due to the nature of the gas atomization process, solute segregation to GBs in gas-atomized powders is almost unavoidable, as discussed in Sect. 5.2.1.1. However, more extensive GB segregation has been reported in as-deposited materials, which is unexpected given the small grain size, short diffusion distances, and transient heat of deformation during CS.

In some cases, blending different powders, such as SS 316 and Co–Cr alloy L605 (AL-Mangour et al. 2013) before CS, and then performing post-CS heat treatment produce composite deposits with superior corrosion and mechanical properties compared to the unblended powder (316 L alone). The low deposition temperature, high deposition rate, and relatively low cost make CS an efficient process for fabrication of composite deposits (Champagne 2007; Grujicic et al. 2004b; Yandouzi et al. 2009; Melendez and McDonald 2013; Karthikeyan 2007; Dykhuizen and Smith 1998; Lupoi and O'Neill 2010). CS of Ti/Al (Novoselova et al. 2007; Zhao et al. 2006; Stoltenhoff et al., 2002), Zn/Al (Wang et al. 2007), Fe/Al (Zhang et al. 2008), and Ni/Al (Zhao et al. 2006) powder blends shows that dense composites can

be produced using blended powder, and subsequent annealing can lead to intermetallic (IM) phase formation.

As shown in Fig. 5.17a, an Fe_2Al_5 IM compound forms during annealing at 450 °C, far below the Fe-Al alloy eutectic temperature (640 °C), due to metastable interfaces resulting from the intense deformation of deposited particles during CS. Increasing the annealing temperature from 450 to 600 °C (Fig. 5.17b) causes the volume fraction of the Fe_2Al_5 phase to increase substantially. Similar results have been published for heat-treated Al/Mg CS deposits (Bu et al. 2011; Spencer and Zhang 2009; Wang et al. 2011; Wang et al. 2012). It has been commonly reported that HT generates the IM phases $Mg_{17}Al_{12}$ (β) and Al_3Mg_2 (γ), which can increase hardness and corrosion resistance.

Like any powder metallurgy product, the sintering/annealing environment is critical to the microstructure and mechanical properties of CS deposits. Vacuum or oxygen-free atmospheres (i.e., argon (Ar) or nitrogen (N_2)) for HT are generally preferred to prevent the formation of oxide layers on the deposit surface and to avoid the formation of sintering necks. Lee et al. (2013) investigated the effect of different HT gas environments on CS Ti deposits. Figure 5.18 shows that vacuum annealing yielded superior densification (3.8% porosity, 156.7 HV) relative to Ar annealing (5.3%, 144.5 HV) and 5% H_2 + Ar gas annealing (5.5%, 153.1 HV). The results also revealed that the use of vacuum environment during post-CS heat treatment can reduce oxide content (purification) in the Ti deposits.

Low annealing temperatures can avoid distortion and residual stress development and, most importantly, preserve the benefits of using a low-temperature

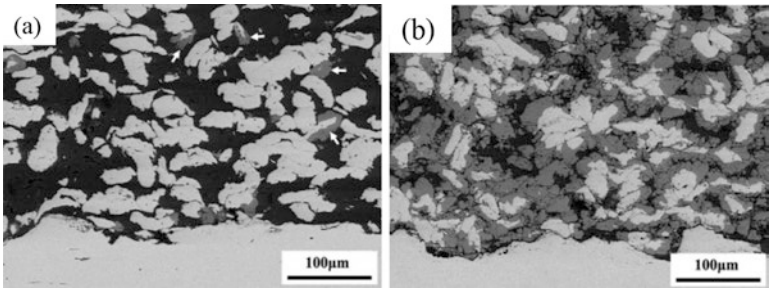

Fig. 5.17 Cross-sectional microstructures of Fe/Al composite coating annealed at (**a**) 450 °C and (**b**) 600 °C for 4 h showing the formation of Fe/Al intermetallic compounds (Zhang et al. 2008)

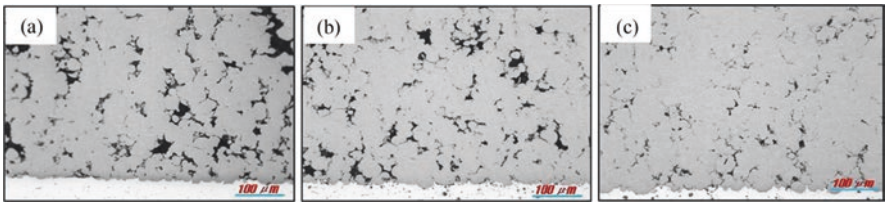

Fig. 5.18 Microstructures of Ti deposits after annealing in (**a**) Ar gas, (**b**) 5% H_2 + Ar gas, and (**c**) vacuum (Lee et al. 2013)

deposition technique. These benefits include overall compressive residual stress, fine microstructure, and superior hardness. Moreover, even if beneficial, a postdeposition anneal can be difficult or unacceptable from a practical perspective because of the component size, base material, or specific production process.

5.3 Mechanical Properties of CS Deposits

5.3.1 Overview of Mechanical Properties Related to Deposit Quality

The mechanical properties and structural integrity of CS deposits are generally one of the main issues for developing CS processes for different industries, like defense, aerospace, and automotive, in which CS is utilized as a repair/refurbishment process (Rokni et al. 2014c; Champagne and Helfritch 2014; Jones et al. 2011). These industries often have strict specifications for the mechanical properties of deposits. As a result, HPCS is finding increasing use for many structural applications, due to the higher strengths, densities, elastic modulus, and ductility exhibited by CS deposits compared to LPCS. Additionally, CS offers distinct advantages over other thermal spray processes, including lower temperatures and the unique solid-state microstructural growth mechanism, which can result in beneficial microstructures. The plastic deformation that occurs during impact and the associated heating and cold working of additional deposited layers, as well as post-CS heat treatments, can further alter the microstructure, opening new opportunities to control and enhance the resultant mechanical properties of CS deposits. In this section, we review fine- and bulk-scale mechanical properties of CS deposits and the effects of post-CS annealing on mechanical properties. Our goal is to provide a useful summary for CS experts as well as to guide students and industrial end users to an understanding of the process characteristics and potential for specific industrial applications.

5.3.2 Local Mechanical Properties

Deformation inhomogeneity in CS deposits creates different regions in the microstructure (Sect. 5.2.2.2). As a result, these regions affect local mechanical properties of CS deposits. As discussed previously, particle–particle interfaces are often 1–4 μm wide. Therefore, nanoindentation is well suited for characterizing local variations in mechanical properties in CS deposits, owing to the fine resolution in load (~ 1 mN) and displacement (~ 1 nm) (Rokni et al. 2015b; Ozdemir et al. 2016; Zou et al. 2009; Goldbaum et al. 2011a, b; Wang et al. 2013; Rolland et al. 2012; Ajdelsztajn et al. 2005).

5.3.2.1 Nanoindentation and Modulus

Nanoindentation has been widely used to measure the elastic modulus of CS deposits (Rolland et al. 2012), as well as the hardness of as-received metal powders (Rokni et al. 2014a, b, Goldbaum et al. 2012), and CS-deposited pure metals and engineering alloys (Rokni et al. 2014e, 2017c; Moy et al. 2010; Yin et al. 2015; Ajdelsztajn et al. 2006b; Liu et al. 2012). Furthermore, nanoindentation studies have reported variations in local mechanical properties of CS deposits (Rokni et al. 2014e, 2015b; Zou et al. 2009, 2010; Goldbaum et al. 2011b; Soer et al. 2005).

Because of grain size differences in the distinct microstructural regions, i.e., particle interiors, PPBs with pancake grains, and PPBs with UFG structures, most studies have reported a nonuniform hardness distribution within CS deposits. Soer et al. (2005) reported that, generally, the hardness increased near particle interfaces and measured 0.7 and 0.8–1.2 GPa greater at particle interfaces than the particle interiors in Fe – 14% Si and Mo, respectively. Zou et al. (2010) and Rokni et al. (2014a) used EBSD along with nanoindentation to measure the local variations of mechanical properties, as shown in Fig. 5.19. They both reported the same trend, greater hardness at particle interface regions, in Cu (Zou et al. 2010), Al alloy (Rokni et al. 2014e; Zou et al. 2010; Yin et al. 2015), and Ti (Goldbaum et al. 2011a) deposits. The mechanisms considered included (1) GB strengthening (lower grain size), (2) precipitate strengthening, and (3) strain hardening and were treated (Zou et al. 2010) using linear superposition. The increased hardness near PPBs was attributed GB-strengthening and strain-hardening mechanisms, owing to the increased density of GBs and dislocations at these regions.

A similar trend was reported for NC cold-sprayed materials. Ajdelsztajn et al. (2005) measured a hardness of ~4 GPa for cryomilled 5083 Al coatings deposited by CS. Rokni et al. (2014e) observed hardness variations between the 5083 substrate (as-cast condition), the NC cryomilled powder, and different regions in cryomilled NC deposits. As shown in Table 5.2, the average hardness of the NC powder was greater than that of the as-cast substrate. Also, the CS NC deposit showed greater hardness than the feedstock NC powder, with the greatest hardness at PPBs. The results indicate that milling/mechanical alloying processes combined with the CS technology may be a viable means of producing both NC deposits and bulk nanostructured materials for engineering applications.

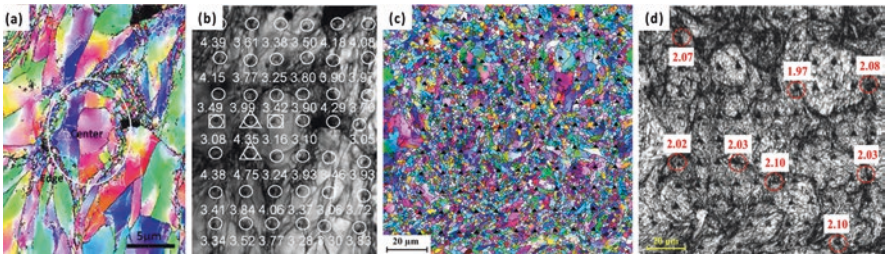

Fig. 5.19 EBSD map and nanohardness distribution map of (**a** and **b**) Ni (Zou et al. 2010) and (**c** and **d**) 7075 Al deposits (Rokni et al. 2015b)

Table 5.2 Hardness values for the 5083 substrate, NC powder, and the NC deposit (Rokni et al. 2014e)

Material	5083 substrate	5083 powder	CSP 5083	
Hardness (GPa)	1.13 ± 0.28	2.52 ± 0.36	*Particle interior*	*High hardness zones*
			2.77 ± 0.21	3.57 ± 0.32

5.3.3 Bulk Mechanical Properties

Bulk mechanical properties of CS deposits affect the performance of repaired/refurbished parts and components which are reused in service. Deposition parameters, including gas temperature and pressure, particle velocity, and substrate material, alter the CS microstructure and cause variations in bulk-scale mechanical properties of CS deposits. Therefore, the relationship between CS parameters and final properties can provide useful insights.

5.3.3.1 Microhardness

Uniformity of mechanical properties across CS deposits affects structural integrity in CS-repaired parts and components. Microhardness measurements provide a useful means to assess the uniformity of basic strength properties. Substrate materials and CS deposits generally show different microhardness values (Rokni et al. 2015b; Li et al. 2007; Li et al. 2006a; Van Steenkiste et al. 2002). When the substrate and CS deposit are the same material, the difference in hardness between substrate and CS deposit stems from three major factors: (1) difference in tempers (for age-hardened alloys) (Rokni et al. 2015b), (2) work hardening because of SPD, and (3) presence of porosity in the deposit (Rokni et al. 2015a; Van Steenkiste et al. 2002). In general, however, the hardness of CS material is usually comparable with that of bulk material in a similar material condition. In the case of dissimilar substrate/deposit materials, the hardness of the deposit and the substrate often differ simply due to intrinsic material differences.

Ghelichi et al. (2014b) investigated dissimilar and similar combinations by depositing Al7075 and pure Al on pure Al substrates. Microhardness measurements across the deposits and substrates showed that the deposits of Al7075 had twice the hardness of the pure Al (see Fig. 5.20a). On the other hand, the substrate surface hardness of specimens coated with pure Al showed a lower microhardness compared to the former series because of greater deformation in the coating/substrate region. Rokni et al. (2015b) investigated the combination of CS 7075/7075-T6 substrate (Fig. 5.20b) and reported that the CS deposit hardness (115 ± 9 Hv) was much lower than the substrate hardness (171 ± 5 Hv). This observation was attributed to the temper difference between the substrate (T6) and both 7075 gas-atomized feedstock powder and the CS deposit (solution treated). They pointed out that, by comparison, the CS deposit microhardness was slightly greater than the reported hardness for solution treated 7075 Al (W temper, 105 Hv) due to the SPD during CS.

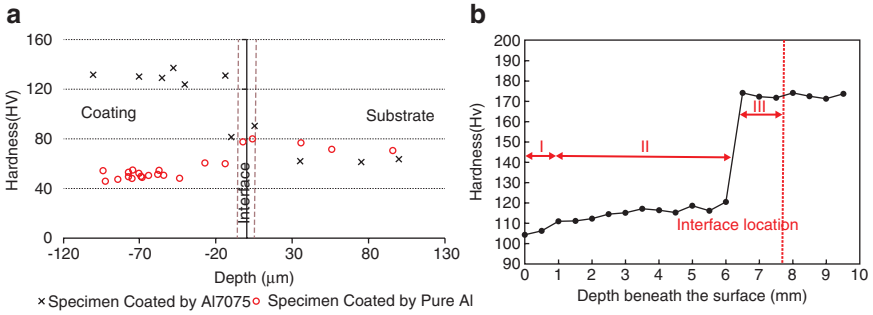

Fig. 5.20 Microhardness distribution from the top of the (**a**) CS 7075 and Al on Al substrates (Ghelichi et al. 2014b) and (**b**) CS 7075 Al on 7075-T6 substrate (Rokni et al. 2015b). The dashed red lines represent the location of the deposit/substrate interface

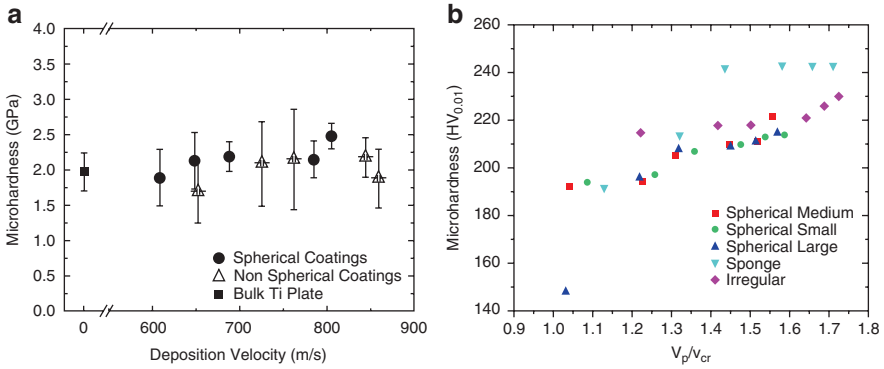

Fig. 5.21 Microhardness difference for (**a**) various deposition velocities and powder states for Ti deposits (Goldbaum et al. 2011a) and (**b**) different powder states (Wong et al. 2013b)

Virtually all CS parameters affecting particle deformation behavior (i.e., particle velocity and temperature) can change deposit hardness. However, there are some discrepancies in the literature regarding the relationship between CS parameters and microhardness. For example, Goldbaum et al. (2011a) showed that microhardness values for spherical and nonspherical Ti deposits were similar for all spray conditions and not significantly greater or less than the hardness of bulk Ti, as shown in Fig. 5.21a. On the other hand, Wong et al. (2013b) reported that powder state and shape affected the resultant hardness of CS deposits (Fig. 5.21b) and attributed this to the level of porosity in the corresponding deposits. In general, sponge and irregular powders show the greatest hardness in deposited materials for different V_p/V_{cr} ratios, as shown in Fig. 5.21b. Note that the same trend has been reported for deposits built from cryomilled NC- vs. gas-atomized powders (Zhang and Zhang 2011). A significantly higher hardness has been achieved in deposits with as-cryomilled powder, since NC grains are produced by mechanical milling under liquid nitrogen and the grain size range is markedly smaller than gas-atomized powder.

Regarding the effect of particle size on the hardness of deposited materials, Zahiri et al. (2009a) showed that deposit microhardness decreases with decreasing average particle size (22–16 μm) under similar spray conditions for Ti deposits. However, Marrocco et al. (2006) and Cinca et al. (2010) showed the opposite trend – deposit microhardness decreased with increasing average particle size (28–47 μm). Thus, it appears that the effect of average particle size on deposit properties may depend on the range of the size distribution.

5.3.3.2 Bond Strength

Adhesive strength or bond strength of CS deposits affects industrial applications. In general, average adhesive/cohesive strengths are determined by bonding (with adhesive) the sprayed area to a respective counter-body of the same size and then pulling the assembly in tension to failure (ASTM C633). Using this method with certain material combinations has shown that deposits can fail cohesively (Irissou et al. 2007) or adhesively (Cinca et al. 2010). There are cases where the test results are limited by the strength of the adhesive. To overcome this case, others (Huang and Fukanuma 2012) have attempted alternative testing techniques which have indicated that CS deposits can display high adhesive strengths (up to 250 MPa for Al alloys (Karthikeyan 2007)). Bond strength has been investigated by assessing the effects of parameters such as particle velocity (Huang and Fukanuma 2012; Cavaliere et al. 2014), carrier gas temperature and pressure (Stoltenhoff et al. 2006; Goldbaum et al. 2011a; Champagne et al. 2005; Binder et al. 2011), standoff distance (Chun et al. 2012; Li et al. 2008), surface roughness (Marrocco et al. 2006; Ghelichi et al. 2012; Ziemian et al. 2014), and spray angle (Binder et al. 2011; Cinca et al. 2010; Schmidt et al. 2009) on the quality of CS deposits. The effects of some of these parameters are summarized below.

Greater bond strength values are measured in the CS deposits sprayed with higher gas temperature and pressure (Stoltenhoff et al. 2006; Goldbaum et al. 2011a; Marrocco et al. 2006; Huang and Fukanuma 2012; Binder et al. 2011; Fukumoto et al. 2010), as shown in Fig. 5.22. This improvement in bond strength has been attributed to two factors. First is the higher kinetic energy of the particles at higher gas pressures, which increases particle deformation (Binder et al. 2011). Second is the greater ductility of the spray material at higher temperature (Champagne 2007; Rokni et al. 2015a; Schmidt et al. 2009), which also increases particle deformation. Note that the effect of gas temperature is reported to be more effective than gas pressure on bond strength, especially with N_2 gas (Huang et al. 2014). By increasing the gas temperature, both particle and substrate are softened by heating. Particles that deeply embed into the substrate increase the material mixing and particle interlocking at the interface, giving rise to superior interface bond strength.

Carrier gas type can also affect the final bond strength of CS deposits. According to Stoltenhoff et al. (2006), the adhesion strength between Cu and SS substrate increased when He was used as a process gas instead of N_2 (marked with blue stars in Fig. 5.23a). Using He as a process gas, particles work hardened more extensively

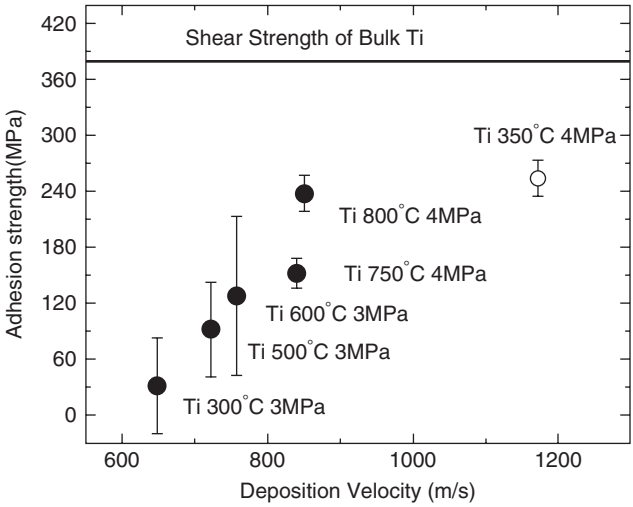

Fig. 5.22 Difference in bond strength of Ti deposits with gas temperature and pressure (Goldbaum et al. 2011a)

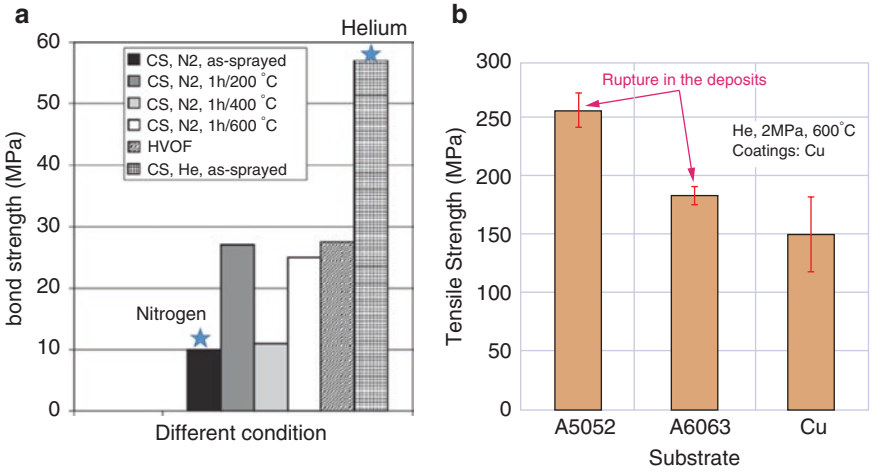

Fig. 5.23 Adhesive strength of CS Cu deposits on (**a**) low-carbon steel substrate with different gas carriers (Stoltenhoff et al. 2006) and (**b**) on different substrate materials (Marrocco et al. 2006)

because of greater particle velocities, producing greater bond strength between deposit and substrate (Champagne 2007).

Substrate material also affects bond strength (Stoltenhoff et al. 2006; Huang and Fukanuma 2012). As shown in Fig. 5.23b, the bond strength of Cu deposits on Al5052 and Al6063 substrates is greater than on a Cu substrate. These results confirm that a greater particle velocity results in more extensive plastic deformation for the Al substrates compared with the Cu substrates, forming stronger bonds.

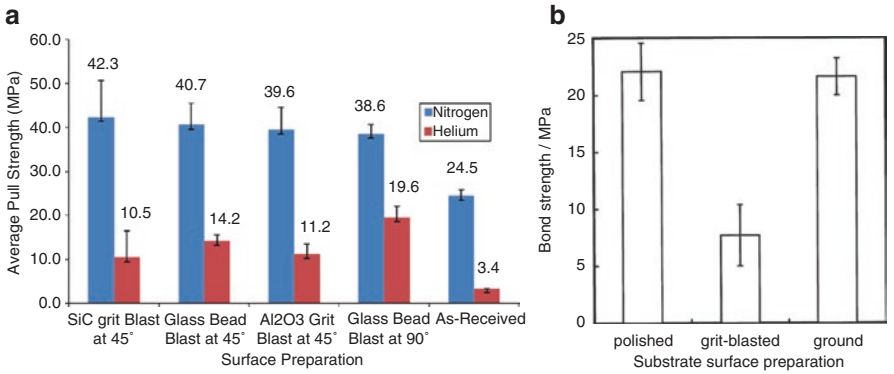

Fig. 5.24 Effect of surface preparation on bond strength of (**a**) CP-Al on AA2024-T3 (Sharma et al. 2015) and (**b**) Ti on Ti (Marrocco et al. 2006) deposits

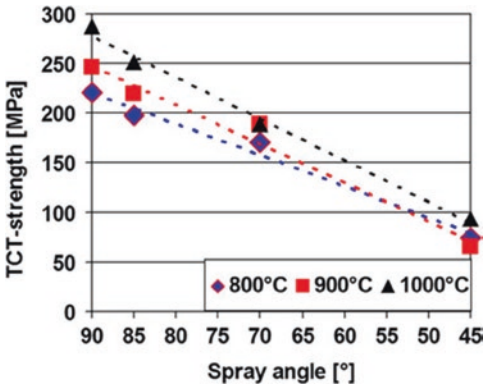

Fig. 5.25 Shear strength of CS Ti deposits on low-carbon steel substrate for different spray angles and process gas temperatures. CS was performed at a gas pressure of 4 MPa (Binder et al. 2011)

There is general agreement that grit blasting of substrates can enhance mechanical interlocking of CS deposits to substrates by increasing surface roughness (Gärtner et al. 2006a, b; Price et al. 2007; Sharma et al. 2015). Sharma et al. (2015) investigated the effect of different surface preparation methods on final bond strength of pure Al deposits on 2024 Al substrates. As shown in Fig. 5.24a, the greatest mean adhesive strengths were achieved by SiC grit blasting at 45° using N_2 carrier gas and glass bead blasting at 90 °C using He gas. However, some discrepancies have been reported in this regard. For example, Marrocco et al. (2006) reported lower bond strength between Ti deposits and substrates (Fig. 5.24b) after grit blasting the substrate, while the polished and ground surfaces resulted in greater bond strengths.

Spray angle can also affect the bond strength of CS deposits. The correlation shown in Fig. 5.25 (Binder et al. (2011)) confirms that the number of well-bonded PPBs decreases with decreasing impact angles. The bond strength decreases from ~290 MPa for perpendicular impacts to ~90 MPa for a spray angle of 45°, demonstrating that impact angles often have a stronger influence on deposit bond strength than other CS process parameters.

Table. 5.3 Effect of thickness on bond strengths of pure Al/2024Al deposits (Sharma et al. 2015)

	Average bond strength	Type of failure	
Deposit thickness (mm)	MPa	SD	
0.152	43.11	±3.86	Adhesion
0.508	39.56	±5.01	Adhesion

CS deposit thickness also reportedly influences bond strength. Huang and Fukanuma (2012) and Sharma et al. (2015) demonstrated that the thicker the deposit, the greater the risk of de-bonding between deposit and substrate because of the accumulated internal stress, as presented in Table 5.3. It was explained that thinner coatings have less residual stresses, contributing to the slightly greater adhesive strength.

5.3.3.3 Tensile Strength and Ductility

CS deposits are usually produced in thicknesses ranging from several hundred microns to a few millimeters, and thus unlike other thinner coating processes, cold spray can be deposited in much greater thicknesses to allow the production of full-size or subsize tensile coupons per standard test methods like ASTM E-8. Most data for ultimate tensile strength (UTS) and ductility of CS deposits have been extracted from this type of tensile test (Cavaliere et al. 2014; Binder et al. 2011; Sharma et al. 2015; Kumar et al. 2016a; Hall et al. 2006).

Process parameters significantly affect the ductility and strength of CS deposits, including particle velocity (Assadi et al. 2003), gas type (DeForce et al. 2011), gas temperature and pressure (AL-Mangour et al. 2013; DeForce et al. 2011; Coddet et al. 2015; Coddet et al. 2016), surface roughness (Ghelichi et al. 2012; Wolfe et al. 2006), and spray angle (Binder et al. 2011). In general, as shown in Fig. 5.26 (Lee et al. 2011), if the particle temperature is too low or too high, the particle can be brittle or too ductile, respectively. This illustrates that there are indeed an ideal particle impact velocity and particle impact temperature to achieve optimal mechanical properties in the CS deposit and that there is a limit to the benefit of increasing temperature in cold spray. Also, gas temperature can affect particles differently depending on their size, since larger particles will retain a higher temperature upon impact (Upadhyaya 1997). Thus, any variable that can affect particle velocity and temperature can affect the resultant ductility and strength of CS deposits.

Huang and Fukanuma (2012) investigated the effects of gas pressure and temperature on tensile strength of CS Cu deposits and showed that the UTS of CS Cu deposits increased with gas temperature and pressure (Fig. 5.27). Their study also revealed the effect of the substrate material on the resultant tensile strength of the CS deposits, which was explained by imposing various levels of deformation on Cu particles with Al alloy and Cu substrates.

In addition, carrier gas type has been shown to have a great impact on tensile strength and ductility of CS deposits due to the velocity differences of the impacting particles. As shown in Fig. 5.28, N_2 and He influenced the mechanical properties of

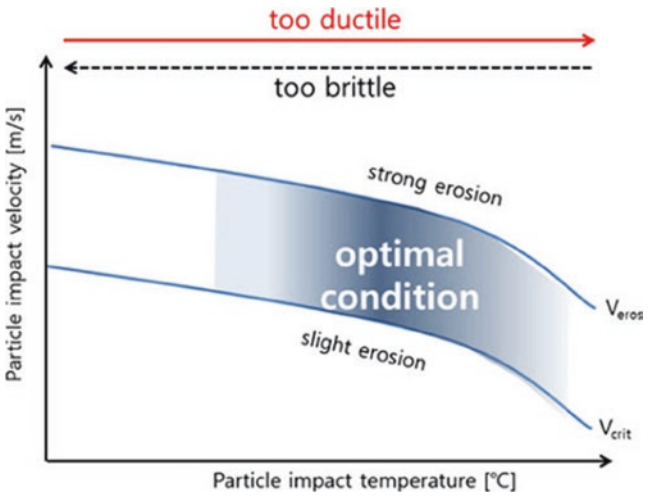

Fig. 5.26 The optimal operating condition in terms of particle impact velocity and temperature (Lee et al. 2011)

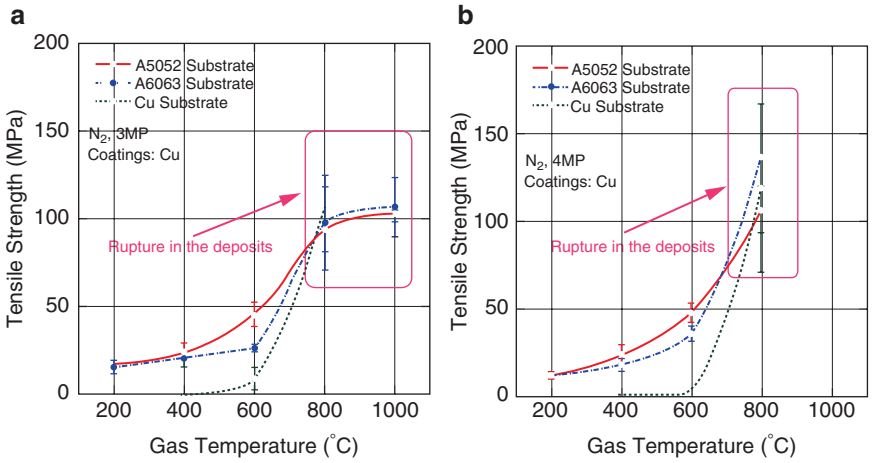

Fig. 5.27 Tensile strength of Cu deposits prepared under different conditions: (**a**) N_2, 3 MPa, and (**b**) N_2, 4 MPa (Marrocco et al. 2006)

Ti-6Al-4 V deposits differently, i.e., He-sprayed deposits showed greater strength and ductility than those of N_2-sprayed deposits (curves #2 and #4, respectively). Similar trends have been reported for other CS-deposited materials (Champagne 2007; Schmidt et al. 2009; Ghelichi et al. 2012; Grujicic et al. 2004a; Vo et al. 2013; Suo et al. 2015). Figure 5.28 also illustrates the difference between the mechanical properties of the CS deposits and the corresponding bulk materials (curve #1). Efforts have been made to improve these properties to those of the bulk materials. One method has been heat treating deposits, which will be discussed later.

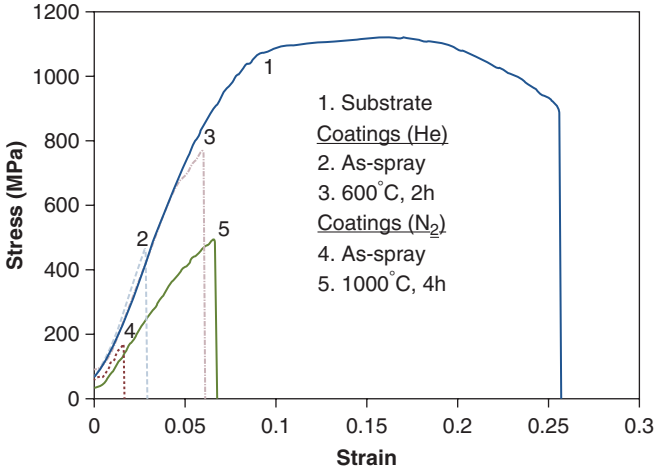

Fig. 5.28 Typical stress–strain curves for Ti-6Al-4 V substrate and deposits in different conditions (Vo et al. 2013)

Schmidt et al. (Schmidt et al. 2008) have also shown that significant increases in the ductility of CS deposits are possible using an optimized nozzle design. They reported increases in tensile strengths of Cu deposits from 50 MPa to as high as 250 MPa with nozzle design improvements with HPCS systems.

5.3.3.4 Residual Stress

Deposit integrity may be loosely defined as the quality of bonding between particles within the deposit and between the deposit and the substrate. Deposit integrity is also influenced by the residual stresses locked within CS deposits. As is the case in all thermal spray deposits, residual stresses can lead to peeling and delamination of the deposit (Champagne 2007; Karthikeyan 2007). As a result, understanding, prediction, and control of internal stress accumulation can contribute to improved CS deposit performance.

A common presumption is that CS deposits have compressive residual stresses. There have been experimental (Ghelichi et al. 2014a, b; Ghelichi et al. 2012; Ziemian et al. 2014; Venkatesh et al. 2011; Schmidt et al. 2006; Lee et al. 2013; Spencer et al. 2012; Luzin et al. 2011) and numerical (Grujicic et al. 2003; Soer et al. 2005; Yandouzi et al. 2008; Jen et al. 2005) studies of residual stress, which confirm this view. Examples of measured residual stress profiles for different combinations of CS deposits and substrates are shown in Fig. 5.29. The plots show that the sign, magnitude, and profile of residual stresses in CS deposits depend on various CS parameters, especially on the hardness of the depositing powder and substrate material. Residual stress relaxation at the interface between the substrate and the deposited material can also be observed in some cases. The residual stress is also greater when the depositing material and the substrate have dissimilar hardness (Fig. 5.29e).

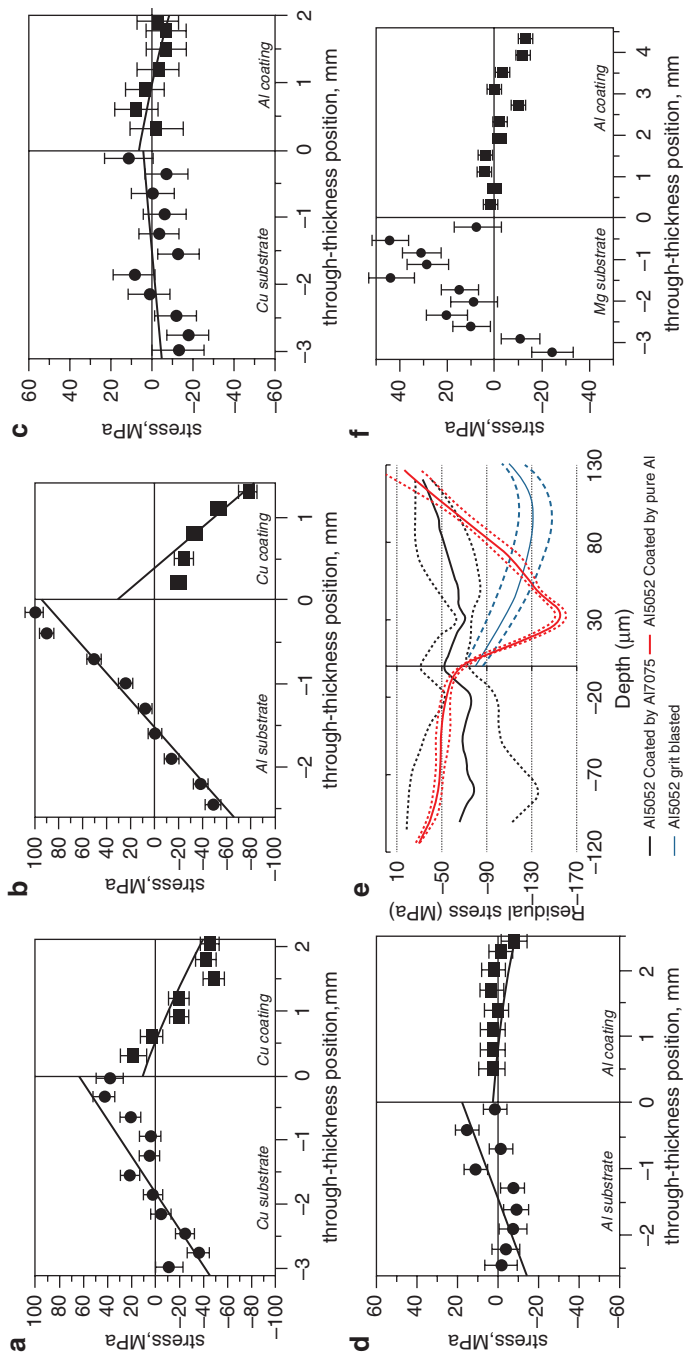

Fig. 5.29 Measurement of residual stress distributions through thickness for (**a**) Cu/Cu, (**b**) Cu/Al, (**c**) Al/Cu, (**d**) Al/Al (Luzin et al. 2011), (**e**) 5052/7075Al and 5052/Al (Ghelichi et al. 2014a, b), and (**f**) Mg/Al (Spencer et al. 2012)

Note that after spraying, the substrate–deposit system is normally cooled to room temperature, so that a thermal misfit strain may arise. Thus, the residual stress can be influenced by the heat input, spraying kinematics, and the associated thermal history. Based on these factors, in addition to substrate and deposit material properties and dimensions, the mean residual stress in the deposit can be compressive or tensile (Lee et al. 2013; Spencer et al. 2012; Luzin et al. 2011).

5.3.3.5 Fatigue Properties

Fatigue strength of CS materials is a major concern, since CS repair parts and components are often used in applications involving cyclic loads. Reports about the influence of CS on fatigue strength are scarce. Furthermore, testing procedures vary widely, and the interpretation of results is generally complex. Not surprisingly, fatigue results are sometimes contradictory. Thus, we choose to report only results from the most thorough studies here.

Multiple factors affect fatigue strength of metallic CS deposits. Both spraying parameters and material properties strongly affect the residual stress in CS materials and, thereby, the fatigue strength (Ghelichi et al. 2012; Sansoucy et al. 2007; Price et al. 2006; Ghelichi et al. 2014a, b). Ghelichi et al. (2012) reported greater fatigue endurance in Al5052 coated with Al7075 compared to specimens deposited with pure Al, as shown in Fig. 5.30a. They concluded that the fatigue strength of the treated specimens followed the fatigue endurance of the stronger of the two materials, i.e., the grit-blasted substrate in the case of pure Al on Al5052 and the deposited material in the case of Al7075 on Al5052.

In the same study, the residual stresses induced by the deposit on the substrate played a minor role in fatigue endurance increase compared to the contribution of the type of the deposited material and coating parameters. However, Sansoucy et al. (2007) studied the fatigue strength of Al–Co–Ce deposits (Fig. 5.30b) and attributed the superior fatigue life of the deposits to the inhibition of crack propagation in the deposit by the residual compressive stresses in the deposit. The presence of compressive residual stress, which is generally generated in CS deposits during deposition, can have beneficial effects in retarding crack propagation under fatigue loading (Binder et al. 2011).

Surface preparation greatly influences the fatigue properties of CS deposits. The standard surface preparation for the CS process involves shot peening or grit blasting, both intended to impart near-surface compressive stresses and increase the surface roughness of the substrate. Ziemian et al. (2014) investigated the effect of surface preparation for Al2024-T351 substrates before depositing pure Al. As shown in Fig. 5.31a, their results indicated that the fatigue strength increased up to 50% with CS Al deposits. They attributed this increase to the work hardening induced by grit blasting and particle impacts. Ghelichi et al. (2012) confirmed this rationale for increased fatigue resistance of 5052 substrates deposited with CS Al7075 deposits (Fig. 5.31b). In their study, the fatigue strength of the coated series increased 13% and 20% with respect to grit-blasted samples. As shown in Fig. 5.31b, they also investigated the effect of powder state, i.e., microcrystalline vs. cryomilled NC, by

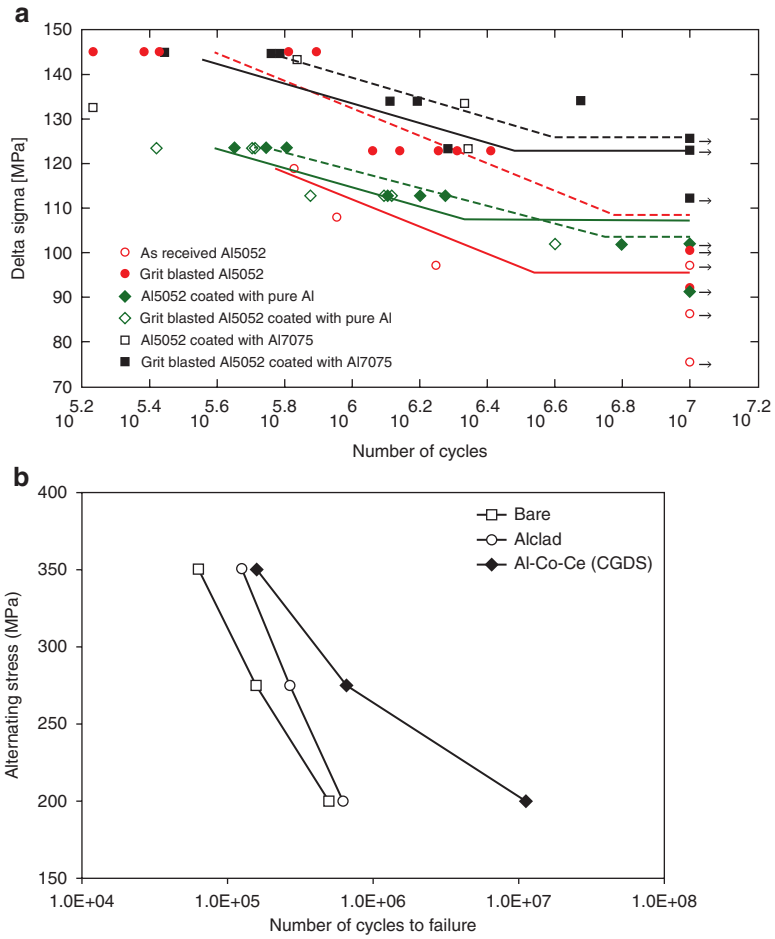

Fig. 5.30 Mean number of cycles prior to failure for (**a**) the bare, Alclad, and CGDS Al–Co–Ce deposits on 2024-T3 (Ghelichi et al. 2012) and (**b**) pure Al and Al7075 deposits on Al 5052 (Sansoucy et al. 2007)

depositing cryomilled NC Al7075 onto Al5052 substrates. They highlighted that using cryomilled NC powder slightly increased the fatigue life with respect to the materials deposited using microcrystalline powders.

5.3.3.6 Corrosion

Published results have demonstrated the potential of the CS process as a technique for refurbishment of various parts and components, especially for corrosion protection applications. This is mainly because CS-deposited materials are highly consolidated (high density) and impermeable (without interconnected porosity) structures. These features are of great importance for obtaining high corrosion resistance with a CS deposit (Bala et al. 2014; Koivuluoto and Vuoristo 2014).

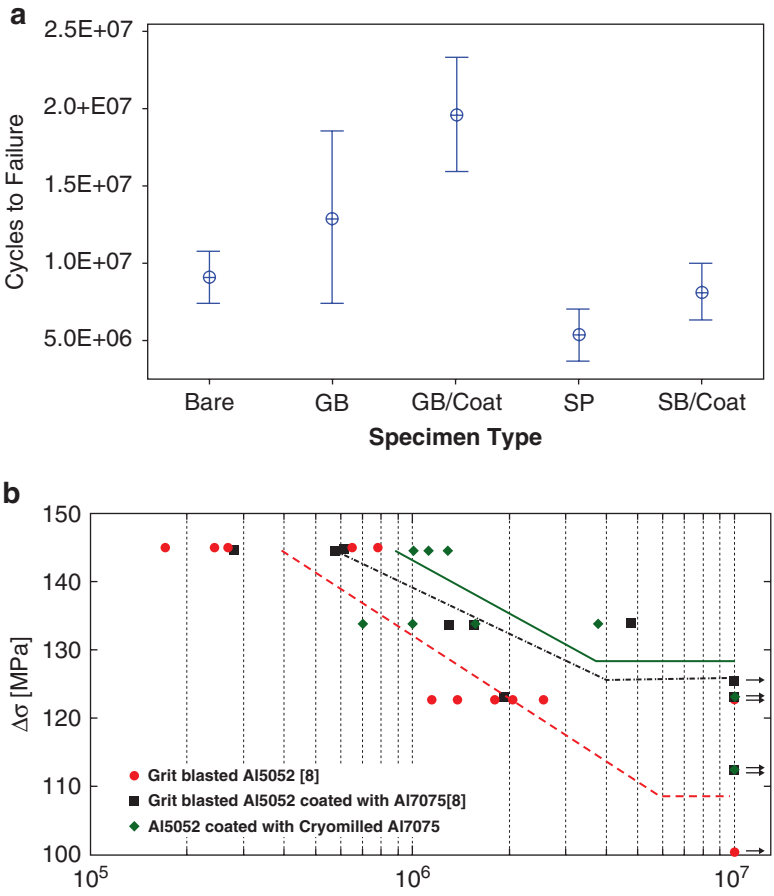

Fig. 5.31 Fatigue life results showing the effect of surface preparation on fatigue life of (**a**) CP-Al/2024-T351 (Ziemian et al. 2014) and (**b**) Al7075/Al5052 deposits (Ghelichi et al. 2012)

CS of materials with potentially high corrosion resistance or anodic protection, such as Zn, Al, Ni, Ta, Ti, SS, Al + Al_2O_3, Al-Mg, and brass, has been examined for various applications including biomedical, medical, marine environments, and hot and high-pressure environments. In all these applications, the CS material acted as either (1) anodic layer with sacrificial behavior for the substrate (Champagne 2007; AL-Mangour et al. 2013; Van Steenkiste et al. 2002; Bala et al. 2014; Koivuluoto and Vuoristo 2014; Balani et al. 2005; Maev and Maeva 2006; Djordjevic and Maev 2006; Karthikeyan et al. 2004; Blose et al. 2005; Xiong et al. 2009; Villafuerte et al. 2009; Kroemmer and Heinrich 2006; Dzhurinskiy et al. 2012; Ma et al. 2014), (2) passive oxide layer (Lahiri et al. 2013; Kumar et al. 2016b; Bu et al. 2012; Spencer et al. 2009), or (3) a dense cathodic or corrosion-resistant protective layer (AL-Mangour et al. 2013; Koivuluoto and Vuoristo 2010; Koivuluoto et al. 2010a; Marx et al. 2005; Hoell and Richter 2008; Bala et al. 2010).

Blose et al. (2005) reported the corrosion protection of steel substrates with CS Zn, Al, and Zn–Al coatings against wet corrosion. Karthikeyan et al. (2004) showed that corrosion resistance of the CS Al deposits was greater than that of Al bulk material. Figure 5.32 shows polarization behavior of CS Al coating and Al bulk material. Passivation of the coatings is first linear and then curving slightly followed by linear behavior again. This indicates repassivation of the coatings (Balani et al. 2005).

HPCS deposits have yielded enhanced corrosion resistance for a variety of materials, such as Cu (Koivuluoto et al. 2010a; Koivuluoto et al. 2012), Cu alumina (Koivuluoto et al. 2010a), Ta (Koivuluoto et al. 2010b; Hassani-Gangaraj et al. 2015), Ti (Wang et al. 2008), Ti + HAP (Zhou and Mohanty 2012), Ni–Cu (Koivuluoto and Vuoristo 2010), Ni–Cr (Bala et al. 2010), SS and SS mixed with Co–Cr (AL-Mangour et al. 2013), and WC–Co (Dosta et al. 2013). Figure 5.33a shows overall dense coating structures of the HPCS Cu and Ta coatings, having superior or a similar open-cell potential behavior with corresponding bulk materials. Ta bulk material and dense HPCS Ta coatings are passivated rapidly, and, above their passivation potential, the corrosion rate falls to a very low value in the passive area due to the stable passive layer formation (Hassani-Gangaraj et al. 2015). Figure 5.33b shows similar anodic corrosion behavior of Ta bulk and cold-sprayed Ta coatings on different substrates (CSTa1 on Al, CSTa2 on Cu, and CSTa3 on steel).

In another study, Al-Mangour et al. (2013) investigated the corrosion properties of mixed SS 316 L particles with particles made of Co–Cr alloy L605 (the latter is known to display superior corrosion resistance to that of 316 L but also is difficult to process). This study reported that CS can be used to consolidate these metals as a blend (67% 316 L – 33% 605 L), and following post-CS heat treatment (HT), both the corrosion and mechanical properties of the resulting composite were superior to 316 L alone. According to Fig. 5.34, composite coatings had lower corrosion rates

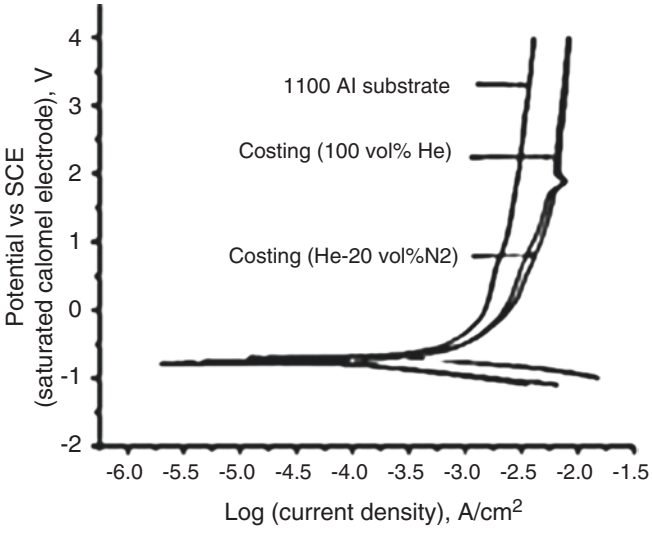

Fig. 5.32 Polarization behavior of CS 1100 Al coatings and 1100 Al bulk material (Balani et al. 2005)

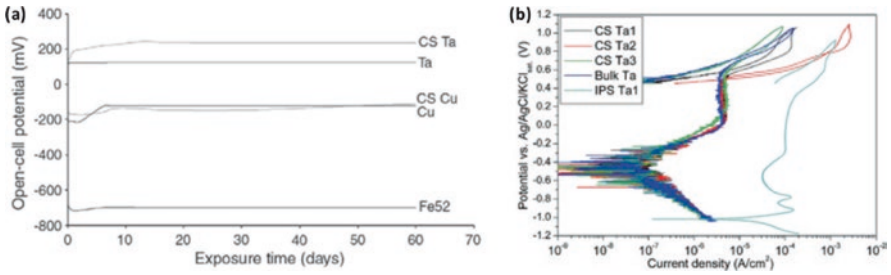

Fig. 5.33 (**a**) Open-cell potentials of HPCS Ta and Cu coatings and Fe52 substrate as a function of exposure time in 3.5%NaCl solution (Koivuluoto et al. 2010a), (**b**) polarization behavior of CS Ta coatings (CSTa1 on Al, CSTa2 on Cu, and CSTa3 on steel) and Ta bulk material in 1 M KOH (Hassani-Gangaraj et al. 2015)

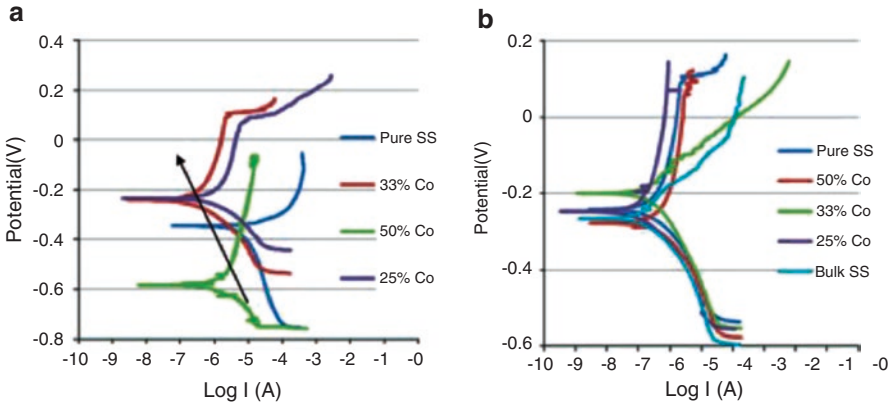

Fig. 5.34 Polarization behavior of CS SS + CoCr coatings in (**a**) as-deposited and (**b**) annealed (1100 °C) coatings (Al-Mangour et al. 2013)

compared to pure stainless steel. Similar results were presented by Chavan et al. (2013) for heat-treated Zn coatings that had reduced corrosion current density, indicating its greater corrosion protection. The main reasons for these improvements are related to the microstructural alteration of the deposit that occurred during an annealing HT, as discussed in Sect. 5.2.3.

5.3.4 Effect of Post-CS Heat Treatments on Mechanical Properties

The effects of heat treatment (HT) on the mechanical properties of cold-worked material have fully been documented (Semiatin 2005), and CS deposits are expected to behave similarly. Generally, residual stresses start to decrease during recovery and are completely relaxed during recrystallization. Furthermore, the largest

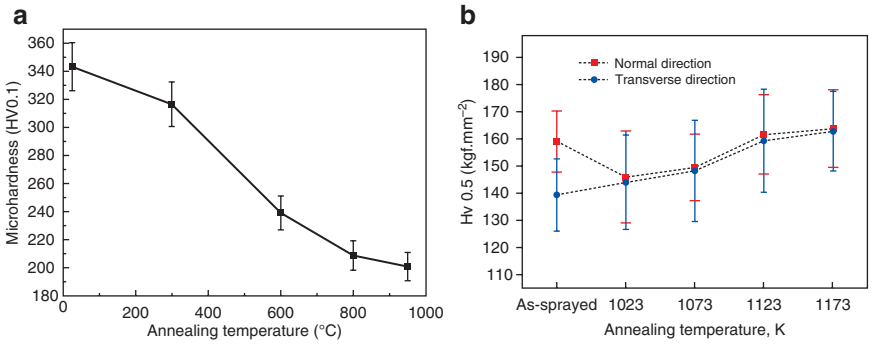

Fig. 5.35 Microhardness variation as a function of heat treatment temperature for (**a**) stainless steel 304 (Meng et al. 2011) and (**b**) Ti deposits (Li et al. 2014)

differences between properties occur after recrystallization. Hardness and strength decrease, while ductility increases. New grains are generated by recrystallization, and the new grains continue to grow if left at elevated temperatures. Hardness and strength are relatively stable in the grain growth regime, while ductility continues to increase (Semiatin 2005). The effects of post-CS HTs on mechanical properties of CS-deposited materials are reviewed in this section.

5.3.4.1 Post-HT Hardness

Post-CS annealing can significantly affect the hardness of CS deposits (Semiatin 2005; Meng et al. 2011). Hardness behavior as a function of annealing temperature is shown in Fig. 5.35. The microhardness of the as-deposited and annealed 304 SS coatings is shown in Fig. 5.35a (Meng et al. 2011). Annealing leads to a decrease in the microhardness of the deposit. The minimum microhardness of the annealed deposit was obtained at 950 °C (~201 HV), a value comparable to that of an annealed bulk 304 SS. The softening is caused by dislocation annihilation, relaxation of peening stress and cold working, and grain growth. Similar trends have been reported for other CS deposits (Champagne 2007; Schmidt et al. 2009; AL-Mangour et al. 2014; Li et al. 2006b; Chavan et al. 2011; Lee et al. 2006).

However, in some cases, the hardness of deposited materials increases with annealing temperature (Goldbaum et al. 2011a; Huang and Fukanuma 2012; Li et al. 2014). Li et al. (2014) measured microhardness values of CS Ti deposits and reported that average values of microhardness gradually increased as the annealing temperature increased from 1023 °K to 1123 °K (Fig. 5.35b). The average hardness remained roughly constant when the annealing temperature was increased to 1173 °K. This behavior was attributed to further consolidation and densification of the deposits during post-CS heat treatments (such as annealing) leading to closure of pores, inter-splat boundaries, and cracks in the microstructure (Zahiri et al. 2009a), especially when nitrogen is used as the carrier gas (Gärtner et al. 2006a, b).

5.3.4.2 Post-HT Bond Strength

To attain greater bond strength and promote coating performance, CS deposits can be heat-treated. Stoltenhoff et al. (2006) studied the effect of annealing of CS Cu deposits on different substrate materials, i.e., Cu/Al, Cu/Cu, and Cu/low-carbon steel. As shown in Fig. 5.36, post-CS HTs strongly influenced the adhesion strength of Cu deposits on different substrate materials. This figure also shows that the increase in bond strength correlates with the annealing temperature. In the case of Al/Cu case, post-CS annealing (1 h at 400 °C) increased the bond strengths from ~40 to ~60 MPa. The adhesion of CS deposits on low-carbon steel substrates did not exceed 10 MPa in the as-deposited state, which is similar to the values achieved by arc or flame spraying, but less than those obtained by HVOF spraying (25–30 MPa). Note that the almost linear increase in adhesion with annealing temperature, which is observed for "soft" substrate materials (e.g., Al or Cu), cannot be confirmed for deposits sprayed onto steel substrates. Hussain et al. (2012) also investigated the adhesive strength of Cu deposits on Al substrates and reported an increase in the bond strength after heat treatment at 400 °C (from 57 to 69 MPa).

However, in some cases, the opposite trend has been observed, i.e., a decrease in bond strength with increasing annealing temperature. As shown in Fig. 5.37a, Al deposits on Mg substrates (black line) show a decrease in bond strength after annealing, and the interfacial bond becomes weaker with increasing annealing time. This finding was attributed to the formation of Al_xMg_y intermetallic at the interface (Wang et al. 2012). According to Fig. 5.37b, the thickness of intermetallic compounds increased with holding time at the anneal temperature (Bu et al. 2011). Because of the brittleness of such IMs, they adversely affect the deposit bond strength.

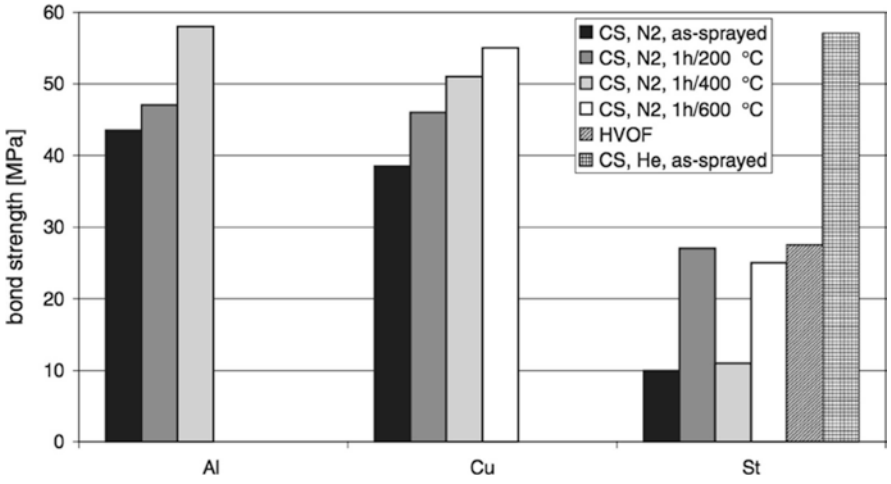

Fig. 5.36 Bond strength of CS Cu deposits on various substrate materials (*Al* aluminum, *Cu* copper, *St* low-carbon steel), as-deposited and annealed states (Stoltenhoff et al. 2006)

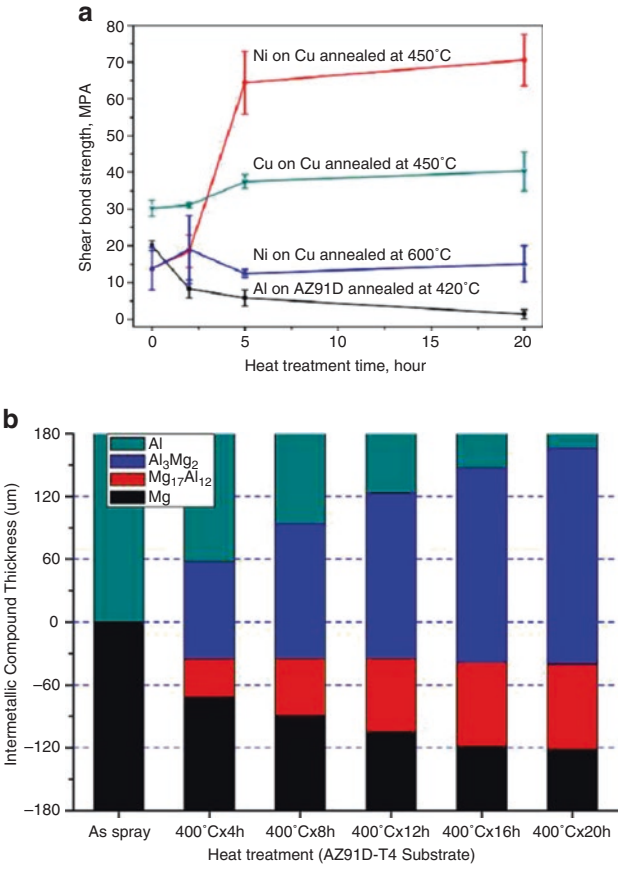

Fig. 5.37 (**a**) Variation of the shear bond strength of different deposit/substrate systems before and after spray annealing treatment (Wang et al. 2012) and (**b**) thickness measurement of the intermetallic layers vs. holding time of the heat treatment at 400 °C under vacuum (Bu et al. 2011)

5.3.4.3 Post-HT Tensile Strength and Ductility

One of the biggest mechanical challenges for CS arises from the reduction or loss of ductility in the deposit because of the high degree of cold work caused by the plastic deformation of the impacting particle. However, ductility can generally be improved with post-CS annealing while also improving the CS deposit strength, as shown in Fig. 5.38 (Rokni et al. 2015a). For example, Ogawa et al. (2008) showed that post-CS annealing of CS Al specimens at temperatures as low as 270 °C restored ductility compared to untreated specimens. Under tensile loading, the strength and ductility of the heat-treated specimens were 2× and 5× greater than that of the untreated specimens, respectively. Similar behavior was reported for CS 7075Al deposits (Rokni et al. 2017a). As shown in Fig. 5.38, the as-deposited (AD) 7075 material shows the lowest UTS and ductility among all the conditions, again as a

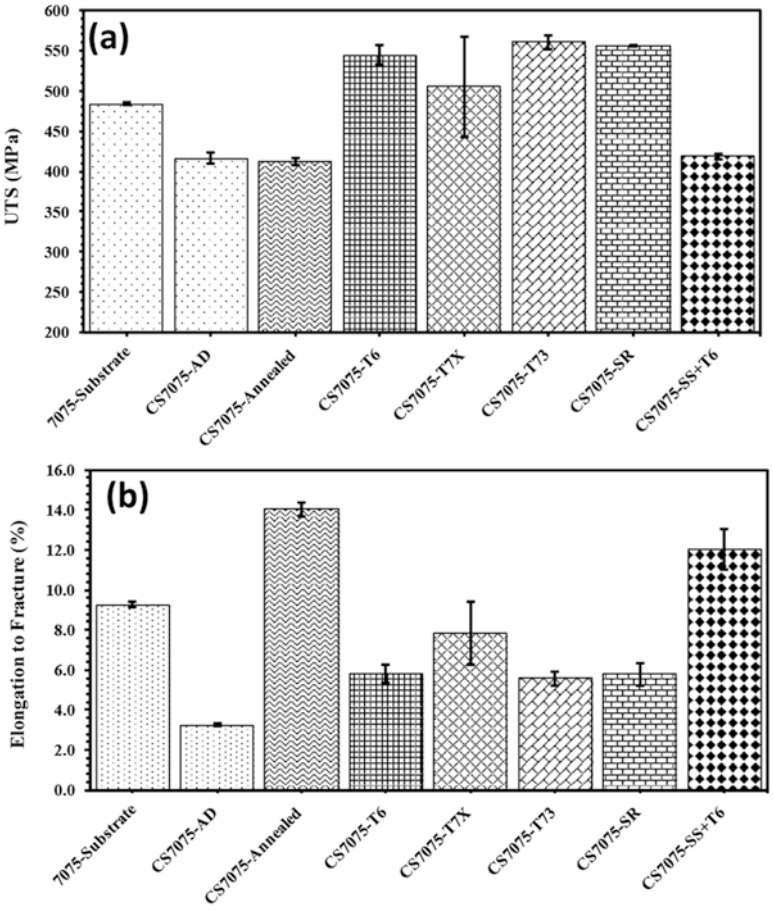

Fig. 5.38 Ultimate strength and the elongation of as-deposited and annealed coatings at different temperatures (Rokni et al. 2017a)

consequence of the extensive cold work introduced into the microstructure during CS. The cold work in the AD material can be seen in the dislocation structures in the microstructure of particle interiors and the UFG structures at the PPBs, shown in Figs. 5.6 and 5.10.

The mechanical properties of the CS 7075Al deposit increase after all of the post-CS HTs (Rokni et al. 2017a). Figure 5.38 shows that low-temperature HTs (T6, T7X, T73, and stress relieve (SR)) increase the UTS and ductility of the CS 7075 Al deposit. The increase in the UTS in these conditions occurs because of precipitation of IM phases, particularly as ή and η. The precipitates impede dislocation movement and thereby increase strength. In all of the low-temperature HT conditions, the hardening effect of aging dominates the softening effects of recovery, and, as a result, samples heat-treated at low temperature are stronger and more ductile. Similar results have been reported for aging of 7075 Al after SPD processing (Kim et al. 2008).

Heat treatments at higher temperatures (annealing and solute solutionizing (SS) + T6) also improved strength and ductility, as shown in Fig. 5.38. Similar approaches have been employed to increase the ductility of CS deposits by annealing (Li et al. 2006b; Li et al. 2009; Sharma et al. 2015; Rokni et al. 2015a; Huang et al. 2015). In most cases, however, annealing led to a decrease in strength due to grain coarsening and relaxation of internal stresses. In contrast, annealing of the CS deposits led to increases in both UTS values and ductility, which increased from ~3.2% in the AD condition to ~14% and 10% in annealed and SS + T6 conditions, respectively.

Mechanical property enhancement occurs because of three main reasons. First, annealing induces diffusion through the particle interface and promotes metallurgical bonding (Rokni et al. 2015a; Rokni et al. 2017a, b; Huang et al. 2015). Second, annealing above optimal temperatures leads to grain growth, increasing the interfaces between particles and resulting in the reduction of voids and unjoint interfaces (Champagne 2007; Schmidt et al. 2006). Third, in CS materials, the stored energy from plastic deformation can drive recrystallization and consolidation when the material is heated (Hall et al. 2006; Rokni et al. 2014a; Semiatin 2005). In certain cases, strength can also occur due to the precipitation of strengthening phases, which can be small in size and with a uniform distribution due to their finer distribution from powder particle grains.

If CS deposits are fully consolidated before post-processing, post-CS annealing decreases the flow stress and increases ductility (Calla et al. 2006; Li et al. 2006b; Li et al. 2009). This behavior has been rationalized by considering the microstructural recovery of the hardened as-deposited splats, diverting plastic strain from the interfaces during indentation, as well as grain growth. Choi et al. (Choi et al. 2007) supported this hypothesis by producing CS Al specimens and subsequently annealing them at 300 °C for 22 h in argon or laboratory air. They found that annealing softened CS Al enough to promote ductile behavior, but the flow stresses decreased in the CS deposits compared to the bulk material. Similar behavior can be observed at 1100 °C in Fig. 5.39a and all temperatures in Fig. 5.39b.

Nevertheless, CS deposits processed with N_2 show brittle failure under relatively low tensile stress, even after thermal annealing. Only the closure of PBBs which were just under compressive contact was observed, and the highest elongation obtained was ~8% (Gärtner et al. 2006a, b; Champagne 2007; Schmidt et al. 2009).

CS of Ni-based superalloys (i.e., Inconel 718) has been challenging because of its high strength and the occurrence of nozzle clogging. One way this problem has been addressed is by using HPCS and a nonclogging nozzle material combined with a nozzle water cooling system for the nozzle, enabling practitioners to deposit Inconel 718 (Levasseur et al. 2012; Wong et al. 2013a) and study the mechanical properties of as-deposited and heat-treated coatings. The difficulty in achieving metallurgical bonding in CS Inconel 718 stems from insufficient deformation and has motivated investigations of post-CS sintering as a means of enhancing mechanical properties. Levasseur et al. (2012) confirmed that upon sintering and conventional aging, the flexural strength of CS Inconel 718 deposits increased from 187 to 1651 MPa and ductility increased from 0.026 to 0.183, as shown in Table 5.4.

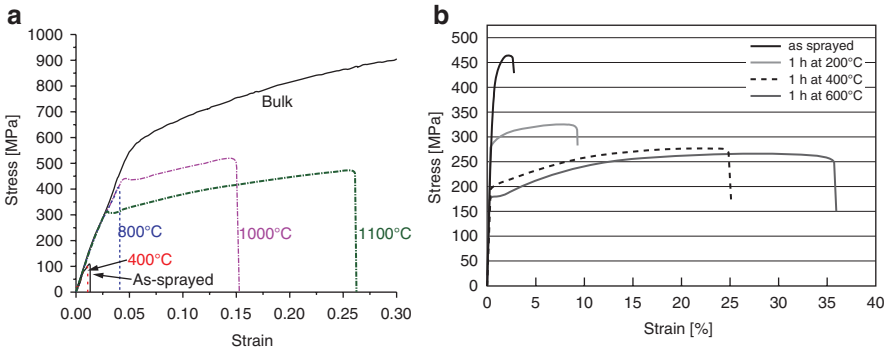

Fig. 5.39 Different UTS and elongation of CS and annealed deposits at different temperatures 316 L (AL-Mangour et al. 2014) and Cu (Gärtner et al. 2006a, b)

Table 5.4 Flexural strength and strain results for the sintered CS samples (Levasseur et al. 2012)

	Flexural strength (MPa)	Flexural strain
As deposited	187 ± 41	0.026 ± 0.022
Sintered 1250 – 60 min	1225 ± 122	0.183 ± 0.037
Sintered 1250 – 180 min	1512 ± 207	0.161 ± 0.025
Sintered 1250 – 60 min + aged	1475 ± 130	0.160 ± 0.046
Sintered 1250 – 180 min + aged	1651 ± 658	0.159 ± 0.045

5.3.4.4 Post-HT Conductivity

In the CS process, the depositing particles do not melt, and thus the deposits absorb little or no oxygen compared to the starting powder O_2 content, which stands in stark contrast to conventional thermal spray deposits. These features enable the production of high conductivity of Cu deposits with low porosity, low oxide content, and low thermal stresses (Champagne 2007; Wong et al. 2013b; Phani et al. 2007a, b). The deposit undergoes SPD and subsequent phenomena, such as dynamic recrystallization and partial chemical reaction (Assadi et al. 2003; Rokni et al. 2014d, 2015b; Schmidt et al. 2009). Thus, in combination with low oxygen content, the thermal conductivity is mainly affected by the high dislocation density and the low mean free path of electrons. Figure 5.40 shows how these features increase the conductivity of CS Cu deposits compared with other thermal spray processes. This figure also shows that post-CS annealing increases electrical conductivity of Cu deposits, and the greater the annealing temperature, the greater the electrical conductivity.

According to the International Annealed Copper Standard (IACS), the conductivity of oxygen-free bulk Cu at room temperature (RT = 20 °C) is $\gamma = 57.14$ m/(Ω cm), which corresponds to a resistivity of $q = 1.7$ Ω V cm (Stoltenhoff et al. 2006). As shown in Fig. 40, CS Cu deposits using nitrogen process gas exhibited 63% of the bulk conductivity. However, HVOF and arc-sprayed coatings reached only 39 and 19% of the bulk conductivity, respectively. The highest reported conductivity (Coddet et al. (2014)), which was 97% of bulk Cu conductivity, was achieved for pure Cu deposits.

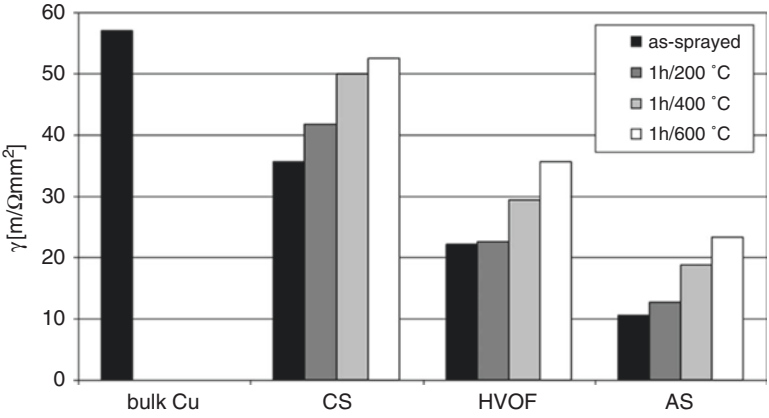

Fig. 5.40 Conductivity of Cu coatings processed by CS, HVOF spraying, and arc spraying in the as-sprayed state and after different annealing conditions. Annealed bulk Cu serves as reference material (Stoltenhoff et al. 2006)

The effects of post-CS annealing on thermal and electrical conductivities of CS alloys and composites are reported to be strictly related to microstructural changes in CS deposits. During annealing, recovery and recrystallization mechanisms reduce defects such as porosity, dislocations, interstitials, vacancies, loosely bonded splat interfaces, and GBs, all of which reduce thermal and electrical conductivities by scattering electrons or photons (Champagne 2007; Schmidt et al. 2006; Sharma et al. 2015; Semiatin 2005). Post-CS HTs also promote bonding between deposited particles, which enhances the coating quality and, consequently, increases the conductivity of CS deposits (Seo et al. 2012; Koivuluoto et al. 2012).

The microstructural anisotropy in CS deposits can also influence electrical resistivity, as demonstrated by Li et al. (2006a, b). However, extensive recrystallization during annealing process, especially at PPBs, leads to equiaxed grain structures in CS deposits. This phenomenon improves the bonding between PPBs and increases electrical conductivity in both directions (see Fig. 5.41). This relationship also provides a method to use conductivity to correlate with increased mechanical properties as a nondestructive inspection method, since the same factors which also improve conductivity are generally good for mechanical properties as well.

However, post-CS annealing above the optimal temperature is not recommended. Soe et al. (2012) studied the effect of post-CS annealing on the thermal conductivity of Cu deposits and concluded that there is an optimal temperature up to which thermal conductivity increases with annealing temperature. Above this temperature, however, voids rearrange and concentrate along GBs, which can degrade mechanical and physical characteristics of the CS deposits.

The annealing environment can affect the extent to which the conductivity of CS deposits can be enhanced (Phani et al. 2007a). Figure 5.4 indicates that annealing Cu deposits in vacuum at 300 ˚C is sufficient to obtain conductivity values similar to that of bulk Cu. On the other hand, even a 4 h anneal at 450 ˚C in air did not yield the required conductivity.

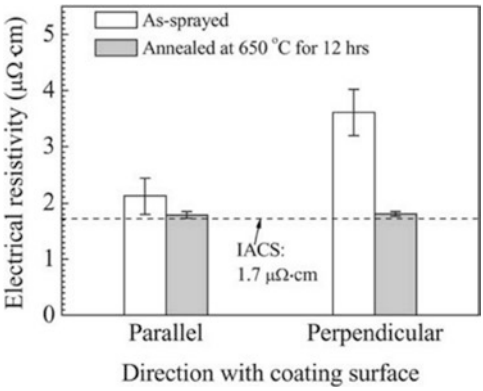

Fig. 5.41 Effect of annealing on the electrical resistivity of Cu coating in the parallel and perpendicular directions (Li et al. 2006b)

5.4 Summary and Conclusions

Cold spray microstructural phenomena are now generally understood to be the result of a complex thermomechanical process, which depends highly on the starting powder microstructure, as well as the particle size, impact velocity, and even temperature. Those incorporated particles are also often inhomogeneous due to both nonequilibrium processing conditions and microstructural differences that can be related to particle size, particularly in gas-atomized powders with different cooling rates resulting from different particle sizes and locations in the powder formation plume. Just as important as the starting powder microstructure are the variations in consolidation microstructure that result from unjoined interfaces at particle–particle interfaces and entrapped porosity from incomplete deformation of a given particle. There is also a much greater understanding of the degree of recrystallization that occurs upon impact of particles at the high-strain interfaces, which is responsible for the formation of metallurgical bonds in addition to mechanical interlocking. Phase transformations and chemical reactions rarely occur during CS because the particles are not heated directly by a thermal source for any significant length of time (<100 ms). Additionally, due to the high degree of dislocations that are imparted to the microstructure, there is also the opportunity to experience additional recrystallization and further increases in both mechanical strength and ductility upon post-CS heating of the coating, even at relatively low temperatures. If the post-CS HT is optimal, the deposit quality can be enhanced, particularly the bond strength, by increasing bonding area between deposited particles and reducing porosity in the microstructure. For the same reasons, the conductivity of CS deposits can match or match the conductivity of bulk materials. The compressive residual stress in CS deposits increases fatigue resistance. Thus, the annealing temperatures should be kept as low as possible to avoid redistribution of residual stress or even part distortion. Low-temperature anneals also help preserve the fine microstructure and superior coating hardness and their related benefits in the as-deposited materials. These low-temperature treatments are also particularly attractive from an industrial perspective for improving properties without a significant reduction of base material

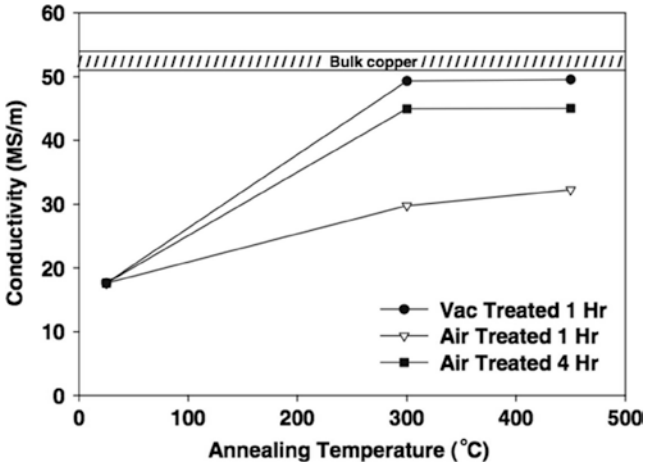

Fig. 5.42 Effect of annealing environment and temperature on the conductivity of CS Cu deposits (Phani et al. 2007a)

properties or distortion. Thus, based on this understanding of CS microstructures, processes under consideration for development should consider opportunities to improve deposit properties by preprocessing feedstock powder or performing post-CS HTs.

Acknowledgments The authors also gratefully acknowledge the helpful comments and suggestions of the reviewers, which have improved the presentation.

References

Ajdelsztajn L, Jodoin B, Kim GE, Schoenung JM (2005) Cold spray deposition of nanocrystalline aluminum alloys. Metal Mater Trans A 6:657–666

Ajdelsztajn L, Jodoin B, Richer P, Sansoucy E, Lavernia EJ (2006a) Cold gas dynamic spraying of a high temperature Al alloy. J Therm Spray Technol 15:495–500

Ajdelsztajn L, Jodoin B, Schoenung JM (2006b) Synthesis and mechanical properties of nanocrystalline Ni coatings produced by cold gas dynamic spraying. Surf Coat Technol 201:1166–1172

Ajdelsztajn L, Zuniga A, Jodoin B, Lavernia EJ (2006c) Cold gas dynamic spraying of a high temperature Al alloy. Surf Coat Technol 201:2109–2116

Alkhimov PA, Kosarev VF, Nesterovich NI, Shushpanov MM (1994) US Patent 5, 302:414

AL-Mangour B, Mongrain R, Irissou E, Yue S (2013) Improving the strength and corrosion resistance of 316L stainless steel for biomedical applications using cold spray. Surf Coat Technol 216:297–307

AL-Mangour B, Vo P, Mongrain R, Irissou E, Yue S (2014) Effect of heat treatment on the microstructure and mechanical properties of stainless steel 316L coatings produced by cold spray for biomedical applications. J Therm Spray Technol 23:641–652

Annavarapu S, Doherty RD (1993) Evolution of microstructure in spray casting. Int J Powder Met 29:331–343

Assadi H, Gärtner F, Stoltenhoff T, Kreye H (2003) Bonding mechanism in cold gas spraying. Acta Mater 51:4379–4394

Bae G, Kumar S, Yoon S, Kang K, Na H, Kim HJ, Lee C (2009) Bonding features and associated mechanisms in kinetic sprayed titanium coatings. Acta Mater 57:5654–5666

Bae G, Kang K, Na H, Kim JJ, Lee C (2010a) Effect of particle size on the microstructure and properties of kinetic sprayed nickel coatings. Surf Coat Technol 204:3326–3335

Bae G, Kang K, Kim JJ, Lee C (2010b) Nanostructure formation and its effects on the mechanical properties of kinetic sprayed titanium coating. Mater Sci Eng A 527:6313–6319

Bala N, Singh H, Murray S (2010) Accelerated hot corrosion studies of cold spray Ni–50Cr coating on boiler steels. Mater Des 31:244–253

Bala N, Singh H, Karthikeyan J, Prakash S (2014) Cold spray coating process for corrosion protection: a review. Surf Eng 30:414–421

Balani K, Laha T, Agarwal A, Karthikeyan J, Munroe N (2005) Effect of carrier gases on microstructural and electrochemical behavior of cold-sprayed 1100 aluminum coating. Surf Coat Technol 195:272–279

Bandar AM, Vo P, Mongrain R, Irissou E, Yue S (2014) Effect of heat treatment on the microstructure and mechanical properties of stainless steel 316L coatings produced by cold spray for biomedical applications. J Therm Spray Technol 23:641–652

Berbon PB, Bingel WH, Mishra RS, Bampton CC, Mahoney MW (2001) Friction stir processing: a tool to homogenize nanocomposite aluminum alloys. Scr Mater 44:61–66

Berube G, Yandouzi M, Zuniga A, Ajdelsztajn L, Villafuerte J, Jodoin B (2012) Phase stability of al-5Fe-V-Si coatings produced by cold gas dynamic spray process using rapidly solidified feedstock materials. J Therm Spray Technol 21:240–254

Binder K, Gottschalk J, Kollenda M, Gartner F, Klassen T (2011) Influence of impact angle and gas temperature on mechanical properties of titanium cold spray deposits. J Therm Spray Technol 20:234–242

Blose R, Vasquez D, Kratochvil W (2005) Metal passivation to resist corrosion using the cold spray process. Thermal spray 2005: explore its surfacing potential. ASM International, Basel

Blum W, Zhu Q, Merkel R, McQueen HJ (1996) Geometric dynamic recrystallization in hot torsion of al-5Mg-0.6Mn (AA5083). Mater Sci Eng A 205:23–30

Borchers C, Gärtner F, Stoltenhoff T, Assadi H, Kreye H (2003) Microstructural and macroscopic properties of cold sprayed copper coatings. J Appl Phys 93:10064–10070

Borchers C, Gärtner F, Stoltenhoff T, Kreye H (2005) Formation of persistent dislocation loops by ultra-high strain-rate deformation during cold spraying. Acta Mater 53:2991–3000

Bu H, Yandouzi M, Lu C, Jodoin B (2011) Effect of heat treatment on the intermetallic layer of cold sprayed aluminum coatings on magnesium alloy. Surf Coat Technol 205:4665–4671

Bu H, Yandouzi M, Lu C, MacDonald D, Jodoin B (2012) Cold spray blended Al+$Mg_{17}Al_{12}$ coating for corrosion protection of AZ91D magnesium alloy. Surf Coat Technol 207:155–162

Calla E, McCartney DG, Shipway PH (2006) Deposition of copper by cold gas dynamic spraying: an investigation of dependence of microstructure and properties of the deposits on the spraying conditions. J Thermal Spray Technol 15:255–262

Cavaliere P, Perrone A, Silvello A (2014) Processing conditions affecting grain size and mechanical properties in nanocomposites produced via cold spray. J Therm Spray Technol 23:1089–1096

Champagne VK (ed) (2007) The CS materials deposition process. Woodhead Publishing Ltd., Cambridge, UK

Champagne VK, Helfritch DJ (2014) Mainstreaming cold spray–push for applications. Surf Eng 30:396–403

Champagne VK, Helfritch D, Leyman P, Grendahl S, Klotz B (2005) Interface material mixing formed by the deposition of copper on aluminum by means of the cold spray process. J Therm Spray Technol 14:330–334

Champagne V Jr, Kaplowitz D, Champagne VK, Howe C, West MK, McNally B, Rokni MR (2017) Dissimilar metal joining and structural repair of ZE41A-T5 cast magnesium by the cold spray (CS) process. Mater Manuf Process:1–10

Chavan NM, Ramakrishna M, Phani PS, Rao DS, Sundararajan G (2011) The influence of process parameters and heat treatment on the properties of cold sprayed silver coatings. Surf Coat Technol 205:4798–4807

Chavan NM, Kiran B, Jyothirmayi A, Phani PS, Sundararajan G (2013) The corrosion behavior of cold sprayed zinc coatings on mild steel substrate. J Therm Spray Technol 22:463–470

Choi WB, Li L, Luzin V, Neiser R, Gnaupel-Herold T, Prask HJ, Sampath S, Gouldstone A (2007) Integrated characterization of cold sprayed aluminum coatings. Acta Mater 55:857–866

Chun DM, Choi JO, Lee CS, Ahn SH (2012) Effect of stand-off distance for cold gas spraying of fine ceramic particles (<5μm) under low vacuum and room temperature using nano-particle deposition system (NPDS). Surf Coat Technol 206:2125–2132

Cinca N, Barbosa M, Dosta S, Guilemany JM (2010) Study of Ti deposition onto Al alloy by cold gas spraying. Surf Coat Technol 205:1096–1102

Coddet P, Verdy C, Coddet C, Lecoutrier F, Debray F (2014) Comparison of the properties of cold-sprayed cu-0.5 Cr-0.05 Zr alloys after various heat treatments versus forged and vacuum plasma-sprayed alloys. J Therm Spray Technol 23:486–491

Coddet P, Verdy C, Coddet C, Debray F, Lecouturier F (2015) Mechanical properties of thick 304L stainless steel deposits processed by He cold spray. Surf Coat Technol 277:74–80

Coddet P, Verdy C, Coddet C, Debray F (2016) On the mechanical and electrical properties of copper-silver and copper-silver-zirconium alloys deposits manufactured by cold spray. Mater Sci Eng A 662:72–79

Debiccari A, Haynes JD, Hobbs DA, Karthikeyan J (2011) European Patent 1942209:B1

DeForce BS, Eden TJ, Potter JK (2011) Cold spray al-5% mg coatings for the corrosion protection of magnesium alloys. J Therm Spray Technol 20:1352–1358

Djordjevic B, Maev R (2006) In: Marple B, Hyland M, Lau YC, Lima R, Voyer J (eds) SIMATTM application for aerospace corrosion protection and structural repair. ASM International, Seattle

Dosta S, Couto M, Guilemany JM (2013) Cold spray deposition of a WC-25Co cermet onto Al7075-T6 and carbon steel substrates. Acta Mater 61:643–652

Dykhuizen RC, Smith MF (1998) Gas dynamic principles of cold spray. J Therm Spray Technol 7:206–212

Dzhurinskiy D, Maeva E, Leshchinsky E, Maev R (2012) Corrosion protection of light alloys using low pressure cold spray. J Therm Spray Technol 21:304–313

Eckert J (1995) Relationships governing the grain size of Nanocrystalline metals and alloys. Nano Struct Mater 6:431–416

Fukumoto M, Mashiko M, Yamada M, Yamaguchi E (2010) Deposition behavior of copper fine particles onto flat substrate surface in cold spraying. J Therm Spray Technol 19:89–94

Gärtner F, Stoltenhoff T, Schmidt T, Kreye H (2006a) The cold spray process and its potential for industrial applications. J Therm Spray Technol 15:223–232

Gärtner F, Stoltenhoff T, Voyer J, Kreye H, Riekehr S, Kocak M (2006b) Mechanical properties of cold-sprayed and thermally sprayed copper coatings. Surf Coat Technol 200:6770–6782

Ghelichi R, MacDonald D, Bagherifard S, Jahed H, Guagliano M, Jodoin B (2012) Microstructure and fatigue behavior of cold spray coated Al5052. Acta Mater 60:6555–6561

Ghelichi R, Bagherifard S, MacDonald D, Fernandez-Pariente I, Jodoin B, Guagliano M (2014a) Experimental and numerical study of residual stress evolution in cold spray coating. Appl Surf Sci 288:26–33

Ghelichi R, Bagherifard S, MacDonald D, Brochu M, Jahed H, Jodoin B, Guagliano M (2014b) Fatigue strength of Al alloy cold sprayed with nanocrystalline powders. Int J Fatigue 65:51–57

Goldbaum D, Ajaja J, Chromik RR, Wong W, Yue S, Irissou E, Legoux JG (2011a) Mechanical behavior of Ti cold spray coatings determined by a multi-scale indentation method. Mater Sci Eng A 530:253–265

Goldbaum D, Chromik RR, Yue S, Irissou E, Legoux JG (2011b) Mechanical property mapping of cold sprayed Ti splats and coatings. J Therm Spray Technol 20:486–496

Goldbaum D, Shockley JM, Chromik RR, Rezaeian A, Yue S, Legoux JG, Irissou E (2012) The effect of deposition conditions on adhesion strength of Ti and Ti6Al4V cold spray splats. J Therm Spray Technol 21:288–303

Grujicic M, Tong C, DeRosset W, Helfritch D (2003) Flow analysis and nozzle-shape optimisation for the cold-gas dynamic-spray process. J Eng Manuf 217:1–11
Grujicic M, Zhao CL, DeRosset WS, Helfritch D (2004a) Adiabatic shear instability based mechanism for particles/substrate bonding in the cold-gas dynamic-spray process. Mater Des 25:681–688
Grujicic M, Zhao CL, Tong C, DeRosset WS, Helfritch D (2004b) Analysis of the impact velocity of powder particles in the cold-gas dynamic-spray process. Mater Sci Eng A 268:222–230
Grujicic M, Tong C, DeRosset WS, Helfritch D (2005) Flow analysis and nozzle-shape optimization for the cold-gas dynamic-spray process. Proc Inst Mech Eng B J Eng Manuf 217(11):1603–1613
Guetta S, Berger MH, Borit F, Guipont V, Jeandin M, Boustie M, Ichikawa Y, Sakaguchi K, Ogawa K (2009) Influence of particle velocity on adhesion of cold-sprayed splats. J Therm Spray Technol 8:331–342
Hall AC, Cook DJ, Neiser RA, Roemer TJ, Hirschfeld DA (2006) The effect of a simple annealing heat treatment on the mechanical properties of cold-sprayed aluminum. J Therm Spray Technol 15:233–238
Hansen N (2001) New discoveries in deformed metals. Metall Mater Trans A 32:2917–2935
Hansen N, Jensen DJ (1999) Philosophical transactions of the Royal Society of London. Series A. Mathematical Physic Eng Sci 357:1447–1469
Hansen N, Huang X, Møller MG, Godfrey A (2008) Thermal stability of aluminum cold rolled to large strain. Mater Sci 43:6254–6259
Hasegawa T, Yakou T, Kocks UF (1982) Length changes and stress effects during recovery of deformed aluminum. Acta Metall 30:235–243
Hassani-Gangaraj SM, Moridi A, Guagliano M (2015) Critical review of corrosion protection by cold spray coatings. Surf Eng 31:803–815
Hayes RW, Witkin D, Zhou F, Lavernia EJ (2004) Deformation and activation volumes of cryomilled ultrafine-grained aluminum. Acta Mater 52:4259–4271
Hoell H, Richter P (2008) KINETIKS® 4000-new perspective with cold spraying. In: Lugscheider E (ed) Thermal spray, thermal spray crossing borders. DVS, Maastricht, pp 479–480
Hu H (1963) Recovery and recrystallization of metals. Gordon, New York
Huang R, Fukanuma R (2012) Study of the influence of particle velocity on adhesive strength of cold spray deposits. J Therm Spray Technol 21:541–549
Huang R, Ma W, Fukanuma H (2014) Development of ultra-strong adhesive strength coatings using cold spray. Surf Coat Technol 258:832–841
Huang R, Sone M, Ma W, Fukanuma H (2015) The effects of heat treatment on the mechanical properties of cold-sprayed coatings. Surf Coat Technol 261:278–288
Humphreys FJ, Hatherly M (2004) Recrystallization and related annealing phenomena, 2nd edn. Pergamon Press, Oxford
Hussain T, McCartney DG, Shipway PH (2012) Bonding between aluminium and copper in cold spraying: story of asymmetry. Mater Sci Technol 28:1371–1378
Irissou E, Legoux JG, Arsenault B, Moreau C (2007) Investigation of Al-Al_2O_3 cold spray coating formation and properties. J Therm Spray Technol 16:661–668
Jen TC, Li L, Cui W, Chen Q, Zhang X (2005) Numerical investigations on cold gas dynamic spray process with nano-and microsize particles. Int J Heat Mass Transf 48:4384–4396
Jodoin B, Ajdelsztajn L, Sansoucy E, Zúñiga A, Richer P, Lavernia EJ (2006) Effect of particle size, morphology, and hardness on cold gas dynamic sprayed aluminum alloy coatings. Surf Coat Technol 201:3422–3429
Jones R, Matthews N, Rodopoulos CA (2011) On the use of supersonic particle deposition to restore the structural integrity of damaged aircraft structures. Int J Fatigue 33:1257–1267
Kairet T, Degrez M, Campana F, Janssen JP (2007) Influence of the powder size distribution on the microstructure of cold-sprayed copper coatings studied by X-ray diffraction. J Therm Spray Technol 16:610–618
Karthikeyan J (2007) The advantages and disadvantages of cold spray coating process. In: Champagne VK (ed) The cold spray materials deposition process: fundamentals and applications, 1st edn. Woodhead, Cambridge

Karthikeyan J, Laha T, Agarwal A, Munroe N (2004) Microstructural and electrochemical characterization of cold-sprayed 1100 aluminum coating. In: Thermal spray, advances in technology and application. ASM International, Osaka

Kassner ME, Barrabes SR (2005) New developments in geometric dynamic recrystallization. Mater Sci Eng A 10:152–155

Kim WJ, Kim JK, Kim HK, Park JW, Jeong YH (2008) Effect of post equal-channel-angular-pressing aging on the modified 7075 Al alloy containing Sc. J Alloys Compd 450:222–228

Kim KH, Watanabe M, Kuroda S (2009) Thermal softening effect on the deposition efficiency and microstructure of warm sprayed metallic powder. Scr Mater 60:710–713

King PC, Zahiri SH, Jahedi M (2009) Microstructural refinement within a cold-sprayed copper particle. Metall mater trans A 40:2115–2123

Ko K, Lee H, Lee JH, Lee J, Yu Y (2013) US Patent 8486496

Ko KH, Choi JO, Lee H (2014) Pretreatment effect of Cu feedstock on cold-sprayed coatings. J Mater Process Technol 214:1530–1535

Ko K, Choi JO, Lee H, Seo Y, Jung S, Yu S (2015) Cold spray induced amorphization at the interface between Fe coatings and Al substrate. Mater Lett 149:40–42

Koivuluoto H, Vuoristo P (2010) Structural analysis of cold-sprayed nickel-based metallic and metallic-ceramic coatings. J Therm Spray Technol 19:975–989

Koivuluoto H, Vuoristo P (2014) Structure and corrosion properties of cold sprayed coatings: a review. Surf Eng 30:404–441

Koivuluoto H, Lagerbom J, Vuoristo P (2007) Microstructural studies of cold sprayed copper, nickel, and nickel-30% copper coatings. J Therm Spray Technol 16:488–497

Koivuluoto H, Lagerbom J, Kylmalahti M, Vuoristo P (2008) Microstructure and mechanical properties of low-pressure cold-sprayed (LPCS) coatings. J Therm Spray Technol 17:721–727

Koivuluoto H, Bolelli G, Lusvarghi L, Casadei F, Vuoristo P (2010a) Corrosion resistance of cold-sprayed ta coatings in very aggressive conditions. Surf Coat Technol 205:1103–1107

Koivuluoto H, Honkanen M, Vuoristo P (2010b) Cold-sprayed copper and tantalum coatings-detailed FESEM and TEM analysis. Surf Coat Technol 204:2353–2361

Koivuluoto H, Coleman A, Murray K, Kearns M, Vuoristo P (2012) High pressure cold sprayed (HPCS) and low pressure cold sprayed (LPCS) coatings prepared from OFHC Cu feedstock: overview from powder characteristics to coating properties. J Therm Spray Technol 21:1065–1075

Kroemmer W, Heinrich P (2006) Cold spraying-potential and new application ideas. In: Marple B, Hyland M, Lau YC, Lima R, Voyer J (eds) Thermal spray, building on 100 years of success. ASM International, Seattle

Kruger U, Ullrich R (2011) Cold gas spraying method. US Patent 8012601 B2, 6 Sept.

Kumar S, Jyothirmayi A, Wasekar N, Joshi SV (2016a) Influence of annealing on mechanical and electrochemical properties of cold sprayed niobium coatings. Surf Coat Technol 296:124–135

Kumar S, Vidyasagar V, Jyothirmayi A, Joshi SV (2016b) Effect of heat treatment on mechanical properties and corrosion performance of cold-sprayed tantalum coatings. J Therm Spray Technol 25:745–756

Lahiri D, Gill PK, Scudino S, Zhang C, Singh V, Karthikeyan J, Munroe N, Seal S, Agarwal A (2013) Cold sprayed aluminum based glassy coating: synthesis, wear and corrosion properties. Surf Coat Technol 232:33–40

Lavernia EJ (1989) The evolution of microstructure during spray atomization and deposition. Int J Rapid Solid 5:47–85

Lee C, Kim J (2015) Microstructure of kinetic spray coatings: a review. J Therm Spray Technol 24:592–610

Lee H, Jung S, Lee S, Ko K (2006) Fabrication of cold sprayed Al-intermetallic compounds coatings by post annealing. Mater Sci Eng A 433:139–143

Lee MW, Park JJ, Kim DY, Yoon SS, Kim HY, James SC, Chandra S, Coyle T (2011) Numerical studies on the effects of stagnation pressure and temperature on supersonic flow characteristics in cold spray applications. J Therm Spray Technol 20:1085–1097

Lee M, Choi HJ, Lee JY, Choi JW (2013) The manufacturing of a disposal canister using a cold spray coating of copper. In: Proceedings of the 14th international high-level radioactive waste management conference: integrating storage transportation, and disposal, Albuquerque, pp 284–290

Levasseur D, Yue S, Brochu M (2012) Pressureless sintering of cold sprayed Inconel 718 deposit. Mater Sci Eng 556:343–350

Li CJ, Li WY (2003) Deposition characteristics of titanium coating in cold spraying. Surf Coat Technol 167:278–283

Li CJ, Li WY, Wang YY (2005) Formation of metastable phases in cold-sprayed soft metallic deposit. Surf Coat Technol 198:469–473

Li CJ, Yang GJ, Gao PH, Ma J, Wang YY, Li CX (2007) Characterization of nanostructured WC-Co deposited by cold spraying. J Therm Spray Technol 16:1011–1020

Li CJ, Li WY, Xing LK, Yang GJ, Li CX (2011) Microstructure features of cold-sprayed NiCoCrAlTaY coating and its high temperature oxidation behavior. Mater Sci Forum 686:595–602

Li WY, Guo XP, Verdy C, Dembinski L, Liao HL, Coddet C (2006a) Improvement of microstructure and property of cold-sprayed Cu–4at.% Cr–2at.% Nb alloy by heat treatment. Scr Mater 55:327–330

Li WY, Li CJ, Liao H (2006b) Effect of annealing treatment on the microstructure and properties of cold-sprayed cu coating. J Therm Spray Technol 15:206–2011

Li WY, Zhang C, Guo XP, Zhang G, Liao HL, Li CJ, Coddet C (2008) Effect of standoff distance on coating deposition characteristics in cold spraying. Mater Des 29:297–304

Li WY, Zhang C, Liao H, Coddet C (2009) Effect of heat treatment on microstructure and mechanical properties of cold sprayed Ti coatings with relatively large powder particles. J Coat Technol Res 6:401–406

Li Z, Yang X, Zhang J, Zheng B, Zhou Y, Shan A, Lavernia E (2014) Microstructure evolution and mechanical behavior of cold-sprayed, bulk nanostructured titanium. Metall Mater Trans A 45:5017–5028

Liu J, Cui H, Zhou X, Wu X, Zhang J (2012) Materials for electrochemical capacitors. Met Mater Int 18:121–128

Luo X, Li CJ (2012) Thermal stability of microstructure and hardness of cold-sprayed cBN/NiCrAl nanocomposite coating. J Therm Spray Technol 21:578–585

Luo XT, Yang GJ, Li CJ, Kondoh K (2011) High strain rate induced localized amorphization in cubic BN/NiCrAl nanocomposite through high velocity impact. Scr Mater 65:581–584

Luo XT, Li CX, Shang FL, Yang GJ, Wang YY, Li CJ (2014) High velocity impact induced microstructure evolution during deposition of cold spray coatings: a review. Surf Coat Technol 254:11–20

Lupoi R, O'Neill W (2010) Deposition of metallic coatings on polymer surfaces using cold spray. Surf Coat Technol 205:2167–2173

Luzin V, Spencer K, Zhang MX (2011) Residual stress and thermo-mechanical properties of cold spray metal coatings. Acta Mater 59:1259–1270

Ma C, Liu X, Zhou C (2014) Cold-sprayed Al coating for corrosion protection of sintered NdFeB. J Therm Spray Technol 23:456–462

Maev RG, Leshchynsky V (1998) Air gas dynamic spraying of powder mixtures: theory and application. J Therm Spray Technol 7:205–212

Maev RG, Maeva V (2006) Air gas dynamic spraying of powder mixtures: theory and application. J Therm Spray Technol 15:198–205

Marrocco T, McCartney DG, Shipway PH, Sturgeon AJ (2006) Production of titanium deposits by cold-gas dynamic spray: numerical modeling and experimental characterization. J Therm Spray Technol 15:263–272

Marx S, Paul A, Köhler A, Hüttl G (2005) Cold spraying-innovative layers for new applications. In: Lugscheider E (ed) Thermal spray, explore its surfacing potential. ASM International, Basel, pp 209–215

McQueen HJ (2002) Elevated-temperature deformation at forming rates of 10^{-2} to 102 s^{-1}. Metall Mater Trans A 33:345–362
McQueen HJ, Mecking H (1987) Hot rolling deformation and recrystallization textures in FCC metals. Z METALLKD 78:387–396
Melendez NM, McDonald AG (2013) Development of WC-based metal matrix composite coatings using low-pressure cold gas dynamic spraying. Surf Coat Technol 214:101–109
Meng X, Zhang J, Han W, Zhao J, Liang Y (2011) Influence of annealing treatment on the microstructure and mechanical performance of cold sprayed 304 stainless steel coating. Appl Surf Sci 258:700–704
Morgan R, Fox P, Pattison J, Sutcliffe C, O'Neill W (2004) Analysis of cold gas dynamically sprayed aluminium deposits. Mater Lett 58:1317–1320
Moy CK, Cairney J, Ranzi G, Jahedi M, Ringer SP (2010) Investigating the microstructure and composition of cold gas-dynamic spray (CGDS) Ti powder deposited on Al 6063 substrate. Surface and coatings technology. Surf Coat Technol 204:3739–2749
Novoselova T, Celotto S, Morgan R, Fox P, O'Neill W (2007) Formation of TiAl intermetallics by heat treatment of cold-sprayed precursor deposits. J Alloys Compd 436:69–77
Ogawa K, Ichimura K, Ichikawa Y, Ohno S, Onda N (2008) Characterization of low-pressure cold-sprayed aluminum coatings. J Therm Spray Technol 17:728–735
Ozdemir OC, Widener CA, Helfritch D, Delfanian F (2016) Estimating the effect of helium and nitrogen mixing on deposition efficiency in cold spray. J Therm Spray Technol 25:660–671
Papyrin AN, Klinkov S, Alkhimov A, Fomin V (2007) Cold spray technology. Elsevier, Amsterdam
Phani PS, Rao DS, Joshi SV, Sundararajan G (2007a) Effect of process parameters and heat treatments on properties of cold sprayed copper coatings. J Thermal Spray Technol 16:425–434
Phani PS, Vishnukanthan V, Sundararajan G (2007b) Effect of heat treatment on properties of cold sprayed nanocrystalline copper alumina coatings. Acta Mater 55:4741–4751
Price TS, Shipway PH, McCartney DG (2006) Effect of cold spray deposition of a titanium coating on fatigue behavior of a titanium alloy. J Therm Spray Technol 15:507–512
Price TS, Shipway PH, McCartney DG, Calla E, Zhang D (2007) A method for characterizing the degree of inter-particle bond formation in cold sprayed coatings. J Therm Spray Technol 16:566–570
Richer P, Zúñiga A, Yandouzi M, Jodoin B (2008) CoNiCrAlY microstructural changes induced during cold gas dynamic spraying. Surf Coat Technol 203:364–271
Rokni MR, Zarei-Hanzaki A, Roostaei AA, Abedi HR (2011) An investigation into the hot deformation characteristics of 7075 aluminum alloy. Mater Des 32:2339–2344
Rokni MR, Zarei-Hanzaki A, Abedi HR (2012) Microstructure evolution and mechanical properties of back extruded 7075 aluminum alloy at elevated temperatures. Mater Sci Eng A 532:593–600
Rokni MR, Widener CA, Ahrenkiel SP, Jasthi BK, Champagne VK (2014a) Annealing behaviour of 6061 aluminium deposited by high pressure cold spray. Surf Eng 30:361–368
Rokni MR, Widener CA, Champagne VK (2014b) Microstructural evolution of 6061 aluminum gas-atomized powder and high-pressure cold-sprayed deposition. J Therm Spray Technol Feb 23:514–524
Rokni MR, Widener CA, Champagne VK (2014c) Microstructural stability of ultrafine grained cold sprayed 6061 aluminum alloy. Appl Surf Sci 290:482–489
Rokni MR, Widener CA, Crawford GA (2014d) Microstructural evolution of 7075 Al gas atomized powder and high-pressure cold sprayed deposition. Surf Coat Technol 251:254–263
Rokni MR, Widener CA, Nardi AT, Champagne VK (2014e) Nano crystalline high energy milled 5083 Al powder deposited using cold spray. Appl Surf Sci 305:797–804
Rokni MR, Widener CA, Champagne VK, Crawford GA (2015a) Microstructure and mechanical properties of cold sprayed 7075 deposition during non-isothermal annealing. Surf Coat Technol 276:305–315
Rokni MR, Widener CA, Crawford GA, West MK (2015b) An investigation into microstructure and mechanical properties of cold sprayed 7075 Al deposition. Mater Sci Eng A 625:19–27
Rokni MR, Widener CA, Champagne VK, Crawford GA, Nutt SR (2017a) The effects of heat treatment on 7075 Al cold spray deposit. Surf Coat Technol 310:278–285

Rokni MR, Widener CA, Ozdemir OC, Crawford GA (2017b) Microstructure and mechanical properties of cold sprayed 6061 Al in As-sprayed and heat treated condition. Surf Coat Technol 309:641–650

Rokni MR, Nutt SR, Widener CA, Champagne VK, Hrabe RH (2017c) Review of relationship between particle deformation, coating microstructure, and properties in high-pressure cold spray. J Therm Spray Technol 26:1308–1355

Rolland G, Sallamand P, Guipont V, Jeandin M, Boller E, Bourda C (2012) Damage study of cold-sprayed composite materials for application to electrical contacts. J Therm Spray Technol 21:758–772

Romanov AE (1995) Continuum theory of defects in nanoscaled materials. Nano Struct Mater 6:125–134

Sansoucy E, Kim GE, Moran AL, Jodoin B (2007) Mechanical characteristics of Al-Co-Ce coatings produced by the cold spray process. J Therm Spray Technol 16:651–660

Semiatin S (2005) Recovery, recrystallization and grain growth structures, metalworking: bulk forming, ASM handbook, vol 14. ASM International, pp 552–562

Schmidt T, Gärtner F, Assadi H, Kreye H (2006) Development of a generalized parameter window for cold spray deposition. Acta Mater 54:729–742

Schmidt T, Gärtner F, Kreye H, Klassen T (2008) In: Lugscheider E (ed) Thermal spray crossing borders. DVS, Maastricht, pp 724–731

Schmidt T, Assadi H, Gärtner F, Richter H, Stoltenhoff T, Kreye H, Klassen T (2009) From particle acceleration to impact and bonding in cold spraying. J Therm Spray Technol 18:794–809

Sellars CM (1987) Recrystallization of metals during hot deformation. Philosophical transactions of the Royal Society of London A. Mathematical, Physical and Engineering Sciences 288:147–158

Seo D, Ogawa K, Sakaguchi K, Miyamoto N, Tsuzuki Y (2012) Parameter study influencing thermal conductivity of annealed pure copper coatings deposited by selective cold spray processes. Surf Coat Technol 206:2316–2324

Sharma MM, Eden TJ, Golesich BT (2015) Effect of surface preparation on the microstructure, adhesion, and tensile properties of cold-sprayed aluminum coatings on AA2024 substrates. J Therm Spray Technol 24:410–422

Shin DH, Kim BC, Park KT, Choo WY (2000) Microstructural changes in equal channel angular pressed low carbon steel by static annealing. Acta Mater 48:3245–5322

Smith MF (2007) Comparing cold spray with thermal spray coating technologies. In: Champagne VK (ed) The cold spray materials deposition process: fundamentals and applications, 1st edn. Woodhead, Cambridge

Soer WA, Aifantis KE, De Hosson JT (2005) Incipient plasticity during nanoindentation at grain boundaries in body-centered cubic metals. Acta Mater 53:4665–4676

Song M, Araki H, Kuroda S, Sakaki K (2013) Reaction layer at the interface between aluminium particles and a glass substrate formed by cold spray. J Physics D: Appl Phys 46:195301

Spencer K, Zhang MX (2009) Heat treatment of cold spray coatings to form protective intermetallic layers. Scr Mater 61:44–47

Spencer K, Fabijanic DM, Zhang MX (2009) The use of Al–Al_2O_3 cold spray coatings to improve the surface properties of magnesium alloys. Surf Coat Technol 204:336–344

Spencer K, Luzin V, Matthews N, Zhang MX (2012) Residual stresses in cold spray Al coatings: the effect of alloying and of process parameters. Surf Coat Technol 206:4249–4255

Stoltenhoff T, Kreye H, Richter HJ (2002) An analysis of the cold spray process and its coatings. J Therm Spray Technol 11:542–550

Stoltenhoff T, Borchers C, Gärtner F, Kreye H (2006) Microstructures and key properties of cold-sprayed and thermally sprayed copper coatings. Surf Coat Technol 200:4947–4960

Sundararajan G, Phani PS, Jyothirmayi A, Gundakaram RC (2009) The influence of heat treatment on the microstructural, mechanical and corrosion behaviour of cold sprayed SS 316L coatings. Mater Sci 44:2320–2326

Suo X, Yin S, Planche MP, Liu T, Liao H (2015) Strong effect of carrier gas species on particle velocity during cold spray processes. Surf Coat Technol 268:90–93

Trivedi R, Jin F, Anderson IE (2003) Dynamical evolution of microstructure in finely atomized droplets of Al-Si alloys. Acta Mater 51:289–300

Upadhyaya GS (1997) Powder metallurgy technology. Cambridge International Science Publishing, Cambridge

Van Steenkiste TH, Smith JR, Teets RE (2002) Aluminum coatings via kinetic spray with relatively large powder particles. Surface and coatings large powder particles. Surf Coat Technol 154:237–252

Vandermeer RA, Hansen N (2008) Recovery kinetics of nanostructured aluminum: model and experiment. Acta Mater 56:5719–5727

Venkatesh L, Chavan NM, Sundararajan G (2011) The influence of powder particle velocity and microstructure on the properties of cold sprayed copper coatings. J Therm Spray Technol 20:1009–1021

Villafuerte J, Dzhurinskiy D, Ramirez R, Maeva E, Leshchynsky V, Maev R (2009) Corrosion behavior and microstructure of the Al–Al_2O_3 coatings produced by low pressure cold spraying. In: Marple B, Hyland M, Lau YC, Li CJ, Lima R, Montavon G (eds) Thermal spray. Expanding thermal spray performance to new markets and applications. ASM International, Las Vegas, pp 908–913

Vo P, Irissou E, Legoux JG, Yue S (2013) Mechanical and microstructural characterization of cold-sprayed Ti-6Al-4V after heat treatment. J Therm Spray Technol 22:954–964

Wang HT, Li CJ, Yang GJ, Li CX, Zhang Q, Li WY (2007) Microstructural characterization of cold-sprayed nanostructured FeAl intermetallic compound coating and its ball-milled feedstock powders. J Therm Spray Technol 16:669–676

Wang HR, Hou BR, Wang J, Li WY (2008) Effect of process conditions on microstructure and corrosion resistance of cold-sprayed Ti coatings. J Therm Spray Technol 17:736–741

Wang F, Xiong B, Liu H, He X (2009) Microstructural development of spray-deposited Al–Zn–Mg–Cu alloy during subsequent processing. J Alloys Compd 477:616–621

Wang Q, Birbilis N, Zhang MX (2011) Interfacial structure between particles in an aluminum deposit produced by cold spray. Mater Lett 65:1576–1578

Wang Q, Birbilis N, Zhang MX (2012) On the formation of a diffusion bond from cold-spray coatings. Metal Mater Trans A 43:1395–1399

Wang Q, Birbilis N, Huang H, Zhang MX (2013) Microstructure characterization and nanomechanics of cold-sprayed pure Al and Al-Al_2O_3 composite coatings. Surf Coat Technol 232:216–223

Wang Q, Qiu D, Xiong Y, Birbilis N, Zhang MX (2014) High resolution microstructure characterization of the interface between cold sprayed Al coating and Mg alloy substrate. Surf Sci 289:366–369

Wolfe DE, Eden TJ, Potter JK, Jaroh AP (2006) Investigation and characterization of Cr^sub 3^C^ sub 2^-based wear-resistant coatings applied by the cold spray process. J Therm Spray Technol 15:400

Wong W, Irissou E, Vo P, Sone M, Bernier F, Legoux JG, Fukanuma H, Yue S (2013a) Cold spray forming of Inconel 718. J Thermal Spray Technol 22:413–421

Wong W, Vo P, Irissou E, Ryabinin AN, Legoux JG, Yue S (2013b) Effect of particle morphology and size distribution on cold-sprayed pure titanium coatings. J Therm Spray Technol 7:1140–1153

Xiong Y, Kang K, Bae G, Yoon S, Lee C (2008) Dynamic amorphization and recrystallization of metals in kinetic spray process. Appl Phys Lett 92:194101

Xiong T, Tao Y, Sun C, Jin H, Du H, Li T (2009) Study on corrosion behavior of cold sprayed al/α Al2O3 deposit on AZ91D alloy. In: Marple B, Hyland M, Lau YC, Li CJ, Lima R, Montavon G (eds) Expanding thermal spray performance to new markets and applications. ASM International, Las Vegas, pp 669–672

Xiong Y, Xiong X, Yoon S, Bae G, Lee C (2011) Dependence of bonding mechanisms of cold sprayed coatings on strain-rate-induced non-equilibrium phase transformation. J Therm Spray Technol 20:860–865

Yandouzi M, Ajdelsztajn L, Jodoin B (2008) WC-based composite coatings prepared by the pulsed gas dynamic spraying process: effect of the feedstock powders. Surf Coat Technol 202:3866–3877

Yandouzi M, Richer P, Jodoin B (2009) SiC particulate reinforced Al–12Si alloy composite coatings produced by the pulsed gas dynamic spray process: microstructure and properties. Surf Coat Technol 203:3260–3270

Yin S, Suo X, Xie Y, Li W, Lupoi R, Liao H (2015) Effect of substrate temperature on interfacial bonding for cold spray of Ni onto Cu. Mater Sci 50:7448–7457

Yoon S, Bae G, Xiong Y, Kumar S, Kang K, Kim JJ, Lee C (2009) Strain-enhanced nanocrystallization of a CuNiTiZr bulk metallic glass coating by a kinetic spraying process. Acta Mater 57:6191–6199

Yu JS, Kim HJ, Oh IH, Lee KA (2013) Oncologic photodynamic therapy: basic principles, current clinical status and future directions. Trans Tech Publications 62:1604–1608

Zahiri SH, Antonio CL, Jahedi M (2009a) Elimination of porosity in directly fabricated titanium via cold gas dynamic spraying. J Mater Process Technol 209:922–929

Zahiri SH, Fraser D, Jahedi M (2009b) Recrystallization of cold spray-fabricated CP titanium structures. J Therm Spray Technol 18:16–22

Zhang YY, Zhang JS (2011) Recrystallization in the particles interfacial region of the cold-sprayed aluminum coating: strain-induced boundary migration. Mater Lett 65:1856–1858

Zhang Q, Li CJ, Wang XR, Ren ZL, Li CX, Yang GJ (2008) Formation of NiAl intermetallic compound by cold spraying of ball-milled Ni/Al alloy powder through postannealing treatment. J Therm Spray Technol 17:715–720

Zhao ZB, Gillispie BA, Smith JR (2006) Coating deposition by the kinetic spray process. Surf Coat Technol 200:4746–4754

Zhou X, Mohanty P (2012) Electrochemical behavior of cold sprayed hydroxyapatite/titanium composite in Hanks' solution. Electrochim Acta 65:134–140

Ziemian CW, Sharma MM, Bouffard BD, Nissley T, Eden TJ (2014) Effect of substrate surface roughening and cold spray coating on the fatigue life of AA2024 specimens. Mater Des 54:212–221

Zou Y, Qin W, Irissou E, Legoux JG, Yue S, Szpunar JA (2009) Dynamic recrystallization in the particle/particle interfacial region of cold-sprayed nickel coating: electron backscatter diffraction characterization. Scr Mater 61:899–902

Zou Y, Goldbaum D, Szpunar JA, Yue S (2010) Microstructure and nanohardness of cold-sprayed coatings: electron backscattered diffraction and nanoindentation studies. Scr Mater 62:395–398

Part II
Future Perspectives

Chapter 6
Cold Spray Additive Manufacture and Component Restoration

Shuo Yin, Barry Aldwell, and Rocco Lupoi

6.1 Introduction

Cold spray as an emerging coating technology was developed in the 1980s. Differing from the conventional thermal spray coating techniques, the formation of cold spray coating relies largely on the particle velocity prior to the impact rather than the temperature. Thereby, the feedstock used for cold spray remains solid state during the entire deposition process. The inevitable defects commonly encountered in the high-temperature deposition processes, e.g., oxidation, thermal residual stress, and phase transformation, can be avoided. Therefore, cold spray coatings have been widely applied in a broad range of industries including aerospace, automotive, energy, medical, marine, and other important fields, providing effective protection against high temperature, corrosion, erosion, oxidation, chemicals, etc. (Champagne and Helfritch 2016, Papyrin 2001; Vilardell et al. 2015). Apart from the aforementioned features, the thickness of cold spray coating almost has no limitation for most metals and metal matrix composites, e.g., the diamond-reinforced metal matrix composites as shown in Fig. 6.1(Yin et al. 2017). Considering this fact, cold spray has been successfully applied as an additive manufacturing technology to fabricate individual components and restore damaged components in recent years (Blose et al. 2006; Champagne et al. 2008). This development shines a new light on the conventional additive manufacturing technologies and significantly broadens application fields of cold spray.

Cold spray additive manufacturing (CSAM) as a new member of additive manufacturing family has great potentials to fabricate components with rotational structures, e.g., cylinder walls and flanges. It also allows for the production of near net-shape structures or complex geometry structures by the aid of well-designed

S. Yin (✉) • B. Aldwell • R. Lupoi
Trinity College Dublin, The University of Dublin, Department of Mechanical and Manufacturing Engineering, Parsons Building, Dublin 2, Ireland
e-mail: yins@tcd.ie; lupoir@tcd.ie

P. Cavaliere (ed.), *Cold-Spray Coatings*,
https://doi.org/10.1007/978-3-319-67183-3_6

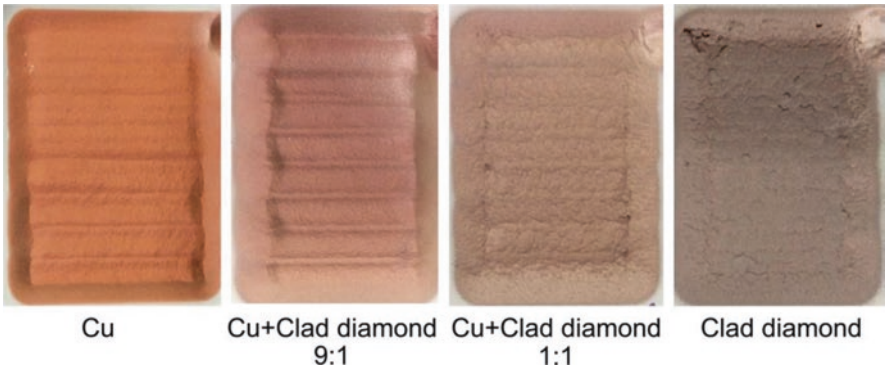

Fig. 6.1 Digital photos of thick Cu + diamond metal matrix composite coatings fabricated via cold spray (Yin et al. 2017)

masks or molds. Similar to the cold spray functional coatings, components fabricated via CSAM have superior advantages, e.g., high adhesive strength, low oxidation, and no phase transformation. Despite having many unique merits, CSAM also has obvious shortcomings. As a process which was originally developed for coating fabrication, the additive materials used for CSAM must be built on a substrate. The as-fabricated CSAM produces, therefore, consist of two parts, i.e., inner base substrate and outer new structure. This unique structure may be favorable to certain special applications, e.g., building a structure on an unweldable base materials. However, in other circumstances, the substrate may have to be removed, which increases the manufacturing cost and time. Moreover, the dimensions and surface condition of the as-fabricated CSAM components are not precise; hence, post-machining is strictly required to finalize the fabrication.

Component damage frequently occurs in service due to corrosion, wear, fatigue, or other causes. Many of the damaged components cannot be reclaimed and have to be replaced due to the lack of effective restoration methods. Cold spray as a cost-effective process has shown great potential in the repair of damaged components because of the capability to prevent adverse influence on the underlying substrate materials and unique merit to retain the feedstock's original properties. During the past decade, cold spray restoration (CSR) as a promising approach has been successfully applied to repair a variety of corroded and damaged components in various fields. The restored components are in good serviceable conditions, significantly reducing the cost by replacing a new component. Similar to other restoration techniques, cold spray feedstock cannot be deposited on the damaged component directly because the complex surface topography and unclean surface on the damaged area may adversely affect the restoration quality. Pre-machining on the damaged zone as a preparation is necessary. By preparing the damaged area, a clean and smooth surface applicable for the further cold spray filling work can be achieved. After material deposition, the as-coated components also have to be post-machined to their original dimensions. The standard CSR process normally includes the

following four stages: pre-machining on the damaged part, coating deposition, post-machining on the backfilling coating, and performance test.

While cold spray for additive manufacturing and repair applications is still an emerging technology, a large amount of research work has been carried out by both the scientific and industrial communities. Existing works mainly focused on applications, product properties, processing parameters optimization, spray strategy, and robot control. So far, a systematic summarization and review on these topics is still lacking. Therefore, in this chapter, the existing CSAM and CSR works were summarized and reviewed for the purpose of systematically introducing the progress of CSAM and CSR techniques.

6.2 Cold Spray Additive Manufacturing Applications

6.2.1 Rotational Structure Fabrication

A broad range of components have a rotational symmetry (e.g., cylinder inner and outer walls and flanges), playing significant roles in the modern industry. CSAM has great capability to fabricate components with such rotational structure. Using an external motor-drive axis to hold the mandrel substrate, the rotational structure can be easily fabricated through a simple definition of nozzle movement. Figure 6.2a shows a photo of the CSAM system located in the cold spray lab of Trinity College Dublin (TCD). The system consists of a conventional homemade cold spray system and a rotational fourth axis which is fixed on a three-axis CNC platform. It has been used for fabricating a variety of rotational structure components since its setup. For instance, an aluminum flange structure was successfully fabricated for an Irish company by this system. This flange shows features which have been manufactured using turning and drilling, including a chamfer which crosses the interface between the substrate and cold spray deposit. This demonstrates the ability to achieve a good surface finish and dimensional accuracy when machining CSAM material.

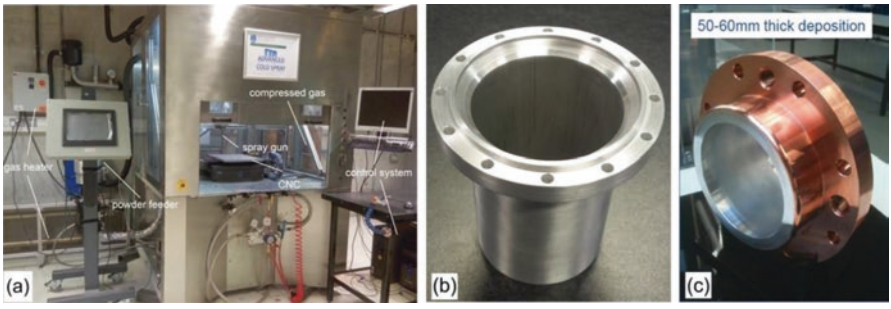

Fig. 6.2 Digital photos of (**a**) CSAM system [TCD], (**b**) CSAM aluminum flange [TCD and Moog Dublin www.moog.com], and (**c**) CSAM copper flange on aluminum tube (Abreeza et al. 2011)

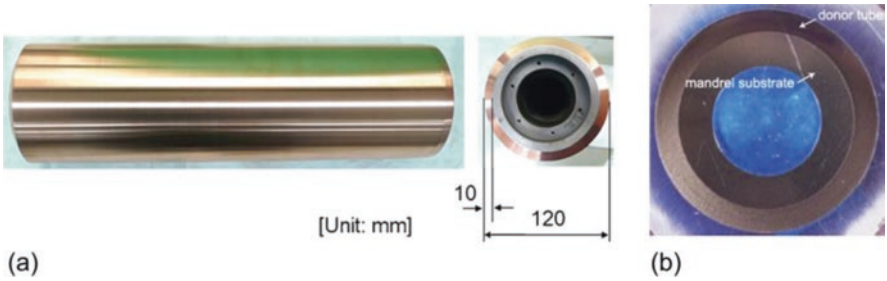

Fig. 6.3 Digital photos of CSAM rotational structure: (**a**) scaled canister for disposal of CANDU spent fuels and (**b**) tantalum-10 tungsten alloy donor tube used for the gun barrel liners (Barnett et al. 2015; Choi et al. 2010)

Subsequent property tests on this flange demonstrated that its quality completely meets the company's requirement. Similar copper flange structure coated on an aluminum tube is also provided in Fig. 6.2c (Abreeza et al. 2011).

Metal cylinder outer and inner walls can also be produced using CSAM. The fabrication process is similar to the flange fabrication, particularly for the additive manufacture or repair of external features. Figure 6.3a provides an example showing a 1/10-scaled canister for disposal of CANDU spent fuels fabricated via CSAM (Choi et al. 2010). A 10 mm thick coating layer with a porosity of 0.3%, density of 8900 kg/m^3, and oxygen content of 0.019% (that of original copper powder was 0.02%) was deposited onto the cast iron cylinder, showing great tensile strength, mechanical stability, and thermal properties. Moreover, in some circumstance, the mandrel substrate may be not needed and have to be removed after the fabrication of rotational structure. An instance is provided in Fig. 6.3b showing a CSAM tantalum-10 tungsten alloy donor tube used for the manufacture of gun barrel liners (Barnett et al. 2015). In this case, the tantalum-10 tungsten alloy layer was deposited onto a cylindrical aluminum mandrel substrate, and then the inner mandrel was removed using deep drilling, honing techniques, and a brief soak in dilute sodium hydroxide. Analogously, single material cylinder walls can be easily fabricated via CSAM with the similar procedure. More rotational outer wall components fabricated via CSAM are shown in Fig. 6.4 (Chad 2014; Kumar and Chavan 2011; May et al. 2013; Richter 2014; Sova et al. 2013).

For the manufacture of internal features, the procedure varies according to the inner diameter. If the inner diameter is sufficiently large to allow for a conventional cold spray nozzle and its holding accessories to fit inside the component, the fabrication process is same as producing the external features. If the internal diameter is too small to allow this, the nozzle can be slightly inclined to fit the limited space at the expense of lower coating quality caused by the spray angle. An example is provided in Fig. 6.5a, b, which shows a copper inner wall of a pressure ring used for food processing machine fabricated via CSAM (May et al. 2013). As can be seen, the nozzle is inclined to the target substrate during the fabrication due to the limitation of the internal diameter. Apart from the aforementioned cases, special-

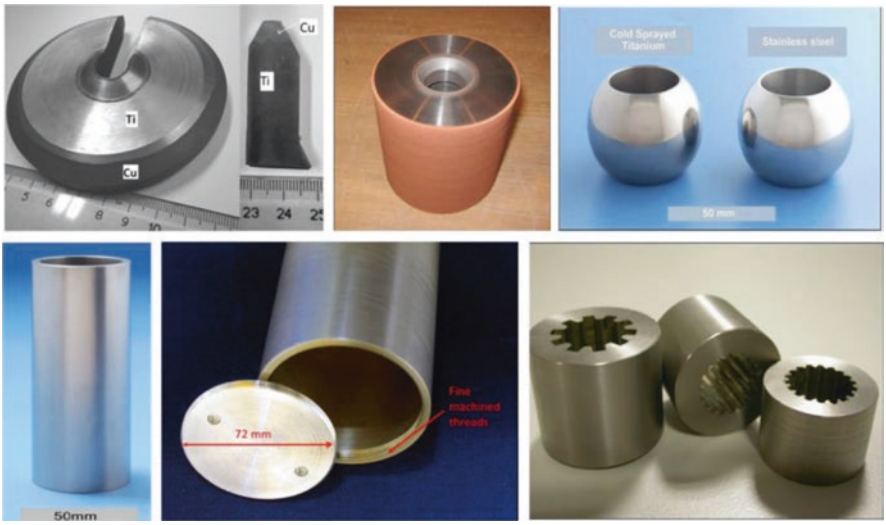

Fig. 6.4 CSAM rotational structures (Chad 2014; Kumar and Chavan 2011; May et al. 2013; Richter 2014; Sova et al. 2013)

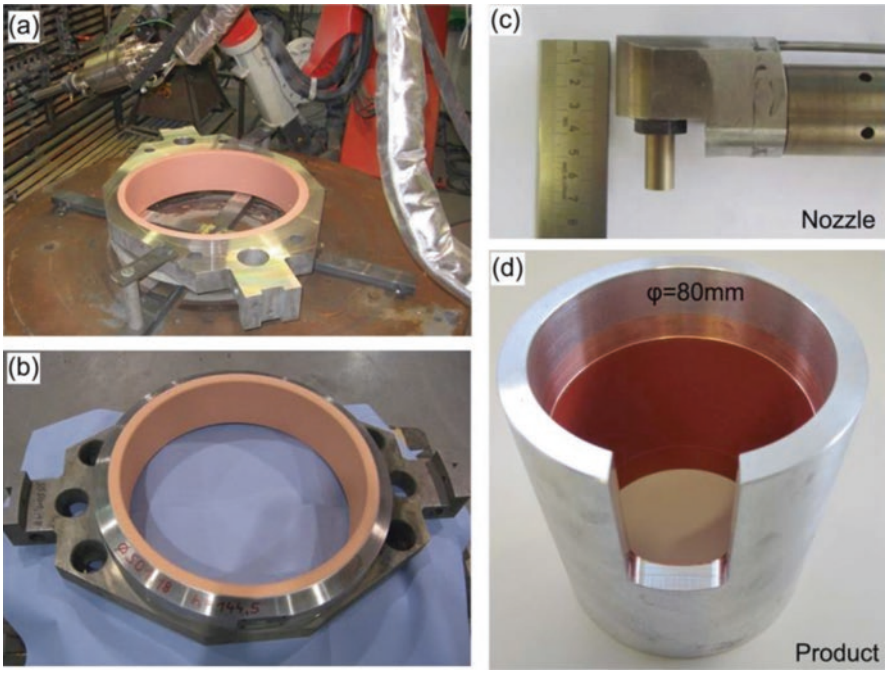

Fig. 6.5 Digital photos of CSAM rotational structures: (**a**, **b**) an inner wall of a pressure ring for food processing machine, (**c**) a micro-size cold spray nozzle, and (**d**) an inner wall of small-space cylinder tube (May et al. 2013; Richter 2014)

Fig. 6.6 Digital photos of CSAM components with complex structure: (**a**) cone structure, (**b**) gear, and (**c**) bracket (Briefing 2013; Champagne and Helfritch 2016; Richter 2014)

designed cold spray nozzles must be used if the inner diameter is very small. As illustrated in Fig. 6.5c, a micro-size cold spray nozzle (5–10 mm in length) is used for the spraying of internal features. The minimum diameter allowed to be fabricated is determined according to the coating thickness and nozzle size. Figure 6.5d shows a copper inner wall on a metal tube with the diameter of 80 mm fabricated using the micro nozzle shown in Fig. 6.5c (Richter 2014).

More complex components may be manufactured using CSAM by accurately defining the nozzle trajectory or designing a mandrel substrate. Figure 6.6 shows some complex structures fabricated via CSAM (Briefing 2013; Champagne and Helfritch 2016; Richter 2014).

The cone structure shown in Fig. 6.6a and gear shown in Fig. 6.6b were made by coordinating the nozzle motion with the rotational movement of the substrate. The bracket structure shown in Fig. 6.6c was fabricated by depositing the additive materials onto a specially designed substrate mold followed by separation of the component from the mold. The use of CSAM to fabricate complex-shape components is

promising, but relevant investigations are very limited. It is necessary to conduct more works in this field including advanced nozzle trajectory and substrate mold development.

6.2.2 *Near Net-shape Structure Fabrication*

CSAM is also capable of producing net-shape or near net-shape components. As shown in Fig. 6.7a, the fabrication process may require the use of a mask or shield to prevent the deposition of redundant materials and hence to obtain a specific pattern that is required. An example of CSAM net-shape structure is the pyramidal fin arrays used for the compact heat exchanger as shown in Fig. 6.7b (Cormier et al. 2016, 2015, 2014a, b, 2013; Dupuis et al. 2016a, b; Farjam et al. 2015). By adjusting the standoff distance and design scheme of the wire mask, the fin array shape and density can be accurately controlled (Cormier et al. 2014a, b, 2013; Farjam et al. 2015). The thermal and mechanical tests suggest that the CSAM fin arrays have superior thermal performance than traditional straight (rectangular) fins due to the higher convective heat transfer coefficient caused by increased turbulence wake behind the fins, and the roughness and porosity of the cold spray surface (Cormier et al. 2013; Farjam et al. 2015; Kotoban et al. 2016). Further studies also suggested that thermal conductance can be improved by increasing the fin height, increasing fin density, or using staggered configurations at the expense of more pressure loss (Cormier et al. 2014a; Dupuis et al. 2016b). In addition, mask-assisted CSAM also can be used to fabricate chip heat sinks, metal markings, or other products with special patterns (Bierk et al. 2011; Birtch 2010; Kashirin et al. 2011).

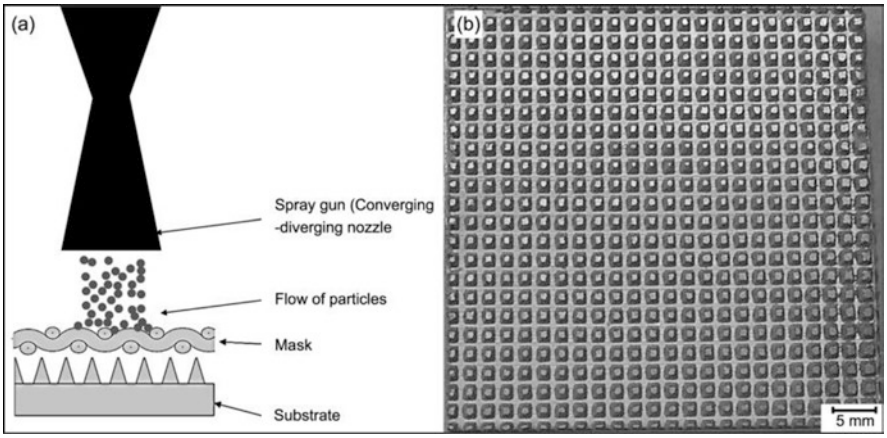

Fig. 6.7 CSAM pyramidal fin arrays heat sink. (**a**) Schematic of the fabrication process and (**b**) digital photo of the CSAM fin array heat sink (Cormier et al. 2014a)

6.3 Cold Spray Restoration Applications

6.3.1 Aircraft Component Restoration

Among all the potential application areas of CSR, the aerospace industry is the largest one because severe corrosion and wear problems always happen in aircraft components due to the harsh operating conditions experienced in service. Magnesium and magnesium alloys possess many merits (e.g., high stiffness, low density, high thermal conductivity, and excellent machinability) over other metals and thus have been widely used for fabricating aircraft transmission gearbox. However, as an electrochemically active material, magnesium and its alloys tend to corrode due to an anode reaction with other metallic materials. Thereby, magnesium gearbox housings frequently suffers from electrochemical corrosion after longtime service. Such corrosion significantly reduces the component lifetime, increasing the maintenance cost and potential failure risk. It is of great importance to properly repair the corroded zone and bring the restored component back to service. By utilizing CSR, the corroded part of the transmission gearbox can be repaired with aluminum or aluminum alloy materials. Figure 6.8 shows some CSR works on the damaged sections of transmission gearboxes (Howe 2014; Kilchenstein 2014; Schell 2016). Mechanical and corrosion tests on the repaired sections confirmed that the backfilling aluminum and aluminum alloy coatings had excellent adhesive strength, wear resistance, and corrosion resistance capability. These restored components are suitable to be

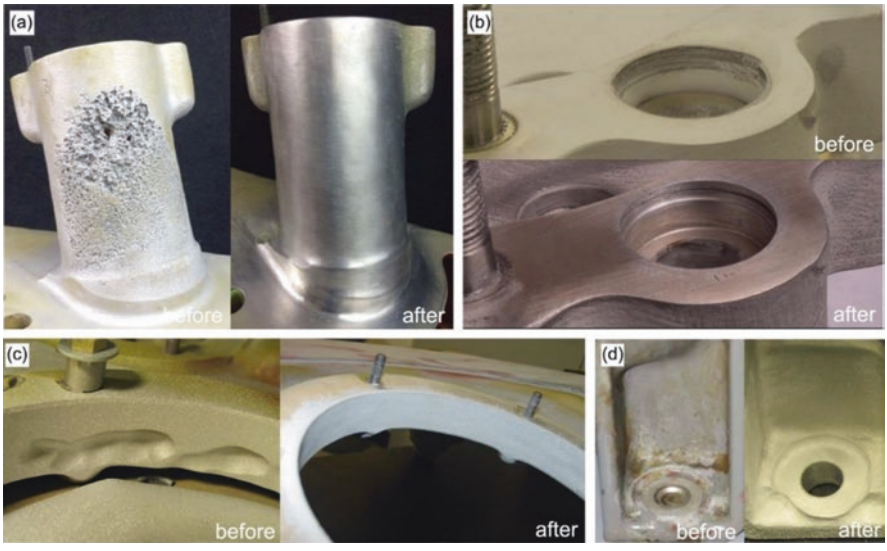

Fig. 6.8 Comparison between damaged and CSR components: (**a**) S-92 helicopter gearbox sump, (**b**) oil tube bores in CH47 helicopter accessory cover, (**c**) UH-60 helicopter gearbox sump, and (**d**) UH-60 rotor transmission housing (Howe 2014; Kilchenstein 2014; Schell 2016)

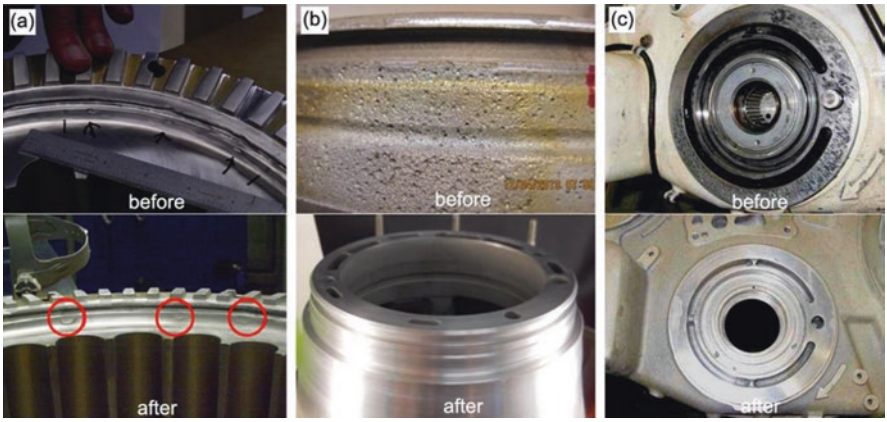

Fig. 6.9 Comparison between damaged and CSR components: (**a**) AH-64 helicopter mast support, (**b**) F18-AMAD gearbox, and (**c**) front frame of T-700 engine (Howe 2015; Kilchenstein 2014; Leyman and Champagne 2009)

returned to service after repair (Champagne et al. 2008; DeForce et al. 2007; Security and Program 2011).

Aluminum and aluminum alloy are also widely used for manufacturing aircraft components due to their low density, high tensile strength, good formability, and excellent corrosion resistance. An example of an aerospace component manufactured from aluminium alloys is the mast support on helicopters. During routine service a helicopter mast support often experiences corrosion pitting on the snap ring groove surface. When the level of the pitting damage exceeds a criterion, the mast support must be repaired or replaced. Significant savings in time and money can be achieved by repairing these components using CSR. Figure 6.9a shows a comparison between a damaged and CSR snap ring groove surface of a mast support (Leyman and Champagne 2009). The detailed restoration procedure consists of blending out corrosion pits, then filling back the removed part using aluminum-based coatings, and finally post-machining the as-coated component. Other examples of repairs using CSR are shown in Fig. 6.9 (Howe 2015; Kilchenstein 2014).

Nickel based superalloys such as Inconel are another important materials frequently used in aerospace industry due to excellent mechanical properties and high chemical and thermal resistance. Aerospace components which are likely to experience high mechanical and/or thermal loading in service are typically manufactured using nickel-based superalloys. These extreme in-service conditions often lead to severe wear and corrosion, and thus a reduction in service life for these components. An example of this is the nose wheel steering actuator barrel, which operates under high loads in a moist, dirty environment. This operating environment causes corrosion in joints. By using CSR, a corroded B737 nose wheel steering actuator barrel was repaired with nickel alloy coating. Figure 6.10 shows the comparison between a damaged and CSR B737 nose wheel steering actuator barrel. The corroded surface became smooth after repair without any pits or cracks (Schell 2016).

Fig. 6.10 Restored B737 nose wheel steering actuator barrel via CSR (Schell 2016)

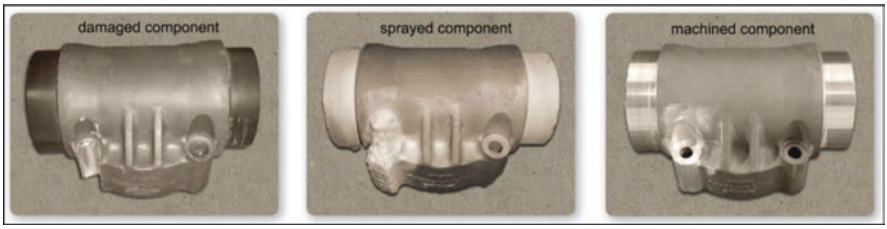

Fig. 6.11 CSR process of a mechanically damaged flap transmission tee box housing of an aircraft (Schell 2016)

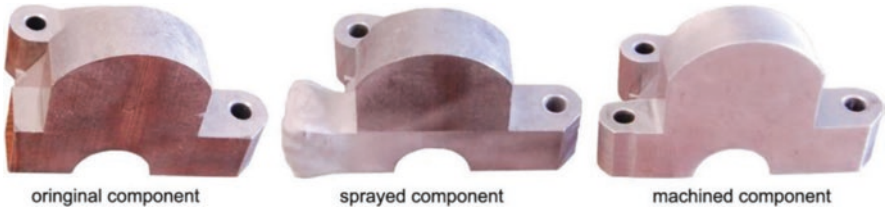

Fig. 6.12 Modification process of adding a new part onto a bearing cap via CSR (Villafuerte 2015)

CSR is also suitable for the repair of components damaged by mechanisms other than corrosion, such as fatigue, wear, or accidental overloading. Figure 6.11 shows the CSR process of a mechanically damaged flap transmission tee box housing of an aircraft (Schell 2016). It is clearly seen that the damaged component was restored to a serviceable condition after repair. Figure 6.12 shows an example of using CSR technology to add a feature to an existing component. As can be seen, a completely new component was obtained after CSR. Visually, there was no obvious boundary between the new part and original body. The new component passed the customer's quality and performance specifications (Villafuerte 2015), demonstrating the feasibility of CSR.

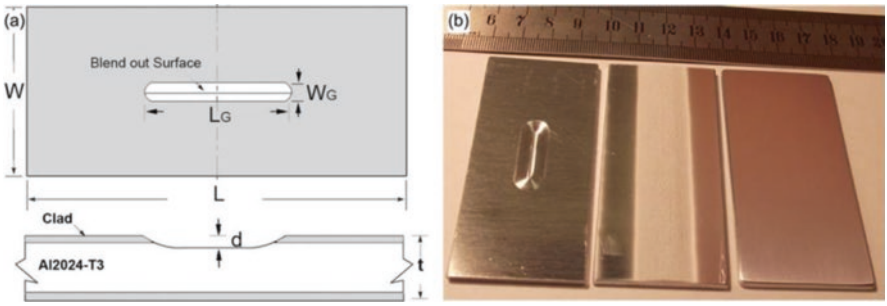

Fig. 6.13 Repair result of aluminum cladding layer on the aluminum alloy panel with self-machined damage via CSR. (**a**) Schematic of the self-machined damage and (**b**) restoration process (Yandouzi et al. 2014)

6.3.2 Aircraft Skin Restoration

Commercial and military aircraft skin are mostly made from sheets of aluminium alloy with an additional aluminum cladding layer to prevent corrosion. During routine flight, the aircraft skin is likely to suffer from erosion and scratch damages due to the high-velocity impact of dust and debris. The damaged area will allow for corrosion to penetrate through the protective aluminum clad layer and down to the base aluminum alloy. Once the base aluminum alloy is seriously corroded, fatigue properties of the component will be compromised. Therefore, it is necessary to repair the damaged aluminum cladding before the corrosion penetrates into the underlying base material. Some thermal spray technologies have been used to repair the damaged aircraft skin. However, the thermal spray coatings suffer from high porosity, high oxidation, and undesirable microstructure due to phase changes. Most importantly, the high-temperature feedstock upon impact may have an adverse effect on the properties of the underlying base material, significantly degrading the aircraft skin performance (D6–51343 2006). CSAM has great potential to resolve this problem (Jones et al. 2014, 2011; Matthews et al. 2014). Figure 6.13 shows the repair result of aluminum cladding layer on the aluminum alloy panel with self-machined damage via CSR (Yandouzi et al. 2014). Visually, the damaged area is completely filled by the cold spray aluminum coating without obvious distinction with the surrounding aluminum cladding. Mechanical tests on the repaired sample suggested that the coating hardness was higher than the original aluminum cladding and the fatigue resistance of the repaired sample was improved. In addition, corrosion testing revealed that the aluminum coating on damaged aluminum cladding provided an effective barrier to corrosion, despite the potential for corrosion to occur at the edge of the repair deposit. The testing results on the self-damaged aircraft skin coupon positively demonstrated the feasibility of CSR for the repair of aircraft skin.

In addition to the skin damage, aircraft fuselage also suffers from multisite damage (MSD) problem. For nearly all kinds of aircraft, the fuselage is fabricated through lap joints of aluminum alloy skin panels. These lap joints may be damaged

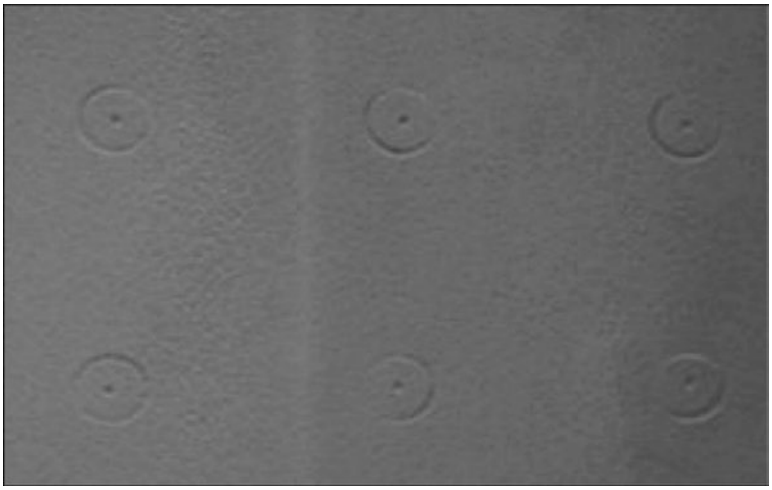

Fig. 6.14 Cold spray coating over the simulated fuselage fasteners (Matthews et al. 2014)

through accidental collisions, or through overloading in service. On one hand, fastener bore corrosion always takes place through the interface between fastener and skin despite the edge sealing between mating panels. On the other hand, multiple fastened strip repairs also act as a weak point, preferentially inducing the generation of cracks. These potential risks work together, finally causing the MSD on the aircraft skin. By using CSR combined with standard sealant, the invasion of the moisture into the joint from the interface between mating panels and also between fasteners and aircraft skin can be prevented (Jones et al. 2014, 2012; Matthews et al. 2014). Figure 6.14 shows a cold spray coating over simulated fuselage fasteners. It can be seen that the surface of the fasteners was completely sealed by the cold spray coating. Subsequent fatigue testing results indicated that the cold spray coating remained intact even when the underlying fuselage joint skin experienced MSD, positively demonstrating the capability of CSR to alleviate the corrosion damage of aircraft skin. Furthermore, CSR presented great potentials to repair the cracks caused by MSD, which helps to enhance the fuselage structural integrity (Jones et al. 2014, 2011; Matthews et al. 2014).

6.3.3 Aircraft Blade Restoration

The restoration of aluminum alloy aircraft blades is another important application of CSR. Similar to the aircraft skin, aircraft blades also suffer from serious erosion due to the high-velocity impact by dust, debris, and water droplets during service. Moreover, relatively large debris raised during aircraft taking off and landing will

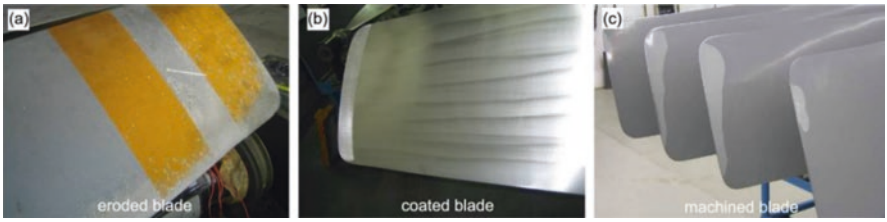

Fig. 6.15 CSR process of aluminum alloy blades (Stoltenhoff and Zimmermann 2012)

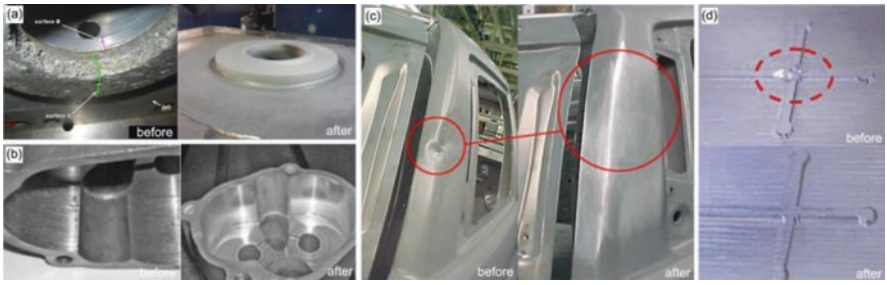

Fig. 6.16 Comparison between damaged and CSR components: (**a**) an internal bore surface of a navy valve actuator, (**b**) an oil pump housing of Caterpillar engine, (**c**) a large cast automotive part, and (**d**) a mold (Lee et al. 2007; Lyalyakin et al. 2016; Maev et al. 2014; Widener et al. 2016)

lead to more serious damage to the blade surface. The current method to repair this damage is to grind the eroded blade to a level that the damaged area has been removed. By using CSR, the lost materials during the grinding process can be filled, which allows the restoration of the original blade dimensions. Figure 6.15 illustrates the repair process of aluminum alloy blades via CSR. The restored blades have passed an extensive airworthiness test program and have been returned to service (Stoltenhoff and Zimmermann 2012).

6.3.4 Other Component Restoration

Some practical CSR works in various industries, e.g., automotive, marine, and energy, are introduced in this section. In terms of marine industry, CSR has been successfully applied to repair a corroded internal bore surface of a navy aluminum alloy valve actuator without thermally affecting the base material, showing superior capability over other traditional repair method (i.e., tungsten inert gas welding, metal inert gas welding, and laser cladding). Figure 6.16a shows the comparison between the damaged and CSR actuator. The CSR actuator has passed all property

tests and is now back in service (Widener et al. 2016). In the automotive industry, CSR has been applied to repair the corroded oil pump housing of Caterpillar-3116 and Caterpillar-3126 engines (Fig. 6.16b). It was reported that more than 30 such corroded pump housings were restored via CSR from 2012 to 2013 in Moscow. All of these reconditioned components have been returned to service without any failure reports so far (Lyalyakin et al. 2016). Moreover, CSR was also used to repair severe cracks in large cast automotive parts as can be seen in Fig. 6.16c (Maev et al. 2014). Additionally, restoration of damaged molds is also possible using CSR as shown in Fig. 6.16d. The repaired mold presented similar results during the cutting force test and even better wear resistance capability than original one (Lee et al. 2007). These are only some of the potential applications for CSR, which is still a developing technique.

6.4 Processing Parameters During Manufacturing

6.4.1 Introduction of Processing Parameters

Processing parameters including nozzle moving speed, spray distance, spray angle, scanning step, and nozzle trajectory play an important role in CSAM and CSR. These parameters are known to pose direct impact on the particle impact velocity and landing footprint; thereby they may affect the consequent coating thickness, coating deposition efficiency, coating cross-sectional profile, and coating properties. Understanding the effects of these parameters is necessary to achieve the desired deposition geometry. Figure 6.17 shows schematic of the processing parameters in CSAM and CSR.

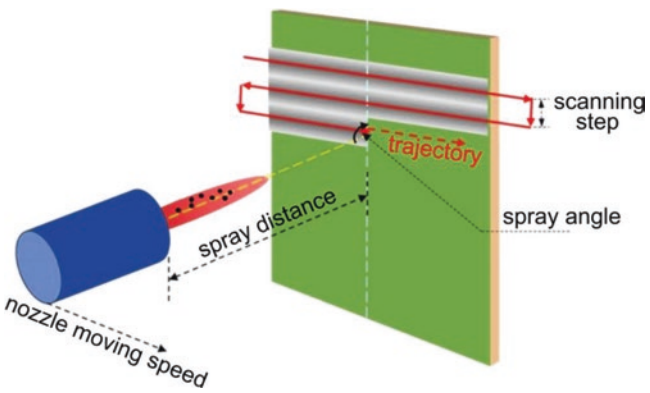

Fig. 6.17 Schematic of the processing parameters in CSAM and CSR

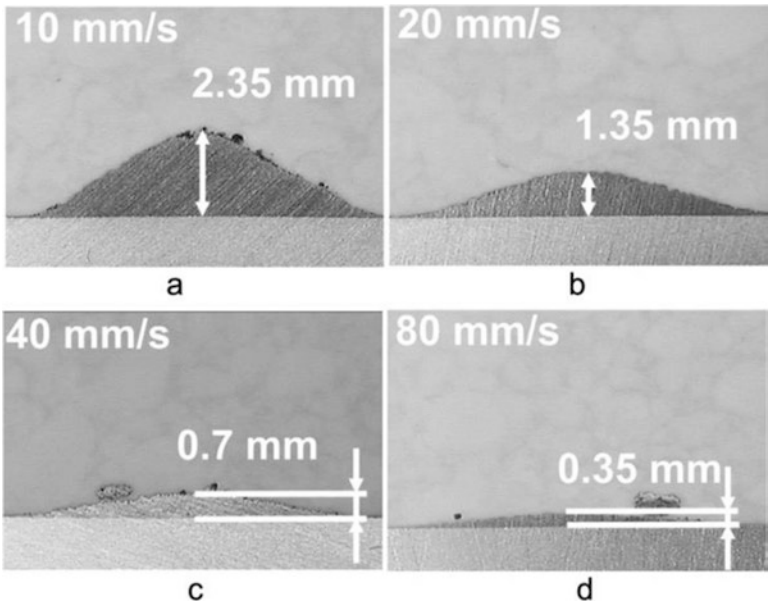

Fig. 6.18 Effect of nozzle moving speed on the single-track coating thickness and cross-sectional profile (Kotoban et al. 2016)

6.4.2 Nozzle Moving Speed

Nozzle moving speed is a parameter that determines the spray duration and amount of feedstock powder impacting onto the target surface. The direct effect of nozzle moving speed is on the coating thickness. Higher nozzle moving speed results in lower single-track coating thickness as shown in Fig. 6.18 (Deng et al. 2014; Fang et al. 2010; Kotoban et al. 2016; Yin et al. 2015). An extreme case is the single particle deposition where the nozzle speed is so high that individual splats are not in contact with each other (Yin et al. 2015). It was reported that increasing coating thickness leads to the increment of residual stress and bonding strength (Moridi et al. 2014; Rech et al. 2014; Xiong et al. 2015); thereby nozzle moving speed also poses indirect impact on these mechanical properties. Moreover, nozzle moving speed was found to influence the single-track coating cross-sectional profile through affecting the deposition efficiency (C. Chen et al. 2016a, b; Kotoban et al. 2016; Pattison et al. 2007; Sova et al. 2013). As can be seen from Fig. 6.18, the cross-sectional profile becomes gradually sharper as the coating thickness increases. The substantial reason behind this phenomenon is the flow characteristic of the propulsive gas passing through a supersonic nozzle. According to fluid dynamics theory, the particle velocity and the consequent deposition efficiency at the central zone are higher than that at the outer zone (Champagne et al. 2011; Tabbara et al. 2011; Yin

et al. 2014). Thereby, the coating cross-sectional profile presents a Gaussian shape as shown in Fig. 6.18a. The slope of this profile causes deposition to occur at angles less than 90 degrees, further decreasing the deposition efficiency. This reduction in deposition efficiency, in turn, leads to preferential deposition along the peak compared to the sloped edges. Finally, the profile becomes increasingly shaper as the nozzle moving speed decreases. In addition, another potential effect of nozzle moving speed is the heating input from the high-temperature impinging jet to the coating and substrate. Low nozzle moving speed helps the temperature increment of the deposited coating and substrate. This fact may contribute to the deposition of subsequent coating (Yin et al. 2015) but in turn may result in the development of thermal stress (Candel and Gadow 2009).

6.4.3 Spray Distance

Spray distance is defined as the distance between the nozzle outlet and the target surface, significantly affecting the particle impact velocity and the consequent coating properties. In a supersonic-free jet, the intensity of the jet core decreases gradually along the jet central axis due to the momentum exchange between the jet and the atmosphere. Inside the jet core, particles achieve positive drag force and thus rapidly accelerate. However, after the jet core length is exceeded, the gas velocity becomes lower than the particle velocity, and the resultant negative drag force causes the deceleration of particles. As a result, the particle impact velocity and deposition efficiency increases with increasing spray distance up until an optimum value is reached, after which the particle velocity and deposition efficiency drop. This fact has been experimentally confirmed (Cai et al. 2014; Pattison et al. 2008). However, different results were also reported in some works, showing a monotonic reduction of coating thickness (deposition efficiency) with increasing the spray distance (Han et al. 2005; Li et al. 2008). Note that coating thickness will increase with the particle impact velocity when the coating deposition efficiency is less than 100%. The different results reported in these publications show that the role of spray distance in the particle velocity upon impact and deposition efficiency is still not quite clear. More research on this subject should be carried out in the future. Despite having different results, a common suggestion is that the spray distance should not be excessively large.

6.4.4 Spray Angle

Spray angle is defined as the angle of the nozzle axis to the target surface. It has a significant influence on the particle impact velocity components and consequent coating properties. When spraying at an angle to the substrate, only the normal velocity component contributes to the coating deposition, while the tangential

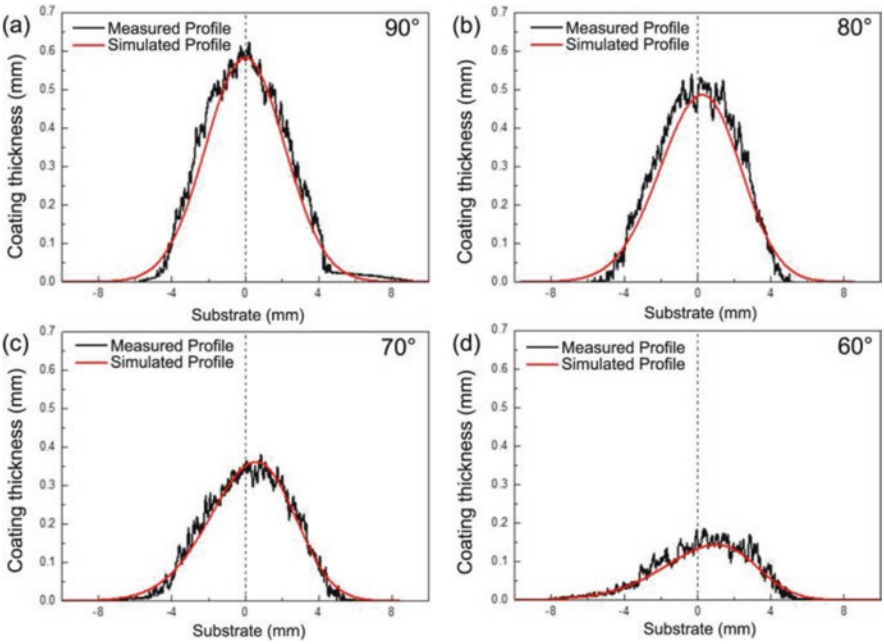

Fig. 6.19 Effect of spray angle on the single-track coating cross-sectional profile (C. Chen et al. 2016a, b)

velocity component plays an opposite role by potentially detaching the deposited particles. As the spray angle decreases, the normal velocity component reduces, while the tangential velocity component increases. As a consequence, coating deposition efficiency and thickness reduce, and the coating bonding strength and porosity decrease (Binder et al. 2011; Gilmore et al. 1999; Li et al. 2006, 2005; Luo et al. 2016; Yin et al. 2013). Therefore, the nozzle should be maintained in a normal orientation to the substrate during the coating fabrication process. Furthermore, spray angle also affects the single-track coating cross-sectional profile due to the variation in spray distance over the particles impact area. Therefore, the cross-sectional profile normally presents a skewed shape as shown in Fig. 6.19 (C. Chen et al. 2016a, b).

6.4.5 Nozzle Scanning Step

Coating buildup is achieved through nozzle scanning over the entire target surface line by line according to a predefined trajectory. The coating is formed by the partial overlapping of many single-track coatings. Scanning step is defined as the interval between two single-track coatings, which is an important parameter that determines the stack process. The main influence of scanning step is the coating thickness

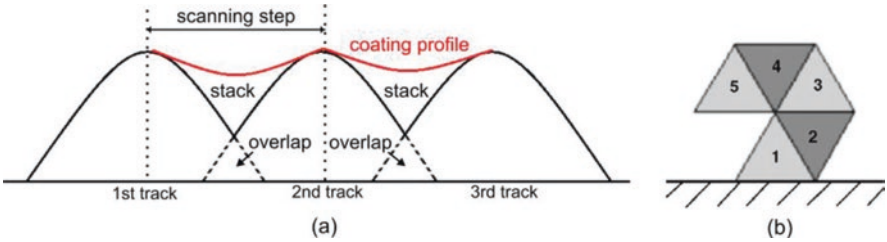

Fig. 6.20 Schematic of scanning strategy (Cai et al. 2014; Pattison et al. 2007)

uniformity and surface morphology. Two scanning strategies are commonly used to achieve a uniform coating thickness. The first approach is to use a scanning step less than half of the width of a single deposited line. When the scanning step is small, the neighboring tracks can overlap each other (Cai et al. 2014). Such overlapping compensates the thickness difference between the central peak and the slope zone of each track as shown in Fig. 6.20a, contributing to the uniformity of coating thickness. The other strategy is to use a larger scanning step, and offset subsequent deposited layers to create a uniform coating thickness. In this way, the neighboring tracks at the first layer do not overlap each other, while the track at the second layer is deposited on the gap between two first-layer tracks as illustrated in Fig. 6.20b (Pattison et al. 2007). In this case, the gap can be perfectly filled, and a smooth coating surface also can be achieved. Investigations on the scanning strategy are still quite limited; more work should be carried out to compare existing strategies, develop new strategy, and explore their influence on the coating properties.

6.4.6 Trajectory Definition

The basic principle of trajectory definition is to maximise the coating homogeneity and quality. The as-sprayed coating should possess a homogenous density, property, and bonding strength. To achieve this objective, the processing parameters must be carefully chosen before spraying and kept constant during the coating fabrication process. When spraying on a flat surface, a simple round-trip trajectory is mostly applied to maximise coating homogeneity. However, for a complex curved surface which could be experienced in CSAM and CSR applications, trajectory definition should maintain the constant spray distance, spray angle, nozzle speed, and other processing parameters over the target surface to avoid the inhomogeneity of coating. Therefore, more advanced nozzle trajectory planning is required. To date, very few attempts have been made for the development of such advanced trajectory in CSR and CSAM (Cai et al. 2016; Chaoyue Chen et al. 2016a, b). A recent study by Chen et al. reported a novel spiral trajectory for a CSR self-damaged aluminum coupon. Figure 6.21 shows the spiral trajectory and the CSR coupon before final machining. The results indicated that spiral trajectory improved the surface

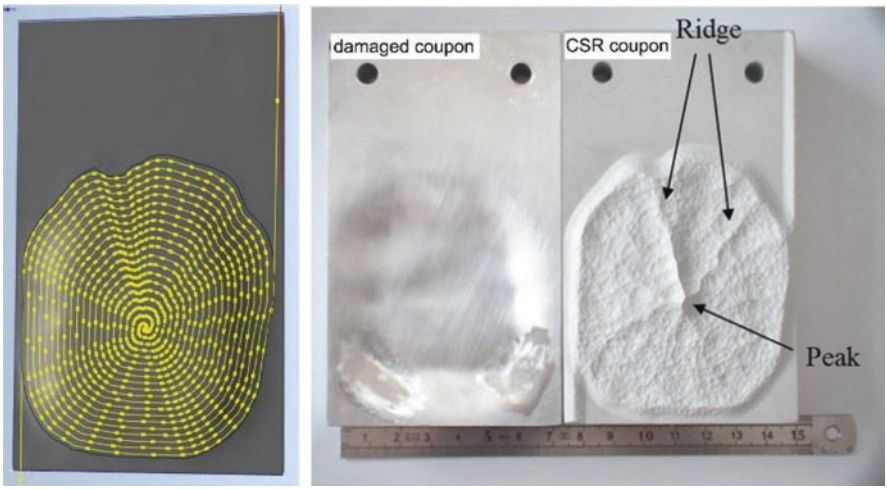

Fig. 6.21 Spiral trajectory and the CSR coupon before final machining (Chaoyue Chen et al. 2016a, b)

condition of as-repaired coupon and reduced deposition of redundant material compared with round-trip trajectory (Chaoyue Chen et al. 2016a, b). This fact indicates that nozzle trajectory is an important parameter for CSR and thus warrants further investigation.

6.5 Robotic Control of Processing Parameters

6.5.1 Introduction of Robotic Control

The precise control of nozzle motion is essential to the fabrication of high-quality CSAM and CSR products. To achieve this, industrial robots (including multi-axes robot arm and computer numerical control platform) are frequently used in cold spray process to control the nozzle or substrate. By properly programming the robot, processing parameters including nozzle moving speed, spray distance, spray angle, and scanning step, as well as nozzle moving trajectory can be accurately planned and executed. Programming also allows for multiple repetitive spraying cycles to be carried out with ease. In addition, the remote control system of a robot allows human operators to work far away from the high-temperature, high-noise, and high-dust environment. Due to these advantages, industrial robots are widely applied to assist the cold spray process for coating fabrication, CSAM, and CSR.

In general, before starting CSAM or CSR work, a spray strategy must be decided upon, and the robot must be programmed to define the processing parameters and nozzle moving trajectory. Then, the compiled program will be uploaded to and

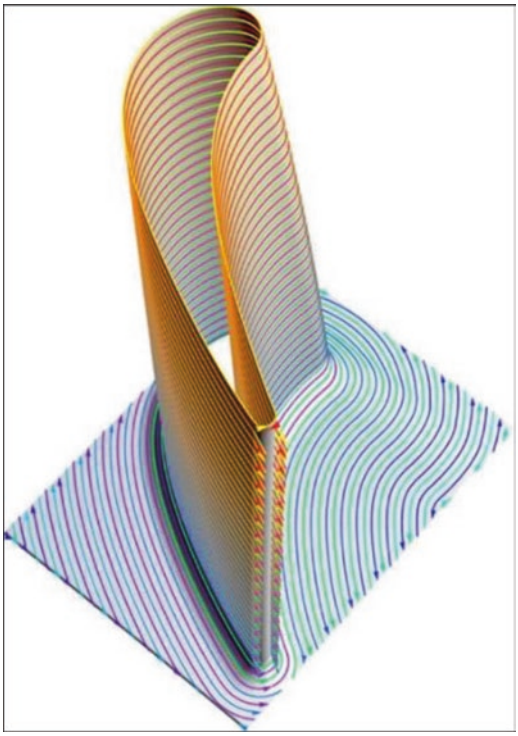

Fig. 6.22 Trajectory on the turbine blade defined by off-line programming method (Stier 2014)

implemented by the robot. According to the complexity of the task, a program can be written in various ways. For a simple task such as when the substrate is a flat surface with a regular shape, the online programming method is always applied, where the processing parameters and trajectory are created through manually defined motion instructions and target points. However, for surfaces with complex topography, e.g., the turbine blade surface shown in Fig. 6.22, the processing parameters and trajectory should be carefully created according to the working strategy, and the off-line programming platform by the aid of CAD/CAM software is more suitable (Cai et al. 2016, 2015; Chaoyue Chen et al. 2016a, b; Deng et al. 2012; Stier 2014). In addition, the trajectory definition must consider the inertia and kinematics of the robot arm to optimize the nozzle moving speed (Deng et al. 2014; Fang et al. 2010).

6.5.2 Online Programming

The online programming method has been widely used to assist cold spray work (Deng and Chen 2015). In this method, the processing parameters and spray trajectory are created by manually defining the motion instructions and target points. The

robot motion instructions which contains the data for motion type, target point details, nozzle traverse speed, and reference coordinate system is firstly created. The nozzle is then moved to the first target point to record its position and orientation information and then moved to the next point. By repeating this procedure until the last target point, all target point locations can be recorded, and the nozzle moving trajectory is finally created. The robot will follow this predefined motion instructions and nozzle moving trajectory to finish the task. The online programming is relatively easy to learn and apply. It is suitable for the simple tasks where trajectory is on a planar surface and only a small quantity of target points need to be defined. However, as most of the programming work is finished on the control panel, the online programming method lacks accuracy and efficiency when the target points are in a large number or on a curved surface. Therefore, as stated previously, this method is only recommended for implementing simple tasks.

6.5.3 Off-Line Programming

Off-line programming is a more advanced and accurate method for trajectory definition compared with online programming (Deng and Chen 2015). It is applicable for tasks where the workpieces have complex geometries and high precision requirement (see Figs. 6.21 and 6.22).

The rapid development of CSAM and CSR brings increasing demands of off-line programming to precisely define the trajectory of the nozzle. For this method, the trajectory can be defined by the aid of graphic operation interface and trajectory generation algorithm. Firstly, the geometry of the workpiece is obtained through either CAD/CAM software or by measurement of the surface geometry depending on the complexity of the task. Afterward, the acquired 3D geometry is input into a simulator platform for trajectory generation and robot moving simulation. In the simulator platform, the trajectory and robot motion data can be easily accessed and adjusted. Finally, these data are converted to the programming language and uploaded to the robot for execution. The detailed flowchart of the off-line programming is provided in Fig. 6.23 (Deng et al. 2012). The off-line programming and robotics simulator tools help robot integrators to create the optimal trajectory for the robot to perform a specific task. For this method, the robot program is created in an external computer and then uploaded to the robot for execution; thus it does not delay the production process.

In order to provide a more intuitive introduction to the off-line programming, the commercial software named RobotStudio™ which designed for use with ABB robots (ABB Automation Technology Products AB, Gothenburg, Sweden) is selected as an example. Figure 6.24 shows the screenshot of working interface in RobotStudio™. As can be seen, the robot and workpieces are represented by 3D geometries in the software to simulate the real working environment. Then, the trajectory generated on the target surface is simulated by the virtual robot system available in RobotStudio™. By analyzing simulation results (i.e., the

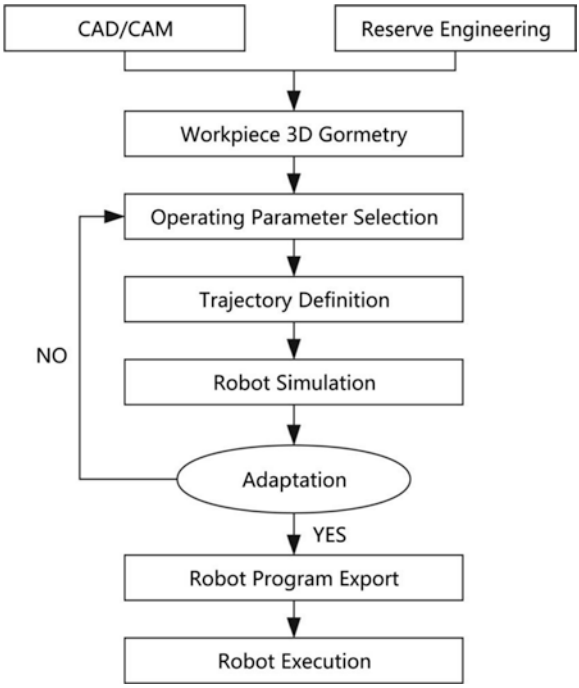

Fig. 6.23 Flowchart of the off-line programming method (Deng et al. 2012)

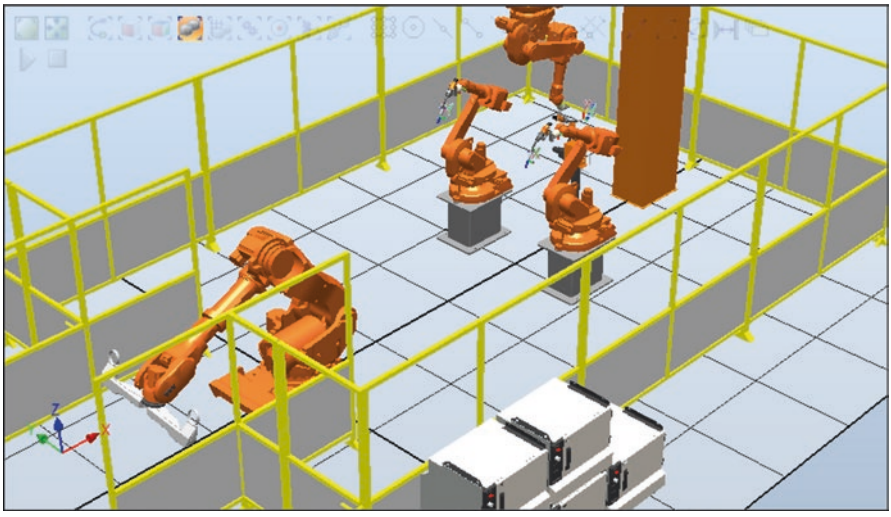

Fig. 6.24 Screenshot of working interface in RobotStudio™ (Deng and Chen 2015)

nozzle speed and the joint position of each axis), the processing parameters and trajectory are optimized. Finally, the optimal trajectory is uploaded to the robot for execution.

6.5.4 External Axis

The mandrel substrate surface often has rotational symmetry in CSAM, but the robot arm is difficult to move in a circular trajectory around the target surface due to its limited reachability. In this regard, an external axis for holding the workpieces is normally required to assist the manufacturing process. Specifically, the robot trajectory can be simplified into a linear motion that cooperates with the rotation of the workpiece by external axis. The coating thickness can be adjusted by controlling the linear movement speed of robot and rotation speed of external axis. For more complicated CSAM tasks, e.g., hook gear and turbo blade, the robot and external axis must be linked through software in order to generate the specific trajectory for fabrication.

6.6 Post-Machining and Finishing Processes

6.6.1 Post-Machining Process

Cold spray typically leaves a rough, undulating, porous surface after spraying. In many applications, such as in repair of a worn surface using cold spray, the as-sprayed surface is not suitable for immediate use, either due to surface finish, wear behavior (Lee et al. 2007), or dimensional accuracy requirements. This necessitates the use of a machining or finishing process. To date, relatively little research has been undertaken into the machinability of cold spray materials.

Cold spray deposits are generally suitable for normal machining processes, such as turning, milling, or drilling (Sova et al. 2013) (Barnett et al. 2015). However, due to the unique properties of cold spray material, careful selection of machining parameters is required to achieve a satisfactory finish. An example of a CSAM component being machined into a finished part is shown in Fig. 6.2b, where turning and drilling operations have been used to manufacture a flange.

In order to understand the machining of cold spray materials, it is important to recognize that unless the coating has been brought to full density, through hot isostatic pressing (HIP) or a similar method, it will machine in a similar manner to a porous, cast material. As a cold spray coating is an amalgamation of individual particles, there will be variations in density and levels of work hardening within the coating, with the potential for small oxide inclusions (Yin et al. 2012). This will cause variations in the physical and thermal loads experienced by any cutting tools.

Many comparisons can be made between the machining of cold spray materials and materials produced through powder metallurgy (Czampa et al. 2013) and electron beam melting (Aziz et al. 2012; Bordin et al. 2014; Montevecchi et al. 2016), which are acknowledged as more difficult to machine than bulk materials. If a deposit has poor inter-particle bonding and little particle deformation, then the cutting process will resemble that of a sintered material, with inter-particle bonds being broken and no chips being formed. The surface finish after machining of any such material would be porous and undulating, though some smearing and densification of the surface may be observed (Tutunea-Fatan et al. 2011). Conversely, a fully dense deposit which has good ductility will form chips and machine in a very similar manner to the bulk material. Thus, the machinability of a cold spray deposit is dependent upon the density and ductility of the cold spray coating created. Cutting forces during the machining of porous cold spray coating will typically be lower than that of bulk material but with more variation during cutting. Porous materials manufactured using other techniques typically show lower but more variable cutting forces (Abolghasemi Fakhri et al. 2012), with the lower magnitude of the forces being at least partially attributable to the lower stiffness of porous materials (Lu et al. 1999) and the variation due to the discontinuous cutting action experienced as the tool disengages and then reengages when passing through pores. Cold spray coatings with higher ductility will show less variation in cutting forces, while coatings with lower porosity will show higher cutting forces. Other issues which are of interest in the machining of cold spray deposits are the potential for debonding of the cold spray coating if overly aggressive cutting parameters are used or if a large portion of the bond area is removed during machining. If it is necessary to remove the deposit from the substrate in order to achieve the geometry required, this should be done first, as the deposit may distort due to residual stresses after debonding. Careful inspection should be carried out of the component after machining, as cut-induced cracking has been observed to cause failure in tensile test samples machined from cold spray coating (MacDonald et al. 2016). Little to no research has been carried out into tool wear during the machining of cold spray materials. It can be expected that due to the discontinuous nature of the machining process, tool wear will be greater than that observed when machining bulk material. The use of tamping materials in cold spray such as alumina, which are typically very hard, will cause excessive tool wear during machining (Ramulu et al. 2002).

6.6.2 Finishing Process

Little research has been carried out into the use of grinding as a manufacturing process for cold spray coatings. However, the use of epoxy resin SiC grinding paper to prepare polished cross-section samples of cold spray samples is common in research (Goldbaum et al. 2016; Jakupi et al. 2015; Morgan et al. 2004; Villa et al. 2013). As with cutting processes, often there will be densification and smearing caused by individual grits plowing the surface rather than cutting (Tutunea-Fatan et al. 2011).

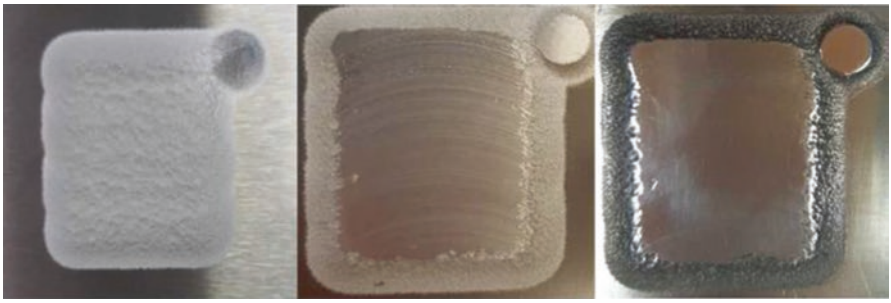

Fig. 6.25 Aluminum cold spray coating, showing as-sprayed, after face milling and after polishing

An example of a machining and finishing process which was carried out in TCD is shown in Fig. 6.25. After face milling the surface has visible machining marks, which are removed after grinding and polishing. Microscope inspection of the surface after polishing shows no visible porosity, which indicates that the material has smeared and flowed to form a fully dense surface layer.

6.7 Conclusions and Future Perspectives

Cold spray technology has shown great potential in additive manufacturing and damaged component restoration due to its great ability to retain the original feedstock properties and prevent adverse influence on the underlying substrate materials. A variety of components have been successfully fabricated or repaired via CSAM and CSR. When compared to materials manufactured using other additive manufacturing techniques, CSAM products were found to possess sufficiently high quality, while CSR components mostly had equal or even better performance in comparison with the original (undamaged) ones. Despite having significant achievements, CSAM and CSR still have a lot of aspects to be explored or improved. CSAM for fabrication of complex components will still be an interesting and challenging subject. Currently, most of the existing CSAM works concern about simple rotational structures, while relatively little work has been done on the manufacture of complex structures, e.g., cone, gear, and bracket. In order to broaden the product variety of CSAM, more works should be done in the coordination of nozzle motion and external axis rotation, mandrel substrate design, and the post-spraying machining of the deposited material. Micro-nozzle development is also encouraged as this is of great importance to the deposition of internal features within existing components. As for the CSR, it is necessary to establish standard testing procedures for restored components and also to explore potential application fields. Nozzle motion parameters, scanning strategy, and trajectory optimization should be another focal point of the future work. This will help to reduce the material's waste and the post-machining work caused by the imprecise

over-deposition on the damaged area. Also, an effective solution of poor deposition on the small-angle corner should be further investigated as it is now a limitation for CSR to broaden its applications.

References

Abolghasemi Fakhri M, Bordatchev EV, Tutunea-Fatan OR (2012) An image-based methodology to establish correlations between porosity and cutting force in micromilling of porous titanium foams. Int J Adv Manuf Technol 60:841–851. https://doi.org/10.1007/s00170-011-3647-1

Abreeza M, Yuji I, Kazuhiro O (2011) Computational simulation for cold sprayed deposition. ELyT Laboratory Workshop, Sendai

Aziz MSA, Ueda T, Furumoto T, Abe S, Hosokawa A, Yassin A (2012) Study on machinability of laser sintered materials fabricated by layered manufacturing system: influence of different hardness of sintered materials. Procedia CIRP 4:79–83. https://doi.org/10.1016/j.procir.2012.10.015

Barnett B, Trexler M, Champagne V (2015) Cold sprayed refractory metals for chrome reduction in gun barrel liners. Int J Refract Met Hard Mater 53:139–143. https://doi.org/10.1016/j.ijrmhm.2015.07.007

Bierk B, Mgr G, Addison G, Elmquist B (2011) Repair Technology Development Projects, In: CSAT Workshop. Worcester, USA

Binder K, Gottschalk J, Kollenda M, Gärtner F, Klassen T (2011) Influence of impact angle and gas temperature on mechanical properties of titanium cold spray deposits. J Therm Spray Technol 20:234–242. https://doi.org/10.1007/s11666-010-9557-1

Birtch W (2010) Practical cold spray. https://www.supersonicspray.com. Accessed 3 June 2014

Blose RE, Walker BH, Walker RM, Froes SH (2006) New opportunities to use cold spray process for applying additive features to titanium alloys. Met Powder Rep 61:30–37. https://doi.org/10.1016/S0026-0657(06)70713-5

Boeing Standards D6-51343 (2006) Thermal spray repair of exterior clad aluminum. USA

Bordin A, Ghiotti A, Bruschi S, Facchini L, Bucciotti F (2014) Machinability characteristics of wrought and EBM CoCrMo alloys. Procedia CIRP 14:89–94. https://doi.org/10.1016/j.procir.2014.03.082

Briefing T (2013) Metal coated particles and defense applications. In: CSAT Workshop. Worcester, USA

Cai Z, Deng S, Liao H, Zeng C, Montavon G (2014) The effect of spray distance and scanning step on the coating thickness uniformity in cold spray process. J Therm Spray Technol 23:354–362. https://doi.org/10.1007/s11666-013-0002-0

Cai Z, Liang H, Quan S, Deng S, Zeng C, Zhang F (2015) Computer-aided robot trajectory autogeneration strategy in thermal spraying. J Therm Spray Technol 24:1235–1245. https://doi.org/10.1007/s11666-015-0282-7

Cai Z, Chen T, Zeng C, Guo X, Lian H, Zheng Y, Wei X (2016) A global approach to the optimal trajectory based on an improved ant Colony algorithm for cold spray. J Therm Spray Technol 25:1631–1637. https://doi.org/10.1007/s11666-016-0468-7

Candel A, Gadow R (2009) Trajectory generation and coupled numerical simulation for thermal spraying applications on complex geometries. J Therm Spray Technol 18:981–987. https://doi.org/10.1007/s11666-009-9338-x

Chad H (2014) CSIRO Titanium Technologies and Additive Manufacturing, Future Manufacturing Flagship. https://www.atse.org.au/Documents/Events/SA%20Manufacturing/chad-henry-titanium-technologies.pdf. Accessed 13 Nov 2016

Champagne V, Helfritch D (2016) The unique abilities of cold spray deposition. Int Mater Rev 6608:1–19. https://doi.org/10.1080/09506608.2016.1194948

Champagne VK, Helfritch D, Leyman PF (2008) Magnesium repair by cold spray. Plat Surf Finish 95:19–28

Champagne VK, Helfritch DJ, Dinavahi SPG, Leyman PF (2011) Theoretical and experimental particle velocity in cold spray. J Therm Spray Technol 20:425–431. https://doi.org/10.1007/s11666-010-9530-z

Chen C, Gojon S, Xie Y, Yin S, Verdy C, Ren Z, Liao H, Deng S (2016a) A novel spiral trajectory for damage component recovery with cold spray. Surf Coat Technol. https://doi.org/10.1016/j.surfcoat.2016.10.096

Chen C, Xie Y, Verdy C, Liao H, Deng S (2016b) Modelling of coating thickness distribution and its application in offline programming software. Surf Coat Technol. https://doi.org/10.1016/j.surfcoat.2016.10.044

Choi HJ, Lee M, Lee JY (2010) Application of a cold spray technique to the fabrication of a copper canister for the geological disposal of CANDU spent fuels. Nucl Eng Des 240:2714–2720. https://doi.org/10.1016/j.nucengdes.2010.06.038

Cormier Y, Dupuis P, Jodoin B, Corbeil A (2013) Net shape fins for compact heat exchanger produced by cold spray. J Therm Spray Technol 22:1210–1221. https://doi.org/10.1007/s11666-013-9968-x

Cormier Y, Dupuis P, Farjam A, Corbeil A, Jodoin B (2014a) Additive manufacturing of pyramidal pin fins: height and fin density effects under forced convection. Int J Heat Mass Transf 75:235–244. https://doi.org/10.1016/j.ijheatmasstransfer.2014.03.053

Cormier Y, Dupuis P, Jodoin B, Corbeil A (2014b) Mechanical properties of cold gas dynamic-sprayed near-net-shaped fin arrays. J Therm Spray Technol 24:476–488. https://doi.org/10.1007/s11666-014-0203-1

Cormier Y, Dupuis P, Jodoin B, Ghaei A (2015) Finite element analysis and failure mode characterization of pyramidal fin arrays produced by masked cold gas dynamic spray. J Therm Spray Technol 24:1549–1565. https://doi.org/10.1007/s11666-015-0317-0

Cormier Y, Dupuis P, Jodoin B, Corbeil A (2016) Pyramidal fin arrays performance using streamwise anisotropic materials by cold spray additive manufacturing. J Therm Spray Technol 25:170–182. https://doi.org/10.1007/s11666-015-0267-6

Czampa M, Markos S, Szalay T (2013) Improvement of drilling possibilities for machining powder metallurgy materials. Procedia CIRP 7:288–293. https://doi.org/10.1016/j.procir.2013.05.049

DeForce B, Eden T, Potter J, Champagne V, Leyman P, Helfritch D (2007) Application of aluminum coatings for the corrosion protection of magnesium by cold spray. In: Tri-Service Corrosion Conference. Denver, USA

Deng S, Chen C (2015) Generation of robot trajectory for thermal spray. In: Adams W (ed) Robot kinematics and motion planning. Nova Science Publishers, New York

Deng S, Cai Z, Fang D, Liao H, Montavon G (2012) Application of robot offline programming in thermal spraying. Surf Coat Technol 206:3875–3882. https://doi.org/10.1016/j.surfcoat.2012.03.038

Deng S, Liang H, Cai Z, Liao H, Montavon G (2014) Kinematic optimization of robot trajectories for thermal spray coating application. J Therm Spray Technol 23:1382–1389. https://doi.org/10.1007/s11666-014-0137-7

Dupuis P, Cormier Y, Fenech M, Corbeil A, Jodoin B (2016a) Flow structure identification and analysis in fin arrays produced by cold spray additive manufacturing. Int J Heat Mass Transf 93:301–313. https://doi.org/10.1016/j.ijheatmasstransfer.2015.10.019

Dupuis P, Cormier Y, Fenech M, Jodoin B (2016b) Heat transfer and flow structure characterization for pin fins produced by cold spray additive manufacturing. Int J Heat Mass Transf 98:650–661. https://doi.org/10.1016/j.ijheatmasstransfer.2016.03.069

Fang D, Deng S, Liao H, Coddet C (2010) The effect of robot kinematics on the coating thickness uniformity. J Therm Spray Technol 19:796–804. https://doi.org/10.1007/s11666-010-9470-7

Farjam A, Cormier Y, Dupuis P, Jodoin B, Corbeil A (2015) Influence of alumina addition to Aluminum fins for compact heat exchangers produced by cold spray additive manufacturing. J Therm Spray Technol 24:1256–1268. https://doi.org/10.1007/s11666-015-0305-4

Gilmore DL, Dykhuizen RC, Neiser RA, Roemer TJ, Smith MF (1999) Particle velocity and deposition efficiency in the cold spray process. J Therm Spray Technol 8:576–582. https://doi.org/10.1361/105996399770350278

Goldbaum D, Manimuda P, Kamath G, Descartes S, Klemberg-Sapieha JE, Chromik RR (2016) Tribological behavior of TiN and Ti (Si,C)N coatings on cold sprayed Ti substrates. Surf Coat Technol 291:264–275. https://doi.org/10.1016/j.surfcoat.2016.02.044

Han T, Zhao Z, Gillispie BA, Smith JR (2005) Effects of spray conditions on coating formation by the kinetic spray process. J Therm Spray Technol 14:373–383. https://doi.org/10.1361/105996305X59369

Howe C (2014) Cold spray repair of the CH-47 accessory cover. In: CSAT Workshop. Worcester, USA

Howe C (2015) Cold spray qualification of T700 engine front frame. In: CSAT Workshop. Worcester, USA

Jakupi P, Keech PG, Barker I, Ramamurthy S, Jacklin RL, Shoesmith DW, Moser DE (2015) Characterization of commercially cold sprayed copper coatings and determination of the effects of impacting copper powder velocities. J Nucl Mater 466:1–11. https://doi.org/10.1016/j.jnucmat.2015.07.001

Jones R, Matthews N, Rodopoulos CA, Cairns K, Pitt S (2011) On the use of supersonic particle deposition to restore the structural integrity of damaged aircraft structures. Int J Fatigue 33:1257–1267. https://doi.org/10.1016/j.ijfatigue.2011.03.013

Jones R, Matthews N, Elston J, Cairns K, Baker J, Wadsley B, Pitt S (2012) SPD repairs to thin aluminium structures. In: 28th International Congress of the Aeronautical Sciences. Brisbane, Australia

Jones R, Molent L, Barter S, Matthews N, Tamboli D (2014) Supersonic particle deposition as a means for enhancing the structural integrity of aircraft structures. Int J Fatigue 68:260–268. https://doi.org/10.1016/j.ijfatigue.2014.03.013

Kashirin A, Klyuev O, Buzdygar T, Shkodkin A (2011) Modern applications of the low pressure cold spray. International Thermal Spray Conference, Hamburg

Kilchenstein G (2014) Cold spray technologies used for repair. In: JTEG Monthly Teleconference. http://jteg.ncms.org/wp-content/gallery/ColdSpray/ColdSpray_SlideDeck.pdf. Accessed 9 Nov 2016

Kotoban D, Grigoriev S, Okunkova A, Sova A (2016) Influence of a shape of single track on deposition efficiency of 316L stainless steel powder in cold spray. Surf Coat Technol. https://doi.org/10.1016/j.surfcoat.2016.10.052

Kumar S, Chavan NM (2011) Cold spray coating technology: activities at ARCI. International Advanced Reserch Centre for Powder Metallurgy and New Materials, Hyderabad

Lee JC, Kang HJ, Chu WS, Ahn SH (2007) Repair of damaged mold surface by cold-spray method. CIRP Ann – Manuf Technol 56:577–580. https://doi.org/10.1016/j.cirp.2007.05.138

Leyman PF, Champagne VK (2009) Cold spray process development for the reclamation of the Apache helicopter mast support. Report No.: ARL-TR-4922. Army Research Laboratory, MD, USA

Li CJ, Li WY, Wang YY, Yang GJ, Fukanuma H (2005) A theoretical model for prediction of deposition efficiency in cold spraying. Thin Solid Films 489:79–85. https://doi.org/10.1016/j.tsf.2005.05.002

Li CJ, Li WY, Liao H (2006) Examination of the critical velocity for deposition of particles in cold spraying. J Therm Spray Technol 15:212–222. https://doi.org/10.1361/105996306X108093

Li WY, Zhang C, Guo XP, Zhang G, Liao HL, Li CJ, Coddet C (2008) Effect of standoff distance on coating deposition characteristics in cold spraying. Materials and DesignMater Des 29:297–304. https://doi.org/10.1016/j.matdes.2007.02.005

Lu G, Lu GQ, Xiao ZM (1999) Mechanical properties of porous materials. J Porous Mater 6:359–368. https://doi.org/10.1023/A:1009669730778

Luo XT, Li YJ, Li CX, Yang GJ, Li CJ (2016) Effect of spray conditions on deposition behavior and microstructure of cold sprayed Ni coatings sprayed with a porous electrolytic Ni powder. Surf Coat Technol 289:85–93. https://doi.org/10.1016/j.surfcoat.2016.01.058

Lyalyakin VP, Kostukov AY, Denisov VA (2016) Special features of reconditioning the housing of a caterpillar diesel oil pump by gas-dynamic spraying. Weld Int 30:68–70. https://doi.org/10.1080/09507116.2015.1030152

MacDonald D, Fernández R, Delloro F, Jodoin B (2016) Cold spraying of Armstrong process titanium powder for additive manufacturing. J Therm Spray Technol. https://doi.org/10.1007/s11666-016-0489-2

Maev RG, Strumban E, Leshchinskiy V, Dzhurinskiy D (2014) Repair applications of the LPCS process. In: CSAT Workshop. Worcester, USA

Matthews N, Jones R, Sih GC (2014) Application of supersonic particle deposition to enhance the structural integrity of aircraft structures. Sci China Phys Mech Astron 57:12–18. https://doi.org/10.1007/s11433-013-5367-z

May C, Marx S, Paul A (2013) Selected R&D results and industrial applications. In: CSAT Workshop, Worcester, USA

Montevecchi F, Grossi N, Takagi H, Scippa A, Sasahara H, Campatelli G (2016) Cutting forces analysis in additive manufactured AISI H13 alloy. Procedia CIRP 46:476–479. https://doi.org/10.1016/j.procir.2016.04.034

Morgan R, Fox P, Pattison J, Sutcliffe C, O'Neill W (2004) Analysis of cold gas dynamically sprayed aluminium deposits. Mater Lett 58:1317–1320. https://doi.org/10.1016/j.matlet.2003.09.048

Moridi A, Hassani Gangaraj SM, Vezzu S, Guagliano M (2014) Number of passes and thickness effect on mechanical characteristics of cold spray coating. Procedia Eng 74:449–459. https://doi.org/10.1016/j.proeng.2014.06.296

Papyrin A (2001) Cold spray technology. Adv Mater Process 159:49–51

Pattison J, Celotto S, Morgan R, Bray M, O'Neill W (2007) Cold gas dynamic manufacturing: a non-thermal approach to freeform fabrication. Int J Mach Tools Manuf 47:627–634. https://doi.org/10.1016/j.ijmachtools.2006.05.001

Pattison J, Celotto S, Khan A, O'Neill W (2008) Standoff distance and bow shock phenomena in the cold spray process. Surf Coat Technol 202:1443–1454. https://doi.org/10.1016/j.surfcoat.2007.06.065

Ramulu M, Rao PN, Kao H (2002) Drilling of (Al_2O_3)p/6061 metal matrix composites. J Mater Process Technol 124:244–254. https://doi.org/10.1016/S0924-0136(02)00176-0

Rech S, Trentin A, Vezzù S, Vedelago E, Legoux JG, Irissou E (2014) Different cold spray deposition strategies: single- and multi-layers to repair aluminium alloy components. J Therm Spray Technol 6061:1237–1250. https://doi.org/10.1007/s11666-014-0141-y

Richter P (2014) New value chain for advanced coatings by using cold spray. In: Industrial Technologies 2014 – Smart Growth through Research and Innovation. Athens, Greece

Schell J (2016) Cold spray aerospace applications. In: CSAT Workshop, Worcester, USA

Security E, Program TC (2011) Cost and performance report cold spray for repair of magnesium. http://www.dtic.mil/dtic/tr/fulltext/u2/a572962.pdf. Accessed 28 Oct 2016

Sova A, Grigoriev S, Okunkova A, Smurov I (2013) Potential of cold gas dynamic spray as additive manufacturing technology. Int J Adv Manuf Technol 69:2269–2278. https://doi.org/10.1007/s00170-013-5166-8

Stier O (2014) Fundamental cost analysis of cold spray. J Therm Spray Technol 23:131–139. https://doi.org/10.1007/s11666-013-9972-1

Stoltenhoff T, Zimmermann F (2012) LOXPlate® coatings for aluminum aerospace components exposed to high dynamic stresses. Praxair Surface Technologies GmbH, Ratingen

Tabbara H, Gu S, McCartney DG, Price TS, Shipway PH (2011) Study on process optimization of cold gas spraying. J Therm Spray Technol 20:608–620. https://doi.org/10.1007/s11666-010-9564-2

Tutunea-Fatan OR, Fakhri MA, Bordatchev EV (2011) Porosity and cutting forces: from macroscale to microscale machining correlations. Proc Inst Mech Eng Part B J Eng Manuf 225:619–630. https://doi.org/10.1177/2041297510394057

Vilardell AM, Cinca N, Concustell A, Dosta S, Cano IG, Guilemany JM (2015) Cold spray as an emerging technology for biocompatible and antibacterial coatings: state of art. J Mater Sci 4441–4462. doi:https://doi.org/10.1007/s10853-015-9013-1

Villa M, Dosta S, Guilemany JM (2013) Optimization of 316L stainless steel coatings on light alloys using cold gas spray. Surf Coat Technol 235:220–225. https://doi.org/10.1016/j.surfcoat.2013.07.036

Villafuerte J (2015) Using cold spray to add features to components. http://www.coldsprayteam.com/files/Villafuerte%20CSAT%20using%20CS%20to%20add%20features.pdf. Accessed 27 Oct 2016

Widener CA, Carter MJ, Ozdemir OC, Hrabe RH, Hoiland B, Stamey TE, Champagne VK, Eden TJ (2016) Application of high-pressure cold spray for an internal bore repair of a navy valve actuator. J Therm Spray Technol 25:193–201. https://doi.org/10.1007/s11666-015-0366-4

Xiong Y, Zhuang W, Zhang M (2015) Effect of the thickness of cold sprayed aluminium alloy coating on the adhesive bond strength with an aluminium alloy substrate. Surf Coat Technol 270:259–265. https://doi.org/10.1016/j.surfcoat.2015.02.048

Yandouzi M, Gaydos S, Guo D, Ghelichi R, Jodoin B (2014) Aircraft skin restoration and evaluation. J Therm Spray Technol 23:1281–1290. https://doi.org/10.1007/s11666-014-0130-1

Yin S, Wang X, Li W, Liao H, Jie H (2012) Deformation behavior of the oxide film on the surface of cold sprayed powder particle. Appl Surf Sci 259:294–300. https://doi.org/10.1016/j.apsusc.2012.07.036

Yin S, Suo X, Su J, Guo Z, Liao H, Wang X (2013) Effects of substrate hardness and spray angle on the deposition behavior of cold-sprayed Ti particles. J Therm Spray Technol 23:76–83. https://doi.org/10.1007/s11666-013-0039-0

Yin S, Liu Q, Liao H, Wang X (2014) Effect of injection pressure on particle acceleration, dispersion and deposition in cold spray. Comput Mater Sci 90:7–15. https://doi.org/10.1016/j.commatsci.2014.03.055

Yin S, Suo X, Xie Y, Li W, Lupoi R, Liao H (2015) Effect of substrate temperature on interfacial bonding for cold spray of Ni onto cu. J Mater Sci 50:7448–7457. https://doi.org/10.1007/s10853-015-9304-6

Yin S, Xie Y, Cizek J, Ekoi E, Hussain T, Dowling D, Lupoi R (2017) Advanced diamond-reinforced metal matrix composites via cold spray: properties and deposition mechanism. Compos Part B Eng. https://doi.org/10.1016/j.compositesb.2017.01.009

Chapter 7
Advances in Titanium on Aluminium Alloys Cold Spray Coatings

Felice Rubino, Valentino Paradiso, Antonello Astarita, Pierpaolo Carlone, and Antonino Squillace

7.1 Introduction

Titanium and titanium alloys are widely employed in the aeronautic industry, due to high specific mechanical properties, corrosion resistance and compatibility with carbon fibre-reinforced plastics (Boyer et al. 1994). Despite of these advantages, high costs and other manufacturing issues pose severe limitations to massive use of titanium alloys. A great deal of attention is currently focused on the possibility to realize titanium coatings on aluminium components to achieve a satisfactory trade-off between the aforementioned features. Thermal spray processes (TSP), such as flame, arc, plasma and high velocity oxygen fuel spraying, already provided good results for some applications (Sampath et al. 2004); however, their feasibility appears quite limited in the considered sectors. Indeed, aluminium alloys used in aeronautics are generally heat treatable and typically age-hardened, whereas the ageing temperature is easily approached and overcome using TSP (Pawlowski 2008). Moreover, some problems related to coating porosity, oxidation and unsatisfactory adhesion are still unsolved (Astarita et al. 2013a, b). Cold gas dynamic spray (CGDS) process has been recently recognized as an effective technology to deposit titanium coatings on aluminium alloys (Irissou et al. 2008; Goyal et al. 2012a, b; Champagne and Helfritch 2014; Vuoristo and Koivuluoto 2014; Bala et al. 2014; Li et al. 2014). A low-pressure cold spray apparatus was employed to deposit titanium grade 2 powders an aluminium alloys substrate. Design of experiments approach

F. Rubino (✉) • V. Paradiso • P. Carlone
Department of Industrial Engineering, University of Salerno,
Via Giovanni Paolo II, 84084 Fisciano, SA, Italy
e-mail: frubino@unisa.it; vaparadiso@unisa.it; pcarlone@unisa.it

A. Astarita • A. Squillace
Department of Chemical, Materials and Industrial Production Engineering,
University of Naples Federico II, P. Tecchio 80, 80125 Naples, Italy
e-mail: antonello.astarita@unina.it; squillac@unina.it

P. Cavaliere (ed.), *Cold-Spray Coatings*,
https://doi.org/10.1007/978-3-319-67183-3_7

and ANOVA analysis were used to assess the influence of process parameters on the properties of coatings and the features of post-deposition manufacturing.

The first section (paragraph 7.2) is focused on the study of the deposition process, the optimization of process parameters that mainly affect the properties of the coatings (i.e. scan speed, standoff distance as well as temperature of carrier gas (helium)) and the analysis of the outcomes. A low-pressure cold spray apparatus was employed to deposit titanium grade 2 powders. Design of experiment approach and ANOVA analysis were used to evaluate the influence of process parameters on physical and mechanical properties of coatings and deposition efficiency. The optimal parameters configuration was also assessed. Experimental results pointed out that both the morphology of the coating and the deposition efficiency are mainly influenced by scan speed and SoD. On the other hand, the temperature affects the hardness and the density of titanium layer.

The second section (paragraph 7.3) is focused on the post-deposition surface treatment on the cold-sprayed titanium coating. The aim is to evaluate the feasibility of laser treatment to produce a dense layer of titanium oxide on the coating in order to improve the surface properties of coating itself, like hardness, wear and corrosion resistance, avoiding the extreme temperatures that could jeopardize the properties of the aluminium alloy substrate. Several processing conditions were tested to evaluate the influence of heat input and dimensional features of coatings on the treated samples following a DOE approach. The analysis of mechanical properties and the surface morphology allowed identifying the optimal processing window taking into account the restriction posed by the low ageing temperature of aluminium alloy. A numerical model was implemented to simulate the laser treatment in order to assess the thermal status established during the process and describe the occurred phenomena. The outcomes have been matched with the experimental results.

The modifications of wear properties of titanium coating induced by the laser treatment were also evaluated. A comparison of wear loss and friction coefficient between aluminium alloy sheet, bulk titanium grade 2, as-deposited cold-sprayed powders and laser-treated coating was performed to assess the influence of laser treatment on tribological behaviour of titanium coating and the effectiveness of the process.

7.2 Cold Spray of Titanium Powders on Aluminium Alloy Substrate

The knowledge of the deposition profile related to the thickness and roughness of the coating is of the utmost importance for the manufacturing. The two most important coating features for a single-pass deposition are the maximum height and the width of the strip of applied coating. The width influences the number of sweeps needed to coat the whole surface, and it is essential to evaluate the deposition rate and coating porosity. This paragraph summarizes the results of previous studies that dealt with the connection between deposition parameters and coating profile as well as the

relationship between the coating thickness and the distance from the nozzle axis. Furthermore, it reports a set of formulas that allow expressing the profile as function of the process parameters. The most recent studies were carried out by using microcrystalline commercial pure titanium grade 2 (density = 4.51 g cm^{-3}) obtained by ball milling and plates of AA 7075-T6 as substrate. Further details concerning the experimental campaign can be found in literature (Prisco et al. 2016). A factorial design was used to study the effects of standoff distance (SoD), gas inlet temperature (*T*) and gun speed (GS) on the morphology of the deposited layer. The relevance of these parameters for cold spraying of Ti was evaluated by measuring the thickness or height (*H*), width (*B*), porosity (*P*) and deposition efficiency (DE) of the coatings obtained. Three different levels for *T* and GS and four different SoD distances were selected, and as a result there are $3^2 \cdot 4 = 36$ different experimental set of parameters. The main results are here reported. The porosity, DE, coating width and height as function of the SoD are shown in Fig. 7.1. The data points reported are the average over four replicates, with the following code adopted: black, red and blue for coating obtained at 300, 400 and 500 °C, respectively, and circle, triangle and square for coatings obtained at gun speed equal to 5, 7.5 and 10 mm/s, respectively. It is evident that the porosity, DE and *H* as function of SoD show a common trend, namely, they present a maximum, in the case of *P*, or a minimum, in the case of DE and *H*, at around 12 mm of SoD. Differently, the coating width, *B*, only increases with the SoD and is (except for the shortest SoD and lowest temperature) always larger than the projection of the nozzle exit section (see Fig. 7.1c).

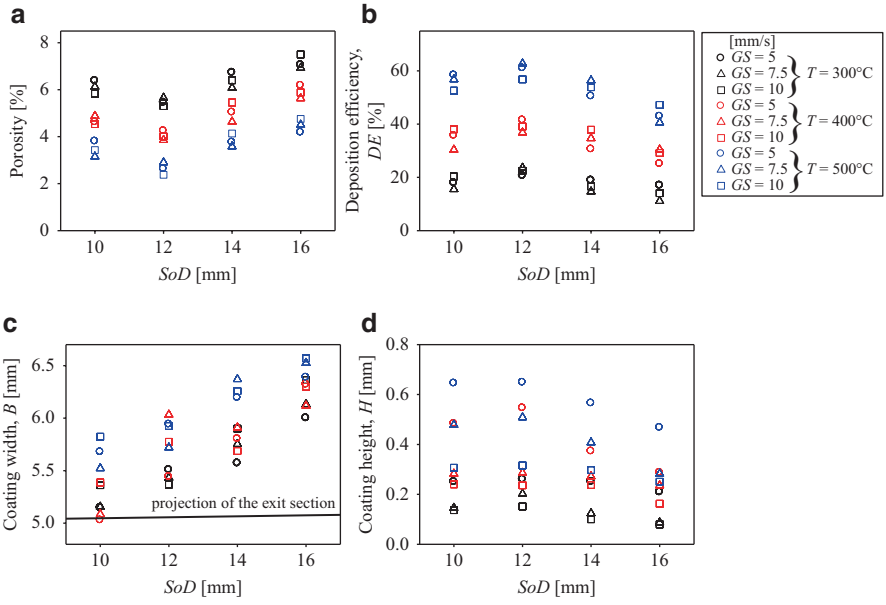

Fig. 7.1 (**a**) Coating porosity, (**b**) deposition efficiency, (**c**) coating height and (**d**) width versus the SoD at different temperatures and gun speed (each plotted point is the average over four measurements)

During the process, the particles are accelerated and heated through the converging-diverging nozzle by the preheated and compressed carrier gas. When the resultant supersonic jet is discharged into the external atmosphere, the consequent turbulent mixing and dragging with the still air produces an intense jet spreading which soon increases its diameter to a value larger than the projection of the exit section of the nozzle. Moreover, the turbulent mixing generates a profile of velocity and temperature along the jet radius in function of the distance from the nozzle exit. Consequently, the sprayed particles are scattered around the nozzle axis over the entire section of the discharging jet, and their in-flight velocities can increase or decrease depending on their inertia and their radial distance from the jet centreline (e.g. small particles in the peripheral part of the jet are decelerated immediately after they exit from the nozzle, while big particles can keep their exit velocity for a longer distance due to their larger inertia).

The in-flight temperature of the particles also varies with the distance downstream from the nozzle, due to their thermal inertia and radial position (e.g. particles at the peripheral part are cooled down by the lower temperatures of the driving gas in this zone). The particle dynamics is complicated by the effect of the bow shock deceleration on the sprayed particles. To this regard, Grujicic et al. (2004) demonstrated that the deceleration effect is dependent on the thickness of the stagnant region due to the impingement of the supersonic jet on the perpendicular substrate for small nozzle-to-plate distance. In addition, Prisco (2015) showed that thickness decreases linearly with the SoD and increases with the exit Mach number. However, it was demonstrated that only particles smaller than around 10–15 μm are appreciably decelerated by the stagnation bubble under usual CGDS conditions. In particular, employing the data about the bow shock height as function of the SoD presented by Pattison et al. (2008), Prisco (2015) found out that over a certain value of SoD, there is no stagnation bubble and that distance is a function of the Mach number and carrier gas density at exit. These limit values of the SoD slightly decrease with the inlet temperature of the carrier gas, because it strongly depends on the carrier gas density at exit, which drops as the preheating temperature rises. The final effect of all these phenomena is the development of size-dependent distributions of particles velocity and temperature at impact. In particular, Prisco (2015) showed that the size-dependent distribution of impact velocity, starting from a small value of SoD, first raises because the height of the stagnation bubble and consequently its deceleration capability then decreases and lowers due to the effect of the increasing distance of the substrate. On the contrary, the size-dependent distribution of temperatures always lowers with the SoD, because particles cool down more and more with the increase of the flight distance. As said before, smaller particles are more strongly affected by these effects. To complicate the picture, these distributions are a function of the radial position from the jet centreline. Only the particles with an impact velocity higher than a threshold value, called critical velocity, achieve the required conditions for successful bonding with the substrate. The critical velocity is strongly dependent on the impact temperature, in particular decreases with this temperature. Summarizing, with the increase of the SoD the impact velocity first increases, reaching a maximum when the deceleration effect of the bow

shock is nullified, and then decreases. Otherwise, the impact temperature always decreases with the SoD. Smaller particles are more subjected to these phenomena. The previous discussion can explain the trends observed in Fig. 7.1. Indeed, coating properties related to a better packing, as DE and *H*, increase with the impact velocity and temperature. Then, the dependence on the SoD of these properties is expected to follow the dependence of the impact velocity, i.e. first increases and then decreases. Differently, because *P* is lowered by a better packing, it is forecast to decrease with the impact velocity and temperature and then to show a minimum with the SoD. The minimum coincides with the SoD that maximizes the impact velocity. Previous studies revealed that the volume fraction of pores in cold sprayed deposits decreases with the increase of the particle velocity at impact, because a high velocity is essential to achieve the necessary plastic deformation needed to minimize the porosity (Zahiri et al. 2009). Taking into consideration the size-dependent distribution of impact velocity above discussed, the relation between porosity and SoD is clearly understood. The porosity first decreases with the SoD, due to the increasing of the mean impact velocity and of the percentage of small particles that exceed the critical velocity. Then it increases because the mean impact velocity distribution at impact lowers due to the increasing distance of the substrate and especially small particles (with diameter lower than 10–15 μm) are unable to bond with the layer. However, the decrease in porosity is due to two different effects: the reduction of the impact velocity and the cooling of the particles at impact. Zahiri et al. (2009) showed that powders with small particle size lead to a decrease in volume fraction of porosity so confirming the importance of the small size particles in reducing the porosity. Increasing the gas inlet temperature causes a higher impact velocity and temperature, which have a positive effect on reducing the coating porosity. This effect for Ti powder deposition was already observed by Goldbaum et al. (2011) and by Yin et al. (2014) who showed that an increase in gas inlet temperature leads to a decrease in porosity. Their observations are confirmed by the data in Fig. 7.1a. The same features are observed for the DE. The only difference is that DE reaches its maximum when the deceleration effect of the bow shock reaches its minimum. Therefore, when the porosity is at its minimum, a maximum for DE is expected. Naturally, a further increase in the SoD determines a decrease of the DE. This decrement is again ascribable to the decrease of impact velocity and temperature for values of SoD larger than the one nullifying the stagnation bubble. Lima et al. (2002) also observed that the DE improves with the impact velocity. The same behaviour is expected for the coating height, reported in Fig. 7.1d. Indeed *H* is straightforward related to DE and porosity. The height presents a maximum for a SoD of 12 mm and then gradually decreases. *H* increases with the gas inlet temperature; in particular this effect was described by (Steenkiste et al. 1999) who reported that the thickness increases with the inlet temperature, a result also confirmed by (Cinca et al. 2010), who showed that an increase in temperature produces an increase in thickness.

It is the first time to the authors' knowledge that the effect of the stagnation bubble upon the coating characteristics is so clearly demonstrated by experiments. Previous studies probably failed in reporting this effect of the SoD on porosity, DE

and height because of the use of a too large spacing for the SoD. Among papers using CGDS conditions similar to the ones presently adopted in the deposition of Ti, Li et al. (2008) directly passes from a SoD of 10 to 30 mm, and Zahiri et al. (2009) directly started their study from a SoD of 20 mm, observing just an increase in P with the SoD. The coating widths B, reported in Fig. 7.1c, are always larger than projection of the nozzle outlet section, reported in the same figure as a continuous line. This is brought about by the spreading of the particles due to the turbulent mixing between the supersonic jet emerging from the nozzle and the external atmosphere, as described by Prisco (2015). This dispersion increases with the length of flight, so that B is expected to increase with the SoD. Prisco (2015) demonstrated that the jet spreading increases with the gas inlet temperature; hence B, having fixed all other parameters, rises with the inlet temperature. Indeed, in Fig. 7.1c, data at 500 °C are in general the highest ones. Likewise, Wu et al. (2005) observed that the width and thickness of the strips increase with the pressure and the temperature of the gas in deposition of Al-12Si powder. The jet spreading is practically negligible at 300 and 400 °C when the SoD is 10 mm, and the difference between the projected exit section and the measured B is almost zero. This difference reaches a maximum of around 1.5 mm at 500 °C and a 16 mm of SoD. In the range considered, GS did not have any influence on the DE, coating porosity and width, as shown in Fig. 7.1a–c because GS does not influence the impact velocity and temperature. On the contrary, Fig. 7.1d shows that GS is a parameter with a high effect on H as a decrease in GS is associated with an increase in the powder mass fed over the unit length of the substrate and, as a consequence, an increase of the coating height. The coating roughness is related to the velocity and temperature at impact due to the former being a function of the packing of the deposited particles. As consequence, the roughness decreases with the DE and then increases with higher velocity and temperature at impact. Figure 7.2, reporting S_a of all the produced coatings as function of the DE, clearly demonstrates this relation. The highest results of S_a are observed for the lowest DE, which were recorded at the largest spray distance and lowest

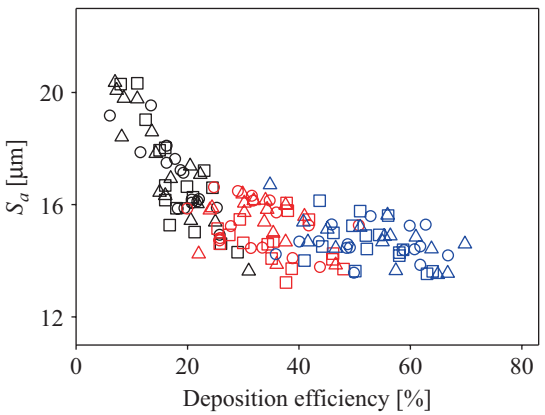

Fig. 7.2 Arithmetical mean height, S_a, versus the deposition efficiency

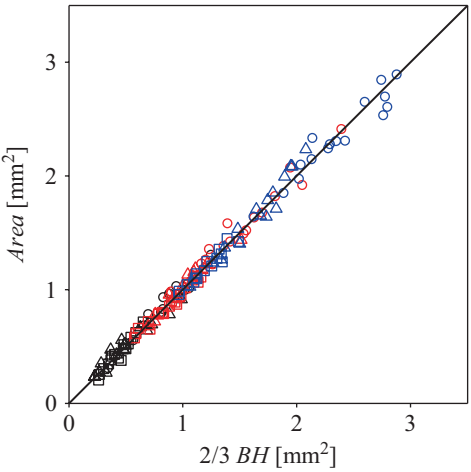

Fig. 7.3 Measured area versus $2/3\ B \cdot H$

temperature of the carrier gas. The plateau presented by the coating roughness for high value of the DE can be explained by the fact that it is not possible to drop below a limit value of roughness, which depends on the powder size distribution and is related to the attainment of the highest performances in term of powder compacting and particle flattening. The amount of data harvested enables to theoretically analyse the coating morphology. Taking into account the process parameters (PFR and GS) and some features of the deposited coatings (i.e. porosity, cross-sectional area), an analytical relation between these parameters and geometrical features (B and H) could be drawn (Prisco 2015):

$$\frac{\mathrm{PRF} \cdot \mathrm{DE}}{\mathrm{GS}} = \left(1 - P\right) \cdot \mathrm{Area} \cdot \rho_p \tag{7.1}$$

where

$$\mathrm{Area} = \frac{2}{3} BH \tag{7.2}$$

Equation (7.2), valid in the limit of $H << B$, relates the cross-sectional area deposited in one pass and the height and width of the coating. Equation (7.2) was checked plotting the measured cross-sectional area versus the area given by the equation (see Fig. 7.3). Data points line up along the bisector of the first quadrant with a coefficient of determination, calculated from this line, larger than 0.9. This testifies that Eq. (7.2) can be satisfactorily used to calculate the cross-sectional area of the deposit. It is very interesting to note that in Fig. 7.3 the largest deviation of the data points from the theoretical line is found for the highest values of H, for which corresponds the highest value of cross-sectional area.

A mathematical formulation of the profile deposited over the substrate as a function of the distance from the nozzle axis is presented in the following. Because the

profile is satisfactorily approximated by a circular arc, it is possible to express the height of the profile at a distance x from the symmetry axis. The relation between $h(x)$ and x can be expressed as a function of DE, GS and P:

$$h(x) = \frac{3}{2}\frac{\text{Area}}{B}\left(1 - 4\frac{x^2}{B^2}\right) = \frac{3}{2}\frac{\text{PRF}\cdot\text{DE}}{\text{GS}\cdot(1-P)\rho_p B}\left(1 - 4\frac{x^2}{B^2}\right) \tag{7.3}$$

In Eq. (7.3), the only terms that need to be measured are B and DE, while all other parameters are chosen in advance. Because the thickness of the coating is the output of the process to be controlled and because the thickness is directly correlated to H, Eq. (7.3) allows the optimization of the cold spray process by means of a few calibration experiments without needing the manufacturing prototypes.

7.3 Post-deposition Laser Treatment Processing

One main drawback of the use of the cold spray process is related to the microporosity induced within the coating layer that negatively affects the performance of the titanium layer as corrosion barrier (Hussain 2013; Hussain et al. 2011). A recent study discussed the capabilities of post-deposition laser remelting treatments to compensate some process drawbacks (Marrocco et al. 2011), reducing coating porosity and improving its corrosion resistance. However, the high heat input required to melt titanium particles may result in excessive temperature increase even in the substrate, making it difficult to perform the treatment assuming this specific material pair. Previous papers demonstrated that laser treatment can also promote the formation of a harder superficial oxidized layer (Bell and Dong 2000; Rubino et al. 2016), whereas experienced temperature represents a key factor to promote the formation of oxides with good mechanical properties and satisfactory adhesion to the substrate (Marrocco et al. 2006). In this paragraph, feasibility and effects of post-deposition laser treatment on grade 2 titanium cold-sprayed layer deposited on an aluminium alloy AA2024-T3 substrate are debated. The aim of the laser treatment is to promote the formation of a titanium oxide layer on the deposited coating. Indeed titanium exhibits high reactivity with the oxygen at elevated temperature, and consequently high temperature holding of titanium in air induces rapid oxidation and formation of thick scale on the hard diffusion layer. This oxide layer is harder than the base material and has better corrosion and wear resistance with respect to bulk titanium (Chaze and Coddet 1986; Frangini et al. 1994). The challenge of this process is to avoid exceeding the ageing temperature of AA2024-T3 (approximately 473 K (200 °C)), which poses hard constraints on the processing window. Several processing conditions were analysed varying the laser heat input and the thickness ratio, TR (defined as the ratio between the coating thickness and the substrate thickness), in order to investigate the effectiveness of laser treatment and evaluate the better process parameters configuration (Rubino et al. 2016). A

numerical model of the laser treatment was employed to assess the temperature distributions established during the laser treatment. The outcomes were discussed and compared with the experimental results. The wear properties of the treated coatings were also studied and discussed. Titanium and its alloys exhibit low tribological properties, but their wear resistance can be improved by surface treatments promoting growth of the surface hardness, leading to changes of the wear mechanism and lowers the wear rate (Bloyce et al. 1994). Frictional contact of titanium alloys both against other materials and titanium alloys themselves, especially under pure sliding conditions, quickly damages the contact surface area and results in the transfer of some particles of the material to the counter face (Bell and Dong 1998; Dong and Bell 1998). Titanium and its alloys are characterized by a high and unstable friction factor, strong adhesion wearing and high tendency to seizure (localized damage due to the diffusion welding between sliding surfaces (ASM Handbook, 1992) and scuffing (damage characterized by surface unevenness and asperities called hillocks (Astarita et al. 2013a, b)). A couple of papers dealing with the tribological properties of cold-sprayed titanium coatings (Kataria et al. 2010; Khun et al. 2015) are also available in literature, but, to date, the coupling between cold-sprayed coating and laser treatment has not been studied and understood. Tribological characteristics of titanium alloys can be improved by different kinds of treatment. Cassar et al. (2012) proposed a triode plasma oxidation treatment on Ti-6Al-4 V, finding reduction in wear rate under a range of different wear test regimes. Wang et al. (2015) studied how different oxidation durations performed on Ti-6Al-4 V alloy affect its surface roughness and wear properties. The fretting tests performed revealed an improvement in fretting wear resistance after oxidation and an optimum time treatment equal to 4 h. Bell and Dong (2000) proved that the oxidation treatment of Ti-6Al-4 V resulted in a significant improvement in wear resistance, but there is no detailed analysis focusing on the application of the laser treatments on cold-sprayed coatings. Friction and wear properties of untreated aluminium sheets, titanium grade 2 sheet, as-sprayed titanium powders and laser-treated coating layer were compared in order to assess the effectiveness of treatment (Rubino et al. 2016; Sun et al. 2003; Astarita et al. 2015; Carlone et al. 2016).

The thermal model employed is based on the solution of an energy balance, using a finite volume approach in a Lagrangian framework. The heat generation rate related to deformation energy or chemical reactions was assumed as negligible, if compared to the laser heat input. Consequently, the conservation of the thermal energy for an isotropic material and neglecting transport phenomena can be expressed using the following equation:

$$\rho c \frac{\partial T}{\partial t} = \nabla \cdot \left(K \nabla T \right), \tag{7.4}$$

where T is the temperature, t is the time, ρ and c are, respectively, the temperature-dependent material density and specific heat capacity and K is the conductivity matrix. Material properties, initial and boundary conditions and other details about the numerical model were described in (Carlone et al. 2016).

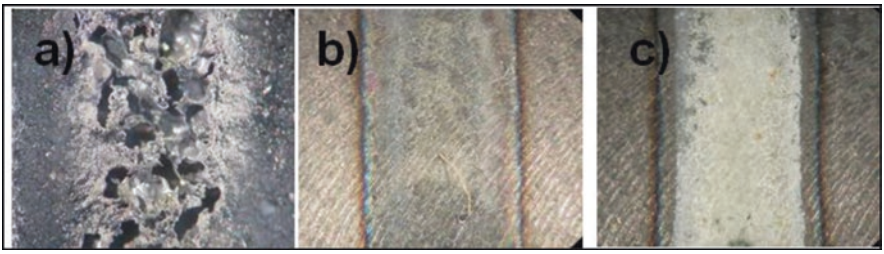

Fig. 7.4 Macrograph of the top surface of three representative tracks: (**a**) material loss, (**b**) ineffective treatment, (**c**) acceptable treatment

Preliminary macroscopical analysis of the treated surfaces and the cross sections highlighted three possible scenarios: (i) acceptable treatment, when an evidence of the direct rutile formation was found; (ii) ineffective treatment, when only a heat-affected zone in the coating, rather than the desired oxidization, was observed; and (iii) specimen damage. The damage of coating occurred according to two behaviours: material loss on top track surface, resulting in apparent macroporosities, and evident cracks on the titanium layer, suggesting the excessive tendency to catastrophic failure. The different colourations of the treated surface highlighted the occurrence of the three scenarios. The oxide colour is ruled by the temperature reached during the process, and colouration ranging from light blue (in correspondence of the lower temperatures achieved on the surface the lower heat input) to white (in correspondence of the higher temperatures the higher heat input) was observed. The track shown in Fig. 7.4c has a regular shape with a light grey colouration, indicating an acceptable treatment promoting the formation of a hard and dense oxide layer. Conversely, the track in Fig. 7.4a is not regular, and some cracks, craters and zones with different oxidations are appreciable. The blue-coloured oxide, in Fig. 7.1b, confirms the hypothesis of a low heat input during the laser post-treatment.

Microscopical observation of the polished and etched cross sections of these specimens (shown in Fig. 7.5) confirmed this trend.

The track in Fig. 7.5c (TR = 1, scan speed 12.5 mm/min) shows a very compact and dense oxide layer which penetrates deep into the titanium coating. The treatments made in the scan speed range from 50 to 400 mm/min led to superficial instability phenomena, which resulted in a loss of material, underlined by some craters on the surface (Fig. 7.5d). Track treated at 800 mm/min (or higher) does not show any remarkable modification of the titanium layer; oxide is confined to the surface and is a few micrometres thick. Concerning the surface quality of the coating, it is possible to observe, for test case C (TR << 1), that tracks treated using scan rate lower than 50 mm/min are not acceptable. Indeed, in these conditions, the high heat input coupled with the low thickness of the coating produced a thick and very brittle oxide layer. As a consequence, a discontinuous layer of oxide characterized by lack of cohesion with the underlying material can be observed (Fig. 7.5f). On the other hand, tracks obtained adopting scan rates equal to or higher than 50 mm/min present a regular shape with a white colouration. Figure 7.5g shows the micrography of

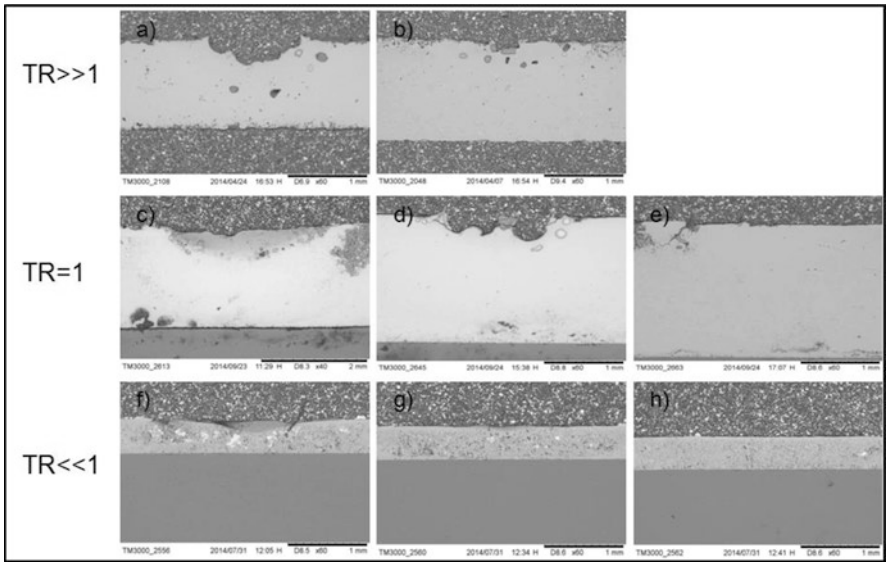

Fig. 7.5 Cross sections of selected tracks realized using scan speed equal to (**a**) 200 mm/min, (**b**) 800 mm/min, (**c**) 12.5 mm/min, (**d**) 100 mm/min, (**e**) 800 mm/min, (**f**) 12.5 mm/min, (**g**) 50 mm/min, (**h**) 400 mm/min

track obtained in the scan speed range from 50 to 200 mm/min. The oxide layer has small thickness, but covers uniformly the underlying titanium coating. For scan speeds equal to or greater than 400 mm/min, the heat input appears too low to provide an effective and acceptable surface treatment. The analysis evidenced that acceptable treatments can be achieved using different processing conditions depending on the geometrical configuration.

Computational simulations evidenced that temperature distributions typically observed in laser processing were established in the coating layer. Numerical outcomes pointed out the relevant role played by thickness ratio and the presence of the substrate material on the predicted thermal peak at the centre of the irradiation line (Fig. 7.6). Indeed, the substrate dissipated the heat away from the titanium layer, lowering the temperature experienced by coating itself. As expected, increasing the scan speed, a reduction of the maximum temperature was predicted. It is worth noting that in some cases a dominant role was played by the sink effect of the aluminium substrate rather than by the heat input.

The same figure summarizes results for all the treated samples, including also some representative microscopical observations of the cross sections. As evidenced, successful treatments were achieved using different processing parameters depending on the geometrical configuration.

In particular, acceptable treatments were observed for test case B (TR = 1) adopting low scan speed (12.5 mm/min). In this case, the temperature peak was estimated as about 983 K (710 °C) that is sufficient to promote the direct rutile formation.

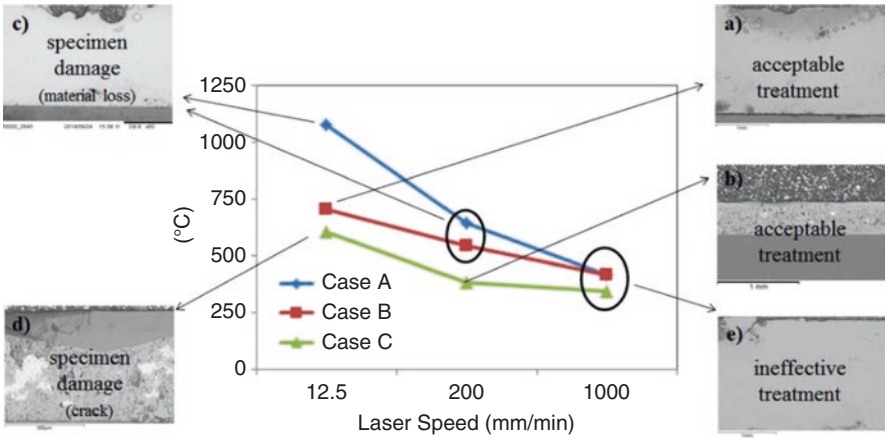

Fig. 7.6 Numerically predicted temperature peaks and summary of experimental outcomes

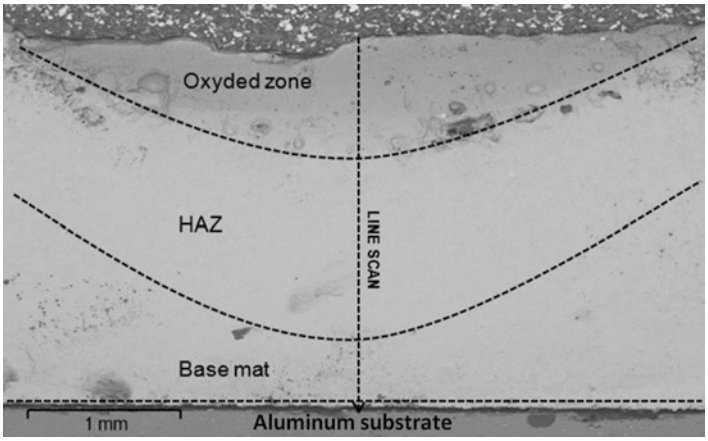

Fig. 7.7 Cross section of laser-treated specimen (magnification 60×)

Moreover, heat conduction inside the titanium coating happened on a time scale comparable with the laser spot movement, reducing thermal gradients and crack nucleation, while the sink effect played by the aluminium substrate contributed to avoid coating overheating. The obtained track was characterized by an apparent compact and dense oxide layer, which penetrates deep into the titanium coating, as visible in Fig. 7.6a. Micrographies of laser-treated specimen (Fig. 7.7) show a dense titanium oxide layer produced on the surface of the titanium coating. In the centre of the treated sample, the oxide penetrates the coating up to about 30% of its thickness. Below the oxide layer, the heat produced by laser source caused the formation

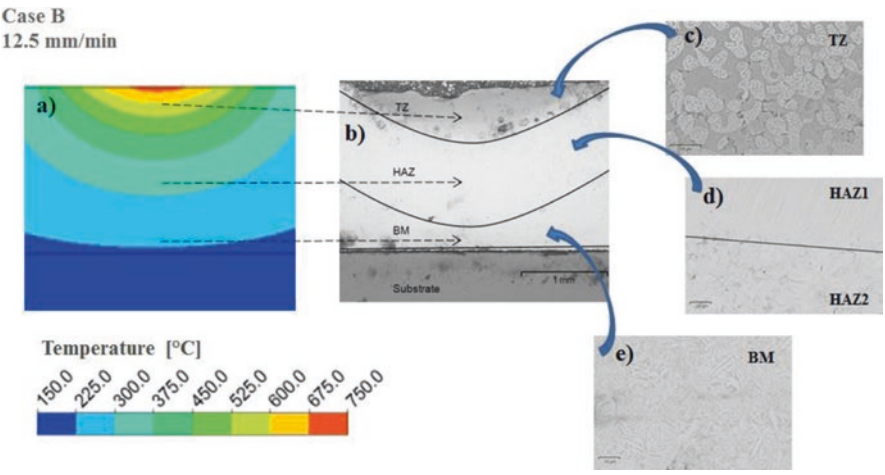

Fig. 7.8 Predicted temperature distributions and microstructures

of a heat-affected zone, characterized by a microstructure with coarser grain than the material base. In the discussion, the following terms will be used to identify the different metallurgical zones:

(i) Oxidized zone is the region of the cold-sprayed layer that was oxidized by the laser treatment.
(ii) Heat-affected zone, similarly to what happens in laser beam welding, is the region of the cold-sprayed layer that was affected by the heat generated during the treatment.
(iii) Base material is the region of the cold-sprayed layer that was not affected by the laser treatment.
(iv) Substrate is the aluminium plate used as substrate for the deposition process.

The final microstructure of each zone was established by the maximum temperature achieved during the process, as highlighted by the contour plot of the numerically predicted temperature distribution (Fig. 7.8a). In Fig. 7.8c the microstructure observed in the TZ, reflecting the typical microstructure of the titanium oxide, is reported. Figure 7.8b shows a micrograph of the HAZ. Interestingly, two different heat-affected zones, namely, HAZ1 and HAZ2, are observable. The microstructure of HAZ1 is characterized by lamellae of coarser dimensions due to grain growth phenomena, promoted by the heat provided during laser treatment. The microstructure of HAZ2 is characterized by almost equiaxed and smaller grains with respect to HAZ1, in agreement with the literature and the physical phenomenon occurring during titanium laser processing (Selvan et al. 1998). Finally, Fig. 7.8e shows a micrograph of the BM, characterized by a fully lamellar microstructure, with very thin lamellae.

Acceptable treatments were also achieved for test case C, using relatively higher scan speed (200 mm/min), if compared to the aforementioned sample. In this case,

the laser treatment promoted the oxide formation on the surface and the establishment of a TZ; however, TZ extent was limited to a very thin surface layer, due to the low heat input provided during the process (Fig. 7.6b). Results obtained in test case A (TR >> 1) appeared strongly conditioned by the absence of the aluminium substrate (Fig. 7.6c).

Indeed, the less effective heat dissipation from the bottom surface of the coating, towards the substrate material and then the ambient, leaded to a heat concentration into the titanium layer. As a consequence the peak temperature resulted the highest detected in this campaign (approximately 1353 K (1080 °C)), assuming 12.5 mm/min as scan speed. This setup induced significant material loss from the irradiated surface and the subsequent formation of spherical craters distributed along the entire length of the treated track. For test case C, the sample treated using scan speed lower than 200 mm/min was not acceptable due to internal damage of the coating. Indeed, in these conditions, the high heat input coupled to the low thickness of the coating produced a thick, but hard and brittle, oxide layer (as also observed in test case B using the same irradiation rate but in presence of the aluminium substrate). However, the subsequent dimensional mismatch between the oxide and the base material, in conjunction with the relatively higher thermal gradients, promoted the formation of evident cracks, resulting into a discontinuous layer of oxide, without satisfactory cohesion with the underlying material (Fig. 7.6d). Further investigations are in progress to rigorously define mechanisms and conditions inducing specimen damage. In authors' opinion, being observed damages mainly attributable to thermal gradients and properties' variations, the implementation of a thermomechanical model of the process could provide a better understanding of the process (Carlone et al. 2008; Hodge et al. 2014). Tracks treated at 1000 mm/min did not show remarkable modification of the titanium layer independently of the thickness ratio. In these cases, the residence time at elevated temperature did not appear as sufficient to promote the direct rutile or anatase formation. The only significant effect of the laser treatment at high speed was the creation of a heat-affected zone, as discussed in what follows (Fig. 7.6e). The extension of the treated zone (TZ) and heat-affected zone (HAZ) was quantified by means of an image analysis software, in terms of maximum width and maximum depth of the affected zones. Obtained results, limited to samples classified as acceptable, are given in Table 7.1. The extension of the treated zone increases with the decrease of the scan rate, i.e. with the increasing of the heat input. Also the TR was found to directly influence the TZ extension. Decreasing the TR, the amount of heat transferred from the coating layer

Table 7.1 Measurements of the treated and affected zone extension

Test case	Scan speed (mm/min)	Max width (mm)	Max depth (mm)
B	12.5	4.23	1.49
	25	4.17	1.38
C	50	2.16	0.27
	100	1.84	0.26
	200	2.1	0.24

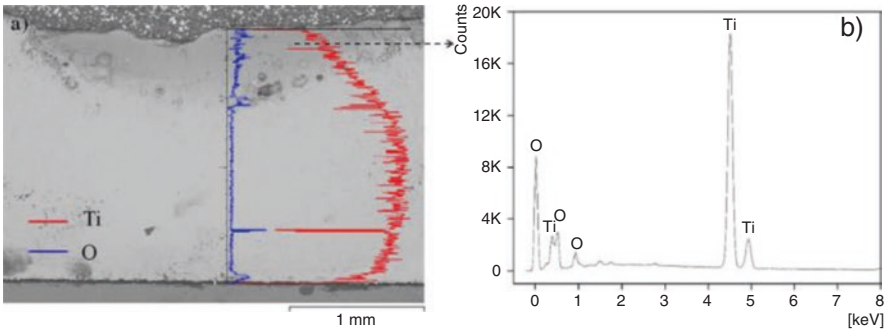

Fig. 7.9 Results of the EDS analysis for case B and v = 12.5 mm/min: (**a**) EDS spectrum through the thickness line scan, (**b**) titanium and oxygen intensities in the TZ

to the substrate increases, lowering the temperature experienced by the titanium layer and reducing the affected area. In other words, decreasing the TR induces the same effect as reducing the heat input.

EDS analysis, carried out through the thickness of the coating, demonstrated an enrichment in oxygen content in proximity of the irradiated surface (Fig. 7.9). The TZ is composed by titanium and oxygen with an atomic fraction (Ti ≈ 37%; O ≈ 63%) corresponding to the stoechiometric composition of the titanium dioxide TiO_2.

The oxygen atomic percentage reached the maximum value in the TZ; then it decreases moving from the surface to the inner layers of the coating. At the interface with the AA2024 substrate, the atomic fractions of Ti and O approached the composition of the BM. Rutile formation in samples corresponding to case B (12.5 mm/min) and case C (200 mm/min) was confirmed by the XRD analysis, as depicted in Fig. 7.10. XRD spectra were acquired using distinct diffraction angles, i.e. at different distances from the top surface. As can be seen, typical rutile peaks were found at the irradiated surface in the aforementioned test case, while a mixture of rutile and other titanium oxides were observed in the inner layers of the treated zone. At higher scan speed, the ineffectiveness of treatment was confirmed by the absence of rutile peaks in the XRD spectra acquired on the coating surface (Fig. 7.10). The suitability of laser treatments to promote rutile formation on titanium surface was proved also in (Marrocco et al. 2011). However, in that case, a laser process was used to achieve the microstructure alteration of the titanium coating on a carbon steel substrate. Obtained outcomes clearly demonstrate that a compact and dense rutile layer can be induced at the surface of the coating also without titanium melting, which requires higher temperature affecting also the aluminium temper state. Oxide formations were found to be consistent with the numerically computed transient temperature profiles, depicted in Fig. 7.11. As can be seen, in case B, adopting 12.5 mm/min as laser velocity, the material in correspondence of the centre of the irradiated surface (point A) experienced a significant temperature increase, exceeding 973 K (700 °C). In the TZ, a minimum temperature of approximately 673 K

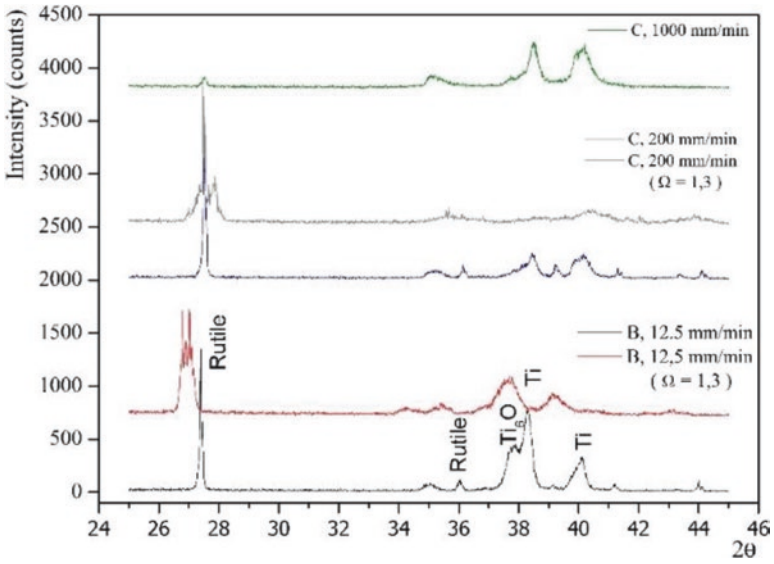

Fig. 7.10 X-ray diffraction spectra in treated samples

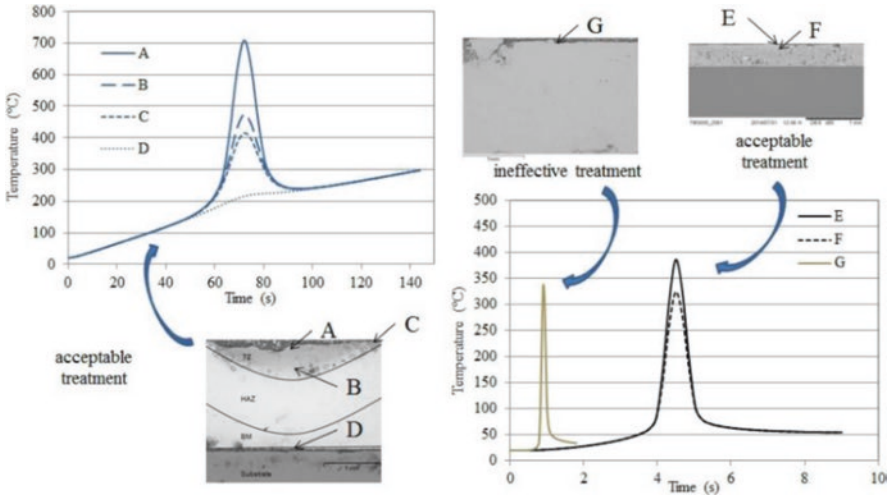

Fig. 7.11 Transient temperature profiles in test case B at 12.5 mm/min (*curves A, B, C, D*), test case C at 200 mm/min (*curves E, F*) and test case C at 1000 mm/min (*curve G*). All points were individuated in the cross section

(400 °C) was found. The variation of the temperature peak well justified the formation of distinct Ti-O compounds in different locations of this zone. Indeed, at higher temperature, a more evident rutile formation (as indicated by XRD spectra in Fig. 7.10) is expected, differently from the oxides mixture observed below the top

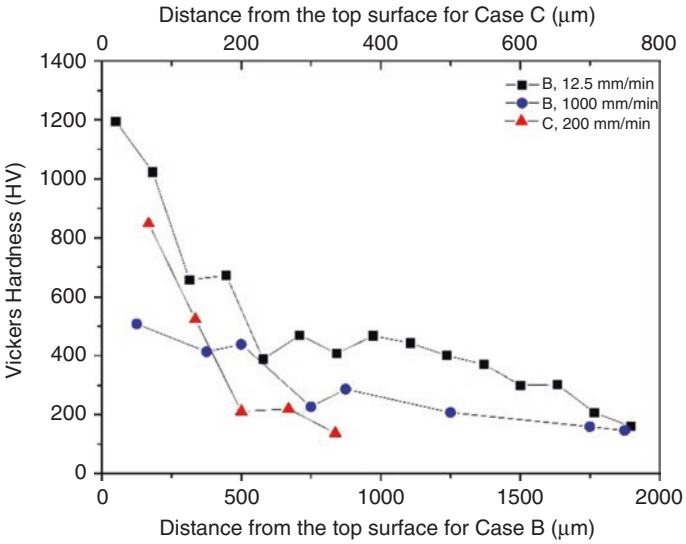

Fig. 7.12 Microhardness profiles in acceptable (case B 12.5 mm/min and case C 200 mm/min) and ineffective (case B – 1000 mm/min) treatments

surface (point B) and moving towards the edge of the laser spot (point C). Finally, point D, defined at the substrate-coating interface, evidenced the reduce heating of the aluminium. Similar considerations apply also to the other acceptable treatment (case C – 200 mm/min).

In this case, the relatively higher travel speed of the heating source, and the subsequent heat input reduction, implied a less pronounced temperature increase at the centre of the irradiated surface (point E), leading to a reduction of the rutile concentration with respect to what found in the same location in the afore-discussed case. Furthermore, the extension of the TZ, i.e. the penetration of the treatment, appeared significantly reduced, being the temperature peak slightly major than 573 K (300 °C) only 0.1 mm below the top surface. As can be seen, assuming 1000 mm/min as laser speed, the residence time at elevated temperature (less than 0.05 s above 573 K (300 °C)) was not sufficient to induce a significant rutile or anatase formation (see Fig. 7.10), providing an ineffective treatment.

Microhardness measurements were performed starting from the oxide layer on the surface of the specimen towards the interface with the aluminium substrate. In Fig. 7.12, Vickers hardness profiles are plotted as a function of the distance from the irradiated surface for three representative samples. As far as acceptable treatments are regarded, hardness values ranging from 700 to 1200 HV were detected, consistently with the rutile formation on top of the coating (Hanaor and Sorrell 2011). A hardness decrease, to approximately 400 HV, was found in the HAZ, indicating the presence of distinct Ti-O compounds. Finally, typical values of as-sprayed titanium (200 HV) were detected in the base material.

At relatively higher scan speed (1000 mm/min), the temperature experienced by the material and the residence time were not sufficient to promote direct anatase or rutile formation, as confirmed by the lower hardness values as well as XRD spectra. In all samples, the aluminium sheet preserved its initial hardness (approximately 135 HV) after the treatment, proving that the temper state of the substrate material was not affected by the laser irradiation and confirming the selective nature of the performed treatment.

7.3.1 Wear Analysis

The main aim of the tribological tests was to evaluate the wear resistance of the materials. Tribological tests have highlighted that the laser treatment can significantly improve the friction and the wear resistance properties of titanium. In Fig. 7.13 the friction coefficient (CoF) progress of treated coating is compared to the cold-sprayed coating, titanium as well as the aluminium plate. The evolution of the friction coefficient is unsteady, and its variation is made of two terms: the trend and the fluctuations around the mean value. The trend is due to several phenomena as the reciprocal adjustment of surface asperities and the following alteration of the real contact area, inclusion of (micro) wear debris (Cassar et al. 2012) – third body wear – and increment of the contact temperature; the fluctuation around the mean is typical of the reciprocating test where the relative velocity is variable.

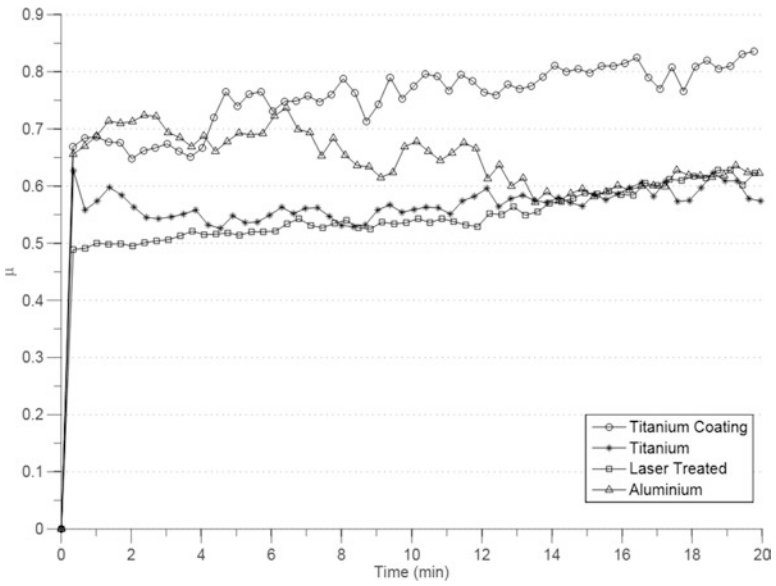

Fig. 7.13 Evolution of friction coefficients for the processed plates with time

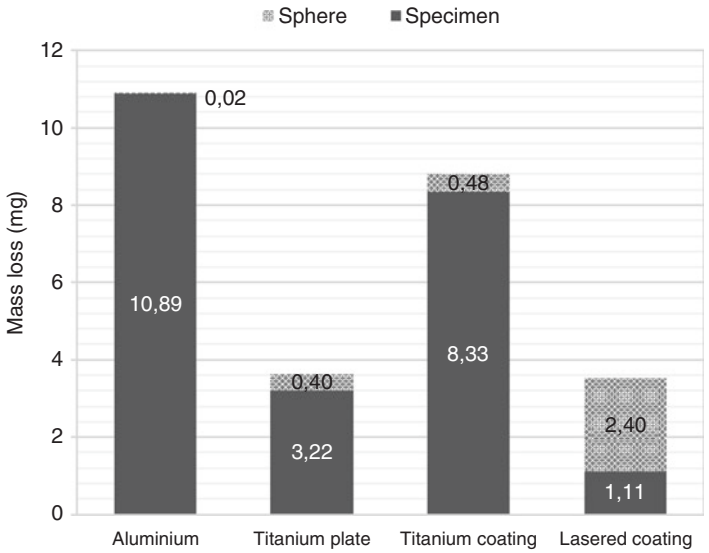

Fig. 7.14 Wear comparison in term of mass loss for the four processing methods

The tribopair couple aluminium plate vs. titanium ball (the latter, hereinafter, omitted for simplicity) presents a slightly increasing trend only after 14 min of test, where μ is nearby 0.60. For the titanium plate all along, the test μ was comprised in the range of 0.50–0.60, ending with a constant trend. In the case of the cold sprayed titanium coating, after 14 min, fluctuations are still noticeable due to the surface unevenness characterizing the as-sprayed coating and the friction coefficient; μ varies in the range of 0.75–0.85 showing also an increasing trend according to (Khun et al. 2015). The measured value CoF, after an initial peak, reached a steady-state value of approximately 0.78. Finally, the development of the laser-treated coating presents a rising trend, reaching – with small fluctuations – the value of 0.62. In Fig. 7.14 the results from gravimetric analysis are presented. Both the values of the specimen wear and the sphere wear are shown and summed up. Concerning the aluminium case, the wear of the ball was almost zero, whereas the flat sample lost a considerable quantity of mass. Laser-treated coating returned the highest wear of the ball with respect to the different tribopairs. On the other hand, this specimen lost very little mass. The overall wear of the tribopair for the laser-treated coating case is comparable to the one relative to the titanium plate; in the latter case though, the main loss was detected on the specimen side. The oxidation of titanium determined significant improvements in its tribological properties. The TiO_2 showed a smoother friction coefficient profile with less fluctuations and reached a lower value of μ compared to the titanium plate, which is characterized by an unstable CoF with evident fluctuations. The same behaviour happened for the cold sprayed coating. The improvements are also highlighted by the limited wear rate of oxidized coating (see Fig. 7.14), which is much lower than the as-sprayed titanium and titanium bulk

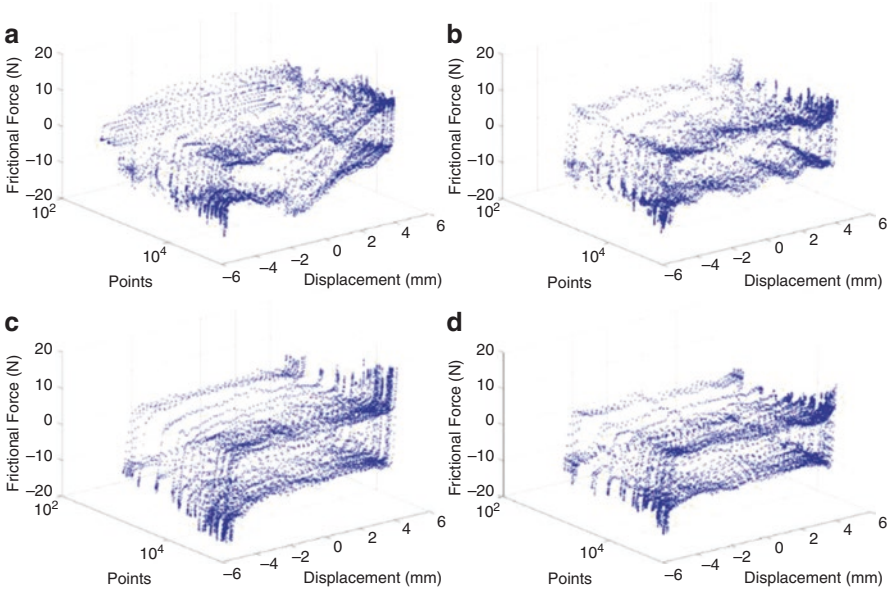

Fig. 7.15 Loop cycles of the frictional force for (**a**) aluminium, (**b**) titanium plate, (**c**) titanium coating and (**d**) laser-treated coating cases

material. Krishna et al. (2007) confirmed this behaviour. They supposed that the improvement in wear resistance is due to the high hardness of oxide layer and its strong adhesion with the underlying material. Dalili et al. (2010) confirmed the role played by the enhanced surface hardness resulted from the formation of a harder oxide layer and a thick oxygen-diffused zone in improving of wear resistance of titanium resulting in a lower friction coefficient and negligible weight loss. They supposed that the oxide layer prevents extensive plastic deformation of titanium changing the nature of the contact surface from ceramic/metallic pair to ceramic/metallic tribopair (Kim and Geringer 2012; Fouvry et al. 1995). The contribution of the rutile is fundamental in the improving of the wear properties of the titanium layer, layer is fundamental in the contribution of the rutile. In this regard, in his papers on the tribological properties of titanium (Sun 2004a, b), Sun proved that the improvement of the tribological properties of the titanium after the thermal oxidation treatment can be attributed to the formation of a rutile layer and also highlighted the correlation between the tribological properties and the characteristics of the rutile. In Fig. 7.15 the typical evolution of the frictional force during sliding is represented for each specimen type. During the inversion of the oscillating motion, the ball is temporary still, which leads to a force peak, corresponding to the static friction phase. The force rapidly decreases and is almost stable during the sliding moment, i.e. the kinetic friction. In the aluminium case (Fig. 7.15a), the cycles are quite irregular; this unpredicted behaviour can be, in first analysis, attributed to an uneven density of the specimen in proximity of the dead centres of the stroke. Also for the

titanium (Fig. 7.15b) in this case, the force has an irregular gait but exhibits the typical hysteresis shape proper of this evolution. More expressly, it has two peaks along the two dead centres, where the ball diverts its motion and, consequently, the friction switches from the kinetic to the static phase. The loop cycles of the last two instances, namely, the titanium coating (Fig. 7.15c) and the laser-treated coating (Fig. 7.15d), are outlined by a smooth hysteresis evolution. These cycles exhibit a regular and flat shape during the sliding of the ball, i.e. the kinetic phase. The values of the energy ratio evaluated all along the test confirmed the gross slip regime (wear-dominated regime), being always greater than 0.2, i.e. from a minimum of 0.3 to the maximum of 0.9

In Fig. 7.16 the images obtained from the topography acquisitions are displayed. The wear track on the aluminium plate (Fig. 7.16a) presents an uneven shape: it is nonsymmetric in respect to the Y-axes (perpendicular to the sliding direction). This observation is congruent with the friction loop cycles, which also exhibited an irregular profile. The wear track is deeper in proximity of the right dead centre, where, in fact, the frictional force was the highest: the maximum wear depth along the midline profile is equal to 470 μm – the deepest recorded among the specimens. The titanium plate exhibits also an irregular shape (Fig. 7.14b), with the deepest wear in proximity of the two dead centres of the ball – 120 μm for the left and 130 μm for the right. It is also noticeable, as red points of the contour image, an area of strong plastic deformation along the border of the wear track. In Fig. 7.16c the worn track of the titanium coating is displayed, and the profile is regular and smooth, presenting a maximum wear of 251 μm. This confirmed the poor resistance of cold sprayed coating against the counter sphere, which results in a higher weight loss of the coat-

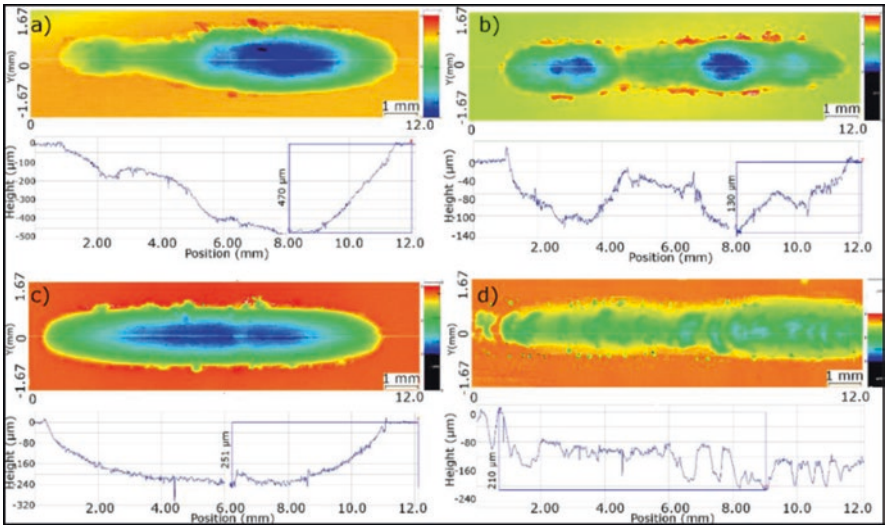

Fig. 7.16 Wear tracks (contours and midline profiles): (**a**) aluminium plate, (**b**) titanium plate, (**c**) as-sprayed titanium coating and (**d**) laser-treated titanium coating

ing itself compared to both titanium plate and oxidized layer (see Fig. 7.14). Figure 7.16d shows the topography images on the laser-treated coating worn surface. As expected the topography did not allow to have an unequivocal estimation of the wear depth, due to the irregular profile produced by the laser operation. As a consequence of this, the surface has an indented profile, and the worn area is distinguishable only thanks to the presence of a large boundary incision.

7.4 Conclusions

Concerning the study of the coating geometry, discussed in the first paragraph, it has been possible to relate the coating cross-sectional area to its height and width, Eq. (7.3). This equation permits to calculate the cross-sectional area by simple experimental measurements and, then, by mean of mass conservation law (Eq. 7.1), to link the DE and the porosity of the coating and to express them as a function of the process parameters. The use of this equation in a manufacturing environment requires only a few calibration tests to find the relation between B and SoD in contrast with the standard operating procedure that involves a lot of prototyping and trials. Furthermore, it has been shown that to reduce the coating roughness, a high deposition efficiency is needed and the latter is independent of the gun speed.

Selective laser treatment can be effectively used to improve surface properties of titanium cold-sprayed coatings, using suitable processing parameters. Scan rate and TR significantly influence the final results. The laser treatment produces a hard oxidized surface layer in the titanium cold-sprayed coating. The formation of rutile and anatase oxides was promoted under specific processing conditions. Three different microstructural zones are visible in the cross section of the irradiated material: TZ, heat-affected zone and base material. The temper state of the aluminium substrate was not affected during the process. Numerical results were consistent with experimental observation. The results of the wear tests are summarized as follows. Both coatings under investigation, the treated one and the untreated one, showed better wear performances relative to the untreated AA2024 alloy. In particular the laser-treated coating showed the best wear resistance, better than the bulk titanium. These enhanced properties can be attributed to the presence of a superficial hard oxidized layer produced by the laser treatment. The presence of this oxide layer was confirmed by the EDS analysis in which an increase in the oxygen content within the treated area was observed. The laser treatment influenced both the friction coefficient and the wear mechanism of the coating. The untreated coating showed an adhesive wear with a noticeable mass loss from the coating itself and a negligible wear of the ball. Abrasive wear mechanisms were observed testing the treated coating, with a negligible wear of the coating, but a severe wear and mass lost on the sphere.

References

ASM Handbook (1992) Materials for Friction and Wear Applications, Nonferrous Metals and Alloys: Friction and Wear of Titanium Alloy. In: Blau PJ (ed) ASM Handbook Volume 18: Friction, Lubrication, and Wear technology, 10th edn. ASM International, Materials Park, p 778. ISBN: 978-0-87170-380-4

Astarita A, Durante M, Langella A, Squillace A (2013a) Improving of steel superficial properties through thermal sprayed coatings. Int J Surf Sci Eng 7(4):366–381

Astarita A, Durante M, Langella A, Squillace A (2013b) Elevation of tribological properties of alloy Ti-6% Al-4%V upon formation of a rutile layer on the surface. Metal Sci Heat Treat 54(11–12):662–666. https://doi.org/10.1007/s11041-013-9567-y

Astarita A, Rubino F, Carlone P, Ruggiero A, Leone C, Genna S, Merola M, Squillace A (2016) On the improvement of AA2024 wear properties through the deposition of a cold sprayed titanium coating. Metals 6(8):185–197. https://doi.org/10.3390/met6080185

Bala N, Singh H, Karthikeyan J, Prakash S (2014) Cold spray coating process for corrosion protection: a review. Surf Eng 30(6):414–421

Bell T, Dong H (2000) Enhanced wear resistance of titanium surfaces by a new thermal oxidation treatment. Wear 238(2):131–137

Bell T, Dong H (1998) Tribological enhancement of titanium alloys. In: State Key Laboratory of Tribology (ed) Proceedings of the first Asian conference on tribology. Tsinghua University Press, Beijing, pp 421–427

Bloyce A, Morton PH, Bell T (1994) In: ASM International (ed) ASM handbook, vol 5. ASM International, Materials Park, pp 835–851

Boyer R, Collings EW, Welsch G (1994) Materials properties handbook: titanium alloys. ASM International, Materials Park. ISBN: 9780871704818

Carlone P, Astarita A, Rubino F, Pasquino N, Aprea P (2016) Selective laser treatment on cold-sprayed titanium coatings: numerical modeling and experimental analysis. Metall Mater Trans B Process Metall Mater Process Sci 47(6):3310–3317. https://doi.org/10.1007/s11663-016-0636-7

Carlone P, Palazzo GS, Pasquino R (2008) Inverse analysis of the laser forming process by computational modelling and methods. Comput Math Appl 55(9):2018–2032

Cassar G, Avelar-Batista Wilson JC, Banfield S, Housden J, Matthews A, Leyland A (2012) Surface modification of Ti–6Al–4V alloys using triode plasma oxidation treatments. Surf Coat Technol 206:4553–4561

Champagne VK, Helfritch DJ (2014) Mainstreaming cold spray – push for applications. Surf Eng 30(6):396–403

Chaze AM, Coddet C (1986) The role of nitrogen in the oxidation behaviour of titanium and some binary alloys. J Less Common Metals 124:73–84

Cinca N, Barbosa M, Dosta S, Guilemany JM (2010) Study of Ti deposition onto Al alloy by cold gas spraying. Surf Coat Technol 205:1096–1102

Dalili N, Edrisy A, Farokhzadeh K, Li J, Lo J, Riahi AR (2010) Improving the wear resistance of Ti–6Al–4V/TiC composites through thermal oxidation (TO). Wear 269:590–601

Dong H, Bell T (1998) Towards designer surfaces for titanium components. Indust Lubrificat Tribol 50:282–289

Frangini S, Mignone A, De Riccardis F (1994) Various aspects of the air oxidation behaviour of a Ti6Al4V alloy at temperatures in the range 600-700°C. J Mater Sci 29:714–720

Fouvry S, Kapsa P, Vincent L (1995) Analysis of sliding behaviour for fretting loadings: determination of transition criteria. Wear 185:35–46

Goldbaum D, Ajaja J, Chromik RR, Wong W, Yue S, Irissou E, Legoux J-G (2011) Mechanical behavior of Ti cold spray coatings determined by a multi-scale indentation method. Mat Sci Eng A-Struct 530:253–265

Goyal T, Walia RS, Sidhu TS (2012a) Effect of parameters on coating density for cold spray process. Mater Manuf Process 27(2):193–200

Goyal T, Walia RS, Sidhu TS (2012b) Study of coating thickness of cold spray process using Taguchi method. Mater Manuf Process 27(2):185–192
Grujicic M, Zhao CL, Tong C, DeRosset WS, Helfritch D (2004) Analysis of the impact velocity of powder particles in the cold-gas dynamic-spray process. Mat Sci Eng A Struct 368:222–230
Hanaor DAH, Sorrell CC (2011) Review of the anatase to rutile phase transformation. J Mater Sci 46:855–874
Hodge NE, Ferencz RM, Solberg JM (2014) Implementation of a thermomechanical model for the simulation of selective laser melting. Comput Mech 54:33–51
Hussain T (2013) Cold spraying of titanium: a review of bonding mechanisms, microstructure and properties. Key Eng Mater 533:53–90
Hussain T, McCartney DG, Shipway PH, Marrocco T (2011) Corrosion behavior of cold sprayed titanium coatings and free standing deposits. J Therm Spray Technol 20(1):260–274. https://doi.org/10.1007/s11666-010-9540-x
Irissou E, Legoux JG, Ryabinin AN, Jodoin B, Moreau C (2008) Review on cold spray process and technology: part I—intellectual property. J Therm Spray Technol 17(4):495–516
Kataria S, Kumar N, Dash S, Tyagi AK (2010) Tribological and deformation behaviour of titanium coating under different sliding contact conditions. Wear 269:797–803
Khun NW, Li RT, Loke K, Khor KA (2015) Effects of Al-Cr-Fe quasicrystal content on tribological properties of cold-sprayed titanium composite coatings. Tribol Trans 58(4):616–624. https://doi.org/10.1080/10402004.2014.991860
Kim K, Geringer J (2012) Analysis of energy dissipation in fretting corrosion experiments with materials used as hip prosthesis. Wear 296:497–503
Krishna DSR, Brama YL, Sun Y (2007) Thick rutile layer on titanium for tribological applications. Tribol Int 40:329–334
Li WY, Zhang DD, Huang CJ, Yin S, Yu M, Wang FF, Liao HL (2014) Modelling of impact behaviour of cold spray particles: review. Surf Eng 30(5):299–308
Li W-Y, Zhang C, Guo XP, Zhang G, Liao HL, Li C-J, Coddet C (2008) Effect of standoff distance on coating deposition characteristics in cold spraying. Mater Design 29:297–304
Lima RS, Kucuk A, Berndt CC, Karthikeyan J, Kay CM, Lindemann J (2002) Deposition efficiency, mechanical properties and coating roughness in cold-sprayed titanium. J Mater Sci Lett 21:1687–1689
Marrocco T, Hussain T, McCartney DG, Shipway PH (2011) Corrosion performance of laser post-treated cold sprayed titanium coatings. J Therm Spray Technol 20(4):909–917. https://doi.org/10.1007/s11666-011-9637-x
Marrocco T, McCartney DG, Shipway PH, Sturgeon AJ (2006) Production of titanium deposits by cold-gas dynamic spray: numerical modeling and experimental characterization. J Therm Spray Technol 15(2):263–272
Pattison J, Celotto S, Khan A, O'Neill W (2008) Standoff distance and bow shock phenomena in the cold spray process. Surf Coat Technol 202:1443–1454
Pawlowski L (2008) The science and engineering of thermal spray coatings. Wiley, The Atrium, Southern Gate, Chichester, West Sussex, England, 597 pp
Prisco U, Squillace A, Astarita A, Carrino L (2016) Morphology of titanium coatings deposited through single pass cold spraying. Mater Manuf Process. https://doi.org/10.1080/10426914.2016.1198035
Prisco U (2015) Size-dependent distributions of particle velocity and temperature at impact in the cold-gas dynamic-spray process. J Mater Process Technol 216:302–314
Rubino F, Astarita A, Carlone P, Genna S, Leone C, Memola Capece Minutolo F, Squillace A (2016) Selective laser post-treatment on titanium cold spray coatings. Mater Manuf Process 31(11):1500–1506
Sampath S, Jiang XY, Matejicek J, Prchlik L, Kulkarni A, Vaidya A (2004) Role of thermal spray processing method on the microstructure, residual stress and properties of coatings: an integrated study for Ni–5 wt.% AL bond coats. Mater Sci Eng A364:216–231. https://doi.org/10.1016/j.msea.2003.08.023

Selvan JS, Subramanian K, Nath AK, Gogia AK, Balamurugan AK, Rajagopal S (1998) Hardness, microstructure and surface characterization of laser gas nitrided commercially pure titanium using high power CO 2 laser. J Mater Eng Perform 7:647–655

Sun Y (2004a) Thermally oxidised titanium coating on aluminium alloy for enhanced corrosion resistance. Mater Lett 58:2635–2639

Sun Y (2004b) Tribological rutile-TiO2 coating on aluminium alloy. Appl Surf Sci 233:328–335

Sun Z, Annergren I, Pan D, Mai TA (2003) Effect of laser surface remelting on the corrosion behavior of commercially pure titanium sheet. Mater Sci Eng 345:293–300

Van Steenkiste TH, Smith JR, Teets RE, Moleski JJ, Gorkiewicz DW, Tison RP, Marantz DR, Kowalsky KA, Riggs WL II, Zajchowski PH, Pilsner B, McCune RC, Barnett KJ (1999) Kinetic spray coatings. Surf Coat Technol 111:62–71

Vuoristo P, Koivuluoto H (2014) Analysis of single spray beads prepared using low-pressure cold spraying. Surf Eng 30(6):451–454

Wu J, Fang H, Yoon S, Kim H, Lee C (2005) Measurement of particle velocity and characterization of deposition in aluminum alloy kinetic spraying process. Appl Surf Sci 252:1368–1377

Wang S, Liao Z, Liu Y, Liu W (2015) Influence of thermal oxidation duration on the microstructure and fretting wear behavior of Ti6Al4V alloy. Mater Chem Phys 159:139–151

Yin S, He P, Liao H, Wang X (2014) Deposition features of Ti coating using irregular powders in cold spray. J Therm Spray Technol 23:984–990

Zahiri SH, Antonio CI, Jahedi M (2009) Elimination of porosity in directly fabricated titanium via cold gas dynamic spraying. J Mater Process Technol 209:922–929

Chapter 8
Characterization, Deposition Mechanisms, and Modeling of Metallic Glass Powders for Cold Spray

John Henao and Mala M. Sharma

8.1 Considerations About Metallic Glasses

Amorphous metals, also known as metallic glasses or glassy metals, possess a lack of grain boundaries and other crystallographic defects that are common weak spots of crystalline materials. This absence of structure lends itself to improved wear and corrosion properties versus traditional crystalline metals and, therefore, makes them excellent candidates to create strong coatings. Metallic glasses (MGs) are materials with great promise for engineering applications due to their unique combination of physical and chemical properties such as high hardness, high elastic limit, high specific strength, high coefficient of restitution, excellent anti-wearing characteristics as well as outstanding corrosion resistance, and good magnetic behavior. Currently, some bulk metallic glasses (BMGs) are commercially available (Vitreloy and Liquidmetal) and used as small parts in devices such as watches and cell phones. However, their fabrication into larger and more complex engineering parts has been a laborious task since MGs are susceptible to thermally activated phenomena in most of the conventional manufacturing processes.

Significant efforts have been made to produce larger MG parts using powder metallurgy methods (Itoi et al. 2001; Pauly et al. 2013). The advantage of the powder metallurgy technique resides in using premanufactured MG powders obtained by atomization techniques. MG alloys, many of them difficult to obtain in a fully amorphous state by conventional casting methods, can be successfully synthetized by gas and water atomization processes. Then, atomized powders are employed to produce bulk parts by powder metallurgy techniques such as cold and hot pressing.

J. Henao
CONACYT-CIATEQ, National Council of Science and Technology and Advanced Center of Technology, Queretaro, Mexico
e-mail: johnpenenrey@gmail.com

M.M. Sharma (✉)
Department of Mechanical Engineering, Bucknell University, Lewisburg, PA, USA
e-mail: mala.sharma@bucknell.edu

P. Cavaliere (ed.), *Cold-Spray Coatings*,
https://doi.org/10.1007/978-3-319-67183-3_8

Nevertheless, processing MG powders into bulk parts is still a serious challenge since the lack of ductility of MGs at low temperatures and the short shaping time before crystallization limit the production of BMGs by this route (Schroers 2010).

As an alternative to powder metallurgy, cold spray technology offers a promising route for processing atomized MG powders without any danger of crystallization due to its short processing time and high cooling rate. Cold spray avoids oxidation of the feedstock powder using inert carrier gases at temperatures below 1000 °C; this affords ideal conditions for the metallic glass coating to be formed. Unlike most metals, MGs are noncrystalline alloys with a short-to-medium range order atomic configuration. During the cold spray process, this amorphous configuration can be preserved, while the MG powder, at high velocities (300–1200 m/s), travels within a nonreactive gas stream toward a substrate material. The MG particles, at temperatures below the melting point, impact the surface and experience severe plastic deformation. Thus, the MG coating is built up by successive impacts of particles (Henao et al. 2016).

Although, at first glance, the cold spray process is relatively simple in terms of the phenomena behind the transport of particles, there are various aspects related to the thermodynamics and mechanical properties of MGs that must be understood for a successful deposition of MGs. For instance, it is well known that MGs crystallize above their crystallization temperature and present a mechanical response which depends on temperature and strain rate (Mridha et al. 2017; Argon 1979). Both crystallization and mechanical behavior change from one MG composition to another. Consequently, it is not a trivial task for engineers to identify the conditions under which a successful deposition will occur. Thus, in the following section, basic concepts related to the thermal and mechanical response of MGs will be introduced with the aim that readers can achieve a better view of how MGs behave during the cold spray process.

8.1.1 Glass Formation and Thermal Behavior of MGs

The formation of MGs is achieved from the liquid melt by means of rapid cooling, i.e., 100 to 10^6 K/s (Wang et al. 2004; Scully et al. 2007). When the alloy, in liquid state, is cooled below the liquidus temperature, it is energetically less stable than the crystalline phase and tends to transform to the more stable crystalline solid. According to the nucleation and growth theory, the driving force for nucleation of crystals is related to the reduced free energy of transforming the molten liquid into a stable crystalline phase. Due to the nucleation, new surfaces appear within the liquid phase, where the surface energy, associated to these new surfaces, opposes to the driving force. As a result, the competition of the driving force and the surface energy establishes a barrier energy which must be surpassed in order to form a stable nucleus. The formation of stable nuclei is associated with the mass transport of the atoms within the molten liquid. Rapid cooling is required since the barrier energy for nucleation and growth is mass transport dependent (Luborsky 1983; Miller et al. 2007). According to the Stokes-Einstein relation (Eq. 8.1), the atomic movement and diffusion in a molten liquid are related by the following expression:

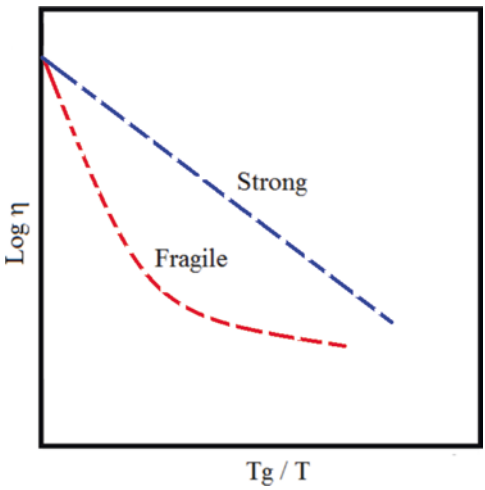

Fig. 8.1 Schematic representation of the MG viscosity according to the VFT equation

$$D = \frac{T * K_B}{3 * \eta * \pi * 1} \tag{8.1}$$

where D is the diffusivity, T is the temperature, K_B is the Boltzmann constant, l is the average atomic diameter, and η is the viscosity of the liquid. In MGs, the viscosity follows an exponential behavior as a function of the inverse of temperature (Fig. 8.1), as described by the Vogel-Fulcher-Tammann (VFT) equation (Eq. 8.2), where D^* is the liquid fragility, η_0 is a constant, and T_0 is referred to as the VFT temperature, i.e., ideal glass transition temperature. D^* describes the degree of deviation of the liquid from the Arrhenius behavior (Takeuchi et al. 2010).

$$\eta = \eta_0 * \exp\left(\frac{D^* T_0}{(T - T_0)}\right) \tag{8.2}$$

Liquids are commonly referred to as strong when $D^* > 20$ and fragile when $D^* < 10$. Fragile liquids have glassy structures that may easily reorganize through fluctuations over a variety of particle orientations and coordination states, without much assistance from thermal excitations. On the other hand, strong liquids intrinsically resist structural changes and show little reorganization even over wide temperature changes (March 2002). In any case, the melting viscosity of MGs is in the order of 100 Pa·s, and it is about three orders of magnitude more viscous than a pure metal, which usually has viscosities in the order of 10^{-3} Pa·s. During cooling, the exponential behavior of viscosity abruptly slows down the atomic diffusion since it may change various orders of magnitude up to 10^{12} Pa·s in a short range of temperatures (Lagogianni et al. 2016; Li et al. 2016). Thus, any increase in viscosity, favored by quenching, reduces the diffusivity of the melting and, consequently, increases the probability of preserving the configuration of the liquid. In this man-

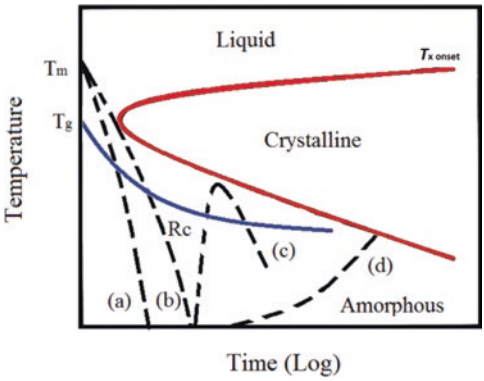

Fig. 8.2 Schematic of a TTT diagram for an amorphous alloy

ner, atomization processes are useful to obtain MG powders in a fully amorphous state. In fact, atomization techniques are the preferred synthesis route in the industry for MG powders.

The formation of an amorphous solid depends on thermodynamic factors (the driving force for nucleation and the nucleation barrier) and kinetic factors (viscosity/mass transport). These are summarized in the following expression (Itoi et al. 2001; Takeuchi et al. 2010; March 2002):

$$I_{\mathrm{v}} = \frac{A_{\mathrm{v}}}{\eta(T)} * \exp\left(\frac{\Delta G^{*}}{T * K_{\mathrm{B}}}\right) \tag{8.3}$$

where I_{v} is the nucleation rate, A_{v} is constant ($\approx 10^{32}$), and ΔG^{*} is the energy barrier for nucleation. According to Eq. 8.3, high cooling rates ease the formation of MGs since viscosity increases rapidly and, consequently, reduces the nucleation rate. The lowest cooling rate required to produce a MG is often called the critical cooling rate (R_{c}). This can be visualized in a TTT diagram, Fig. 8.2.

The location of the curve in the TTT diagram (onset of crystallization) is associated with the thermodynamics and depends on each alloy. If an alloy can form a MG, then the driving force for nucleation in the supercooled liquid state must be low. Since the driving force for nucleation is associated with the entropy of the system, it will be reduced if the number of elements in the liquid is increased. Adding more elements will also make the structure more complex and, consequently, make the needed atomic rearrangement for crystallization more difficult. Therefore, the liquid will have a stronger behavior, and the onset of crystallization will be shifted to longer times (Gheiratmand et al. 2016; Lagogianni et al. 2016; Li et al. 2016). Based on thermodynamics and experimental observations, Inuoe (2000) proposed some empirical rules for the formation of MGs: (1) the alloy must be made up of more than two elements, (2) the diameters of the atomic elements must differ from each other by more than 12%, and (3) the heat of mixing between the elements must be negative. In this manner, hundreds of MGs such as lanthanide metals-, Au-, Mg-, Zr-, Ti-, Hf-, Fe-, Pd-, Pt-, Co-, Ni-, Al-, and Cu-based alloy systems have been

developed. Another beneficial aspect to producing MGs is using near-eutectic alloys. A multicomponent alloy near to the eutectic point minimizes the difference between the glass transition and the liquidus temperature and, therefore, stabilizes the liquid at lower temperatures.

Figure 8.2, curve (c), illustrates the behavior of MGs during heating. MGs can be heated above the glass transition where they can recover their atomic mobility, while their viscosity decreases exponentially (Fig. 8.1). The temperature range, from the glass transition up to crystallization, is called the supercooled liquid region. This property is commonly benefited in the cold spray technology to deposit MG particles. Heating must be sufficiently high and must be combined with rapid cooling to avoid crystallization. In the cold spray process, rapid heating and rapid cooling are associated with gas temperature, nozzle geometry, standoff distance, and substrate material. A good control of these factors allows processing the MG particles while avoiding the onset of crystallization. Otherwise, crystallization can take place as shown in Fig. 8.2, curve (d). The crystallization of MGs is accompanied by a densification of 1%, a decrease of enthalpy, and significant changes in most physical and chemical properties (Afonin et al. 2016).

8.1.1.1 Concluding Remarks

The thermodynamic properties of MGs have been used in recent studies to evaluate the state of particles during the cold spraying process (Henao et al. 2017). The nucleation and growth theory through the construction of a TTT diagram is useful to determine if crystallization takes place before particles impact onto the substrate. By utilizing this thermodynamic approach, theoretically any MG can be cold sprayed – and by avoiding the onset of crystallization, the amorphous structure can be preserved. Moreover, thermodynamic data through the VFT equation can be useful to know the viscosity of particles at impact. As it will be discussed further in this chapter, a low viscosity of particles at impact is desired to get a good bonding of particle/substrate.

8.2 Metallic Glass Feedstock Powders for Cold Spray

A critical initial step in a successful cold spray deposit is the proper development of the feedstock powders; as previously stated, these are typically manufactured through gas and water atomization, although recent advances in solid-state processing have also yielded developmental alloys suitable for cold spraying. Although similar in composition and size, feedstock powders can result in different morphologies owing to the manufacturing process; these can vary from spherical to irregular or blocky. Blocky particles which possess an elongation ratio close to unity are known to be dense, whereas spherical and irregular particles can be dense or may vary in void content (Salman et al. 2007). Powder properties such as hardness can have a direct impact on the quality and successful buildup of the subsequent coating (Jodoin et al.

2006). Other factors which influence the deposition efficiency of the coating are the morphology and size of the particle which affect how well it is accelerated through the supersonic gas stream. These qualities affect the critical particle velocity required to ensure proper adhesion to the substrate (Xiao-Tao et al. 2016). In general, rough and irregular particles have higher drag coefficients, thus making them more responsive to the cold spray process. In addition to the aerodynamic effect the particle shape can have, the variation in porosity can also affect the particle specific mass, which in turn will have a direct influence on the thermal properties (i.e., conductivity and diffusivity) (Fauchais et al. 2010). Finally, flowability through the powder feeder and nozzle can also be affected by the morphology of the particle; poor flowability resulting from fluctuations in powder feed rate may result in an undesirable nonhomogeneous coating. Therefore, characterization of the feedstock powders in terms of phase composition, particle size distribution, morphology, and SEM is extremely important for successful deposition. For metallic glasses, thermal properties should also be identified and can be executed using differential scanning calorimetry (DSC) and X-ray diffraction. The resulting data is often used to identify optimized spray parameters by modeling predicted coating properties and individual particle impact behavior.

8.2.1 Characterization of Metallic Glass Feedstock Materials

In the present study, characterization of a water-atomized Fe-based MG composition (FeSiCrBC) was executed to help identify optimum process parameters for cold spray deposition. Powder particles were evaluated for average size, distribution, and morphology, in addition to chemical composition and verification of amorphicity (Fig. 8.3a–c). Particles are mostly spherical in nature, but several irregular-shaped particles can also be observed, and this is characteristic of water-atomized powders. The irregular morphology positively affects in-flight particle velocity (Sun et al. 2006) and can have an effect on the subsequent coating microstructure and hardness given the same processing parameters. Studies (Xiao-Tao et al. 2016; Fauchais et al. 2010; Sun et al. 2006) have ascribed higher deposition efficiencies to porous and irregular feedstock particle microstructures in cold-sprayed powders that were preheated. This behavior is not clearly understood and has been attributed to the lower critical velocity in previous studies (Xiao-Tao et al. 2016) and to the flow properties (heat transfer and drag) in this study; consequently, they present higher impact velocity and particle temperature. This effect that powder morphology has on the particle velocity has been observed to be more significant for larger particle size ranges between 25 and 38 μ (Jodoin et al. 2006).

In general, for optimum deposition efficiency during the cold spray process, the feedstock particle size should range between 5 and 45 μm. Studies have indicated that particle size is directly related to cooling rate and glass formation in metallic glasses (Johnson 2002). Consequently, it is advantageous for the powder distribution of MG feedstock to contain a majority of finer particles of similar diameter. This is due to the correlation between viscosity, temperature, and velocity. Ideally, the range of the particle size should be as narrow as possible with the majority of the particles between 20 and 30 μm, but this is not always possible.

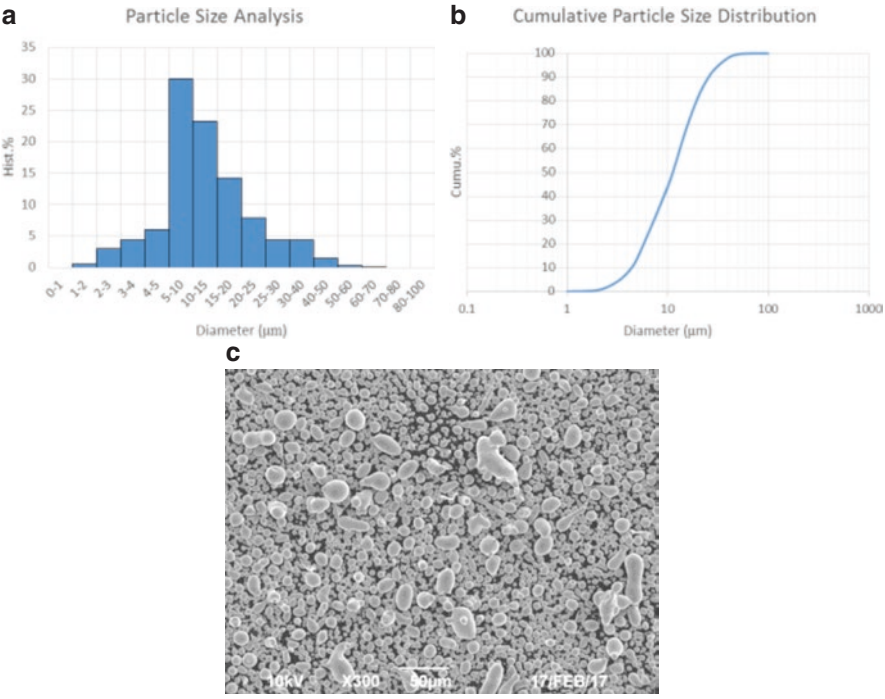

Fig. 8.3 (**a**) Particle size analysis, (**b**) particle size distribution, and (**c**) SEM morphology of water-atomized powders

The FeSiCrBC metallic glass particles in this study ranged from approximately 5 to 60 μm with an average particle size diameter of approximately 15 μm. Powders were verified amorphous as evidenced by the broadband halo of the X-ray diffraction pattern (Fig. 8.4). DSC measurements shown in Fig. 8.5 revealed an endothermic heat flux corresponding to the glass transition temperature at approximately 475 °C (T_g) and an exothermic peak due to crystallization of the supercooled liquid at approximately 543 °C (T_x).

Characterization of the surface structure of the metallic glass powder particles is also important to understanding the deposition mechanics. In this study, FeSiCrBC particles were investigated using BSE, and the chemical composition at various locations on a single particle was investigated using EDS. Figure 8.6a–c shows the structure to be very smooth, which is a factor of the water atomization process.

A number of various spots that were examined on the BSE image of a round particle (shown in Fig. b) and results indicated that, as expected, the elements were consistently showing high amounts of Fe and Si with more trace amounts of Cr and C. However, oxygen is also present in very small quantities, a factor of the water atomization process (Dunkley 1998). Sphericity and particle oxidation in-flight during atomization are connected and more so with water atomization than in inert gas atomization (Dunkley 1998). To the extent possible, oxidation should be avoided because it serves to destabilize the metallic glass particle. The chemical composition is dependent on the cooling

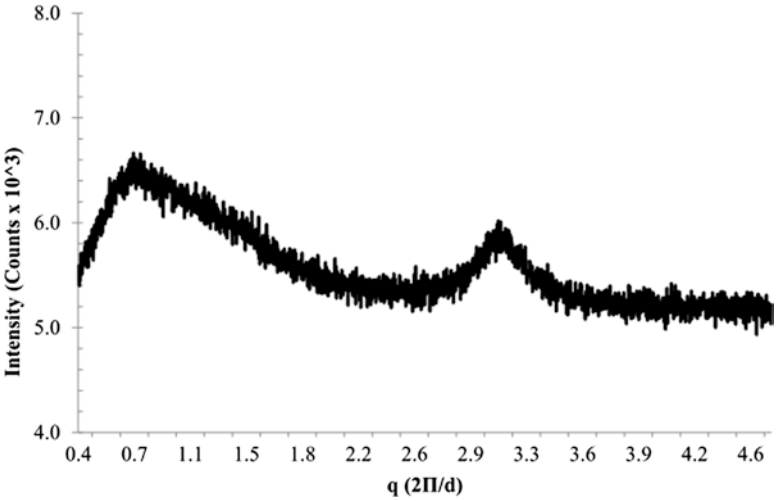

Fig. 8.4 XRD pattern showing broadband halo indicative of an amorphous structure

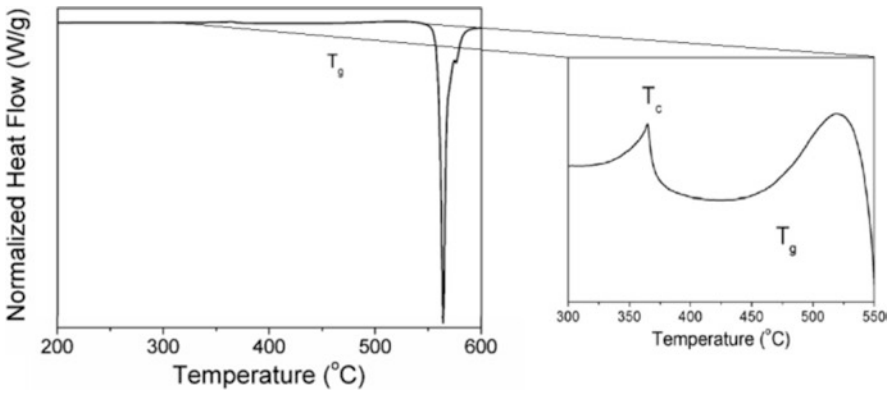

Fig. 8.5 DSC curve identifying various thermal properties of the powder

rate, which in turn controls the amorphous phase stability and glass-forming ability (Fauchais et al. 2010). These properties affect the resulting mechanical deformation of the particle and buildup for the potential metallic glass coating.

8.2.2 Identifying Spray Parameters for Metallic Glass Feedstock

Various amorphous powders have been successfully deposited on to different substrates via the cold spray process utilizing feedstock powders produced by gas and water atomization (List et al. 2012; Sanghoon et al. 2009). Previous work done in this

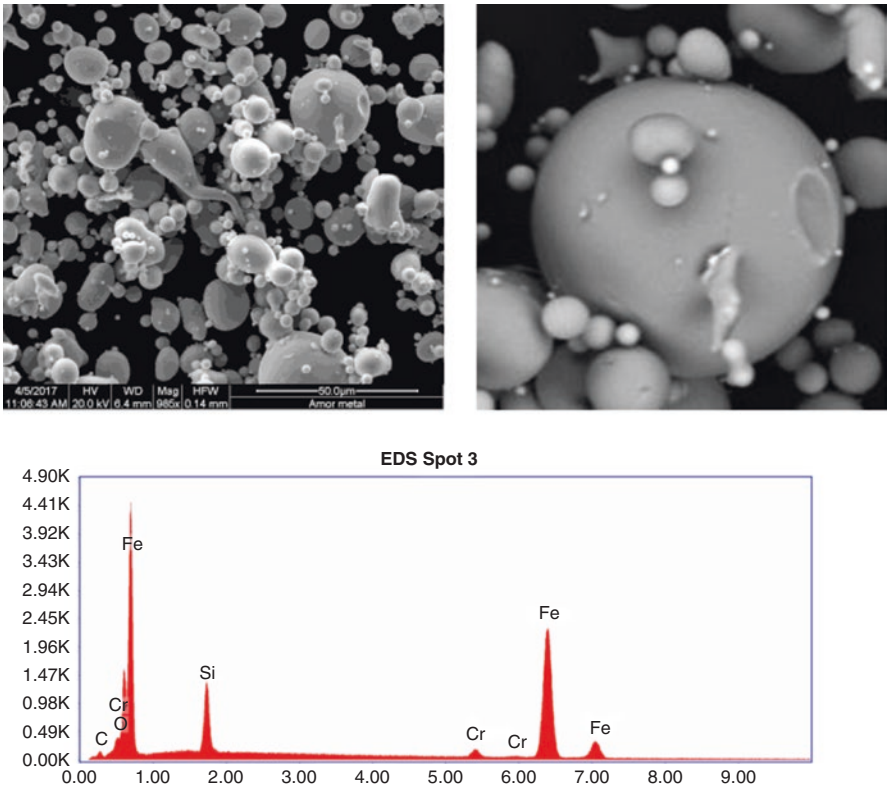

Fig. 8.6 Showing (**a**) SEM pic of MG particles, (**b**) closeup BSE of particle, and (**c**) corresponding EDS spectrum of particle surface

area has focused on impact conditions of the particle on the substrate while recognizing that the mechanism for amorphous particle deformation will be different whether above or below the glass transition temperature (Ashby and Greer 2006). Localized plastic flow will occur below the glass transition temperature, while homogeneous deformation occurs above the glass transition temperature (List et al. 2012; Sanghoon et al. 2009). Generally speaking, targeting impact conditions above the glass transition and below the crystallization temperature is believed to produce the most efficient deposition with the lowest associated porosity. Figure 8.7 demonstrates these phenomena with SEM micrographs of impact particles at different initial temperatures.

8.2.3 Deformation Mechanisms of Metallic Glass Feedstock Particles

Since cold spray coating buildup involves plastic deformation of particles, it is crucial to understand the mechanical behavior of MGs. The amorphous atomic configuration of MGs fundamentally makes their mechanical behavior different from

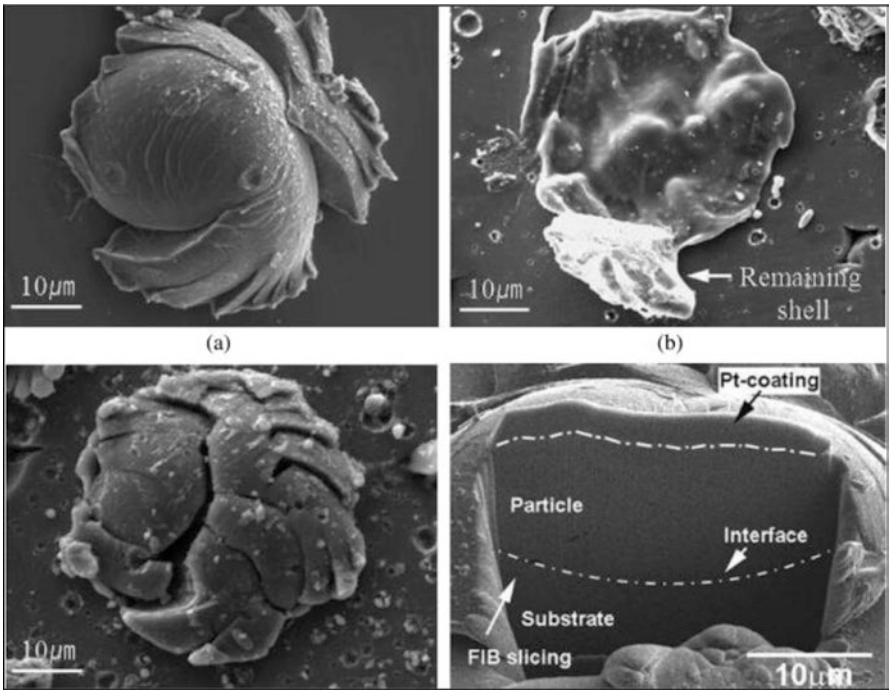

Fig. 8.7 Metallic glass impact particles with different initial temperatures: (**a**) room temperature; (**b**) between T_g and T_x ; (**c**) above T_x (Sanghoon et al. 2009)

their crystalline counterparts, i.e., the absence of grain boundaries and crystal defects. Although the elastic response of MGs is considered as instantaneous and reversible as with crystalline materials, the plastic response of MGs is defined as irreversible and temperature and time dependent. The Hookean elastic strain of MGs is approximately four times higher than of crystalline alloys with similar density. This fact is responsible for the high storage density of elastic energy which is almost 10–20 times higher in MGs with respect to crystalline alloys (Ashby and Greer 2006; Schuh et al. 2007).

On the other hand, the mechanisms of plastic deformation of MGs show two different modes: inhomogeneous deformation and homogeneous deformation (Zhong et al. 2016; Trexler and Thadhani 2010). Inhomogeneous deformation is present in the plastic flow confinement of thin shear bands, while the rest of the specimen deforms elastically. The lack of microstructure-based work hardening renders MGs susceptible to plastic instabilities. Shear bands represent the localization of shear strain under an applied stress which occurs via local rearrangements of atoms around free-volume regions (Huang et al. 2002; Liu et al. 2016). The shear bands are characterized to be very thin, between 20 and 100 nm, and form quickly once the yield stress is reached. Alternatively, homogenous flow is nonlocalized, while the

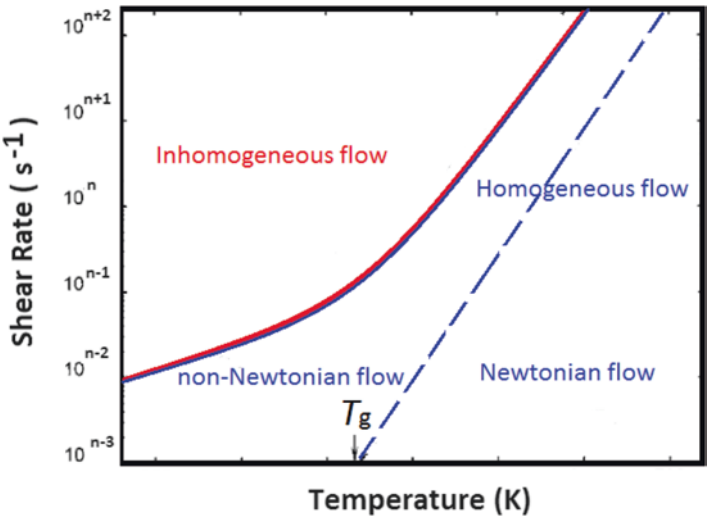

Fig. 8.8 Schematic deformation map for a metallic glass

applied stress is distributed along the material, resulting in long uniform plastic deformation (Nieh and Wadsworth 2006). The occurrence of homogeneous and/or inhomogeneous plastic deformation is illustrated on a schematic deformation mechanism map (Demetriou and Johnson 2004) (Fig. 8.8).

The map displays that, for a given temperature, the type of plastic flow depends on the strain rate. Shear localization is favored by high strain rates and low temperatures, while homogeneous deformation is given under high temperatures and lower strain rates. Inhomogeneous deformation may also occur above the glass transition. The map is also interesting since it includes the sub-regimes of homogeneous deformation corresponding to non-Newtonian and Newtonian flow. The transition from inhomogeneous deformation to homogeneous deformation occurs through non-Newtonian flow. Non-Newtonian flow takes place at moderate and high temperatures and is essentially strain rate dependent (Huang et al. 2002).

The enhanced plasticity of MGs at high temperatures has been widely useful as a net-shape processing method (Liu et al. 2016). This method has been used to produce MGs into simple shapes such as sheets or powders. The simple MG shapes are heated up within the supercooled liquid region, and subsequently, a second process, based on applied pressure, is used to produce a more complex MG shape. Other methods commonly used for MG net shape are extrusion and hot isostatic pressure from amorphous MG powder (Liu et al. 2016). These methods require alloy compositions with a wide supercooled liquid region and good stability of the amorphous phase and often present problems of crystallization during the plastic forming and lack of powder's compressibility. In case of the cold spray process, the enhanced plasticity of MGs within the supercooled liquid region is used to deposit the MG particles and get dense coatings.

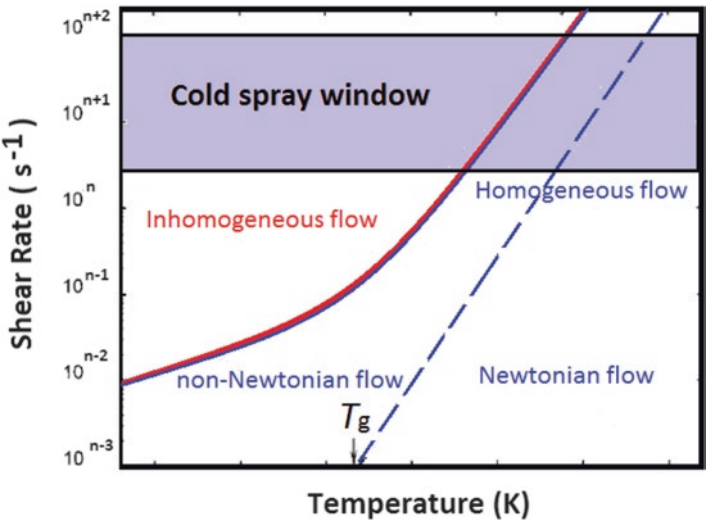

Fig. 8.9 Schematic deformation map for a metallic glass in the cold spray process. The window of shear rates depends on the spraying conditions (standoff distance, substrate hardness, gas pressure, and gas temperature)

8.2.3.1 Concluding Remarks

The knowledge about the mechanical response of MG is fundamental to evaluate the conditions at which MGs can be deposited by cold spray. Early experimental studies have shown that spraying MGs at room temperature is not efficient since particles undergo severe localized deformation and fracture (Yoon et al. 2006). Deformation maps, as the schematic deformation map in Fig. 8.9, can be useful to predict the type of mechanical response of MGs at impact during the cold spray process. Even at temperatures close to the glass transition, the deformation of the particles can be inhomogeneous at the strain rates experienced in the cold spray process (10^6–10^8 s^{-1}). Thus, either higher impact temperatures or lower strain rate conditions should be set to promote homogeneous plastic deformation. As it will be discussed further in this chapter, homogeneous deformation is related to the deposition and coating growth of MGs by cold spray.

8.3 Deposition Mechanisms of Metallic Glasses by Cold Gas Spray

Although deposition of particles in the cold spray process in a general way involves acceleration, heating, high strain rates, rapid cooling, and intimate contact of particle/substrate, deposition and bonding mechanisms of MGs are found to differ from accepted theories of deposition of crystalline metal coatings (Assadi et al. 2016). For crystalline metals, the deposition and coating growth is determined by the

critical velocity at impact. The critical velocity is defined as the impact velocity where most of the particles, above 50% of the sprayed material, start to be deposited onto the substrate during the spraying process (Assadi et al. 2016). The concept of critical velocity arises from ballistic expression of hydrodynamic penetration of particles at impact, combined with the Johnson-Cook model for softening of crystalline materials, which is often used for modeling and simulation of deforming metals (Meng et al. 2016). The critical velocity is a parameter used to control and to predict the optimum deposition conditions of a given material in cold spray. In this manner, the conversion of kinetic energy, at conditions predicted by the critical velocity, results into plastic deformation and subsequent heat generation, localized at the impact region, promoting bonding at the interface of particle/substrate (Assadi et al. 2016; Grujicic et al. 2004). The localized plastic deformation and the subsequent heat generation at the impact surface are commonly known as adiabatic shear instabilities. Bonding and deposition of crystalline metals are then associated with the occurrence of adiabatic shear instabilities (Grujicic et al. 2004). When the impact velocity is two to three orders of magnitude of the critical velocity, erosion of the substrate occurs, and therefore, no deposition of particles is observed.

In the case of MGs, the deposition mechanisms are different with respect to those of crystalline metals due to the lack of long-range atomic ordering, their particular thermal behavior and mechanisms of deformation, i.e., they do not present strain hardening and defects such as dislocations involved in the plasticity of crystalline materials (Trexler and Thadhani 2010). In this manner, the concept based on the critical velocity derived from dislocation-based model results is inappropriate, since plasticity of MGs differs vastly from that in crystalline metals. Using experimental observations, Concustell et al. proposed a model based on the impact of a liquid droplet onto a surface to correlate the experimental deposition efficiency with the Reynolds number (Re) of the MG particle before impact (Concustell et al. 2015). The Re is defined by the ratio between the inertial and viscous forces of MGs at impact and is useful to predict the window of deposition of MGs from the velocity and viscosity of the particles at impact:

$$\mathrm{Re} = \frac{\rho v_0 d}{\eta(T)} \tag{8.4}$$

where ρ, v_0, d, and η are density of the liquid, impacting velocity, particle diameter, and viscosity of the liquid. The Re is a good engineering tool for the fabrication of MGs, substituting the impact velocity as the main parameter to control coating buildup. Experimental observations of the deposition of MG coatings prepared by CGS (Henao et al. 2016, 2017; Yoon et al. 2006; Concustell et al. 2015) have shown that at low impact temperatures (low Re numbers), MG particles show typical structures related to shear bands, molten phases, and low deformation.

At high temperatures, above the glass transition, shear bands tend to disappear and the flattening ratio of MG particles increases as shown in Fig. 8.10. High deposition efficiencies are obtained when homogeneous flow is the main mechanism of deformation (high Re numbers).

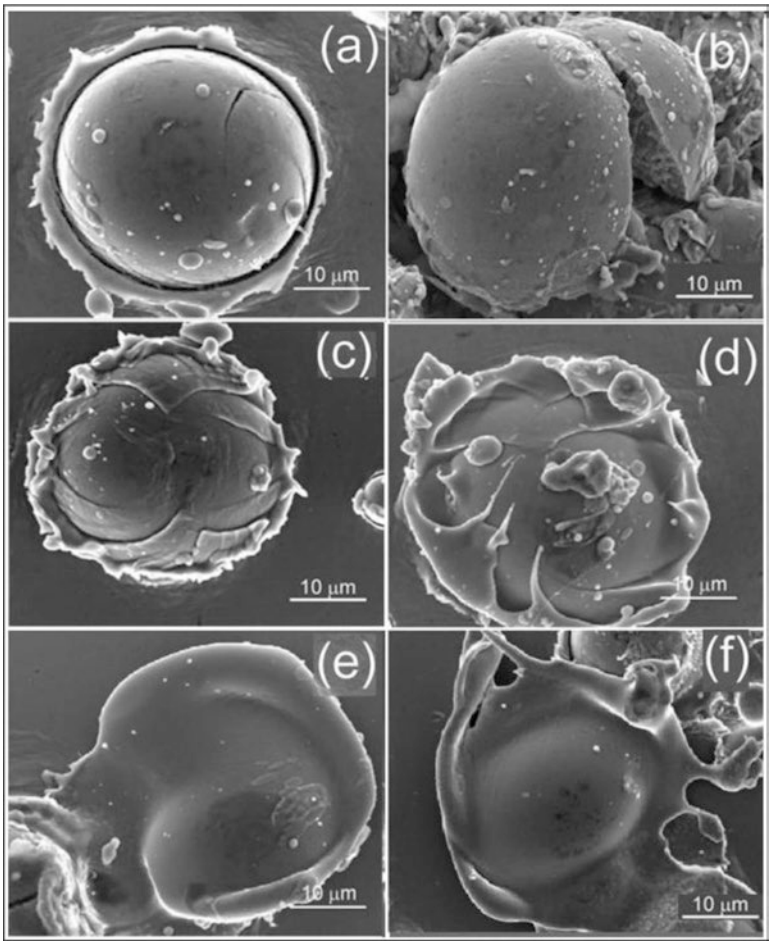

Fig. 8.10 Single impact morphologies corresponding to different deformation regimes typical for a Fe-base MG (FeSiBCCr): (**a**) elastic deformation (Re = 10^{-10}), (**b**) inhomogeneous deformation with failure (Re = 10^{-8}), (**c**) multiple shear band formation (Re = 10^{-6}), (**d**) mixed shear bands and homogeneous flow ($10^{-5} < 10^{-4}$), (**e**, **f**) homogeneous flow (Re > 10^{-4})

Using the Re to predict the conditions for coating buildup suggests that the deposition of MG particles is mainly activated by their viscosity and the inertial forces. In the first case, when MG particles reach temperatures above the glass transition point, their viscosity decreases and can flow more easily at impact. During impact, inertial forces are transformed to shear stresses at the impact surface which favor viscous flow. Figure 8.11 is an example of how deposition efficiency of MG coatings increases at high Re values.

Therefore, mechanisms of deposition of MGs are a consequence of the dynamic impact conditions and rheological behavior of MGs during the cold spray process. At low Re numbers, localized deformation with shear band formation occurs, mean-

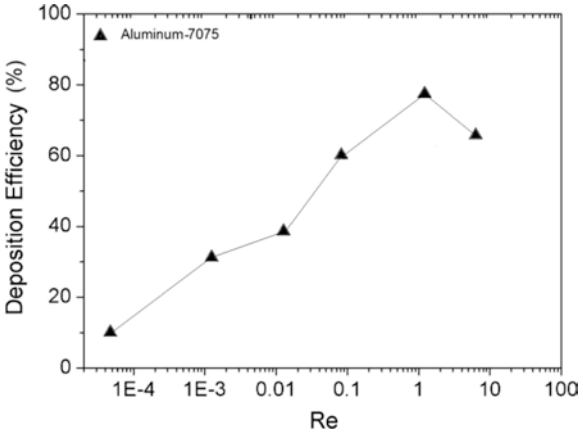

Fig. 8.11 Deposition efficiency of a Fe-base MG coating (FeSiBCCr) prepared onto Al7075-T6 substrate as a function of the Re number

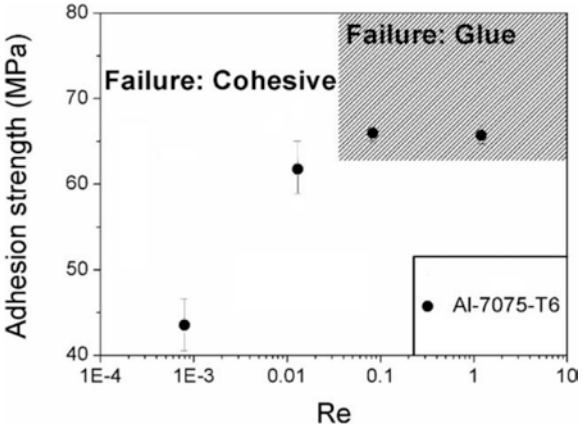

Fig. 8.12 Adhesion strength of an Fe-base MG coating (FeSiBCCr) prepared onto Al7075-T6 as a function of the Re number. Measurements were carried out under the ASTM C633–13 standard

while at high Re, homogeneous flow is the main mechanisms associated with deposition of particles. Under homogeneous flow, shear thinning can appear because of the high strain rate in cold spray process. However, due to the nonstationary conditions, shear thinning is followed by Newtonian flow due to stress relaxation and internal heating. Shear thinning and Newtonian flow mostly promote a cooperative lateral viscous flow of MG particles as a consequence of the viscosity dependence on the shear strain rate and temperature (Demetriou and Johnson 2004; Kawamura et al. 1999). High deposition efficiency and high bonding strength of MG coatings are attributed to the emergence of shear thinning with the subsequent Newtonian flow at high Re numbers (Henao et al. 2016, 2017) (Figs. 8.11 and 8.12).

8.3.1 Finite Element Modeling for the Improvement of Metallic Glass Coatings

Cold spray coatings are formed by the impact and consolidation of particles, and therefore, the state of particles just before impact, the interaction with the substrate, the particle boundaries, and their degree of adhesion to one another determine coating mechanical properties. Finite element (FE) modeling is a powerful technique to get a better understanding of the formation process of MG coatings by cold spray. FE analysis can be useful to estimate certain quantities such as impact velocity, impact temperature, local particle or substrate temperature rise, and some other parameters which are not easily accessible in experiments. That information can be processed and is valuable to improve characteristics of the obtained coatings. First attempts to simulate metallic glass by cold spray have been devoted to the impact phenomenon of the particles on the substrate (Zhou et al. 2010).

For modeling MGs, a combination of analytical and numerical analyses must be developed. A subsequent successful simulation requires the appropriate selection of the model. Unlike crystalline metals, the adhesion of MG particle is not based on adiabatic shear instabilities, but it is based on appearing viscous flow which stands for all circumstances in the material during impact. Thus, a good FE simulation of MGs must account for its thermal and mechanical behavior.

Recently, a model based on the well-known free-volume mechanism has been employed to recreate the impact of MG particles by cold spray (Henao et al. 2017). The free-volume model, Eq. 8.5, is based on the concept of excess space among atoms, which facilitates atomic motion and rearrangements. Plastic flow occurs via stress-induced creation and diffusion-controlled annihilation of free volume and describes the stress-strain relation, stress overshoot, and the transition from non-Newtonian to Newtonian flow in MGs (Henann and Anand 2008; Spaepen and Turnbull 1974; Lu et al. 2003):

$$\eta\left(\dot{\varepsilon},T\right)=\frac{4k_{\mathrm{B}}T}{3V\dot{\varepsilon}}\sin h^{-1}\left(\frac{\dot{\varepsilon}}{2v_0}\exp\left(\frac{1}{\varsigma}\right)\exp\left(\frac{\Delta F}{k_{\mathrm{B}}T}\right)\right) \tag{8.5}$$

Equation 8.5 describes the viscosity of metallic glasses in the supercooled liquid state, where K_{B} is the Boltzmann constant, V is the active volume, i.e., atomic volume needed to activate viscoplastic flow, T is the temperature, $\dot{\varepsilon}$ is the strain rate, v_0 is the reference strain rate, ς is a free-volume parameter, and ΔF corresponds to the energy barrier for the annihilation and the creation of free volume. In recent studies, FE simulation has been carried out using a Lagrangian approach and the model in Eq. 8.5 to study the impact of a MG particle at low and high Reynolds numbers (Henao et al. 2017). Those simulations could describe the formation of shear thinning and Newtonian flow due to stress relaxation and internal heating. It was found that shear thinning and Newtonian flow mostly promote a cooperative lateral viscous flow of MG particles because of the viscosity dependence on the shear strain rate and temperature (Henao et al. 2016, 2017). Therefore, high deposition efficiency and high bonding strength of MG coatings are attributed to the emergence of shear thinning with the subsequent Newtonian flow.

FE analysis is also important to evaluate the effect of the substrate properties on the formation of MG coatings. For instance, mechanical properties of the substrate material can affect the strain rate conditions and rebound energy, while thermal properties affect the heat dissipation rate and, indirectly, the average temperature and deformation of MG particles. To illustrate the effect of the substrate properties on the deposition mechanisms of MGs, a simulation was performed to recreate the impact of a Vitreloy-1 particle onto aluminum-7075-T6 utilizing the same approach from previous researchers (Henao et al. 2017).

Figure 8.13 displays the final deformation state of the Vitreloy-1 particle onto 4340 steel and aluminum-7075-T6 substrates. Plastic deformation of the aluminum-7075-T6 substrate increases, while the deformation of the MG particle decreases. Moreover, the accumulated plastic strain within the MG particle is low and can only be evidenced at high Re (Fig. 8.13f).

Figure 8.14a, b illustrates the evolution of viscosity at different nodes (A, B, C, and D) within the Vitreloy-1 particle during the impact onto the steel and aluminum substrates. Interestingly, shear thinning is significantly reduced in all of the nodal points when the MG particle is deposited onto the aluminum substrate. Viscosity decreases three orders of magnitude at nodes (B, C, and D) onto steel, but it only decreases one order of magnitude at nodes (C and D) onto aluminum. It is also interesting to note that viscosity of the nodal point B, Fig. 8.14b, rapidly increases, while the central point A remains almost constant during most of the impact. This fact is attributed to the thermal interaction of particle/substrate.

Figure 8.15 shows the temperature contour plot of the MG particle during impact onto aluminum-7075-T6 substrate, where rapid cooling is evidenced at the impact surface of the Vitreloy-1 particle from the first impact. Overall, the different behavior of viscosity at nodal points (A, B, C, and D) between the aluminum and steel substrates (Fig. 8.14) is a consequence of the higher thermal conductivity of the aluminum which suppresses shear thinning at the impact point and reduces adiabatic heating within the MG particle during impact. (Certainly, the low resistance to penetration of the Al substrate also contributes to the reduction of shear thinning.)

Therefore, the present results support and validate experimental observations and conclusions reported recently in the literature (Henao et al. 2016, 2017; Zhong et al. 2016; Yoon et al. 2006). A hard substrate increases shear thinning and, consequently, larger deformation of particles is obtained. On the other hand, a substrate with a high thermal diffusivity and/or low hardness (<150 Hv) improves the heat dissipation out of the particle from the first impact because a higher contact area of particle/substrate is developed. Especially for substrates with high thermal conductivity, this fact leads to reduced and/or suppressed shear thinning and, therefore, lower deformation states are obtained.

FE analysis and simulation tools have helped to prove experimental observations and to understand mechanisms leading to the deposition of MGs by cold spray. It is also interesting that FE tools can be used to optimize spraying conditions and coating properties. Analytical models are often used to predict the gas flow features inside the cold spray nozzles. One-dimensional (1D) isentropic equations for the ideal gas flow and particle motion equations (Newton's second law) are widely used to estimate the flow properties and particle velocity and temperature at impact.

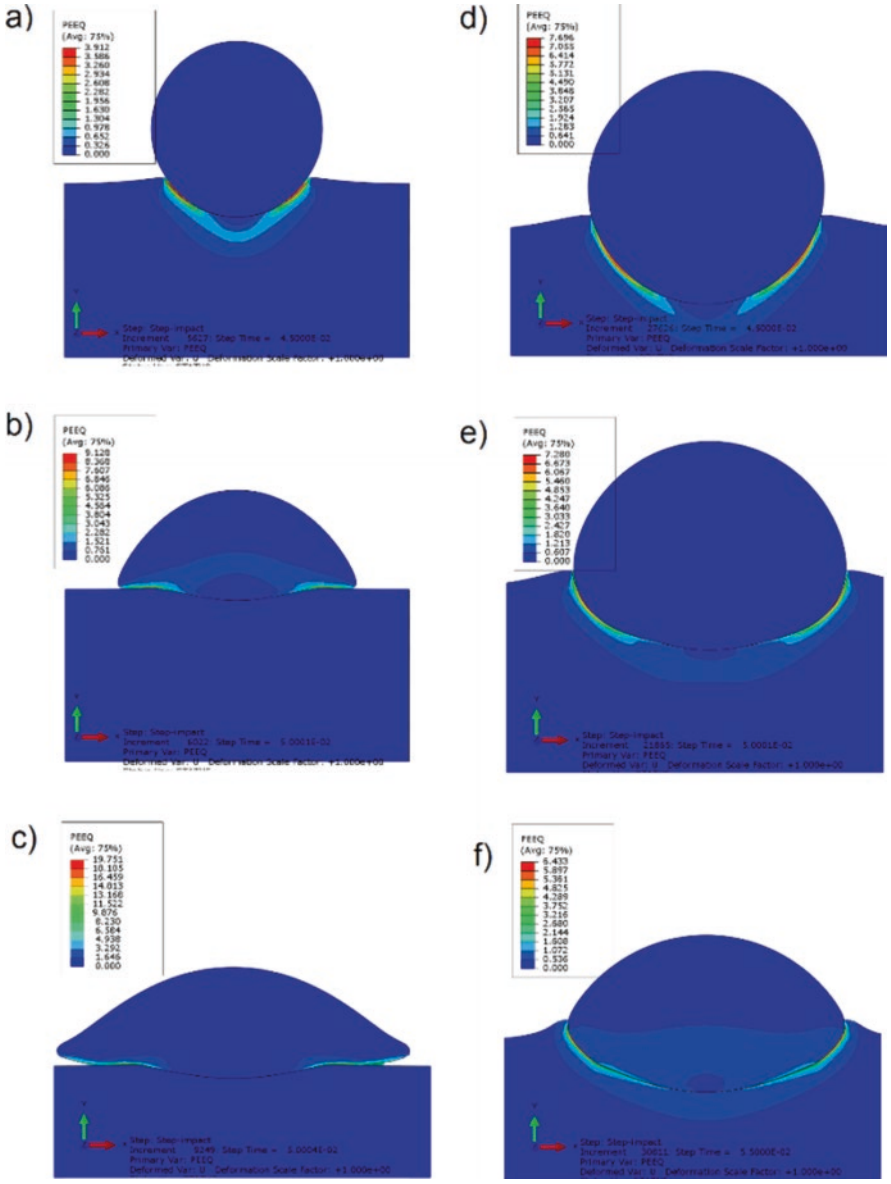

Fig. 8.13 Simulation of the impact of a Vitreloy-1 particle onto 4130 steel (**a**–**c**) and Al-7075-T6 (**d**–**f**) substrates. The contour plot shows the equivalent plastic strain for (**a**, **d**) Re = 10^{-9}, (**b**, **e**) Re = 10^{-3}, (**c**, **f**) Re = 1

Those analytical models are simple and easy to use and result in a prediction that is within tolerable engineering error in some cases, thus attracting many users. For instance, the development of special nozzles for MGs is an area that still requires further investigation in the cold spray industry. Nozzles can be especially designed

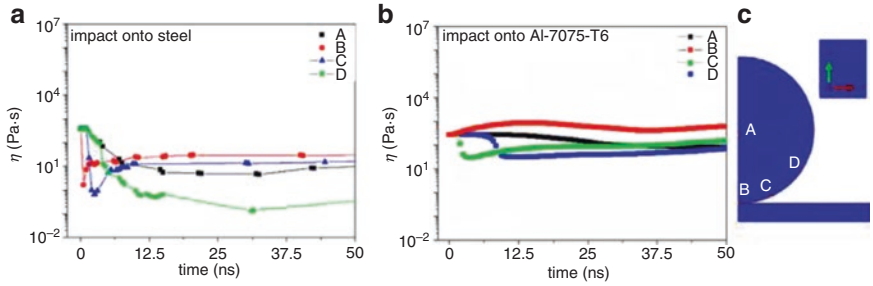

Fig. 8.14 Viscosity evolution during impact for: (**a**) Re = 1 onto 4340 steel substrate, (**b**) Re = 1 onto Al-7075-T6 substrate at nodal points displayed in (**c**)

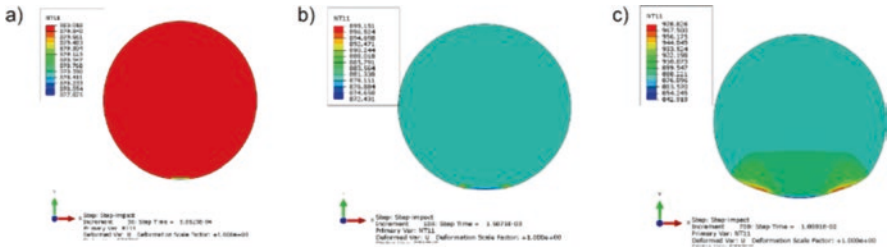

Fig. 8.15 Temperature contour for Re = 1 onto Al-7075-T6 substrate at (**a**) 0.5 ns, (**b**) 1.5 ns, and (**c**) 10 ns during impact

to produce high Re with the minimum energy spent. In this sense, analytical models and FE analysis are a good option to find out new solutions.

In the present study, some experiments with a Fe-base MG composition (FeSiCrBC) were carried out using two different de Laval nozzles in order to reveal the importance of having a proper nozzle for spraying MGs (dimensions are not revealed due to confidentiality reasons). The experimental results are shown in Fig. 8.16. The deposition efficiency, at similar spraying conditions (gas pressure, gas temperature, and standoff distance), is lower when nozzle 2 is used. This result is attributed to the lower gas compression produced with the new nozzle. Thus, higher gas temperature or higher gas pressure would be required to increase deposition.

8.3.1.1 Concluding Remarks

FE analysis and simulation is a powerful tool for improving and understanding the phenomena behind the formation of MG coatings. The model defined for MGs must be able to consider strain rate and temperature dependence of MGs under different conditions. The FE simulation consists of an axisymmetric dynamic explicit FE model coupled with an equation that describes MG behavior. With the numerical

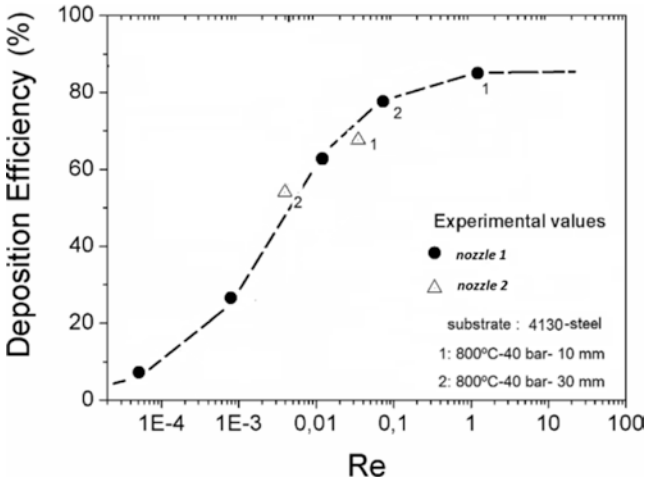

Fig. 8.16 Experimental deposition efficiency as a function of the Re number for an Fe-base MG coating (FeSiBCCr) prepared using two different nozzle geometries

approach, simulations provide information of plastic strain, temperature, strain rate, and viscoplastic dissipation, among others. Of course, the obtained results will help to fabricate coatings with better microstructure. Using analytical models is also of great interest in order to optimize spraying conditions (gas pressure, gas temperature, standoff distance, Reynolds number). Further work must be developed in the field of new nozzle designs for optimizing the cold spray process for MGs.

Acknowledgments The authors gratefully acknowledge the Epson Atmix Corporation (Japan) for supplying the MG powders, the Thermal Spray Center of Barcelona, the Department of Engineering "Enzo Ferrari" (Modena, Italy), and the Universidad Nacional Autonoma de Mexico (UNAM) – campus Morelos.

References

Afonin GV, Mitrofanov YP, Makarov AS, Kobelev NP, Wang WH, Khonik VA (2016) Universal relationship between crystallization-induced changes of the shear modulus and heat release in metallic glasses. Acta Mater 115:204–209. https://doi.org/10.1016/j.actamat.2016.06.002

Argon AS (1979) Plastic deformation in metallic glasses. Acta Metall 27(1):47–58. https://doi.org/10.1016/0001-6160(79)90055-5

Ashby MF, Greer AL (2006) Metallic glasses as structural materials. Scr Mater 54(3):321–326. https://doi.org/10.1016/j.scriptamat.2005.09.051

Assadi H, Kreye H, Gärtner F, Klassen T (2016) Cold spraying–a materials perspective. Acta Mater 116:382–407. https://doi.org/10.1016/j.actamat.2016.06.034

Concustell A, Henao J, Dosta S, Cinca N, Cano IG, Guilemany JM (2015) On the formation of metallic glass coatings by means of cold gas spray technology. J Alloys Compd 651:764–772. https://doi.org/10.1016/j.jallcom.2015.07.270

Demetriou MD, Johnson WL (2004) Modeling the transient flow of undercooled glass-forming liquids. J Appl Phys 95(5):2857–2865. https://doi.org/10.1063/1.1645669

Dunkley JJ (1998) Atomization: in ASM handbook, powder metal technologies and applications. ASM International, Materials Park, pp 35–52

Fauchais P, Montavon G, Bertrand G (2010) From powders to thermally sprayed coatings. J Therm Spray Technol 19:57–80

Gheiratmand T, Hosseini HM, Davami P, Sarafidis C (2016) Fabrication of FINEMET bulk alloy from amorphous powders by spark plasma sintering. Powder Technol 289:163–168. https://doi.org/10.1016/j.powtec.2015.11.060

Grujicic M, Zhao CL, DeRosset WS, Helfritch D (2004) Adiabatic shear instability based mechanism for particles/substrate bonding in the cold-gas dynamic-spray process. Mater Des 25(8):681–688. https://doi.org/10.1016/j.matdes.2004.03.008

Henann D, Anand L (2008) A constitutive theory for the mechanical response of amorphous metals at high temperatures spanning the glass transition temperature: application to microscale thermoplastic forming. Acta Mater 56(13):3290–3305. https://doi.org/10.1016/j.actamat.2008.03.007

Henao J, Concustell A, Dosta S, Cinca N, Cano IG, Guilemany JM (2016) Influence of the substrate on the formation of metallic glass coatings by cold gas spraying. J Therm Spray Technol 25(5):992–1008. https://doi.org/10.1007/s11666-016-0419-3

Henao J, Concustell A, Dosta S, Bolelli G, Cano IG, Lusvarghi L, Guilemany JM (2017) Deposition mechanisms of metallic glass particles by cold gas spraying. Acta Mater 125:327–339. https://doi.org/10.1016/j.actamat.2016.12.007

Huang R, Suo Z, Prevost JH, Nix WD (2002) Inhomogeneous deformation in metallic glasses. J Mech Phys Solids 50(5):1011–1027. https://doi.org/10.1016/S0022-5096(01)00115-6

Inoue A (2000) Stabilization of metallic supercooled liquid and bulk amorphous alloys. Acta Mater 48(1):279–306. https://doi.org/10.1016/S1359-6454(99)00300-6

Itoi T, Takamizawa T, Kawamura Y, Inoue A (2001) Fabrication of Co 40 Fe 22 Nb 8 B 30 bulk metallic glasses by consolidation of gas-atomized powders and their soft-magnetic properties. Scr Mater 45(10):1131–1137. https://doi.org/10.1016/S1359-6462(01)01122-8

Jodoin B, Ajdelsztajn L, Sansoucy E, Zúñiga A, Richer P, Lavernia EJ (2006) Effect of particle size, morphology, and hardness on cold gas dynamic sprayed aluminum alloy coatings. Surf Coat Technol 201:3422–3429

Johnson WL (2002) Bulk amorphous metal—an emerging engineering material. JOM 54(3):40–43. https://doi.org/10.1007/BF02822619

Kawamura Y, Nakamura T, Inoue A, Masumoto T (1999) High-strain-rate superplasticity due to Newtonian viscous flow in La55Al25Ni20 metallic glass. Mater Trans JIM 40(8):794–803. https://doi.org/10.2320/matertrans1989.40.794

Lagogianni AE, Krausser J, Evenson Z, Samwer K, Zaccone A (2016) Unifying interatomic potential, g (r), elasticity, viscosity, and fragility of metallic glasses: analytical model, simulations, and experiments. J Stat Mech Theory Exp 2016(8):084001. https://doi.org/10.1088/1742-5468/2016/08/084001

Li N, Chen W, Liu L (2016) Thermoplastic micro-forming of bulk metallic glasses: a review. JOM 68(4):1246–1261. https://doi.org/10.1007/s11837-016-1844-y

List A, Gartner F, Schmidt T, Klassen T (2012) Impact conditions for cold spraying of hard metallic glasses. J Therm Spray Technol 21:531–540

Liu Z, Chen W, Carstensen J, Ketkaew J, Mota RMO, Guest JK, Schroers J (2016) 3D metallic glass cellular structures. Acta Mater 105:35–43. https://doi.org/10.1016/j.actamat.2015.11.057

LuJ,RavichandranG,JohnsonWL(2003)DeformationbehaviorofthеZr41.2Ti13.8Cu12.5Ni10Be22.5 bulk metallic glass over a wide range of strain-rates and temperatures. Acta Mater 51(12):3429–3443. https://doi.org/10.1016/S1359-6454(03)00164-2

Luborsky FE (1983) Metallic glass formation. In: Davies HA (ed) Amorphous metallic alloys, 1st edn. Butterworth and Co(Publishers), London

March, N.H., Tosi, M.P., (Ed.). (2002). Introduction to liquid state physics. Qualitative description of liquid properties, World Scientific, London

Meng F, Hu D, Gao Y, Yue S, Song J (2016) Cold-spray bonding mechanisms and deposition efficiency prediction for particle/substrate with distinct deformability. Mater Des 109:503–510. https://doi.org/10.1016/j.matdes.2016.07.103

Miller MK, Liaw P (2007) Development and application of late transition metal bulk metallic glass. In: Inuoe A (ed) Bulk metallic glasses: an overview. Springer Science & Business Media, New York

Mridha S, Arora HS, Lefebvre J, Bhowmick S, Mukherjee S (2017) High temperature in situ compression of thermoplastically formed nano-scale metallic glass. JOM 69(1):39–44. https://doi.org/10.1007/s11837-016-1961-7

Nieh TG, Wadsworth J (2006) Homogeneous deformation of bulk metallic glasses. Scr Mater 54(3):387–392. https://doi.org/10.1016/j.scriptamat.2005.04.052

Pauly S, Löber L, Petters R, Stoica M, Scudino S, Kühn U, Eckert J (2013) Processing metallic glasses by selective laser melting. Mater Today 16(1):37–41. https://doi.org/10.1016/j.mattod.2013.01.018

Salman AD, Ghadiri M, Hounslow MJ (2007) In: Lausanne BV (ed) Handbook of powder technology, particle breakage. Elsevier, Switzerland Lausanne

Sanghoon Y, Yuming X, Hwijun K, Changhee L (2009) Dependence of initial powder temperature on impact behaviour of bulk metallic glass in a kinetic spray process. J Phys D Appl Phys 42:1–5

Schroers J (2010) Processing of bulk metallic glass. Adv Mater 22(14):1566–1597. https://doi.org/10.1002/adma.200902776

Schuh CA, Hufnagel TC, Ramamurty U (2007) Mechanical behavior of amorphous alloys. Acta Mater 55(12):4067–4109. https://doi.org/10.1016/j.actamat.2007.01.052

Scully JR, Gebert A, Payer JH (2007) Corrosion and related mechanical properties of bulk metallic glasses. J Mater Res 22(02):302–313. https://doi.org/10.1557/jmr.2007.0051

Spaepen F, Turnbull D (1974) A mechanism for the flow and fracture of metallic glasses. Scr Metall 8(5):563–556. https://doi.org/10.1016/0036-9748(74)90070-2

Sun B, Huang RZ, Ohno N, Fukanuma H (2006) Effect of spraying parameters on stainless steel particle velocity and deposition efficiency in cold spraying. In: International thermal spray conference and exposition: science, innovation, and application. ASM International, Seattle, WA, pp 209–214

Takeuchi A, Kato H, Inoue A (2010) Vogel–Fulcher–Tammann plot for viscosity scaled with temperature interval between actual and ideal glass transitions for metallic glasses in liquid and supercooled liquid states. Intermetallics 18(4):406–411. https://doi.org/10.1016/j.intermet.2009.08.015

Trexler MM, Thadhani NN (2010) Mechanical properties of bulk metallic glasses. Prog Mater Sci 55(8):759–839. https://doi.org/10.1016/j.pmatsci.2010.04.002

Wang WH, Dong C, Shek CH (2004) Bulk metallic glasses. Mater Sci Eng R Rep 44(2):45–89. https://doi.org/10.1016/j.mser.2004.03.001

Xiao-Tao L, Yu-Juan L, Chang-Jiu L (2016) A comparison of cold spray deposition behavior between gas atomized and dendritic porous electrolytic Ni powders under the same spray conditions. Mater Lett 163:58–63

Yoon S, Lee C, Choi H, Jo H (2006) Kinetic spraying deposition behavior of bulk amorphous NiTiZrSiSn feedstock. Mater Sci Eng A 415(1):45–52. https://doi.org/10.1016/j.msea.2005.08.132

Zhong C, Zhang H, Cao QP, Wang XD, Zhang DX, Ramamurty U, Jiang JZ (2016) Deformation behavior of metallic glasses with shear band like atomic structure: a molecular dynamics study. Sci Rep 6. https://doi.org/10.1038/srep30935

Zhou X, Wu X, Mou SJ, Liu J, Zhang J (2010) Simulation of deposition behavior of bulk amorphous particles in cold spraying. Mater Trans 51(10):1977–1980. https://doi.org/10.2320/matertrans.M2010213

Part III
Cold Spray Composites Coatings

Chapter 9
Cold-Sprayed Metal Matrix Composite Coatings

Yik Tung Roy Lee, Tanvir Hussain, Gary A. Fisher, and André G. McDonald

9.1 Introduction

Metal matrix composites (MMCs) are advanced materials that are composed of two or more phases. The matrix phase is typically metal or alloy, while the reinforcing phase or disperse phase can be another metal, a ceramic, or another material, such as a polymer. This introduction will explore the advantages of ceramic-reinforced MMCs, methods of fabricating these MMCs, and a more detailed description of cold spraying as an option for MMC fabrication. This chapter will focus specifically on the use of cold spraying as a method to deposit and develop MMCs that contain ceramic reinforcing phases.

9.1.1 Advantages of MMC

The combination of materials into a MMC can result in material properties that are not obtainable with a single material phase (Chawla and Chawla 2013; Balasubramanian 2013; Kar 2016). The improvements in material properties can be directed at higher hardness, lighter weight, higher strength, and improved wear resistance (Ibrahim et al. 1991; Chawla and Chawla 2013; Balasubramanian 2013; Kar 2016), to name a few. These improvements can be tailored in the MMC by

Y.T.R. Lee • A.G. McDonald (✉)
Department of Mechanical Engineering, University of Alberta,
T6G 2G8 Edmonton, AB, Canada
e-mail: andre.mcdonald@ualberta.ca

T. Hussain
Faculty of Engineering, University of Nottingham, NG7 2RD Nottingham, UK

G.A. Fisher
Innotech Alberta, T6N 1E4 Edmonton, AB, Canada

P. Cavaliere (ed.), *Cold-Spray Coatings*,
https://doi.org/10.1007/978-3-319-67183-3_9

varying the composition and microstructure of the composite (Ibrahim et al. 1991; Chawla and Chawla 2013; Balasubramanian 2013; Kar 2016).

The prediction of MMC material properties has been extensively studied by using the rule of mixtures (ROM) (Ibrahim et al. 1991; Kim 2000; Melendez and McDonald 2013; Melendez et al. 2013). ROM is based on two generalized models: iso-stress and iso-strain models. By considering the material hardness as an example, the iso-strain model describes a theoretical maximum hardness for a MMC based on the volume-weighted average of the hardness of the constituent phases as shown in the following equation:

$$H_{\max} = V_{\mathrm{r}} H_{\mathrm{r}} + V_{\mathrm{m}} H_{\mathrm{m}} \tag{9.1}$$

Similarly, the theoretical minimum for the hardness is defined by

$$H_{\min} = \left(\frac{V_{\mathrm{r}}}{H_{\mathrm{r}}} + \frac{V_{\mathrm{m}}}{H_{\mathrm{m}}} \right)^{-1} \tag{9.2}$$

where H is the hardness of the material and V is the volume fraction. The subscripts r and m denote the reinforcing and matrix phases, respectively.

9.1.2 MMC Fabrication Methods

There are a variety of methods that are available to produce MMCs, including solid-state methods, liquid-state methods, and thermal spraying methods. Liquid-state methods include techniques such as pressure infiltration or squeeze casting. Solid-state methods include powder processing techniques such as sintering or hot pressing. Thermal spraying techniques include high-velocity oxy-fuel (HVOF) spraying, plasma spraying, or cold spraying. Each technique has their own distinctive advantages and disadvantages. Liquid-state methods, such as infiltration, have the advantage of fabricating near net shape structures, which allow for rapid processing of the MMC-based parts and structures (Ibrahim et al. 1991; Chawla and Chawla 2013; Balasubramanian 2013; Kar 2016). However, the use of molten metal during processing results in reduced control of the microstructure of the metal matrix and the distribution of the reinforcing particles (Ibrahim et al. 1991; Chawla and Chawla 2013; Balasubramanian 2013; Kar 2016). Solid-state methods, such as sintering, allow for the fabrication of high-density MMCs and facilitate the mixing and blending of the metal and ceramic powders (Ibrahim et al. 1991; Chawla and Chawla 2013; Balasubramanian 2013; Kar 2016). Sintering does not fully melt the particles and allows for greater control of the final microstructural outcome.

Thermal spraying techniques are similar to the liquid-state and solid-state methods; however, the thermal spray processes are highly scalable with respect to the fabrication and manufacture of coatings. Higher-temperature processes such as

HVOF spraying and plasma spraying can cause unfavorable phase transformations which can negatively impact the properties of the material (Chen and Hutchings 1998; Stewart et al. 1999; Guilemany et al. 1999; Qi et al. 2006; Al-Mutairi et al. 2015). Cold spraying, however, is a lower-temperature spraying technique that minimizes the probability of these unwanted phase transformations in the feedstock material.

9.1.3 Cold Spraying of MMCs

Cold spraying is a deposition method where small powder particles are accelerated in a supersonic gas flow to attain high velocities to enable successful particle deposition into coatings. In high-pressure cold-spray systems, the gas is pressurized to between 1 and 4 MPa and accelerated through a converging diverging de Laval nozzle, and low-pressure cold-spray systems use gas pressures below 1 MPa (Papyrin 2007; Fauchais et al. 2014; Maev and Leshchynsky 2016). Both high- and low-pressure cold-spray systems typically use powders that possess a particle size range of 1–50 μm, which are introduced to the gas stream and are accelerated to velocities between 300 and 1400 m/s (Papyrin 2007; Moridi et al. 2014; Maev and Leshchynsky 2016). Additionally, the temperature of the feedstock materials is maintained well below the melting temperature of the feedstock materials, therefore minimizing undesirable phase transformation and chemical reactions (Kim et al. 2005; Melendez and McDonald 2013). The adhesion of the cold-spray particles relies on the plastic deformation of the metal or alloy particles due to the high impact force of the high-velocity particles.

The spraying and powder parameters that influence the degree of plastic deformation of the metal powders have been studied extensively. Studies have shown that there is a window of deposition that is based on the velocity of the metal powders (Assadi et al. 2003; Schmidt et al. 2006, 2009). For metal powders, the window of deposition is based on a critical velocity and an erosion velocity (Schmidt et al. 2006). Between these velocities, there is an optimum velocity range where the change in particle momentum upon impact produces a force that plastically deforms the particle. This plastic deformation occurs very quickly and can also cause adiabatic shear instability along the interface between the particle and the surface (Schmidt et al. 2006). This adiabatic heating allows for thermal softening and facilitates plastic deformation (Schmidt et al. 2006). The plastic deformation of the impacting metal particle and the surface led to metallurgical bonding and mechanical interlocking of the particles and the subsequent formation of a dense coating (Schmidt et al. 2006). Deposition efficiency of the metal particles is low outside of the window of deposition that is based on the so-called critical velocity of the particles. The critical velocity defines the velocity where particles have sufficient change in momentum to cause the plastic deformation needed for particle adhesion (Schmidt et al. 2006). The erosion velocity defines the velocity where the impacting particles experience sufficient adiabatic shear heating to cause hydrodynamic penetration which erodes the surface (Schmidt et al. 2006).

Exploration of the factors affecting the deposition of ceramic powders in cold spraying has recently been initiated. Various studies have shown the successful deposition of MMC coatings via the cold-spray deposition of metal-ceramic mechanical powder blends (Irissou et al. 2007; Sova et al. 2009, 2011; Hodder et al. 2012) and metal-ceramic composite powders (Gao et al. 2008; Wang and Villafuerte 2009; Feng et al. 2012; Melendez and McDonald 2013). The composition of the MMC material can be controlled to produce the desired MMC composition. However, detailed analysis of the parameters affecting the deposition efficiencies of ceramic powders within the metal-ceramic composite feedstock powder blend is limited. This chapter aims to assemble the research on the cold spraying of MMC coatings by exploring the benefits of spraying with ceramic reinforcing particles in the powder blend and the parameters that affect ceramic particle deposition efficiencies.

9.2 Benefits of Cold Spraying with Ceramics

There are multiple benefits that arise from the inclusion of ceramic powders in the cold spraying MMC coatings. The ceramic powder particles in the feedstock powder have been shown to increase the deposition efficiency of the metal powder and powder mixture. It has also been shown that adhesion and cohesion of the coating improve as a result of including ceramics in the feedstock powder material.

9.2.1 Deposition Efficiency

The improvement in deposition efficiency caused by the inclusion of ceramic powders in the feedstock has been observed in multiple studies (Shkodkin et al. 2006; Irissou et al. 2007; Sova et al. 2009). The specific details of each study are explored further in this section. In each of the studies, ceramic and metal powders were mechanically blended and deposited using cold spraying. The impact of the ceramic powder on the deposition efficiency of the blended powder and of the metal component of the feedstock powder was investigated (Irissou et al. 2007). Further analysis was also conducted by varying the gas temperature of the cold-spray system (Shkodkin et al. 2006). In a study with high-pressure cold-spray system, the ceramic content was fixed and the gas temperature was varied to investigate the impact on the deposition efficiency of the blended powder and the deposition efficiency of the metal component of the feedstock powder (Sova et al. 2009).

Aluminum oxide (Al_2O_3)-aluminum (Al) coatings were deposited by using a low-pressure cold spraying system (Irissou et al. 2007). Pure Al_2O_3 powders and Al powder were blended at 0, 7, 10, 20, 30, 50, and 75 wt.% of the ceramic. Two different Al powders, with mean diameters of 81.5 and 36.2 μm, were investigated. The Al powders were individually mixed with a single Al_2O_3 powder, which had a

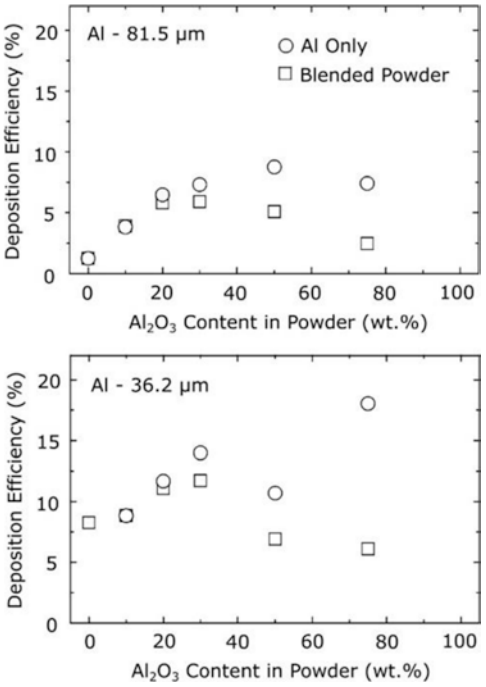

Fig. 9.1 Deposition efficiency of the blended Al_2O_3-Al powder and of the Al metal component (Figure adapted from Irissou et al. (2007))

mean diameter of 25.5 µm. These powders were then fed into a cold spraying unit that used nitrogen as a carrier gas at a pressure of 0.62 MPa and temperature of 773 K. With both sizes of Al powder, the deposition efficiency of both the metal component and the powder mixtures increased with increasing ceramic content up to 30 wt.% ceramic in the feedstock powder as shown in Fig. 9.1. Above 30 wt.% ceramic, the deposition efficiency of the powder mixture decreased. With 75 wt.% of Al_2O_3 in the powder blend, a maximum of 26 wt.% Al_2O_3 in the coating was obtained as shown in Fig. 9.2.

Similar results were found in low-pressure cold-sprayed Al_2O_3-Al and Al_2O_3-copper (Cu) (Shkodkin et al. 2006). The cold-spray system that was used was set to an air pressure of 0.5 MPa, while the gas temperature was between 300 and 900 K. The powders were blended at approximately 0, 12, 16, 28, 54, 70, 78, 88, and 100 wt.% Al_2O_3. Similar to Irissou et al. (2007), Shkodkin et al. (2006) found that the maximum mixture deposition efficiency was observed at 28 wt.% Al_2O_3 in the powder, for the 600, 700, and 800 K cold-sprayed depositions, as shown in Fig. 9.2. As the ceramic content in the powder increased above 28 wt.% Al_2O_3, the deposition efficiency of the powder mixture also decreased (Fig. 9.3).

These results show that the ceramic may have a roughening affect that may create micro-asperities to improve the adhesion of subsequent impacting particles, therefore improving the deposition efficiency (Shkodkin et al. 2006; Irissou et al. 2007). The small-scale roughness or micro-asperities increase the impact pressure at the peaks of the micro-asperities allowing for facilitated plastic deformation of

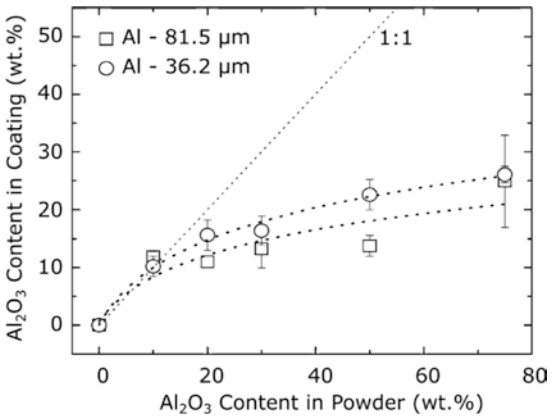

Fig. 9.2 Coating Al_2O_3 content (Figure adapted from Irissou et al. (2007))

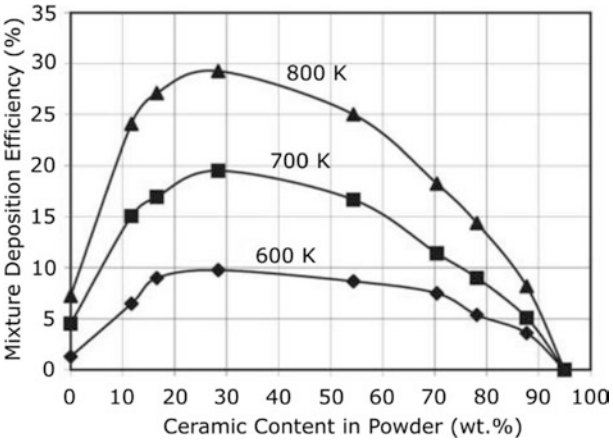

Fig. 9.3 Deposition efficiency of the blended Al_2O_3-Al powder at various temperatures (Figure adapted from Shkodkin et al. (2006))

the substrate and enhanced mechanical interlocking of the incoming particles to the substrate (Shkodkin et al. 2006). This enhanced particle adhesion was noticeable when lower gas deposition temperatures were used. There, the impacting particles have lower velocity, lower impact momentum, and lower impact pressure; therefore, the increased impact pressure at the peaks of the micro-asperities improved plastic deformation and mechanical interlocking (Shkodkin et al. 2006). However, at high ceramic contents, the roughening transitions to material removal resulting in erosion of the coating leading to the observed decrease in deposition efficiency (Irissou et al. 2007).

The improvements to the cold-spray deposition efficiency are not limited to low-pressure cold spraying. High-pressure cold-sprayed Al_2O_3 and silicon carbide (SiC)-based MMC coatings were investigated (Sova et al. 2009). Al_2O_3 and SiC

powders were mixed with Al and Cu powders. The feed rates were controlled such that the cold-sprayed mass composition was 16.5 wt.% Al + 83.5 wt.% ceramic and 37.5 wt.% Cu + 62.5 wt.% ceramic. The powder mixtures were sprayed using nitrogen gas at a pressure of 1.6 MPa. The stagnation gas temperature was varied depending on the metal component. For Al powder deposition, the stagnation gas temperatures used were 373, 423, 473, and 503 K. For Cu powder deposition, the stagnation gas temperatures used were 473, 573, 643, and 698 K. Using fine ceramic powders, with an average particle diameter between 19 and 25 μm, there was a decrease in the critical temperature required for deposition. The decrease in the critical temperature required for deposition is likely due to the activation and roughening of the surface. The activation and roughening caused the formation of micro-asperities that allowed for facilitated plastic deformation and improved particle adhesion.

These studies have shown that the addition of ceramic powders to the cold spraying of metal powders can improve the deposition efficiency of the metal powder (Shkodkin et al. 2006; Irissou et al. 2007; Sova et al. 2009). The roughening of the deposition surface improves the mechanical interlocking between impacting particles and the surface and improves particle adhesion. The roughening of the deposition surface also allows for a decrease in the critical temperature required to deposit the material.

9.2.2 Improving Pull-Off Bond Strength

Activation of the surface and the creation of micro-asperities on the surface can also improve the pull-off bond strength of the deposited coatings. In order to measure the pull-off bond strength of the coatings, tests according to ASTM C633-13 (ASTM International 2013) are typically used. ASTM C633 uses a 1 inch diameter cylinder where the coating is deposited onto the circular flat section. Another cylinder is attached to the coated surface using an epoxy adhesive. The pull-off bond strength of the coating is then measured by pulling the two cylinders apart in a universal tensile frame. Failure can occur at the coating-substrate interface, within the coating, or at the epoxy-coating interface.

An increase in pull-off bond strength with increasing ceramic content in the coatings was found in Al_2O_3-Al coatings (Lee et al. 2005; Irissou et al. 2007). The lowest pull-off bond strength was observed for the metal coating that was devoid of ceramic reinforcement, where the failure was at the coating substrate interface (Lee et al. 2005; Irissou et al. 2007). When the ceramic content was 10 wt.% in the powder blend, the pull-off bond strength increased (Lee et al. 2005; Irissou et al. 2007). As the weight percentage of ceramic in the powder increased further, Irissou et al. (2007) showed that coatings began to fail within the epoxy layer or at the epoxy-coating interface. This suggested that the pull-off bond strength of the coating was higher than the adhesion strength of the epoxy. The results showed that an increase of up to 15 wt.% of Al_2O_3 content in the coating resulted in an

increase in the coating pull-off bond strength (Irissou et al. 2007). For ceramic contents above 15 wt.% of Al_2O_3, the pull-off bond strength was higher than that of the epoxy adhesion strength, but an exact value cannot be determined since failure occurred at the epoxy-coating interface (Irissou et al. 2007). As such the change in pull-off bond strength with increasing ceramic content beyond 15 wt.% was not determined (Irissou et al. 2007). The roughening of the surface from the impacting ceramic particles creates micro-peaks that increase the amount of mechanical interlocking between particles. The increased mechanical interlocking between particles improves the pull-off bond strength of the coating. Using cold-spray parameters similar to Irissou et al. (2007), Lee et al. (2005) found that the pull-off bond strength of the Al_2O_3 coatings increased as the Al_2O_3 content in the powder increase to 50 wt.%.

The effect of Al_2O_3 reinforcement particles on the bond strength of cold-sprayed Al- and 316 L stainless steel-based coatings was investigated (Spencer et al. 2009, 2012). For the cold-spray deposition of Al_2O_3-Al coatings, helium was used as a carrier gas at a pressure of 0.62 MPa and a temperature of 398 K (Spencer et al. 2009). For the Al_2O_3-316 stainless steel coatings, the same gas and pressure was used at a temperature of 593 K (Spencer et al. 2012). The powders were mixed by mass to obtain 0, 25, 50, and 75 vol.% Al_2O_3 in the feedstock powder (Spencer et al. 2009, 2012). For the Al_2O_3-Al coatings, the failures were found to occur within the coating (Spencer et al. 2009). Similarly, for the cold-sprayed steel with no Al_2O_3 reinforcement, the failure was also within the coating. This suggests that the bonding between the deposited particles was weak and the coating had delaminated and failed at the particle interfaces (Spencer et al. 2012). For the Al_2O_3-Al coatings, there was an increase in coating pull-off bond strength with increasing Al_2O_3 content in the feedstock powder (Spencer et al. 2009). This result showed that the impacting ceramic particles create micro-asperities or small-scale roughness, which facilitate mechanical interlocking between the deposited particles and increased the adhesion strength of the coatings (Spencer et al. 2009). For the Al_2O_3-316 stainless steel coatings, with 25 vol.% Al_2O_3 in the feedstock, the adhesion tests showed signs of mixed failure with characteristics of both adhesive and cohesive failure (Spencer et al. 2012). At 50 and 75 vol.% Al_2O_3 in the feedstock powder, there were signs of only adhesive failure (Spencer et al. 2012). These results indicated that the bonding within the coatings had increased. This was likely due to the creation of micro-asperities from the impacting ceramic particles that facilitate the mechanical interlocking between the particles, producing the increased bonding within the coatings (Spencer et al. 2009, 2012).

Improvements in adhesion strength of cold-sprayed coatings were observed by multiple studies (Lee et al. 2005; Shkodkin et al. 2006; Irissou et al. 2007; Spencer et al. 2009, 2012). The activation of the surface by the creation of micro-asperities allows for improved mechanical interlocking between deposited particles, which strengthens the bond between deposited particles and the substrate leading to higher bond strengths.

9.3 Particle Morphology and Spray Parameters

Extensive studies have focused attention on the impact of particle morphology and spray parameters on the deposition and quality of the metal matrix composite coatings (Sova et al. 2009, 2011; Leger et al. 2016). By varying particle parameters, such as size, velocity, and shape, it has been found that ceramic deposition efficiency, the metal deposition efficiency, and in some cases the performance and quality of the coating will be affected.

9.3.1 Particle Size

Particle size may affect the overall deposition due to the interaction between the hard ceramic particle and the soft metal surface. The effect of ceramic particle size was investigated by using aluminum oxide (Al_2O_3) and silicon carbide (SiC) ceramic particles with aluminum (Al) and copper (Cu) metal matrices (Sova et al. 2009). The average diameters of the metal powder particles were 28 μm and 39 μm for the Al and Cu, respectively. For the ceramic powders, two different sizes were tested for both materials. The Al_2O_3 powders had average particle diameters of 19 and 141 μm, while the SiC particles had average particle diameters of 25 and 135 μm. The powders were then fed into a specialty cold-spray nozzle where the metal powder was introduced axially and the ceramic powder radially (see Fig. 9.4). The feed rates were controlled such that the sprayed weight composition was 16.5 wt.% Al + 83.5 wt.% ceramic and 37.5 wt.% Cu + 62.5 wt.% ceramic. Four different mixtures were tested for each metal by varying the size and type of the ceramic. The powder mixtures were sprayed using nitrogen at a pressure of 1.6 MPa. The stagnation gas temperature was varied depending on the metal component. For the Al powders, the stagnation gas temperatures used were 373, 423, 473, and 503 K. For the Cu powders, the stagnation gas temperatures used were 473, 573, 643, and 698 K.

The overall deposition efficiency of the powder mixture and the effective deposition efficiency of the metal component were measured (Sova et al. 2009). Figure 9.5 shows the deposition efficiencies of the cold-sprayed Cu-based MMC. As discussed

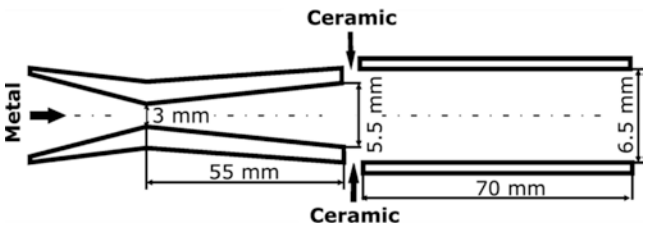

Fig. 9.4 Specialty nozzle design from Sova et al. (2009) (Figure adapted from Sova et al. (2009))

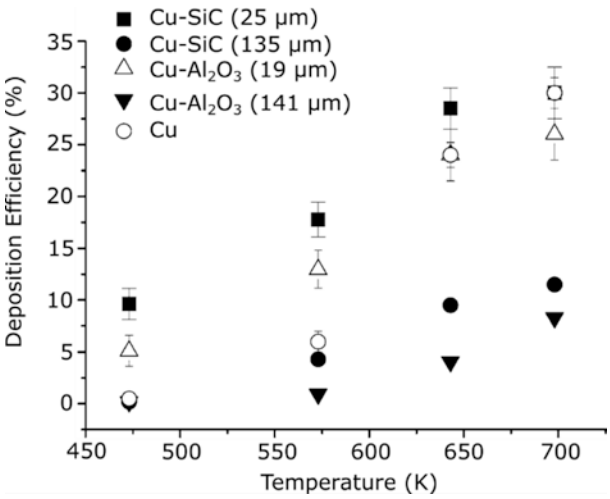

Fig. 9.5 Deposition efficiency of Cu-based MMC deposited by Sova et al. (2009) (Figure adapted from Sova et al. (2009))

previously, the results showed that the fine ceramic particles improved the deposition efficiency of the metal component and of the blended powder.

The coarse ceramic particles were found to impact the deposition efficiencies negatively at the higher temperatures (Sova et al. 2009). At lower temperatures, there was little change in deposition efficiency with the addition of coarse ceramic particles, as shown in Fig. 9.5. The impacting ceramic particles acted as erosive media against the surface, and the fine ceramic particles cause small volumes of material to be removed and create micro-peaks where plastic deformation can easily occur resulting in more mechanical interlocking and improved adhesion for subsequent impacting particles. The coarse ceramic particles more material and the peaks that remain are larger and may not improve mechanical interlocking of subsequent particles. Although the purpose of the study by Sova et al. (2009) was not to investigate specifically the deposition efficiency of the ceramic component, overall, the results do show that the coarse ceramic particles will erode the surface and removed the previously deposited layers, which negatively impacts the metal deposition efficiency and the overall deposition efficiency.

9.3.2 Particle Velocity

In order to study the effect of particle velocity, the particles were introduced at different locations in the nozzle (Sova et al. 2011). The three different nozzle configurations in Fig. 9.6 were investigated (Sova et al. 2011). The first and third nozzles were the same with a critical section diameter of 2.7 mm and an exit diameter of 6.5 mm; only the ceramic injection point was varied. The first

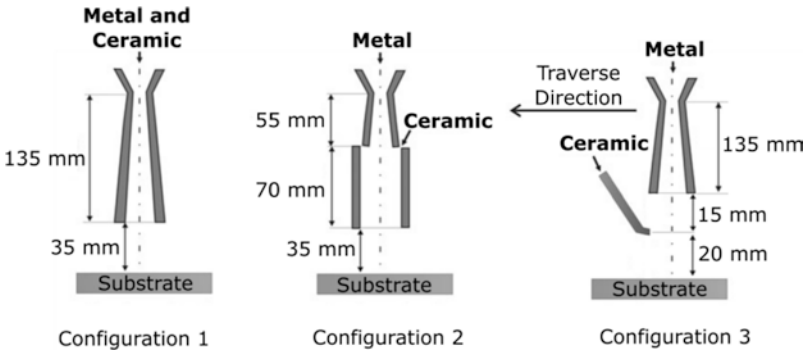

Fig. 9.6 Specialty nozzle configurations from Sova et al. (2011) (Figure adapted from Sova et al. (2011))

configuration had the ceramic powder introduced axially along with the metal powder. The third nozzle configuration had the ceramic powder introduced after the gas exited the nozzle in the free gas jet. The second nozzle configuration is the nozzle used in the Sova et al. (2009) in Fig. 9.4, where the ceramic powder is introduced perpendicular to the gas flow. The ceramic powders that were investigated are Al_2O_3 and SiC. The average particle diameters of the Al_2O_3 powder were 19 and 127 μm, while the SiC particles had average diameters of 25 and 135 μm. The ceramic powders were mixed with Al and Cu with a targeted 50 vol.% metal and 50 vol.% ceramic mix. These metal-ceramic mixtures were deposited in a high-pressure cold-spray unit with 3 MPa nitrogen gas at a stagnation temperature of 700 K for Cu blends and 500 K for Al blends.

The location at which the ceramic particles were introduced influenced their velocity. The velocities of the particles were measured using a CCD-camera-based diagnostic measurement system. It was found that the ceramics introduced in configuration 1 had the highest velocities, followed by configuration 2. Configuration 3 had the slowest particles due to the shortest interaction with the high-velocity gas stream. Additionally, it was also found that the smaller particles had a higher velocity than the larger particles. This is due to their lower mass that allows for them to be accelerated to higher velocities. The small particles, with an average diameter of 19 and 25 μm, had the highest velocity of approximately 600 m/s in the first nozzle configuration at a gas stagnation temperature of 700 K. The large particles, with an average diameter of 127 and 135 μm, had the lowest velocity of approximately 100 m/s in the third nozzle configuration at a gas stagnation temperature of 500 K. These velocity results are summarized in Fig. 9.7.

In turn these velocities affect the resultant ceramic content in the coatings. The ceramic volume contents are also summarized in Fig. 9.4. The maximum ceramic content was approximately 16 vol.%; it was achieved with small (25 μm) SiC particles and Cu powder in configuration 1. This was the ceramic powder with the highest velocity. The coarse ceramic particles had the lowest velocities in configuration 3, and this resulted in ceramic contents below 1 vol.%. Overall the ceramic

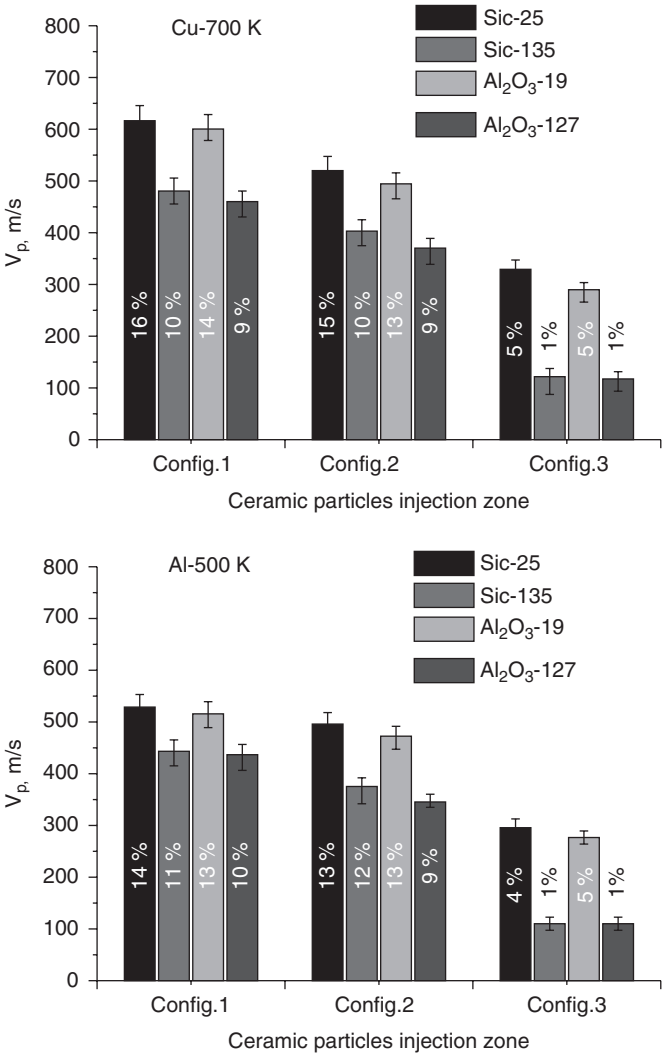

Fig. 9.7 Ceramic particle velocities and coating ceramic volume contents from Sova et al. (2011) (Figure adapted from Sova et al. (2011))

contents within the coatings were similar in configurations 1 and 2 where the same ceramic type, ceramic size, and metal binder were compared. In configuration 3, there is a significant drop in the ceramic content within the coatings. The mixtures with the fine ceramic powders obtain a ceramic content of approximately 5 vol.%, while the coarse ceramic powder mixtures in configuration 3 had less than 1 vol.% in the coating.

These results show that the ceramic content within the coating is affected by the velocity of the particles. When comparing the result of configurations 2 and 3, with

an increase in the velocity of both the coarse and fine ceramic particles, there is an increase in the ceramic content within the coating. The velocity difference between configurations 1 and 2 is less significant, and the difference in ceramic content is also less significant. It was suggested that for a given particle size of ceramic, there exists a minimum velocity for ceramic deposition (Sova et al. 2011). The large ceramic particles, between 50 and 100 μm, require a velocity of between 350 and 500 m/s for the ceramics to deposit (Sova et al. 2011). Smaller ceramic particles, between 10 and 30 μm, the critical velocity for ceramic deposition is below 300 m/s (Sova et al. 2011). The velocity of the particles affects the momentum of the particles, which in turn affects the force upon which the particles impacts. The critical velocity for smaller particles is lower as there is more surface activation from the surface-roughening effect that the ceramic particles have on the substrate or coating surface to improve substrate side plastic deformation.

9.3.3 Particle Morphology

Particle morphology may impact the ceramic content within a coating. The effect of powder morphology on the microstructure of the coatings was investigated during the deposition of Al_2O_3-Al coatings (Shockley et al. 2015; Leger et al. 2016). Al_2O_3-Al powder blends were deposited using a high-pressure cold-spray system. The cold-spray system parameters were nitrogen gas at a pressure of 2.5 MPa (Leger et al. 2016) or 3 MPa (Shockley et al. 2015) and temperature of 673 K. The powder blends were a combination of spherical and irregular Al and Al_2O_3 powders.

The ceramic contents of these cold-sprayed Al_2O_3-Al coatings were investigated (Shockley et al. 2015; Leger et al. 2016). Table 9.1 summarized the Al_2O_3 content in the coating obtained by these studies (Shockley et al. 2015; Leger et al. 2016). Higher ceramic contents in the coatings were found when angular ceramic particles were used (Shockley et al. 2015; Leger et al. 2016). Some hollow spherical Al_2O_3 particles were found within the coating. Thus, it was concluded that other hollow spherical Al_2O_3 particles may have exploded due to the high momentum impact of the particles (Leger et al. 2016). The explosion may cause small fragments of Al_2O_3 to disperse in every direction; therefore, a lower amount of Al_2O_3 would be found in

Table 9.1 Al_2O_3 content in the cold-sprayed Al_2O_3-Al coatings

	Al_2O_3 content coating (wt.%)			
	With irregular Al – 15 wt.% Al_2O_3 (Leger et al. 2016)	With spherical Al – 15 wt.% Al_2O_3 (Leger et al. 2016)	With spherical Al – 10 wt.% Al_2O_3 (Shockley et al. 2015)	With spherical Al – 50 wt.% Al_2O_3 (Shockley et al. 2015)
Spherical Al_2O_3	3.5	2.7	3	11
Angular Al_2O_3	8.1	5.3	10	22

the final coating (Leger et al. 2016). Another possibility presented by Shockley et al. (2015) is based on the work on solid particle erosion by Getu et al. (2012). In order for an impacting ceramic particle to embed into a surface, the frictional forces between the particle and substrate must be larger than the elastic rebound forces of the particle (Getu et al. 2012). For spherical particles, this means that the particle must impact to a depth greater than its radius to be embedded (Getu et al. 2012). The angular ceramic particles may also embed better due to the increased roughness of the surface from impacting angular particles. The roughness has an activation effect on the surface which could improve substrate side deformation and increase the ceramic content of the coating sprayed with angular Al_2O_3 particles.

The effects of the powder morphology and spray parameters were investigated by multiple studies (Sova et al. 2009, 2011; Shockley et al. 2015; Leger et al. 2016). It was found that smaller particles of approximately 20 μm improved the deposition efficiency and reduced the critical temperature required to deposit metals and larger particles of approximately 130 μm reduced deposition efficiency by eroding the surface. Additionally, the smaller particles required lower particle velocity to deposit successfully within the coating. In terms of the morphology of the ceramic particles, it was found that angular particles were better retained in the coatings than spherical particles.

9.4 Composite Powders

In lieu of mechanically blending a ceramic powder and a metal powder for cold-spray deposition, composite powders can also be used. Composite powders are powders that are already MMCs before the cold-spray deposition process. The composite powders can be ceramic powders that are coated with metal or a composite powder with ceramic sub-particles held together by a metal matrix. The use of composite powders allows for further increase in the ceramic content obtained within the coatings. Ceramic powders are friable and have low fracture toughness, which causes the particles to fracture upon impact, therefore decreasing the ceramic content in the coating. The use of metal-ceramic composite powders or coated ceramic powders may offer protection for the ceramic and can reduce ceramic fracture.

9.4.1 Coated Ceramic Powders

The ceramic powders can be coated in metal to create a composite powder made of a ceramic core and a metal shell. Diamond particles were incorporated into a bronze matrix using cold-spray (Na et al. 2009). The diamond content of the feedstock powder was 20 vol.% diamond. The cold-spray parameter used was nitrogen gas at a pressure of 2.5 MPa and a temperature of 773 K. The original diamond powder had a particle size of +15–25 μm, where the Ni coating the particles increases to a

size range of +20–30 μm. In order to compare the amount of fracture in the deposited diamond particles, a broken ratio was developed and was calculated based on the following equation:

$$\text{Broken Ratio}(\%) = \left(1 - \frac{d_c}{d_p}\right) * 100 \tag{9.3}$$

where d_c is the diameter of diamond in the coating and d_p is the diameter of diamond in the powder. The results showed that the uncoated diamond particles had a broken ratio of 68%, while the Ni-coated diamond particles had a broken ratio of 12%. Although not measured directly, it was also observed that the Ni-coated diamond resulted in a higher diamond content in the coatings as shown in Fig. 9.8. This higher diamond content and lower broken ratio are due to lower impact stress. The impact stress of the coated and uncoated diamond particles was also simulated using finite element analysis (FEA). The Ni layer acted as a protective impact layer. The FEA showed that the uncoated diamond particles experienced an impact stress of 122.5 GPa and the Ni coating decreased the stress experienced by the diamond particle down to 11.32 GPa. This decrease in impact stress allowed for the decreased fracturing and increased diamond content in the coating.

The coated diamond coatings did not achieve high ceramic contents, but a method for decreasing the impact stress experienced by the ceramic powders was developed. Ni-coated boron carbide (B_4C) and B_4C-Ni powder blends were deposited using high-pressure cold spraying (Feng et al. 2012). The feedstock powders used contained high ceramic content between 54 and 87 vol.% (Feng et al. 2012). The coated B_4C powders were coated with Ni using chemical vapor deposition, while the uncoated B_4C powders were mechanically blended with Ni powder to obtain the same B_4C contents in the feedstock powder. The results showed that for a mechanical powder blend, the maximum B_4C content obtained in the coating was 18.7 vol.%; this was produced using a powder blend with 87 vol.% B_4C. For the same 87 vol.% B_4C in the Ni-coated B_4C powder, a B_4C content of 32.7 vol.% was obtained. However, the maximum B_4C content obtained with the Ni-coated B_4C was 44 vol.% using a Ni-coated powder with 78 vol.% B_4C. These results show that higher ceramic contents in the coating can be obtained by protecting the ceramic powder using a metal coating which reduces the impact stress on the ceramic particles, reduces the amount of fracturing, and increase the ceramic deposition efficiency.

Wang and Villafuerte (2009) also investigated the cold-spray deposition of metal-coated ceramic powders. A low-pressure cold-spray system was used to deposit tungsten carbide (WC) with Cu or Al as the metal matrix. Compressed air was used as the carrier gas at a pressure of 0.5–0.6 MPa and a temperature of 648–813 K. The metal-coated powders were prepared by chemical vapor deposition (CVD) for the WC-Al powder, while electroplating was used to coat the WC particles with Cu. The WC-Al composite powder had a WC content of 70 wt.%, and the WC-Cu composite powder had a WC content of 80 wt.%. Mechanically blended powders with

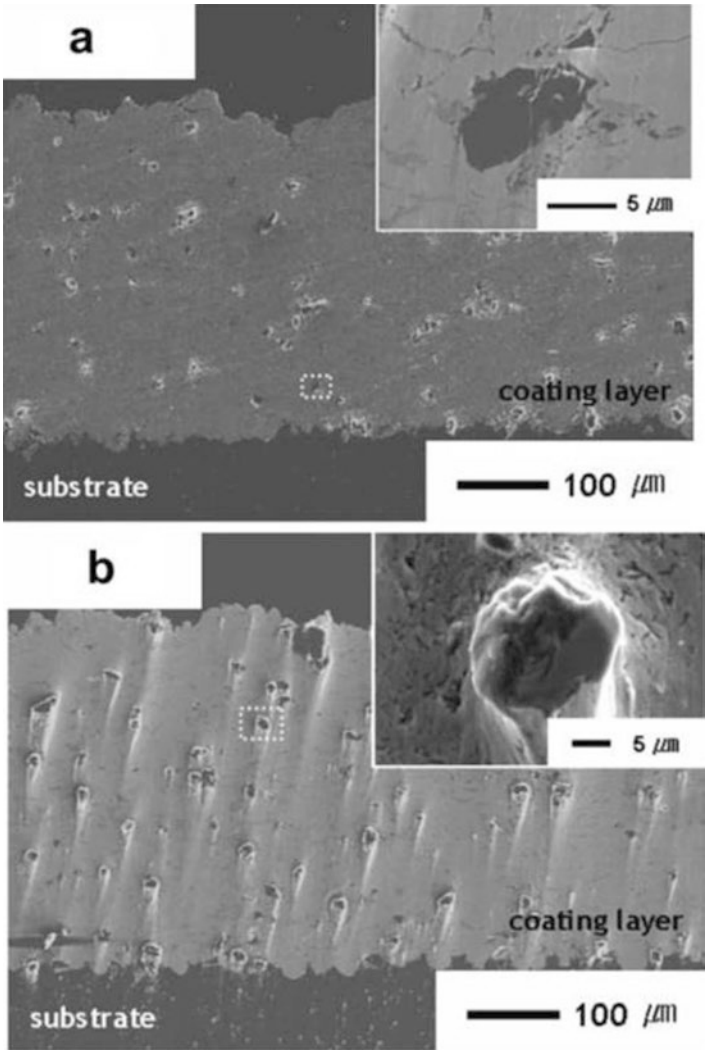

Fig. 9.8 Diamond-bronze composite with (**a**) uncoated diamond and (**b**) Ni-coated diamond (Figure from Na et al. (2009))

70 wt.% WC were also deposited using the same cold-spray parameters. It was observed that the coated ceramic particles had sufficient soft metal around the carbide particle to deposit similarly to a soft metal powder during cold spraying. The cold spraying of Al- and Cu-coated WC composite powders obtained an estimated 55 vol.% WC within the coating, and the WC particles were well dispersed within the coating. By comparison, the mechanically blended WC-Al powder with 70 wt.% ceramic phase resulted in a WC content of approximately 30 vol.% in the coating, while the mechanically blended WC-Cu powder with 70 wt.% ceramic phase

resulted in a WC content of approximately 65 vol.% in the coating. However, both the Al- and Cu-based coatings, deposited from metal-coated WC composite powders blended powders, had greater homogeneity in the dispersion of WC and were estimated to have lower porosity.

9.4.2 Agglomerated Powders

Although these results are promising, using chemical vapor deposition to create powder can be expensive; Melendez and McDonald (2013) showed that using commercially available composite powders with high ceramic content within the coatings can be obtained. A commercially available WC-cobalt (Co) composite powder was mechanically blended with Ni for cold-spray deposition. The mechanical powder blends were fed into a cold-spray system with air as the working gas, at a pressure of 0.63 MPa and temperature of 823 K. A maximum of ceramic content of 52 vol.% WC was obtained within the coating using a feedstock powder that contained 93 vol.% WC-Co. The high ceramic content is likely due to the Co metal protecting the WC particles from high impact stresses. Additionally, due to the sintered and agglomerated nature of the composite WC-Co powder, there was likely increased malleability of the composite powder. This malleability results from the Co metal that was located between the WC sub-particles within the larger WC-Co powder. As such, when the WC-Co particles impact upon the surface, the Co plastically deforms allowing for the WC sub-particles to realign and fabricate a coating.

The effect of the WC sub-particle size on the deposition of cold-sprayed WC-Co particles was investigated (Ang et al. 2011). A high-pressure cold-spray system was used with helium gas at a pressure of 1.2–1.5 MPa and temperature of approximately 873 K. The WC-17 wt.% Co composite powders used had a mean particle size of approximately 30 μm, and the WC sub-particles were either 2–3 μm or 80–700 nm. By using only two passes of the cold-spray nozzle, deposition of the WC-Co coating using the micron-sized WC sub-particles resulted in a coating that was approximately 20 μm thick, while the powder with nanosized WC sub-particles resulted in a coating that was over 500 μm thick as shown in Fig. 9.9. This result indicates that the smaller sub-particles improve the cold-spray deposition of the WC-Co. The nanostructured WC sub-particles were found to deposit better due to their increased contact area to the ductile Co. The increased contact area allowed for the impacting WC sub-particles to embed into the already deposited soft Co matrix, thereby improving the adhesion of subsequent particles to the surface. In the WC-Co composite powder with micron-sized sub-particles, the lower contact area between Co and WC resulted in an increased probability that the impacting WC sub-particle would impact another WC sub-particle, resulting in particle fracture and erosion instead of adhesion. There was evidence of particle fracture from the peak broadening in the XRD analysis of the coating fabricated from the WC-Co powder with micron-sized sub-particles when compared to the coating fabricated from the WC-Co powder with micron-sized sub-particles. Additionally, the smaller size of

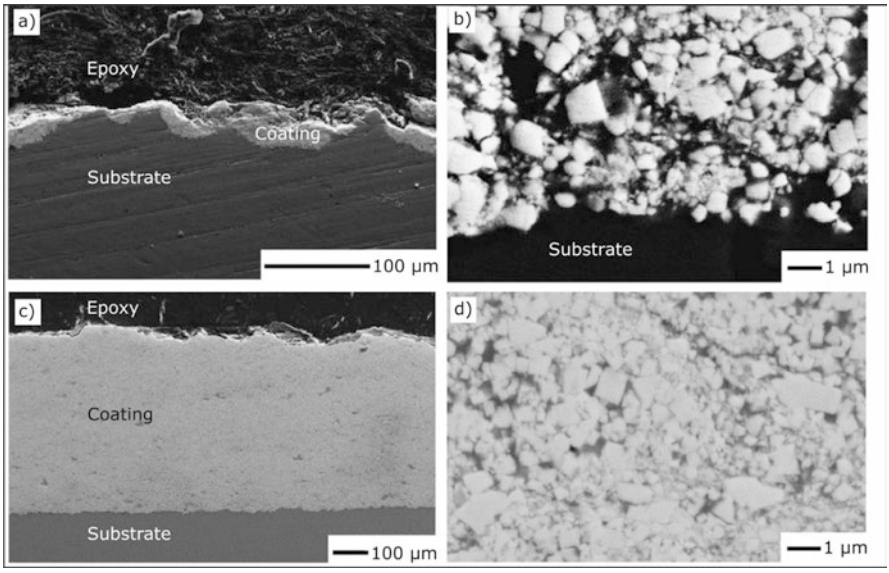

Fig. 9.9 Morphology of the WC-Co coatings deposited with (**a**, **b**) micron-sized WC sub-particles and (**c**, **d**) nanosized WC sub-particles (Figure adapted from Ang et al. (2011))

the WC sub-particles allowed for the realignment of WC sub-particles during the impact, which likely improved the deformability of the WC-Co particle.

The importance of composite powder deformability was investigated by Gao et al. (2008). The deformability of a WC-12 wt.% Co powder was controlled by varying the porosity of the powder. Three WC-12 wt.% Co powders with 44, 30, and 5% porosity were deposited using a high-pressure cold-spray system, where helium carrier gas was used at a pressure of 2.0–2.5 MPa and a temperature of 913 K. It was found that the high-porosity particle collapsed upon impact, which allowed for high particle deformability. However, the high porosity results in low particle hardness, which reduced the ease at which the particle embedded itself into the previously deposited layers, reducing the overall deposition efficiency of the coating. Low-porosity particles have high hardness and can easily embed themselves into the substrate. However, at the second layer of deposition, the low-porosity and high-hardness particles create high impact pressure which may cause the propagation of existing cracks, which may cause spallation within the coating. As such, a thick coating using low porosity powder was not obtained. The medium porosity powder produced the thickest coating after two passes, as it had sufficient hardness to embed into previously deposited layers and sufficient deformability not to cause significant spallation within the coating. The results show that by controlling the porosity, deformability, and hardness of a composite powder, the deposition behavior of that powder can also be controlled.

These studies have shown that by using composite powders, the retention of ceramics in cold-sprayed MMC coatings can be improved. Metal coatings on

ceramic powders will reduce the impact stress experienced by the ceramic particle and improve ceramic retention. Designing agglomerated composite powders with small ceramic sub-particles and controlling the porosity of the agglomerated particles can also improve the deformability of the composite powder and improve the deposition efficiency of the powder.

9.5 Conclusion

This work has explored the fabrication of MMC using cold-spray deposition. The inclusion of ceramic powder in the cold spraying process improved the deposition efficiency and lowered the critical temperature required for material deposition. The use of small ceramic powders, on the order of 10 and 50 μm, activated the deposition surface. The impacting ceramic particles created micro-asperities which concentrated the impact pressure at the peaks, thereby facilitating the plastic deformation and mechanical interlocking required for the fabrication of cold-spray coatings. The increased mechanical interlocking also improved the bond strength between particles and between the coating and the substrate. Large ceramic particles, on the order of 130 μm, eroded the surface and reduced the deposition efficiency of the cold-sprayed powder.

Obtaining the desired ceramic content within a cold-sprayed MMC can be accomplished by varying powder morphology, cold-spray parameters, and powder composition. Angular particles have been found to have higher ceramic retention during cold-spray deposition. Ceramic deposition efficiency also depends on the size of the ceramic particle, wherein larger particles require higher velocity. It was found that particles between 50 and 100 μm required velocities between 350 and 500 m/s for the ceramics to deposit, while ceramic particles between 10 and 30 μm required velocities below 300 m/s. However, high velocities will produce high impact forces which may result in ceramic particle fracture and a decrease in the ceramic deposition efficiency. Metal coatings on the ceramic particles protected the ceramic particle from high impact stress and improved the deposition efficiency of the MMC. The use of agglomerated composite powders also improved the deposition efficiency of the MMC. High deformability within the agglomerated composite powder is desirable in the cold-spray deposition. The deformability of an agglomerated composite particle can be increased by decreasing the ceramic sub-particle size or by increasing the porosity of the agglomerate.

References

Al-Mutairi S, Hashmi MSJ, Yilbas BS, Stokes J (2015) Microstructural characterization of HVOF/plasma thermal spray of micro/nano WC–12%co powders. Surf Coat Technol 264:175–186. https://doi.org/10.1016/j.surfcoat.2014.12.050

Ang ASM, Berndt CC, Cheang P (2011) Deposition effects of WC particle size on cold sprayed WC–Co coatings. Surf Coat Technol 205:3260–3267. https://doi.org/10.1016/j.surfcoat.2010.11.045

Assadi H, Gärtner F, Stoltenhoff T, Kreye H (2003) Bonding mechanism in cold gas spraying. Acta Mater 51:4379–4394. https://doi.org/10.1016/S1359-6454(03)00274-X

ASTM International (2013) ASTM C633–13, standard test method for adhesion or cohesion strength of thermal spray coatings. ASTM International, West Conshohocken

Balasubramanian M (2013) Composite materials and processing. Taylor & Francis, Boca Raton, Florida

Chawla N, Chawla KK (2013) Metal matrix composites. Springer New York, New York

Chen H, Hutchings I (1998) Abrasive wear resistance of plasma-sprayed tungsten carbide–cobalt coatings. Surf Coat Technol 107:106–114. https://doi.org/10.1016/S0257-8972(98)00581-7

Fauchais PL, Heberlein JVR, Boulos MI (2014) Thermal spray fundamentals. Springer US, Boston

Feng C, Guipont V, Jeandin M et al (2012) B_4C/Ni composite coatings prepared by cold spray of blended or CVD-coated powders. J Therm Spray Technol 21:561–570. https://doi.org/10.1007/s11666-012-9774-x

Gao P-H, Li Y-G, Li C-J et al (2008) Influence of powder porous structure on the deposition behavior of cold-sprayed WC-12Co coatings. J Therm Spray Technol 17:742–749. https://doi.org/10.1007/s11666-008-9258-1

Getu H, Spelt JK, Papini M (2012) Conditions leading to the embedding of angular and spherical particles during the solid particle erosion of polymers. Wear 292–293:159–168. https://doi.org/10.1016/j.wear.2012.05.017

Guilemany JM, de Paco JM, Miguel JR, Nutting J (1999) Characterization of the W_2C phase formed during the high velocity oxygen fuel spraying of a WC + 12 pct Co powder. Metall Mater Trans A 30:1913–1921. https://doi.org/10.1007/s11661-999-0002-3

Hodder KJ, Izadi H, McDonald AG, Gerlich AP (2012) Fabrication of aluminum–alumina metal matrix composites via cold gas dynamic spraying at low pressure followed by friction stir processing. Mater Sci Eng A 556:114–121. https://doi.org/10.1016/j.msea.2012.06.066

Ibrahim IA, Mohamed FA, Lavernia EJ (1991) Particulate reinforced metal matrix composites – a review. J Mater Sci 26:1137–1156. https://doi.org/10.1007/BF00544448

Irissou E, Legoux J-G, Arsenault B, Moreau C (2007) Investigation of Al-Al_2O_3 cold spray coating formation and properties. J Therm Spray Technol 16:661–668. https://doi.org/10.1007/s11666-007-9086-8

Kar KK (ed) (2016) Composite materials: processing, applications, characterizations, 1st edn. Springer, New York

Kim H-J, Lee C-H, Hwang S-Y (2005) Fabrication of WC–Co coatings by cold spray deposition. Surf Coat Technol 191:335–340. https://doi.org/10.1016/j.surfcoat.2004.04.058

Kim HS (2000) On the rule of mixtures for the hardness of particle reinforced composites. Mater Sci Eng A 289:30–33. https://doi.org/10.1016/S0921-5093(00)00909-6

Lee HY, Jung SH, Lee SY et al (2005) Correlation between Al_2O_3 particles and interface of Al–Al_2O_3 coatings by cold spray. Appl Surf Sci 252:1891–1898. https://doi.org/10.1016/j.apsusc.2005.03.148

Maev RG, Leshchynsky V (eds) (2016) Cold gas dynamic spray. CRC Press/Taylor & Francis Group, Boca Raton

Melendez NM, McDonald AG (2013) Development of WC-based metal matrix composite coatings using low-pressure cold gas dynamic spraying. Surf Coat Technol 214:101–109. https://doi.org/10.1016/j.surfcoat.2012.11.010

Melendez NM, Narulkar VV, Fisher GA, McDonald AG (2013) Effect of reinforcing particles on the wear rate of low-pressure cold-sprayed WC-based MMC coatings. Wear 306:185–195. https://doi.org/10.1016/j.wear.2013.08.006

Moridi A, Hassani-Gangaraj SM, Guagliano M, Dao M (2014) Cold spray coating: review of material systems and future perspectives. Surf Eng 30:369–395. https://doi.org/10.1179/1743294414Y.0000000270

Na H, Bae G, Shin S et al (2009) Advanced deposition characteristics of kinetic sprayed bronze/diamond composite by tailoring feedstock properties. Compos Sci Technol 69:463–468. https://doi.org/10.1016/j.compscitech.2008.11.015

Papyrin A (2007) Cold spray technology. Elsevier, Amsterdam/London

Leger P-E, Borit F, Fabregue N, Jeandin M (2016) Influence of powder characteristics on the microstructure and bond strength of cold-sprayed aluminum coating. ASM International, Shanghai

Qi X, Eigen N, Aust E et al (2006) Two-body abrasive wear of nano- and microcrystalline TiC–Ni-based thermal spray coatings. Surf Coat Technol 200:5037–5047. https://doi.org/10.1016/j.surfcoat.2005.05.007

Schmidt T, Assadi H, Gärtner F et al (2009) From particle acceleration to impact and bonding in cold spraying. J Therm Spray Technol 18:794–808. https://doi.org/10.1007/s11666-009-9357-7

Schmidt T, Gärtner F, Assadi H, Kreye H (2006) Development of a generalized parameter window for cold spray deposition. Acta Mater 54:729–742. https://doi.org/10.1016/j.actamat.2005.10.005

Shkodkin A, Kashirin A, Klyuev O, Buzdygar T (2006) Metal particle deposition stimulation by surface abrasive treatment in gas dynamic spraying. J Therm Spray Technol 15:382–386. https://doi.org/10.1361/105996306X124383

Shockley JM, Descartes S, Vo P et al (2015) The influence of Al2O3 particle morphology on the coating formation and dry sliding wear behavior of cold sprayed Al–Al2O3 composites. Surf Coat Technol 270:324–333. https://doi.org/10.1016/j.surfcoat.2015.01.057

Sova A, Kosarev VF, Papyrin A, Smurov I (2011) Effect of ceramic particle velocity on cold spray deposition of metal-ceramic coatings. J Therm Spray Technol 20:285–291. https://doi.org/10.1007/s11666-010-9571-3

Sova A, Papyrin A, Smurov I (2009) Influence of ceramic powder size on process of cermet coating formation by cold spray. J Therm Spray Technol 18:633–641. https://doi.org/10.1007/s11666-009-9359-5

Spencer K, Fabijanic DM, Zhang M-X (2009) The use of Al–Al_2O_3 cold spray coatings to improve the surface properties of magnesium alloys. Surf Coat Technol 204:336–344. https://doi.org/10.1016/j.surfcoat.2009.07.032

Spencer K, Fabijanic DM, Zhang M-X (2012) The influence of Al_2O_3 reinforcement on the properties of stainless steel cold spray coatings. Surf Coat Technol 206:3275–3282. https://doi.org/10.1016/j.surfcoat.2012.01.031

Stewart DA, Shipway PH, McCartney DG (1999) Abrasive wear behaviour of conventional and nanocomposite HVOF-sprayed WC–Co coatings. Wear 225–229:789–798. https://doi.org/10.1016/S0043-1648(99)00032-0

Wang J, Villafuerte J (2009) Low pressure cold spray of tungsten carbide composite coatings. Adv Mater Process 167:54–56

Chapter 10
Metal Matrix Composite Coatings by Cold Spray

Min Yu and Wenya Li

10.1 Introduction

Having the advantage of alleviating problems associated with high-temperature processing of materials, cold spray (CS) shows its remarkable potential in fabricating composite materials. Its low deposition temperature effectively avoids the oxidation, decomposition, phase transformation, and/or grain growth of the sprayed materials, more importantly, the deleterious chemical interactions between the reinforcement and matrix. In addition, making composites by CS is relatively inexpensive, with a cost that is usually intermediate between melt stirring and powder metallurgy processes.

The characteristics of cold-sprayed composites are attributed to their special building-up process (Sevillano et al. 2013). In most cases, the mixed two or more powders are accelerated to a high velocity by a high-speed jet flow and subsequently deposit on a substrate or the previously deposited layers in a solid state. The "soft" matrix with extensive plastic deformation adheres on the substrate surface as well as on previously deposited layers. The hard particles only peen the layers and mechanically wedge in the deposited matrix or being embedded by the incoming "soft" matrix (Sova et al. 2010, 2016). The whole process is on an order of dozens of milliseconds. The microstructure of cold-sprayed composite coatings usually is composed of highly deformed matrix and non-deformed reinforcement (Bakshi et al. 2008; Li et al. 2008a; Sansoucy et al. 2008; Shen et al. 2009; Spencer et al. 2009; Yandouzi et al. 2009).

M. Yu
Research Center of Sichuan Advanced Welding and Surface Engineering,
Southwest Jiaotong University, Chengdu 610031, People's Republic of China
e-mail: yumin@swjtu.edu.cn

W. Li (✉)
State Key Laboratory of Solidification Processing, Shaanxi Key Laboratory of Friction Welding Technologies, Northwestern Polytechnical University,
Xi'an 710072, People's Republic of China
e-mail: liwy@nwpu.edu.cn

P. Cavaliere (ed.), *Cold-Spray Coatings*,
https://doi.org/10.1007/978-3-319-67183-3_10

The co-deposition of discontinuous hard particles would influence the deposition process involving three main functions: Firstly, the hard particles keep the spray nozzle clean and eliminate the nozzle clogging. Secondly, they activate the surfaces to be coated by removing impurities, contamination, and oxide layers from the surface (Triantou et al. 2015). Thirdly, the hard particles roughen the surface and increase the contact area of particles. These functions can improve the deposition efficiency (Shkodkin et al. 2006) and the compactness of the coatings, yielding a product that usually has some very attractive properties. The addition of hard particles in the coating can strengthen its mechanical and physical properties in the form of work hardening, dispersion strengthening, and grain refinement (Luo et al. 2011). Moreover, the properties of the composite coatings can be tailored by change the reinforcement material type, content, morphology, etc.

There are numerous examples of cold-sprayed composite coatings. In most cases, there is a metallic component that is to provide deformability and binding between the harder particulates (Assadi et al. 2016). Thus the cold-sprayed composite coatings will be listed according to the most-reported matrix materials of Al, Cu, Ni, WC, Ti, etc.

10.2 Metal Matrix Composite Coatings

10.2.1 Al Matrix Composite Coatings

The high strength-to-weight ratio of Al alloy makes it an attractive material for industrial applications (Sansoucy et al. 2008). However, the Al alloy can become susceptible to corrosion, wear, and other degradation over time via galvanic corrosion or by abrasives (Hodder et al. 2014). In order to improve the mechanical and physical properties, numerous studies have been performed on the Al matrix composite coatings with the aim to increase hardness, wear resistance, as well as corrosion resistance. The improved properties of the Al matrix composite coatings are strongly related to the characteristics of the reinforcement used.

10.2.1.1 Hardness

Ceramic powders are excellent reinforcement materials for Al matrix composite coatings due to the high hardness and chemical and thermal stability (Lashgari et al. 2010). The hardness of the Al coating can be improved through incorporating micro-sized SiC, B_4C,TiN, and Al_2O_3 hard particles (Sansoucy et al. 2008; Tao et al. 2009) (Irissou et al. 2007; Spencer et al. 2009; Yu et al. 2013, 2014). The main reinforcing principle is attributed to the severe plastic deformation of Al matrix due to the tamping effect of hard ceramics, as shown in Fig. 10.1. Meanwhile, the ceramic particles can restrict the further deformation of the soft Al matrix during the loading process (Wang et al. 2013). Predominantly, the hard particles allow for load sharing

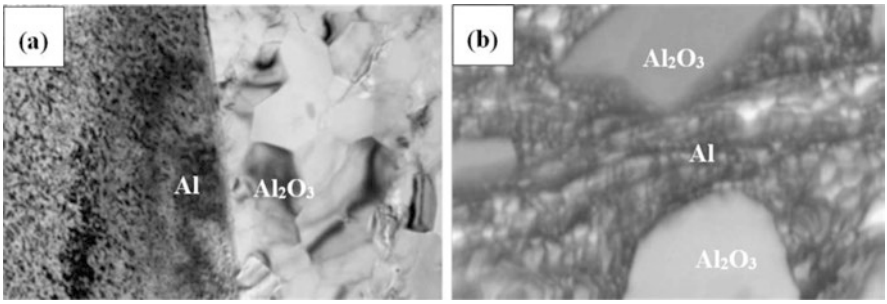

Fig. 10.1 Micrographs of Al-50wt.%Al_2O_3 composite coating: (**a**) TEM micrograph of the Al/Al_2O_3 interface and (**b**) EBSD pattern map (Wang et al. 2013). An intimate interface was formed between Al and Al_2O_3, and the Al particles trapped between Al_2O_3 particles underwent severe plastic deformation due to the tamping effect the Al_2O_3 particles

with the matrix coating. The use of nano-agglomerated hard powders could be a more efficient alternative than the conventional micro-sized reinforcement particles. Hodder et al. (2014) reported the hardness of the Al matrix composite coatings reinforced by 38 wt.% 20 nm Al_2O_3 were comparable to those containing 10 μm Al_2O_3 with the content of 48 wt.%. The increased spreading of the nano-agglomerated particles in the coating increased load-sharing and reinforcing capability of the particles. The nano-diamond (ND) is another reinforcement material for increasing the coating hardness. Woo et al. (2013) reported that the Al matrix composite coatings with the homogenous ND dispersion showed high hardness values. It should be noted that the nanoparticles generally are co-deposited in the coating after a milling process; thus, the hardness of the cold-sprayed nano-coatings would be determined by milling conditions and powder compositions (Woo et al. 2015). Considering the size effect of reinforcements on the coating hardness, some researchers employed friction stir processing (FSP) as a post-spray treatment technique to change Al matrix composite coating's hardness. FSP redistributed the Al_2O_3 particles trapped within the grain boundaries of the Al matrix and thus increased the hardness of the composite coating (Hodder et al. 2012). However, FSP-refined SiC particles exhibited a homogeneous distribution but a decreased microhardness for cold-sprayed Al5056-SiC composite coatings (Huang et al. 2016). Therefore, the suitable FSP process parameters could determine the hardness improvement for the Al matrix composite coatings.

10.2.1.2 Wear Resistance

The addition of ceramic particles is also of great significance to improve coating tribological performance. The addition of TiN particles contributed to a third-body abrasion and decreased friction coefficient by rolling action partially instead of sliding action for the cold-sprayed Al2319-TiN composite coating (Li et al. 2008a). As using the same Al matrix, the differences of the ceramic powders in elastic modulus and particle size can

produce different reinforcing effects. It was reported that the 7075Al composite coating reinforced by the B_4C powder exhibited slightly better wear property than that reinforced by the SiC powder (Meydanoglu et al. 2013). The B_4C particles in the coating promoted strain localization during reciprocating sliding and produced more uniform third-body microstructures than the SiC particles, thus protecting the underlying Al matrix from deformation. Interestingly, as using the same reinforcement powder, the difference in particle morphology could produce different reinforcing effect on wear resistance of the coatings. It was reported that the spherical Al_2O_3 morphology was associated with superior wear property to the angular morphology when comparing similar Al_2O_3 content in the coating (Shockley et al. 2013, 2015). Figure 10.2 elaborated that the spherical Al_2O_3 morphology benefited to form a stable third-body material with a thin, hardened, coherent layer of fine-grained material, exhibiting low wear rate and friction (Godet 1984). Furthermore, increasing the Al_2O_3 content in the coating generally increases the wear resistance (Shockley et al. 2013, 2015) and gradually changed the wear mode from adhesive to abrasive for the Al-Al_2O_3 composite coating (Spencer et al. 2009). Researchers reminded that the cold-sprayed composite coatings could not exhibit sufficient wear resistance especially at relatively high wear loads; thus, water as an environment-friendly lubrication remarkably enhanced the tribological performance as compared to the dry sliding condition (Paksoy et al. 2016).

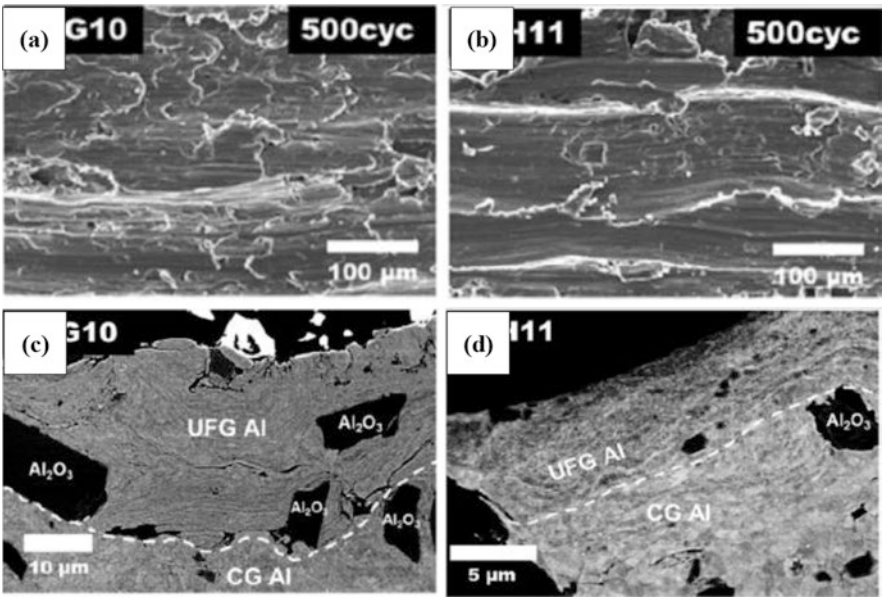

Fig. 10.2 Wear track morphologies and cross sections of the near-surface microstructures after 500 sliding cycles for the ANG10 (Al-10 wt.% angular Al_2O_3) and SPH11 (Al-11 wt.% spherical Al_2O_3) coatings. The SPH11 showed a superior wear resistance to the ANG10. The SPH11 revealed the formation of smooth, coherent third-body layers with 5–10 μm thick of UFG Al that partially enveloped the spherical Al_2O_3 particles (Shockley et al. 2013, 2015)

10.2.1.3 Corrosion

The success of Al matrix composite coating in providing a good combination of mechanical strength and corrosion resistance has attracted much attention in the coating industry (Sansoucy et al. 2008; Wang et al. 2010; Li et al. 2011).

The addition of α-Al_2O_3 decreased the current density of the pure Al coating and offered a good protection for the AZ91D substrate (Tao et al. 2009). However, the content of Al_2O_3 in the coating did not make a difference to its corrosion property (Irissou et al. 2007; Spencer et al. 2009). The similar result was also found as adding the SiC particles in the Al5056 coating, and the SiC content in the coating had no significant effect on the anodic polarization behavior (Wang et al. 2014). It was explained that the coating compactness due to tamping effect of the hard particles improved the corrosion resistance of coatings. However, Meydanoglu et al. (2013) reported that the addition of B_4C and SiC into 7075 Al matrix led to increased corrosion current densities when compared to that of unreinforced 7075 Al coating. Besides the ceramic reinforcement particles, intermetallic $Mg_{17}Al_{12}$ powder was also co-deposited into the Al matrix by CS. The Al-$Mg_{17}Al_{12}$ composite coating showed a comparable electrochemical characteristic to the bulk Al, and the composite coating can provide suitable protection for the as cast AZ91D substrate (Bu et al. 2012). Additionally, cold-sprayed Al-Al_2O_3 composite coatings on magnesium alloys presented the improved wear and corrosion resistance, as well as a high-cycle fatigue limit (Xiong and Zhang 2014). To guarantee the good corrosion resistance given by the pure aluminum at the interface and good mechanical resistance on the surface, CS shows great feasibility of preparing bilayer composite coatings. Al-Al_2O_3/Al composite coating with a top layer of Al-Al_2O_3 composite and a bottom layer of Al coating was fabricated on the steel substrate. The novel coating construction protected the substrate for immersion times more than 2000 h due to the dense structure obtained (Silva et al. 2016).

10.2.1.4 Other Property

Combined with ball-milling technique, CS can deposit homogeneously dispersed CNT-reinforced Al matrix composite coating. The original property of this thermally sensitive material can be well retained by CS. The Al-MWCNT composite showed lower electrical resistivity than the Al coating (Kang et al. 2016). In addition, the Al coating shows an improved thermal property after the addition of oxide ceramic particles; thus, it has a potential application in harsh serving environment. Heimann et al. (2014) reported the Al-Al_2O_3 composite coating has been selected as potential coating material for the outer space application due to the very low thermal conductivity (λ), comparatively high infrared emittance (ε), and oxidation stability. The coating also can resist a combined synergistic action of aggressive environmental factors. Finally, the Al matrix composite coating also shows the excellent magnetic property with certain reinforcement materials. Cold-sprayed Al-FeSiBNbCu

coating presented a soft magnetic character (Hc < 1000 A/m), and the 25 wt.% FeSiBNbCu in the coating was optimal to produce a homogenous coating with the suitable magnetic property (Cherigui et al. 2008).

10.2.2 Cu Matrix Composite Coatings

Cu is an attractive material for electrical applications because of its high electrical and thermal conductivities (Mirazimi et al. 2016). However, poor mechanical properties, including hardness, strength, and wear resistance, limit the service life. The addition of proper reinforcements can improve its mechanical strength and conductivity of the Cu coating. Some researchers reported that the SiC particles increased the coating hardness but reduced the wear resistance of the Cu-SiC composite coatings due to pullout of the ceramic particles during sliding (Tazegul et al. 2013). While the addition of the Al_2O_3 particles increased the wear resistance of the Cu coating, increasing Al_2O_3 fractions increased the hardness and bond strength of the Cu-Al_2O_3 coatings (Koivuluoto and Vuoristo 2010a). Furthermore, the wear rate of the Cu matrix composite coating containing fine Al_2O_3 particles was lower than that containing coarse Al_2O_3 particles (Triantou et al. 2015). Nevertheless, these composite coatings exhibited poorer electrical conductivity than that of unreinforced Cu coating. Both the cold-working of the deformed Cu matrix due to the shot peening and the presence of ceramic particles in the coating impaired the electrical conductivity of the coating. Therefore, mostly oxide and carbide ceramic powders generally are not suitable to reinforce the Cu matrix composite coatings for electrical applications. In recent, some other reinforcement materials were attempted to achieve good physical compatibility and binding with the Cu matrix as compared to ceramic powders. Al_2Cu-reinforced Cu matrix composite coatings have been successfully deposited on commercially pure Cu by CS. The Cu matrix composite coatings reinforced by 5 vol.% and 10 vol.% Al_2Cu exhibited both better electrical conductivity and wear resistance than the Cu coating (Tazegul et al. 2016). CNT is another attempt to improve the electrical conductivity of the Cu coating. Cold-sprayed Cu-MWCNT composite showed superior wear resistance and electrical resistivity to the thermal-sprayed coating (Kang et al. 2015a, b).

CNT is also used to improve the thermal conductivity of the cold-sprayed Cu coating (Cho et al. 2012). With an intention for thermal applications of Cu-CNT composite coating in the boiling heat transfer, the ceramic powders of SiC (Pialago et al. 2015a) and TiN (Pialago et al. 2015a, b) as additional filler were co-deposited in Cu-CNT composites with the help of feasibility of CS. These ceramic particles promoted the formation of surface micro-pores, and the presence of these pores would assist the bubble nucleation during boiling heat transfer. Figure 10.3 shows the ternary Cu-CNT composite coatings, respectively, reinforced by SiC and AlN (Pialago et al. 2016). Additionally, some other reinforcements, such as metal glass, quasicrystal, and amorphous, also can be co-deposited into the Cu coating sans any crystallization drawing back of low deposition temperature of CS. ZrCuAlNiTi metal glass (MG) powders improved the wear resistance of the Cu coating (Kang

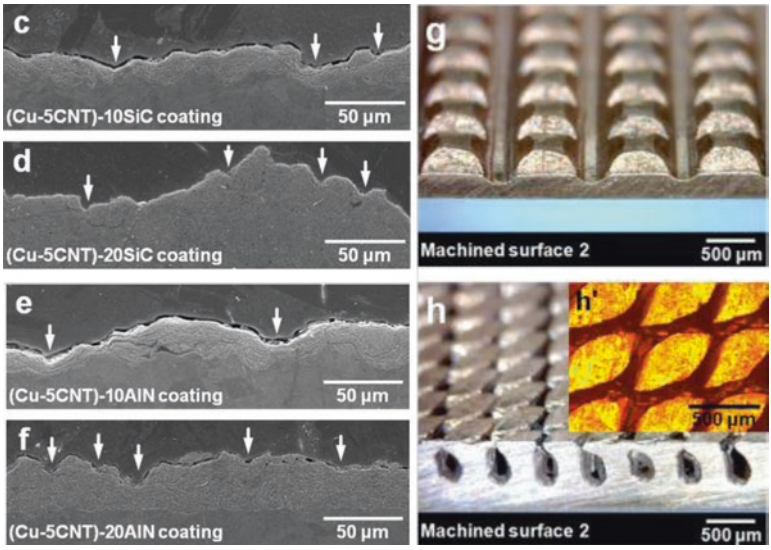

Fig. 10.3 Morphology of the ternary Cu-CNT composite coating, respectively, reinforced by SiC and AlN (Pialago et al. 2016)

et al. 2015a). Amorphous (CuZrTiNi)-reinforced Cu matrix composite coating showed three times higher of wear resistance than the pure Cu coating (Lee et al. 2009). AlCuFeB quasicrystal (QC) improved the wear resistance of the CuSn8 coating, but the relatively high content of the low-loading QC phase adversely aggravated the wear resistance (Guo et al. 2016).

In addition, Cu and its alloys have been used as lubricating metallic materials by combing with self-lubricating materials such as MoS_2. CS can avoid high-temperature-induced decomposition of MoS_2 and/or other phase transformations that could be detrimental for tribological performance. This kind of composite coating can be used as self-lubricating dry-bearing materials, where the friction coefficients vary in a range of 0.04–0.26 depending on the MoS_2 content (Yamada et al. 2009). The low content of MoS_2 had no significant impact on steady-state value of COF, but the MoS_2 exceeded a certain concentration, and the wear resistance of the Cu-MoS_2 composite coating decreased as well because of mechanical property lost as shown in Fig. 10.4 (Zhang et al. 2016).

10.2.3 Ni Matrix Composite Coatings

Ni alloys are widely employed in marine engineering and power generation (Gschneidner et al. 2001). High denseness and low oxide content are among the most important properties guaranteeing the high corrosion resistance of the Ni coating. Koivuluoto and Vuoristo (2010a, b) and Koivuluoto et al. (2014) reported that

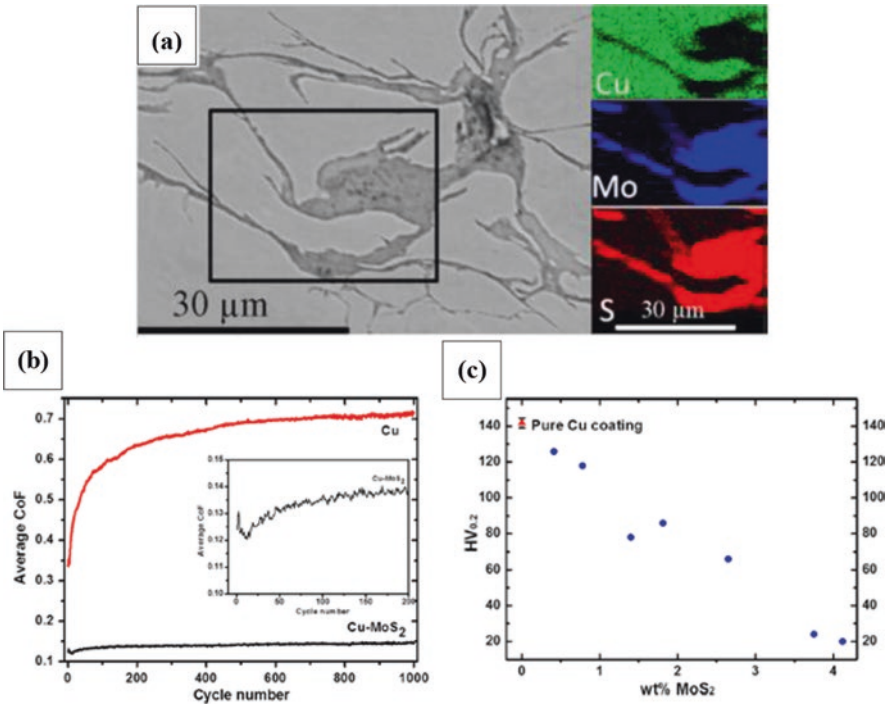

Fig. 10.4 (**a**) Cross section of the as-sprayed Cu-MoS_2 composite coating, (**b**) COF comparison between the Cu-MoS_2 coating and Cu coating, and (**c**) effect of MoS_2 content on coating microhardness. Dark contrast around the particles was identified as MoS_2 by EDX mapping. The Cu-MoS_2 coating showed a much lower COF than the Cu coating and the coating hardness linearly decreased with the increase of MoS_2 concentration (Zhang et al. 2016)

the addition of the Al_2O_3 particles compacted the NiCr coating, thereby improving the corrosion resistance. With the versatility of CS in depositing two or more materials, the Ni-20Cr coating blended with TiC and Re powders were successfully deposited on a boiler steel (SAE 213-T22). Cold-sprayed Ni-20Cr-TiC showed excellent hot corrosion resistance and the addition of Re in the Ni-20Cr-TiC coating not only solved the hot corrosion but also erosion-corrosion problems in power plant boilers (Singh et al. 2015).

The addition of Al_2O_3 in the Ni coating can improve the coating's hardness as well as the resistance to cavitation erosion (Hu et al. 2011). It is reported that the Ni-Al_2O_3 coatings with good oxidation resistance could represent a very promising basis for application in power generation systems (Sevillano et al. 2013; Sacks 2016). When a nickel-coated Al_2O_3 powder was used, a higher volume fraction of Al_2O_3 can be retained in the coating by CS (Li et al. 2008a, b) and the as-sprayed Ni-Al_2O_3 coating provided good protection from oxidation corrosion and also showed an excellent wear performance (Li et al. 2014).

Combined with mechanical alloying process, CS is also an effective approach to prepare ceramic dispersion reinforced Ni matrix nanocomposite coatings with high quality. The NiCrAl matrix nanocomposite reinforced by 40 vol.% cubic boron nitride

ceramic particle (cBNp) was prepared by cold spraying the mechanically alloyed nanostructured composite powders. The nanostructure of the powders was well remained into the coating. No phase transformation and grain growth of the NiCrAl matrix occurred during the spraying process (Luo et al. 2011, 2014; Luo and Li 2012).

In addition, Ni was another metal matrix for producing self-lubricating coating by being deposited with MoS_2 and hBN (Aggarwal 2007). The cold-sprayed Ni-hBN composite coating showed higher-temperature capability than the traditional MoS_2-matrix system (Segall et al. 2008). Using mixed Ni/Ni-coated hBN powder can further increase the distribution uniformity and content of the hBN particles into the Ni-hBN self-lubricating coating (Smid et al. 2012).

10.2.4 WC Matrix Composite Coatings

WC matrix coatings are widespread because of good combination of hardness and excellent wear resistance. CS can suppress WC decarburization and avoid introducing undesirable brittle phases such as W_2C and amorphous binder (Kim et al. 2005; Gao et al. 2008). An elaborated state of the art of WC matrix composite coating can be reviewed in the newly published literature (Sacks 2016).

10.2.5 Ti, Mg, and Ag Matrix Composite Coatings

Ti alloys are widely used as structural materials in aerospace and marine industries because of their high mechanical strength and excellent corrosion resistance (Boyer 1996). The good biocompatibility of the Ti alloys makes them highly suitable for biomedical applications (Long and Rack 1998). However, the poor wear resistance limits the tribological application (Dong and Bell 2000). Khun et al. (2015) incorporated quasicrystalline Al-Cr-Fe particles in the Ti matrix with different contents to form a new type of wear-resistant Ti matrix composite coating. Carbide ceramic powders were co-deposited in the AZ91D at different contents to fabricate Mg matrix composite coating with excellent wear resistance (Suo et al. 2014). In addition, Cold-sprayed Ag-SnO_2 composite coating showed a superior electrical property to that fabricated by conventional powder metallurgy (P/M), which opens a new and cost-attractive production route for electrical contacts (Rolland et al. 2012).

10.2.6 Intermetallic Matrix Composite Coatings

Intermetallics have high creeping strength and high oxidation and corrosion resistance, and thus they are widely used as high-temperature structural materials in aerospace industry. Due to the intrinsic brittleness of intermetallics at room temperature, it is very difficult to directly deposit intermetallic particles by CS

(Cinca et al. 2014). The produce of intermetallic coating was usually realized through post-spray-heat-treatment (PSHT) of as-sprayed metal-metal and metal-intermetallic composite coatings. The metal-metal material systems mainly cover Ni-Al, Ti-Al, Fe-Al, and Cu-Al. The intermetallics of Al_3Ni and Al_3Ni_2 (Lee et al. 2007; Novoselova et al. 2007), $TiAl_3$ (Wang et al. 2012), and Fe_2Al_5 (Wang et al. 2012) are reported being from the annealed Ni-Al, Ti-Al, and Fe-Al coatings, as shown in Fig. 10.5. Furthermore, the cold-sprayed Ni/Al-Al_2O_3 composite can be

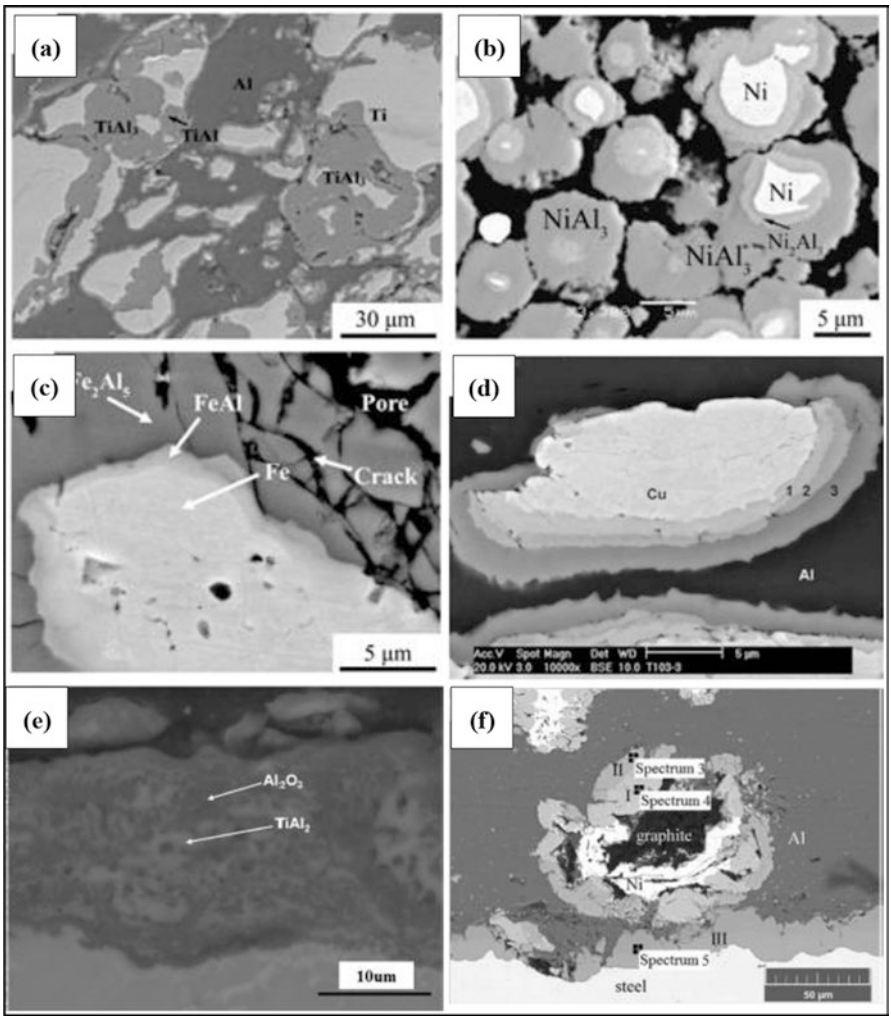

Fig. 10.5 SEM images of coatings underwent intermetallic transformation: (**a**) Ti-Al (Novoselova et al. 2007), (**b**) Ni-Al (Spencer and Zhang 2009), (**c**) Fe-Al (Wang et al. 2012), (**d**) Cu-Al (Price et al. 2007), (**e**) TiAl3-Al_2O_3 composite coating (Wang et al. 2016), and (**f**) Ni-Al intermetallic-coated graphite/Al composite coating (Huang et al. 2017)

transferred as NiAl-Al_2O_3 intermetallic matrix composite coating through PSHT (Yang et al. 2013). Another $TiAl_3$-Al_2O_3 composite coating was fabricated by cold spraying the high-energy ball-milled Al/TiO_2 composite powders (40 wt.% TiO_2), followed by heat treatment. The kind of composite coatings showed good oxidation resistance (Wang et al. 2016).

Recently, a new Ni-Al intermetallic-coated graphite/Al composite coating was prepared by PSHT of the cold-sprayed Al matrix composite coating reinforced by nickel-coated graphite powder. The lubrication phase (graphite) improved the formation of a graphite film during sliding friction and decreased the COF, while the hard Ni-Al intermetallic phases contributed to the increase of COF (Huang et al. 2017).

10.2.7 Hydroxyapatite and Polymer Matrix Composite Coatings

Hydroxyapatite (HAP) is the most researched bio-ceramic material in the field of biomedical engineering. The heat sensitivity and lack of plastic deformation of HAP limit the choice of surface coating techniques. Choosing Ti as the binder phase, the HAP-Ti composite coating can be cold sprayed on Ti substrate. The HAP-Ti composite coating showed good bio-integration (Tlotleng et al. 2015) and excellent electrochemical corrosion resistance in a simulated biomedical environment (Zhou and Mohanty 2012). The HAP-Ti composite coating is very promising for load-bearing implant applications. Furthermore, HAP-graphene-nanosheet composite coatings were deposited by vacuum cold spray (VCS) with inherited nanostructures and enhanced properties. The VCS HA-GN coatings show potential for the repair or replacement of hard tissues (Liu et al. 2014a, b).

Driven by economical and ecological reasons, polymer matrix coatings become a potential solution for anti-wear purpose (Zhang et al. 2007). A very few works have been done with polymer particles as feedstock in CS, mainly because polymer deposition is difficult to achieve (Xu and Hutchings 2006). In recent, with the addition of nano-alumina and nano-ceramic powders in the feedstock, an ultra-high molecular weight polyethylene (UHMWPE) matrix composite coating was fabricated by CS on Al and PP substrates. It was reported that the thickness of UHMWPE coatings reached 4 and 1 mm on Al and PP substrates, respectively, as shown in Fig. 10.6 (Ravi et al. 2016).

Finally, due to the versatility of CS, multiphase composite coatings have been developed, such as W/Ni/Fe alloy coating (Xia et al. 2016) and stainless steel 316 L, Cu, and Tribaloy T-700 composite coating (Maestracci et al. 2016). Cold-sprayed Cu50Ti20Ni30 metallic glassy coating can be used as antibacterial protective coating in medical and food sectors (Maestracci et al. 2016).

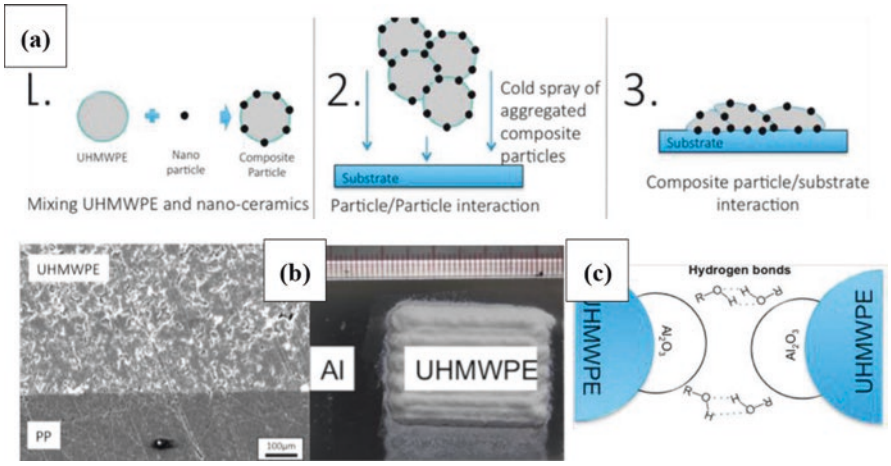

Fig. 10.6 (**a**) The addition of nano-ceramic particles to the feedstock UHMWPE aided in the coating building up. (**b**) UHMWPE matrix composite coatings on Al and PP substrates, and (**c**) a bridge bond between UHMWPE particles was created by a network of finely dispersed nanoparticles, which were strongly bonded to the polymer matrix (Ravi et al. 2016)

10.3 Key Issues

The microstructure and properties of the cold-sprayed coating can be tailored by judicious choice of the reinforcement materials. For example, the addition of TiC to A1 is most effective in reducing the CTE followed by Al_2O_3 and SiC. The property of the composite coating also depends on the volume fraction, the morphology, and the distribution of the reinforcements in the coatings. In early studies, reinforcement particles usually were mechanically blended with the matrix powder before spraying. The mechanical blending is a simple and easy way to operate, and economical for preparation of composite powders, but it encountered two key issues of the content loss (Fig. 10.7) and fragmentation of the hard particles (Fig. 10.8), especially for the metal-ceramics composite coatings. Figure 10.7 shows the content of hard particles in some representative metal-ceramics coatings comparing to the feedstock powder mixture. It is seen that the hard particle content in the coating is generally lower than that in the feedstock powder. Hard particles do not participate in the adiabatic shear instability process, so the particles must be embedded by the "soft" phase during deposition process, and thus the recovery of hard particles may be less than in the initial feedstock (Irissou et al. 2007; Spencer et al. 2009). Figure 10.9 further pointed out the particle size in a certain range had no effect on the content of the hard particles in the coating, but the particle morphology did influence the hard particle content.

As such, powder preparation techniques and strategies could alleviate the difference in hard particle content between the coatings and feedstock powders. The ball-milling method was reported enabling finer and more homogeneous powders than

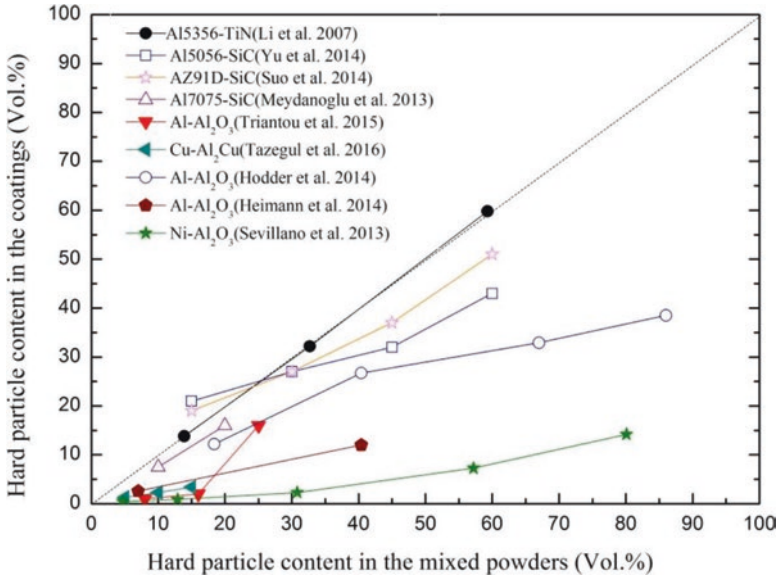

Fig. 10.7 Content of hard particles in the coatings compared to the feedstock powder mixture

the mechanical blending, as shown Fig. 10.10a, b. In this way, one can control the concentration, size, and distribution of the two phases, thus control the composition of the coatings. The ball-milling method can also be used to produce nanostructured powders (Luo et al. 2011; Luo and Li 2012). It should be concerned with the possibility that the powders experienced some degree of strain hardening during milling that made them less likely to deform and/or yield; this could have allowed the particles to act more like an erosive media (Smid et al. 2012); therefore, the milling process could be crucial.

Pre-coated (or cladding) is another effective way to produce composite powders. Through regulating the thickness of the coated layer, one can obtain various volume fractions of the hard particles. It was reported that the coatings prepared from the cladding powders had a higher content of hard particles than that from the mechanical blending, as shown in Fig. 10.10c, d. Furthermore, the pre-coated composite powders enabled preventing the fragmentation of Al_2O_3 (Li et al. 2008a, b, c) and B_4C (Feng et al. 2012) with a thickness of about a few to dozens of micrometer Ni layer, as shown in Fig. 10.11a, b. However, Feng et al. (2012) pointed out that the Ni layer had a beneficial influence of protecting the B_4C particles against fragmentation, but the increase of B_4C content in the feedstock powder induced the fragmentation. The fragmentation of diamond particles in Cu-coated diamond powders was also reported, as shown in Fig. 10.11c, d. An alternative powder combination of pre-coated powder with a metal binder, i.e., Ni-coated diamond power mixed with bronze (Na et al. 2009), Ti-coated diamond mixed with Fe (Kim et al. 2007), and Cu-coated diamond mixed with Cu (Yin et al. 2017) and Al-TiB_2-blended powder

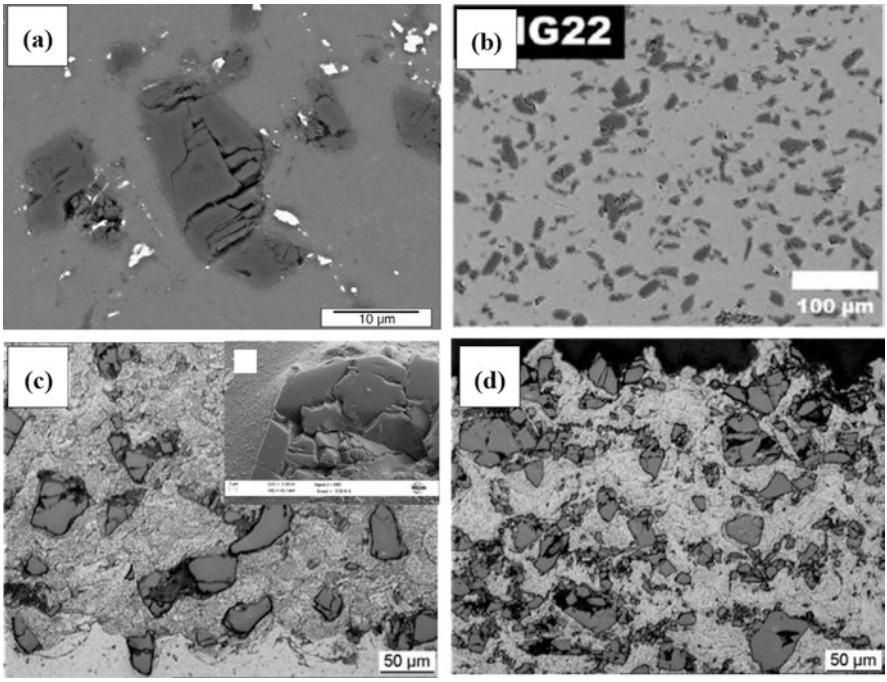

Fig. 10.8 Images showing cracked ceramic particles from coatings of (**a**) Al-12Si + 20% vol.% SiC (Sansoucy et al. 2008), (**b**) Al + 30 vol.% Al_2O_3 (Shockley et al. 2015), (**c**) Al5056 + 30 vol.% SiC, and (**d**) Al5056 + 60 vol.% SiC. The fragmenting degree of the SiC particles increased as the SiC content in the coating increased (Yu et al. 2014)

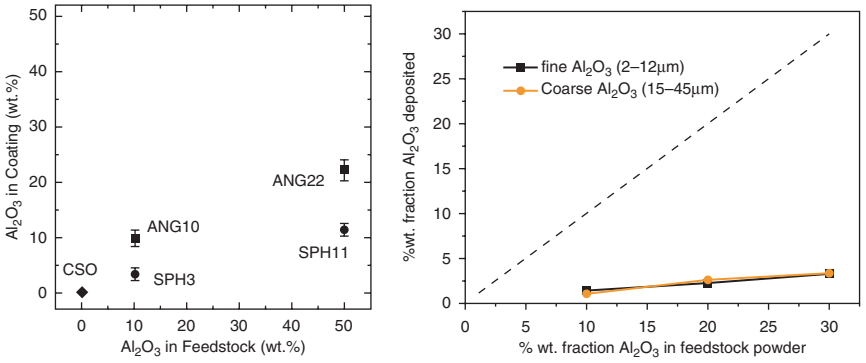

Fig. 10.9 (**a**) Effect of Al_2O_3 particle morphology on its content in the Al-Al_2O_3 coating (Shockley et al. 2015) and (**b**) effect of Al_2O_3 particle size on its content in the Cu-Al_2O_3 coating (Triantou et al. 2015). The amount of recovery of spherical Al_2O_3 was considerably lower than that of angular Al_2O_3. Cu-Al_2O_3 fraction in the coatings depended on the mass fraction of Al_2O_3 in the feedstock powder, but it was almost independent on the Al_2O_3 particle size used

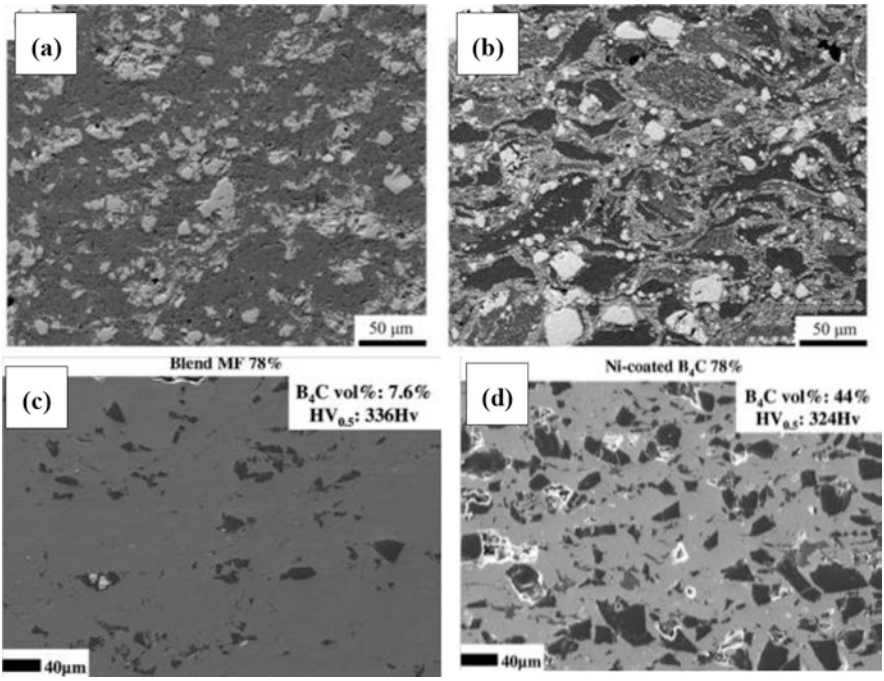

Fig. 10.10 Cross sections of Al5356-TiN composite coatings with feedstock powders prepared by (**a**) mechanical blending (Li et al. 2007) and (**b**) ball milling (Li et al. 2008a, c). The ball-milled powder yielded a dense and homogeneous coating with super fine TiN particles dispersed into Al5356 matrix. Cross sections of Ni-B_4C composite coating prepared by (**c**) mechanical blending powder and (**d**) Ni-coated B_4C composite powder (Feng et al. 2012). The coated power effectively retained the B_4C content in the coating

with Al (Chen et al. 2017), was employed for avoiding the fracture of hard particles but being at the expense of the hard particle content in the coating. Therefore, the most promising path could be to encapsulate much smaller hard particles (micro- to nanoscale) with thinner levels of metals to avoid the fracture and loss of the hard particles. Besides seeking a higher and higher content of hard particles in the composite coating, the distribution of hard particle is also a crucial factor affecting the coating property. Melendez and McDonald (2013) and Melendez et al. (2013) pointed out that the coating with the highest WC content and shortest mean free path between the reinforcing particles had the lowest wear rate. It should be noted that achieving uniform and meaningful distributions of the hard particles in the coatings is found to be problematic and must be resolved before the coatings can have an impact on the economy and longevity of any intended application. Therefore, researches related to achieving uniform and meaningful distributions of the hard particles should be emphasized.

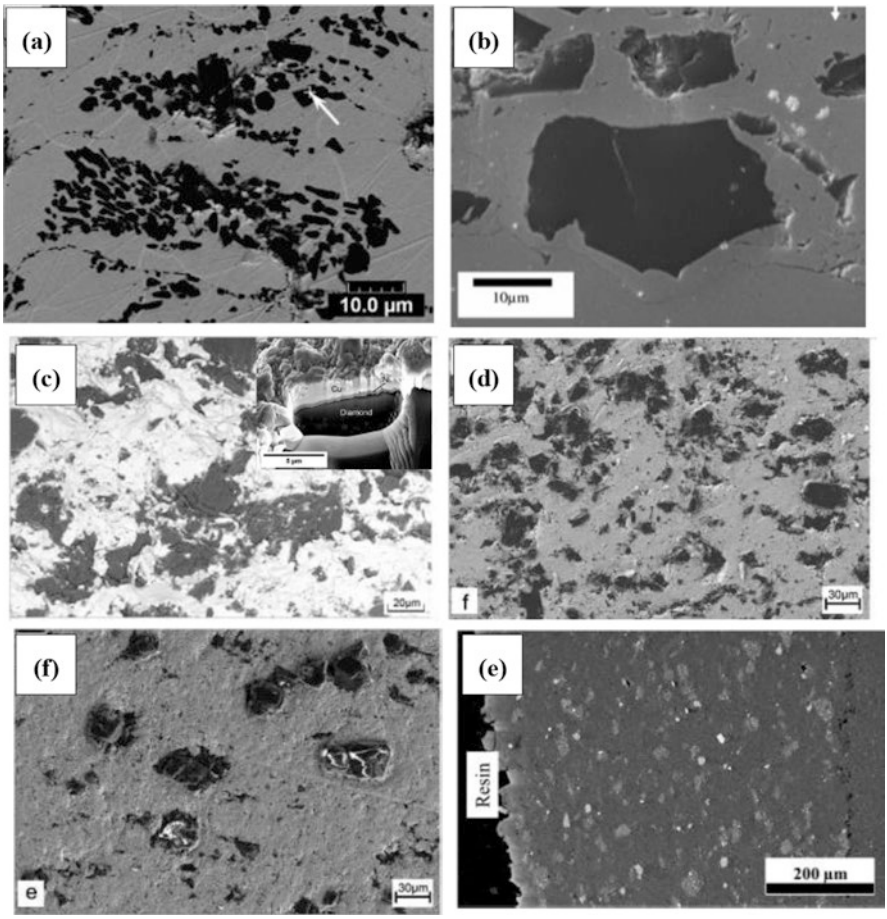

Fig. 10.11 Microstructure of (**a**) Ni-coated Al_2O_3 coating (Li et al. 2008a, b, c), (**b**) Ni-coated B_4C coating (Feng et al. 2012), (**c**) Cu- and Ni-coated diamond coating (Aldwell et al. 2016), (**d**) Cu-coated diamond coating, and (**e**) Cu + 50 wt.% Cu-coated diamond coating (Yin et al. 2017) and (**f**) Al + 50 wt.% Al-TiB_2-blended powder (Chen et al. 2017)

10.4 Conclusions and Outlook

CS shows its remarkable advantages in fabricating composite materials. Its low deposition temperature avoids the deleterious effect of chemical interactions between the reinforcement and matrix. The versatility of CS has produced a great wide range of applicable materials, such as Al, Cu, Ni, WC, Ti, hydroxyapatite, and even polymer. The judicious choice of the reinforcement material type can tailor the microstructure of the metal matrix composite coatings and obtain some attractive properties.

Combined with mechanical alloying process, CS is also the effective approach to prepare nanocomposite coatings with high quality. The PSHT can well transform

cold-sprayed metal-metal and metal-ceramic composite coatings to metal-intermetallic and intermetallic matrix composite coatings. In addition, effectively using cladding powders or mixed with metal binder has potential of fabricating fragmentation-free composite coating with high content and uniform distribution of hard particles.

Issues related to achieving uniform and meaningful distributions of the hard particles are found to be problematic and must be resolved before the composite coatings can have an impact on the economy and longevity of any intended applications. Researches about deposition mechanism of the hard particle, which substantially determines its content, distribution, and interface characteristics of the matrix and hard particle, are urgent to be considered. In addition, the combinations of powder preparation strategies and other post-spray techniques with CS would play a crucial role in expanding the application of cold-sprayed coating with distinct and stable properties.

Acknowledgments This work is supported by the Fundamental Research Funds for the Central Universities (2682015RC01) and the National Natural Science Foundation of China (51601157). The authors also gratefully acknowledge the helpful comments and suggestions of the reviewers of Prof. HL Liao and Dr. CJ Huang from Université de Technologie de Belfort-Montbéliard for their help and useful discussions.

References

Aggarwal G (2007) Development of self-lubricating coatings via cold spray process: feedstock formulation and deformation modeling. Dissertation, The Pennsylvania State University

Aldwell B, Yin S, McDonnell KA, Trimble D, Hussain T, Lupoi R (2016) A novel method for metal-diamond composite coating deposition with cold spray and formation mechanism. Scrip Mater 115:10–13

Assadi H, Kreye H, Gartner F, Klassen T (2016) Cold spraying -a materials perspective. Acta Mater 116:382–407

Bakshi SR, Singh V, Balani K, McCartney DG, Seal S, Agarwal A (2008) Carbon nanotube reinforced aluminum composite coating via cold spraying. Surf Coat Technol 202(21):5162–5169

Boyer RR (1996) An overview on the use of titanium in the aerospace industry. Mater Sci Eng A 213(1–2):103–114

Bu H, Yandouzi M, Lu C, MacDonald D, Jodoin B (2012) Cold spray blended Al + $Mg_{17}Al_{12}$ coating for corrosion protection of AZ91D magnesium alloy. Surf Coat Technol 207:155–162

Chen H, Pala Z, Hussain T, McCartney DG (2017) Fabrication and microstrain evolution of Al-TiB_2 composite coating by cold spray deposition. In: Proceedings of the institution of mechanical engineers, Part L: Journal of Materials: Design and Applications, pp 1–9

Cherigui M, Li W, Hamzaoui R, Ji V, Fenineche N, Coddet C (2008) Microstructure and magnetic properties of FeSiBNbCu-Al cold spray coatings. Eur Phys J Appl Phys 43(1):79–86

Cho S, Takagi K, Kwon H, Seo D, Ogawa K, Kikuchi K, Kawasaki A (2012) Multi-walled carbon nanotube-reinforced copper nanocomposite coating fabricated by low-pressure cold spray process. Surf Coat Technol 206(16):3488–3494

Cinca N, List A, Gartner F, Guilemany JM, Klassen T (2014) Influence of spraying parameters on cold gas spraying of iron aluminide intermetallics. Surf Coat Technol 268:99–107

Dong H, Bell T (2000) Enhanced wear resistance of titanium surfaces by a new thermal oxidation treatment. Wear 238(2):131–137

Feng C, Guipont V, Jeandin M, Amsellem O, Pauchet F, Saenger R, Bucher S, Iacob C (2012) B_4C/Ni composite coatings prepared by cold spray of blended or CVD-coated powders. J Therm Spray Technol 21(3–4):561–570

Gao P-H, Li Y-G, Li C-J, Yang G-J, Li C-X (2008) Influence of powder porous structure on the deposition behavior of cold-sprayed WC-12Co coatings. J Therm Spray Technol 17(5–6):742–749

Godet M (1984) The third-body approach: a mechanical view of wear. Wear 100(1):437–452

Gschneidner KA, Beaudry BJ, Capellen J (2001) Properties and selection: nonferrous alloys and special-purpose materials. ASM International, Book News, Inc., Portland, OR, pp 889–896

Guo X, Chen J, Yu H, Liao HL, Coddet C (2016) A study on the microstructure and tribological behavior of cold-sprayed metal matrix composites reinforced by particulate quasicrystal. Surf Coat Technol 268:94–98

Heimann RB, Kleiman JI, Litovsky E, Marx S, Ng R, Petrov S, Shagalov M, Sodhi RNS, Tang A (2014) High-pressure cold gas dynamic (CGD)-sprayed alumina-reinforced aluminum coatings for potential application as space construction material. Surf Coat Technol 252:113–119

Hodder KJ, Izadi H, McDonald AG, Gerlich AP (2012) Fabrication of aluminum-alumina metal matrix composites via cold gas dynamic spraying at low pressure followed by friction stir processing. Mater Sci Eng A 556:114–121

Hodder KJ, Nychka JA, McDonald AG (2014) Comparison of 10 um and 20 nm Al-Al_2O_3 metal matrix composite coatings fabricated by low-pressure cold gas dynamic spraying. J Therm Spray Technol 23(5):839–848

Hu HX, Jiang SL, Tao YS, Xiong TY, Zheng YG (2011) Cavitation erosion and jet impingement erosion mechanism of cold sprayed Ni-Al_2O_3 coating. Nuclear Eng Design 241(12):4929–4937

Huang C, Li W, Zhang Z, Planche MP, Liao H and Montavon G (2016) Effect of tool rotation speed on microstructure and microhardness of friction-stir-processed cold-sprayed SiC_p/Al5056 composite coating. J Therm Spray Technol 25(7):1–8

Huang C, Li W, Planche M-P, Liao H, Montavon G (2017) In-situ formation of Ni-Al intermetallics-coated graphite/Al composite in a cold-sprayed coating and its high temperature tribological behaviors. J Mater Sci Tech. https://doi.org/10.1016/j.jmst.2017.01.026

Irissou E, Legoux J-G, Arsenault B, Moreau C (2007) Investigation of Al-Al2O3 cold spray coating formation and properties. J Therm Spray Technol 16(5–6):661–668

Kang N, Coddet P, Liao H, Coddet C (2015a) The effect of heat treatment on microstructure and tensile properties of cold spray Zr base metal glass/Cu composite. Surf Coat Technol 280:64–71

Kang K, Park H, Kim J, Lee C (2015b) Role of spray processes on microstructural evolution, and physical and mechanical properties of multi-walled carbon nanotube reinforced cu composite coatings. Appl Surf Sci 356:1039–1051

Kang K, Kim J, Park H, Lee C (2016) Formation and heat treatment of kinetic sprayed nanocrystalline al coatings reinforced with multi-walled carbon nanotubes: the relationship between microstructural features and physical properties. Surf Coat Technol 289:124–135

Khun NW, Li RT, Loke K, Khor KA (2015) Effects of Al-Cr-Fe Quasicrystal content on Tribological properties of cold-sprayed titanium composite coatings. Tribol T 58:616–624

Kim H-J, Lee C-H, Hwang S-Y (2005) Superhard nano WC-12%Co coating by cold spray deposition. Mater Sci Eng A 391(1–2):243–248

Kim HJ, Jang JH, Chang HL (2007) Assessment of metal/diamond composite coating by cold spray deposition. J Korean Inst Metals Mater 45(7):409–415

Koivuluoto H, Vuoristo P (2010a) Effect of powder type and composition on structure and mechanical properties of Cu+Al_2O_3 coatings prepared by using low-pressure cold spray process. J Therm Spray Technol 19(5):1081–1092

Koivuluoto H, Vuoristo P (2010b) Structural analysis of cold-sprayed nickel-based metallic and metallic-ceramic coatings. J Therm Spray Technol 19(5):975–989

Koivuluoto H, Milanti A, Bolelli G, Lusvarghi L, Vuoristo P (2014) High-pressure cold-sprayed Ni and Ni-Cu coatings: improved structures and corrosion properties. J Therm Spray Technol 23(1):98–103

Lashgari HR, Sufizadeh AR, Emamy M (2010) The effect of strontium on the microstructure and wear properties of A356-10%B_4C cast composites. Mater Design 31(4):2187–2195

Lee HY, Jung SH, Lee SY, Ko KH (2007) Alloying of cold-sprayed Al-Ni composite coatings by post-annealing. Appl Surf Sci 253(7):3496–3502
Lee KA, Jung DJ, Park DY, Kang WG, Lee JK, Kim HJ (2009) Study on the fabrication and physical properties of cold-sprayed, Cu-based amorphous coating. J Phys Conf Ser 144:012113
Li WY, Zhang G, Guo X, Liao H, Coddet C (2007) Characterizations of cold-sprayed TiN particle-reinforced Al alloy-based composites – from structures to tribological behaviour. Adv Eng Mater 9(7):577–583
Li WY, Zhang G, Liao HL, Coddet C (2008a) Characterizations of cold sprayed TiN particle reinforced Al2319 composite coating. J Mater Process Technol 202(1–3):508–513
Li W-Y, Zhang C, Liao H, Li J, Coddet C (2008b) Characterizations of cold-sprayed nickel-alumina composite coating with relatively large nickel-coated alumina powder. Surf Coat Technol 202(19):4855–4860
Li WY, Zhang G, Zhang C, Elkedim O, Liao H, Coddet C (2008c) Effect of ball milling of feedstock powder on microstructure and properties of TiN particle-reinforced Al alloy-based composites fabricated by cold spraying. J Therm Spray Technol 17(3):316–322
Li WY, Yang C, Liao H (2011) Effect of vacuum heat treatment on microstructure and microhardness of cold-sprayed TiN particle-reinforced Al alloy-based composites. Mater Design 32(1):388–394
Li W, Huang C, Yu M, Liu D, Feng Y, Liao H (2014) Investigation of high temperature oxidation behavior and tribological performance on cold sprayed nickel-alumina composite coating. Surf Coat Technol 239:95–101
Liu Y, Dang Z, Wang Y, Huang J, Li H (2014a) Hydroxyapatite/graphene-nanosheet composite coatings deposited by vacuum cold spraying for biomedical applications: inherited nanostructures and enhanced properties. Carbon 67:250–259
Liu Y, Huang J, Li H (2014b) Nanostructural characteristics of vacuum cold-sprayed hydroxyapatite/graphene-nanosheet coatings for biomedical applications. J Therm Spray Technol 23(7):1149–1156
Long M, Rack HJ (1998) Titanium alloys in total joint replacement – a materials science perspective. Biomaterials 19(19):1621–1639
Luo XT, Li CJ (2012) Thermal stability of microstructure and hardness of cold-sprayed cBN/NiCrAl nanocomposite coating. J Therm Spray Technol 21(3):578–585
Luo X-T, Yang G-J, Li C-J (2011) Multiple strengthening mechanisms of cold-sprayed cBNp/NiCrAl composite coating. Surf Coat Technol 205(20):4808–4813
Luo XT, Yang EJ, Shang FL, Yang GJ, Li CX, Li CJ (2014) Microstructure, mechanical properties, and two-body abrasive wear behavior of cold-sprayed 20vol.% cubic BN-NiCrAl nanocomposite coating. J Therm Spray Technol 23(7):1181–1190
Maestracci R, Sova A, Jeandin M, Malhaire JM, Movchan I, Bertrand P, Smurov I (2016) Deposition of composite coatings by cold spray using stainless steel 316L, copper and Tribaloy T-700 powder mixtures. Surf Coat Technol 287:1–8
Melendez NM, McDonald AG (2013) Development of WC-based metal matrix composite coatings using low-pressure cold gas dynamic spraying. Surf Coat Technol 214:101–109
Melendez NM, Narulkar VV, Fisher GA, McDonald AG (2013) Effect of reinforcing particles on the wear rate of low-pressure cold-sprayed WC-based MMC coatings. Wear 306(1–2):185–195
Meydanoglu O, Jodoin B, Kayali ES (2013) Microstructure, mechanical properties and corrosion performance of 7075 Al matrix ceramic particle reinforced composite coatings produced by the cold gas dynamic spraying process. Surf Coat Technol 235:108–116
Mirazimi J, Abachi P, Purazrang K (2016) Spark plasma sintering of ultrafine YSZ reinforced cu matrix functionally graded composite. Acta Metall Sin 29(12):1–8
Na H, Bae G, Shin S, Kumar S, Kim H, Lee C (2009) Advanced deposition characteristics of kinetic sprayed bronze/diamond composite by tailoring feedstock properties. Compos Sci Technol 69(3–4):463–468
Novoselova T, Celotto S, Morgan R, Fox P, ONeill W (2007) Formation of TiAl intermetallics by heat treatment of cold-sprayed precursor deposits. J Alloy Compd 436(1–2):69–77

Paksoy AH, Deprem O, Tazegul O, Cimenoglu H (2016) Tribology of SiCp reinforced Al-12Si matrix composite coatings in water. Tribo Int. https://doi.org/10.1016/j.triboint.2016.10.037
Pialago EJT, Kwon OK, Kim M-S, Park CW (2015a) Ternary Cu-CNT-AlN composite coatings consolidated by cold spray deposition of mechanically alloyed powders. J Alloy Compd 650:199–209
Pialago EJT, Kwon OK, Park CW (2015b) Cold spray deposition of mechanically alloyed ternary Cu-CNT-SiC composite powders. Ceram Int 41(5, Part B):6764–6775
Pialago EJT, Kwon OK, Jin JS, Park CW (2016) Nucleate pool boiling of R134a on cold sprayed Cu-CNT-SiC and Cu-CNT-AlN composite coatings. Appl Therm Eng 103:684–694
Price TS, Shipway PH, McCartney DG, Calla E, Zhang D (2007) A method for characterizing the degree of inter-particle bond formation in cold sprayed coatings. J Therm Spray Technol 16(4):566–570
Ravi K, Ichikawa Y, Ogawa K, Deplancke T, Lame O, Cavaille J-Y (2016) Mechanistic study and characterization of cold-sprayed ultra-high molecular weight polyethylene-nano-ceramic composite coating. J Therm Spray Technol 25(1):160–169
Rolland G, Sallamand P, Guipont V, Jeandin M, Boller E, Bourda C (2012) Damage study of cold-sprayed composite materials for application to electrical contacts. J Therm Spray Technol 21(5):758–772
Sacks N (2016) Low pressure cold gas dynamic spraying of tungsten carbide-nickel coatings. Metal Powder Rep 71(5):356–358
Sansoucy E, Marcoux P, Ajdelsztajn L, Jodoin B (2008) Properties of SiC-reinforced aluminum alloy coatings produced by the cold gas dynamic spraying process. Surf Coat Technol 202(16):3988–3996
Segall AE, Smid I, Walia P, Eden TJ (2008) Self-lubricating coatings for elevated temperature applications using a high-velocity-particle-consolidation (hvpc) process. AFRL-RX-WP-TR-2008-4380
Sevillano F, Poza P, Munez CJ, Vezzu S, Rech S, Trentin A (2013) Cold-sprayed Ni-Al 2 O 3 coatings for applications in power generation industry. J Therm Spray Technol 22(5):772–782
Shen L, Kong L-y, Xiong T-y, Du H, Li T-f (2009) Preparation of TiAl3-Al composite coating by cold spraying. T Nonferr Metal Soc 19(4):879–882
Shkodkin A, Kashirion A, Kulyuev O, Buzdygar T (2006) Metal particle deposition stimulation by surface abrasive treatment in gas dynamic spraying. J Therm Spray Technol 15(3):382–386
Shockley JM, Strauss HW, Chromik RR, Brodusch N, Gauvin R, Irissou E, Legoux JG (2013) In situ tribometry of cold-sprayed Al-Al_2O_3 composite coatings. Surf Coat Technol 215:350–356
Shockley JM, Descartes S, Vo P, Irissou E, Chromik RR (2015) The influence of Al_2O_3 particle morphology on the coating formation and dry sliding wear behavior of cold sprayed Al-Al_2O_3 composites. Surf Coat Technol 270:324–333
Silva FS, Bedoya J, Dosta S, Cinca N, Cano IG, Guilemany JM, Benedetti AV (2016) Corrosion characteristics of cold gas spray coatings of reinforced aluminum deposited onto carbon steel. Corros Sci 114:57–71
Singh H, Bala N, Kaur N, Sharma SK, Kim DY, Prakash S (2015) Effect of additions of TiC and Re on high temperature corrosion performance of cold sprayed Ni-20Cr coatings. Surf Coat Technol 280:50–63
Smid I, Segall AE, Walia P, Aggarwal G, Eden TJ, Potter JK (2012) Cold-sprayed Ni-hBN self-lubricating coatings. Tribol Trans 55(5):599–605
Sova A, Kosarev VF, Papyrin A, Smurov I (2010) Effect of ceramic particle velocity on cold spray deposition of metal-ceramic coatings. J Therm Spray Technol 20(1-2):285–291
Sova A, Maestracci R, Jeandin M, Bertrand P, Smurov I (2016) Kinetics of composite coating formation process in cold spray: modelling and experimental validation. Surf Coat Technol. https://doi.org/10.1016/j.surfcoat.2016.06.084
Spencer K, Zhang MX (2009) The use of kinetic metallization to form intermetallic reinforced composite coatings by post-spray heat treatment. Surf Coat Technol 203(20–21):3019–3025
Spencer K, Fabijanic DM, Zhang MX (2009) The use of Al-Al2O3 cold spray coatings to improve the surface properties of magnesium alloys. Surf Coat Technol 204(3):336–344

Suo XK, Suo QL, Li WY, Planche MP, Liao HL (2014) Effects of SiC volume fraction and particle size on the deposition behavior and mechanical properties of cold-sprayed AZ91D/SiC_p composite coatings. J Therm Spray Technol 23(1):91–97

Tao Y, Xiong T, Sun C, Jin H, Du H, Li T (2009) Effect of α-Al_2O_3 on the properties of cold sprayed Al/α-Al_2O_3 composite coatings on AZ91D magnesium alloy. Appl Surf Sci 256(1):261–266

Tazegul O, Meydanoglu O, Kayali ES (2013) Surface modification of electrical contacts by cold gas dynamic spraying process. Surf Coat Technol 236(24):159–165

Tazegul O, Dylmishi V, Cimenoglu H (2016) Copper matrix composite coatings produced by cold spraying process for electrical applications. Arch Civ Mech Eng 16(3):344–350

Tlotleng M, Akinlabi E, Shukla M, Pityana S (2015) Microstructural and mechanical evaluation of laser-assisted cold sprayed bio-ceramic coatings: potential use for biomedical applications. J Therm Spray Technol 24(3):423–435

Triantou KI, Pantelis DI, Guipont V, Jeandin M (2015) Microstructure and tribological behavior of copper and composite copper+alumina cold sprayed coatings for various alumina contents. Wear 336-337:96–107

Wang Q, Spencer K, Birbilis N, Zhang M-X (2010) The influence of ceramic particles on bond strength of cold spray composite coatings on AZ91 alloy substrate. Surf Coat Technol 205(1):50–56

Wang HT, Li CJ, Ji GC, Yang GJ (2012) Annealing effect on the intermetallic compound formation of cold sprayed Fe/Al composite coating. J Therm Spray Technol 21(3–4):571–577

Wang Q, Birbilis N, Huang H, Zhang M-X (2013) Microstructure characterization and nano-mechanics of cold-sprayed pure Al and Al-Al2O3 composite coatings. Surf Coat Technol 232:216–223

Wang Y, Normand B, Mary N, Yu M, Liao H (2014) Microstructure and corrosion behavior of cold sprayed SiCp/al 5056 composite coatings. Surf Coat Technol 251:264–275

Wang J, Kong L, Li T, Xiong T (2016) A novel TiAl 3 /Al $_2$ O $_3$ composite coating on r-TiAl alloy and evaluating the oxidation performance. Appl Surf Sci 361:90–94

Woo DJ, Sneed B, Peerally F, Heer FC, Brewer LN, Hooper JP, Osswald S (2013) Synthesis of nanodiamond-reinforced aluminum metal composite powders and coatings using high-energy ball milling and cold spray. Carbon 63:404–415

Woo DJ, Heer FC, Brewer LN, Hooper JP, Osswald S (2015) Synthesis of nanodiamond-reinforced aluminum metal matrix composites using cold-spray deposition. Carbon 86:15–25

Xia M, Huang P, Cu R-K, Ge C-C (2016) Cold sprayed W/Ni/Fe alloy coating: microstructure and mechanical properties. Surf Coat Technol 291:376–381

Xiong Y, Zhang MX (2014) The effect of cold sprayed coatings on the mechanical properties of AZ91D magnesium alloys. Surf Coat Technol 253(9):89–95

Xu Y, Hutchings IM (2006) Cold spray deposition of thermoplastic powder. Surf Coat Technol 201(6):3044–3050

Yamada M, Wakabayashi J, Kitamura J, et al. (2009) Fabrication of Cu-MoS_2 composite coating by cold spraying and evaluation of its property [C]. International thermal spray conference

Yandouzi M, Richer P, Jodoin B (2009) SiC particulate reinforced Al-12Si alloy composite coatings produced by the pulsed gas dynamic spray process: microstructure and properties. Surf Coat Technol 203(20–21):3260–3270

Yang GJ, Zhao SN, Li CX, Li CJ (2013) Effect of phase transformation mechanism on the microstructure of cold-sprayed Ni/Al-Al_2O_3 composite coatings during post-spray annealing treatment. J Therm Spray Technol 22(2):398–405

Yin S, Xie Y, Cizek J, Ekoi E, Hussain T, Dowling D, Lupoi R (2017) Advanced diamond-reinforced metal matrix composites via cold spray: properties and deposition mechanism. Compos Part B-Eng. https://doi.org/10.1016/j.compositesb.2017.01.009

Yu M, Li WY, Suo XK, Liao HL (2013) Effects of gas temperature and ceramic particle content on microstructure and microhardness of cold sprayed SiC_p/Al 5056 composite coatings. Surf Coat Technol 220:102–106

Yu M, Suo XK, Li WY, Wang YY, Liao HL (2014) Microstructure, mechanical property and wear performance of cold sprayed Al5056/SiCp composite coatings: effect of reinforcement content. Appl Surf Sci 289(0):188–196

Zhang G, Li WY, Cherigui M, Zhang C, Liao H, Bordes JM, Coddet C (2007) Structures and tribological performances of PEEK (poly-ether-ether-ketone)-based coatings designed for tribological application. Prog Org Coat 60(1):39–44

Zhang Y, Shockley JM, Vo P, Chromik RR (2016) Tribological behavior of a cold-sprayed Cu-MoS_2 composite coating during dry sliding wear. Tribol Lett 62(1):1–12

Zhou X, Mohanty P (2012) Electrochemical behavior of cold sprayed hydroxyapatite/titanium composite in Hanks solution. Electrochim Acta 65:134–140

Part IV
Wear Resistant Coatings

Chapter 11
Tribological Coatings Prepared by Cold Spray

Richard R. Chromik, Sima Ahmad Alidokht, J. Michael Shockley, and Yinyin Zhang

11.1 Introduction

Many industries, such as aerospace, mining, forestry, and automotive, actively utilize coatings and surface modifications to protect components from damage. The form of this damage can be chemical or mechanical. The former is related to corrosion, oxidation, or other phase changes at the surface that are detrimental to the lifetime of the component. When protecting surfaces from corrosion, one strategy is barrier coatings that are corrosion resistant and essentially seal and isolate the base material from the corrosive media. Barrier coatings can be noble metals or metals that naturally form stable protective oxides or ceramic coatings. The latter form of damage (i.e., mechanical) is related to interacting parts in machinery that lead to forces applied to the surface in various mode (e.g., sliding, rolling, or normal contacts) but also environmental interactions such as hard particles or slurries striking the surfaces that can lead to damage. This is the field of tribology, where the damage is most often referred to as "wear." Coating strategies to protect from wear are wide ranging and can include hard metal or ceramics, solid lubricants, or some form of composite. These strategies seek to provide better mechanical properties at the surface, lubrication, or both. There can also be dual modes of damage, where a component experiences both mechanical and chemical attacks, and these are likely the harshest operating conditions that provide significant challenges for surface engineers.

R.R. Chromik (✉) • S.A. Alidokht • Y. Zhang
Department of Mining and Materials Engineering, McGill University,
3610 University Street, Montreal, QC H3A 0C5, Canada
e-mail: richard.chromik@mcgill.ca

J.M. Shockley
Department of Mining and Materials Engineering, McGill University,
3610 University Street, Montreal, QC H3A 0C5, Canada

NRC Postdoctoral Research Associate in Chemistry Division, US Naval Research Laboratory, Washington, DC, USA

P. Cavaliere (ed.), *Cold-Spray Coatings*,
https://doi.org/10.1007/978-3-319-67183-3_11

Historically, protective coatings have been fabricated by many processes. These range from physical or chemical vapor depositions (PVD and CVD), which deposit thin, micron-scale coatings, to thermal spray processes, which deposit thicker coatings up to hundreds of microns. Another workhorse process for the surface engineering industry is electroplating, which can fabricate metallic coatings in the range of microns to 10s of microns. Thicker coatings fabricated by laser-based techniques that can approach millimeter-length scales are often called claddings and are commonly found in pipeline and mining industries.

One of the most recent coating technologies, which falls into the family of thermal spray processes, is the cold spray process (Champagne 2007; Papyrin et al. 2006). This technique, which is described in detail elsewhere in this book, accelerates powder through a de Laval nozzle such that the powder reaches supersonic velocities. No heat source, plasma, or electrical discharge is present, like in many of the thermal spray processes, so the powder remains in the solid state throughout the process. The mechanism for coating deposition is the mechanical deformation of the powders. As such, cold spray is most useful for metals, which under a high-speed impact will deform and experience adiabatic shear at the particle extremities leading to jetting, local temperature rises, and, when the process is optimized, the creation of metallurgical bonding. Some desirable characteristics of cold spray coatings are nearly full density and minimal chemical reaction or oxidation. The process itself is quite rapid and potentially economical.

In terms of applications for cold spray for the deposition of protective coatings, there were immediate applications for common metals used for corrosion protection (e.g., Al, Ta, Ti). However, for protection from wear, metallic coatings generally are not the primary choice as discussed above. This naturally led cold spray researchers to explore the possibility of the fabricating of composite coatings with a metal matrix and ceramic reinforcements and/or solid lubricant inclusions (Champagne et al. 2015; Jeandin et al. 2015). The cold spray process is capable of fabricating coatings of this type, but there are significant challenges in optimizing the process such that coatings are robust in their structure and properties to provide good wear resistance.

The focus of this chapter is a review of the recent progress in the fabrication of metal matrix composite coatings by cold spray and their tribological behavior. Following this introduction, a brief review of important tribology concepts and a review of coating fabrication principles are presented. This is followed by three sections reviewing work on important composite coatings. Firstly, aluminum metal matrix composites (MMCs) are reviewed, which have a long history of fabrication by other methods, and as such were one of the first systems attempted by cold spray and are well researched. Secondly, MMCs containing carbide reinforcements are presented. This is an important system from an industrial perspective as carbide reinforcements in MMCs are commonly applied by many other methods. Cold spray is considered as either a replacement or a repair method for coatings and claddings of this type. Lastly, MMCs with solid lubricants are reviewed, which are perhaps the most recent system actively studied by cold spray. This also has significant

technological relevance for self-lubricating coatings which are commonly applied on bearings, seals, etc. A summary will also be presented that will identify the future challenges for the development of tribological coatings made by the cold spray process and identify new research directions.

11.2 Tribology Concepts

The vast majority of contacts made in moving mechanical assemblies are metal-metal contacts (Scharf and Prasad 2012). Dry metallic contacts are known for high friction and unacceptable wear rates for systems requiring long lifetime and reliability. Strategies to modify the metal-metal contacts to improve the tribological performance include (i) liquid lubrication (most often oils), (ii) application of solid coatings, or (iii) modification of the bulk materials. Increasingly, engineers are being challenged to develop solutions that are green and sustainable. Thus the first option, absent environmentally friendly lubricants, is less desirable than the latter two. Modification of the bulk material is an option, but a complete replacement to another material is often not possible. In some instances, the same metal or alloy system could be used but manufactured as a "bulk" composite with either ceramic reinforcements to increase the strength or solid lubricant phases to reduce friction. For the second option, there are a host of coating materials available that can be fabricated by many processes. The most common strategies for coating tribology are either a hard coating to enhance the surface hardness and protect from wear or a solid lubricant coating that reduces friction (Holmberg and Matthews 2009). A more recent development is the fabrication of composite coatings, which may utilize both strategies (Erdemir and Voevodin 2010).

Cold spray is capable of fabricating MMCs with ceramics, solid lubricants, or both. This makes the process ideal for fabrication of surface coatings for tribology applications. While tribology of cold spray coatings is a relatively recent area of research, tribology concepts used for many decades can be extended readily to these materials. Figure 11.1 presents an example of a sliding contact on an MMC. As the two surfaces slide past one another, mechanical forces will induce plasticity. Near surface, the microstructure of the metal will be modified. For coarse-grained metals, there is often a refinement to a near-surface nanocrystalline structure, while the reverse takes place for an initially nanocrystalline metal (Argibay et al. 2017). This top layer of modified materials goes by many names in the open literature, with the most common being the general term "tribofilm" or "tribolayer" and "mechanically modified layer (MML)" (Biswas 2005), which is commonly used in the metal tribology community. Besides surface modification to the parent material, there is also transfer of material to the counterface. This can be due to adhesion but also the successive damage of the coating leading to eventual fracture and material removal. Material that transfers to the counterface is termed "transfer film." Material that leaves the tribological

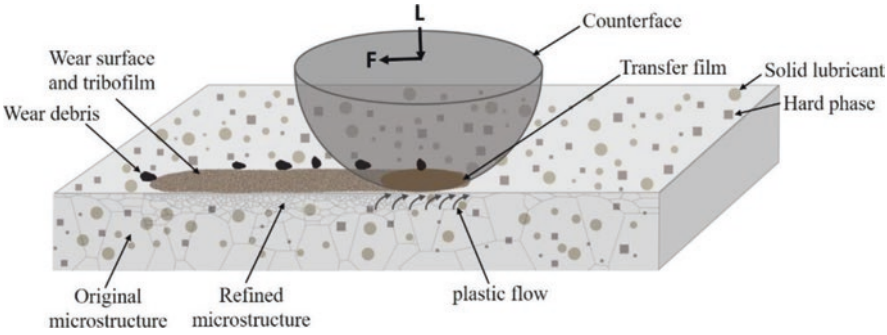

Fig. 11.1 A schematic of a bulk MMC under service. Tribofilms and, in some cases, transfer films are formed. Also, sliding usually generates refined microstructure on the subsurface of the wear track

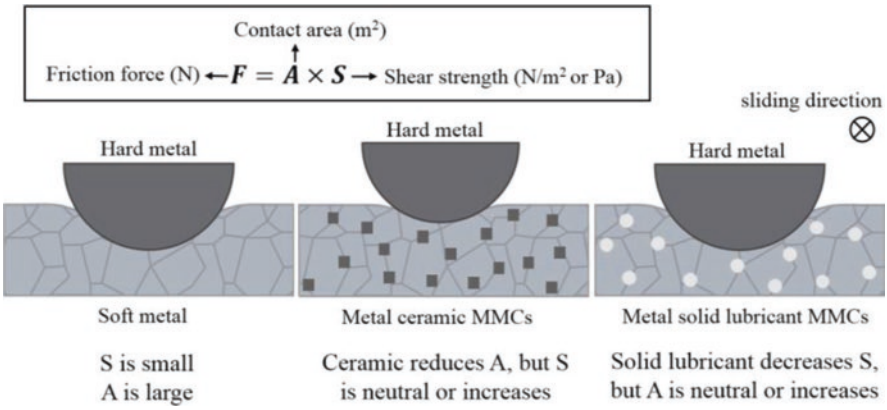

Fig. 11.2 A schematic of contact between metal slider and soft metal (*left*), metal ceramic MMC (*middle*), and metal solid lubricant MMC (*right*), indicating how incorporation of ceramics and solid lubricants modifies friction force. Sliding direction is into the image (Adapted from Singer (1992))

system entirely is termed "wear debris." Collectively, all of these modified materials (i.e., tribofilm, transfer film, wear debris) are known as "third bodies" (Godet 1984, 1990), which are any materials that are mechanically or chemically modified by the wear process.

When engineering a MMC for tribological applications, one is taking advantage of an enhancement of the load-carrying capacity provided by ceramic inclusions or the ability of solid lubricants to develop low-friction tribofilms and accommodate the velocity. In both cases, the friction coefficient will be modified, and depending on other factors (e.g., running speed, load, environment), there may also be an accompanying reduction in wear. Figure 11.2 presents conceptually how friction is modified for MMCs compared to a metal-metal contact. When a hard metal pin slides on a softer metal, there is a relatively large area of contact formed. Due to the low mechanical properties of the softer

metal, the interfacial shear strength will be low, but overall low friction may not be realized due to the creation of many junctions in the large contact area. For a ceramic-based MMC, the contact area will be reduced, but the effect on interfacial shear strength may be an increase due to hard contact between ceramic fragments and the slider. In the case of a solid lubricant-based MMC, there is surely a decrease in shear strength. However, depending on the level of solid lubricant additions, there may be a debit of mechanical properties that leads to an increase in the contact area. When engineering an MMC with high solid lubricant content, mechanical properties can sometimes be retained by addition of ceramic phases as well.

Both strategies shown in Fig. 11.2 also present the possibility of reducing wear. This can be understood in terms of the tribological circuit (see Fig. 11.3) (Berthier 2005; Descartes and Berthier 2002). A reduction in contact area reduces the number of friction junctions that can provide initiation points for fracture and creation of a third body. A reduction in interfacial shear strength is also desirable as it will reduce the forces on the test material that attempt to initiate fracture, which will again reduce the creation of a third body. However, it must be emphasized that these strategies are concentrating entirely on control of the "source flow" in Fig. 11.3. Wear is a very dynamic process, and the controlling factors in determining tribological performance are often tied to the nature of those third bodies once they enter the contact. The stability of tribofilms and transfer films will minimize the "internal flow" in Fig. 11.3 and determines if friction and wear are well controlled and minimized. When tribofilms and transfer films are unstable, are broken down, and are reformed often, there can be a corresponding increase in the "wear flow" (Singer et al. 2003). Thus, minimizing source and internal flows is often helpful in reducing overall wear. In theory, including hard ceramics and solid lubricants can improve the stability of transfer films and tribofilms, but only after studying the tribological performance can this be determined.

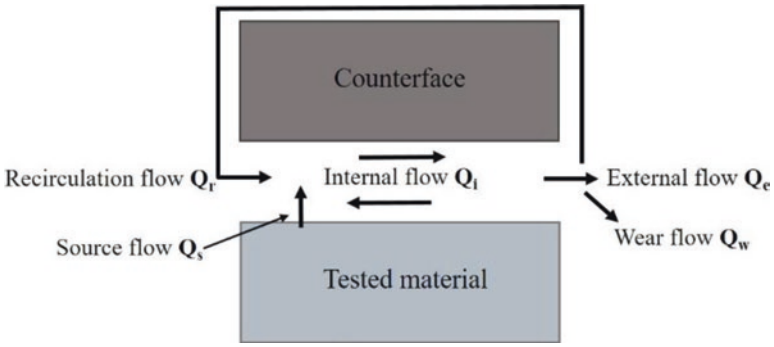

Fig. 11.3 Tribological circuit depicts third body dynamics in the contact: Q_s represents detachment of tested material to become third bodies; Q_i is movement of material across the interface; Q_e is material ejected from the contact; Q_r is ejected material that has been reintroduced to the contact; and Q_w is material permanently removed from the tribosystem (Berthier 2005; Descartes and Berthier 2002)

11.3 Synthesis of Composite Coatings by Cold Spray

The vast majority of research on cold spray for the first decade after its invention was on metallic materials (Champagne 2007; Papyrin et al. 2006). Materials applicable for cold spray are limited to those that have some degree of ductility at high strain rate (Assadi et al. 2003; Schmidt et al. 2006). However, it did not take long for researchers to attempt fabrication of MMCs, which is a common class of coatings made by thermal spray. Some of the very first successful reports of MMCs fabricated by cold spray were naturally coating materials that are commonly fabricated by other methods, such as Al-Al_2O_3, Al-SiC, and WC-Co (Eesley et al. 2003; Lee et al. 2004; Lima et al. 2002; Shukla et al. 2000). Research quickly spreads to other materials, and a wide range of composite systems have been sprayed, including MMCs with various ceramics, solid lubricants, carbon nanotubes, and polymers (Bakshi et al. 2008; Champagne 2007; Moridi et al. 2014; Papyrin et al. 2006; Smid et al. 2012; Stark et al. 2012). Many of the researchers identified the low temperature of cold spray as advantageous. There were minimal oxidation, less evidence of carbide decomposition that commonly occurs in thermal spray, and, similarly, the ability to retain MoS_2 without thermal degradation. Researchers also noted the densified coatings produced by cold spray in comparison to thermally sprayed counterparts of similar materials.

There are three main strategies when spraying MMCs by cold spray: (a) sintered, crushed, or otherwise manufactured metal-ceramic composite powders, (b) pretreatment of pure ceramic powders with metallic claddings, and (c) mechanical blends of metal and ceramic powders. For the first two strategies, the pretreated powders may still be admixed with metal powders to achieve a coating, but some researchers have demonstrated coating fabrication directly from composite or clad powders (Couto et al. 2013; Gao et al. 2008; Kim et al. 2005; Li et al. 2007; Lima et al. 2002).

Cold spray of mechanically blended ceramic and metallic powders is the most commonly applied method. Co-deposition of metallic particles with oxides and carbides has been accomplished, especially with SiC or Al_2O_3 as reinforcement particles (Sova et al. 2010, 2011; Irissou et al. 2007; Sansoucy et al. 2008; Spencer et al. 2009; Yu et al. 2013). The Al-Al_2O_3 system especially was studied extensively and even optimized for use in a MIL standard for repair of magnesium gearboxes (Champagne 2008). This system has relatively good "cold sprayability" due to Al being ductile with a low melting point making simple admixing of the two powders a sufficient approach. Even with this well-behaved system, in all reports, the recovered Al_2O_3 concentration is generally lower than that in the initial feedstock (see Fig. 11.4) (Sova et al. 2011; Irissou et al. 2007; Spencer et al. 2009). Using standard powders, the maximum recoverable Al_2O_3 concentration has been shown to be on the order of 25 wt.% when feedstock concentrations were at 75 wt.% and prepared by admixing (Irissou et al. 2007).

Lower retention of the ceramic in the coating compared to the feedstock composition is generally expected as the ceramic does not plastically deform upon impact. For the ceramic to be retained, it generally requires embedding into pre-deposited

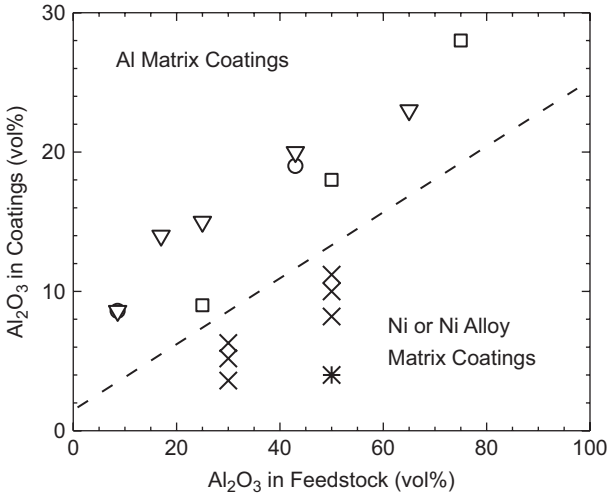

Fig. 11.4 Volume fraction of Al_2O_3 retained in cold spray coatings as a function of the volume fraction in the feedstock. Coatings with Al matrix (∇ – (Irissou et al. 2007), ○ – (Shockley et al. 2015), □ – (Spencer et al. 2009)) retain more alumina than a Ni or Ni alloy matrix (× – (Koivuluoto et al. 2015), ∗ – (Koivuluoto and Vuoristo 2009))

metal particles or by a so-called "burial" mechanism by which a rebounding ceramic particle is trapped by later-arriving metal particles. To take advantage of the embedding mechanism, many studies use angular ceramic particles that will more easily cut into the metal when sprayed. However, angular morphology is not always preferred for the engineering application, and researchers have also sprayed with spherical ceramic particles (Alidokht et al. 2016; King et al. 2007; Shockley et al. 2015). Particle morphology certainly has an effect where the retention of angular ceramic particles is higher than spherical of same size (Shockley et al. 2015). Particle size can also have a profound effect, where finer size ceramic particles are more prone to embed into substrate due to higher velocities attained in gas stream (Sova et al. 2009). However, one cannot use too fine a particle size because the bow shock effect at the substrate can prevent deposition for very small particles (Koivuluoto and Vuoristo 2009).

The metal used at the matrix can have a profound effect on ceramic retention as well. Figure 11.4 presents the volume fraction of Al_2O_3 retained plotted versus the volume fraction in the feedstock for both Al matrix (Irissou et al. 2007; Shockley et al. 2015; Spencer et al. 2009) and Ni or Ni alloy matrices (Koivuluoto et al. 2015; Koivuluoto and Vuoristo 2009). In all cases, the Al_2O_3 is an angular shape. There is a clear difference in the retention, where the Al matrix retains significantly more ceramic compared to the Ni matrix. When ceramic retention is affected by the metal being sprayed, it is linked to the deformability of the metal. Al feedstock powder (Shockley et al. 2015) is relatively soft compared to Ni feedstock powders (Alidokht et al. 2016). Ceramic particles impacting on a softer metal can embed further and have better chance of being retained rather than rebounding.

Metal-carbide-type MMCs often make use of harder metallic matrices and also require a much higher volume fraction of carbide than the typical retention found for simple admixing of ceramic powders with Ni, NiC, steel, etc. Because of this difficulty, most of the studies on cold-sprayed MMCs with carbides have used agglomerated, sintered, and crushed powders. However, this approach has its own issues in that composite powders with significant carbide content will be very non-deformable and will lead to low deposition efficiency and unsatisfactory bonding quality. As such researchers have attempted tailoring the powder to enhance deformability, such as porous powder (Gao et al. 2008; Li et al. 2007; Lima et al. 2002), sufficient metal binder (Couto et al. 2013), and preheating prior to spray (Kim et al. 2005; Li et al. 2007). All of these approaches can enhance deposition but have a corresponding effect on properties of the coating. As such there continues to be significant efforts on powder engineering and process optimization for carbide containing MMCs manufactured by cold spray (Ang et al. 2011; Champagne 2007; Gao et al. 2010; Ji et al. 2013; Kim et al. 2005; Lioma et al. 2015; Melendez et al. 2013; Papyrin et al. 2006; Wang et al. 2014; Yandouzi et al. 2007).

Compared to other MMC systems, self-lubricating metal matrix composites (SLMMCs) application with cold spray initiated the most recently (Aggarwal 2007; Botef and Villafuerte 2015; Champagne 2007; Papyrin et al. 2006). So far, only nickel and copper have been cold sprayed with hexagonal boron nitride (h-BN) and molybdenum sulfide (MoS_2). Deposition mechanism of solid lubricant with metal was explored by Zhang et al. using a mechanical blend of Cu and MoS_2 (Zhang et al. 2016a). Firstly, MoS_2 particles were fractured upon impact, with a subsequent high-velocity impact of a Cu particle, Cu-Cu bonding occurred if its plastic deformation could push MoS_2 flakes aside so that adiabatic shear took place. Otherwise Cu particles rebounded, resulting in craters, and no more deposition can be further developed. The MoS_2 recovery under optimized spraying condition was found to be around 2 wt.% by mechanical blends. They found preheating the substrate improved significantly deposition efficiency and surface roughness (Zhang et al. 2016a, b). Pretreatments of solid lubricant with metallic claddings by electrodeposition have been used to fabricate Ni-h-BN powder for cold spray. Micro- and nano-scale h-BN were the optimized solid lubricant core in order to improve deposition efficiency (Neshastehriz 2014; Neshastehriz et al. 2014; Weyant 2008). The highest h-BN recovery of around 10 vol.% was achieved. However, the best combination of hardness and friction was the one with 1 vol.% h-BN (Stark et al. 2012).

11.4 Tribology of Al MMCs Fabricated by Cold Spray

The low density, high thermal conductivity, and inherent corrosion resistance of aluminum and many of its alloys make them attractive as coating materials. However, the tribological performance is too poor for many applications unless the alloy is chosen judiciously or the matrix is reinforced using hard secondary phases such as Al_2O_3 or SiC particles to make Al MMCs (Deuis et al. 1997). The corrosion resistance of pure aluminum has made it an important coating material in the

aerospace industry. For instance, thermal-sprayed aluminum coatings have been used to prevent stress corrosion cracking in aluminum alloy 7075-T6 structural elements (Irissou et al. 2007), and similar techniques have been applied to corrosion-prone magnesium alloys (Parco et al. 2006; Pardo et al. 2009; Spencer et al. 2009). However, due to its affinity for oxygen, aluminum has a tendency for in-flight oxidation during high temperature thermal spray processes, leading to porosity and poor cohesion between coating layers (Irissou et al. 2007). As an alternative, cold-sprayed Al-MMC coatings maintain aluminum's corrosion resistance while substantially lowering wear rates (Irissou et al. 2007), the latter being the role of hard particles in Al-MMCs (Alpas and Zhang 1992, 1994; Deuis et al. 1997; Venkataraman and Sundararajan 1996).

11.4.1 Trends for Tribological Performance of Cold-Sprayed Al-MMCs

Most Al-MMC materials are produced through casting or sintering techniques, and the friction and wear behavior of Al-MMC materials reinforced with hard particles or fibers has been a subject of interest for at least 40 years (Sato and Mehrabian 1976). Relatively soft aluminum-based matrix materials such as pure Al, Al-4Cu, Al-4Cu-0.75 Mg, AA6061, AA2014, Al-10Zn, A356, AA7091, and various other alloys have been paired with comparatively harder reinforcements made most commonly from SiC, Si, or Al_2O_3 (Deuis et al. 1997). Generally speaking, the presence of hard particles is associated with lower wear rates and lower friction compared to the unreinforced matrix material. One early study explored the influence of concentration and particle size for Al_2O_3 and SiC reinforcements in an AA2014 alloy matrix. It was found that in the ranges of 2–30 wt.% and 1–142 μm particle sizes, the wear rate decreased as reinforcement concentration increased, and at a given weight fraction, wear rate decreased as reinforcement size increased (Hosking et al. 1982). The optimum Al_2O_3 particle content for wear resistance was found to fall in the range of 25–35% (Chung and Hwang 1994). The influence of particle size is not as clear, as some subsequent studies have found that increasing the particle size can lead to slightly higher wear rates (Sato and Mehrabian 1976). The friction coefficient was found to be affected by the presence of hard particles as well, with the composite materials exhibiting 30% lower friction coefficients than the aluminum matrix alone (Roy et al. 1992).

Al-MMCs by cold spray are relatively new, but a few studies have been dedicated specifically to their tribological behavior. In general, coating hardness increases as a function of Al_2O_3 content due to load bearing by Al_2O_3 particles (Irissou et al. 2007; Shockley et al. 2013; Spencer et al. 2009). Spencer et al. (2009) focused on the dry sliding wear rates of cold-sprayed Al-Al_2O_3, using a unidirectional pin-on-disk tribometer with a 6 mm steel ball and a 3 N deadweight load. The presence of Al_2O_3 particles was associated with stable friction coefficients, while the un-reinforced pure Al and AA6061 coatings they tested showed unstable friction, with frequent fluctuations in the measured friction force. Wear rate measurements showed that the presence of Al_2O_3 particles was associated with significant reduction

in wear rates of up to several orders of magnitude. The application of a 2 h heat treatment at 400 °C resulted in very little change in the measured wear rates (Spencer et al. 2009).

Various studies by Shockley et al. have focused on the friction and wear behavior of cold-sprayed Al-Al_2O_3, studying the effect of Al_2O_3 particle concentration and morphology (Shockley et al. 2013, 2014, 2015, 2016) and linking this to the third body behavior through in situ tribometry, microstructural analysis through focused ion beam (FIB-SEM) and transmission electron microscopy (TEM), and nanoindentation of third bodies. A reciprocating ball-on-flat tribometer was used to perform dry sliding wear tests. A 1.0 N deadweight load was applied to polycrystalline Al_2O_3 or monocrystalline sapphire counterfaces. The friction and wear behavior was found to be relatively similar between pure cold-sprayed aluminum (sample CS0) and low quantities of reinforcement (10 wt.% angular Al_2O_3 and 3 wt.% spherical Al_2O_3). In these cases the friction was highly unstable (see Fig. 11.5). With higher reinforcement contents of 22 wt.% angular and 11 wt.% spherical, the friction was considerably more stable, and wear rates were lower by an order of magnitude.

11.4.2 Third Body Aspects for Cold-Sprayed Al-MMC Tribology

Two regimes of tribological behavior were determined for the cold-sprayed Al-Al_2O_3 material system: high, unstable friction and high wear rates, associated with no or low Al_2O_3 contents, and lower, more stable friction and low wear rates with high

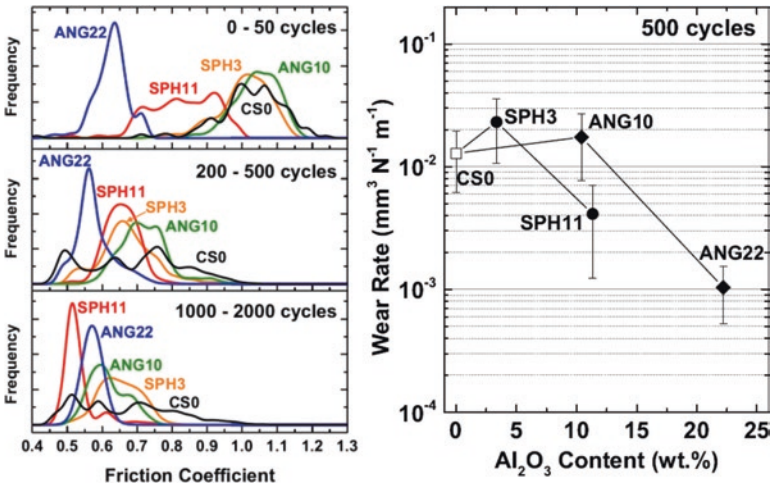

Fig. 11.5 Friction (*left*) and wear rates (*right*) of pure cold-sprayed aluminum (CS0), 10 and 22 wt.% angular Al_2O_3 (ANG10 and ANG22), and 3 and 11 wt.% spherical Al_2O_3 (SPH3 and SPH11) (Adapted from Shockley et al. (2015))

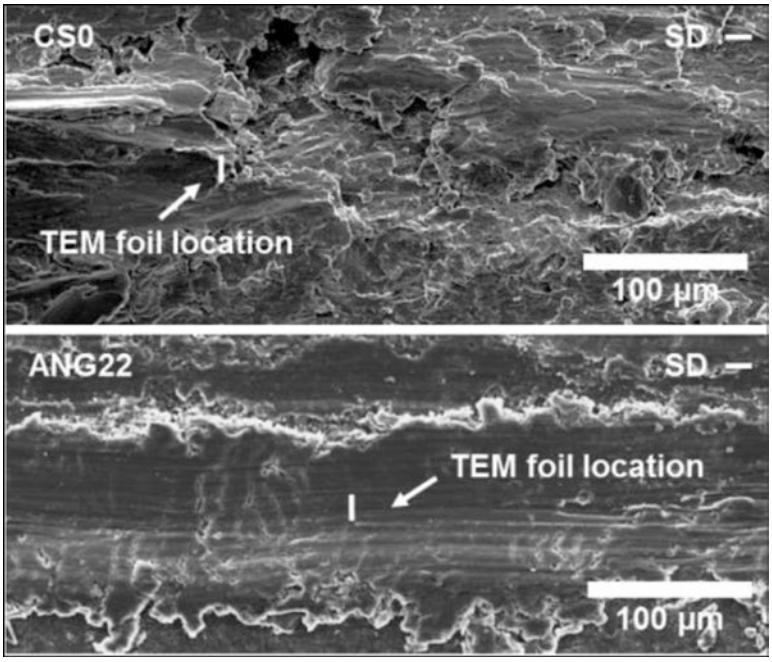

Fig. 11.6 Surface analysis of regions within a wear track: cold-sprayed pure aluminum sample CS0 and cold-sprayed Al-22 wt.% Al_2O_3 sample with angular morphology (Adapted from Shockley et al. (2016))

Al_2O_3 amounts. To determine mechanisms associated with the transition between the two regimes, surface and near-surface material changes were examined. From Fig. 11.6, pure cold-sprayed aluminum showed evidence of adhesive wear, transfer, and plastic deformation, while the presence of 22 wt.% angular Al_2O_3 was associated with the formation of a smooth surface on sample ANG22.

The subsurface microstructure of CS0 and ANG22 after 500 sliding cycles was analyzed using TEM methods. Low-magnification TEM of sample CS0 revealed a layered microstructure consisting of clusters of multiple grain sizes (see Fig. 11.7). The bottom region of the image shows larger grain sizes with a grain size gradient, separated from the rest of the microstructure by a series of horizontal cracks. Above these cracks the grain sizes were mixed, with regions of ultrafine and nanocrystalline grain sizes. The lower region is the deformed first body. The upper region is the third body, which was smeared over the first body during the adhesive wear process (Shockley et al. 2014).

The microstructure of the first body region of CS0 showed a grain size gradient indicative of plastic deformation (see Fig. 11.7). The smallest apparent grain sizes in the first body were on the order of roughly 50 nm. In the CS0 third body region, there are many grain sizes visible with the smallest on the order of about 20 nm (see Fig. 11.7 right). Selected area electron diffraction (SAED) reveals that no amorphous material is present and that the material is entirely nanocrystalline and ultrafine grain aluminum.

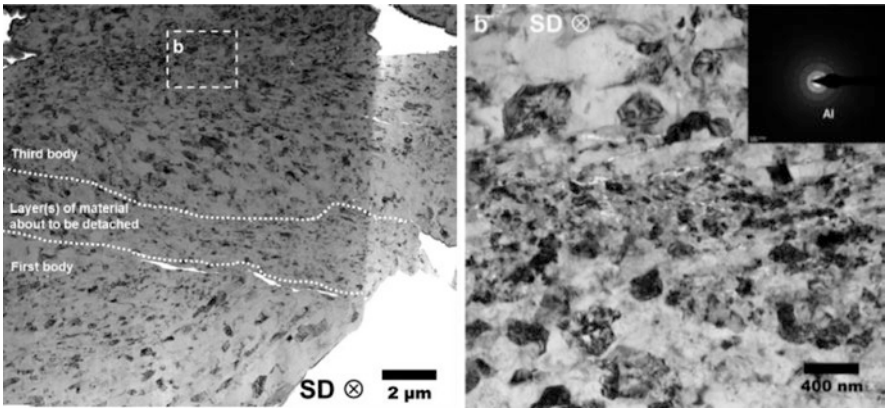

Fig. 11.7 TEM micrographs from sample CS0, showing low and high magnification views (*left* and *right*, respectively) and SAED (*inset*) (Adapted from Shockley et al. (2016))

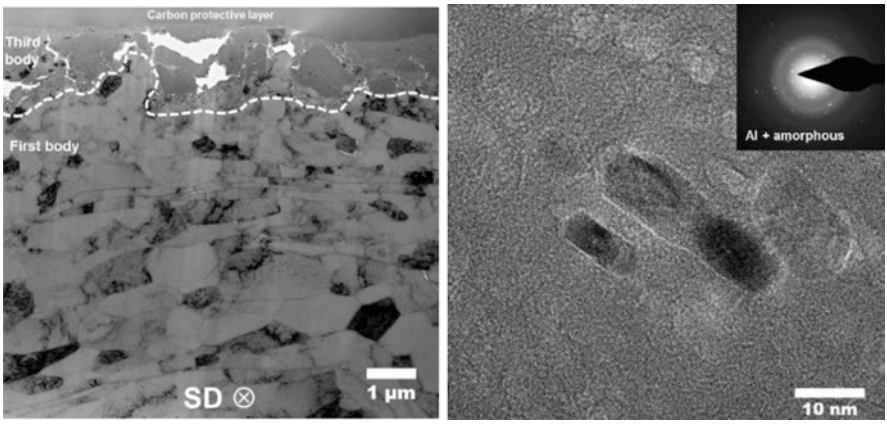

Fig. 11.8 TEM micrographs from sample ANG22, showing low and high magnification views (*left* and *right*, respectively) and SAED (*inset*) (Adapted from Shockley et al. (2016))

Low-magnification TEM of sample ANG22 revealed distinct contrasts between the first and third body material (Fig. 11.8). In the first body, grain sizes remain more or less microscale until close vicinity of the third body material, becoming refined to no less than roughly 500 nm until immediately adjacent to the third body material. A severely deformed region was observed between the first and third bodies and varied from roughly 50 to 500 nm thick, with a clear gradient of grain size within this region (Shockley et al. 2016). Third body material is present in discrete pieces embedded in the third body sitting at the surface. Several pieces of third body material in Fig. 11.8 detached and were lost during the FIB thinning process. No Al_2O_3 particles happened to be captured in the region where the FIB foil was extracted, but previous observations by FIB-SEM observed fragments of Al_2O_3 surrounded by deformed material (Shockley et al. 2014). A discrete section of ANG22 third body was analyzed by

higher-magnification TEM (Fig. 11.8 right). This revealed that the microstructure of the third body particle consisted predominantly of an amorphous matrix with small, nanocrystalline (~5–20 nm) phases present. Selected area electron diffraction (pictured) and plane spacing measurements (not pictured) revealed that these phases within the amorphous matrix were aluminum. The elevated oxygen in this region indicated that at an amorphous, oxidized structure developed, shrinking the size of the aluminum grains to the nanoscale "islands" remaining.

11.4.3 Nanoindentation of Third Bodies from Cold-Sprayed Al-MMC

Nanoindentation was performed on discrete regions of third body material in the near-surface microstructure of various samples, as well as the undeformed aluminum in the first body of all samples (see Fig. 11.9). The hardness of the third body material was always higher than that of the unworn aluminum, with the highest hardness on the order of 3.8 GPa for samples SPH11 and ANG22. This value is lower than that of polycrystalline α-Al_2O_3 (~21 GPa), but the similar hardness between SPH11 and ANG22 indicates that the same amorphous, highly oxidized material observed in Fig. 11.8 is required to reach the low wear, stable friction regime observed for these samples.

The concentration and morphology of Al_2O_3 play a large role in the tribological behavior of cold-sprayed Al-Al_2O_3, affecting the third body dynamics, microstructural transformations, and mechanical properties. A major shift in behavior

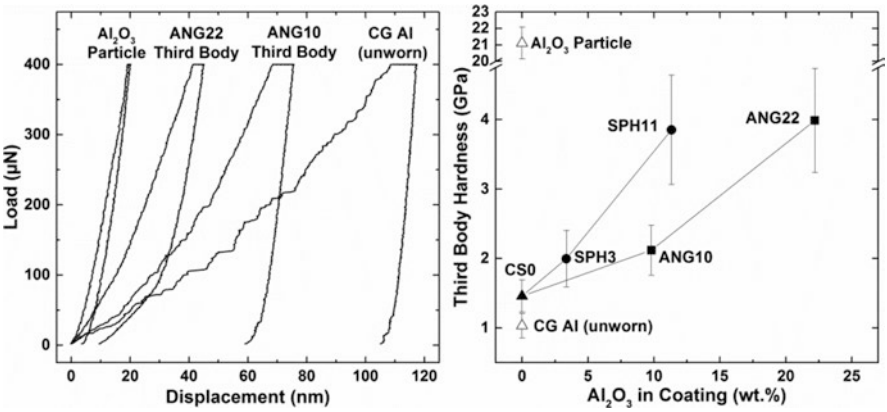

Fig. 11.9 *Left*: representative load-displacement curves from nanoindentation of ANG10 and ANG22 third body layers, compared to an α-Al_2O_3 particle and coarse-grained aluminum (CG Al) (Shockley et al. 2014). *Right*: hardness of the third body layers from pure cold-sprayed aluminum (CS0) as well as spherical and angular reinforced cold-sprayed Al-Al_2O_3, compared to that of coarse-grained aluminum and an α-Al_2O_3 particle (Shockley et al. 2015)

between a high wear, unstable friction regime and a low wear, stable friction regime occurs due to enhanced grain refinement and subsequent oxidation at the subsurface, and this only occurs in the vicinity of a sufficient concentration of hard particles. The lower concentrations of spherical Al_2O_3 needed compared to angular Al_2O_3 were found to be due to crack formation at the corners of Al_2O_3 particles, where stress concentration is known to be highest (Shockley et al. 2015), a hypothesis which was confirmed using high-pressure torsion (Shockley et al. 2017) on the same materials.

11.5 Tribology of Cold-Sprayed Metal-Carbide MMCs

Transition metal carbides, such as WC and TiC, have been widely used to reinforce metallic matrix for wear resistance applications (Pierson 1996). Coatings in this class are considered for applications where there are aggressive wear conditions such as solid particle erosion, slurry erosion, or abrasive contacts. Traditionally, these materials are manufactured by thermal spray, laser cladding, or powder metallurgy methods. Cold spray processing of these materials has been a recent development, but there are quite a few researchers that have researched wear with various tests, including sliding, abrasive, and erosive. Table 11.1 summarizes some of the recent work on tribology of cold-sprayed metal-carbide coatings.

Couto et al. (2013, 2014, 2015) and Dosta et al. (2013) reported cold spray deposition of WC-based composite coatings with different Co contents, including 12, 17, and 25 wt% Co. They studied the sliding (ASTM G99-04) and abrasive (ASTM G65-00) wear resistances of the coatings. Benchmarking of the cold spray coatings was made against conventional high-velocity oxygen fuel (HVOF) WC-Co coatings. The HVOF coatings were thicker and harder than cold-sprayed coatings due to the thermal decomposition of the WC-Co powder and formation of the hard Co_6W_6C or Co_3W_3C phases. However, HVOF coatings were also more brittle due to the depletion of the ductile Co matrix and the presence of fragile phases such as W_2C, W, and/or η phases. Comparing the sliding wear resistance of coatings made by the two processes, cold-sprayed WC-Co coatings showed higher wear resistance with an improvement of approximately 72% for WC-17Co, 60% for WC-12Co, and 80% for WC-25Co coatings. This was attributed to the absence of the brittle phases in cold spray coatings. For HVOF coatings, the higher wear rate was primarily due to cracking along the preferential crack paths provided by brittle phases (Stewart et al. 1999).

Abrasive wear behavior of WC-Co coatings, obtained by cold spray and HVOF, was also investigated by Couto et al. Even though HVOF coatings were harder than cold-sprayed ones, the abrasive wear resistance of cold-sprayed coatings proved to be higher. Cold spray coatings had a uniform distribution of the WC carbide particles in the metallic Co matrix and the homogeneous and sub-micrometric size of the carbide particles that led to a very high abrasion resistance. By decreasing the Co binder content, a higher Vickers hardness and even better abrasive wear resistance were observed.

Table 11.1 Summary of wear test types, configurations, and parameters

Material systems	Wear test type	Wear test parameters	References
Microstructured WC-25, WC-17, and WC-12Co coatings	Abrasive (ASTM G65–00) Ball-on-disk (BoD) sliding ASTM G99–04	Abrasion Three-body abrasive wear: rubber wheel rotation speed, 139 rpm; load, 50 N; abrasive SiO_2 flux, 250–310 g/min Sliding WC-12Co ball, sliding velocity, 131 rpm; total testing distance, 1000 m; load, 25 N; relative humidity and temperature 20% and 25 °C	Couto et al. (2013, 2014, 2015), Dosta et al. (2013)
Multimodal WC-12Co with 30 vol.% nano- and 70 vol.% microstructured WC WC-17Co containing 10, 30, and 50 wt.% nanostructured WC	Pin-on-disk two-body abrasive wear	Pin sample, abrasive paper SiC 300 grit; load, 10 N; wear distance, 16 m; and rotation speed, 60 rpm	Ji et al. (2013) Wang et al. (2014)
Ni and Ni-10.5 vol.% WC composite coatings sprayed using unmodified spherical powders	Ball-on-flat reciprocating sliding wear Solid particle erosion (SPE) (ASTM standard G76)	Sliding WC-12Co ball, sliding velocity, 3 mm/s; load, 5 N; relative humidity and temperature 0% and 25 °C Erosion Erodent, angular Al_2O_3, 50–70 μm; impact angles, 30 and 90°; stand of distance, 20 mm; feeding rate, 0.8 g/min	Alidokht et al. (2016, 2017)
Ni and Ni-WC (WC-Co) containing 7–66 wt.% WC	Abrasive (ASTM G65–04)	Three-body abrasive wear, rubber wheel rotation speed, 200 rpm; load, 130 N; abrasive SiO_2 flux, 365 g/min	Melendez et al. (2013)

One of the advantages of the cold spray technique over other thermal spray processes is deposition of coatings that retain the original nanostructure of the feedstock powders. Ji et al. (2013) reported deposition of a WC-12Co coating, using a bimodal WC-12Co powders composed of 30 vol. % nano- and 70 vol. % microstructured WC particles. Average microhardness obtained on the coating cross section was 1525.3 ± 143.05 $HV_{0.3}$, which was higher than that of HVOF multimodal WC-12Co coating (1100 $HV_{1.0}$). This was due to the dense structure of the cold-sprayed coatings. The multimodal distribution of WC particles resulted in a coating with high fracture toughness. Abrasive wear tests showed an enhanced wear resistance for multimodal distribution of WC particles that was attributed to a synergetic strengthening effects of the multiscale WC particles. Nano-sized WC particles improved the abrasion resistance of the Co matrix by reducing its deformation and cutting, and micro-sized WC particles were more resistant to being pulled out and retarded the propagation of cracks. The abrasive wear resistance of cold-sprayed

multimodal WC-12Co was greatly enhanced when comparing to the HVOF coating. The weight loss of cold-sprayed and HVOF-sprayed coatings was 1.8 ± 0.44 mg and 15.93 ± 0.12 mg, respectively. The wear mechanism was mainly an initial selective removal of soft Co followed by WC removal or fracture.

Wang et al. (2014) studied abrasion wear performance of cold-sprayed multimodal WC-17Co coating with different content of nanostructured WC. The microhardness and fracture toughness increased and decreased, respectively, with increasing the content of nano-sized WC. Nevertheless, overall a higher fracture toughness was recorded compared to HVOF coatings, which was due to the dense microstructure and the absence of brittle phase (η phase). The weight loss from abrasive wear for the cold-sprayed coatings decreased from 5.53 ± 0.11 to 3.8 ± 0.06 and 2.67 ± 0.15 mg with increasing nanostructured WC content in feedstock. Also, due to the better hardness and fracture toughness, the abrasive wear resistance of cold-sprayed coatings was higher than HVOF coatings.

Melendez et al. (2013) studied dry abrasion wear performance of low-pressure cold-sprayed Ni and Ni-WC (WC-Co) composite coatings containing 7–66 wt% WC. They reported that the addition of WC to the coating minimized the wear damage to the surface. Higher wear resistance of the coatings was recorded with increasing WC percentages due to the enhanced hardness and fracture toughness. As the WC content in the coating increased, the number of cracks around hardness indents, as well as, in the subsurface of worn coatings decreased. It was reported that the cold-sprayed Ni-WC coatings containing 66 wt% WC can compete with a HVOF WC-12Co coating in terms of abrasive wear resistance. Although the latter had a higher WC content (83wt%WC), and thus, a higher hardness (~1100 HV), but hardness is not always the sole indicator of coating ability to withstand wear. Embrittlement of the HVOF WC-Co coatings due to detrimental phase reaction decreased wear resistance. Abrasion wear resistance of low-pressure cold-sprayed coating that contained 66 wt% WC was comparable to that of the WC-25Co coatings fabricated using high-pressure cold spray suggesting that the former could be used as a low-cost alternative.

Alidokht et al. (2016) studied dry sliding wear behavior of cold-sprayed Ni and Ni-10.5 vol% WC coatings. The incorporation of WC particles didn't increase hardness significantly, due to low percentage of WC particles, decreased bonding between Ni particles, and fragmented/cracked WC particles. Nevertheless, the presence of WC stabilized the friction (Fig. 11.10a) and decreased wear rate by a factor of seven (Fig. 11.10b). Significant plastic flow and adhesive wear were observed for both coatings for initial cycles. For the Ni-WC composite, Ni was preferentially worn early in the test and squeezed onto WC particles. This led to an earlier formation of a protective tribofilm, consisting of compacted Ni wear particles rich in oxygen and WC fine fragments. Whereas, for the Ni coating, an adhesive wear mechanism persisted longer, and the tribofilm formed later in the test. At higher cycles, the coverage of the tribofilm on the worn surface was lower for pure Ni than the composite coating.

From observation of mechanical cross sections of wear tracks, subsurface micro-cracking was observed in the cross section of the wear track for Ni coating (Fig. 11.11a). Shear stresses were more easily transferred to the bulk material underneath the tribofilm due to low load-bearing capacity of Ni. The

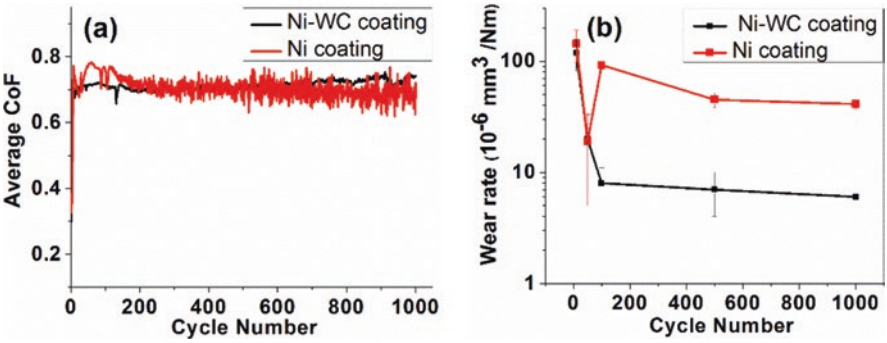

Fig. 11.10 Average CoF (**a**) and volumetric wear rate (**b**) plotted versus number of cycles for tests run to 1000 cycles

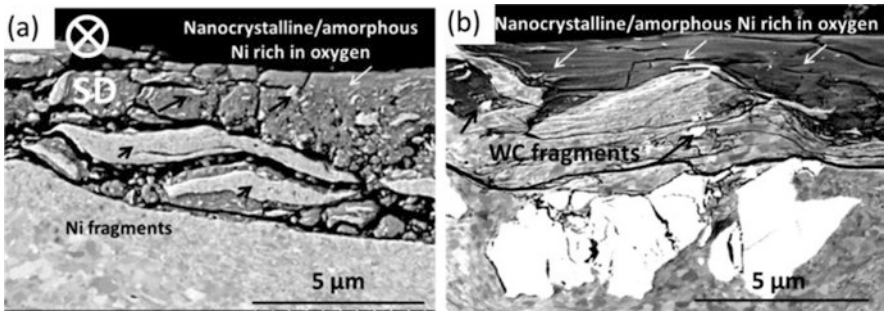

Fig. 11.11 Cross sections of the near-surface microstructures after 1000 sliding cycles for (**a**) Ni, where *black arrows* indicate Ni fragments and *white arrows* indicate oxygen-rich regions, and (**b**) Ni-10.5vol%WC coatings, where *black arrows* indicate WC fragments and *white arrows* indicate oxygen-rich regions. *SD* indicates sliding direction

intersection of these cracks led to detachment of wear particles, which induced wear on the surface by abrasion. In the case of the Ni-WC composite coating, the development of a coherent and stable tribofilm, which is evident from Fig. 11.11b, contributed to superior wear resistance of the Ni-WC coating compared to the Ni coating. The presence of fine redistributed WC particles in the tribofilm improved friction stability as well. Using nanoindentation, the tribofilm of the Ni coating had a hardness of 6.2 ± 0.7 GPa which was 1.4 times higher than that of the underlying Ni (4.6 ± 1.0 GPa). The strain hardening due to grain refinement and surface oxidation are the possible contributions to the increased hardness of tribofilm. The hardness of the Ni-WC coating tribofilm was 11.2 ± 3.6 GPa which was 2.2 times harder than the bulk of the tested material (5.2 ± 1.0 GPa). A large value of hardness of the worn surface was due to the redistributed fine WC particles and strain hardening. In addition, the higher oxygen content in the load-bearing areas of Ni-WC composite coating and fine debris around these areas compared to those of the Ni coating was obtained

using EDX chemical analysis. This was attributed to a more localized plastic deformation of Ni adjacent to WC particles, which resulted in large density of sliding-induced defects and harder tribofilm.

Erosive wear was studied on same coatings, i.e., cold-sprayed Ni and Ni-10.5 vol% WC coatings (Alidokht et al. 2017). Detailed microstructural analyses and wear loss measurements were conducted to study the mechanism involved in solid particle erosion (SPE) of Ni and Ni-WC coatings under two impact angles, 30 and 90°. Ni and Ni-WC coatings exhibited ductile erosion. Higher erosion resistance of coatings under normal angle compared to oblique angle was related to the formation of a protective tribofilm. However, 10.5 vol% WC content was not sufficient to reinforce Ni against erosion under oblique angle. Under normal angle, the addition of 10.5 vol% WC actually deteriorated erosion resistance by preventing tribofilm formation and providing mechanisms for brittle fracture.

11.6 Self-lubricating Metal Matrix Composites (SLMMCs)

Currently there are two main research groups including Pennsylvania State University and McGill University who explore cold sprayability of solid lubricants with metals. The former group focused on pretreatments of different length scales of hexagonal boron nitride (h-BN) encapsulated with nickel in order to improve deposition efficiency and h-BN recovery (Stark et al. 2012; Weyant 2008), while the latter group observed extensively tribological performance of cold-sprayed Cu-MoS_2 fabricated by mechanically blended feedstock (Zhang et al. 2016a, b). Although the best solid lubricant concentration in the composites was reported as around 10 vol.% using nano-engineered h-BN encapsulated with Ni, Ni-1 vol.% h-BN composite exhibited the lowest friction coefficient and highest hardness (Stark et al. 2012).

Figure 11.12 summarizes friction coefficient varies with solid lubricant content of SLMMCs made by cold spray (Zhang et al. 2016a) as well as other techniques such as powder metallurgy (Kovalchenko et al. 2012; Li and Xiong 2008; Raadnui et al. 2008; Zhang et al. 2008), thermal spray (Du et al. 2010, 2011), and laser cladding (Zhang et al. 2008). In general, the friction coefficient decreases with solid lubricant content, and the lowest friction value for most of the composites was around 0.4.

Another feature observed from Fig. 11.12 is that the lowest attainable friction coefficient is much higher than that rubbing against blankets of solid lubricant films (Dvorak et al. 2007; Martin et al. 1993). This suggests the metal matrices play an important role on friction of the SLMMCs. Early contribution by Rohatgi et al. (1992) has analyzed theoretically the effect of metal matrix component on friction coefficient, and the friction of a SLMMC can be written as:

$$f = \left(1 - A_f\right) f_m + A_f f_f \tag{11.1}$$

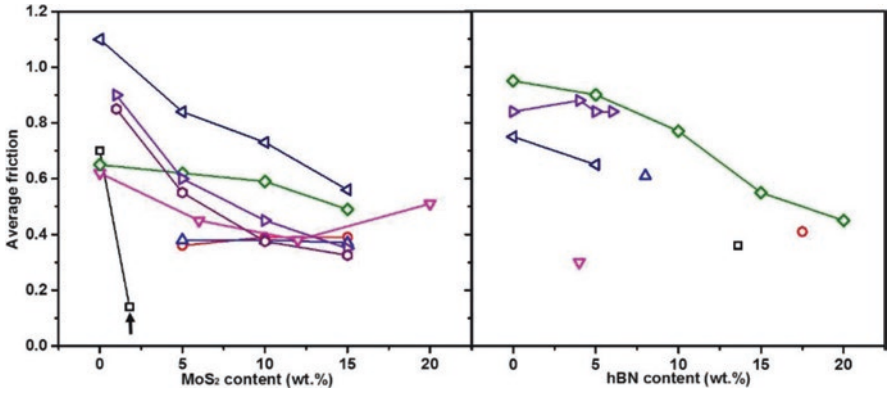

Fig. 11.12 A summary of average friction coefficients that vary with MoS_2 (*left*) and h-BN (*right*) content from SLMMCs with different matrix materials and produced by different techniques. The *arrow* indicates data points of cold-sprayed Cu-MoS_2 composite

where A_f is fraction of lubricating tribofilm in the contact, f_f and f_m are friction coefficients of tribofilm and matrix, respectively. Therefore, the coefficient of friction of composites may vary between f_m and f_f, depending on solid lubricant content and ability of development and stability of lubricating film over sliding. In addition, most of the manufacturing methods such as thermal spray and powder metallurgy inevitably cause oxidation and/or other phase transformations of solid lubricants, which could prevent solid lubricants to be effective (Kato et al. 2003; Kovalchenko et al. 2012; Lansdown 1999).

As friction behavior is largely determined by the coverage of solid lubricant film on the worn surface, Zhang et al. (2016b) related spatially resolved friction to local solid lubricant content in a cold-sprayed Cu-MoS_2 composite during reciprocating sliding wear tests. As shown in Fig. 11.13, once sliding commenced, MoS_2 was smeared out and formed discontinuous MoS_2 films on the wear track. The locations that had more MoS_2 films showed lower coefficient of friction. These results demonstrate the concepts described by Rohatgi et al. (1992) for SLMMCs. Inhomogeneous distribution of coefficient of friction was also observed after a longer test (1000 cycles) even though MoS_2 was further spread over the wear track. Based on the Raman spectroscopy results, the local MoS_2 content probably decreased with sliding, and Cu was oxidized forming Cu_2O. Due to low MoS_2 content, i.e., 1.8 wt.%, and tribochemical reaction of Cu when testing in ambient, no stable MoS_2 transfer film was observed on the counterfaces, which made it different from that found rubbing against blanket films of MoS_2 (Lince 2004; Stoyanov et al. 2012; Wahl and Singer 1995). The main feature of these latter coatings is to form transfer films on the counterfaces, which leads to MoS_2 sliding versus MoS_2 and friction coefficients in the range of 0.02–0.06 in dry air at similar test conditions (Wahl and Singer 1995).

Wear rates were also determined and correlated to local MoS_2 content, as summarized in Table 11.2 (Zhang et al. 2016b). It is worth to note that substantial wear rate was initiated during the first 100 cycles, and it was directly related to local

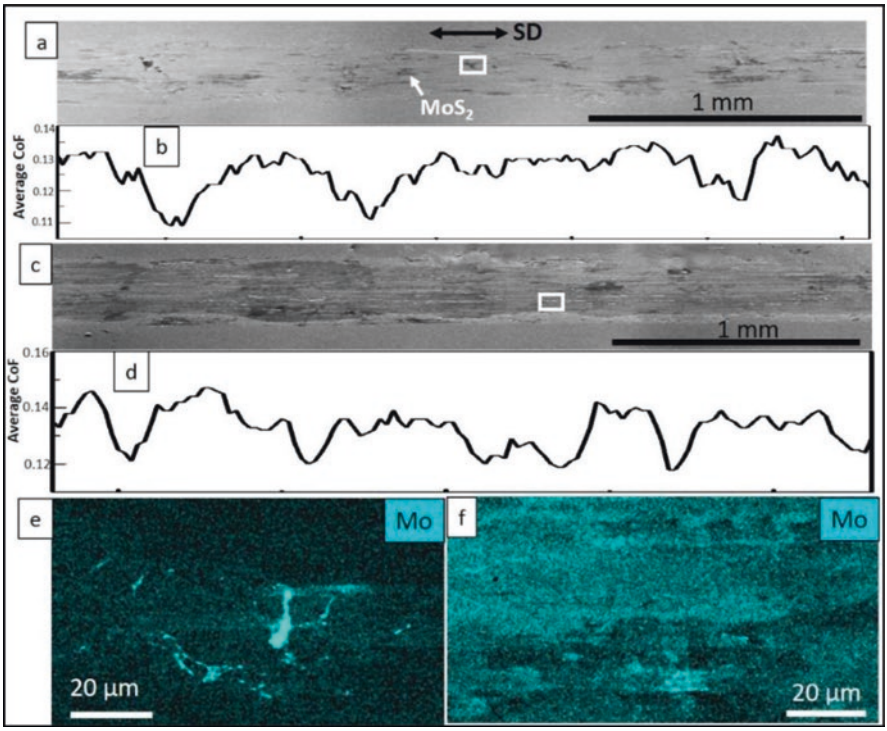

Fig. 11.13 Top-down view of the Cu-MoS_2 wear tracks after a 100-cycle (**a**, **b**, **e**) and a 1000-cycle (**c**, **d**, **f**) tests. (**a**, **b**) Overall morphology and spatial friction along the wear track at the 100th cycle, respectively. (**c**, **d**) Overall morphology and spatial friction along the wear track at the 1000th cycle, respectively. (**e**, **f**) EDX maps of the white rectangles in (**a**) and (**c**), respectively (Zhang et al. 2016b)

Table 11.2 Mean wear rates

	Wear rate (nm/cycle)	
Coatings	0–100 cycles	100–1000 cycles
Cu-MoS_2 (D)	12.8 ± 3.41	0.22 ± 0.47
Cu-MoS_2 (S)	8.61 ± 3.15	0.12 ± 0.55
Cu	2.04 ± 0.31	0.26 ± 0.22

D, high MoS_2 content region; *S*, low MoS_2 content region

MoS_2 content. The high MoS_2 content regions produced high wear rate, while low wear rate was found in the low MoS_2 content zones. This was attributed from MoS_2-induced mechanical property loss. Hardness of composites decreased linearly with MoS_2 content, and the degradation was due to weak bonding strength between Cu and MoS_2. The presence of MoS_2 hindered adiabatic shear, leading to inadequate bonding between Cu particles and therefore decreased hardness with increase in MoS_2 content (Zhang et al. 2016b). This has been observed commonly

in SLMMCs reinforced with MoS_2 and other lamellar solid lubricants such as graphite and WS_2. Even though in some cases a small amount of solid lubricant reinforcement could improve mechanical property by filling out pores of the metal matrix, there are thresholds beyond which mechanical properties, e.g., hardness and fracture toughness, decrease and wear rate increases (Dhanasekaran and Gnanamoorthy 2007; Li and Xiong 2009; Omrani et al. 2016) (Kato et al. 2003). Dhanasekaran et al. showed a 3 wt.% addition of MoS_2 to Fe-C-Cu alloy achieved optimized wear resistance, while 5 wt.% MoS_2 caused high wear due to decreased strength (Dhanasekaran and Gnanamoorthy 2007). Kato et al. found consistently decreased hardness and wear resistance once MoS_2 content was higher than 10 vol.% in copper-tin-based composites (Kato et al. 2003).

Moreover, the limit of the load-bearing capacity of SLMMCs gives rise to a critical running condition above which the form of wear changes in an undesirable way. Zhang et al. (2016b) reported a critical normal load of around 100 N for a cold-sprayed Cu-1.8 wt.% MoS_2 subjected to fretting wear. Severe wear was initiated once increased the normal load up to 150 N due to weak bonding between Cu and MoS_2. In order to improve load-bearing capacity, adding hard phase like ceramics to form hybrid composites is an effective method (Miracle 2005; Suresha and Sridhara 2010; Rajkumar and Aravindan 2011; Xu et al. 2006). Moreover, some online or post-spray techniques can be used to improve mechanical property and therefore wear resistance of SLMMCs. Laser-assistant low-pressure cold spray system had the potential to improve bonding strength between the splats and deposition efficiency. It was used to deposit fully dense Cu-Al_2O_3 and Ni-Al_2O_3 composites (Kulmala and Vuoristo 2008). Post-spray treatments, e.g., extrusion, were capable to improve mechanical property effectively and therefore have a potential to improve wear resistance (Kumar et al. 2016).

Observations on structural, chemical, and mechanical changes of third bodies over sliding permit better understanding on wear processes that determine the ability of a material to resist wear or exhibit high or low friction. A combination of several techniques such as scanning electron microscopy, energy-dispersive X-ray spectroscopy, Raman spectroscopy, and nanoindentation allows an extensive examination on third bodies. Following this method, dry sliding wear behavior of cold-sprayed Cu-MoS_2 composites was studied by Zhang et al. (2016b). Powdery MoS_2 flakes on the wear track and a lack of transfer film at the counterface made it different from that sliding against blanket films of solid lubricants. Therefore, the friction mechanism was fracturing of MoS_2. Some MoS_2 that was deposited onto the counterface during the early stage of sliding (~100 cycles) was trapped back to the contact and served as reservoirs to replenish MoS_2. However, with oxidation of Cu and further material mixing, the local MoS_2 concentration decreased gradually. MoS_2 helped to improve endurance of the first steady-state low friction, which could be due to high lifetime of MoS_2 (Wahl and Singer 1995). Cross-sectional micrographs (Fig. 11.14) showed minor modifications in terms of subsurface microstructure and oxidation occurred in the Cu-MoS_2 coating comparing to the Cu coating after 3000 cycles. That suggests the presence of MoS_2 helped to stabilize tribolayer and prevent subsurface microstructure to be yielded and transferred.

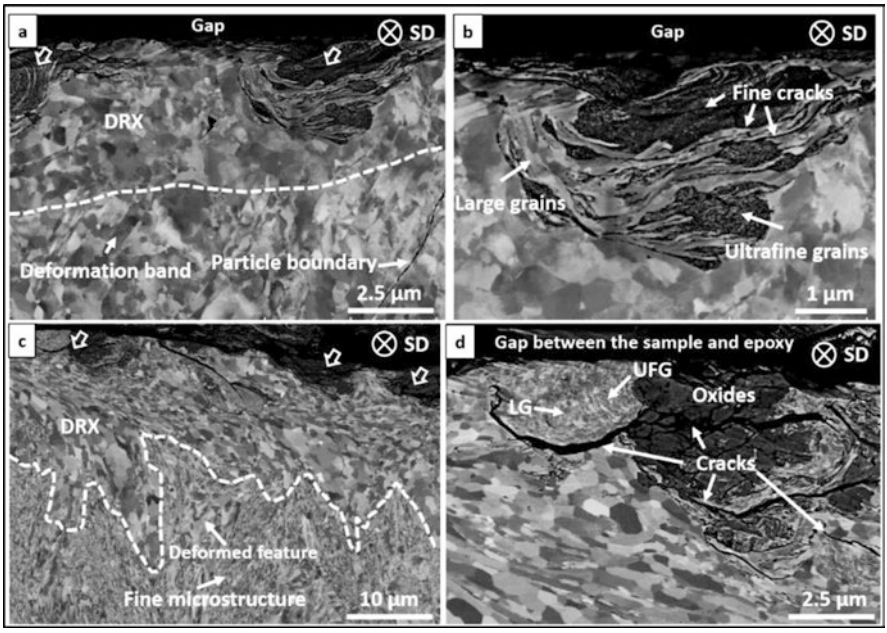

Fig. 11.14 Micrographs of cross sections of the Cu-MoS_2 (**a**, **b**) and Cu (**c**, **d**) wear tracks after a 3000-cycle test. The *hollow arrows* denote MML, and the *dashed lines* the interface of the sliding-induced microstructure and as-sprayed microstructure. (**b**, **d**) are closer views of the sliding-induced microstructure in (**a**) and (**c**), respectively. *SD* indicates sliding direction (Zhang et al. 2016b)

The influence of ceramics on tribological performance of cold-sprayed SLMMCs was also explored by the tribology group at McGill University. A hybrid composite of Cu-2.2wt.% MoS_2-12wt.%WC was cold-sprayed, and its fretting wear performance was tested under a gross slip contact condition. Comparing to their previous study (Zhang et al. 2016b), where a critical normal load of 100 N was observed in Cu-MoS_2, improved wear resistance was observed at an elevated normal load of 150 N for Cu-MoS_2-WC. As was found in Al-Al_2O_3 composites (Shockley et al. 2014), the crashed WC fragments forced plastic deformation to be concentrated and led to a continuous hardened tribolayer. Nanoindentation from the cross section of the wear scars showed the hardness of the tribolayer was as high as 3.8 GPa, while the as-sprayed Cu was around 2.3 GPa. This, coupled with a more stable transfer film, was believed to give rise to less material removal, namely, source flow, and therefore improved wear resistance of Cu-MoS_2-WC.

To summarize, this section presented friction and wear behavior of cold-sprayed SLMMCs. A small amount of MoS_2 reduces friction significantly, yet it causes high wear due to degradation of mechanical property. For fretting, there is a critical running condition for Cu-MoS_2, but adding WC particles improved effectively the wear resistance. On manufacturing side, although challenges exist, cold spray is a promising manufacturing method for SLMMCs.

11.7 Summary and Future Directions

Metal matrix composites have been fabricated by cold spray for over a decade. While most of the applications for these coatings involve tribology, research has often focused more on cold sprayability, microstructure, and basic coating properties, such as hardness and bond strength. This is because dual spraying of a metal and ceramic complicates the cold spray deposition process and makes it more difficult to optimize the structure and properties of the coatings. Even with the significant research already carried out on this topic, there remain challenges for MMCs made by cold spray to be adopted as replacement or repair options for more mature coating processes. Many of these challenges have been alluded to in the previous sections, and they can be categorized into two major themes that are tied closely to one another: optimization of the cold spray process for deposition of MMCs and measurement, analysis, and interpretation of the tribological properties of the MMC coatings.

Deposition of MMCs with cold spray, as reviewed here, is becoming a viable process, with a wide range of coating systems studied. In terms of applications, the most mature MMC is Al-Al_2O_3, which is used for repair of aerospace components. For most of the other applications, including the other two reviewed here (i.e., metal-carbide and metal-solid lubricant), there remains a need for optimization of powder characteristics and cold spray process parameters to obtain a robust coating. For example, with the metal-carbide system, to retain high-volume fractions of carbide, researchers turned to composite powders. This assists in retention of the ceramic but at the expense of overall deposition efficiency. Nevertheless, researchers have demonstrated the possibility of high retention of carbides, which make prospects good for this coating system as an erosion- or abrasion-resistant option. Similarly, the metal-solid lubricant system has required researchers to consider powder modifications prior to spraying, such as cladding and sintered powders. In some instances, this has allowed greater retention of solid lubricant phases, up to 10 vol.%. However, commercially available self-lubricating composites often contain above 20 vol.%. Significant powder engineering may be required to realize similar retention of solid lubricant as SLMMCs made by other processes. Overall, despite research on optimization of the cold spray process for composites, with some trend and general rules for spray optimization identified, significant work remains.

While the processing changes suggested above are intended to improve the coating quality and the retention of the ceramic or solid lubricant, the measures taken may lead to unintended consequences for the tribological properties of the coatings. These changes can be best understood in terms of third body flows (Fig. 11.3). What is desired is a reduction in source flow and a relatively well-controlled or small internal flow. This can be accomplished with MMCs by inclusion of more hard particles, to make the material stronger, or by more solid lubricants to reduce the shearing forces on the third bodies. However, the strategies used thus far for cold spray to retain higher-volume fractions of nonmetallic phases generally lead to a potential

reduction in the cohesion strength of the coating itself. Composite metal-carbide powders do not undergo much adiabatic shear and as such, while they may deposit, are actually not strongly bonded to one another. This would lead to a significant increase in source flow and may also lead to third bodies that are not mechanically robust and a stronger internal flow. Similarly, for solid lubricants, it is known that higher-volume fraction leads to a debit in mechanical properties. This could also lead to an increase in source flow, depending on how effective the lubricating tribofilms are in limiting the friction forces. Online and post-spray treatments may also be needed to improve mechanical property and wear resistance of the material.

For the three systems that were reviewed here, tribofilms were generated that were harder than the parent coating. This is a common phenomenon for metal tribology, where an MML is formed that leads to a reduction in the source flow and better wear resistance. Despite being commonplace, it is still very important to understand the effectiveness of these tribofilms. As was seen in this review, they can result in improved tribological performance even for moderate volume fractions of the ceramic or solid lubricant phases. Thus, it is important that a desire for higher retention of the nonmetallic phases does not override other considerations like cohesion strength. For future tribological applications of cold-sprayed metal matrix composites, ultimately, both process optimization and characterization of the tribological performance will be required.

References

Sova A, Kosarev VF, Papyrin A, Smurov I (2011) Effect of ceramic particle velocity on cold spray deposition of metal-ceramic coatings. J Therm Spray Technol 20:285–291

Aggarwal G (2007) Development of self-lubricating coatings via cold spray process: feedstock formulation and deformation modeling. Dissertation, The Pennsylvania State University

Alidokht S, Manimunda P, Vo P, Yue S, Chromik R (2016) Cold spray deposition of a Ni-WC composite coating and its dry sliding wear behavior. Surf Coat Technol 308:424–434

Alidokht S, Vo P, Yue S, Chromik RR (2017) Erosive wear behavior of cold-sprayed Ni-WC composite coating. Wear 376-377:566–577

Alpas A, Zhang J (1992) Effect of SiC particulate reinforcement on the dry sliding wear of aluminium silicon alloys (A356). Wear 155:83–104

Alpas AT, Zhang J (1994) Effect of microstructure (particulate size and volume fraction) and counterface material on the sliding wear resistance of particulate-reinforced aluminum matrix composites. Metall Mater Trans A 25A:969–983

Ang ASM, Berndt CC, Cheang P (2011) Deposition effects of WC particle size on cold sprayed WC–Co coatings. Surf Coat Technol 205(10):3260–3267

Argibay N, Chandross M, Cheng S, Michael JR (2017) Linking microstructural evolution and macro-scale friction behavior in metals. J Mater Sci 52(5):2780–2799

Assadi H, Gärtner F, Stoltenhoff T, Kreye H (2003) Bonding mechanism in cold gas spraying. Acta Mater 51(15):4379–4394

Bakshi SR, Singh V, Balani K, McCartney DG, Seal S, Agarwal A (2008) Carbon nanotube reinforced aluminum composite coating via cold spraying. Surf Coat Technol 202(21):5162–5169

Berthier Y (2005) Third-body reality – consequences and use of the third-body concept to solve friction and wear problems. In: Stachowiak GW (ed) Wear – materials, mechanisms and practice. Wiley, West Sussex/England, pp 291–316

Biswas SK (2005) Wear of metals: a material approach. In: Stachowiak GW (ed) Wear: materials, mechanisms and practice. Wiley, West Sussex/England, pp 21–36
Botef I, Villafuerte J (2015) Overview. In: Villafuerte J (ed) Modern cold spray: materials, process, and applications. Springer International, Cham, pp 1–29
Champagne VK (2007) The cold spray materials deposition process: Fundamentals and applications. Woodhead Publishing, Cambridge/England
Champagne VK (2008) The repair of magnesium rotorcraft components by cold spray. J Fail Anal Prev 8(2):164–175
Champagne VK, Koh PK, Eden TJ, Wolfe DE, Villafuerte J (2015) Applications. In: Villafuerte J (ed) Modern cold spray. Cham, Springer International
Chung S, Hwang BH (1994) A microstructural study of the wear behaviour of SiC/al composites. Tribol Int 24:307–314
Couto M, Dosta S, Fernández J, Guilemany JM (2014) Comparison of the mechanical and electrochemical properties of WC-25Co coatings obtained by high velocity oxy-fuel and cold gas spraying. J Therm Spray Technol 23(8):1251–1258
Couto M, Dosta S, Guilemany JM (2015) Comparison of the mechanical and electrochemical properties of WC-17 and 12Co coatings onto Al7075-T6 obtained by high velocity oxy-fuel and cold gas spraying. Surf Coat Technol 268:180–189
Couto M, Dosta S, Torrell M, Fernández J, Guilemany JM (2013) Cold spray deposition of WC–17 and 12Co cermets onto aluminum. Surf Coat Technol 235:54–61
Descartes S, Berthier Y (2002) Rheology and flows of solid third bodies: background and application to an $MoS_{1.6}$ coating. Wear 252(7–8):546–556
Deuis RL, Subramanian C, Yellup JM (1997) Dry sliding wear of aluminium composites – a review. Compos Sci Technol 57:415–435
Dhanasekaran S, Gnanamoorthy R (2007) Dry sliding friction and wear characteristics of Fe–C–Cu alloy containing molybdenum di sulphide. Mater Des 28(4):1135–1141
Dosta S, Couto M, Guilemany JM (2013) Cold spray deposition of a WC-25Co cermet onto Al7075-T6 and carbon steel substrates. Acta Mater 61(2):643–652
Du L, Huang C, Zhang W, Li T, Liu W (2011) Preparation and wear performance of NiCr/Cr_3C_2–NiCr/h-BN plasma sprayed composite coating. Surf Coat Technol 205(12):3722–3728
Du L, Zhang W, Liu W, Zhang J (2010) Preparation and characterization of plasma sprayed Ni 3 Al–h-BN composite coating. Surf Coat Technol 205(7):2419–2424
Dvorak S, Wahl K, Singer I (2007) In situ analysis of third body contributions to sliding friction of a Pb–Mo–S coating in dry and humid air. Tribol Lett 28(3):263–274
Eesley GL, Elmoursi A, Patel N (2003) Thermal properties of kinetic spray Al-SiC metal-matrix composite. J Mater Res 18(4):855–860
Erdemir A, Voevodin AA (2010) Chapter 14: Nanocomposite coatings for severe applications* A2. In: Martin PM (ed) Handbook of deposition technologies for films and coatings, 3rd edn. William Andrew Publishing, Boston, pp 679–715
Gao P-H, Li C-J, Yang G-J, Li Y-G, Li C-X (2010) Influence of substrate hardness transition on built-up of nanostructured WC–12Co by cold spraying. Appl Surf Sci 256(7):2263–2268
Gao P-H, Li Y-G, Li C-J, Yang G-J, Li C-X (2008) Influence of powder porous structure on the deposition behavior of cold-sprayed WC-12Co coatings. J Therm Spray Technol 17(5–6):742–749
Godet M (1984) The third-body approach: a mechanical view of wear. Wear 100:437–452
Godet M (1990) Third-bodies in tribology. Wear 136(1):29–45
Holmberg K, Matthews A (2009) Coatings tribology: properties, mechanisms, techniques and applications in surface engineering. Elsevier, Amsterdam
Hosking FM, Portillo FF, Wunderlin R, Mehrabian R (1982) Composites of aluminium alloys: fabrication and wear behaviour. J Mater Sci 17:477–498
Irissou E, Legoux J-G, Arsenault B, Moreau C (2007) Investigation of Al-Al_2O_3 cold spray coating formation and properties. J Therm Spray Technol 16(5–6):661–668
Jeandin M, Koivuluoto H, Vezzù S (2015) Coating properties. In: Villafuerte J (ed) Modern cold spray. Cham, Springer International

Ji G-C, Wang H-T, Chen X, Bai X-B, Dong Z-X, Yang F-G (2013) Characterization of cold-sprayed multimodal WC-12Co coating. Surf Coat Technol 235:536–543

Kato H, Takama M, Iwai Y, Washida K, Sasaki Y (2003) Wear and mechanical properties of sintered copper–tin composites containing graphite or molybdenum disulfide. Wear 255(1):573–578

Kim H-J, Lee C-H, Hwang S-Y (2005) Fabrication of WC–Co coatings by cold spray deposition. Surf Coat Technol 191(2–3):335–340

King PC, Zahiri SH, Jahedi MZ (2007) Rare earth/metal composite formation by cold spray. J Therm Spray Technol 17(2):221–227

Koivuluoto H, Bolelli G, Milanti A, Lusvarghi L, Vuoristo P (2015) Microstructural analysis of high-pressure cold-sprayed Ni, NiCu and NiCu + Al_2O_3 coatings. Surf Coat Technol 268:224–229

Koivuluoto H, Vuoristo P (2009) Effect of ceramic particles on properties of cold-sprayed Ni-20Cr+Al_2O_3 coatings. J Therm Spray Technol 18(4):555–562

Kovalchenko A, Fushchich O, Danyluk S (2012) The tribological properties and mechanism of wear of Cu-based sintered powder materials containing molybdenum disulfide and molybdenum diselenite under unlubricated sliding against copper. Wear 290:106–123

Kulmala M, Vuoristo P (2008) Influence of process conditions in laser-assisted low-pressure cold spraying. Surf Coat Technol 202(18):4503–4508

Kumar P, Manisekar K, Vettivel S (2016) Effect of extrusion on the microstructure and tribological behavior of copper-tin composites containing MoS_2. Tribol Trans 59:1016–1030

Lansdown AR (1999) Chapter 12: Composites. In: Lansdown AR (ed) Tribology series, vol 35. Elsevier, Amsterdam, pp 207–244

Lee HY, Yu YH, Lee YC, Hong YP, Ko KH (2004) Cold spray of SiC and Al2O3 with soft metal incorporation: a technical contribution. J Therm Spray Technol 13(2):184–189

Li C-J, Yang G-J, Gao P-H, Ma J, Wang Y-Y, Li C-X (2007) Characterization of nanostructured WC-co deposited by cold spraying. J Therm Spray Technol 16(5–6):1011–1020

Li J, Xiong D (2009) Tribological behavior of graphite-containing nickel-based composite as function of temperature, load and counterface. Wear 266(1):360–367

Li JL, Xiong DS (2008) Tribological properties of nickel-based self-lubricating composite at elevated temperature and counterface material selection. Wear 265(3):533–539

Lima R, Karthikeyan J, Kay C, Lindemann J, Berndt C (2002) Microstructural characteristics of cold-sprayed nanostructured WC–Co coatings. Thin Solid Films 416(1):129–135

Lince JR (2004) Tribology of co-sputtered nanocomposite Au/MoS_2 solid lubricant films over a wide contact stress range. Tribol Lett 17(3):419–428

Lioma D, Sacks N, Botef I (2015) Cold gas dynamic spraying of WC–Ni cemented carbide coatings. Int J Refract Met Hard Mater 49:365–373

Martin J, Donnet C, Le Mogne T, Epicier T (1993) Superlubricity of molybdenum disulphide. Phys Rev B 48(14):10583

Melendez NM, Narulkar VV, Fisher GA, McDonald AG (2013) Effect of reinforcing particles on the wear rate of low-pressure cold-sprayed WC-based MMC coatings. Wear 306(1–2):185–195

Miracle DB (2005) Metal matrix composites – From science to technological significance. Compos Sci Technol 65(15–16):2526–2540

Moridi A, Hassani-Gangaraj S, Guagliano M, Dao M (2014) Cold spray coating: review of material systems and future perspectives. Surf Eng 30(6):369–395

Neshastehriz M (2014) Influence of pre-process work hardening of nickel encapsulated hexagonal boron nitride powders on cold spray coatings. Dissertation, The Pennsylvania State University

Neshastehriz M, Smid I, Segall A (2014) In-situ agglomeration and de-agglomeration by milling of nano-engineered lubricant particulate composites for cold spray deposition. J Therm Spray Technol 23(7):1191–1198

Omrani E, Moghadam AD, Menezes PL, Rohatgi PK (2016) Influences of graphite reinforcement on the tribological properties of self-lubricating aluminum matrix composites for green tribology, sustainability, and energy efficiency—a review. Int J Adv Manuf Technol 83(1–4):325–346

Papyrin A, Kosarev V, Klinkov S, Alkhimov A, Fomin VM (2006) Cold spray technology. Elsevier, Amsterdam

Parco M, Zhao L, Zwick J, Bobzin K, Lugscheider E (2006) Investigation of HVOF spraying on magnesium alloys. Surf Coat Technol 201:3269–3274
Pardo A, Merino MC, Mohedano M, Casajus P, Coy AE, Arrabal R (2009) Corrosion behaviour of Mg/Al alloys with composite coatings. Surf Coat Technol 203:1252–1263
Pierson HO (1996) Handbook of refractory carbides and nitrides : properties, characteristics, processing, and applications. Noyes Publications, Park Ridge
Raadnui S, Mahathanabodee S, Tongsri R (2008) Tribological behaviour of sintered 316L stainless steel impregnated with MoS_2 plain bearing. Wear 265(3):546–553
Rajkumar K, Aravindan S (2011) Tribological performance of microwave sintered copper–TiC–graphite hybrid composites. Tribol Int 44(4):347–358
Rohatgi PK, Ray S, Liu Y (1992) Tribological properties of metal matrix-graphite particle composites. Int Mater Rev 37:129–152
Roy M, Venkataraman B, Bhanuprasad VV, Mahajan YR, Sundararajan G (1992) The effect of particulate reinforcement on the sliding wear behavior of aluminum matrix composites. Metall Trans A 23A:2833–2847
Sansoucy E, Marcoux P, Ajdelsztajn L, Jodoin B (2008) Properties of SiC-reinforced aluminum alloy coatings produced by the cold gas dynamic spraying process. Surf Coat Technol 202(16):3988–3996
Sato A, Mehrabian R (1976) Aluminum matrix composites: fabrication and properties. Metall Trans B 7B:443–451
Scharf TW, Prasad SV (2012) Solid lubricants: a review. J Mater Sci 48(2):511–531
Schmidt T, Gärtner F, Assadi H, Kreye H (2006) Development of a generalized parameter window for cold spray deposition. Acta Mater 54(3):729–742
Shockley JM, Chromik RR, Descartes S (2016) TEM microanalysis of interfacial structures after dry sliding of cold sprayed Al-Al_2O_3. Wear 376-377:1411–1417
Shockley JM, Descartes S, Irissou E, Legoux JG, Chromik RR (2014) Third body behavior during dry sliding of cold-sprayed al-Al_2O_3 composites: in situ tribometry and microanalysis. Tribol Lett 54(2):191–206
Shockley JM, Descartes S, Vo P, Irissou E, Chromik RR (2015) The influence of Al_2O_3 particle morphology on the coating formation and dry sliding wear behavior of cold sprayed Al–Al_2O_3 composites. Surf Coat Technol 270:324–333
Shockley JM, Desrayaud C, Chromik RR, Descartes S (2017) Significance of Al_2O_3 particle morphology in the microstructure evolution of cold-sprayed Al-Al_2O_3 during unconstrained high-pressure torsion. Mater Sci Eng A 684:510–516
Shockley JM, Strauss HW, Chromik RR, Brodusch N, Gauvin R, Irissou E, Legoux JG (2013) In situ tribometry of cold-sprayed Al-Al_2O_3 composite coatings. Surf Coat Technol 215:350–356
Shukla V, Elliott GS, Kear BH (2000) Nanopowder deposition by supersonic rectangular jet impingement. J Therm Spray Technol 9(3):394–398
Singer IL (1992) Solid lubrication processes. In: Singer IL, Pollock H (eds) Fundamentals of friction. Kluwer Academic, Dordrecht, pp 237–261
Singer IL, Dvorak SD, Wahl KJ, Scharf TW (2003) Role of third bodies in friction and wear of protective coatings. J Vac Sci Technol A 21(5):S232–S240
Smid I, Segall A, Walia P, Aggarwal G, Eden T, Potter J (2012) Cold-sprayed Ni-h-BN self-lubricating coatings. Tribol Trans 55(5):599–605
Sova A, Kosarev VF, Papyrin A, Smurov I (2010) Effect of ceramic particle velocity on cold spray deposition of metal-ceramic coatings. J Therm Spray Technol 20(1–2):285–291
Sova A, Papyrin A, Smurov I (2009) Influence of ceramic powder size on process of cermet coating formation by cold spray. J Therm Spray Technol 18(4):633–641
Spencer K, Fabijanic DM, Zhang M-X (2009) The use of Al-Al_2O_3 cold spray coatings to improve the surface properties of magnesium alloys. Surf Coat Technol 204(3):336–344
Stark L, Smid I, Segall A, Eden T, Potter J (2012) Self-lubricating cold-sprayed coatings utilizing microscale nickel-encapsulated hexagonal boron nitride. Tribol Trans 55(5):624–630
Stewart D, Shipway P, McCartney D (1999) Abrasive wear behaviour of conventional and nanocomposite HVOF-sprayed WC–Co coatings. Wear 225:789–798

Stoyanov P, Strauss HW, Chromik RR (2012) Scaling effects between micro-and macro-tribology for a Ti–MoS 2 coating. Wear 274:149–161

Suresha S, Sridhara BK (2010) Wear characteristics of hybrid aluminium matrix composites reinforced with graphite and silicon carbide particulates. Compos Sci Technol 70(11):1652–1659

Venkataraman B, Sundararajan G (1996) The sliding wear behaviour of Al-SiC particulate composites – I. Macrobehaviour. Acta Mater 44(2):451–460

Wahl KJ, Singer IL (1995) Quantification of a lubricant transfer process that enhances the sliding life of a MoS2 coating. Tribol Lett 1(1):59–66

Wang H, Chen X, Bai X, Ji G, Dong Z, Yi D (2014) Microstructure and properties of cold sprayed multimodal WC–17Co deposits. Int J Refract Met Hard Mater 45:196–203

Weyant J (2008) Nano-engineered encapsulated-particles for the creation of self lubricating coatings and alloys. Dissertation, The Pennsylvania State University

Xu J, Liu W, Zhong M (2006) Microstructure and dry sliding wear behavior of MoS2/TiC/Ni composite coatings prepared by laser cladding. Surf Coat Technol 200(14–15):4227–4232

Yandouzi M, Sansoucy E, Ajdelsztajn L, Jodoin B (2007) WC-based cermet coatings produced by cold gas dynamic and pulsed gas dynamic spraying processes. Surf Coat Technol 202(2):382–390

Yu M, Li WY, Suo XK, Liao HL (2013) Effects of gas temperature and ceramic particle content on microstructure and microhardness of cold sprayed SiC/Al 5056 composite coatings. Surf Coat Technol 220:102–106

Zhang S, Zhou J, Guo B, Zhou H, Pu Y, Chen J (2008) Friction and wear behavior of laser cladding Ni/h-BN self-lubricating composite coating. Mater Sci Eng A 491(1):47–54

Zhang Y, Descartes S, Vo P, Chromik RR (2016a) Cold-sprayed Cu-MoS_2 and its fretting wear behavior. J Therm Spray Technol 25(3):473–482

Zhang Y, Shockley JM, Vo P, Chromik RR (2016b) Tribological behavior of a cold-sprayed cu–MoS_2 composite coating during dry sliding wear. Tribol Lett 62(1):1–12

Part V
Corrosion Resistant Coatings

Chapter 12
Fundamentals of Corrosion Mechanisms in Cold Spray Coatings

Niraj Bala and Harpreet Singh

12.1 Introduction

Cold spraying is one of the latest and upcoming thermal spray techniques. The conventional thermal spraying processes being used like arc spraying, flame spraying, and plasma spraying utilize the principle of melting the powder to be sprayed. High velocity oxygen fuel (HVOF) spraying uses only partial melting to achieve a coating with high quality. This is due to the fact that the particle velocities upon impact on the substrate are comparatively higher in HVOF spraying. Similar to HVOF spraying, this new process, cold spraying, also known as cold gas dynamic spraying (CGDS), also uses higher particle velocities combined with reduced and controlled heat input of the spray material. In this the gas temperature is lesser than the melting temperature of the material, which leads to a negligible melting of particles in the jet (Stoltenhoff et al. 2001).

The discovery of cold spray process dates back to the mid-1980s. It was developed at the Institute of Theoretical and Applied Mechanics of the Russian Academy of Science in Novosibirsk by A. Papyrin and colleagues (Alkimov et al. a, b, 1987, 1990). They succeeded in the deposition of a variety of pure metals, metallic alloys, and composites onto a wide range of substrate materials and also established the feasibility of the use of cold spray for various applications. A US patent on the cold spray technology was allotted in 1994 (Alkimov et al. 1997) and a European one in 1995 (Alkimov et al. 1995).

N. Bala (✉)
Baba Banda Singh Bahadur Engineering College, Fatehgarh Sahib, Punjab, India
e-mail: nirajbala@gmail.com

H. Singh
Indian Institute of Technology Ropar, Rupnagar, India
e-mail: harpreetsingh@iitrpr.ac.in

P. Cavaliere (ed.), *Cold-Spray Coatings*,
https://doi.org/10.1007/978-3-319-67183-3_12

12.1.1 Cold Spray: The Process

A cold spray system comprises a compressor or a high-pressure gas delivery system, a gas heater, a powder hopper, a control console, and cold spray gun. The purpose of gas delivery system is to supply nitrogen and/or helium up to 60 SCFM with the pressure range of 200–500 psi. The gas is heated in an electric gas heater up to a maximum temperature of 1200 ° F (648.9 °C). The coating material in the form of a powder is delivered by the powder hopper and transported by a carrier gas to the gun. All the controls used to meter the gas flow rates, pressures, powder feed rate, etc. are housed in the control console. Cold spray gun constitutes the heart of the system. It is a precision engineered device, which converts the mechanical energy of the gas jet into kinetic energy of the jet and transfers a part of the kinetic energy from the jet to the powder particles. The gun mainly consists of a gun body and an easily removable/mountable nozzle assembly. The gun body contains one or more chambers and houses all the inlet ports for the gas and powder supplies. The gas and powder jets mix in the gun body, and this two-phase flow goes through the converging/diverging expansion to result in a high velocity powder jet. The gun body also houses the sensors for recording the gas temperature and pressure (Li et al. 2007). A typical cold spray process is shown in Fig. 12.1 (Raletz et al. 2006).

12.1.2 Mechanism of Formation of Coating

The actual mechanisms of deposition of coatings in cold spray process have not been well defined, how the solid-state particles deform, and the bond has not been well characterized. It seems believable, though it has not yet been demonstrated, that plastic deformation may disrupt thin surface films, for example, oxides, and provide an intimate conformal contact as a result of high local pressure, leading to

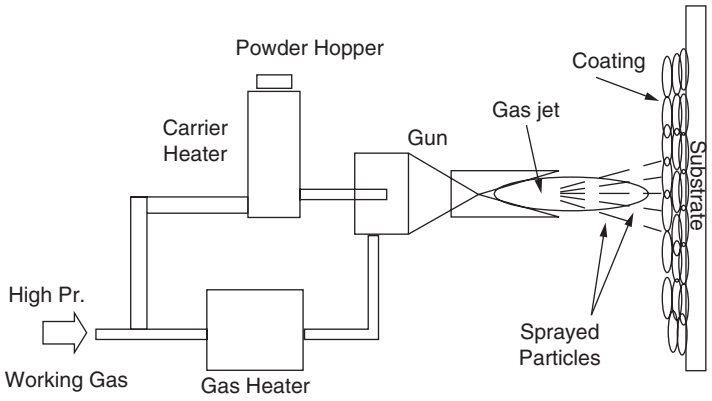

Fig. 12.1 A schematic of cold spray coating process (Raletz et al. 2006)

the formation of a bond. Though it has not been proved, this hypothesis is consistent with the fact that a variety of ductile materials have been deposited by cold-spray method (Dykhuizen and Smith 1998; Shukla et al. 1999). This theory also verifies the fact that a critical velocity (V_c) is needed to achieve deposition, because sufficient kinetic energy is required to plastically deform the solid material. For each coating and substrate combination, there is a V_c. Above this V_c, particles have enough kinetic energy to be incorporated into a coating. Below the V_c, the particles will be either bounced off from the surface or may lead to the erosion of the substrate or any coating buildup which has begun. For particle velocities V greater than V_c, the coating process takes place and the deposition efficiency also increases with increasing V (Mccune et al. 1995; Dykhuizen and Smith 1998; Shukla et al. 1999). With the increase of the particle velocity to the critical value, the process of adhesion of the particle to the surface begins, and the probability of particle attachment increases with an increase in particle velocity. The results of the experiments performed showed that the critical value of particle velocity depends on many factors, which include type of particle and substrate materials, temperature and size of the particle, substrate surface state, etc. The different stages of coating formation were described by Steenkiste et al. (2002); this gives a better understanding of the kinetics of cold spraying (Fig. 12.2).

12.1.3 Characteristics of Cold Spray Process

One of the characteristics of the cold spray process is that the temperature of the gas stream is always lower than the melting point of the particulate material, which provides coatings developed primarily from particles in the solid state with very little oxidation (Mccune et al. 1995; Alkimov et al. 1994; Dykhuizen and Smith 1998). Since cold spray is known to be 100% solid-state process, the coatings are deposited with negligible oxidation which represents an important technical achievement.

McCune et al. (2000) discovered that an exceptional aspect of cold gas dynamic spraying is its capability to produce a vast range of deposited layer thicknesses which may range from few microns up to as much as a centimeter. In this regard the process extends beyond the concept of coating of a substrate and possesses the capability to develop three-dimensional structures.

According to Lima et al. (2002), no phase transformation takes place during the cold spray process since it is a 100% solid-state process; this implies no particle melting. Hence, in general, oxidation, decarburizing, nitriding, and any type of decomposition are avoided in this process. The phase composition obtained for the as-sprayed coating should be the same as the powder phase composition.

As discussed before cold spray is a solid-state process; therefore it produces coatings which possess many advantageous characteristics. Absence of high temperature makes it suitable for spray depositing temperature-sensitive materials including nanophase, amorphous materials; oxygen-sensitive materials like

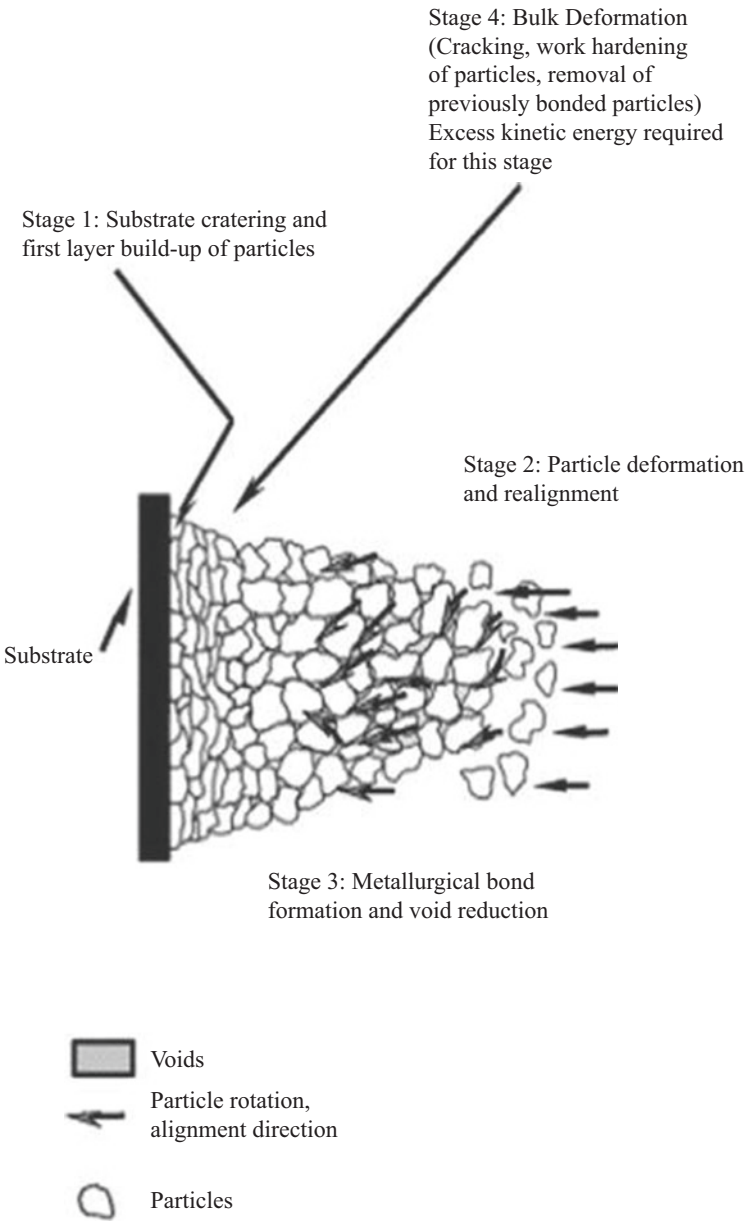

Fig. 12.2 Stages of coating formation in the cold spray process (Steenkiste et al. 2002)

aluminum, copper, and titanium; and phase-sensitive materials such as carbide composites. In cold spray process, the size of the nozzle (10–15 mm^2) and the spray distance (5–25 mm) spray beam is very small, typically, 5 mm diameter, which translates into precise control over the area of deposition over the substrate surface.

The working of the cold spray process can be compared to a microshot peening devise, which produces coatings with compressive stresses. Hence, ultrathick (5–50 mm) coatings can be produced without any adhesion failure. The characteristic high-energy low-temperature formation of coating leads to formation of a wrought-like microstructure with near theoretical density values. The particles can be collected and reused in this technique. Further the absence of high temperature jets increases operational safety. The high feed rate leads to high productivity and high deposition rates and efficiencies. Eliminating the harmful effects of high temperature on coatings and substrates in case of cold spray process offered significant advantages and new possibilities (Papyrin et al. 2007). These include avoiding oxidation and undesirable phases, retainment of properties of the stock powder, and minimum of residual stresses. Another feature includes the good conduction of heat and electricity through the coatings. The coatings obtained possess higher density, better hardness, and cold-worked microstructure; all these advantages allow the spraying of thermally sensitive materials and powders with a particle size <5–10 μm. Cold spray can be worked with vastly dissimilar materials. For the start of the process, the preparation of the substrate is very less and it involves short standoff distance. In the process the heating of the substrate is very minute. Since the powder feed rate is high, the productivity is also high. It further enables deposition of many types of materials at high deposition rates and efficiencies. Unlike other thermal spray processes, the absence of high-temperature gas jets, radiation, and explosive gases increases operational safety. Cold spray process enables the collection and reuse of particles which avoid wastage and near 100% utilization of powder with recycling. When compared with other powder spraying methods like detonation, plasma, etc., it is quite similar, but at the same time, there are certain features, for example, the particles are in solid state before their deposition on the substrate. The cold spray method can be used for deposition of coating at room temperature. These features enable one to track the effect of particle velocity (in pure form) on the deposition process and to eliminate temperature from consideration, which is not possible in other gas-thermal methods. The coatings which are produced by the traditional thermal spray methods like high velocity oxygen fuel (HVOF) spraying and atmospheric plasma spray (APS) contain porosity and oxides, which lowers the corrosion resistance of the as-sprayed coatings. This new emerging cold spraying technique provides a perspective to produce these coatings (Li et al. 2007).

12.1.4 Applications of Cold Spray Process

The advantages mentioned above enable cold spray a promising technique for producing and repairing various industrial parts (Papyrin et al. 2007). These include the blades of turbine, pistons, cylinders, various pump elements, valves, rings, and bearing components, sleeves, shafts, and seals for many industries. Further the coatings may add to the increase in strength, hardness, wear, and corrosion resistance, both electromagnetic and thermal conduction, and other properties. The process is

also suitable for production of compact powder materials and for direct fabrication of parts (Papyrin et al. 2007).

According to Karthikeyan (2004), cold spray process is suitable for corrosion protection applications where the absence of process-induced oxidation may offer superior performance. Further this process is suitable for applications requiring good thermal conductivity for example in electrical and thermal field.

12.2 Studies of Cold Spray Coatings for Corrosion Protection

A composite coating consisting of $TiAl_3$ in the matrix of residual aluminum ($TiAl_3$-Al) was deposited by cold spray technique on high-temperature titanium Al-based alloy. The coating consisted of an interlayer of (Ti, Nb) Al_3 of about 10 μm which was formed in between the coating and the substrate during heat treatment. The porosity for the coating was found to be 14.69%. Oxidation tests were carried out under quasi-isothermal conditions at 950 °C for 150 cycles in static air. The results of the weight change indicated that the coating was successful to significantly improve the high temperature oxidation resistance of the substrate alloy (Kong et al. 2010).

Bala et al. (2009a, b, 2010, 2011) and Bala (2011) investigated the hot corrosion behavior of cold-sprayed Ni20Cr and Ni50Cr coatings deposited on boiler steels, namely, SA 213-T22 and SA 516 (grade 70). The hot corrosion performance of the coatings and uncoated boiler steels was evaluated in the simulated boiler environment of Na_2SO_4-$60V_2O_5$ and air oxidation under cyclic conditions at temperature of 900 °C. The rate of the corrosion was calculated by measuring the weight change after each cycle for a total period of 50 cycles. Each cycle constituted of 1 h heating in a tube furnace followed by 20 min cooling in ambient air. The XRD and SEM/EDS techniques were used for the analysis of the corrosion products. It was observed that the uncoated boiler steels suffered intensive spallation in the form of removal of their oxide scales. The phases revealed in the oxide scales of the coated specimens were mainly oxides of chromium and nickel and their spinels, which are reported to be protective against the hot corrosion. A diagram representing the hot corrosion mode for the cold-sprayed Ni50Cr coating on SA 516 boiler steel exposed to Na_2SO_4-$60V_2O_5$ at 900 °C for 50 cycles has been represented in Fig. 12.3 (Bala 2011).

Similar cyclic studies were also performed in actual boiler environment where promising results were obtained for the cold-sprayed coatings. Similar type of cyclic high temperature studies was also performed by some other authors, and positive results were obtained (Rahman et al. 2012; Kaushal et al. 2013; Mahesh et al. 2011; Kaur et al. 2010). A comparison of cyclic hot corrosion behavior of Ni20Cr coating in molten salt environment at 900 °C for 50 cycles by various thermal spray processes has been depicted in Table 12.1.

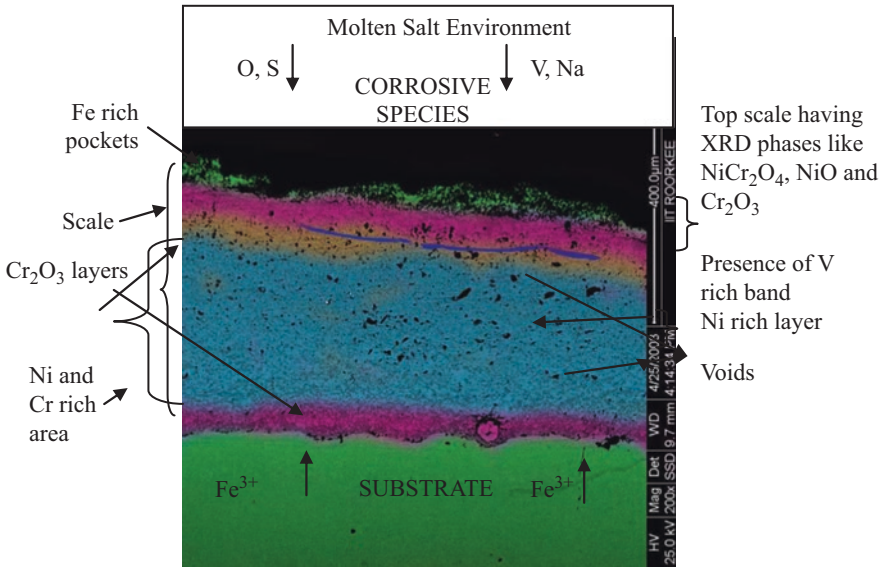

Fig. 12.3 Schematic diagram showing probable hot corrosion mode for the cold-sprayed Ni-50Cr coating on SA 516 boiler steel subjected to Na_2SO_4-60%V_2O_5 at 900 °C for 50 cycles (Bala 2011)

In the study done by Singh et al. (2015), three types of powders Ni20Cr, Ni20Cr blended with TiC, and Ni20Cr blended with TiC and Re powder were cold sprayed on a boiler steel (SAE 213-T22). The specimens were subjected to a molten salt environment of Na_2SO_4-60wt.%V_2O_5 at 900 °C under cyclic conditions. The rate of the corrosion was calculated by measuring the weight change after each cycle for a total period of 50 cycles. Each cycle constituted of 1 h heating in a tube furnace followed by 20 min cooling in ambient air. The XRD and SEM/EDS techniques were used for the analysis of the corrosion products. It was observed that all the cold spray coatings performed much better than the uncoated steel. The improved hot corrosion resistance of the coatings was attributed to the formation of oxides and spinels of nickel and chromium. Among all the coatings, the cold-sprayed Ni20CrTiCRe coating showed a maximum resistance to the hot corrosion, hence establishing the effectiveness of combined blending of TiC and Re in the Ni20Cr coating. Diagram representing the hot corrosion mode for the cold-sprayed Ni20CrTiCRe coating on T22 boiler steel after exposure to simulated boiler environment at 900 °C for 50 cycles has been shown in Fig. 12.4. The same coatings when deposited on SA 516 steel were then exposed to the actual environment of the boiler by the authors (Bala et al. 2017). The trend shown by erosion-corrosion resistance in the boiler environment was similar to that observed for hot corrosion studies.

Cold spray coating technique was used to deposit composite coatings of pure aluminum blended with 25 wt.% and 50 wt.% α-Al_2O_3 on AZ91D magnesium alloy substrates in the work done by Tao et al. (2009). The potentiodynamic polarization

Table 12.1 A comparison of cyclic hot corrosion behavior of Ni-20Cr coating in molten salt environment at 900 ° C for 50 cycles by various thermal spray processes

Authors	Coating technique	Substrate	Wt change (mg/cm^2)	$K_p \times 10^{-8}$ g^2 cm^{-4} s^{-1}	XRD phases	Remarks
Bala et al. (2010), Bala (2011)	Cold spray technique	SA 516 boiler steel	31.41	0.52	NiO, Cr_2O_3	Some oozing out of substrate material, no visible crack formation or spallation of the oxide scale
		T22 boiler steel	51.95	1.4	NiO	Some oozing out of material on one edge was observed at the end of 6th cycle. At the end of 24th cycle, a little flux in form of 2–3 particles seen
Bala (2011)	HVOF spray technique	SA 516 boiler steel	12.12	0.08	NiO, $Ni(VO_3)_2$	Some protruding lines were observed on one of the edges of the specimen at the end of 26th cycle
		T22 boiler steel	96.97	1.879	NiO, Fe_2O_3, $NiCr_2O_4$	Small amount of scale spallation observed at the end of 22nd cycle, along with oozing out of material
Kaushal (2011)	HVOF spray technique	347 boiler steel	0.358	–	NiO, Cr_2O_3, $NiCr_2O_4$, Fe_2O_3	After the completion of 12th cycle, small amount of flux was seen in the boat
Sidhu et al. (2006a)	HVOF spray technique	ASTM SA210 GradeA1	10.56	6.36	NiO, $NiCr_2O_4$,Cr_2O_3, Fe_2O_3	Blackish-gray scale indicated minor spalling toward the end in form of powder, integrity between coating and base alloy preserved after corrosion run
		ASTM SA213 T11	13.96	10.17	Cr_2O_3, NiO, $NiCr_2O_4$,Fe_2O_3	Blackish-gray scale indicated minor spalling in form of powder, integrity between coating and base alloy preserved after corrosion run

Sidhu et al. (2006b, c)	HVOF spray technique	Superni 75	7.121	2.21	Cr_2O_3, NiO, $NiCr_2O_4$, Fe_2O_3, TiO_2	The dark gray color surface scale found to be smooth and intact. Contact between the coating and the base alloy found to be excellent during and after the cyclic hot corrosion runs
		Superni 600	7.16	3.05	NiO, $NiCr_2O_4$, Fe_2O_3, Cr_2O_3, $Ni(VO_3)_2$	A very shiny silver gray scale formed after 15th cycle. The surface scale smooth and intact with maintained continuity and adherence with the base alloy during cyclic exposure
		Superni 601	6.97	3.089	NiO, $NiCr_2O_4$, Fe_2O_3, Al_2O_3, $Ni(VO_3)_2$, Cr_2O_3	Shining silver gray color continuous and adherent oxide scale formed. Contact between coating and base alloy found to be excellent during and after the cyclic exposures
		Superni 718	4.72	1.44	Cr_2O_3, $NiCr_2O_4$	A smooth and very shining silver gray scale formed during cyclic exposures found to be adherent and intact. No indication of any adherence loss between the coating and the substrate alloy observed
		Superfer 800H	4.33	1.180	NiO, Cr_2O_3, $NiCr_2O_4$	A uniform continuous oxide scale formed. Excellent coating-substrate contact with during and after exposures
Singh et al. (2005a, b), Singh (2005)	Plasma spray technique	Superni 75	7.121	22.95; 9.36 and 4.49	NiO, Cr_2O_3, $NiCr_2O_4$	Smooth and intact greenish scale without spalling, sound contact between coating and base alloy maintained after exposure
		Superni 600	7.16	5.05	NiO, Cr_2O_3, $NiCr_2O_4$	Smooth, intact greenish scale without spalling, sound contact between coating and base alloy
		Superni 601	6.97	4.72	NiO, Cr_2O_3, $NiCr_2O_4$	Smooth and intact greenish scale without spalling, sound contact between coating and base alloy

(continued)

Table 2.1 (continued)

Authors	Coating technique	Substrate	Wt change (mg/cm^2)	$K_p \times 10^{-8}\ g^2\ cm^{-4}\ s^{-1}$	XRD phases	Remarks
		Superni 718	4.72	8.32	NiO, Cr_2O_3, $NiCr_2O_4$	Smooth and intact greenish scale without spalling, sound contact between coating and base alloy
		Superfer 800H	4.33	5.04	NiO, Cr_2O_3, $NiCr_2O_4$	Smooth and intact greenish scale without spalling, sound contact between coating and base alloy
Sidhu (2003), Sidhu and Prakash (2006)	Plasma spray technique	Grade A1 boiler steel	25.771	0.340	NiO, Cr_2O_3, Al_2O_3, Fe_2O_3, $NiCr_2O_4$	Very less cracks appeared during 40th cycle. Oxide protrusion appeared from beneath
		T22 boiler steel	76.746	Behavior not parabolic	NiO, Cr_2O_3, Al_2O_3, Fe_2O_3, $NiCr_2O_4$	Cracks appeared during 15th cycle and some spalling was observed during last 10 cycles. Oxide protrusion appeared from beneath
		T11 boiler steel	21.653	0.227	NiO, Cr_2O_3, Al_2O_3, Fe_2O_3, $NiCr_2O_4$	Cracks appeared during 30th cycle. Oxide protrusion appeared from beneath
Kaushal et al. (2011a)	Detonation spray gun	T22	6.276	0.019	NiO, Cr_2O_3, Fe_2O_3, $NiCr_2O_4$, FeV_2O_4	A small flake seemed to get detached by the end of cyclic studies and some flux in powder form observed in the boat
Kaushal et al. (2011b)	Detonation spray gun	347 boiler steel	2.914	–	NiO, $NiCr_2O_4$, FeV_2O_4, Cr_2O_3, Fe_2O_3	Oxide scale adherent at all other surfaces with no tendency for spallation

Bala et al. (2014)

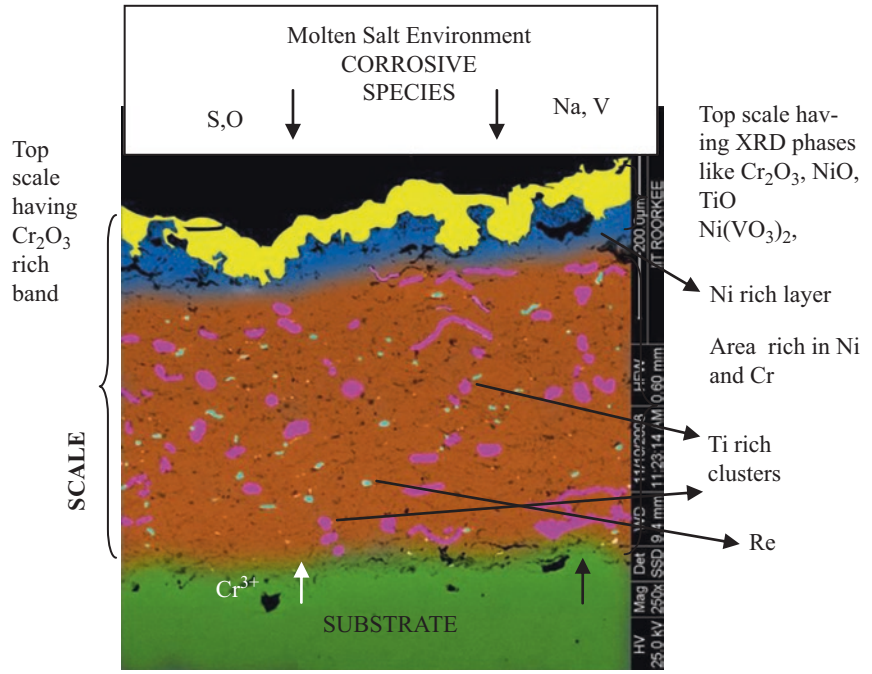

Fig. 12.4 Schematic diagram showing probable hot corrosion mode for the cold-sprayed Ni20CrTiCRe coating on T22 boiler steel subjected to Na_2SO_4-60%V_2O_5 at 900 °C for 50 cycles (Singh et al. 2015)

technique was used to evaluate the corrosion behavior of the coatings in neutral 3.5 wt.% NaCl solution. It was concluded that the corrosion current densities of the composite coatings were comparable to the pure Al coating and three orders lower than that of the bare AZ91D alloy substrate. Therefore, the addition of α-Al_2O_3 has relatively no passive effect on anti-corrosion ability of the composite coatings in comparison to that of the pure Al coating.

In another investigation done by Wang et al. (2010), pure Al and composite coatings of 6061 aluminum alloy with Al_2O_3 particle as reinforcement were produced on AZ91E substrates using cold spray process. Corrosion resistance of the coatings was evaluated in a neutral 5%NaCl solution visually by using salt spray testing and electrochemically using linear potentiodynamic polarization. ASTM B117 standard was used for the salt spray tests. The corrosion resistance of the Al-Al_2O_3 composite coatings was found to be similar to that of pure Al alloys, and much better than the AZ91E Mg substrate.

In the work done by Kumar et al. (2015), erosion-corrosion (E-C) behavior of cold spray nanostructured Ni20Cr coatings on two boiler steels SAE 213-T22 and SA 516 Grade 70 was evaluated under actual boiler environment. A nanostructured Ni20Cr powder was synthesized using a ball milling technique. The coated and uncoated steels were exposed to the super heating zone of actual power plant boiler at 750 ° C under cyclic conditions for 15 cycles. Each cycle consisted of 100 h of

heating followed by 1 h of cooling. The weight change and thickness loss data of the specimens were used to study the kinetics of E-C. For the characterization of the eroded-corroded samples, XRD, SEM/EDS, and X-ray mappings analyses were used. The nanostructured coating on the T22 and SA 516 steels was found to possess higher hardness (2.5 times) in comparison with their conventional counterparts. The coating was found to be successful in reducing the E-C rate of T22 and SA 516 steels by 100% in terms of thickness loss. The higher hardness was found to be useful in enhancing the erosion resistance of the coatings. Further, the nanostructured Ni20Cr coating was found to provide more E-C resistance to the steels in comparison to its conventional micron-size counterpart. The higher erosion-corrosion resistance shown by the investigated coating in the current conditions was attributed to the presence of protective oxides of NiO and Cr_2O_3 as well as its superior as-sprayed microhardness.

Al-Al_2O_3 coatings were produced on the carbon steel pipe surface by cold spray (CS) technology in the work done by Bai et al. (2017). The corrosion resistance of cold spray Al-Al_2O_3 composite coatings was studied under thermal insulation. Experimental apparatus was built to test the corrosion resistance of coatings beneath mineral wool insulation under isothermal, thermal cycling, and wet/dry conditions. The results showed that when α-Al_2O_3 was added in spraying powder, the coating could obtain higher hardness and a denser microstructure. Hardness was highest at the interface of the coating and substrate because in this region the deposited particles were repeatedly impinged upon by the subsequently deposited particles. From corrosion-under-insulation (CUI) tests, Al-Al_2O_3 CS coatings proved to be efficient in protecting carbon steel pipe from CUI mainly owning to lamellar microstructures of coatings. During exposure to the corrosive environment, coatings degraded in forms of general thinning, pores, and cracks, but the remaining coatings could protect substrate from the corrosive medium as a result of the lamellar microstructures. Additionally, there was no evidence that the addition of α-Al_2O_3 might bring any negative effect on corrosion resistance.

Pure aluminum powder was successfully sprayed on AZ31B extrusion flat and round coupons at low temperature. The corrosion and corrosion fatigue behavior of the coated and uncoated samples were examined by performing accelerated corrosion tests. The corrosion resistance of AZ31B samples with and without coating was investigated based on ASTM B117 standard salt spray with a concentration of 5% NaCl at 36 °C, 100% relative humidity. The corrosion fatigue of bare and coated round samples was examined by producing a thin film of 3.5% NaCl solution on the surface of the fatigue samples via integrating a corrosion chamber into a rotating bending fatigue testing machine. Pure Al coating provided significant corrosion protection for AZ31B in 5% NaCl fog environment by improving its corrosion resistance from 90% average weight loss in 33 days for bare samples to less than 10% average weight loss in 90 days of continuous corrosion cycles. The strong adhesion and very low porosity of the Al coating were the main factors that resulted in the excellent corrosion performance of the coated AZ31B (Diab et al. 2017)

Ni-based coatings of the type Inconel 625 sprayed with high-kinetic spray processes are applied as protective coatings in many industrial fields where high

corrosion resistance is required. High velocity oxygen fuel (HVOF) and arc spray are common thermal spray methods used in the industry of power generation. Conversely, high velocity air fuel (HVAF) and cold spray are nowadays technologies of rising interest because of their possibilities to create highly dense and low oxidized metallic coatings. In the work done by Fantozzi et al. (2017), the effect of the different high-kinetic spray systems on chlorine-induced high-temperature corrosion protection of Inconel 625 coatings under KCl salt deposit at 550 °C for 168 h was evaluated. The study aimed to evaluate the effect of chlorine corrosion on the complex microstructure of thermally sprayed coatings. All the coatings performed well preventing the corrosion of the substrate and acting as a barrier against the corrosive chlorine-containing environment. HVOF and TWAS coatings experienced the lowest corrosion degradation and the HVAF-sprayed coating the highest. For the cold spray coatings, the finest particle size distributions and the use of He as process gas seemed beneficial. All the coatings were subjected to the corrosion mechanism of high temperature chlorine active oxidation with formation of porous and non-protective oxides and chromate layers on the surface. The corrosion products were mainly composed of K_2CrO_4 and mixed Cr, Ni, and Mo oxides.

Microstructural evolutions, mechanical properties, and corrosion performance of coatings made of 7075 Al matrix with B_4C or SiC reinforcement deposited on T6 6061 Al alloy using the cold gas dynamic spraying process were investigated in the work done by Meydanoglu et al. (2013). Microstructural surveys showed that coatings with no discontinuity at the interface as well as with fine grains were obtained, and the addition of ceramic particles enhanced the coating density for a prescribed set of spray parameters and nozzle configuration. 7075 Al alloy matrix ceramic particle (B_4C and SiC) reinforced composite coatings were successfully produced on T6 6061 Al alloy substrate without any discontinuity at the coating/substrate interface and with uniform distribution of ceramic particles in the 7075 Al matrix. According to the XRD patterns of the coatings besides the main phases of Al, B_4C, and SiC, there are no other phases in the coatings. It can be concluded that no phase transformation occurs during spraying. Broadening and shifting of Al diffraction peaks were noticed by XRD analyses when compared with those of initial 7075 Al powders suggesting that grain refinement was generated. Unreinforced 7075 Al coating exhibited much higher hardness in comparison with 7075 Al alloy due to severe plastic deformation and strain hardening of the 7075 Al matrix. The addition of ceramic particles into 7075 Al matrix increased the hardness of the cold-sprayed coatings. The hardness values of the composite coatings moderately increased as the volume content of ceramic particles retained in the coating increased. The cold-sprayed coatings showed more noble corrosion potentials but higher corrosion current densities than those of the T6 6061 Al substrate. The addition of ceramic particles into 7075 Al matrix led to increased corrosion current densities when compared to that of unreinforced 7075 Al coating.

Cold spray process was used to deposit NiCrAlY and NiCoCrAlY powders on Fe-based Superfer 800H superalloy. The hot corrosion behavior of the cold spray coatings was studied on Fe-based superalloy in Na_2SO_4-10%NaCl environment at 900 °C under cyclic conditions for 50 cycles. The weight-change technique was

used for the study of kinetics of corrosion. The XRD, SEM/EDAX, and X-ray mapping techniques were used to study the corrosion products. The porosity of both the coatings was found in the range 0.8–0.9%. The NiCoCrAlY coating performed relatively better than NiCrAlY coating against hot corrosion in the given environment. Formation of Cr_2O_3 scale at the top and Al_2O_3 scale underneath was observed for the cold-sprayed NiCrAlY coating after exposure to Na_2SO_4-10%NaCl molten salt environment. Better hot corrosion resistance of cold-sprayed NiCoCrAlY was found to be due to the formation of oxides of chromium and cobalt, with some spinels of cobalt-chromium and nickel-chromium. The dense coating structure obtained by the cold spray coating was partially responsible for higher corrosion resistance (Kalsi et al. 2014).

The defects in the cold-sprayed coatings are critical in the case of corrosion performances of the coatings in aggressive conditions. To understand the influence of coating defects on corrosion, immersion tests were carried out in 5 wt % HF solution for the cold-sprayed and heat-treated titanium, tantalum, and niobium coatings by Kumar and Rao (2017). Long-duration immersion tests revealed inhomogeneous weight losses of the samples prepared at different heat treatment conditions. The weight loss for different coatings was well corroborated with the coating defects and microstructures. Chemical and microstructural analysis elucidates the reason behind the inhomogeneous performance of different type of cold-sprayed coatings in corrosion medium. In the case of cold-sprayed titanium, formation of stable oxide along the inter-splat boundary hindered the aggressive attack of the corrosion medium which was not so in other cases. As-coated titanium performed superiorly in the immersion test as compared with heat-treated coatings. In the case of titanium, the corrosion medium percolates through inter-splat boundaries and forms oxide layer which prevents bulk titanium from further corrosion. Since the inter-splat boundary fraction has been reduced to isolated pores for the coatings heat treated at higher temperature, the corrosion reaction is severe on the surfaces. In the case of tantalum and niobium coatings, as-sprayed samples performed better than most of the heat-treated samples; a clear understanding could not be derived. It was believed that the formation of protective layer in the as-coated case and closure of inter-splat boundaries at extreme heat treatment conditions protects coatings from corrosion attack.

Al-based bulk metallic glasses (Al-BMG) have attracted a lot of attention due to their superior mechanical properties, low density, and corrosion resistance in the past (Inoue 1998, 2000; Mu et al. 2009). Cold spraying technique was used to synthesize Al-based glassy coatings to protect 6061 aluminum surface from wear and corrosion. Gas atomized Al90.05Y4.4Ni4.3Co0.9Sc0.35 (at.%) powder was used as the starting powder. Dense (98%) coatings with a uniform thickness of ~250 μm were deposited. Potentiodynamic studies of the coatings were done in varying NaCl concentrations; results displayed 5 times better corrosion resistance than 6061 Al substrate, which was attributed to the active passivation and the chemical homogeneity of the coating. The improved corrosion resistance was attributed to the chemical homogeneity of the amorphous structure with embedded nanocrystals. Cold-sprayed Al-based amorphous coating showed great promise in protecting aluminum surface from corrosion and wear (Lahiri et al. 2013).

Aluminum/copper contacts occur in power networks made of aluminum alloy busbars. Bolted joints of aluminum and copper cause galvanic corrosion of aluminum in the presence of electrolyte. The work done by Winnicki et al. (2016) focused on the effect of different powder morphology and the addition of ceramics on coating porosity and consequently on corrosion resistance and electrical conductivity behavior. The corrosion protection of copper coatings deposited by low-pressure cold spraying (LPCS) onto AA 1350 aluminum alloy was examined. The coatings were sprayed using two copper powders of different morphology, namely, spherical and dendritic ones. These powders were mixed with alumina before spraying in a 50:50 weight ratio, and composite coatings were deposited. The coating microstructures were characterized by the scanning electron microscopy (SEM). The measurements of coating hardness in the middle of the coating thickness were carried out. The coating corrosion protection was analyzed by polarization measurements. All the coatings showed increased corrosion potential as compared to the substrate. The metal, as well as composite copper coatings, increased the open cell potential of coated Al samples. Moreover, all copper coatings showed a higher corrosion potential than the substrate material. The addition of ceramics insignificantly decreased the corrosion potential of both metal powders.

The morphology, chemical, mechanical, and corrosion characterization of starting materials and Al and Al-Al_2O_3/Al coatings obtained by cold gas spray and applied on common steel substrate were performed. An Al coating on a ground or grit-blasted substrate and Al-Al_2O_3/Al coating on ground mild carbon steel were compared in the work done by Silva et al. (2017). Coatings of Al and Al-Al_2O_3/Al composite applied on ground or grit-blasted steel substrates with low porosity were successfully prepared by cold spray technology. All the studied Al-based coatings protected the substrate against corrosion for a long time such as 3000 h in salt fog tests. In solution and at immersion times (<200 h), the Al-Al_2O_3/Al composite coating showed higher corrosion resistance, probably due to the lower active area of Al, and it showed lower corrosion performance for immersion times higher than 200 h due to the severe corrosion of Al matrix surrounding the alumina particles. For immersion time higher than around 600 h, the Al/grit-blasted steel showed the highest corrosion performance. The detection of aluminum ions in the solution (aluminum test) at around 1 h of immersion indicated that Al is easily oxidized; however, the coating/substrate interface was not corroded up to 1200 h of immersion, and for the Al/grit-blasted steel, some spots of corrosion were observed at the coating/substrate interface after 2200 h of immersion, indicating that Al-based coatings can protect steel against corrosion for a long immersion time.

Cold spraying shows a great potential in the fabrication of metal matrix composites. In the study done by Li et al. (2014), a nickel-coated Al_2O_3 powder produced with the hydrothermal hydrogen reduction method was employed aiming to increase the volume fraction of ceramic particles in the cold-sprayed composites. The effect of oxidation temperatures on the microstructure and microhardness of as-cold-sprayed and vacuum heat-treated Ni/Al_2O_3 composite coatings was characterized. The high temperature oxidation behaviors of as-sprayed and heat-treated coatings were compared and discussed. Results showed that the oxidized coatings were

denser compared with the as-sprayed coating. The oxide films morphologies of as-sprayed coatings were different under different oxidizing temperatures. Moreover, the as-sprayed coating has a similar oxide film feature to the heat-treated coating when oxidized at 850 °C, which may suggest the direct use of coating after deposition without any heat treatment. It was observed that the pores and interlamellar cracks in the as-sprayed composite coating tend to be closed during oxidizing. The oxide film morphologies of as-sprayed coatings were different when the oxidation temperature increased to 850 °C.

Cold spray (CS) technique was used to deposit pure Al coating on AZ91D magnesium alloy in the work done by Tao et al. (2010). Scanning electron microscopy (SEM) and transmission electron microscopy (TEM) techniques were used to characterize the microstructure of the coating. The grain interfaces and subgrains were found to have formed close to the particle/particle boundaries. Electrochemical tests were performed in neutral 3.5 wt.% NaCl solution. The cold-sprayed pure Al coating showed better pitting corrosion resistance than the bulk pure Al with similar purity. During 10-day immersion, a mass-transfer step was found to be involved in the corrosion. The onset of pitting (Epit) is defined by the potential at an anodic current density of 25 μA/cm^2 from the forward scanning curve, while repassivation potential (Er) is determined at the same current density from the backward scanning curve. Table 12.2 gives the estimated potentials from the cyclic polarization curves. The difference between Epit and Ecorr gives a measure of the tendency to pitting nucleation (Kiourtsidis et al. 1999). If there is an increase in this difference, it implies improved resistance to pitting corrosion. Therefore, the difference between Er and Ecorr is an indication of the repassivation ability. In this study, the Al coating has larger values of (Epit-Ecorr) and (Er-Ecorr) than the bulk Al, which indicates that the Al coating possessed better pitting corrosion resistance and repassivity than the bulk Al.

It was concluded that after 10 days of immersion in the aggressive solution, the coating offered enough corrosion protection for AZ91D substrate which was owed to its dense and fine-grain microstructure (Tao et al. 2009).

Titanium coating was successfully deposited by cold spraying. The microstructure and corrosion performance of cold-sprayed Ti coating were examined. The experimental results showed that a dense Ti coating could be formed with a porous surface layer. The as-sprayed Ti coating presents a more negative open circuit potential and a larger corrosion current than that of TA2 (pure Ti metal) owing to its porous surface structure and high surface activity compared with TA2. The polarization behavior of the polished Ti coating was a little different with that of TA2 because of the limited bonding between the deposited particles in coating (Wang et al. 2007).

Table 12.2 Results of cyclic polarization measurements for the material subjected to 3.5 wt.% NaCl solution for 1 h

	Ecorr (VSCE)	Epit (VSCE)	Er (VSCE)	Epit-Ecorr (V)	Er-Ecorr (V)
Pure Al coating	−0.915	−0.744	−0.779	−0.171	−0.136
Bulk pure Al	−0.630	−0.616	−0.789	−0.014	−0.159

Cold spraying technique was used to deposit an aluminum coating on the surface of a friction stir welded 2024-T351 aluminum alloy joint for corrosion protection. Cold spray coating leads to the formation of a relatively dense coating except some pores on the coating surface layer, and further a good bonding between the coating and the weld surface was formed. Immersion tests were carried out in the exfoliation solution which established that the presence of pure Al coating considerably reduced the corrosion attack. A new innovation in the form of application of CS to FSW to improve the corrosion resistance of the FSWed joints was formed. Hence it was concluded that the presence of the Al coating offers exceptional corrosion protection for welds, while without protection joints are terribly corroded. Besides, the strength of joints with coating protection did not lower (Li et al. 2015).

The micro-arc oxidation (MAO) technology has been increasingly recognized as one of the novel and nontraditional approaches for increasing both the corrosion and wear resistance of Al, Ti, Mg, and their alloys. These MAO coatings deposited on Mg in general are porous; hence various techniques of duplexing the MAO with other conventional and non-conventional methods have been investigated for increasing the corrosion protection of Mg and its alloys. For the first time the cold gas dynamic spray (CGDS) technique was used as a pre-MAO treatment for deposition of Al on AZ91 Mg alloy. A duplex coating on Mg alloy with Al topcoat was obtained. The microstructure was studied by employing scanning electron microscopy (SEM); the elemental concentration and their distribution across the coating thickness were evaluated using energy dispersive spectroscopy (EDS) coupled with SEM. This coating forms a duplex in the way of combining two different methods, i.e., CGDS and MAO, further in terms of the elemental distribution across the coating thickness which exhibit a compositionally graded nature. The potentiodynamic polarization studies were carried out in 3.5 wt.% NaCl solution which revealed that the corrosion current density gets decreased by 1–2 orders of magnitude compared to the bare magnesium substrate. Hence the duplex coating (CGDS + MAO) offered considerably higher corrosion protection with the polarization resistance of duplex coating about 14 times higher than the plain MAO coating. Hence it was concluded that the cold gas dynamic spraying can be successfully combined with MAO (Krishna et al. 2013).

12.3 Conclusions

The chapter gives a brief introduction to the cold spray coating technique and its applications with respect to corrosion resistance. It is well known that cold spray technique has developed extensively over the last two decades; still modifications and improvements of the technology have been introduced. Nowadays, cold spray process is being accepted by many industries due to its advantages of being 100% solid-state process, no particle melting, negligible oxidation, decarburizing, nitriding, etc. Presently, high-temperature oxidation resistant and corrosion resistance coatings are produced in vacuum plasma spray systems, physical vapor deposition,

or other spraying systems. These systems are extremely expensive to both install and operate. Moreover, cold spray process may lend itself to collect the overspray and reprocess these expensive raw materials. Hence, it is expected that this well-founded cold spray technology will be able to compete for a good market share of other thermal spray coatings for various corrosion protection applications. Detailed review of various applications of the cold spray coatings has been discussed in detail. The coatings can be successfully deposited on wide range of substrates like boiler steels, Al, Ti, Mg, and their alloys. Ni-, Cr-, Al-, and Ti-based pure and composite coatings have been successfully deposited on these alloys. These coating systems were tested in the corrosive mediums, and results have shown better corrosion resistance of these coatings than the bare substrates. Studies by various authors prove that for aggressive corrosion environments including cyclic studies, coatings deposited by cold spray process have shown very good and impressive corrosion resistance results. However, further experimental studies are required for studying the feasibility of the process for corrosion protection in other aggressive conditions especially in actual working conditions. In the near future, cold spray process may serve the overall field of thermal spray technology as a specialized tool for novel applications and devices, otherwise unachievable with existing materials and practices.

References

Alkimov AP, Kosarev VF, Nesterovich NI, Papyrin AN (1986a) Method of applying coatings, Russian Patent No 1618778, Sept 8, 1990 (Priority of the Invention: Jun 6, 1986)

Alkimov AP, Kosarev VF, Nesterovich NI, Papyrin AN, Shushpanov MM (1986b) Device for applying coatings, Russian Patent No 1618777, Sept 8, 1990 (Priority of the Invention Jun 18, 1986)

Alkimov AP, Kosarev VF, Nesterovich NI, Papyrin AN (1987) Method of applying of metal powder coatings, Russian Patent No 1773072, Jul 1, 1992 (Priority of the Invention: Oct 5, 1987)

Alkimov AP, Kosarev VF, Papyrin AN (1990) A method of cold gas-dynamic deposition. Sov Phys Dokl 35(12):1047–1049

Alkimov AP, Papyrin AN, Dosarev VP, Nesterovich NI, Shushpanov MM (1994) US Patent 5,302,414, April 12, 1994

Alkimov AP, Papyrin AN, Kosarev VF, Nesterovich NI, Shushpanov MM (1995) Method and device for coating, European Patent No 0484533, Jan 25, 1995

Alkimov AP, Kosarev VF, Nesterovich NI, Papyrin AN, Shushpanov MM (1997) Gas dynamic spraying method for applying a coating, U.S. Patent No. 5, 302, 414, Apr 12, 1994, Re-examination Certificate, Feb 25, 1997

Bai X, Tang J, Gong J, Lu (2017) Corrosion performance of Al-Al_2O_3 cold sprayed coatings on mild carbon steel pipe under thermal insulation. Chin J Chem Eng 25:533–539

Bala N (2011) Investigations on the hot corrosion behaviour of cold spray and HVOF spray coatings on T22 and SA 516 steels'. PhD thesis, Punjab Technical University, Jalandhar

Bala N, Singh H, Prakash S (2009a) High-temperature oxidation studies of cold-sprayed Ni–20Cr and Ni–50Cr coatings on SAE 213-T22 boiler steel. Appl Surf Sci 255(15):6862–6869

Bala N, Singh H, Prakash S (2009b) Accelerated hot corrosion studies of cold spray Ni-50Cr coating on boiler steels. Mater Des 31:244–253

Bala N, Singh H, Prakash S (2010) High temperature corrosion behavior of cold spray Ni-20Cr coating on boiler steel in molten salt environment at 900°C. J Therm Spray Technol 19:110–118

Bala N, Singh H, Prakash S (2011) Characterisation and high temperature oxidation behavior of cold sprayed Ni-20Cr and Ni-50Cr coatings on boiler steels. Metall Mater Trans A 42A:3399–3416

Bala N, Singh H, Karthikeyan J, Prakash S (2014) Cold spray coating process for corrosion protection: A review. Surf Engg 30:414–421

Bala N, Singh H, Prakash S (2017) Performance of cold sprayed Ni based coatings in actual boiler environment. Surf Coat Technol 318:50–61

Diab M, Pang X, Jahed H (2017) The effect of pure aluminum cold spray coating on corrosion and corrosion fatigue of magnesium (3% Al-1%Zn) extrusion. Surf Coat Technol 309:423–435

Dykhuizen RC, Smith MF (1998) Gas dynamic principles of cold spray. J Therm Spray Technol 7(2):205–212

Fantozzi D, Matikainen V, Uusitalo M, Koivuluoto H, Vuoristo P (2017) Chlorine-induced high temperature corrosion of Inconel 625 sprayed coatings deposited with different thermal spray techniques. Surf Coat Technol 318:33–243

Inoue A (1998) Amorphous, nanoquasicrystalline and nanocrystalline alloys in Al-based systems. Prog Mater Sci 43:365–520

Inoue A (2000) Stabilization of metallic supercooled liquid and bulk amorphous alloys. Acta Mater 48:279–306

Kalsi SS, Sidhu TS, Singh H (2014) Performance of cold spray coatings on Fe-based superalloy in Na_2SO_4–NaCl environment at 900 °C. Surf Coat Technol 240:456–463

Karthikeyan J (2004) Cold spray technology: international status and USA efforts, 1–14

Kaur M, Singh H, Prakash S (2010) Role of detonation-gun spray Cr_3C_2-NiCr coating in improving high temperature corrosion resistance of SAE-213-T22 and SAE-347H steel in the presence of Na_2SO_4-82%$Fe_2(SO_4)_3$ salt deposits. Surf Eng 26(6):428–439

Kaushal G (2011) Erosion-corrosion studies on high-velocity oxy-fuel thermal spray coatings over some boiler steels. PhD thesis, Mech. Engg. Dept., Punjab Technical University, Jalandhar

Kaushal G, Singh H, Prakash S (2011a) Comparative high temperature analysis of HVOF sprayed and detonation gun sprayed Ni-20Cr coating in laboratory and actual boiler environments. Oxid Met 76:169–191

Kaushal G, Singh H, Prakash S (2011b) Surface engineering by detonation-gun spray coating of 347H boiler steel to enhance its high temperature corrosion resistance. Mater High Temp 28(1):1–11

Kaushal G, Kaur N, Singh H, Prakash S (2013) Effect of zirconium addition in HVOF-sprayed Ni-20Cr coating. Surf Eng 29(1):46–54

Kiourtsidis GE, Skolianos SM, Pavlidou EG (1999) A study on pitting behaviour of AA2024/SiCp composites using the double cycle polarization technique. Corros Sci 41:1185–1203

Kong LY, Shen L, Lu B, Yang R, Cui XY, Li TF, Xiong TY (2010) Preparation of TiAl3-Al composite coating by cold spray and its high temperature oxidation behavior. J Therm Spray Technol 19(6):1206–1210

Krishna LR, Poshal G, Jyothirmayi A, Sundararajan G (2013) Compositionally modulated CGDS + MAO duplex coatings for corrosion protection of AZ91 magnesium alloy. J Alloys Compd 578:355–361

Kumar S, Rao AA (2017) Influence of coating defects on the corrosion behavior of cold sprayed refractory metals. Appl Surf Sci 396:760–773

Kumar M, Singh H, Singh N, Joshi RS (2015) Erosion–corrosion behavior of cold-spray nanostructured Ni–20Cr coatings in actual boiler environment. Wear 332-333:103–1043

Lahiri D, Gill PK, Scudino S, Zhang C, Singh V et al (2013) Cold sprayed aluminum based glassy coating: synthesis, wear and corrosion properties. Surf Coat Technol 232:33–40

Li WL, Liao H, Douchy G, Coddet C (2007) Optimal design of a cold spray nozzle by numerical analysis of particle velocity and experimental validation with 316L stainless steel powder. Mater Des 28:2129–2137

Li W, Huang C, Yu M, Liu D, Feng Y, Liao H (2014) Investigation of high temperature oxidation behavior and tribological performance on cold sprayed nickel–alumina composite coating. Surf Coat Technol 239:95–101

Li WY, Jiang RR, Huang CJ, Zhang ZH, Feng Y (2015) Effect of cold sprayed Al coating on mechanical property and corrosion behavior of friction stir welded AA2024-T351 joint. Mater Design 65:757–761

Lima RS, Karthikeyan J, Kay CM, Lindemann J, Berndt CC (2002) Microstructural characteristics of cold-sprayed nanostructured WC-Co coatings. Thin Solid Films 416:129–135

Mahesh RA, Jayaganthan R, Prakash S (2011) High temperature oxidation studies on HVOF sprayed NiCrAl coatings on superalloys. Surf Eng 28(5):332–339

McCune RC, Papyrin AN, Hall JN, Riggs WL, Zajchowski PH (1995) In: Berndt CC, Sampath S (eds) An exploration of the cold-gas dynamic spray method for several material systems in Advances in thermal spray science and technology. ASM International, Materials Park, pp 1–5

McCune RC, Donlon WT, Popoola OO, Cartwright EL (2000) Characterization of copper layers produced by cold gas-dynamic spraying. J Therm Spray Technol 9(1):73–82

Meydanoglu O, Bertrand Jodoin B, Kayali ES (2013) Microstructure, mechanical properties and corrosion performance of 7075 Al matrix ceramic particle reinforced composite coatings produced by the cold gas dynamic spraying process. Surf Coat Technol 235:108–116

Mu J, Fy H, Zhu Z et al (2009) Synthesis and properties of Al-Ni-La bulk metallic glass. Adv Eng Mater 11:530–532

Papyrin A, Kosarev V, Klinkov S, Alkhimov AP, Fomin V (2007) Current status of the cold spray process. In: Papyrin A (ed) Cold spray Technology. Elsevier, Amsterdam

Rahman A, Chawla V, Jayaganthan R, Chandra R, Tewari VK, Ambardar R (2012) Surf Eng 28(4):249–256

Raletz F, Vardelle M, Ezo'o G (2006) Critical particle velocity under cold spray conditions. Surf Coat Technol 201:1942–1947

Shukla V, Elliott G, Kear B (1999) 37th AIAA aerospace sciences meeting and exhibit, January 11–14, 1999, Reno, 1

Sidhu BS (2003) Studies on the role of coatings in improving resistance to hot corrosion and degradation. PhD thesis, Metals and Materials Engineering Department, IITR, Roorkee

Sidhu BS, Prakash S (2006) Performance of NiCrAlY, Ni–Cr, stellite-6 and Ni_3Al coatings in Na_2SO_4–60% V_2O_5 environment at 900°C under cyclic conditions. Surf Coat Technol 201(3-4):1643–1654

Sidhu HS, Sidhu BS, Prakash S (2006a) The role of HVOF coatings in improving hot corrosion resistance of ASTM-SA210 GrA1 steel in the presence of Na_2SO_4–V_2O_5 salt deposits. Surf Coat Technol 200(18-19):5386–5394

Sidhu TS, Prakash S, Agrawal RD (2006b) Characterisations of HVOF sprayed NiCrBSi coatings on Ni- and Fe-based superalloys and evaluation of cyclic oxidation behaviour of some Ni-based superalloys in molten salt environment. Thin Solid Films 515(1-2):95–105

Sidhu TS, Prakash S, Agrawal RD (2006c) Hot corrosion studies of HVOF sprayed Cr_3C_2-NiCr and Ni-20Cr coatings on a nickel based superalloy at 900°C. Surf Coat Technol 201(3-4):792–800

Silva FSD, Bedoya J, Dosta S, Cinca N, Cano IG, Guilemany JM, Benedetti AV (2017) Corrosion characteristics of cold gas spray coatings of reinforced aluminum deposited onto carbon steel. Corr Sci 114:57–71

Singh H (2005) Hot corrosion studies on plasma spray coatings over some Ni- and Fe-based superalloys. PhD thesis, Metals and Materials Engineering Department, IITR, Roorkee

Singh H, Puri D, Prakash S (2005a) Some studies on hot corrosion performance of plasma sprayed coatings on a Fe-based superalloy. Surf Coat Technol 192:27–38

Singh H, Puri D, Prakash S (2005b) Hot corrosion behaviour of plasma sprayed coatings on a Ni-based superalloy in Na_2SO_4-60%V_2O_5 environment. ISIJ Int 45(6):886–895

Singh H, Bala N, Kaur N, Sharma SK, Kim DY, Prakash S (2015) Effect of additions of TiC and Re on high temperature corrosion performance of cold sprayed Ni-20Cr coatings. Surf Coat Technol 280:50–63

Steenkiste TH, Smith JR, Teets RE, Moleski JJ et al (2002) Aluminum coating via kinetic spray with relatively large powder particles. Surf Coat Technol 154(2-3):237–252

Stoltenhoff T, Kreye H, Richter HJ, Assadi H (2001) In: Berndt CC, Khor KA, Lugscheider EF (eds) Optimization of the cold spray process in thermal spray 2001: new surfaces for a millennium. ASM International, Materials Park, pp 409–416

Tao Y, Xiong T, Sun C, Jin H, Du H, Li T (2009) Effect of α-Al2O3 on the properties of cold sprayed Al/α-Al2O3 composite coatings on AZ91D magnesium alloy. Appl Surf Sci 256:261–266

Tao Y, Xiong T, Sun C, Kong L, Cui X, Li T, Song GL (2010) Microstructure and corrosion performance of a cold sprayed aluminium coating on AZ91D magnesium alloy. Corros Sci 52:3191–3197

Wang HR, Li WY, Ma L, Wang J, Wang Q (2007) Corrosion behavior of cold sprayed titanium protective coating on 1Cr13 substrate in seawater. Surf Coat Technol 201:5203–5206

Wang Q, Spencer K, Birbilis N, Zhang MX (2010) The influence of ceramic particles on bond strength of cold spray composite coatings on AZ91 alloy substrate. Surf Coat Technol 205(1):50–56

Winnicki M, Małachowska A, Baszczuk A, Gorczyca MR, Kukla D, Lachowicz M, Ambroziak A (2016) Corrosion protection and electrical conductivity of copper coatings deposited by low-pressure cold spraying. Surf Coat Technol. https://doi.org/10.1016/j.surfcoat.2016.12.101

Chapter 13
Corrosion Resistance of Cold-Sprayed Coatings

Heli Koivuluoto

13.1 Introduction

This chapter presents the corrosion properties of cold-sprayed coatings. Cold spraying has shown its potential producing corrosion-resistant coatings for several operation conditions due to the fact that dense and protective metallic and composite coatings can be manufactured by using cold spray processes, examples are presented in Fig. 13.1. This enables the use of cold-sprayed coatings as corrosion barrier coatings. In addition to corrosion resistance, other advantages of cold-sprayed coatings are dealing with high strength, electrical conductivity and minimal or compressive residual stresses as well as repairing and additive manufacturing (Papyrin et al. 2007; Champagne and Helfritch 2016; Champagne 2007; Koivuluoto 2010; Villafuerte 2015). Corrosion properties and behavior of the cold-sprayed coatings are increasingly reported in the literature during last years. Recently, review papers concerning corrosion properties of cold-sprayed coatings have been published by Bala et al. (2014), Koivuluoto and Vuoristo (2014), and Hassani-Gangaraj et al. (2015). Furthermore, cold spraying can be used for corrosion protection as well as repairing of corrosion defects (Vardelle et al. 2016).

13.2 Corrosion Generally

An extractive metallurgy in reverse is the definition of corrosion, and it is related to the chemical or electrochemical reaction between material and its environment (Jones 1996). Due to the damages or material losses caused by corrosion, it is to design and manufacture corrosion-resistant and protective materials and coatings with specific

H. Koivuluoto (✉)
Tampere University of Technology, Faculty of Engineering Sciences, Laboratory of Materials Science, Tampere, Finland
e-mail: heli.koivuluoto@tut.fi

P. Cavaliere (ed.), *Cold-Spray Coatings*,
https://doi.org/10.1007/978-3-319-67183-3_13

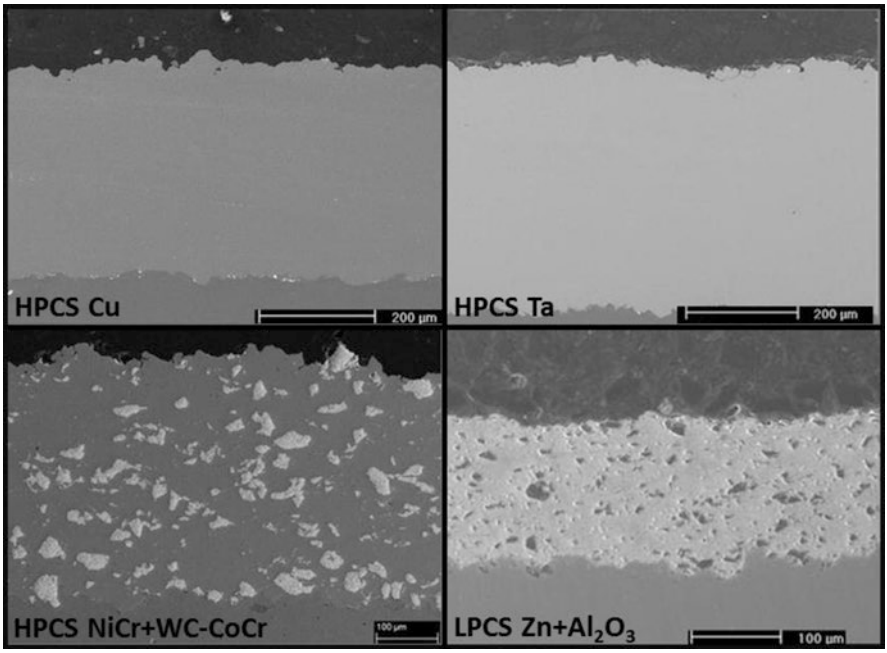

Fig. 13.1 Examples of dense cold-sprayed metallic and composite coatings (Modified after Koivuluoto et al. (2008, 2009a, 2012) and Koivuluoto and Vuoristo (2010b))

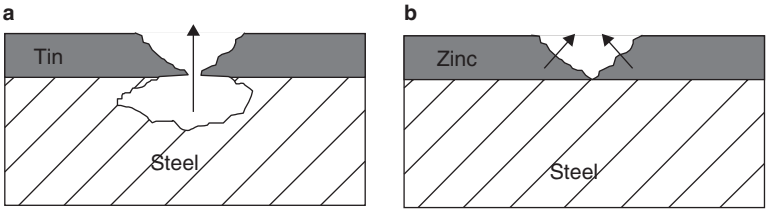

Fig. 13.2 Example of galvanic corrosion at the damaged coatings. Corrosion behavior of (**a**) anodically and (**b**) cathodically protective coating. Steel is more active than tin and thus, steels corrode strongly, whereas damaged zinc coating acts as a sacrificial anode being less noble than steel (Chatterjee et al. 2001)

requirements, e.g., high reliability, quality, and low costs. High corrosion resistance is necessary in several industrial sectors such as in chemical and process equipment and energy production systems. Corrosion protection of metals and metallic coatings is based on anodic protection by passivity or cathodic protection by sacrificial anode behavior. Figure 13.2 presents an example of galvanic corrosion at the damaged coatings. Basically, corrosion starts if protection fails or breaks down, making metal vulnerable to attacks of corrosion (Talbot and Talbot 1998). Corrosion can be prevented by using dense corrosion barrier coatings, which can be produced by using cold spray techniques.

Corrosion can occur in different forms. For coatings, uniform, pitting, crevice, and galvanic corrosion are typical forms of corrosion. The most common forms of localized corrosion are pitting and crevice corrosion in which corrosive conditions could penetrate relatively rapidly (Jones 1996). Pitting corrosion occurs if the passive layer of protecting material is locally damaged, pits form on the surface, and underlying metal is open for the attack (Frankel 2003). Furthermore, pitting corrosion causes highly localized damages (Schweitzer 1996). For nonuniform and poorly adhered coatings, pitting corrosion takes place relatively easily. In addition, porosity in the anodically protective coatings accelerates pitting corrosion by opening the way for aqueous solution to penetrate inside the coating structure to a substrate material (Chatterjee et al. 2001). Crevice corrosion is said to be the one of the most damaging forms of corrosion, and it causes localized corrosion (Kelly 2003). Whereas galvanic corrosion occurs when two dissimilar metals form an electrical couple in the same electrolyte. In the electrical couple, corrosion starts in the less corrosion resistant material (more active) which becomes the anode whereas the more resistant material (nobler) will be cathode (Baboian 2003). Material, metallographic structure, and microstructural properties have an influence on corrosion behavior (Jones 1996) which can be controlled by correct material selection together with protective coating properties.

Galvanic series of materials shows anodic-cathodic behavior of materials compared with each other. The nobler the material, the higher it is on the order. Cathodic materials protect less noble materials anodically, whereas anodic materials give cathodic protection to the nobler material. It is known that cathodic protection is based on sacrificial behavior of anodic material, e.g., zinc coating on steel substrate. In this case, porosity is not so critical, whereas in the anodically protective coatings, impermeability of the coating and passive layer on its surface is crucial for corrosion resistance.

The best way to protect steel components (active metal) is to deposit the protective coating on its surface (Talbot and Talbot 1998). For that purpose, cold spraying enables the production of dense coatings for applications where corrosion resistance is needed. Denseness of the anodically protective coatings is the first criterion required for corrosion protection (Koivuluoto et al. 2009b). Anodic protection is based on passivation of metals. This, in turn, is based on a formation of thin, protective oxide layer, acting as a corrosion barrier film (Jones 1996). Existence of passive film is the requirement for corrosion protection (Kruger 2003). Many metals can form a protective film on their surface, which inhibits interactions between metal and corrosive atmosphere due to passivation. Coverage of passive layer is crucial because if it is not or passive layer breaks down, corrosion can damage the structure. Metals' passivity is usually based on the formation of thin oxide layer typically in the air. It is very important to have a continuous and coherent oxide film. In electrochemical polarization behavior of passivated metals, passivation potential E_p indicates critical potential and above that corrosion rate of metal decreases. The area is called passivation range. Below E_p corrosion occurs at a higher rate. If the passive layer fractures, it opens the way for localized forms of corrosion (Jones 1996). Anodic polarization behavior shows material active-passive behavior and, therefore, corrosion protection (Schweitzer 1996).

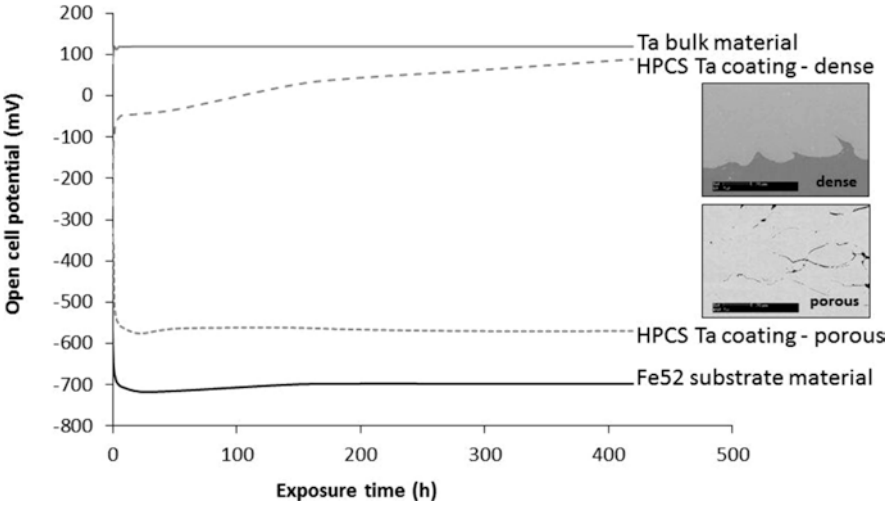

Fig. 13.3 Open-cell potential behavior of Ta bulk material, dense and porous high-pressure cold-sprayed Ta coatings and Fe52 substrate material in 3.5% NaCl solution (Ag/AgCl reference electrode) (Modified after Koivuluoto et al. (2009a))

Corrosion behavior of the coatings can be studied by using electrochemical or accelerated corrosion tests. Open-cell potential measurements and salt spray (ASTM B117 standard) tests as wet corrosion tests are relevant methods to evaluate the denseness (density, impermeability) of the coatings on corrodible substrate (e.g., carbon steel in saltwater conditions). Additionally, salt spray testing is a commonly used test method to evaluate the quality of various coatings. This particular test enables the use of different corrosive solutions and different test temperatures in a controlled test condition. Furthermore, corrosion protectiveness and corrosion rates can be estimated with polarization behavior of the coatings (Schweitzer 1996). Polarization measurements are widely used in the corrosion studies of cold-sprayed coatings. Furthermore, corrosion properties can be studied with more application related tests, e.g., hot corrosion tests and electrochemical corrosion tests in certain specific exposure conditions.

Existing interconnected porosity (through-porosity or open-porosity) can be evaluated by using, e.g., open-cell potential measurements. If the coating contains interconnected porosity, potential behavior is composed of potentials of both coating and substrate which is seen as mixed potential (Vreijling 1998). If the open-cell potential value of the coating approaches the value of the corresponding bulk material, it indicates impermeable and dense coating structure. In the other case, if the value of the coating approaches the value of the substrate material, it reflects the through-porosity in the coating structure. In such situation, testing liquid has an open access to penetrate from the surface of the coating to the interface between coating and substrate, it will corrode the substrate, and corrosion products will come up to the surface. Figure 13.3 presents the open-cell potential behavior of dense and porous cold-sprayed Ta coatings.

13.3 Anodic Protection by Cold-Sprayed Coatings

Dense and impermeable coating structures are the first criterion for the corrosion resistance of coatings that are nobler than substrate material. For example, Cu, Ta, Ni, and Ni-based alloys are nobler than steel substrate. Cold-sprayed Ni, Ta, Ti, stainless steel, brass, and bronze coatings with non-existing or low porosity in their structures are reported to have potential to use for corrosion resistance applications (Koivuluoto et al. 2010b; Koivuluoto and Vuoristo 2010b; Bala et al. 2010a; Wang et al. 2006, 2008; AL-Mangour et al. 2013).

13.3.1 Cold-Sprayed Cu Coatings

Copper is a corrosion-resistant material against seawater, waters, dilute sulfuric acid, phosphoric acid, acetic acid, and other non-oxidizing acids and, in addition, generally atmospheric exposure (Schweitzer 1996). Cold-sprayed Cu coatings have similar corrosion resistance compared with Cu bulk material in seawater conditions (3–5% NaCl). This is seen in Fig. 13.4. Hence, dense and protective Cu and Cu alloy coatings can be produced by cold spray processes (Koivuluoto et al. 2012; Partovi-Nia et al. 2015). For example, overall dense coating structures of the HPCS Cu coatings, having a similar open-cell potential behavior with corresponding bulk material, have been presented (Koivuluoto et al. 2012). The coatings remained

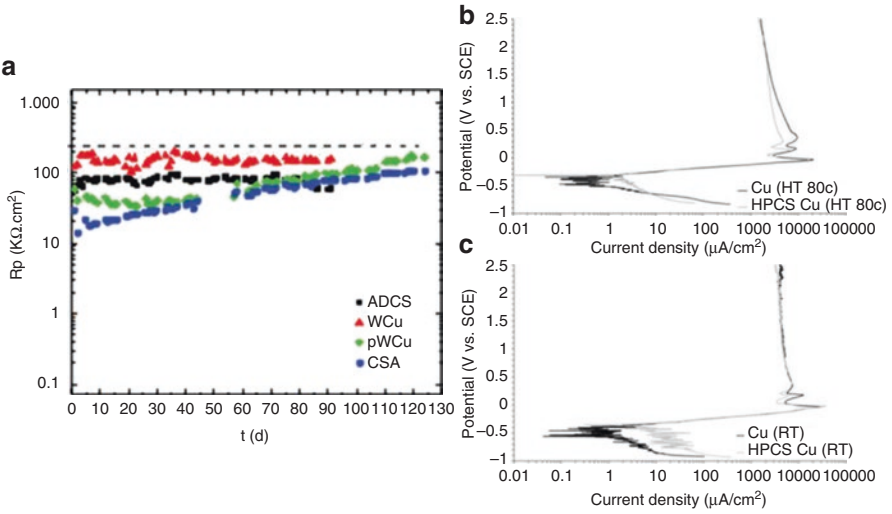

Fig. 13.4 Corrosion behavior of cold-sprayed Cu coatings: (**a**) polarization resistance for wrought Cu (WCu and pWCu (polished)) and cold-sprayed ADCS (as-sprayed) and CSA (heat-treated and polished) Cu coatings in 3.0 mol/L NaCl (Modified Partovi-Nia et al. (2015)), (**b**) polarization behavior of heat-treated HPCS Cu coating and Cu bulk material in 3.5% NaCl and (**c**) polarization behavior of as-sprayed HPCS Cu coating and Cu bulk material in 3.5% NaCl. (Modified Koivuluoto et al. (2012))

stable in the long-time exposure, indicating their structural durability (Koivuluoto et al. 2010b). The open-cell potential measurements and salt spray tests showed that the LPCS Cu and Cu + Al_2O_3 coatings contained through-porosity in their structures. Open-cell potentials of the coatings were close to the values of Fe52 substrate material (Koivuluoto et al. 2008; Koivuluoto and Vuoristo 2010a). Regardless, in the cold spray process, powder type and composition had strong influence on the denseness of the coatings. Denseness of the coatings was improved with Al_2O_3 particle addition. Optimal composition of metallic and ceramic particles in the powder mixture depends on sprayed material combination and powder type of metallic particles (Koivuluoto and Vuoristo 2010a).

13.3.2 Cold-Sprayed Ni and Ni Alloy Coatings

Nickel and nickel alloys have excellent corrosion, oxidation, and heat resistance, and thus, they are used in the chemical processing, pollution control, power generation, electronic, and aerospace industries (Caron and Staley 1997). In addition, Ni-30Cu alloy (Monel 400) has good corrosion resistance in sulfuric, hydrochloric, phosphoric, and hydrofluoric acids. In Monel alloy, Cu improves corrosion resistance better than pure Ni (Schweitzer 1996). Furthermore, Ni-Cr alloys have high oxidation and corrosion resistance in high temperatures, and therefore, they are used in boilers and electrical furnaces. The suitability of cold-sprayed Ni-50Cr coatings for these conditions has been studied with accelerated hot corrosion tests in molten salt Na_2SO_4–60%V_2O_5 paste (900 °C, 1 h) (Bala et al. 2010a). The cold-sprayed Ni-50Cr coatings had dense and oxygen-free structures, and they showed better corrosion resistance than uncoated boiler steels (Bala et al. 2010a). Furthermore, cold-sprayed Ni-20Cr coating had better corrosion-erosion resistance than uncoated T22 boiler steel substrate (Bala et al. 2012). However, in the comparison between cold-sprayed and HVOF-sprayed Ni-20Cr coatings, HVOF coatings behave better due to the protective surface layer (Bala et al. 2012). Hot corrosion resistance of cold-sprayed Ni-20Cr coating was better than uncoated steel substrate, which is explained by the formation of protective oxides (Bala et al. 2010b). Under actual boiler environment, Bala et al. (2017) have showed that cold-sprayed NiCr, NiCrTiC, and NiCrTiCRe coatings successfully decreased the erosion-corrosion rate of substrate SA 516 steel by 58%, 76%, and 78%, respectively. The cold-sprayed NiCrTiCRe coating provided the highest erosion-corrosion resistance in actual boiler environment. This was speculated to relate to its higher hardness and continuously protective Cr_2O_3 layer on the surface (Bala et al. 2017). Furthermore, cold-sprayed NiCrAlY coating provides the protection to Superni-600 against erosion-corrosion in the medical waste incinerator. Degradation rate of cold-sprayed NiCrAlY coating on Superni-600 heat exchanger tube was 2.8 times lower compared to that of uncoated material. This is due to the formation of even Al_2O_3 layer on the surface (Kalsi et al. 2016).

Nickel-based amorphous coatings with high corrosion resistance were prepared by using kinetic metallization (cold spraying). For example, cold-sprayed NiNbTiZrCoCu coating had extremely low passive current density and wide passive

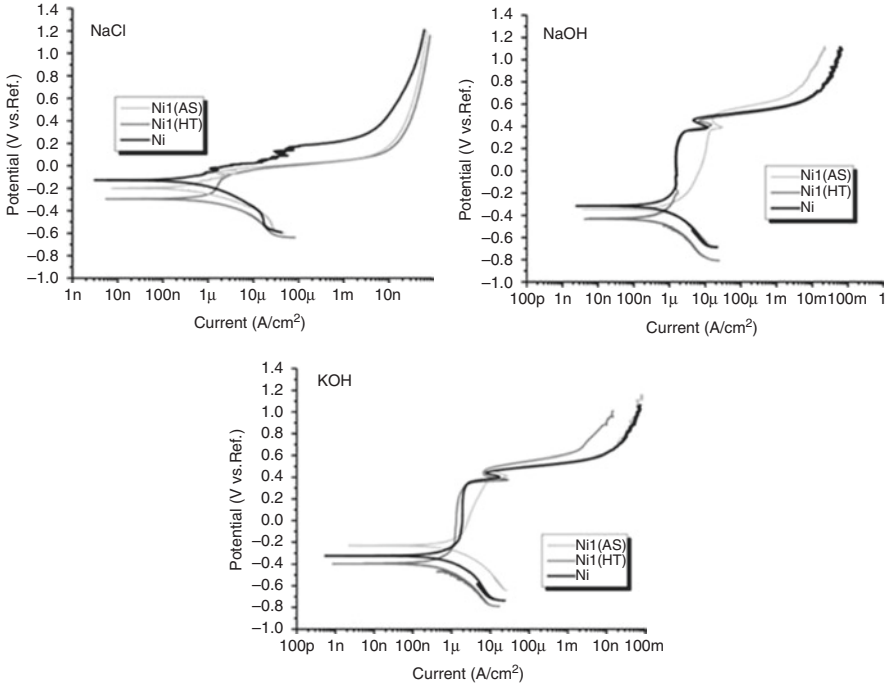

Fig. 13.5 Polarization behavior of as-sprayed and heat-treated cold-sprayed Ni (Ni1) coatings and Ni bulk in 3.5 wt.% NaCl, 1 M NaOH, and 1 M KOH solutions (Modified Koivuluoto et al. (2014))

region, indicating extreme corrosion resistance (Wang et al. 2006). Open-cell potentials of as-sprayed and heat-treated HPCS Ni and Ni-20Cu coatings have been reported to be closer to the bulk materials (Ni and Ni-30Cu) than to the substrate material (Fe52), indicating high coating quality (Koivuluoto and Vuoristo 2010b). The denseness of Ni and Ni-Cu coatings was improved with heat treatments. Heat treatment densified the coating structures due to recovery, recrystallization, and void reduction by the softening and rearrangement of grains (Koivuluoto and Vuoristo 2010b, 2014). Furthermore, corrosion behavior of cold-sprayed Ni coatings both in as-sprayed and heat-treated conditions was comparative to corresponding Ni bulk material in 3.5 wt.% NaCl, 1 M NaOH, and 1 M KOH solutions (Fig. 13.5). This indicates the capability of cold-sprayed Ni coatings acting as corrosion barrier coatings in these conditions. As similar to Fig. 13.6, corrosion behavior of cold-sprayed NiCu and NiCu + Al_2O_3 coatings (as-sprayed and heat-treated) is close to that of NiCu bulk material in seawater solution (Koivuluoto et al. 2014).

The denseness of cold-sprayed coatings can be improved by using optimized spraying parameters (Koivuluoto and Vuoristo 2010b). In addition to that, one way to improve the denseness of the cold-sprayed coatings is to add hard particles into the metallic powder (Koivuluoto and Vuoristo 2009, 2010b; Koivuluoto et al. 2015). As an example, denseness of cold-sprayed NiCu was improved with the addition of Al_2O_3 particles. This behavior was confirmed with 80 h Corrodkote corrosion test. Figure 13.7 presents coating surfaces after 80 h corrosion exposure.

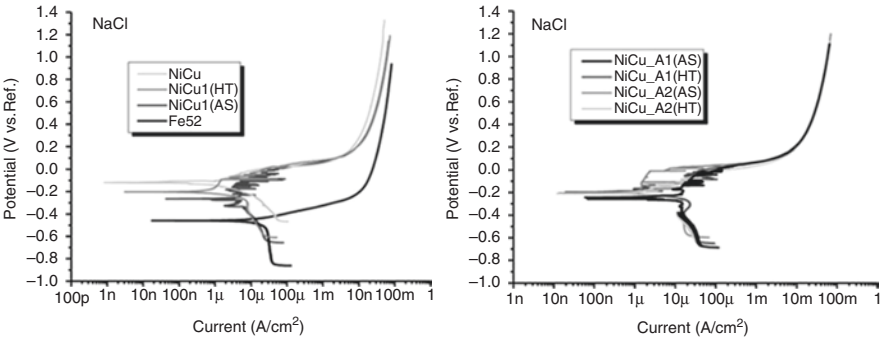

Fig. 13.6 Polarization behavior of as-sprayed and heat-treated cold-sprayed NiCu1 coating, NiCu, and Fe52 bulks and NiCu + Al_2O_3 (NiCu_A1 and NiCu_A2) coatings in 3.5 wt.% NaCl solution (Modified Koivuluoto et al. (2014))

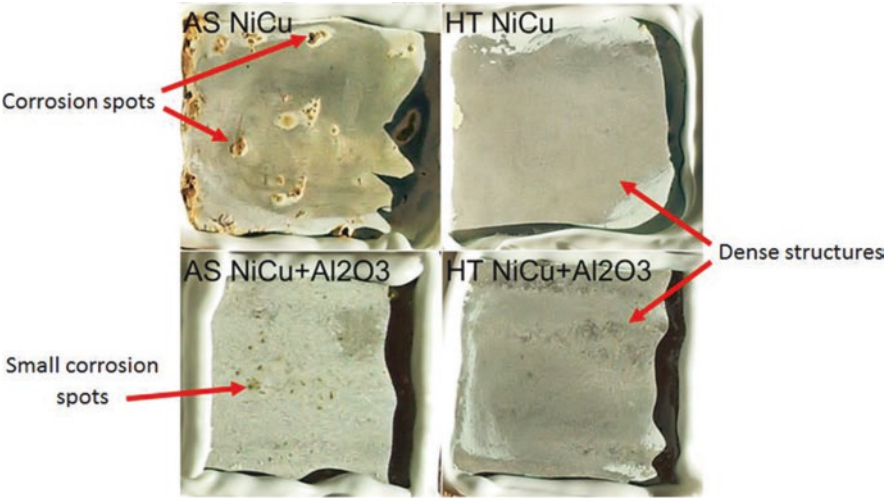

Fig. 13.7 As-sprayed and heat-treated HPCS NiCu and NiCu + Al_2O_3 coating surfaces after 80 h exposure in Corrodkote test (Modified Koivuluoto et al. (2015))

Denser structures were achieved with heat treatment and Al_2O_3 addition. Corrodkote test is 100 times more aggressive test than salt spray fog test, showing very clearly the corrosion protection possibility of the coatings (Koivuluoto et al. 2015).

13.3.3 Cold-Sprayed Ti and Ti Alloy Coatings

Titanium and its alloys have an excellent corrosion resistance in the severe seawater environment, and they have been widely used for the protection of steel structure and are widely used in marine environments (Wang et al. 2007, 2008).

Therefore, cold-sprayed Ti and Ti alloy coatings offer interesting possibilities for corrosion protection. Spray parameters need to be optimized, and cold-sprayed Ti coating sprayed with high pressure and high temperature had the lowest porosity and, thus, better corrosion properties. As-polished Ti coating sprayed with optimized spray parameters showed similar behavior than Ti bulk material. Only, polarization current density was higher caused by differences between densities of coating (Wang et al. 2007, 2008).

Titanium is also used in biomedical applications due to its good corrosion resistance and biocompatibility. Formation of passive titanium dioxide layer on the surface is crucial for corrosion protection. Furthermore, addition of hydroxyapatite (HAP) improves bioactivity. As reported in (Zhou and Mohanty 2012), corrosion resistance of cold-sprayed Ti + 50HAP was better than cold-sprayed Ti + 20HAP. In addition, heat treatment improved corrosion behavior of the Ti + 20HAP coating. Passivation was detected with all coatings and cold-sprayed Ti + 50HAP coating was the most stable (Zhou and Mohanty 2012). Additionally, cold-sprayed Ti coatings were densified by vacuum heat treatment as posttreatment (Hussain et al. 2011). On the other hand, Marrocco et al. (2011) have improved corrosion resistance of cold-sprayed Ti coatings by posttreating the coatings with laser. The top of the coatings were densified and that way interconnected porosity was eliminated. Figure 13.8 shows that posttreated cold-sprayed Ti coatings had similar corrosion resistance that corresponding bulk Ti had showed with the polarization tests. Indeed, the laser-treated cold-sprayed Ti coating performed as corrosion barrier layer and has OCP, E_{corr}, and I_{pp} corrosion values very close to those of bulk titanium (Marrocco et al. 2011).

13.3.4 Cold-Sprayed Ta Coatings

Tantalum has extraordinary corrosion resistance (Cramer and Covino 2005) due to the formation of highly stable passivating layer (Schweitzer 1996). Tantalum resists corrosion effectively in acids (not HF), salts, and organic chemicals even at elevated temperatures (Cramer and Covino 2005). Furthermore, tantalum as a dense coating acts like corrosion barrier coating on a steel substrate, providing high corrosion resistance in many environments (Jones 1996).

Cold-sprayed Ta coatings are fully dense (Koivuluoto et al. 2009a, b, 2010a), and they can be serve as corrosion barrier layers. For instance, Ta bulk material and dense HPCS Ta coating have been passivated rapidly, and above their passivation potential, corrosion rate falls to very low value in the passive area due to the stable passive layer (Jones 1996). Cold-sprayed Ta coatings and Ta bulk material had similar corrosion characteristics in NaCl and H_2SO_4 solutions at 22 °C and at 80 °C (Koivuluoto et al. 2009a). Due to the fact that dense HPCS Ta coatings behaved like the bulk material, real corrosion resistance of the coatings is reality and can be produced by using cold spray processes. In addition, the electrochemical tests in 1 M KOH solution revealed stable passive behavior of the HPCS Ta coatings due to the fully dense coating

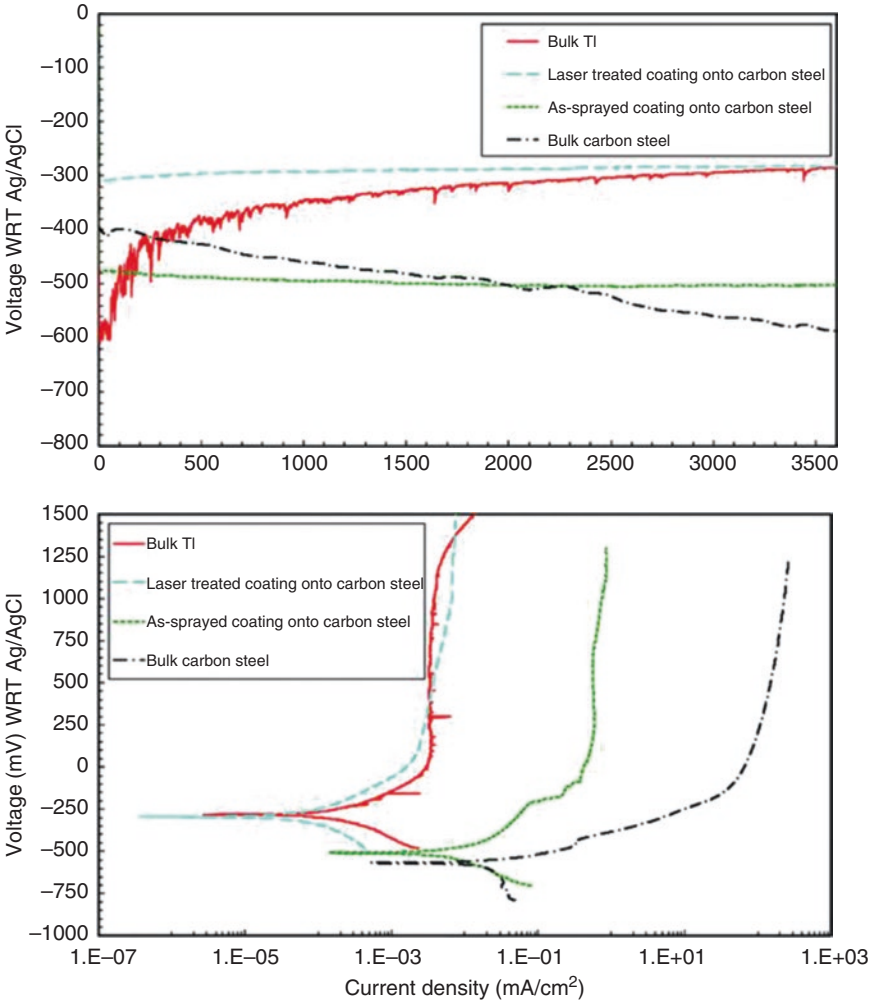

Fig. 13.8 Open circuit potential (OCP) and potentiodynamic polarization scans of bulk Ti, carbon steel, as-sprayed cold-sprayed Ti coating (on carbon steel), and laser-treated cold-sprayed Ti coating in aerated 3.5% NaCl (Marrocco et al. 2011)

structures. Figure 13.9a shows similar anodic corrosion behavior of Ta bulk and cold-sprayed Ta coatings on different substrates (CSTa1 on Al, CSTa2 on Cu, and CSTa3 on steel). In addition, etched cross sections of CS Ta and IPS Ta coatings after hot corrosion/oxidation are presented in Fig. 13.9b. CS Ta coating is fully dense with no through-porosity; the original homogeneous fine-grained structure of the steel substrate was unaltered under the coating after hot corrosion/oxidation testing. By contrast, the IPS Ta coating contains defects, and therefore, air and corrosive salts can penetrate down to the steel substrate, which undergoes remarkable microstructural alterations (grain coarsening) (Koivuluoto et al. 2010a).

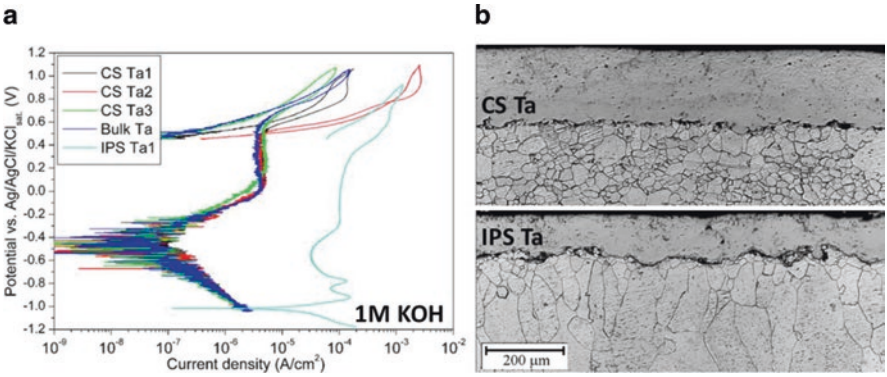

Fig. 13.9 Polarization behavior of cold-sprayed and inert-plasma-sprayed Ta coatings (**a**) CS Ta1 on Al, CS Ta2 on Cu, CS Ta3 on steel substrates, Ta bulk material, and IPS Ta1 (inert-plasma-sprayed) coatings in 1 M KOH and (**b**) OM micrographs of the etched cross section of CS Ta3 and IPS Ta1 coatings after hot corrosion/oxidation testing (Modified Koivuluoto et al. (2010a))

13.3.5 Cold-Sprayed Stainless Steel and Hard Metal Coatings

It is possible to produce protective stainless steel coatings by cold spraying. For instance, cold-sprayed stainless steel coatings sprayed with optimized powder properties had similar polarization behavior with corresponding bulk material. Spencer and Zhang (2011) have showed the highest corrosion resistance of cold-sprayed stainless steel coating sprayed with mixed powders (mixing of two particle sizes: −10 and −22 µm). Figure 13.10a presents polarization behavior of cold-sprayed stainless steel coatings compared to that of bulk material. For the optimization, two 316 L powders with different particle size distributions were mixed and cold-sprayed on the substrate. This, in turn, improved the corrosion resistance of coating being close to that of bulk material (Spencer and Zhang 2011). Corrosion properties were also detected to coating thickness and coating with higher thickness showed higher corrosion resistance analyzed by polarization behavior (Fig. 13.10b) (Spencer and Zhang 2011). Furthermore, surface finishing has seed to affect corrosion properties. Coatings with polished surfaces had higher corrosion resistance than as-sprayed coatings with certain roughness. The rough outer layer including small pores has been removed by polishing treatment, leading to the considerable improvement of corrosion resistance (Wang et al. 2008).

Additionally, AL-Mangour et al. (2013) have cold-sprayed stainless steel (SS) mixed with Co-Cr particles. Stainless steels and Co-Cr alloys due to their high corrosion resistance have used in medical applications, and thus, there is high interest of produce corrosion-resistant coatings from these compositions. Porosity was reduced by optimizing composition of the composite (33%Co-Cr) and by heat-treating the coatings. Improvement of the corrosion resistance was detected with the polarization behavior. Composite coatings had lower corrosion rate compared with pure stainless steel coatings (Fig. 13.11). In addition, cold-sprayed SS + 33%Co-Cr coating had

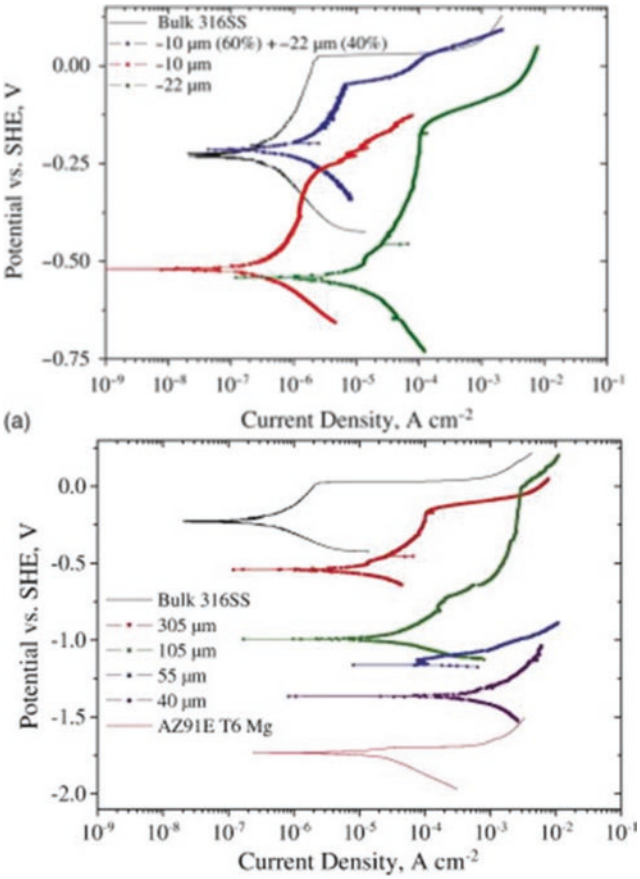

Fig. 13.10 Anodic polarization behavior of cold-sprayed 316 stainless steel coatings (**a**) using different powder particle sizes and (**b**) with different thicknesses compared to bulk type 316SS and AZ91E T6 substrate material. Coatings were sprayed using −22 μm powder (Modified Spencer and Zhang (2011))

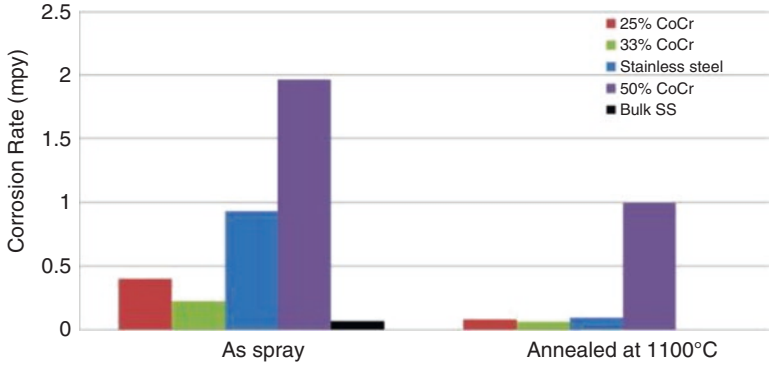

Fig. 13.11 Corrosion rate of as-sprayed and heat-treated cold-sprayed SS and SS + CoCr coatings (AL-Mangour et al. 2013)

corrosion rate very close to bulk stainless steel, indicating potential to use in medical implants (AL-Mangour et al. 2013). Similarly, Dosta et al. (2013) have studied corrosion properties of cold-sprayed WC-25Co coatings. Dense hard metal coatings were produced, and any sign of corrosion was not detected in the coatings after electrochemical studies in NaCl solutions (Dosta et al. 2013).

13.4 Cathodic Protection by Cold-Sprayed Coatings

Corrosion behavior of cold-sprayed coatings is increasingly reported in the literature during the last years. Most of these studies are concentrated on the corrosion protection of coatings which give cathodic protection based on sacrificial behavior, e.g., Zn, Al, and Al-based composites (Maev and Leshchynsky 2006; Champagne 2007; Karthikeyan et al. 2004; Blose et al. 2005; Xiong et al. 2009; Kroemmer and Heinrich 2006; Chavan et al. 2013; Bu et al. 2012; DeForce et al. 2011; Spencer et al. 2009; Dzhurinskiy et al. 2012). For example, Blose et al. (2005) have presented the successful corrosion protection of steel substrates with cold-sprayed Zn, Al, and Zn-Al coatings against wet corrosion. Also, Karthikeyan et al. (2004) have shown that corrosion resistance of the cold-sprayed Al coatings was higher than that of Al bulk material analyzed using polarization measurements. Furthermore, cold-sprayed Al coating on Mg alloy substrate had dense structure and, due to that, sufficient corrosion protection in NaCl solution (Tao et al. 2010; Diab et al. 2017). One of the most popular Mg casting alloys is AZ91D alloy due to its relative high fatigue strength (Song et al. 1999). However, corrosion commonly causes deterioration of fatigue property for AZ91D alloy. Therefore, it is important to prevent AZ91D alloy from corrosion attack by cold-sprayed coatings. Reportedly, cold-sprayed Al-based coatings on Mg alloy have shown high corrosion resistance (Spencer et al. 2009; Tao et al. 2009).

Aluminum and magnesium alloys are widely used in aircraft industry due to their low weight. Especially, in Mg alloys, pitting corrosion is general but can be eliminated by using cold-sprayed coatings (Nooririnah et al. 2012). The use of the cold spray process to deposit commercially pure aluminum for providing dimensional restoration and protection to magnesium has been developed by the US Army Research Laboratory Center for Cold Spray Technology (Champagne 2007; Champagne and Helfritch 2016). As an example, cold-sprayed Al coating gives corrosion protection to Mg substrate studied by salt spray exposure. Figure 13.12 shows coating behavior compared to substrate material in salt spray test. No corrosion of CS Al coating was detected (Champagne and Helfritch 2016).

Cold-sprayed Al- and Zn-based coatings give cathodic protection to Mg-alloy substrate. Interestingly, the corrosion rate in AZ31 Mg-alloy joints is significantly reduced by using LPCS 75Ni–25Zn and 60Ni–20Zn–20Al_2O_3 coatings. Additionally, these coating compositions show considerably higher protection from corrosion of NaCl solution as compared to pure Al coatings (Fig. 13.13) (Dzhurinskiy et al. 2015).

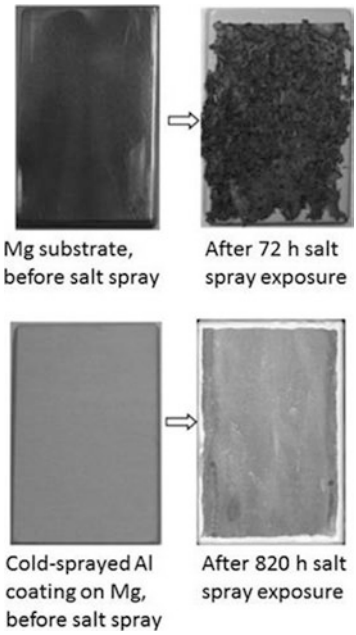

Fig. 13.12 Salt spray testing. Mg substrate before and after 72 h exposure and cold-sprayed Al coating on Mg substrate before and after 820 h exposure (Modified after Champagne and Helfritch (2016))

The cold-sprayed Al + Al_2O_3 coatings had improved anticorrosion properties compared with Al bulk material (Xiong et al. 2009; Spencer et al. 2009). Generally speaking, cold-sprayed Al and Al alloy/composite coatings can be applied to protect metal surface from atmospheric degradation, e.g., in seawater conditions (Balani et al. 2005; Villafuerte et al. 2009). This is caused by formation of thin oxide layer on the Al surface. This, in turn, is beneficial in repairs and be a cost-effective and fast solution instead of replacing structure (Balani et al. 2005; Jones et al. 2011). In addition, dense cold-sprayed Al coating has shown to protect sintered NdFeB magnets for the corrosion (Ma et al. 2014), whereas dense structures and good corrosion resistances of LPCS Al, Al + Al_2O_3, and Al + Zn + Al_2O_3 coatings have been also achieved by Dzhurinskiy et al. (2012). Addition of hard particles to the powder mixture has three main functions: (i) to keep the nozzle clean (eliminate nozzle clogging), (ii) to activate the sprayed surface, and (iii) to hammer the coating structure (densification) (Koivuluoto et al. 2008). In the other study, denseness of cold-sprayed Al coatings was improved by using Al + $Mg_{17}Al_{12}$ blended powders. Addition of hard intermetallic particles decreased porosity and improved corrosion resistance. Behavior of the coatings is closer to the Al bulk, reflecting corrosion protection behavior over substrate material (Bu et al. 2012). Also, corrosion properties of cold-sprayed Al-5 Mg coatings have been studied (Spencer et al. 2009). Coatings behave very well in corrosion study and after 1000 h exposure in salt spray test, and there was not any sign of Mg corrosion observed on the coating surfaces. In addition, coating had minimal galvanic reaction coupled with Mg, indicating galvanic compatibility (Spencer et al. 2009).

Zinc coatings are widely used as corrosion protection of steel components in aqueous and marine environments. Zinc gives sacrificial protection over steel due to its more negative corrosion potential. Chavan et al. (2013) have studied polarization

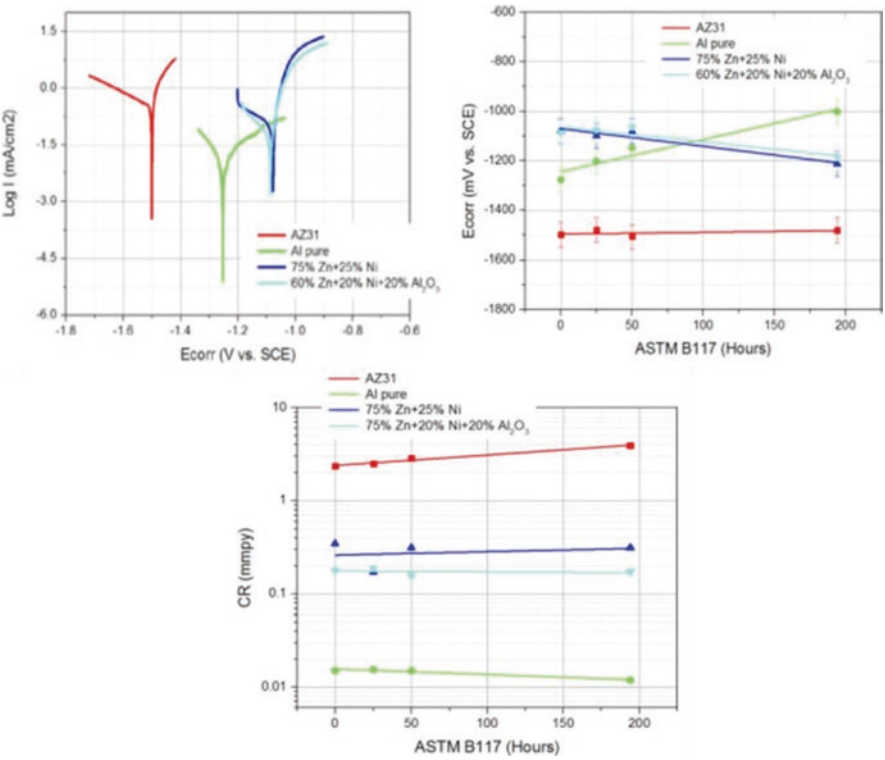

Fig. 13.13 Corrosion behavior of LPCS Al, Zn + Ni, and Zn + Ni + Al_2O_3 coatings and AZ31 substrate material exposed in salt fog corrosion environment (Modified Dzhurinskiy et al. (2015))

behavior of as-sprayed and heat-treated cold-sprayed Zn coatings in 3.5%NaCl solution. Lifetime of coatings was increased as sacrificial coating due to that as-sprayed and heat-treated cold-sprayed Zn coatings formed protective passive layer, which improved corrosion resistance of Zn coatings. Furthermore, heat-treated Zn coating had reduced corrosion current density, indicating its longer corrosion protection (Chavan et al. 2013).

13.5 Corrosion Resistance Improvements by Assisting Processes

As stated, cold spraying enables to produce corrosion resistant coatings. However, sometimes there is still some porosity in the coating structures. This, in turn, can be diminished by using laser-assisted cold spray processes or by posttreatments, e.g., annealing (Koivuluoto and Vuoristo 2010b, 2014; Zhou and Mohanty 2012). The hybrid processes connect the benefits of the cold spraying as solid-state process and softening by laser. This assists higher particle deformation, which in turn

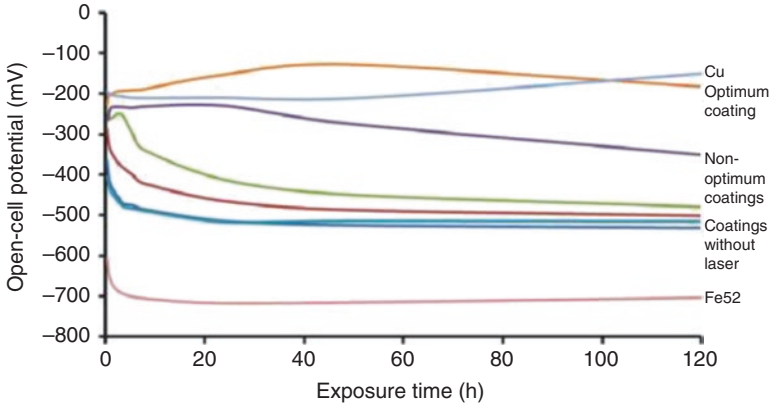

Fig. 13.14 Open-cell potential of LACS CuSn coatings, Cu, and Fe52 bulk materials in 3.5% NaCl solutions (Allen et al. 2015)

improves denseness of the coating and adhesion between particles (Kulmala and Vuoristo 2008; Allen et al. 2015; Olakanmi and Doyoyo 2014). As showed earlier, laser posttreatment improved corrosion behavior of CS Ti coatings (Marrocco et al. 2011). In addition to posttreatments, laser-assisted cold spraying has shown the improvements of corrosion properties of low-pressure cold-sprayed Cu coatings (Kulmala and Vuoristo 2008) and high-pressure cold-sprayed CuSn coatings (Fig. 13.14) (Allen et al. 2015) by forming the fully dense coating structures.

One way to improve coating quality is to use a novel in situ shot peening (SP)-assisted cold spraying. Plastic deformation can be significantly enhanced by using SP particles with spray powder. As the SP particle content increases to 60 vol.%, the Al606l coating prepared by the novel process reveals a completely dense microstructure of Al6061 coating which was achieved while spraying with 60 vol.% SP particles. In this case, also corrosion properties were good, and coating on AZ31B alloy showed similar open-circuit potential and dynamic polarization behavior than Al6061 bulk material as presented in Fig. 13.15. This, in turn, reflects high corrosion protection (Wei et al. 2017).

13.6 Conclusions

Summing up, cold spraying has shown its potential for corrosion protection. Coatings with anodic or cathodic protection can be manufactured by using several cold spray processes. Denseness of the coatings is crucial in anodic protection. With optimized spray parameters and powders together with posttreatments, it makes producing fully dense coatings from different materials, e.g., Cu, Ta, Ti, and Ni-based coatings possible. In the cathodic protection, denseness is not so critical due to the sacrificial behavior of the coatings. Therefore, there can be some porosity in the structures. Cold-sprayed Al- and Zn-based coatings have shown good corrosion properties and

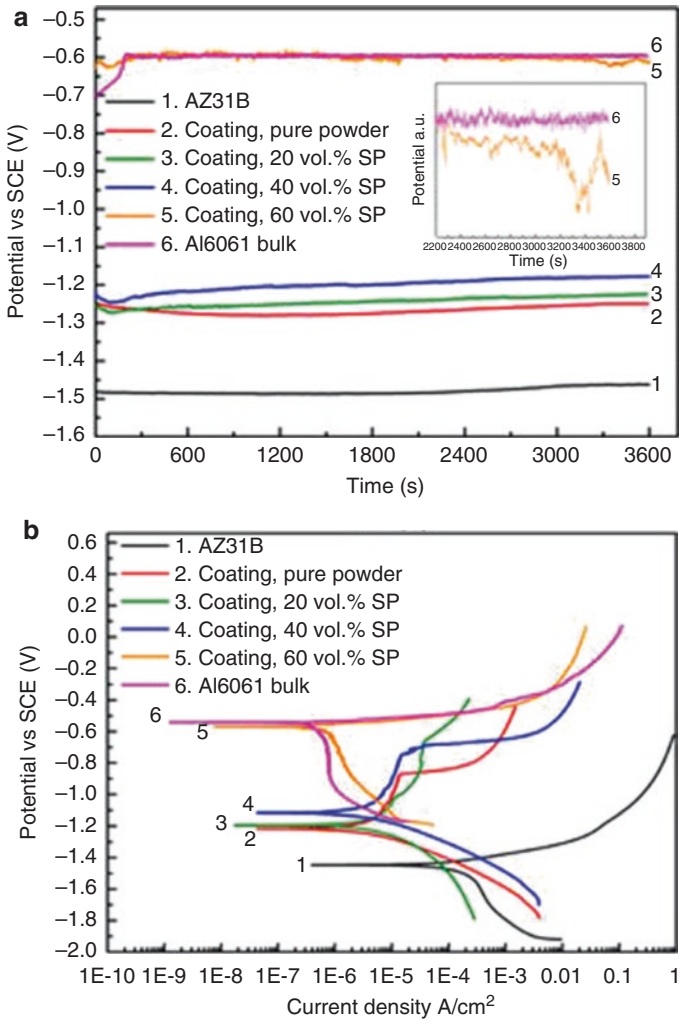

Fig. 13.15 AZ31B and Al606l bulk materials and CS Al6061 coating with SP particles (**a**) open-circuit potential and (**b**) potentiodynamic polarization behavior (Wei et al. 2017)

can act as corrosion barrier coatings. In addition to corrosion resistance itself, corrosion damages can be repaired with highly corrosion resistant materials by using cold spraying, and this way, lifetime of components will be improved.

References

Allen C, Marrocco T, McNutt P, Koivuluoto H, Latokartano J, Vuoristo P, Olsson R (2015) A novel coaxially laser-assisted (COLA) cold spray system, ITSC2015: International Thermal Spray Conference, 11–14 May 2015, Long Beach, California, USA, pp 210–216

AL-Mangour B, Mongrain R, Irissou E, Yue S (2013) Improving the strength and corrosion resistance of 316L stainless steel for biomedical applications using cold spray. Surf Coat Technol 216:297–307

Baboian R (2003) Galvanic corrosion, corrosion: fundamentals, testing, and protection, ASM handbook, 13A, pp 210–213

Bala N, Singh H, Prakash S (2010a) Accelerated hot corrosion studies of cold spray Ni–50Cr coating on boiler steels. Mater Des 31:244–253

Bala N, Singh H, Prakash S (2010b) High temperature corrosion behavior of cold spray Ni-20Cr coating on boiler steel in molten salt environment at 900 °C. J Therm Spray Technol 19(1–2):110–118

Bala N, Singh H, Prakash S, Karthikeyan J (2012) Investigations on the behavior of HVOF and cold sprayed Ni-20Cr coating on T22 boiler steel in actual boiler environment. J Therm Spray Technol 21(1):144–158

Bala N, Singh H, Karthikeyan J, Prakash S (2014) Cold spray coating process for corrosion protection: a review. Surf Eng 30(6):414–421

Bala N, Singh H, Prakash S (2017) Performance of cold sprayed Ni based coatings in actual boiler environment. Surf Coat Technol 318:50–61

Balani K, Laha T, Agarwal A, Karthikeyan J, Munroe N (2005) Effect of carrier gases on microstructural and electrochemical behavior of cold-sprayed 1100 aluminum coating. Surf Coat Technol 195:272–279

Blose R, Vasquez D, Kratochvil W (2005) Metal passivation to resist corrosion using the cold spray process, thermal spray 2005: explore its surfacing potential!, 2–4 May 2005, Basel, Switzerland, pp 126–134

Bu H, Yandouzi M, Lu C, MacDonald D, Jodoin B (2012) Cold spray blended Al + $Mg_{17}Al_{12}$ coating for corrosion protection of AZ91D magnesium alloy. Surf Coat Technol 207:155–162

Caron RN, Staley JT (1997) Effects of composition, processing, and structure on properties of nonferrous alloys, materials selection and design, ASM handbook, 20, pp 383–415

Champagne V (ed) (2007) The cold spray materials deposition process: fundamentals and applications. Woodhead Publishing Ltd., Cambridge, 362 p

Champagne V, Helfritch D (2016) The unique abilities of cold spray deposition. Int Mater Rev 61(7):437–455

Chatterjee U, Bose S, Roy S (2001) Environmental degradation of metals. Marcel Dekker Inc, New York

Chavan NM, Kiran B, Jyothirmayi A, Sudharshan Phani P, Sundararajan G (2013) The corrosion behavior of cold sprayed zinc coatings on mild steel substrate. J Therm Spray Technol 22(4):463–470

Cramer SD, Covino Jr BS (eds) (2005) Corrosion of Tantalum and Tantalum alloys, corrosion: materials, ASM handbook, 13B, pp 337–353

DeForce BS, Eden TJ, Potter JK (2011) Cold spray Al-5% Mg coatings for the corrosion protection of magnesium alloys. J Therm Spray Technol 20(6):1352–1358

Diab M, Pang X, Jahed H (2017) The effect of pure aluminum cold spray coating on corrosion and corrosion fatigue of magnesium (3% Al-1% Zn) extrusion. Surf Coat Technol 309:423–435

Dosta S, Couto M, Guilemany JM (2013) Cold spray deposition of a WC-25Co cermet onto Al7075-T6 and carbon steel substrates. Acta Mater 61:643–652

Dzhurinskiy D, Maeva E, Ev L, Maev RG (2012) Corrosion protection of light alloys using low pressure cold spray. J Therm Spray Technol 21(2):304–313

Dzhurinskiy D, Leshchinsky V, Strumban E, Maeva E, Maev RG (2015) Protective coatings for mechanical aluminum–magnesium joints. Surf Eng 31(10):740–746

Frankel G (2003) Pitting corrosion, corrosion: fundamentals, testing, and protection, ASM handbook, 13A, pp 236–241

Hassani-Gangaraj SM, Moridi A, Guagliano M (2015) Critical review of corrosion protection by cold spray coatings. Surf Eng 31(11):803–815

Hussain T, McCartney DG, Shipway PH, Marrocco T (2011) Corrosion behavior of cold sprayed titanium coatings and free standing deposits. J Therm Spray Technol 20:1–2, 260–274 (Hussain et al. 2011)

Jones D (1996) Principles and prevention of corrosion. Prentice-Hall, Upper Saddle River

Jones R, Matthews N, Rodopoulos CA, Cairns K, Pitt S (2011) On the use of supersonic particle deposition to restore the structural integrity of damaged aircraft structures. Int J Fatigue 33(9):1257–1267

Kalsi SS, Sidhu TS, Singh H, Karthikeyan J (2016) Behavior of cold spray coating in real incineration environment. Mater Manuf Process 31(11):1468–1475

Karthikeyan J, Laha T, Balani K, Agarwal A, Munroe N (2004) Microstructural and electrochemical characterization of cold-sprayed 1100 aluminum coating, thermal spray 2004: advances in technology and application, 10–12 May 2004, Osaka, Japan, pp 241–246

Kelly R (2003) Crevice corrosion, corrosion: fundamentals, testing, and protection, ASM handbook, 13A, pp 242–247

Koivuluoto H (2010) Microstructural characteristics and corrosion properties of cold-sprayed coatings. Doctoral thesis, Tampere University of Technology, Tampere, p 153

Koivuluoto H, Vuoristo P (2009) Effect of ceramic particles on properties of cold-sprayed Ni-20Cr+Al2O3 coatings. J Therm Spray Technol 18(4):555–562

Koivuluoto H, Vuoristo P (2010a) Effect of powder type and composition on structure and mechanical properties of Cu+Al_2O_3 coatings prepared by using low-pressure cold spray process. J Therm Spray Technol 19(5):1081–1092

Koivuluoto H, Vuoristo P (2010b) Structural analysis of cold-sprayed nickel-based metallic and metallic-ceramic coatings. J Therm Spray Technol 19(5):975–989

Koivuluoto H, Vuoristo P (2014) Structure and corrosion properties of cold sprayed coatings: a review. Surf Eng 30:404–414

Koivuluoto H, Lagerbom J, Kylmälahti M, Vuoristo P (2008) Microstructure and mechanical properties of low-pressure cold-sprayed coatings. J Therm Spray Technol 17(5–6):721–727

Koivuluoto H, Näkki J, Vuoristo P (2009a) Corrosion properties of cold-sprayed tantalum coatings. J Therm Spray Technol 18(1):75–82

Koivuluoto H, Näkki J, Vuoristo P (2009b) Structure and corrosion behavior of cold-sprayed tantalum coatings, thermal spray 2009: expanding thermal spray performance to new markets and applications. In: Marple B, Hyland M, Lau YC, Li CJ, Lima R, Montavon G (eds) ASM International, 4–7 May 2009, Las Vegas, Nevada, USA, pp 314–319

Koivuluoto H, Bolelli G, Lusvarghi L, Casadei F, Vuoristo P (2010a) Corrosion resistance of cold-sprayed Ta coatings in very aggressive conditions. Surf Coat Technol 205(4):1103–1107

Koivuluoto H, Honkanen M, Vuoristo P (2010b) Cold-sprayed copper and tantalum coatings – detailed FESEM and TEM analysis. Surf Coat Technol 204(15):2353–2361

Koivuluoto H, Coleman A, Murray K, Kearns M, Vuoristo P (2012) High-pressure cold sprayed (HPCS) and low pressure cold sprayed (LPCS) coatings prepared from OFHC Cu feedstock – overview from powder characteristics to coating properties. J Therm Spray Technol 21(5):1065–1075

Koivuluoto H, Milanti A, Bolelli G, Lusvarghi L, Vuoristo P (2014) High-pressure cold-sprayed Ni and Ni-Cu coatings: improved structures and corrosion properties. J Therm Spray Technol 23(1):98–103

Koivuluoto H, Bolelli G, Milanti A, Lusvarghi L, Vuoristo P (2015) Microstructural analysis of high-pressure cold-sprayed Ni, NiCu and NiCu+Al_2O_3 coatings. Surf Coat Technol 268:224–229

Kroemmer W, Heinrich P (2006) Cold spraying – potential and new application ideas, thermal spray 2006: pushing the envelope of materials performance. ASM International, 15–18 May 2006, Seattle, USA

Kruger J (2003) Passivity, corrosion: fundamentals, testing, and protection. ASM Handbook, vol 13A. ASM International, Materials Park, pp 61–67

Kulmala M, Vuoristo P (2008) Influence of process conditions in laser-assisted low-pressure cold spraying. Surf Coat Technol 202(18):4503–4508

Ma C, Liu X, Zhou C (2014) Cold-sprayed Al coating for corrosion protection of Sintered NdFeB. J Therm Spray Technol 23(3):456–462

Maev R, Leshchynsky V (2006) Air gas dynamic spraying of powder mixtures: theory and application. J Therm Spray Technol 15(2):198–205

Marrocco T, Hussain T, McCartney DG, Shipway PH (2011) Corrosion performance of laser posttreated cold sprayed titanium coatings. J Therm Spray Technol 20(4):909–917

Nooririnah O, Rohana A, Nazrul HN, Suhana M (2012) Supersonic particle deposition as potential corrosion treatment method for helicopter part in Malaysia. Int J Adv Res Eng Technol 3(2):275–279

Olakanmi EO, Doyoyo M (2014) Laser-assisted cold-sprayed corrosion- and wear-resistant coatings: a review. J Therm Spray Technol 23(5):765–785

Papyrin A, Kosarev V, Klinkov S, Alkimov A, Fomin V (eds) (2007) Cold spray technology, 1st edn. Elsevier, Amsterdam, 328 p

Partovi-Nia R, Ramamurthy S, Zagidulin D, Chen J, Jacklin R, Keech P, Shoesmith DW (2015) Corrosion of cold spray deposited copper coating on steel substrates. Corrosion 71(10):1237–1247

Schweitzer PA (ed) (1996) Corrosion engineering handbook. Marcel Dekker, Inc., NY, USA

Song GL, Atrens A, Dargusch M (1999) Influence of microstructure on the corrosion of diecast AZ91D. Corros Sci 41:249–273

Spencer K, Zhang M-X (2011) Optimisation of stainless steel cold spray coatings using mixed particle size distributions. Surf Coat Technol 205:5153–5140

Spencer K, Fabijanic DM, Zhang M-X (2009) The use of Al–Al_2O_3 cold spray coatings to improve the surface properties of magnesium alloys. Surf Coat Technol 204:336–344

Talbot D, Talbot J (1998) Corrosion science and technology. CRC Press LLC, Boca Raton

Tao YS, Xiong TY, Sun C, Jin HZ, Du H, Li TF (2009) Effect of alpha-Al_2O_3 on the properties of cold sprayed Al/alpha-Al2O3 composite coatings on AZ91D magnesium alloy. Appl Surf Sci 256:261–266

Tao Y, Xiong T, Sun C, Kong L, Cui X, Li T, Song G-L (2010) Microstructure and corrosion performance of a cold sprayed aluminium coating on AZ91D magnesium alloy. Corros Sci 52:3191–3197

Vardelle A, Moreau C, Akedo J, Ashrafizadeh H, Berndt CC, Oberste Berghaus J, Boulos M, Brogan J, Bourtsalas AC, Dolatabadi A, Dorfman M, Eden TJ, Fauchais P, Fisher G, Gaertner F, Gindrat M, Henne R, Hyland M, Irissou E, Jordan EH, Aik Khor K, Killinger A, Lau YC, Li CJ, Li L, Longtin J, Markocsan N, Masset PJ, Matejicek J, Mauer G, McDonald A, Mostaghimi J, Sampath S, Schiller G, Shinoda K, Smith MF, Ansar Syed A, Themelis NJ, Toma FL, Trelles JP, Vassen R, Vuoristo P (2016) The 2016 thermal spray roadmap. J Therm Spray Technol 25(8):1376–1440

Villafuerte J (ed) (2015) Modern cold spray – materials, process, and applications. Springer International Publishing, Cham, p 429

Villafuerte J, Dzhurinskiy D, Ramirez R, Maeva E, Leshchynsky V, Maev R (2009) Corrosion behavior and microstructure of the Al-Al_2O_3 coatings produced by low pressure cold spraying, thermal spray 2009: expanding thermal spray performance to new markets and applications. In: Marple B, Hyland M, Lau YC, Li CJ, Lima R, Montavon E (eds) May 4–7. ASM International, Las Vegas, Nevada, USA, pp 908–913

Vreijling M (1998) Electrochemical characterization of metallic thermally sprayed coatings, printed in the Netherlands, p 143

Wang AP, Zhang T, Wang JQ (2006) Ni-based fully amorphous metallic coating with high corrosion resistance. Philos Mag Lett 86(1):5–11

Wang H-R, Li W-Y, Ma L, Wang J, Wang Q (2007) Corrosion behavior of cold sprayed titanium protective coating on 1Cr13 substrate in seawater. Surf Coat Technol 201:5203–5206

Wang H-R, Hou B-R, Wang J, Li W-Y (2008) Effect of process conditions on microstructure and corrosion resistance of cold-sprayed Ti coatings. J Therm Spray Technol 17(5–6):736–741

Wei Y-K, Luo X-T, Li C-X, Li C-J (2017) Optimization of in-situ shot-peening-assisted cold spraying parameters for full corrosion protection of Mg alloy by fully dense Al-based alloy coating. J Therm Spray Technol 26:173–183

Xiong T, Tao Y, Sun C, Jin H, Du H, Li T (2009) Study on corrosion behavior of cold sprayed Al/α-Al_2O_3 deposit on AZ91D alloy, thermal spray 2009: expanding thermal spray performance to new markets and applications. In: Marple B, Hyland M, Lau YC, Li CJ, Lima R, Montavon G (eds) May 4–7. ASM International, Las Vegas, Nevada, USA, pp 669–672

Zhou X, Mohanty P (2012) Electrochemical behavior of cold sprayed hydroxyapatite/titanium composite in Hanks´ solution. Electrochim Acta 65:134–140

Chapter 14
High Temperature Oxidation Performance of Cold Spray Coatings

Lingyan Kong

14.1 Introduction

Cold spray technique has been developed widely in recent years. The main distinguishing feature of cold spray compared with conventional thermal spray processes is the ability to produce coatings while maintaining the particles in solid state. Therefore, the coatings prepared by cold spray usually have low porosity, low oxidation, and low residual stress (Victor 2007). Nowadays, a great variety of powders could be deposited by cold spray, such as Ni-20Cr (Niraj et al. 2010; Kaur et al. 2015), CoNiCrAlY (Chen et al. 2011; Lima et al. 2015), Cr_3C_2/NiCr (Wolfe and Eden 2007), TiO_2 (Yang et al. 2008; Yamada et al. 2010), and WO_3/Y_2O_3 (Lee et al. 2004), except those metal powders of high ductility which have been well studied. However, cold spray coatings are still seeking their ways for wide applications. For those well-studied coatings such as aluminum coating, which has shown great advantage in corrosion resistance (Berti et al. 2002), their applications for low-temperature corrosion protection are mainly hindered by the economical inferiority compared to other alternative coating technologies, as well as the disadvantage for application on complex structure components under certain conditions. MCrAlY (Chen et al. 2011; Lima et al. 2015) coatings were prepared by cold spray recently for hot corrosion or for high-temperature oxidation combined with thermal barrier coating (TBC). Nevertheless, much effort is still needed to explore new applications for cold-sprayed coatings for high-temperature protection.

As we can see, the γ-TiAl-based alloys are promising lightweight materials in the future advanced aeroengines (Kothari et al. 2012). However, experimental evidence

L. Kong (✉)
Surface Engineering Division, Institute of Metal Research,
Chinese Academy of Sciences, Shenyang, China
e-mail: lykong@imr.ac.cn

P. Cavaliere (ed.), *Cold-Spray Coatings*,
https://doi.org/10.1007/978-3-319-67183-3_14

has shown that γ-TiAl-based alloys with aluminum content less than 25 at. % suffered from poor high temperature oxidation resistance and interstitial embrittlement (Rahmel et al. 1995; Pflumm et al. 2015). Therefore, they must be protected for application at elevated temperatures.

Usually protective coatings are expected to provide effective protections without significant negative influence on the mechanical properties of the matrix. Several coating systems were applied onto the titanium-based alloys. Xu et al.(2014) reported a NiCrAlY coating with and without Al interlayer. Zhang et al. (2012) reported the superior long-term oxidation resistance of a Ni-Al-coated TiAl alloy. It has been found that the Ni element in these types of coatings would suffer from great interdiffusion with the γ-TiAl substrate. The TiAlCr/TiAlCrY was also found to have the same problem (Braun et al. 2013). Ceramic composite coatings were also studied by many research groups. Gao et al. (2012) reported the oxidation behavior of γ-TiAl-based alloy with an Al_2O_3-Y_2O_3composite coating. Zeng et al. (2015) studied the performance of ZrO_2-8wt.% Y_2O_3 coating on γ-TiAl. Nitride coatings were also studied for the oxidation protection on γ-TiAl (Braun et al. 2010). $TiAl_3$ intermetallic as a potential oxidation resistance coating for γ-TiAl substrate also attracted great interests, for the thermal expansion coefficient of $TiAl_3$(15 × 10–6 °C − 1) is very close to that of γ-TiAl (12 × 10–6 °C − 1). Many techniques were used to prepare the TiAl3 coatings. The most common method to prepare TiAl3 coating was aluminizing, including pack cementation (Xiang et al. 2002), thermal spray aluminum and annealing (Sasaki et al. 2011), sputtering aluminum and annealing (Chu and Wu 2003), deposition of aluminum by PVD and annealing (Varlese et al. 2013), and electrodeposition of aluminum and annealing (Miyake et al. 2011). Xiong et al. (2004, 2005) reported a liquid-phase siliconizing by Al-Si alloy on TiAl-based alloy and studied its oxidation resistance. Swadzba et al. (2004) studied the long-term cyclic oxidation of Al-Si diffusion coating deposited by Arc-PVD. Xiang et al. (2003) studied co-deposition of Al and Si to form an oxidation-resistant coating by pack cementation. All types of coatings exhibited certain improvements and some problems as well.

Considering the facts that cold spray has shown great advantages in depositing aluminum and it is difficult to obtain TiAl3 powders suitable for spraying, we developed a new approach to prepare TiAl3 composite coatings by cold spray and subsequent heat treatment. The performances of coatings for oxidation resistance at high temperature for γ-TiAl were investigated.

14.2 Preparation of $TiAl_3$ Composite Coatings by Cold Spray

Cold spray was carried out on a stationary system, which was manufactured by the Institute of Theoretical and Applied Mechanics of the Siberian Branch of the Russian Academy of Science (ITAM SB RAS). The de Laval nozzle was a rectangle exit equipped with a cross section of 2 mm × 10 mm and a throat of 2 mm × 2 mm.

The parameters for cold spraying process were 10–30 mm, 220–550 °C, and 1.8–2.0 MPa for stand-off distance, temperature, and air pressure, respectively. The substrates were coated both on flat and side. The thickness of the coating was about 100 μm. The as-sprayed specimens were subjected to a heat treatment under Ar gas flow of 40 ml/min. The furnace was heated from room temperature to a set temperature at a heating rate of 3 °C/min and was held at this level for 5 h. The furnace was then cooled down to room temperature at its natural rate by switching off the power supply while maintaining the Ar gas flow.

The γ-TiAl substrate with nominal composition of Ti-47Al-2Cr-2Nb-0.15B (at. %) and the orthorhombic Ti-22Al-26Nb (at. %) were provided by the Titanium Alloys Division, Institute of Metal Research, Chinese Academy of Sciences. The ingot was cut into 15 mm × 10 mm × 2 mm coupons. The surface of all the specimens was grounded with SiC paper up to 800 grit, cleaned ultrasonically in anhydrous alcohol, dried, and then pilled before cold spray.

Several types of powders or their mixture were deposited on titanium-based alloys by cold spraying:

1. *Al powders*. The aluminum powders (99.5 wt. %) were sieved to an average size of 20 μm and then dried at 80 °C for 4 h before use.
2. Mixture of Al and Al_2O_3 powders. Commercially pure aluminum powders (99.5 wt.%) produced by gas atomization were blended with α-Al_2O_3 particles as feedstock materials for coatings. The spherical pure Al powders and the rectangular α-Al_2O_3 particles were in the size range of 1–30 μm. The weight percentage of α-Al_2O_3 in the feedstock was 50%. The mixed powders were dried at 80 °C for 4 h before cold spraying.
3. *Al-Si powders*. Commercial Al-12Si (wt.%) and Al-20Si (wt.%) alloy powders (Changsha Tianjiu Metallic Materials Co., Ltd., China) were used for cold spray. Both types of the powders were dried at 80 °C for 4 h before use.
4. *Mixture of Ti and Al powders*. The powders of the commercial titanium (90.0% wt.) and aluminum (99.5% wt.) were sieved to an average size of 20 μm and then premixed in a V-mixer for 48 h. The molar ratio of Ti/Al was settled as 1:3. The mixture obtained was dried at 80 °C for 4 h before use.
5. Mixture of Ti, Al, and Al_2O_3 powders. The powders are composed of Al_2O_3 (30 wt.%) and mixture of Ti/Al (70 wt.%, Ti/Al atom ratio = 1:3). The mixed powders were premixed in a V-mixer for 24 h and then dried at 80 °C for 12 h before use.
6. Ball-milled Al and $TiAl_3$ powders. The raw materials used for high-energy ball milling were pure Al and TiO_2 powders. The Al powders (Changsha Tianjiu Metallic Materials Co., Ltd., China) were sieved to −400 and +500 mesh. The TiO_2 powders were commercial P25 without any further treatment. Al/TiO_2composite powders (40 wt. % TiO_2) were fabricated by high-energy ball milling using a shaker mill (QM-3A, Nanjing Nanda Instrument Co, China). The high-energy ball milling was carried out with 5 mm agate balls at a ball-to-powder mass ratio of 5:1. The mixture was milled at the speed of 1200 rpm for 2 h. After ball milling, the as-prepared composite powders were subjected to a

heat treatment at 750 °C for 8 h in an annealing furnace under Ar gas flow of 40 ml/min. After heat treatment, the composite powders turned to be agglomerate. The agglomerates were smashed by high-energy ball milling again for 15 min under the aforementioned conditions.

14.3 Characterization of TiAl3 Composite Coatings

14.3.1 Deposition of Pure Aluminum

The temperature used to deposit pure aluminum powders by cold spray should be lower. In a typical run, the aluminum coating was deposited at 220 °C by cold spray. The microstructure showed that a compact Al coating was deposited on the

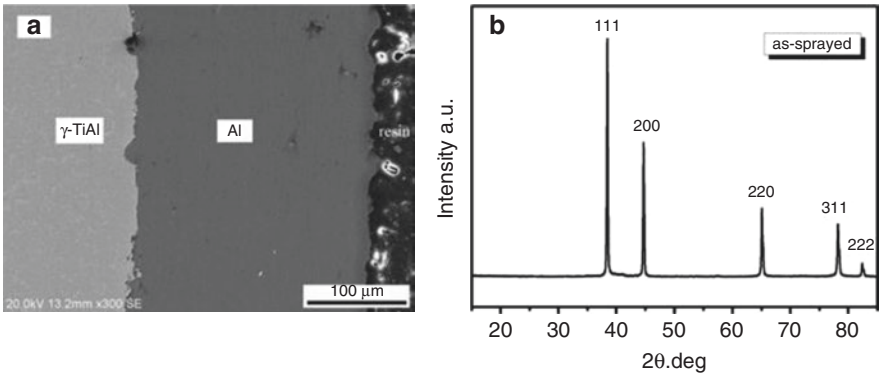

Fig. 14.1 SEM image of cross section (**a**) and XRD patterns (**b**) of γ-TiAl with Al coating by cold spray (Yang et al. 2011)

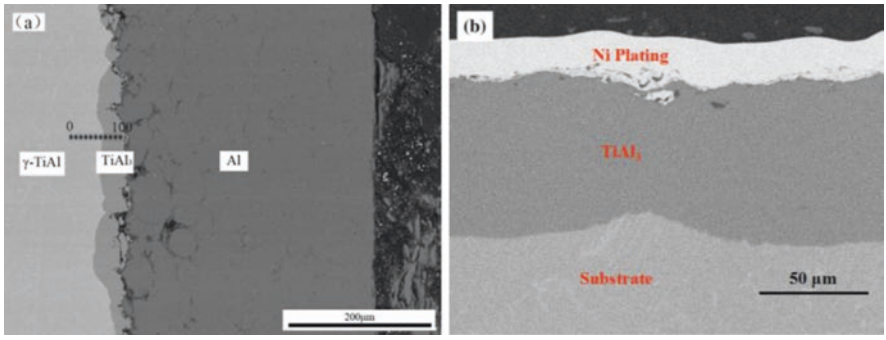

Fig. 14.2 SEM images of cross section of coatings after heat treatment (**a**) at 630 °C for 5 h and (**b**) at 700 °C for 12 h (Yang et al. 2011)

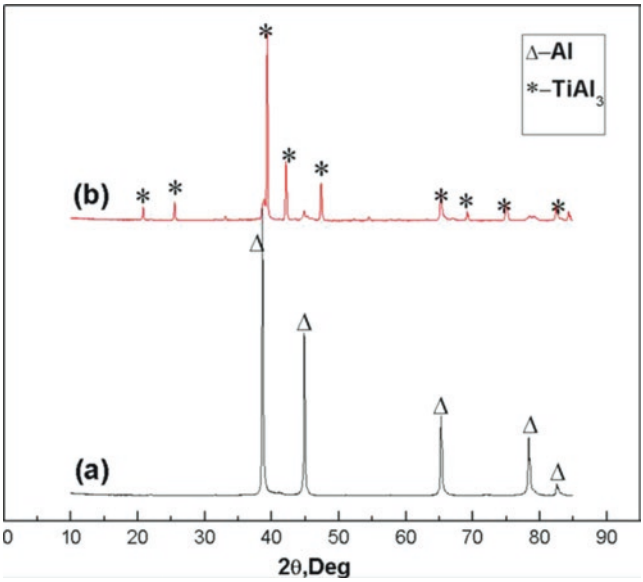

Fig. 14.3 XRD patterns of coatings after heat treatment at 700 °C for 12 h

substrate with few pores and voids (Fig. 14.1a). The XRD analysis showed that no detectable oxide was found in the as-sprayed coating (Fig. 14.2b).

After heat treatment in Ar atmosphere at 630 °C for 5 h, the interdiffusion reaction between the deposited aluminum coating and the substrate alloy took place, and $TiAl_3$ was formed at the interface of the coating and the substrate (Eq. 14.1).

The outer aluminum maintained observable plastic deformation of the original particle structure (Fig. 14.2a). No $TiAl_2$ was detected at this stage. Raising the temperature and extending the treating time for heat treatment, the deposited aluminum was reacted completely with the substrate alloy and transformed to $TiAl_3$ layer. The newly formed coating was uniform and compact (Fig. 14.2b) and was only composed of $TiAl_3$ (Fig. 14.3).

$$\mathrm{TiAl(s)} + \mathrm{Al(s)} \rightarrow \mathrm{TiAl_3(s)} \tag{14.1}$$

According to the phase diagram of Ti-Al (Murray 1987), there are two phases existing between TiAl and Al, which are $TiAl_2$ and $TiAl_3$. It has been proved that $TiAl_3$ is the only phase formed at the beginning of the reaction between TiAl and Al. The $TiAl_3$ will not stop growing until Al is consumed completely, and then the $TiAl_2$ begins to appear. Figure 14.2a shows that the newly formed $TiAl_3$ interlayer was dense and combined with the substrate very well, while voids could be observed between the $TiAl_3$ phase and the cold-sprayed Al. These are Kirkendall voids that resulted from the accumulation of vacancies, which were formed by the diffusion of aluminum. The bulk that expanded with the formation of $TiAl_3$ could fill up part of the voids limitedly, and voids were formed finally between $TiAl_3$ and external deposited Al.

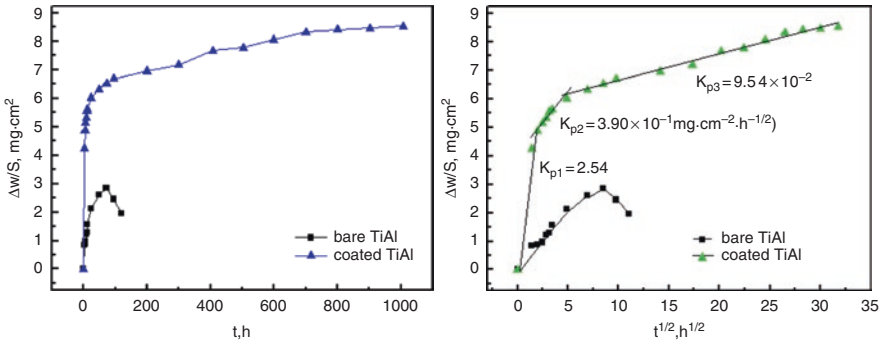

Fig. 14.4 Quasi-isothermal oxidation kinetics and parabolic rate constant plots of γ-TiAl and $TiAl_3$-Al composite coatings at 950 °C in air

The coatings after heat treatment at 630 °C are actually composed of $TiAl_3$ and cold-sprayed Al and are defined as $TiAl_3$-Al composite coatings. The high temperature oxidation resistance of the so-called $TiAl_3$-Al composite coatings was tested at 950 °C in air under quasi-isothermal condition.

It can be seen from Fig. 14.4 that after being oxidized for 70 h, the yellow oxides on the bare γ-TiAl began to fall off, which lost its oxidation resistance.

For the coatings, the initial weight gaining (0–4 h) was relatively large due to the quick oxidation of the aluminum in the composite at high temperature. After a transition period (4–24 h), the oxidation rate for the composite coatings obviously slowed down, and the kinetics of oxidation followed quasi-parabolic law (24–1000 h) with a parabolic constant of 9.54×10^{-2} mg·cm^{-2}·h$^{-1/2}$.

After oxidation, the structure of the composite coatings changed greatly. The XRD analysis shows that there are three main phases in the oxidized coatings, $TiAl_3$, $TiAl_2$, and Al_2O_3, with small amount of TiO_2 and $AlTi_2N$ (Fig. 14.5). Figure 14.6 shows that three parts can be distinguished in the composite coating, the $TiAl_2$ interlayer, the $TiAl_3$ phase with dispersing Al_2O_3 particles, and the Al_2O_3 out layer. The $TiAl_3$ in the initial composite coatings was transformed to uniform and compact $TiAl_2$ interlayer due to the interdiffusion. The pure Al out layer was transformed to $TiAl_3$ and Al_2O_3 due to interdiffusion and oxidation. A continuous Al_2O_3 scale was formed at the surface of the coatings and provided high-temperature protection for the base alloys. The Cr in the substrate alloys also diffused outward and formed a Cr-rich net zone between $TiAl_2$ and $TiAl_3$. The TEM and diffraction analyses proved that the Cr-rich net phase is a cubic phase $Ti(Al,Cr)_3$ $L1_2$ (Fig.14.7). It is proposed that the difference between the grain boundary diffusion (Dg) and the lattice diffusion (Dl), as well as the difference of grain direction and width, resulted in the inhomogeneous diffusion of Cr and led to the formation of the net structure (Danielewski et al. 1980).

It should be noted that although there was large amount of pure Al in the $TiAl_3$-Al composite coatings, no flow of the liquid aluminum on the coating surface was observed. This is possible because the diffusion and reaction of the coating was very

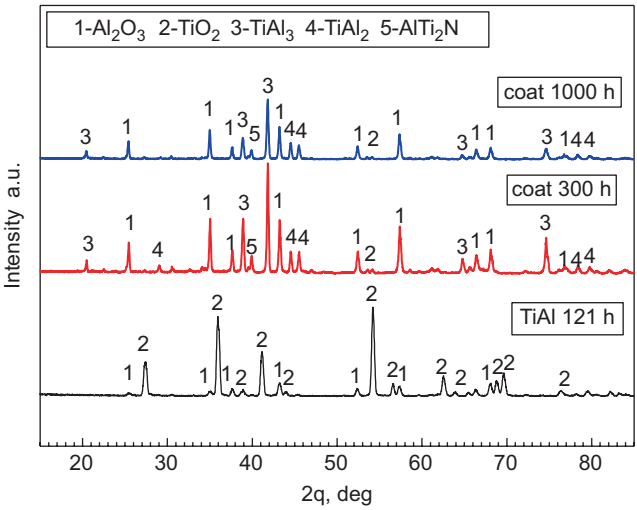

Fig. 14.5 XRD spectra of γ-TiAl and Al diffusion coating oxidized at 950 °C for different times

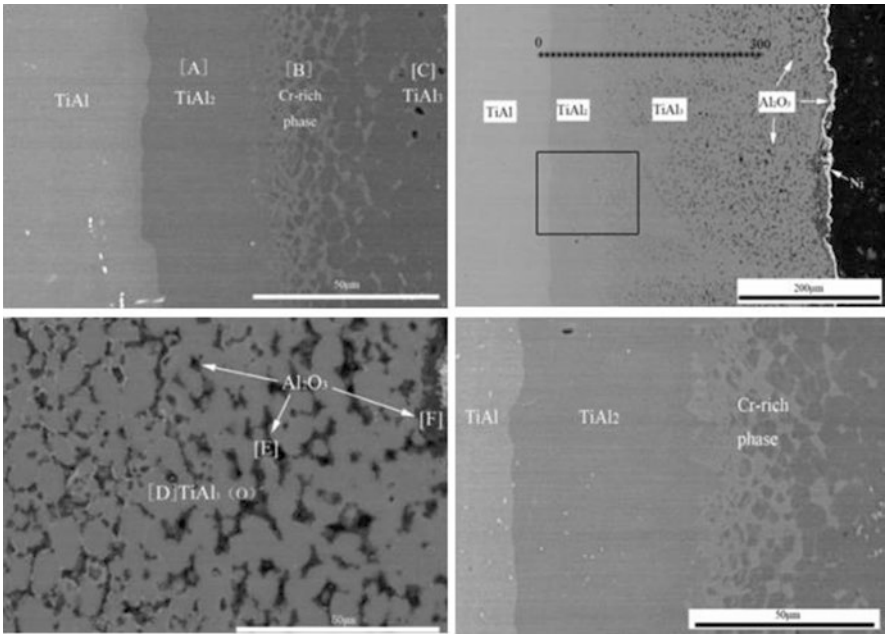

Fig. 14.6 SEM images of cross section of the $TiAl_3$-Al composite coating oxidized at 950 °C in air for (**a**) 300 h and (**b**) 1000 h; (**c**) enlarged SEM image in the black square zone in (**a**); (**d**) enlarged SEM image of the interdiffusion zone

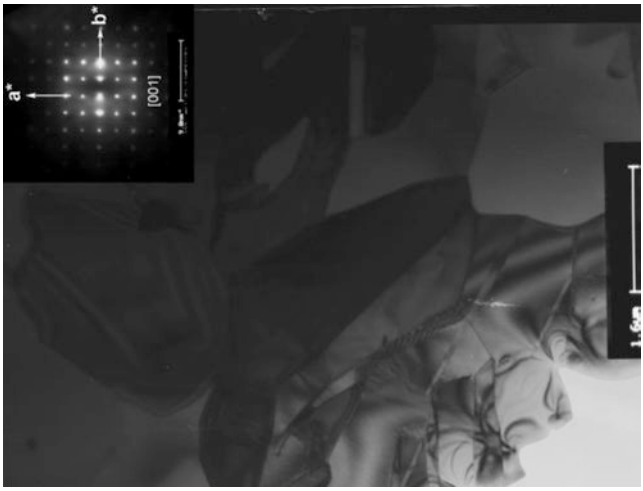

Fig. 14.7 The planner TEM image of the Cr-rich phase

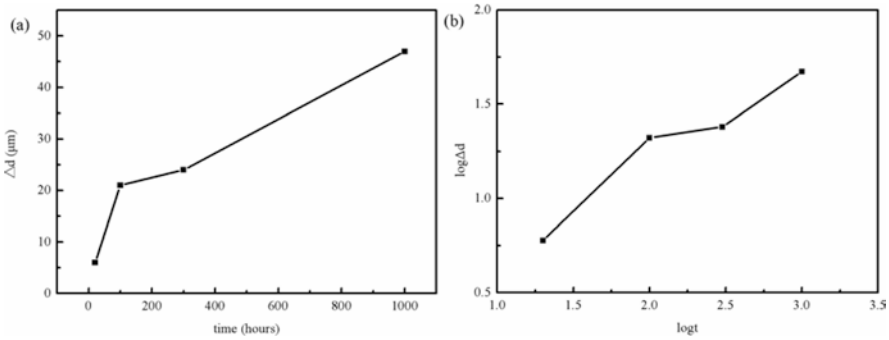

Fig. 14.8 Relationship between thickness of $TiAl_2$ and its growth time

fast at 950 °C and the coating was too thin to flow for the surface tension (Zhang et al. 2009). From the thickness of the $TiAl_2$ growth with time, it can be seen that the $TiAl_2$ phase grew fast at first and then slowed down. But the log ($\triangle d$) – t graph was not a straight line (Fig. 14.8), which was probably due to the influence of other elements (Van Loo and Rieck 1973b).

14.3.2 Deposition of the Mixture of Al and Al2O3

Al_2O_3 is used to enhance the strength of cold spraying coatings through their compaction over metal coatings by impacting and promoting deformation (Tao et al. 2009). The $TiAl_3$-Al_2O_3 composite coatings were prepared by cold spraying

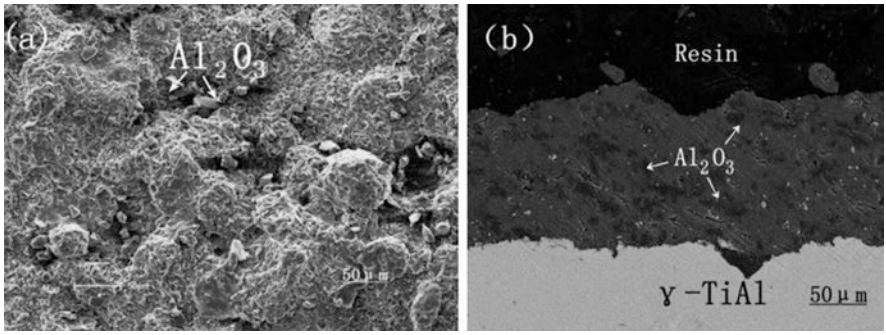

Fig. 14.9 SEM images of surface (**a**) and cross section (**b**) of Al-Al_2O_3 composite coating by cold spray

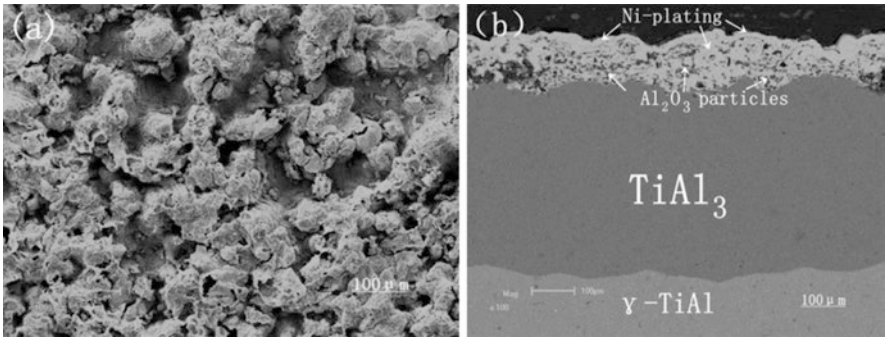

Fig. 14.10 SEM images of surface (**a**) and cross section (**b**) of Al-Al_2O_3 coating after heat treatment at 700 °C for

Al-Al_2O_3 powders on γ-TiAl-based alloy (Zhang 2013). Figure 14.9a shows that the surface of the as-sprayed coatings was relatively flat, with the irregular Al_2O_3 particles scattered in the Al coating. The particles of Al_2O_3 did not deformed obviously and part of them were embedded into the coatings. However, the fraction of Al_2O_3 decreased a lot compared to that of original powder mixture, for the ceramics are relatively difficult to deposit by cold spray. The cross image of the as-deposited coatings shows that the coating was about 100 μm in width with low pore ratio and small amount of cracks (Fig. 14.9b).

After heat treatment at 700 °C for 12 h in Ar, the surface of the coating became rather rough than before (Fig. 14.10a), and the coating was mainly composed of the deposited Al_2O_3 particles, which were left at the surface, while the Al diffused inwardly and reacted with the substrate alloy. Figure 14.10b shows the cross-sectional image of the coatings after heat treatment. It can be seen that the Al in the original coating reacted with the substrate alloy and transformed to $TiAl_3$ completely. The newly formed $TiAl_3$ were compact without pores and cracks. The Al_2O_3 particles, which were embedded in the aluminum in the sprayed coating, were left at the surface as a porous layer but bonded with the $TiAl_3$ layer well.

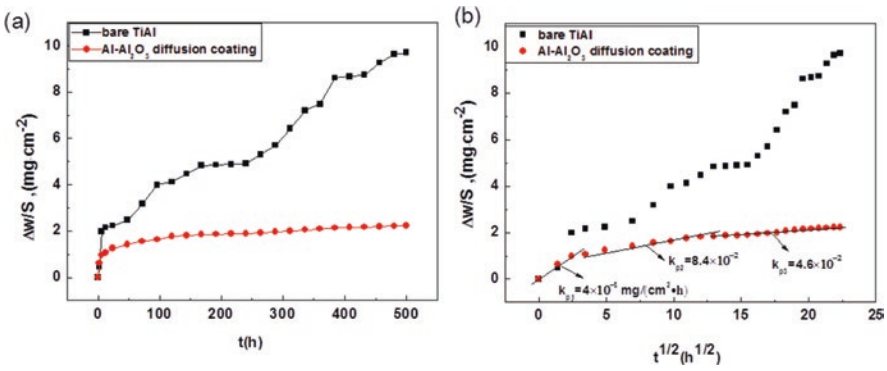

Fig. 14.11 Quasi-isothermal oxidation kinetics (**a**) and oxidation parabolic rate constant (**b**) plots of bare γ-TiAl and $TiAl_3$-Al_2O_3 composite coating at 900 °C in the air

The high temperature oxidation performance of the $TiAl_3$-Al_2O_3composite coatings is shown in Fig. 14.11. The coatings improved the oxidation resistance of the base alloy significantly, and the kinetic plot of the coatings was similar to that of the $TiAl_3$-Al composite coatings.

After oxidation at 900 °C for 500 h, the cold-sprayed Al_2O_3 particles were still scattered on the surface of the coatings and bonded well with the newly formed needle-like θ-Al_2O_3 scale (Fig. 14.12a, c). The cross-sectional image shows that outside the $TiAl_3$ layer, the dense Al_2O_3 scale was about 5 μm thick and some of them prorogated into the network of the deposited Al_2O_3 particles without pores or cracks. It is proposed that the aluminum in the $TiAl_3$ layer would diffuse into the pores of the deposited Al_2O_3 porous network and oxidize there at 900 °C.

Most of $TiAl_3$ phase still existed in the coatings; however, the $TiAl_3$ connected with the substrate were degraded into $TiAl_2$ interlayer after oxidation for 500 h (Fig. 14.12b, d). Fortunately, the two layers were very dense without pores and cracks and prevented the substrate alloy from the oxidation. The performance of the deposited Al_2O_3 layer was not very clear. It seems to reinforce the dense Al_2O_3 protective scale by way of pinning into the scale as hard inclusion and preventing them from scaling (Li et al. 2003).

14.3.3 Deposition of Al-Si Alloy

Besides the aluminide coatings, siliconizing coatings were also studied in order to improve the oxidation resistance of the bare alloys. Thus, to combine the effects of Al and Si on the improvement in oxidation resistance of γ-TiAl, co-deposition of Al and Si to form oxidation-resistant coatings was also studied by cold spray(Wang 2015). The powders of Al-12Si and Al-20Si were used for cold spray. The microstructures of the powders are shown in Fig. 14.13, showing both particles are near

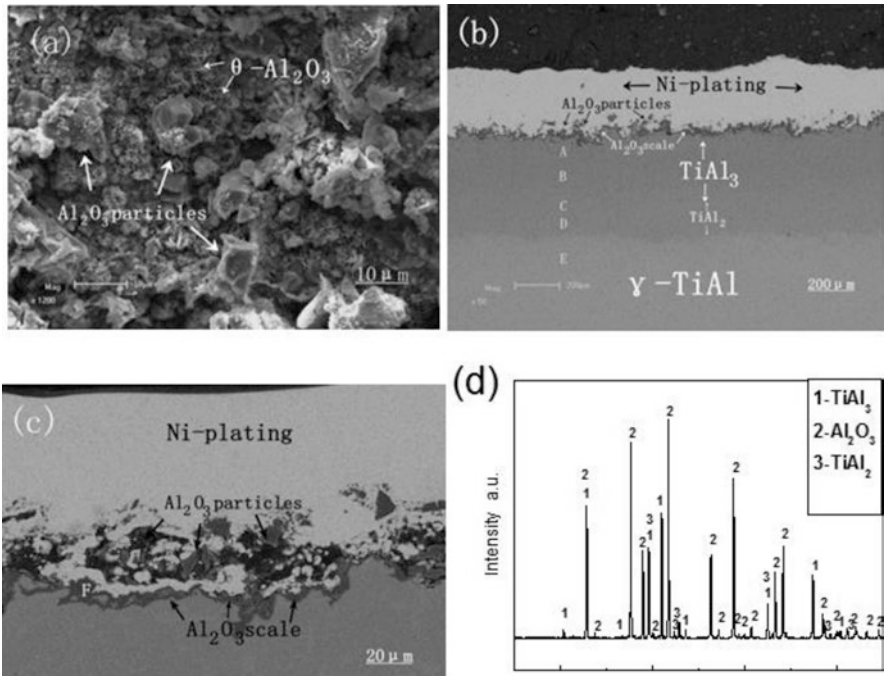

Fig. 14.12 SEM images of surface (**a**) and cross section (**b**), a magnified morphology of the zone between the coating and substrate (**c**), and XRD pattern (**d**) of the $TiAl_3$-Al_2O_3 composite coatings oxidized at 900 °C for 500 h in the air

spherical (Fig. 14.13a, c). After etching by HF (15 wt. %, hydrous), it can be seen that the Al-12Si is composed of two phase and shows typical eutectic structure (Fig. 14.13b), and the Al-20Si has a typical hypereutectic structure with large amount of α-Si in the alloy (Fig. 14.13d).

The surface of the as-sprayed coating of Al-12Si showed that all the particles of Al-12Si were fully deformed (Fig. 14.14a), while the surface of Al-20Si was rather rough with observable rebounding craters and undeformed particles (Fig. 14.14b). This difference in surface morphology resulted from different plasticity.

Figure 14.15 shows the cross-sectional image of the as-sprayed coatings. It can be seen that the thickness of the as-sprayed Al-12Si coating is nearly 30 μm that bonds well with the substrate alloy. There are no obvious pores or cracks in the coating. After etching, the Al phase of Al and the Si-rich phase are observed in the seriously deformed particles, meaning that the feedstock of alloy particles did not experience a phase change during cold spray. But the change was observed on the as-sprayed Al-20Si.

After heat treatment at 750 °C for 12 h, the as-sprayed Al-12Si diffused into the substrate alloy and formed a dark phase of $Ti(Al,Si)_3$(Fig. 14.16a). The white sediments with a diameter of several nanometers were dispersed in the dark phase (Fig. 14.16b). They were the Si-rich phase analyzed by EDS. The coatings after heat treatment for Al-20Si was only composed of formed phase of $Ti(Al,Si)_3$ (Fig. 14.16c).

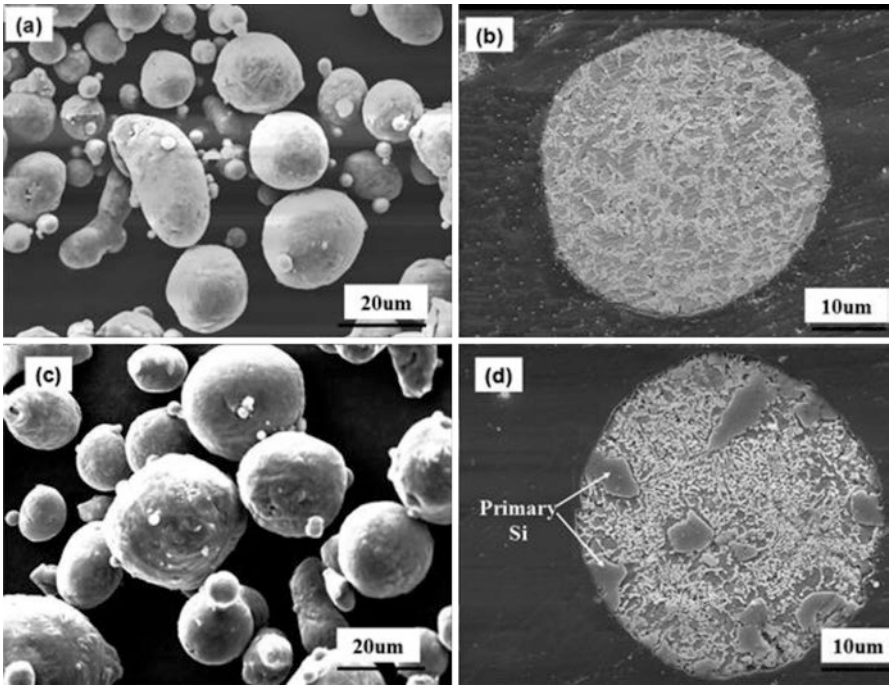

Fig. 14.13 SEM images of (**a**) Al-12Si and (**c**) Al-20Si powders and etched cross sections of (**b**) Al-12Si and (**d**) Al-20Si particles

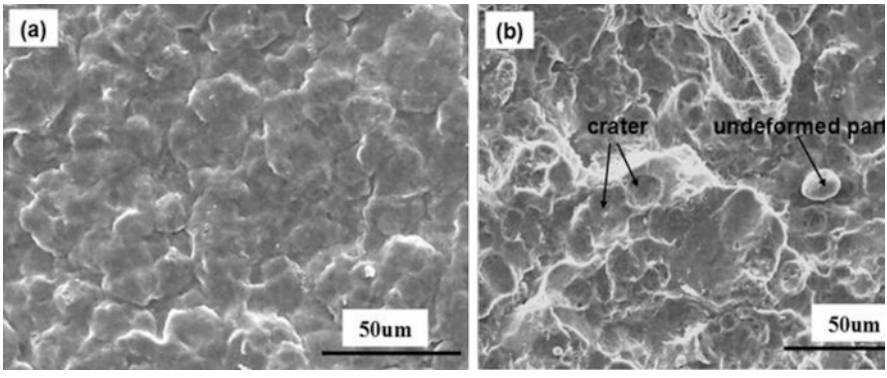

Fig. 14.14 Surface morphologies of the as-sprayed (**a**) Al-12Si and (**b**) Al-20Si alloy coatings

After oxidation at 900 °C for 50 h, oxides began to form on the diffusion coatings of Al-12Si. The main phase of the coatings was also $TiAl_3$. The phase of Ti5Si3 began to grow, and part of them formed a continuous diffusion layer just outside the $TiAl_2$ diffusion layer (Fig. 14.17a). After oxidation for 300 h, the

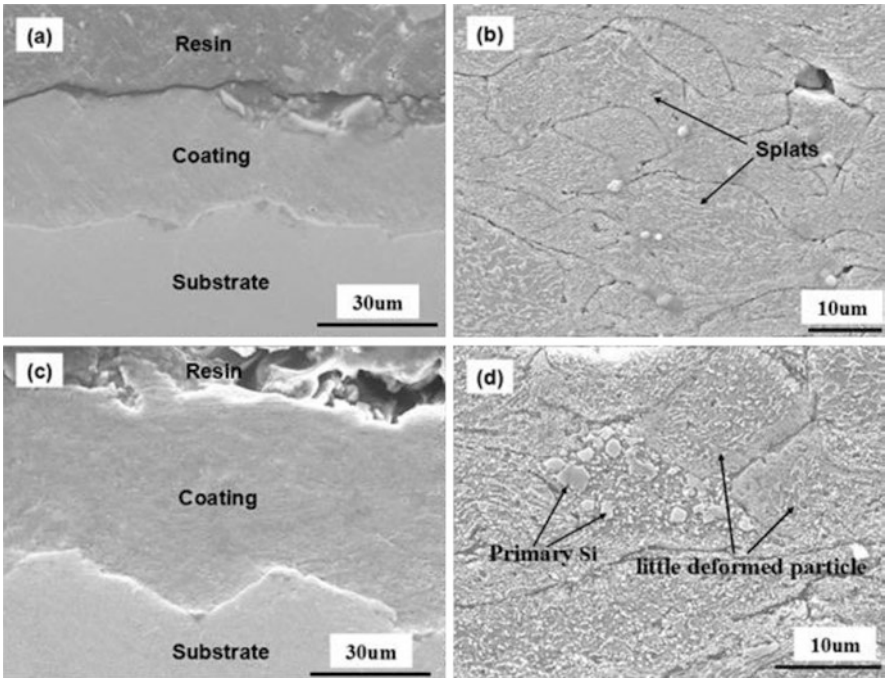

Fig. 14.15 Cross sections of (**a**) the as-sprayed and (**b**) etched Al-12Si alloy coating and (**c**) the as-sprayed and (**d**) etched Al-20Si alloy coating

continuous layer rich in Si near $TiAl_2$ layer was degraded (Fig. 14.17b). After oxidation for 500 h, $TiAl_2$ phase and the Ti5Si3 phase grew quickly (Fig. 14.17c). After oxidation for 1000 h, $TiAl_3$ almost vanished and was degraded into $TiAl_2$ entirely. The Ti5Si3 phase disappeared completely (Fig. 14.18d). TiO_2 also came into being in the coatings after oxidation. θ-Al_2O_3 was formed on the surface of the coating, and the metastable scale was transformed to α-Al_2O_3 scale as extending the oxidation time.

The SiO_2 phase was not detected at all tested time. The $Ti(Al,Si)_3$ phase degraded into $TiAl_2$ phase and a Si-rich phase after oxidation, and the continuous SiO_2 scale was not detected. The benefit of the Si-rich phase was to form the Ti5Si3 phase, which was very stable at high temperature and thus reduced the outward diffusion of Ti because of the affinity between Si and Ti (Goral et al. 2009).

There are large amount of vertical cracks in the Al-20Si coatings for the large difference in thermal coefficiency of the diffusion coating and the γ-TiAl-based alloy. However, these cracks were prevented by the Si-rich phase from propagating, and no severe internal oxidation occurred.

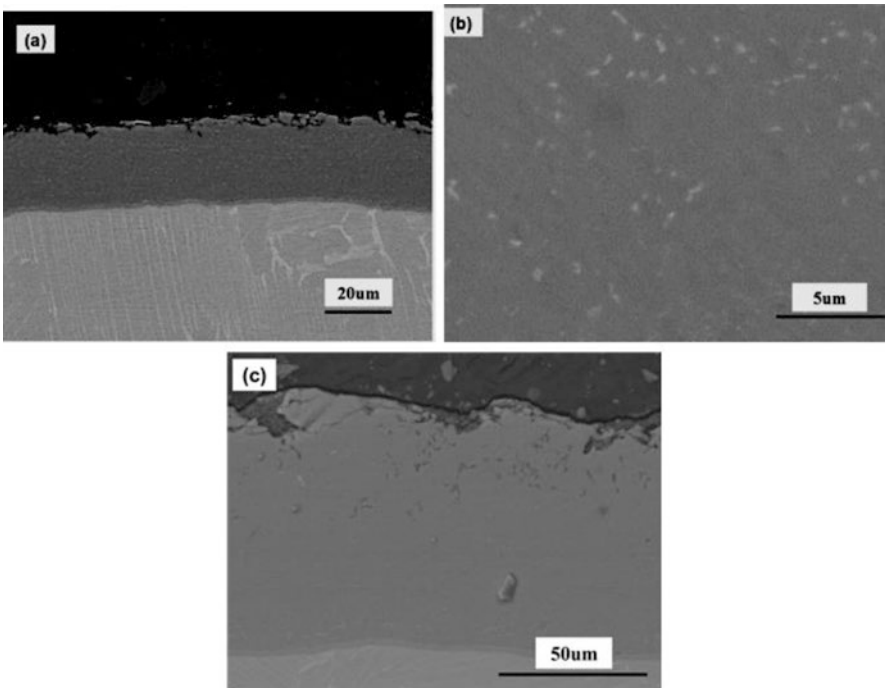

Fig. 14.16 Microstructures of (**a**, **b**) Al-12Si alloy and (**c**) Al-20Si alloy coatings after heat treatment at 750 °C for 12 h

14.3.4 Deposition of Mixture of Ti and Al Powders

When depositing pure Al by cold spray and subsequent heat treatment, higher temperature for heat treatment has to be chosen due to the long transport path lengths for growth of the $TiAl_3$ coating. The diffusion temperature for Al and Ti was set at 700 °C to make sure to obtain uniform $TiAl_3$ coatings at a reasonable time. However, cracks would be prone to be generated during cooling the coating from temperature above the melting point of Al for the $TiAl_3$ (Smialek 1993). This could be avoided by depositing mixture of Ti and Al powders, for the diffusion route of Al was not very long.

Figure 14.18a shows the morphology of the as-sprayed coating. It shows that the Ti particles (Fig. 14.19a, B) are embedded in the continuous Al matrix (Fig. 14.18a, A) for the as-sprayed coating. The as-sprayed coating was compact with a porosity of about 0.17% (Shen 2008). After heat treatment at 630 °C, the components in the as-sprayed coating experienced solid reaction and were transformed to $TiAl_3$-Al (Fig. 14.18b, C). The newly formed $TiAl_3$ phase as well as the residual Al (Fig. 14.18b, D) composed the composite coating with a porosity of 14.69 %. A new interdiffusion zone was formed after heat treatment, which was compact with a broadness of 10 μm and the (Ti, Nb)Al_3 phase (Fig. 14.18b, B). The Nb was derived

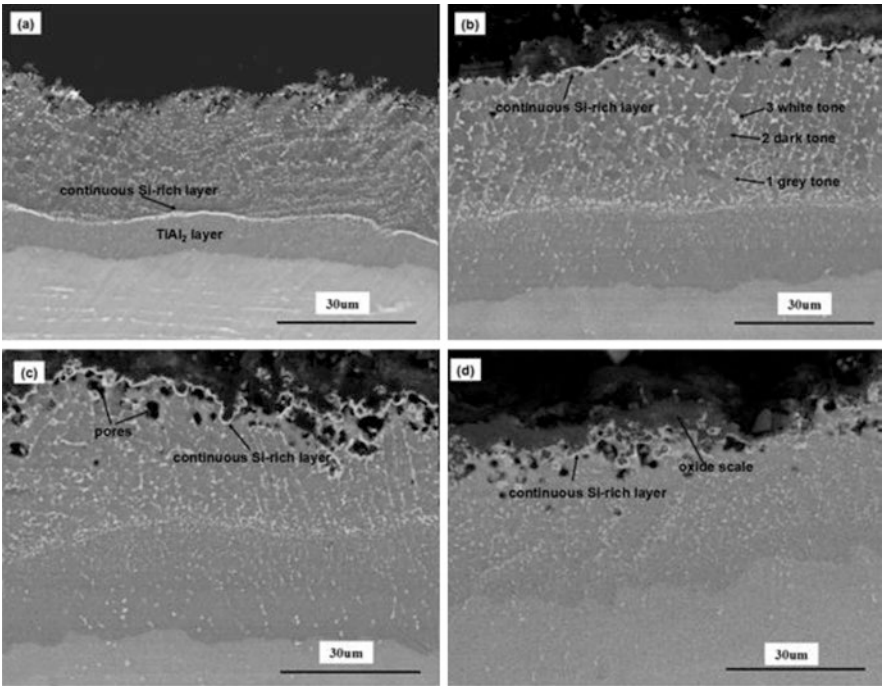

Fig. 14.17 Cross sections of Al-12Si diffusion coating at 900 °C for (**a**) 50 h, (**b**) 300 h, (**c**) 500 h, and (**d**) 1000 h

from the substrate alloy. The surface morphology of the as-sprayed coating and the coating after heat treatment did not change a lot; both were rough surfaces without crack (Fig. 14.18c).

The quasi-isothermal oxidation test for the $TiAl_3$-Al composite coatings showed that the mass gaining mainly occurred at the initial 20 h. After that period, the weight gaining rate decreased greatly. The oxidation kinetic curve followed the parabolic rate law and did not present unsteady weight gaining even after oxidation at 950 °C for 300 h (Fig. 14.19). These results indicate that the composite coating could provide good protection for the substrate alloy at 950 °C and good adherence of the coating as well.

Figure 14.20 shows the surface morphology and cross-sectional morphology of the oxidized bare alloy at 950 °C(Kong et al, 2010). It can be seen from Fig. 14.21a that the oxide on the surface tended to scale off obviously because of the growth of cracks induced by the thermal tension under cyclic oxidation condition. The cracks tended to occur most likely on the TiO_2 strip area. For the $TiAl_3$-Al coating, the residual Al in the $TiAl_3$-Al composite coating was oxidized very fast to form a matrix Al_2O_3 in the oxidized composite coating (Fig. 14.20b). After being oxidized for a while, the $TiAl_3$ acted as the Al source for continuous generation of Al_2O_3 and itself was consumed to turn into $TiAl_2$. The cross section of the coating shows that

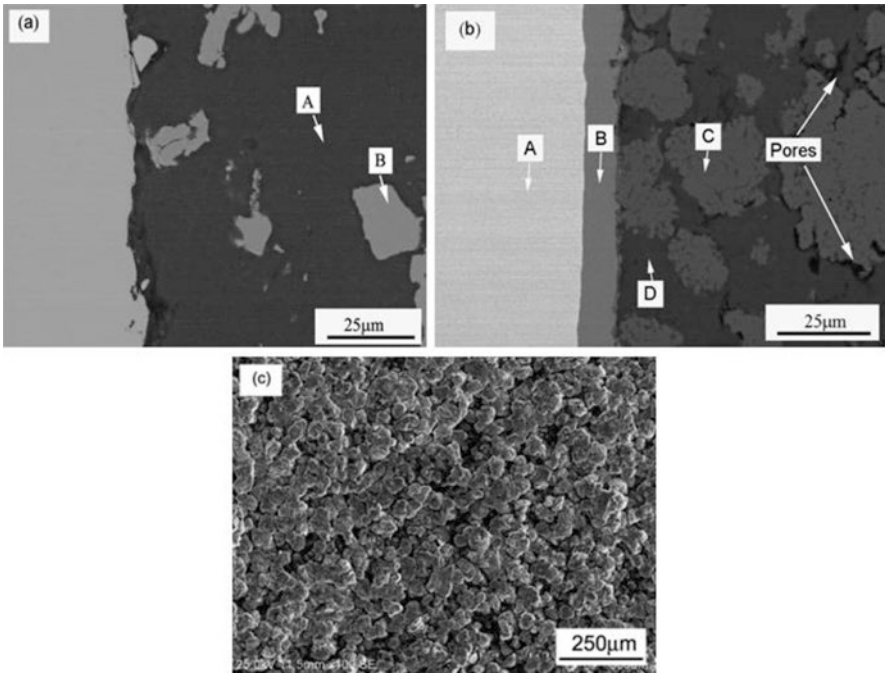

Fig. 14.18 SEM images of the $TiAl_3$-Al coating prepared by cold spray, (**a**) cross-sectional image of as-sprayed coating, (**b**) cross-sectional image of the coating after heat treatment, and (**c**) surface morphology of the coating after heat treatment

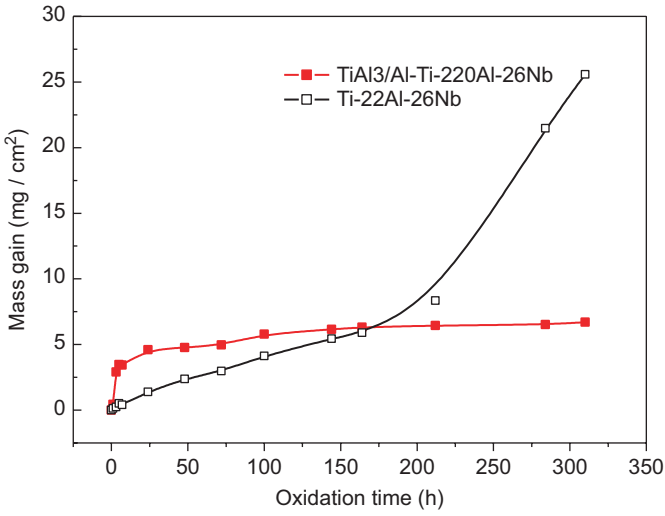

Fig. 14.19 Mass change vs. time curves of the Ti-22Al-26Nb alloy and the $TiAl_3$-Al coating at 950 °C for 300 h in the air under quasi-isothermal condition

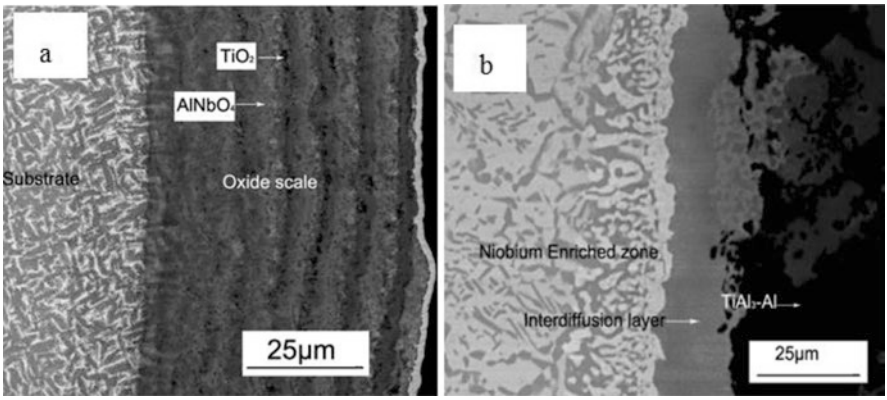

Fig. 14.20 SEM images of the bare alloy and the coating after oxidation at 950 °C for 150 cycles in air, (**a**) cross section of the Ti-22Al-26Nb, and (**b**) cross section of the $TiAl_3$-Al coating

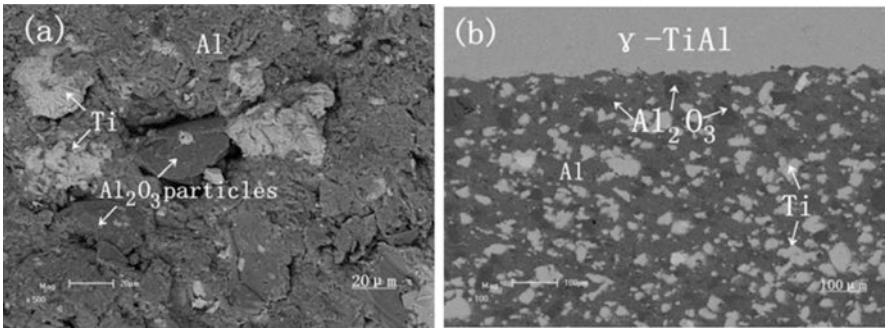

Fig. 14.21 SEM images of surface (**a**), cross section (**b**) of as-deposited $TiAl_3$-Al_2O_3 composite coatings by cold spray

the interdiffusion zone was kept at 10 μm with change in phase but was degraded to (Ti,Nb)Al_2. No vertical crack was observed in the cross section of the coating at 950 °C for 150 cycles, and no inner oxide could be detected beneath the coating. It can be concluded from the above analysis that the $TiAl_3$-Al composite coating effectively protects the base alloy from high-temperature oxidation.

The diffusion routes for the cold-sprayed pure Al and Ti/Al mixture were different. For the as-sprayed Al coating, the $TiAl_3$ was formed through the reaction of Al with the Ti of the substrate, and the diffusion route was very long and needed much high temperature to obtain a uniform $TiAl_3$ coating. While for the cold-sprayed mixture of Ti and Al, the Al could react with the Ti in the matrix next to them, and the diffusion route was just about the size of the particle radius. This made it possible to obtain a uniform $TiAl_3$ coating at the temperature below the melting point of Al for a reasonable heat-treating time, which was formed through solid-solid diffusion.

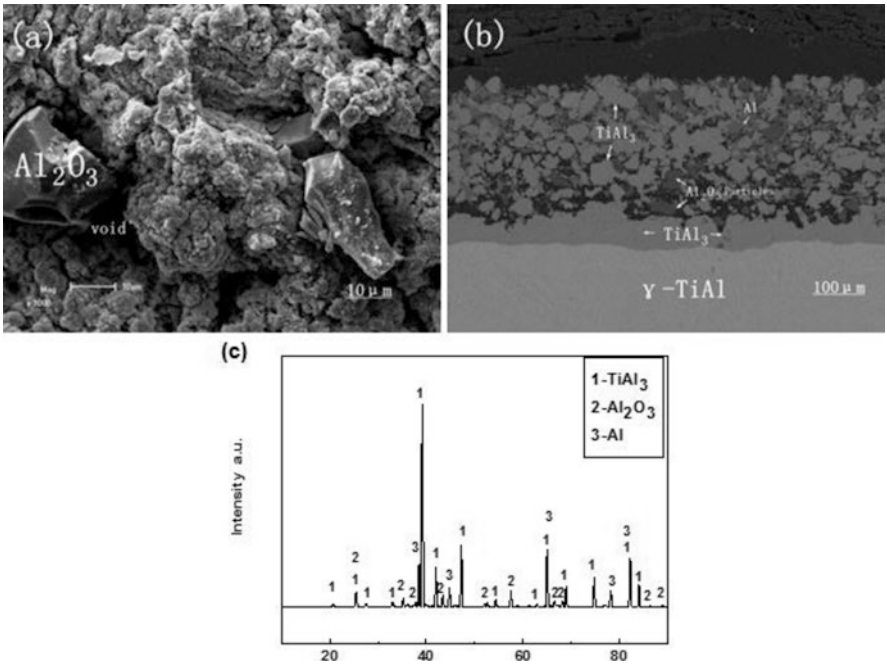

Fig. 14.22 SEM images of surface (**a**), cross section (**b**) of as-deposited $TiAl_3$-Al_2O_3 composite coatings by cold spray

It was reported that the interdiffusion between the $TiAl_3$ coating and the substrate alloy was the main reason for the coatings' degradation (Leyens et al. 2006), which determined the life span of the coating. It could be seen that the $TiAl_3$ composite coatings obtained from deposited Ti/Al mixture degraded much slowly. The interdiffusion zone was only about 10 μm and did not change very much as the oxidation proceeded.

14.3.5 Deposition of Mixture of Al/Ti/Al2O3

An Al-Ti-Al_2O_3 mixture was deposited on the γ-TiAl to obtain Al_2O_3-assisted $TiAl_3$ composite coatings. Figure 14.21a shows the surface of the as-sprayed coatings. It can be seen that the white Ti and black Al_2O_3 particles are scattering in the Al matrix. The deposition efficiency of the mixtured powders was relatively high and much easy to obtain thick coatings. The cross-sectional image shows that the as-sprayed coating is about 300 μm thick and bonded well with the base alloy (Fig. 14.21b).

After heat treatment at 650 °C for 12 h, the surface becomes very rough and was full of black Al_2O_3 particles and many gray tiny bulges which were the newly formed $TiAl_3$ (Fig. 14.22a). The Al_2O_3 particles did not react with Ti or Al. Voids

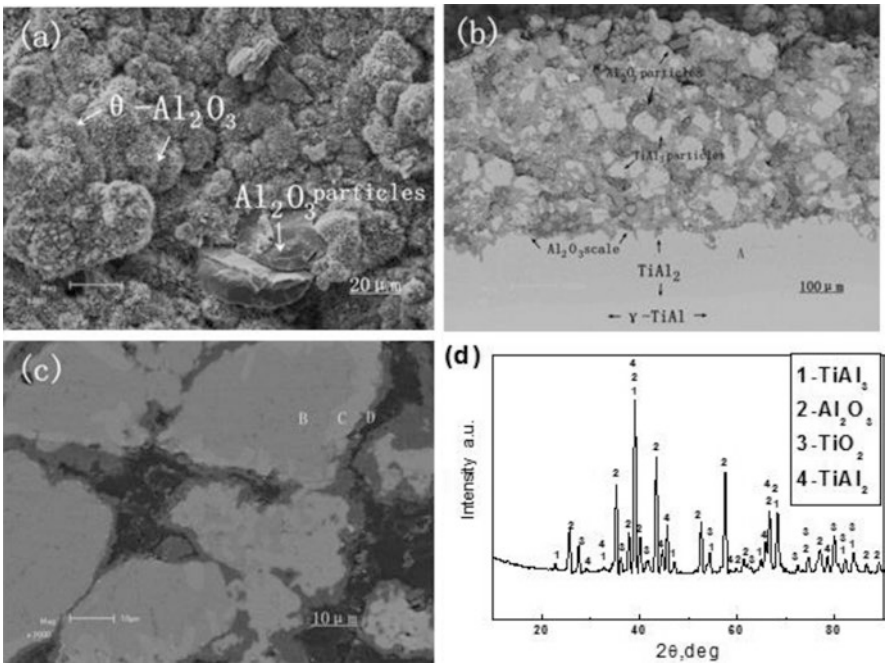

Fig. 14.23 SEM images of surface (**a**), cross section (**b**), a magnified morphology of the zone between the coating and substrate (**c**), and XRD patterns (**d**) of the Al-Ti-Al_2O_3 composite coating oxidated at 900 °C for 500 h in the air

appeared around the Al_2O_3 for the diffusion of Al to Ti. Figure 14.22b shows the cross-sectional image of the coating. The Ti particles were completely converted to $TiAl_3$phase. The Al_2O_3 were still embedded in the coatings, unlike those observed in the deposited Al-Al_2O_3 (Sect. 14.3.2) when the Al_2O_3 were gathering at the surface of the coatings. Voids are around the newly formed $TiAl_3$ phase for the diffusion of Al. Next to the substrate is still the $TiAl_2$ interdiffusion layer. The XRD analysis shows that there are rest Al in the coating, except $TiAl_2$, $TiAl_3$, and Al_2O_3 (Fig. 14.22c).

After oxidation at 900 °C for 500 h, needle-like θ-Al_2O_3 formed and overlapped on the surface (Fig. 14.23a) with a little bit deposited Al_2O_3 scattering around. No TiO_2 can be observed on the surface. The rest Al in the coating after heat treatment had been oxidized to Al_2O_3 (Fig. 14.23b). $TiAl_3$ was degraded by oxidation. Figure 14.23c shows clearly that a thin dark Al_2O_3 scale has enclosed the $TiAl_3$ phase, and between the Al_2O_3 and $TiAl_3$, it was light-gray phase of $TiAl_2$ (Fig. 14.23c, Table 14.1). The continuous protective Al_2O_3 scale was formed right on top of $TiAl_2$ interdiffusion layer.

Table 14.1 EDS analysis results of different positions in Fig. 14.22

Position	Al (at.%)	Ti (at.%)	O (at.%)	Phase
A	66.182	33.818	/	$TiAl_2$
B	74.418	25.258	/	$TiAl_3$
C	65.987	34.013	/	$TiAl_2$
D	40.118	/	59.882	Al_2O_3

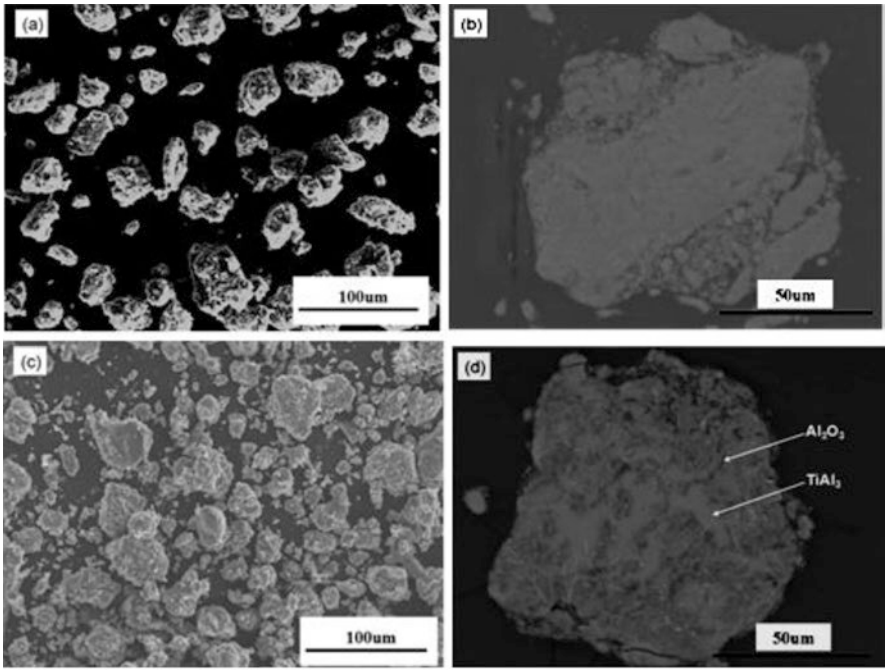

Fig. 14.24 SEM images of ball-milled Al/TiO_2 composite powders before (**a**, **b**) and after (**c**, **d**) the heat treatment

14.3.6 Deposition of Ball-Milled Al and TiAl3 Powders

To enhance the toughness of $TiAl_3$ coatings, a new method to prepare Al_2O_3-dispersed $TiAl_3$ coatings was investigated by cold spray $TiAl_3/Al_2O_3$ powders, which was obtained by ball milling Al/TiO_2 powders. Specifically, the powders used for cold spray were produced first by ball milling mixture of Al/TiO_2 and then by conventional diffusion method. After the treatment, the mixture of $TiAl_3/Al_2O_3$ was obtained and then used as the powders for cold spray(Wang 2016).

After ball milling, the particles of Al/TiO_2 exhibited irregular shapes with an average size of 60 μm (Fig. 14.24a). They were homogeneous in microstructure without observable separated phase (Fig. 14.24b). This indicated that the chemical composition of the particles was uniform after balling for 2 h. It could be proposed

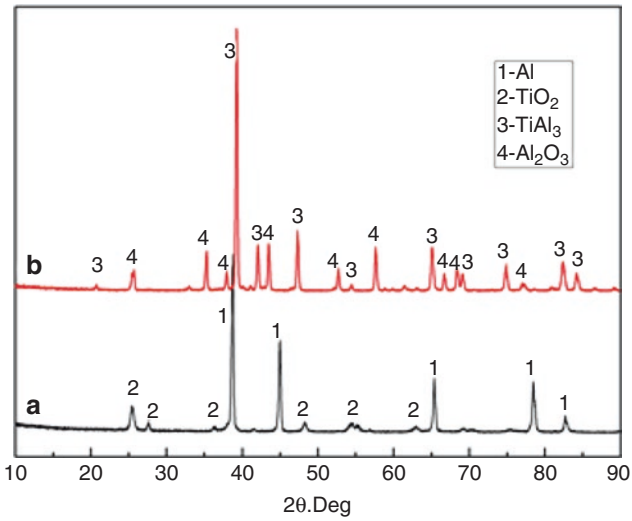

Fig. 14.25 XRD patterns of ball-milled Al/TiO_2 composite powders before (**a**) and after (**b**) the heat treatment

that ductile Al particles were successively flattened, cold welded, fractured, and re-welded, while the brittle nano-TiO_2 particles were difficult to deform during balling. So they were trapped and embedded in the Al particles. With continued milling, the nano-TiO_2 particles uniformly dispersed in Al particles (Zhang et al. 2004). From the XRD patterns as shown in Fig. 14.25(a), it can be seen that there are diffraction peaks of Al and TiO_2 phases, and no other diffraction peak was found, which indicates that no reaction occurred during the high-energy ball milling.

After heat treatment, the shape and size of the mixed particles were similar to those of the as ball-milled particles (Fig. 14.24c). The microstructure of the particle was composed of two phases. The gray parts were identified as $TiAl_3$-rich phase and the dark parts were identified as Al_2O_3-rich phase (Fig. 14.24d). The XRD patterns further demonstrated that the particles were composed of $TiAl_3$ and Al_2O_3 phases (Fig. 14.25b). The formation of $TiAl_3$ and Al_2O_3 phases was attributed to the reaction in Eq. 14.2.

$$13Al + 3TiO_2 \rightarrow 3TiAl_3 + 2Al_2O_3 \tag{14.2}$$

The powders after heat treatment were used for cold spray. Figure 14.26 shows the surface morphology and cross section of the as-sprayed $TiAl_3/Al_2O_3$ composite coating. It can be seen that the surface of the composite coating was very rough with lots of craters which were created by the rebound particles (Fig. 14.26a). It demonstrated that the deposition efficiency was not high because of the low ductility of the $TiAl_3/Al_2O_3$ mixture. From the cross section of the composite coating in Fig. 14.26(b), it can be seen that the coating had good adhesion to the substrate with

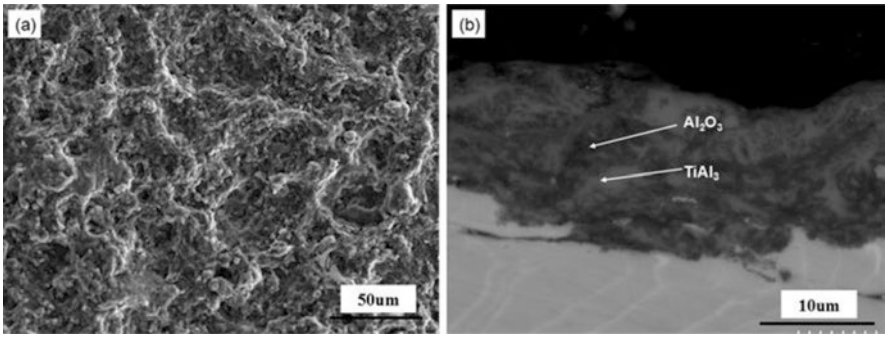

Fig. 14.26 SEM images of surface morphology (**a**) and cross section (**b**) of the as-sprayed $TiAl_3$/Al_2O_3 composite coating

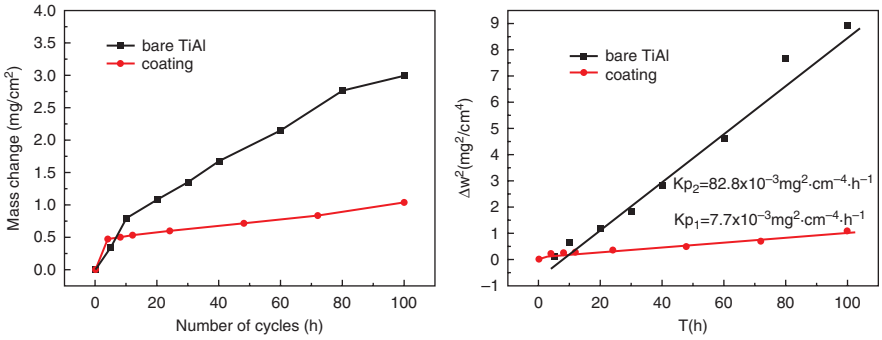

Fig. 14.27 Cyclic oxidation kinetic curves of γ-TiAl alloy with and without the composite coating at 900 °C for 100 cycles

thickness of about 18 μm. The coating was compact without observable pores. Its microstructure was similar to that of the $TiAl_3$/Al_2O_3 coating according to the EDS analysis. This result demonstrated that the microstructure of the particles did not change during the cold spray process.

The composite coating was tested at 900 °C for 100 cycles for its oxidation performance. As other composite $TiAl_3$ coatings prepared by cold spray and subsequent heat treatment, the weight gain of the composite coating increased quickly, even higher than that of the bare alloy at initial oxidation stage (Fig. 14.27a). After that period, the weight gain of the bare alloy increased quickly with oxidation time, while the weight gain rate of the composite coating decreased largely. The total weight gain of the bare γ-TiAl alloy after 100 cycles of oxidation at 900 °C was 2.99 mg/cm^2, while the total weight gain of the composite coating after 100 cycles of oxidation was 1.04 mg/cm^2, only one third of that of the bare alloy. From Fig. 14.27b, it can be seen that both kinetic curves of the bare alloy and coating similarly followed parabolic law because the square of weight gain increased linearly with the oxidation time. The parabolic rate constant of the composite coating

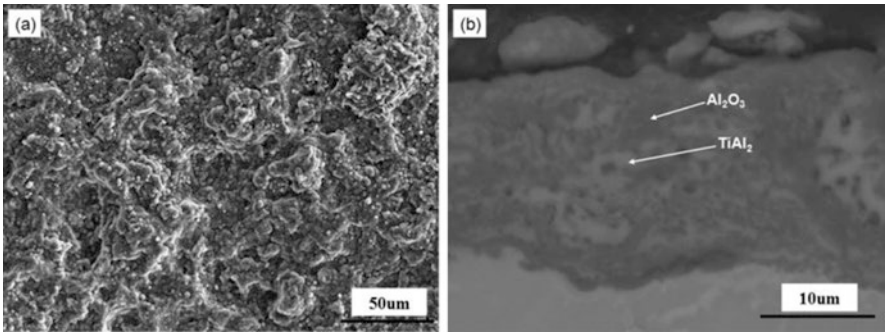

Fig. 14.28 SEM images of surface morphology (**a**) and cross section (**b**) of the oxidized $TiAl_3$/Al_2O_3 composite coating

was only one-tenth of that of the bare alloy. This result indicated that the composite coating decreased the oxidation rate of the bare alloy significantly.

After oxidation at 900 °C for 100 cycles, the composite coating had a rough surface free of cracks and spallation (Fig. 14.28a). The composite coating after the oxidation was also composed of two phases. The gray parts were $TiAl_2$ rich which were derived from the degradation of the $TiAl_3$ phase in the coatings. The dark parts were Al_2O_3-rich phase (Fig. 14.28b). This newly formed Al_2O_3 oxide scale and the original Al_2O_3 phase could serve as a diffusion barrier to decrease the inward diffusion of oxygen and thus protect the γ-TiAl substrate from high-temperature oxidation. During the oxidation process, significant interdiffusion occurred between the conventional $TiAl_3$ coating and substrate because of the inward diffusion of Al. However, no interdiffusion layer was observed between the composite coating and γ-TiAl substrate as shown in Fig. 14.28b.

14.4 Conclusions

$TiAl_3$ coating which can form a stable and continuous Al_2O_3 scale during oxidation has attracted great concerns because of its good compatibility with γ-TiAl substrate. Aluminizing such as pack cementation and hot-dip process is an economical and well-established technique used in the industry for mass production. Aluminizing using pack cementation has been used to establish the alumina-forming $TiAl_3$ phase on the surface of Ti-50Al (Smialek 1993; Pflumm et al. 2015). Gauthier et al. (Pflumm et al. 2015) confirmed the formation of an alumina layer on top of the substrate in isothermal tests at 900 °C for up to 100 h but also the presence of brittle $TiAl_3$ and $TiAl_2$ layers as a consequence of interdiffusion of Al and Ti. The failure mechanism of this type of coating was determined by significant cracks in the $TiAl_2$ coating, which propagated toward the Al_2O_3/$TiAl_2$ interface and induced spallation of the oxide scale. The presence of Nb or Cr in the alloy could

diminish the negative effect of the $TiAl_2$ phase due to a reduction of the Ti activity; however, severe interdiffusion between the $TiAl_3$ coating and the substrate could not be restrained, leading to failure of the coating. Coatings prepared by pack cementation, Arc-PVD, or AIP were degraded within 300 h because of interdiffusion (Zhang et al. 2006). Furthermore, mismatches regarding the coefficients of thermal expansion of the Al-rich coating and substrate could negatively affect the mechanical stability of the deposited layer.

The coatings prepared by cold spray were relatively dense and thick compared to the coatings prepared by other alternative methods. Especially for the coatings prepared by depositing powders of Ti/Al, Ti/Al/Al_2O_3, or Al/TiO_2, the microstructure of coatings was much different from that prepared by the technique through aluminizing. Specifically, the coatings were composed of a $TiAl_2$ interlayer (about 10 μm) and $TiAl_3$ phase surrounded by Al, which was oxidized to Al_2O_3 at the initial stage of oxidation. Thus, the coatings could also be described as $TiAl_2$/$TiAl_3$/Al_2O_3 composite coatings. The new Al_2O_3matrix in the composite coating could inhibit further interdiffusion of $TiAl_3$ and the substrate alloy, and therefore, the growth of the $TiAl_2$interlayer was kept very slow even after oxidation at 900 °C for 1000 h.

The coefficients of thermal expansions (CTEs) of γ-TiAl, $TiAl_3$, and Al_2O_3 are 10–12, 12–15, and 8–9 10^{-6}/K, respectively. The incorporation of Al_2O_3could decrease the CTE of the composite coating. The composite coating prepared by cold spray and subsequent heat treatment showed good adhesion to the substrate, and no crack was observed even after 100 cycles of oxidation, while the conventional $TiAl_3$ coating was apt to produce cracks because of the low ductility of $TiAl_3$ phase and high CTE compared with the substrate (Smialek 1993; Pflumm et al. 2015).

Acknowledgments The financial support from the National Natural Science Foundation of China (No. 50971127, No. 50902131) is gratefully acknowledged. This work was made possible through collaborative efforts in my laboratory. I gratefully acknowledged my colleagues Prof. Tianying Xiong and Prof. Tiefan Li. I gratefully acknowledged the students L. Shen, J. Yang, Zhenguo Zhang, and Jiqiang Wang for their hard work in coating preparation and the assessment of coating performance. I also gratefully acknowledge the helpful comments and suggestions of Prof. Ke Yang and the reviewers, who have improved the presentation of chapter.

References

Berti S, Shaw BA, Shaw WW (2002) Corrosion evaluation of aluminum sacrificial coatings applied by various sprayed metal techniques. Corrosion, Houston

Braun R, Rovere F, Mayrhofer PH et al (2010) Environmental protection of γ-TiAl based alloy Ti-45Al-8Nb by CrAlYN thin films and thermal barrier coatings. Intermetallics 18:479–486

Braun R, Kelm K, Frohlich M, Leyens C (2013) Oxidation resistance of gamma-TiAl based alloy Ti-45Al-8Nb coated with intermetallic Ti-Al-Cr-Y layers and EB- PVD zirconia topcoats at 950 degrees in air. Surf Coat Technol 222:128–134

Chen WR, Irissou E, Wu X et al (2011) The oxidation behavior of TBC with cold spray CoNiCrAlY bond coat. J Therm Spray Technol 20:132–138

Chu MS, Wu SK (2003) The improvement of high temperature oxidation of Ti-50Al by sputtering Al film and subsequent interdiffusion treatment. Acta Mater 51:3109–3120

Danielewski M, Mrowec S, Stokosa A et al (1980) Defect structure and diffusion in nonstoichiometric ferrous sulphide. Solid State Ion 1:287–309
Gao J, He Y, Gao W (2012) Electro-codeposition of Al2O3–Y2O3 composite thin film coatings and their high-temperature oxidation resistance on γ-TiAl alloy. Thin Solid Films 520:2060–2065
Goral M, Swadzba L, Moskal G et al (2009) Si-modified aluminide coatings deposited on Ti46Al7Nb alloy by slurry method. Intermetallics 17:965–967
Kaur N, Kumar M, Sanjeev K et al (2015) Study of mechanical properties and high temperature oxidation behavior of a novel cold-spray Ni-20Cr coating on boiler steels. Appl Surf Sci 328:13–25
Kong LY, Qi JZ, Lu B et al (2010) Oxidation resistance of TiAl3–Al composite coating on orthorhombic Ti2AlNb based alloy. Surf Coat Technol 204:2262–2267
Kothari K, Radhakrishnan R, Wereley N (2012) Advances in gamma titanium aluminides and their manufacturing techniques. Prog Aerosp Sci 55:1–16
Lee HY, Yu YH, Lee YC et al (2004) Interfacial studies between cold-sprayed WO3, Y2O3 films and Si substrate. Appl Surf Sci 227:244–249
Leyens C, Braun R, Fröhlich M et al (2006) Recent progress in the coating protection of gamma titanium aluminides. JOM 58:17–21
Li ZW, Gao W, Ying DY et al (2003) Improved oxidation resistance of Ti with a thermal sprayed Ti3Al(O)-Al2O3 composite coating. Scr Mater 48:1649–1653
Lima CRC, Belém MJX, Crespo V et al (2015) High Temperature Oxidation of Cold Gas Sprayed Bond Coats for TBC Application. ITSC 2015-Pro. Inter Therm Spray Confer, Long Beach, California, USA
Miyake M, Tajikara S, Hirato T (2011) Fabrication of TiAl3 coating on TiAl-based alloy by Al electrodeposition from dimethylsulfone bath and subsequent annealing. Surf Coat Technol 205:5141–5146
Murray JL (1987) Diagrams of binary titanium alloys. ASM International, Materials Park, Ohio
Niraj B, Harpreet S, Prakash S (2010) Accelerated hot corrosion studies of cold spray Ni–50Cr coating on boiler steels. Mater Design 31:244–253
Pflumm R, Friedle S, Schütze M (2015) Oxidation protection of γ-TiAl-based alloys. Intermetallics 56:1–14
Rahmel A, Schütze M, Quadakkers W (1995) Fundamentals of TiAl oxidation–a critical review. Mater Corros 46:271–285
Sasaki T, Yagi T, Watanabe T et al (2011) Aluminizing of TiAl-based alloy using thermal spray coating. Surf Coat Technol 205:3900–3904
Shen L (2008). Investigation on cold gas dynamic sprayed TiAl3-Al composite coating and its oxidation resistance. Dissertation, Institute of Metal Reaserch
Smialek JL (1993) Oxidation behavior of TiAl3 coatings and alloys. Corros Sci 35:1199–1208
Swadzba L, Moskal G, Hetmanczyk M et al (2004) Long-term cyclic oxidation of Al–Si diffusion coatings deposited by arc-PVD on TiAlCrNb alloy. Surf Coat Technol 184:93–101
Tao YS, Xiong TY, Sun C et al (2009) Effect of a-Al2O3 on the properties of cold sprayed Al/a--Al2O3 composite coatings on AZ91D magnesium alloy. Appl Surf Sci 256:261–266
Van Loo FJJ, Rieck GD (1973a) Diffusion in the titanium-aluminum system--I. Interdiffusion between solid Al and Ti or Ti-Al alloys. Acta Metall 21:61–71
Van Loo FJJ, Rieck GD (1973b) Diffusion in the titanium-aluminium system--II. Interdiffusion in the composition range between 25 and 100 at.% Ti. Acta Metall 21:73–84
Varlese FA, Tului M, Sabbadini S et al (2013) Optimized coating procedure for the protection of TiAl intermetallic alloy against high temperature oxidation. Intermetallics 37:76–82
Victor KC (2007) The cold spray materials deposition process fundamentals and applications. WP, New York
Wang JQ, Kong LY, Li TF et al (2015) Microstructure Evolution of Cold- Sprayed Al - Si Alloy Coatings on γ-TiAl During Heat Treatment. J Therm Spray Technol 24:1071–1080
Wang JQ (2016) Study of silicon-aluminizing coating prepared by cold spray and subsequent heat-treatment. Dissertation, Institute of Metal Research

Wolfe D, Eden T (2007) Cold spray particle deposition for improved wear resistance. In: Victor KC (ed) The cold spray materials deposition process fundamentals and applications. WP, New York

Xiang ZD, Rose SR, Datta PK (2002) Pack deposition of coherent aluminide coatings on γ-TiAl for enhancing its high temperature oxidation resistance. Surf Coat Technol 161:286–292

Xiang Z, Rose S, Datta P (2003) Codeposition of Al and Si to form oxidation-resistant coatings on γ-TiAl by the pack cementation process. Mater Chem Phys 80:482–489

Xiong HP, Mao W, Xie YH et al (2004) Liquid-phase siliconizing by Al-Si alloys at the surface of a TiAl-based alloy and improvement in oxidation resistance. Acta Mater 52:2605–2620

Xiong HP, Wei M, Xie YH et al (2005) Formation of silicide coatings on the surface of a TiAl-based alloy and improvement in oxidation resistance. Mater Sci Eng A 391:10–18

Xu Y, Miao Q, Liang W et al (2014) A comparison of oxidation behavior of Al coatings prepared by magnetron sputtering and arc ion plating on γ-TiAl. Rare Met Mater Eng 43:2652–2656

Yamada M, Isago H, Shima K et al (2010) Deposition of TiO2 ceramic particles on cold spray process. Inter Therm Spray Confer Exp 2010. Singapore

Yang GJ, Li CJ, Han F et al (2008) Low temperature deposition and characterization of TiO2 photocatalytic film through cold spray. Appl Surf Sci 254:3979–3982

Yang J, Kong LY, Cui XY et al (2011) Improvement in the oxidation resistance of TiAl based alloy by cold spraying Al coating and subsequent interdiffusion treatment. Adv Mater (Rus) 13:295–299

Zeng S, Zhao A, Jiang H (2015) Oxidation of conventional and nanostructured 8 wt.% yttria-stabilized zirconia coating surface coatings on γ-TiAl. Appl Surf Sci 332:362–367

Zhang ZG (2013) Preparation and oxidation behavior of high-temperature protective coatings on TiAl alloy. Dissertation, Institute of Metal Research

Zhang DL, Cai ZH, Adam G (2004) The mechanical milling of Al/TiO2compositepowders. JOM 56:53–56

Zhang K, Sun C, Wang FH (2006) Preparation and protection of Al diffusion coatings on matrixγ-TiAl. Acta Metall Sin 42:355–360

Zhang P, Flores-Renteria A, Wild E et al (2009) Oxidation-resistant Ti-90Al coatings with lotus effect surface morphology deposited on a gamma-TiAl alloy. Scr Mater 61:1156–1159

Zhang H, Peng X, Wang F (2012) Fabrication of an oxidation-resistant beta-NiAl coating on gamma-TiAl. Surf Coat Technol 206:2454–2458

Part VI
Mechanical Properties

Chapter 15
Understanding Adhesion

Daniel MacDonald, Aleksandra Nastic, and Bertrand Jodoin

15.1 Introduction

One of the most attractive features of the cold spray (CS) process is its flexibility in substrate/powder material combinations. This chapter aims to develop a thorough understanding of the particle to substrate adhesion process, which is fundamental to the development of high adhesion coatings.

15.1.1 The Physics of Particle Impact

The particle impact time, from initial contact to complete dissipation of kinetic energy, is typically less than 100 ns (Gärtner et al. 2003; Assadi et al. 2016). As the particle strikes the substrate, a small portion of the available kinetic energy is used for viscoplastic deformation and elastic energy storage, while the remaining 90% is converted into heat. It has been suggested that the amount of energy dissipated into heat increases with increasing strain rates (Kapoor and Nemat-Nasser 1998). The heat generated through dissipation of plastic strain energy can produce strain localization and ultimately shear instability. With increasing local temperature, thermal softening alters the capacity of the material to transmit shear forces and eventually the softening process dominates over strain hardening. Beyond this point, the strain increases, while the stress drastically drops

D. MacDonald (✉) • A. Nastic (✉) • B. Jodoin
Ottawa Cold Spray Laboratory, Department of Mechanical Engineering,
University of Ottawa, Ottawa, ON, Canada
e-mail: Daniel.MacDonald@uottawa.ca; Aleksandra.Nastic@uottawa.ca;
Bertrand.Jodoin@uottawa.ca

P. Cavaliere (ed.), *Cold-Spray Coatings*,
https://doi.org/10.1007/978-3-319-67183-3_15

leading to the state of shear instability. The process can be adiabatic; however, its adiabacity relies on the following relation:

$$\frac{\chi^2}{\alpha t} = \beta \gg 1 \tag{15.1}$$

which suggests that the process falls under adiabatic condition only if the system dimensions (χ) are considerably greater than the thermal diffusion distance (αt), in which χ relates to the particle dimensions, α is the thermal diffusivity, and t is the process time (Assadi et al. 2016; Schmidt et al. 2006b). This type of material response to impact leads to the formation of material jet and ejection. The powerful material ejection is thought to provide removal of oxide layers at the particle periphery and consequently delivers clean metal-to-metal intimate contact zones required to get metallurgical bonding. Thus, material jetting is considered to be the main factor leading to bonding in both the CS and explosive welding (EW) processes (Kim et al. 2009; Assadi et al. 2003). However, the particle deformation behavior in response to impact becomes more complicated when two dissimilar materials are to be bonded.

15.1.2 Critical Velocity

Optimization of the CS process continuously strives toward increasing the deposition efficiency (DE) of a given material, defined as the fraction of deposited mass over the overall sprayed mass. DE is closely related to the material adhesion behavior and therefore provides insight to the particle bonding process.

Since the discovery of CS in the 1980s (Alkhimov 1994; Papyrin 2001), it has been recognized that particles need to exceed a so-called critical velocity, V_c, to deposit. This critical velocity is dependent on the substrate and particle material properties and particle size and geometry (Assadi et al. 2003; Raletz et al. 2006; Li et al. 2006; Huang and Fukanuma 2009). The concept of critical velocity in collision-like deposition methods is not novel and has been studied for the explosion welding (EW) process (Akbarimousavi and Alhassani 2005). The velocity of impacting materials establishes the type of pressure field generated at contact zones, the time available for interatomic bonding, and the available energy for oxide layer disruption and material deformation. A minimum velocity, V_c, is needed for bonding to occur; however, too high of an impact velocity leads to substrate surface erosion (Schmidt et al. 2006a; b) as a result of excess elastic energy available for particle rebounding. The velocity range bound by those two criteria defines the deposition window of a given material in CS (Stoltenhoff et al. 2002).

Materials with low mechanical strength and low melting points, such as aluminum, copper, nickel, tin, zinc, and silver, have shown to exhibit low V_c. These metals share the same face-centered cubic (FCC) crystal structure characterized by 12 slip systems occurring along closed packed planes allowing increased lattice deformation. Critical velocities of 570 m/s for copper (5–25μm) (Assadi

et al. 2003; Stoltenhoff et al. 2002), 500 to 660 m/s for aluminum (20 μm) (Klinkov and Kosarev 2006; Assadi et al. 2003), 512 m/s for nickel (10–33 μm) (Raletz et al. 2006), and 350 m/s zinc and silver particles (25 μm) are required to reach a suitable DE. In contrast, body-centered cubic (BCC) and hexagonal close packed (HCP) metals exhibit considerably less deformation under similar impact velocities due to the reduced amount of slip planes and consequently require larger impact velocities to allow for deposition. For example, a V_c of 750 m/s was measured for titanium (Schmidt et al. 2009). Ceramic materials tend to be difficult to spray due to their brittleness; however, few studies have successfully deposited ceramic coatings with limited thickness: TiO_2 on Ti under 1 μm (Schmidt et al. 2017), ZrO_2 on Al under 10 μm (Vlcek et al. 2005), and TiO_2 on soft SS400 substrate close to 10 μm (Yamada et al. 2010). Moreover, studies have shown successful deposition of metals onto ceramics, and the atomic-scale structural alignment was given to be the source of bonding (Drehmann et al. 2014a; King et al. 2008).

In addition, the particle size also affects the V_c of a given material. The critical velocity increases with decreasing particle size (Schmidt et al. 2006a; b; Schmidt et al. 2009). Although small particles can easily reach their V_c at the exit of the nozzle, they can undergo deceleration due to the bow shock at the substrate surface vicinity, which can hinder their deposition. Larger surface oxygen contents are also expected for smaller particles due to their larger specific surface area, which obstructs the bonding process at impact and as a result increases the V_c. In addition to high cooling rates, small particles undergo increased strain-rate hardening, which limits the localized jetting and increases the V_c. Typical particle size for CS applications is in the range of 10–45 μm for ductile materials (Schmidt et al. 2006a, b).

Apart from crystal structure, particle size and inherent thermal and mechanical properties, both the particle purity and substrate material influence the V_c for a given substrate/particle material combination. Alloy materials tend to reduce the particle deformability by hindering the motion of dislocations through impurity atoms, which gives rise to higher V_c. Similarly, oxidized particles with increased oxide layer thickness reduce material ductility and impede intimate metal-to-metal contact (Li and Gao 2009). Particle to substrate softness ratio influences the total amount of deformation that both surfaces will experience, which will result in either full/partial particle flattening or embedment (King et al. 2010; Bae et al. 2008; Schmidt et al. 2009).

15.1.3 The Nature of Adhesion

Despite the minute time and length scales of the CS process, numerous interfacial features have been detected using high-end analysis equipment. The following section will provide examples and summarize the observed microstructural characteristics that relate to the existing type of bonding between the particle and substrate.

15.1.3.1 Metallic Bonds

In a metallic bond, the valence electrons from adjacent atoms are shared in a common cloud. Outside the sphere of influence, the atoms are too far to induce any repulsive or attractive interaction forces. The magnitude of both forces and their respective influence on two isolated atoms depends on interatomic distances and atomic charge. High pressure developed at contacting oxide-free surfaces allows the valence electrons from both materials to cross each other's sphere of influence, resulting in the creation of metallic bonds. In a bonded region, an equilibrium state exists in which the repulsive and attractive forces are balanced, and an equilibrium spacing (~ 0.3 nm) separates the atoms (Callister and Rethwisch 2008). In a metallic bond, the cloud of free electrons shields the positively charged ion core from mutually repulsive electrostatic forces, which makes the metallic bond nondirectional in nature. The resulting bonding energy represents the energy required to separate two atoms to an infinite distance. In a more complex system comprising of more than two interacting atoms, a similar but more complex state exists that considers all energy interactions between influencing forces.

The development of an atom-to-atom bond between metals has been investigated for decades through theoretical and experimental models of one of the simplest kind of mating process known as solid-state pressure welding, also referred to as cold welding (CW). The commonly accepted theory states that the primary requirement for the creation of a bond between two surfaces is intimate, oxide-free, pressurized contact, deprived of organic contaminants (Semenov 1961; Mohamed and Washburn 1975) However, at room temperature and in an atmospheric environment, all metals, except gold, possess a thin oxide layer that would need to be removed either prior or during the CW process (Mohamed and Washburn 1975).

The CS process also has the ability to bond together dissimilar materials with different crystal structures and inherent properties. Figure 15.1 shows successful cold-bonded material combinations based on their crystalline structure and hardness. Metals with face-centered cubic (FCC) lattice structure exhibit the highest ability to create bonds (adapted from Li et al. 2008). This was associated to their lower strength and higher threshold deformation based on the FCC's closed packed lattice configuration, provided that the work hardening is not a dominating process.

In CS, the particle impact generates extreme strain rates, up to 10^9 s^{-1} (Schmidt et al. 2006a; b; Assadi et al. 2003), which provides sufficient deformation and pressure to remove native oxides on both material surfaces (Grujicic et al. 2004; Xie et al. 2016b). The particle deformation process is difficult to accurately characterize, as the process is within the nanoscale. Consequently, establishing whether or not the required conditions (general and localized temperature, pressure, stress, and strains) are reached at the contacting surfaces is difficult to assess.

15.1.3.2 Mechanical Interlocking

Mechanical interlocking is defined as the physical connection between two materials in contact through the linkage of common surface features. Its presence is known to increase coating adhesion and in some cases has been shown to be responsible for

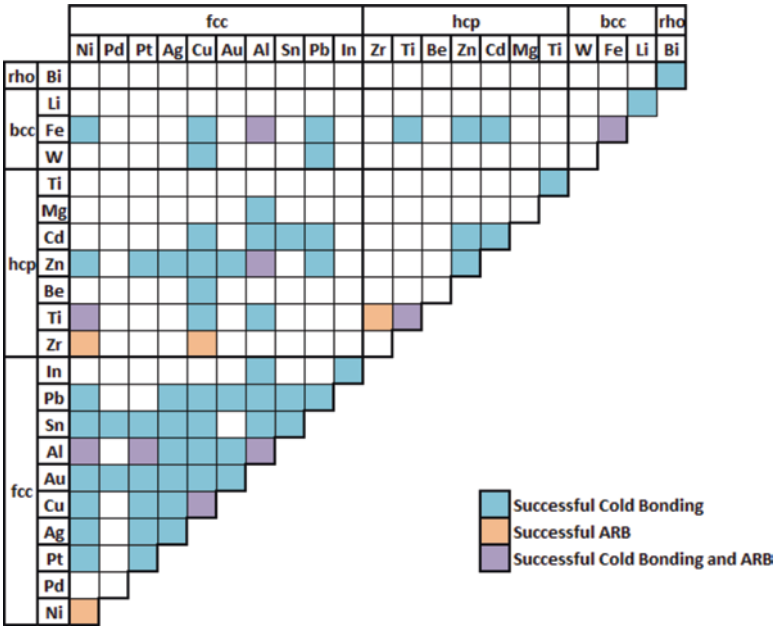

Fig. 15.1 Successful bonding formed during cold bonding and/or accumulative rolling bonding (ARB) processes according to the lattice structure and hardness of different metals

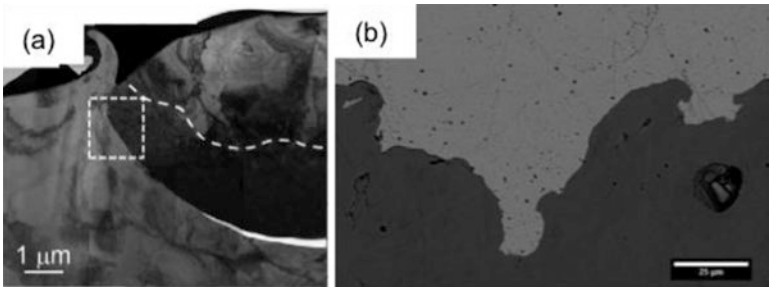

Fig. 15.2 (**a**) Mechanical interlocking of copper particles into the aluminum substrate during the deposition process, (**b**) FPWJ-treated substrate surface providing mechanical interlocking (Reproduced with permission of Springer)

the majority of the adhesion strength (Fernandez et al. 2016; Grujicic et al. 2003; Hussain et al. 2009). Interlocking can occur during metal jetting of a softer substrate surface around a harder impacting particle as shown in Fig. 15.2a for titanium sprayed on aluminum (Kim et al. 2010). Additionally, mechanical anchoring can also be created prior to deposition through substrate surface roughening procedures (Fernandez et al. 2016; Hussain et al. 2009; King and Jahedi 2010; Sharma et al. 2014; Samson et al. 2015) as shown in Fig. 15.2b for a copper coating deposited onto a forced pulsed waterjet (FPWJ)-treated steel substrate (Fernandez et al. 2016). The interlocking strength relies on the properties of the surface features and capacity to hold the underlying coating under an applied stress.

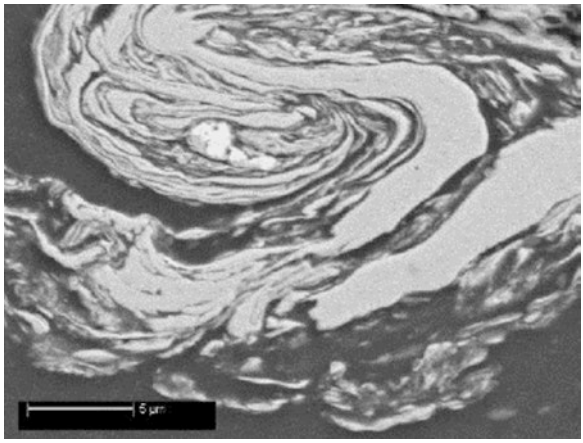

Fig. 15.3 Interface instabilities forming vortex-like features (Reproduced with permission of Springer)

Mechanical interlocking may also result from interfacial perturbations, resulting from viscous-like material flow that result in material mixing, as depicted in Fig. 15.3 (Ajdelsztajn et al. 2005). The onset of interfacial perturbation follows the Kelvin-Helmholtz instability principle (Grujicic et al. 2003). The surface instabilities are developed due to a large difference in velocities and densities between the lower and upper layers of the substrate surface.

15.1.3.3 Other Adhesion Mechanisms

Studies have shown that small particles with average diameter ranging between 0.1 and 1 μm and traveling velocity of 100 m/s are able to deposit and adhere successfully to the impacted surface (Rollot et al. 1999). It was proposed that adhesion was governed by Van der Waals (VDW) and electrostatic forces. VDW forces, also known as dispersion or electrodynamic forces, are weak long-range repulsive or attractive atomic level forces that act between neutral or charged atoms. VDW forces are always present and dominant in absence of electrostatic forces in restricted simple systems (Israelachvili 1974; Hamaker 1937). In more complex systems, when the atoms are charged, strong long-range electrostatic attraction also leads to their interaction, as explained in Sect. 1.3.1. The atomic separation distance and the charge sign govern the resulting interplay between VDW and electrostatic forces and the consequential equilibrium state. However, in CS applications, the coatings adhesion considerably exceed the level of VDW forces such that they are considered, if present, to have limited influence on adhesion.

15.2 The Influence of Cold Spray Parameters on Adhesion

The inherent properties of the substrate and powder materials have a significant influence on adhesion. However, the CS process parameters also significantly affect the adhesion strength of coatings by modifying the prevalence of metallically

bonded and/or mechanically interlocked regions. For a particular powder/substrate combination, the adhesion strength is influenced by the impact conditions: mainly the particle velocity, the particle temperature, and the substrate temperature. Impact conditions are directly affected by process parameters: primarily the nature, temperature, and pressure of the propellant gas, velocity of the spray gun, standoff distance, powder preheating, nozzle material, and nozzle geometry.

15.2.1 Effect of Impact Conditions on Adhesion

15.2.1.1 Particle Velocity

Since the introduction of CS, the idea that particle velocity influences adhesion has been well established (Huang and Fukanuma 2012; Wu et al. 2006; Goldbaum et al. 2012). Particles traveling at higher velocities are more likely to develop zones of high plastic deformation, resulting in the intimate contact of oxide-free surfaces as well as interfacial mechanical anchors. Figure 15.4 presents a typical result from tensile tests, showing an increase in adhesion strength of a copper coating on A5052 substrate with an increase in particle velocity (Huang and Fukanuma 2012).

15.2.1.2 Particle Temperature

The low temperatures and high velocities in CS have prevented experimental measurement of particle temperature. This has limited the investigation of the effect of particle temperature on adhesion strength. However, increased particle

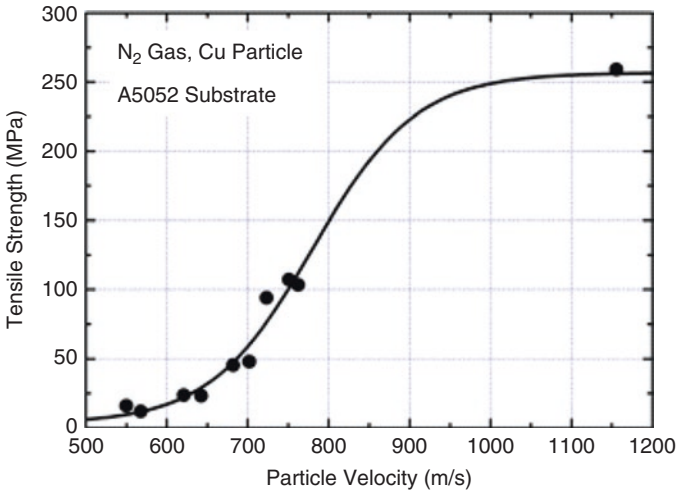

Fig. 15.4 Tensile adhesion strength of a copper coating on A5052 substrate for different particle velocities (Reproduced with permission of Springer)

temperatures have been shown to reduce the critical velocity required for bonding (Schmidt et al. 2006a; b). This reduction of critical velocity would result in a higher ratio of particle velocity to critical velocity, which was shown to increase general coating properties such as deposition efficiency, flattening ratio, and cohesive strength for titanium and copper deposits (Assadi et al. 2011). It has also been demonstrated that the cohesive strength of copper deposits was increased with an increase in particle temperature (Schmidt et al. 2006a, b). Although no data could be found directly on adhesion strength, it is likely that the phenomenon responsible for an increase in cohesive strength would also result in an increase of adhesion strength.

15.2.1.3 Substrate Temperature

An increase in substrate temperature will soften the substrate material, reducing the stresses required for plastic deformation. It has also been shown to increase peak interface temperatures during deposition (Yin et al. 2015). This indicates a higher probability of mechanical interlocking and metallurgical bonding. Most studies (Xie et al. 2016a; Goldbaum et al. 2012; Watanabe et al. 2014; Yin et al. 2015; Danlos et al. 2010) are in agreement that increased substrate temperature does result in an increased adhesion strength, as was shown for 316 stainless steel (Xie et al. 2016a), presented in Fig. 15.5.

Although most publications agree on this trend, it has been demonstrated that high substrate temperatures can increase oxide layer thickness on steel substrates, resulting in a decreased adhesion strength (Watanabe et al. 2014). However, Yin et al. did not observe this result in their research, stating "the thickness of the oxide film barely influences the interfacial bonding…" (Yin et al. 2015). Although the conclusion is not clear, the oxidation of the substrate should be carefully considered when preheating substrates for deposition.

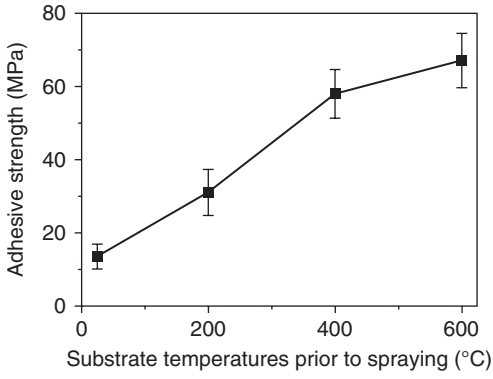

Fig. 15.5 Adhesion strength for different substrate temperatures (Reproduced with permission of Springer)

15.2.2 The Effect of CS Process Parameters on Impact Conditions

Section 2.1 outlined the effects of particle velocity, particle temperature, and substrate temperature on adhesion. Understanding how those conditions can be modified through the optimization of the process parameters is of key importance to maximize adhesion strength of coatings.

15.2.2.1 The Nature of the Propellant Gas

From the inception of the CS process, it has been known that the propellant gas nature has a significant effect on particle velocity (Alkhimov 1994). This relationship stems from the 1D isentropic model for the gas velocity in an expanding supersonic nozzle (Dykhuizen and Smith 1998):

$$V = M\sqrt{kRT} \tag{15.2}$$

where M is the gas local Mach number, R is the specific gas constant, T is the local gas temperature, and k is the gas heat capacity ratio. This relationship demonstrates that the gas velocity, and ultimately the particle velocity, can be greatly influenced by the molecular weight of the propellant gas, as the molecular weight influences both the specific gas constant and the heat capacity ratio.

Helium, nitrogen, and air are primarily used as CS process gasses. Helium has a substantially lower molecular weight (4.0126 g/mol) when compared to nitrogen gas (28.013 g/mol) and air (approximately 29 g/mol). This generally results in higher particle velocities when using helium for fixed spray conditions as stated in the original CS patent (Alkhimov 1994).

The use of helium will result in higher particle velocities; however, its usage may be prohibitively expensive. However, in recent years helium recycling systems have been shown to keep the costs competitive with nitrogen (Wong et al. 2011). It has also been demonstrated that the blending of helium and nitrogen results in an increase in particle velocity with an increase in helium concentration (Ozdemir et al. 2016), as shown in Fig. 15.6.

While it is established that the use of lower molecular weight gasses increases the particle velocity, few studies have reported the effect the gas nature has on the other impact conditions. It was recently demonstrated, through CFD modeling, that particle temperature decreases with higher concentrations of helium, with particle temperature decreasing from 450 to 300 K with the addition of 70% helium volume to nitrogen (Ozdemir et al. 2016). Although studies have been published on the heat transfer of the gas stream to the substrate (McDonald et al. 2013), no clear conclusion has been found stating the effect of gas nature on the substrate temperature.

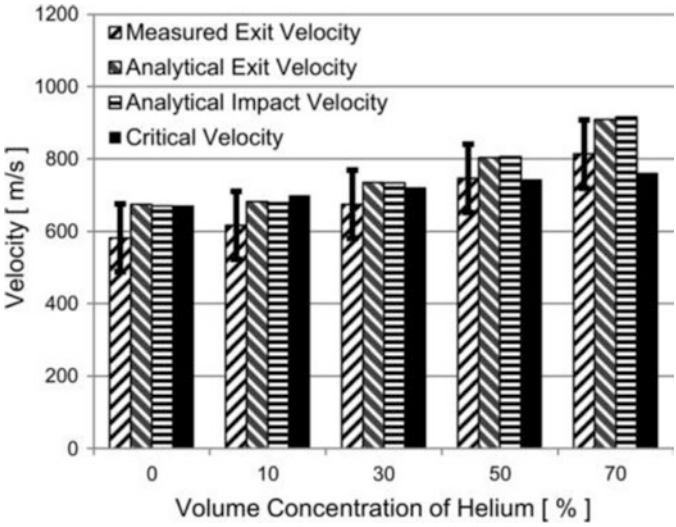

Fig. 15.6 Particle (26 μm) velocity for different helium concentrations with nitrogen (Reproduced with permission of Springer)

15.2.2.2 The Stagnation Temperature of the Propellant Gas

The local gas temperature has a significant effect on the gas stream velocity, as seen in Eq. 15.2. The local gas temperature is related to the stagnation temperature through the 1D isentropic relationship:

$$\frac{T_o}{T} = 1 + \frac{(k-1)}{2} M^2 \tag{15.3}$$

where T_o is the gas stagnation temperature. The effect of increasing the gas stagnation temperature has been established by many authors to increase particle velocity (Legoux et al. 2007; Gilmore et al. 1999; Kwon et al. 2005; Van Steenkiste and Smith 2004; Fukumoto et al. 2007; Stoltenhoff et al. 2002; Alkhimov 1994; Jodoin et al. 2006).

As expected, studies have shown that substrate temperature also increases with gas temperature (Legoux et al. 2007; McDonald et al. 2013). CFD modeling has demonstrated that the particle temperature increases with an increase in gas stagnation temperature (Kwon et al. 2005; Van Steenkiste and Smith 2004; Stoltenhoff et al. 2002).

15.2.2.3 The Stagnation Pressure of the Propellant Gas

According to the 1D approximation, shown in Eq. 15.2, the gas velocity is completely independent from gas stagnation pressure. However, the particles do not necessarily travel at gas velocity but are accelerated by the drag force induced by this high velocity gas, which can be estimated through the equation:

$$m\frac{\mathrm{d}V_\mathrm{p}}{\mathrm{dt}} = \frac{1}{2}\rho\left(V - V_\mathrm{p}\right)^2 C_\mathrm{d} A_\mathrm{p} \tag{15.4}$$

where m is the particle mass, V_p is the particle velocity, t is time, ρ is the propellant gas density, V is the propellant gas velocity, C_d is the drag coefficient, and A_p is the particle cross-sectional area.

The cross-sectional area and particle mass are not considered process parameters in the way this chapter defines them; therefore, they can be considered a constant. The drag coefficient varies depending on the instantaneous conditions, but it can be assumed constant for simplicity (Dykhuizen and Smith 1998). As such, the particle velocity is only influenced by the gas density and velocity. The 1D isentropic relationship for the gas density relates it to the local gas Mach number and the gas stagnation density:

$$\frac{\rho_\mathrm{o}}{\rho} = \left(1 + \frac{(k-1)}{2}M^2\right)^{\frac{1}{k-1}} \tag{15.5}$$

where this stagnation density is given by the ideal gas law:

$$P_\mathrm{o} = \rho_\mathrm{o} R T_o \tag{15.6}$$

For this reason, the increase in gas stagnation pressure should result in an increased drag force and a potentially higher particle velocity. Obviously, the particle velocity will always be limited to the gas velocity (Dykhuizen and Smith 1998).

The effect of stagnation pressures on particle temperature has also been studied. It has been concluded, through CFD modeling, that the gas stagnation pressure has minimal effects on the particle temperature (Kwon et al. 2005; Stoltenhoff et al. 2002).

15.2.2.4 The Nozzle Geometry

The nozzle geometry establishes the local Mach number inside the nozzle at any axial location, which is determined by the nozzle area ratio and is related by the following 1D approximation:

$$\frac{A}{A^*} = \frac{1}{M}\left[\left(\frac{2}{k+1}\right)\left(1 + \frac{(k-1)}{2}M\right)\right]^{k+1/2(k-1)} \tag{15.7}$$

where A is the local nozzle area and A^* is the nozzle throat area. From Eq. 15.7, a larger area ratio will increase the local Mach number and therefore the flow velocity.

However, it has been stated that there is a limit to the maximum nozzle Mach number (approximately Mach = 3) due to complex shockwave/particle interactions (Jodoin 2002).

Nozzle length will also determine the particle residence time in the fast moving flow. This can result in higher particle velocities for longer nozzles. However, when increasing the nozzle length, the friction between the nozzle wall and gas will increase, and new phenomena must be taken into account (Alkhimov et al. 2001).

15.2.2.5 The Nozzle Material

Very few studies have been done on the influence of nozzle material on the particle impact conditions. Typically, nozzle material is thought to only have an effect on the wear and clogging during deposition (MacDonald et al. 2016). However, a correlation between nozzle material and particle velocity has been shown in a recent study (MacDonald et al. 2016). In this study, nozzles were produced with different materials with the exact same geometries. Tests were done under the same spray conditions, and the median particle velocity for the polymer nozzle was 616 m/s, while it was 448 m/s for the copper nozzle. In contrast to expected results, the highest DE was found for the copper nozzle and the lowest for the polymer nozzle. The study concluded that in many cases, the particles have direct contact with the nozzle walls, which can lower the particle velocity but increase the temperature.

15.2.2.6 Particle Preheating

Purposely raising particle temperature is typically accomplished in two ways: through an external particle preheater or by changing the location at which particles are injected into the spray nozzle gas stream. It was demonstrated that exiting particle temperatures increased when particles are injected further upstream of the nozzle throat (Schmidt et al. 2006a, b). This effect was amplified for larger particles and it was shown to have significant effect on the coatings quality.

Separate powder preheating can be accomplished by passing the powder through a heating coil before being injected into the main gas flow. In these cases, it is usually assumed that the particles are at powder feeding gas temperature prior to injection.

15.2.2.7 The Nozzle Traverse Velocity

Traverse velocity has been shown to have no effect on the particle velocity or temperature. However, lower traverse velocities increase the time for heat transfer to occur between the propellant gas and substrate, resulting in possibly higher substrate temperatures (Wong et al. 2011; Yin et al. 2011; McDonald et al. 2013).

15.2.2.8 The Nozzle Standoff Distance

The nozzle standoff distance (SOD) must be in a certain range to effectively deposit particles on a substrate. It has been shown that there are three regions when it comes to SOD: Region 1, where the SOD is too small and particle velocities are reduced as a consequence of a strong bow shock; Region 2, where for a medium SOD the particle velocities increase; and Region 3, where a large SOD results in particles decelerating as they are now traveling faster than the gas stream (Pattison et al. 2008; Stoltenhoff et al. 2002). It is therefore recommended to operate in Region 2. However, the distances for these regions will change depending on spray conditions and nozzle geometry and must be determined experimentally or through modeling. As is expected, the substrate temperature was also shown to decrease with an increase in standoff distance (Yin et al. 2013).

15.3 Surface Preparation

It is often stated that CS substrates do not require any surface preparation as the particle impacts typically provide the necessary cleaning and roughening. However, this does not appear to agree with all experimental results, as the substrate surface condition has been shown to be of great influence in many cases (Samson et al. 2015; Fernandez et al. 2016; Hussain et al. 2009). The effect of substrate preparation on adhesion strength is a complex issue, fielding different results depending on the particle/substrate material combinations and the particle impact conditions.

15.3.1 Roughening Surface Preparations

CS substrate surfaces are typically roughened to improve the mechanical anchoring of a deposited coating. The substrate surface roughness is typically quantified by the arithmetic average roughness (*Ra*), defined as the arithmetic average of the absolute values of the profile height deviations from the mean line. The root mean square average (*Rq*) and the maximum height (*Ry*) are also used occasionally. These values ignore the three-dimensional aspects of the surface features, taking into account only height deviations. This can complicate data interpretation, as two substrates may have very similar arithmetic average roughness values but have drastically different surface characteristics and resulting adhesion (Samson et al. 2015). Substrate roughness is typically modified using abrasive blasting or more recently through forced pulsed waterjet.

15.3.1.1 Abrasive Blasting

Cold spray, being one of the newer thermal spray technologies, has adapted many of the thermal spray practices that have come before it, most notably the preparation of substrates using abrasive (grit) blasting. Abrasive blasting is the operation of propelling a stream of abrasive (usually ceramic) material against a substrate. The main purpose of this process is to obtain a level of surface roughness that improves mechanical anchoring of the coatings as well as cleaning contaminants to promote metallic bonding. However, proper cleaning by abrasive blasting is not the ideal method; organic contaminants are better removed with organic solvents, native oxides normally present in metals will quickly reform after the process, and abnormal oxides and inorganic products are better removed by chemical methods (Wigren 1988). Typical roughness values for abrasive blasting are on the order of 2–7 μm, depending on the substrate and grit materials and blasting process parameters (Harris and Beevers 1999).

Although the vast majority of CS studies use abrasive blasting as the default surface preparation method, the use of grit blasting to improve adhesion can be controversial (Day et al. 2005), and very few studies demonstrate the need or benefit of this surface preparation method. Abrasive blasting is also known to result in grit residue on the surface (grit embedment), which can remain at the interface between the coating and substrate. Day et al. demonstrated that up to 10% of the substrate surface area can be covered with this residue for steel surfaces (Day et al. 2005). Studies have attributed a sharp decrease in adhesion to this residue (Samson et al. 2015). It was suggested that in order to minimize grit embedment, the finest grit possible should be used with the lowest pressure and shortest blasting time (Day et al. 2005). This is in agreement with previous work that shows higher blasting times significantly increases the percentage of residue (up to 32% residue coverage) (Wigren 1988). It has also been suggested to perform the blasting procedure at an impact angle of 45° for minimal embedment (Wigren 1988).

15.3.1.2 Forced Pulsed Waterjet

In recent years, the use of the forced pulsed waterjet (FPWJ) system to roughen surfaces before deposition has been studied. This process can provide roughness values much higher than those typically found in abrasive blasting (up to Ra = 80 μm) while eliminating the risk of abrasive residue at the surface (Fernandez et al. 2016; Samson et al. 2015).

The FPWJ prepares substrates through the impacting of a high-frequency, high-pressure water jet. This results in noncontinuous discrete packets of water, known as “slugs” (Vijay et al. 2013). These slugs result in a rapid water hammer over-pressure waves upon the target surface. This water hammer phenomenon greatly enhances the erosive capacity of the pulsed waterjet compared to con-

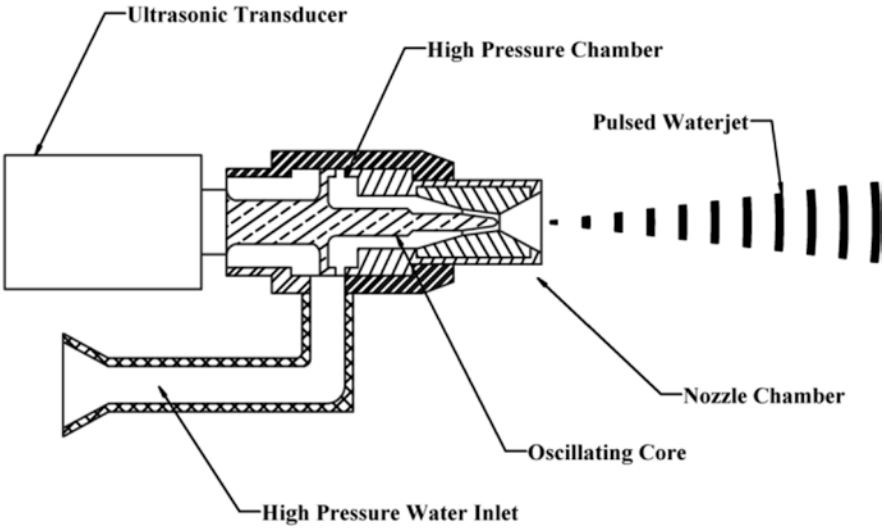

Fig. 15.7 Schematic of the pulsed waterjet system (Reproduced with permission of Springer)

tinuous waterjet applications. The mechanism of mass loss is similar to material removal due to cavitation erosion (Karimi and Martin 1986). A schematic of the system is presented in Fig. 15.7 (Samson et al. 2015).

15.3.2 Non-roughening Substrate Preparations

Some surface preparation methods do not involve changing the substrate surface roughness but focus on cleaning the surface of oxides and contaminants to improve the probability of metallic bonding. This is typically achieved through means such as laser or chemicals.

15.3.2.1 Laser Preparation

Laser substrate preparation can serve two distinct purposes: to clean contaminants immediately prior to particle impact though ablation and to heat the substrate locally. Typically, these purposes require different types of lasers, but are often combined in multi-laser systems.

In the laser ablation surface preparation process, a pulsed laser irradiates the substrate which removes the contaminants. This ablation process can also eliminate the native oxide layers of the substrate, which could improve the likelihood of metallic bonding. This ablation process has been shown to have a minimal effect on surface roughness, while having a significant effect on adhesion strength

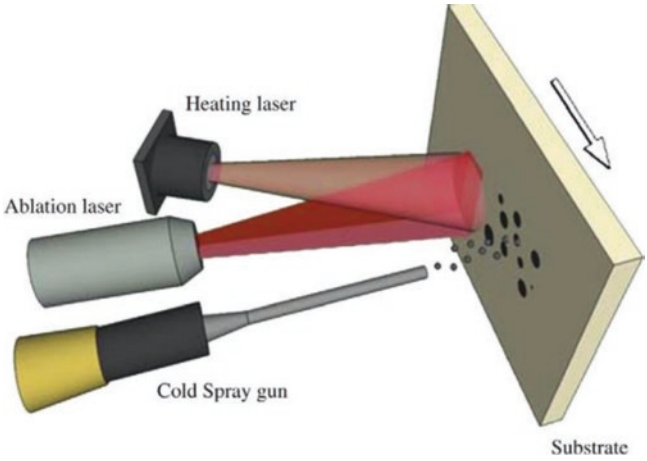

Fig. 15.8 Schematic of the combined heating and ablating laser cold spray system (Reproduced with permission of Springer)

(Villafuerte 2015). A commercial system has been developed for thermal spray processes (PROTAL, Quantel, Lannion, France) as a solution for laser ablation.

In laser heating, a CS gun is paired with a diode laser pointed directly in front of the powder beam. The laser is controlled to heat the substrate from 450 to 900 °C, and significant improvements in adhesion and densification are observed (Bray et al. 2009).

The two types of laser preparations were successfully combined, with one laser ablating the surface directly in front of the impacting particle jet and the other laser simultaneously heating the deposition area, as shown in Fig. 15.8 (Danlos et al. 2010). Higher adhesion was observed for substrates treated in these conditions when compared to conventional surface preparation methods (Danlos et al. 2017; Christoulis et al. 2010).

15.3.2.2 Chemical Cleaning

Chemical cleaning to remove contaminants and native oxides can be done with various acids or bases (typically sulfuric, nitric, or hydrochloric acid). However, it is not common due to safety/environmental hazards and application complexity. It has been demonstrated that adhesion strength can be increased for pure aluminum coatings on aluminum 7075 through chemical deoxidation of the substrate using both a solution of 25% v/v of 85% H3PO4 and a solution of 50% v/v of 70% HNO3 + 2% v/v of 40% HF (Irissou and Arsenault 2007). These solutions would have removed the native oxide, the hydroxide film, and the secondary phases of the Al-alloy on top surface, allowing for an improved likelihood of metallic bonding.

15.4 The Mechanism of Adhesion

While studies about CS and its applications are continuously increasing in number, the fundamentals of interfacial bonding and critical aspects governing the adhesion are still not well understood. Figure 15.9 (Bae et al. 2008) summarizes four possible impact deformation processes based on the relative particle/substrate mechanical properties. Figure 15.9 shows that various distinct bonding mechanisms can arise during deposition and that the ensuing deformation extent of both the particle and substrate will consequently lead to different thermal and kinetic resulting energies. Both energies play key roles in the bond strength of coatings.

As discussed in previous sections, both the cold spray parameters and surface treatment methods influence the particle impact process and as a consequence affect the bonding at the interface. As such, the current section aims at explaining the processes arising at the impact surface that lead to either mechanical and/or metallic bonding of particles. Moreover, observations linked to the occurrence of both adhesion mechanisms and FEM results are presented.

15.4.1 Metallic Bonding

15.4.1.1 Oxide Removal

Many experimental observations (King et al. 2014; Yin et al. 2015; Xie et al. 2016b; Grujicic et al. 2004; Assadi et al. 2003) have shown discontinuous native oxide film disruption with intermittent metallic bonding at the clean interface. For cases where

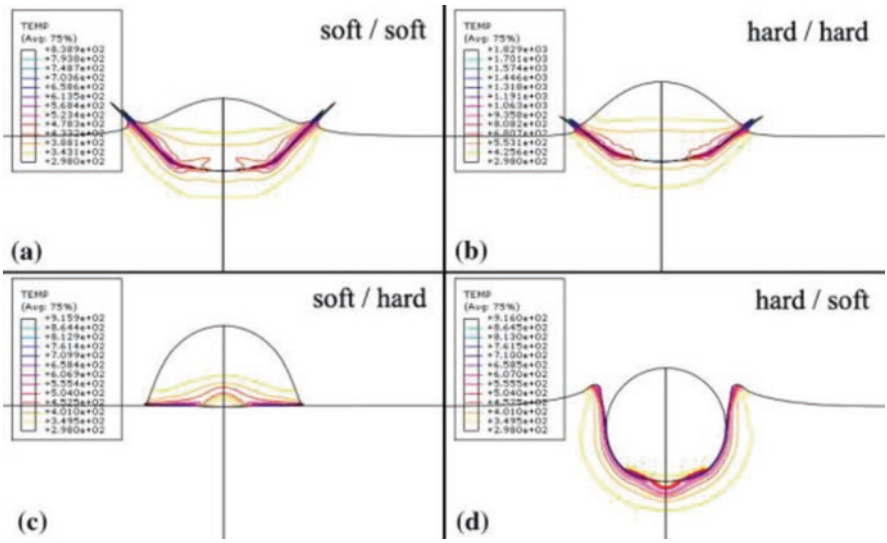

Fig. 15.9 FEA resulting temperature distribution for four cases of particle impact giving rise to different bonding and surface activation processes (Reproduced with permission of Elsevier)

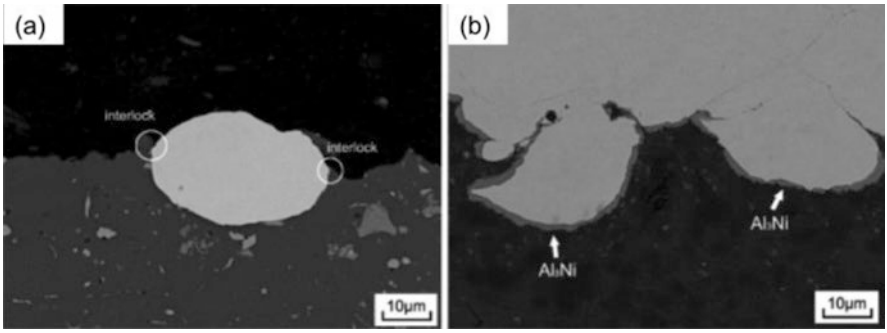

Fig. 15.10 Cross-sectional images of Ni particles deposited onto Al substrates for (**a**) single particle impacts and (**b**) full coating depositions after heat treatment (Reproduced with permission of Elsevier)

the particles and substrates experience large thermal softening, such as Al/Al (Li et al. 2007b; Yin et al. 2012) and Cu/Cu (Li et al. 2010), the metal-to-metal contact was associated to large deformation from material viscous plastic flow. However, many have shown that bonding still occurs despite the absence of large particle deformations for cases where the jetting mechanisms are found at the substrate surface (Yin et al. 2015; Xie et al. 2016b). Studies have shown that oxide disruption was absent for single particle impacts of Ni deposited onto Al substrates, but was obtained for full coating depositions through peening effects (Xie et al. 2016b) as shown in Fig.15.10. In full coatings, fresh metal is exposed at the interface from the impingement of subsequent deposited coating layers that promote further cracking of the oxide scale.

15.4.1.2 Melting

Interfacial melting has been associated to multiple surface features found on the substrate (Li et al. 2005; Ning et al. 2008; King et al. 2008, 2014; King and Jahedi 2010; Bae et al. 2009). Very fine molten aluminum ejecta have been found on the surface resulting from spheroidization and driven by surface tension (King and Jahedi 2010). The presence of spherical Zn particles of several hundred of nanometers on the coating surface was also observed. Splashing during liquid metal jetting was said to induce their formation (Li et al. 2005). In subsequent studies, possible melting zones were observed through dimple like ductile fracture surfaces of Ti coatings (Li et al. 2007b). The presence of cold weld regions at the peripheral interface of Ni particle and Cu substrate with a resulting intermixed region of 15 nm has been observed (Xiong et al. 2011). Considering the short impact time and the metal-metal interdiffusion coefficients of both materials, an interdiffusion distance of less than 0.1 nm was calculated possible and consequently fast quenching of strain-rate-induced melts and solid-state amorphization were assumed to occur alongside the limited interdiffusion process.

In dynamic amorphization, the enthalpy of fusion is reached through the shock-induced kinetic energy rather than thermal energy (Ikeda et al. 1999). In other words, the kinetic energy per atom imparted to the system through deformation is high enough to break the atomic bond and leave the atom in random position creating an amorphous state. The strain rates observed in cold spray can reach 10^9 s^{-1}, which is near the critical values of $5 \times 10^{10} s^{-1}$ and $7 \times 10^{10} s^{-1}$ found necessary for strain-rate-induced amorphization of metallic monocrystal nanowire (Ikeda et al. 1999; Branicio and Rino 2000).

15.4.1.3 Intermetallics

In multiple publications, intermetallic layers at the interface have been identified using TEM and chemical composition analysis (Kim et al. 2010; Guetta et al. 2009; Barradas et al. 2007; Bolesta et al. 2001; Wank et al. 2006). Al_2Cu and Al_4Cu_9 nanocrystalized phases were detected in a 500 nm diffusion layer between Al and Cu (Guetta et al. 2009). A 20–50 nm chemisorptional Ni_3Al intermetallic compound bond was found at the interface of Al particles deposited on Ni substrate (Bolesta et al. 2001). Equiaxed intermetallic grains at the interface of copper-aluminum over 400 nm thick were also discovered (Barradas et al. 2007). The thick intermetallic zones could not have been a result of solid-state diffusion alone but must have included interfacial melting (King and Jahedi 2010). Even at the melting temperature, the layer formation is too slow to generate a thick layer under 100 ns (Barradas et al. 2007).

15.4.1.4 Recrystallization

As a result of severe plastic deformation, through migration of grain boundaries, lattice and subgrain rotation and dislocation rearrangement, dynamic recrystallization (<100 nm), and recovery processes have also been detected after impact (Xiong et al. 2008; Borchers et al. 2004; Luo et al. 2014; Zou et al. 2009). The dynamic recrystallization process at the particle/substrate can improve the bonding by facilitating epitaxial and heteroepitaxial growth of crystals. The latter refers to the growth of one crystal into another of different chemical compositions but similar atomic arrangement and interatomic distances (Drehmann et al. 2014a, b; Rafaja et al. 2009). Successful deposition of Al onto Al_2O_3 was observed, and the resulting high adhesion was explained through heteroepitaxy between (0001)-oriented Al_2O_2 and (111)-oriented Al lattices found using HRTEM (Drehmann et al. 2014b). Similarly, deposited Ti can grow heteroepitaxially on corundum and that the energy stored in microstructural defects increases the crystal interaction between the nanocrystalline Ti (<10 nm) and Al_2O_3 (Rafaja et al. 2009). The occurrence of dynamic recrystallization for various FCC metals (Al, Cu, and Ni) has been studied. The differences in resulting microstructure characteristics between materials have been correlated to their respective stacking fault energy (SFE) and consequent resulting local conditions such as dislocation density, arrangement and orientation, and temperature rise (Borchers et al. 2004).

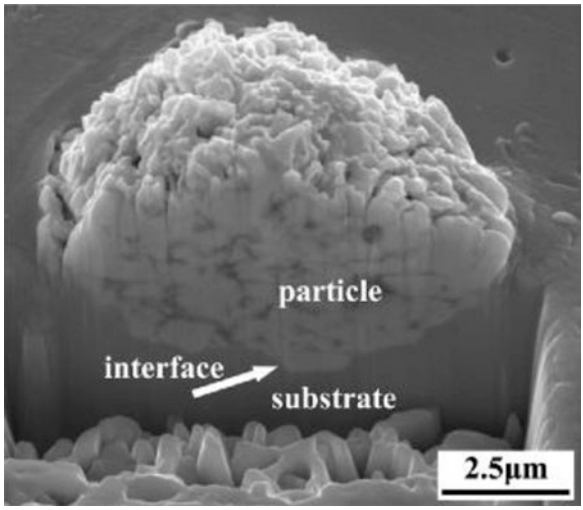

Fig. 15.11 FIB cut of WC-12Co particle infiltration into stainless steel substrate surface (Reproduced with permission of Elsevier)

15.4.2 Mechanical Interlocking

15.4.2.1 Spray-Induced Mechanical Interlocking

The in situ change in substrate topography can be caused by a hardness difference between the particle and substrate. This is the case for TiO_2 deposited onto polymer matrix composites (PMC) substrate, which drastically deformed and wrapped around the particle during impact (Burlacov et al. 2007). Another case is the deposition of Al-Al_2O_3 composite powders on Al6061 substrates, which induced cratering at the interface during impact and consequently led to an increase in adhesion to approximately 45 MPa compared to only 24 MPa for pure aluminum depositions (Lee et al. 2005). Similarly, Al-Al_2O_3 coatings produced on AZ91D magnesium alloy substrates show increasing shear strength properties with increasing Al_2O_3 volume fraction percentage. However, the optimal strength is reached at a composition of 50% with values around 45 MPa and then decreases to 35% for a 75% Al_2O_3 volume fraction (Wang et al. 2010). On the other hand, the adhesion strength of Al-Al_2O_3 deposited on Al7075 substrates shows a continuous increase with ceramic content up to 60 MPa (glue failure) for a 16.4 Al_2O_3 wt.% (Irissou et al. 2007). Another example of hard particle impact onto soft substrates was WC-Co coatings onto Al7075. The WC-Co coatings were tested in adhesion and all have failed at the glue, which signified an adhesion above 60 MPa (Dosta et al. 2017). The WC-Co particles deep penetration roughened the substrate surface, which resulted in mechanical anchoring (Dosta et al. 2017). Similarly, as shown in Fig. 15.11, CS of WC-12Co onto SS led to the successful deposition of a 400 μm coating along with a good interfacial adhesion (Ji et al. 2013). TiO_2 was also deposited onto Ti substrates, and the nano- and microscale roughness created at the surface was linked to the successful deposition of small particles with a resulting coating thickness of less

than 1μm (Schmidt et al. 2017). Moreover, interlocking and surface mixing between copper particles and aluminum substrate have been seen at their interface and associated to their high shear adhesion strength of 49 MPa in average (Champagne et al. 2005). Copper has also been deposited onto A5052 substrates, and severe mechanical anchoring from particle penetration resulted into a coating tensile strength of 250 MPa (Huang and Fukanuma 2012).

The second case of in situ substrate surface roughening is through change of spray parameters that allow substrate softening and increased particles velocities for proper surface cratering. This process applies during the surface metallization of PMCs, which considerably rely on the interfacial mechanical interlocking principles for successful coating deposition and buildup. Accurate control of the CS process temperature and pressure can lead to PMC surface softening, distortion, and particle penetration. Al and Al/Cu were deposited onto PMC surfaces, and clear softening and mechanical anchoring were detected at the interface (Zhou et al. 2011). For deposition onto very soft substrates such as polymers, the particle velocity and temperature must be minimized in order to avoid erosion. A Cu layer with a 50 μm average embedment depth on polyurethane and high-density polyethylene was also created, but without successful coating buildup (King et al. 2013). However, thanks to strong mechanical interlocking, dendritic copper coatings of 800 to 1000 μm were successfully deposited on PVC by using a tin and spherical Cu bond coat (Ganesan et al. 2012).

15.4.2.2 Surface Preparation-Induced Mechanical Interlocking

The effect of the substrate topography obtained through the application of various surface preparation procedures on the adhesion strength has been studied by many (Hussain et al. 2009; Marrocco et al. 2006; Samson et al. 2015; Fernandez et al. 2016). The adhesion of pure aluminum on Al6061-T6511 substrate treated with 177 μm Al_2O_3 grit has shown a decrease from 25.5 ± 5.5 MPa to 12.8 ± 1.4 MPa on a polished and GB surface, respectively (Samson et al. 2015). Similarly, the deposition of Ti-6Al-4 V onto grit-blasted Ti-6Al-4 V substrates has shown a resulting adhesion of only half the adhesion when CS on mirror-finish surfaces (Marrocco et al. 2006). Copper deposited onto Al6082 also show a decrease in adhesion from 57.4 ± 5.3 MPa on polished surfaces to 35.5 ± 4.7 MPa for grit-blasted surfaces with 500 μm Al_2O_3. Contrary to those results, the adhesion of CS copper coatings on copper substrates showed a significant increase from 5.4 MPa on as-received substrates to 36 MPa on grit-blasted substrate surfaces (Mäkinen and Lagerbom 2007). Likewise, grit blasting or glass beading the surface of AA 2024-T351 substrates increased the pure aluminum coating adhesion by 17.8% when compared to the as-received surfaces (Sharma et al. 2014).

The use of FPWJ surface treatment has shown an increase in coating adhesion over polished and grit-blasted samples. Pure aluminum deposited on FPWJ-treated Al6061-T6511 substrates reached an adhesion of 51.0 ± 4.3 MPa (Samson et al. 2015), while the adhesion was of 12.8 ± 1.4 and 25.5 ± 5.5 on grit-blasted and

polished surfaces, respectively. Similarly, the deposition of copper on FPWJ-treated low-carbon steel A519 Grade 70 reaches an adhesion of 56.5 ± 2.5 MPa, while on polished this adhesion was only of 0.7 ± 0.2 MPa (Fernandez et al. 2016).

Laser surface texturing and ablation has proven to increase the CS coating adhesion strength through the additional contact area and anchoring regions (Danlos et al. 2017; Kromer et al. 2016). The adhesion of CS Al6061 on laser ablated Al2017 substrates was shown to be 51.2 MPa, while it only reached 36.1 MPa for sand-blasted substrates (Danlos et al. 2017). Similarly, the adhesion strength of Al-alloy, Mg-alloy, and Al-SiC deposited on laser-textured substrates made of 7000 series Al, RZ5 magnesium alloy, and Al-SiC 20% vol. composite has shown increase over their deposition on grit-blasted samples. The Al-alloy coating adhesion was increased to approximately 51 MPa when deposited on laser-treated surfaces, while it reached only approximately 18 MPa on grit-blasted samples (Kromer et al. 2016).

15.4.3 Finite Element Modeling

15.4.3.1 Modeling of Particle/Substrate Interaction

Numerical simulations in CS use Lagrangian, Eulerian, arbitrary Lagrangian-Eulerian (ALE), coupled Lagrangian-Eulerian (CLE), smoothed particle hydrodynamics (SPH), or coupled thermal-mechanical/hydrodynamic (CTH) algorithms to solve particle impact processes. The Johnson-Cook (JC) plasticity model (Johnson and Cook 1983) has been widely used to describe the material response to deformation of single CS particle impact (Assadi et al. 2003; Grujicic et al. 2003; Schmidt et al. 2006a, b; Ghelichi et al. 2011; Li and Gao 2009; King et al. 2010). The plastic flow strength, σ, is given by the following equation:

$$\sigma = \left(A + B\varepsilon_p^n\right)\left(1 + Cln\left(\frac{\dot{\varepsilon}_p}{\dot{\varepsilon}_{\text{ref}}}\right)\right)\left(1 - \left(\frac{T - T_{\text{ref}}}{T_{\text{m}} - T_{\text{ref}}}\right)^m\right) \tag{15.8}$$

where ε is the plastic strain, $\dot{\varepsilon}$ is the plastic strain rate, T_{m} is the material melting temperature, T_{ref} is the transition reference temperature, and A, B, n, and C are constants determined from low strain-rate experiments ($<10^4 s^{-1}$). However, the JC hardening model does not adequately describe material behavior for deformations occurring at extremely high strain-rate regimes (Rahmati and Ghaei 2014). In CS, strain rates in the order of 10^7 to 10^9 s^{-1} are encountered at the particle periphery (Assadi et al. 2003). At strain rates exceeding 10^4 s^{-1}, experimental studies have shown the presence of a sharp increase in material flow stress attributed to the change in mechanisms governing the material dislocation process from thermally activated to phonon drag principles, also known as Wallace's theory of overdriven shocks. This is not derived and taken into consideration in the JC model. As a consequence, the Preston-Tonks-Wallace constitutive model (PTW) (Preston et al. 2003)

has been used for hypervelocity impact (Price et al. 2013) and recently in CS FEM studies (Rahmati and Ghaei 2014; Cormier et al. 2015). The plastic flow strength in the PTW model is given by:

$$\sigma = 2\left[\hat{\tau}_s + \alpha ln\left[1 - \varphi exp\left(-\delta - \frac{\theta \varepsilon_p}{\alpha \varphi}\right)\right]\right] G_p \tag{15.9}$$

where $\hat{\tau}_s$ is the normalized work-hardening saturation stress, θ represents the strain hardening rate, G_p is the plastic shear modulus, and the other terms are described as follow:

$$\alpha = \left(\frac{s_0 - \hat{\tau}_y}{p}\right) \tag{15.10}$$

$$\delta = \left(\frac{\hat{\tau}_s - \hat{\tau}_y}{\alpha}\right) \tag{15.11}$$

$$\varphi = \exp(\delta) - 1 \tag{15.12}$$

where s_0 is the saturation stress at 0 K, $\hat{\tau}_y$ is the normalized yield stress, and p is the strain hardening constant. The yield (τ_y) and work-hardening (τ_s) stresses are defined based on the strain-rate regime and consequently the mechanisms controlling the motion of dislocations. The model has shown acceptable correlation and prediction of flow stress results with respect to strain rate for various materials. However, data on plastic constitutive properties of materials at strain rates exceeding 10^9 s^{-1} are limited, even more so for micron-sized particles, which makes the selection of a "perfect" material model arduous.

FEM in CS has been used to evaluate the equivalent plastic strain (PEEQ), temperature, contact pressure, and velocity gradients at the particle/substrate surface. From a point of view of FEM, the susceptibility of particles to create metallic bonds at the impact has been based on the occurrence of interfacial shear instabilities, formation of jetting, and resulting interfacial properties such as pressure, temperature, and strain rate (Assadi et al. 2003; Grujicic et al. 2004). FEM analysis along with experimental observations has shown that the location of the adiabatic shear instability (ASI) is restricted to the outer circumferential areas of the impact zone. Additionally, a correlation has been found between the FEM results of the onset of shear instability and the experimental occurrence of particle bonding for various combinations of particle/substrate materials as they reach their V_c (Grujicic et al. 2004; Assadi et al. 2003). Experimental observations have also shown that preferential bonding occurs at the particle periphery (King et al. 2008). These zones also conform to regions free of oxide layers, which tend to indicate that the bonding process results from outcomes of ASI due to the large deformation they induce.

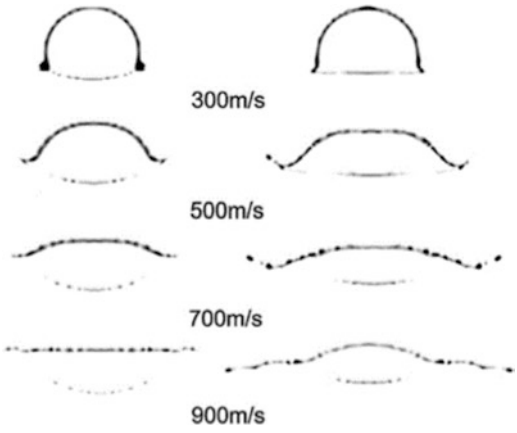

Fig. 15.12 Oxide layer shape evolution during Al 6061-T6 particle impact on Cu (*left*) and SS (*right*) at different velocities. The remaining oxide layer after impact is shown in *black* (Reproduced with permission of Elsevier)

The evolution of the native oxide film removal on single particles during the impact process has been modeled (Yin et al. 2012). The Johnson-Holmquist damage model (Johnson and Holmquist 1994), developed initially for brittle materials traveling at ballistic velocity, has been used to simulate the behavior of Al_2O_3 oxide film layer around Al 6061-T6 particles. As shown in Fig. 15.12 (Yin et al. 2012), as a result of ASI, the viscous-like metal jetting created at the particle rim carries the fractured oxides away from the contact surface. As displayed, the extent of removed oxides at the interface increases with the degree of particle plastic flow and associatively to particle velocity and temperature. Portions of the oxide films however remain at the periphery of the interface at the region of initial contact, which obstructs the creation of metallurgical bonds.

Despite the ability to simulate realistic material deformation processes, the modeled interaction between the impacting particle and substrate is of artificial nature. A bonding criterion can be added to the FEA model and forced at the interface without representing the real physical phenomena. Simulation of bonding and rebounding of superficially oxidized Cu particles on Cu substrates has been modeled using Eulerian-based FEM (Assadi et al. 2016). The oxide layer properties were described by a pressure-dependent yield model, which monitored the rebound to occur only at a set specific particle velocity.

Additionally, molecular dynamics simulations (MDS) have been used to understand cold spray deposition of nanoparticles (Gao et al. 2013). The results from cold spray MDS are limited and confirm previous findings obtained in micro-simulations in terms of stress, strain, and temperature requirements for material bonding.

15.4.3.2 Modeling of Mechanical Anchoring

The substrate surface deformation during impact has been simulated in multiple studies (Li et al. 2007a; King et al. 2010; Wang et al. 2014). Modeling of severe substrate jetting has been achieved in multiple studies, which demonstrates the

occurrence of spray induced mechanical interlocking. Computational analysis has also been used to explain the experienced interfacial mixing at the contact zones of copper particles and aluminum substrate (Grujicic et al. 2003). FEM focusing on anchored coatings and their respective purely mechanical adhesion strength has been modeled for copper deposited onto FPWJ-treated steel substrates (Fernandez et al. 2016). The substrate surface cross-sectional profile has been extracted from SEM images as shown in Fig.15.13, where the boundary conditions replicated the ASTM C633 standard pull test process. The work hardened CS coating property was estimated using the measured hardness of the deposited copper and subsequently represented by a predefined strain field value through the JC model equation and $H \approx c \times \sigma_y$ relation. The resultant strain was found using the following relation:

$$\varepsilon_p = \left(\frac{H}{c \times B \left[1 - \frac{T - T_{ref}}{T_m - T_{ref}} \right]} - \frac{A}{B} \right)^{1/n} \tag{15.13}$$

The obtained simulated strength of 46.1 ± 6.7 MPa was close to the measured 49.0 ± 5.8 MPa value, which suggested that mechanical anchoring was the main, if not the only, mechanism through which the coating was attached to the substrate surface.

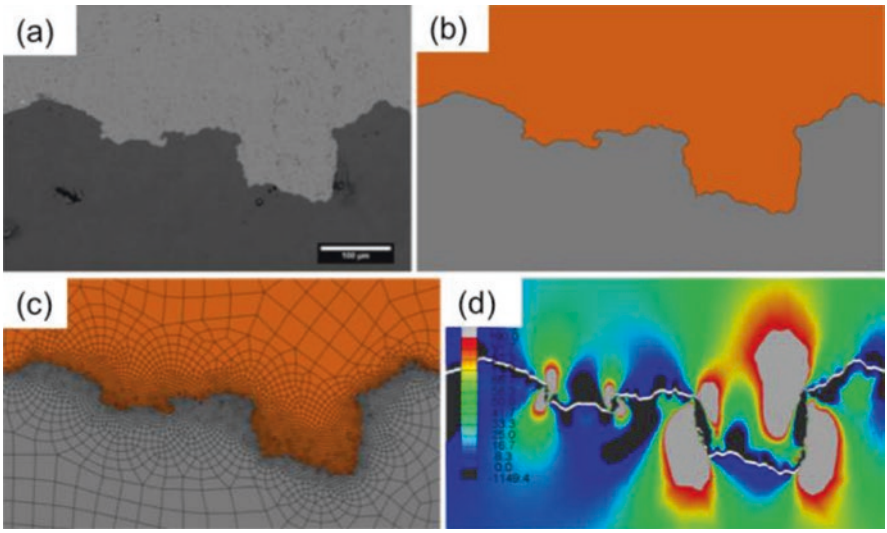

Fig. 15.13 Substrate surface treated using FWPJ with resulting roughness (*Ra*) of 32.0±4.9 μm. (**a**) Profile cross section, (**b**) interface digitalization, (**c**) FEM meshing, and (**d**) magnitude of stresses at the interface (Reproduced with permission of Springer)

15.5 Conclusion

In order to promote the highest adhesion in cold spray coatings, one must first understand the mechanisms by which adhesion occurs. Two adhesion mechanisms dominate this property: the prevalence of metallic bonds and the presence of mechanical anchoring. The optimization of this bonding is specific for every powder/substrate combination and can be influence through the CS process parameters and surface modification methods discussed in this chapter. The FEA models assist in this understanding but cannot model the metallic bonding process properly. These models should be developed toward incorporating crystal structure of metals to predict the conformity of the particle/substrate interface to form metallic bonds.

References

Ajdelsztajn L et al (2005) Cold spray deposition of nanocrystalline aluminum alloys. Metall Mater Trans A 36A:657–662

Akbarimousavi A, Alhassani S (2005) Numerical and experimental studies of the mechanism of the wavy interface formations in explosive/impact welding. J Mech Phys Solids 53(11):2501–2528

Alkhimov AP (1994) US patent-gas-dynamic spraying method for applying a coating. US5302414 A

Alkhimov AP, Kosarev VF, Klinkov SV (2001) The features of cold spray nozzle design. J Therm Spray Technol 10:375–381

Assadi H et al (2003) Bonding mechanism in cold gas spraying. Acta Mater 51(15):4379–4394

Assadi H et al (2011) On parameter selection in cold spraying. J Therm Spray Technol 20(6):1161–1176

Assadi H et al (2016) Cold spraying – a materials perspective. Acta Mater 116:382–407

Bae G et al (2008) General aspects of interface bonding in kinetic sprayed coatings. Acta Mater 56(17):4858–4868

Bae G et al (2009) Bonding features and associated mechanisms in kinetic sprayed titanium coatings. Acta Mater 57(19):5654–5666

Barradas S et al (2007) Laser shock flier impact simulation of particle-substrate interactions in cold spray. J Therm Spray Technol 16(4):548–556

Bolesta AV et al (2001) Investigation of interface boundary occurring during cold gas-dynamic spraying of metallic particles. Nucl Instrum Methods Phys Res, Sect A 470(1–2):249–252

Borchers C et al (2004) Microstructural bonding features of cold sprayed face centered cubic metals. J Appl Phys 96(8):4288

Branicio PS, Rino JP (2000) Large deformation and amorphization of Ni nanowires under uniaxial strain: a molecular dynamics study. Phys Rev B: Condens Matter Mater Phys 62(24):16950–16955

Bray M, Cockburn A, Neill WO (2009) Surface and coatings technology the laser-assisted cold spray process and deposit characterisation. Surf Coat Technol 203(19):2851–2857

Burlacov I et al (2007) Cold gas dynamic spraying (CGDS) of TiO 2 (anatase) powders onto poly(sulfone) substrates: microstructural characterisation and photocatalytic efficiency. J Photochem Photobiol A Chem 187:285–292

Callister W, Rethwisch D (2008) Materials science and engineering: an introduction, 8th edn. Wiley, Hoboken

Champagne VK et al (2005) Interface material mixing formed by the deposition of copper on aluminum by means of the cold spray process. J Therm Spray Technol 14(3):330–334

Christoulis DK et al (2010) Cold-spraying coupled to nano-pulsed Nd-YaG laser surface pretreatment. J Therm Spray Technol 19(5):1062–1073
Cormier Y et al (2015) Finite element analysis and failure mode characterization of pyramidal fin arrays produced by masked cold gas dynamic spray. J Therm Spray Technol 24(8):1549–1565
Danlos Y et al (2010) Ablation laser and heating laser combined to cold spraying. Surf Coat Technol 205(4):1055–1059
Danlos Y et al (2017) Surface & coatings technology ablation laser and heating laser combined to cold spraying. Surf Coat Technol 205(4):1055–1059
Day J, Huang X, Richards NL (2005) Examination of a grit-blasting process for thermal spraying using statistical methods. J Therm Spray Technol 14(4):471–479
Dosta S et al (2017) Plastic deformation phenomena during cold spray impact of WC-Co particles onto metal substrates. Acta Mater 124:173–181
Drehmann R et al (2014a) Interface characterization and bonding mechanisms of cold gas-sprayed Al coatings on ceramic substrates. J Therm Spray Technol 24(1–2):92–99
Drehmann R et al (2014b) Splat formation and adhesion mechanisms of cold gas-sprayed al coatings on Al2O3 substrates. J Therm Spray Technol 23(1-2):68–75
Dykhuizen RC, Smith MF (1998) Gas dynamic principles of cold spray. J Therm Spray Technol 7(June):205–212
Fernandez R et al (2016) Enhancement and prediction of adhesion strength of copper cold spray coatings on steel substrates for nuclear fuel repository. J Therm Spray Technol 25(8):1577–1587
Fukumoto M et al (2007) Effect of substrate temperature on deposition behavior of copper particles on substrate surfaces in the cold spray process. J Therm Spray Technol 16(5–6):643–650
Ganesan A et al (2012) Bonding behavior studies of cold sprayed copper coating on the PVC polymer substrate. Surf Coat Technol 207:262–269
Gao H, Liu C, Song FH (2013) Molecular dynamics simulation of the influence factors of particle depositing on surface during cold spray. Adv Mater Mater Processing Pts 1-3:1916–1924
Gärtner F et al (2003) Numerical and microstructural investigations of the bonding mechanisms in cold spraying. In: Prodceedings of the 2003 Thermal Spray Conference "Thermal Spray 2003: advancing the science and applying the technology.", ITSC 2003. ASM International, Materials Park USA
Ghelichi R et al (2011) Numerical simulation of cold spray coating. Surf Coat Technol 205(23–24):5294–5301
Gilmore DL et al (1999) Particle velocity and deposition efficiency in the cold spray process. J Therm Spray Technol 8(December):576–582
Goldbaum D et al (2012) The effect of deposition conditions on adhesion strength of Ti and Ti6Al4V cold spray splats. J Therm Spray Technol 21(2):288–303
Grujicic M et al (2003) Computational analysis of the interfacial bonding between feed-powder particles and the substrate in the cold-gas dynamic-spray process. Appl Surf Sci 219(3–4):211–227
Grujicic M et al (2004) Adiabatic shear instability based mechanism for particles/substrate bonding in the cold-gas dynamic-spray process. Mater Des 25(8):681–688
Guetta S et al (2009) Influence of particle velocity on adhesion of cold-sprayed splats. J Therm Spray Technol 18(3):331–342
Hamaker HC (1937) The London—van der Waals attraction between spherical particles. Physica 4(10):1058–1072
Harris AF, Beevers A (1999) The effects of grit-blasting on surface properties for adhesion. J Adhes 19(November 1998):445–452
Huang RZ, Fukanuma H (2009) The influence of spray conditions on deposition characteristics of aluminum coatings in cold spraying. Proceeding of the International Thermal Spray Conference:279–284. Available at: http://plasma.co.jp/about/pdf/2009-3.pdf
Huang R, Fukanuma H (2012) Study of the influence of particle velocity on adhesive strength of cold spray deposits. J Therm Spray Technol 21(3–4):541–549
Hussain T et al (2009) Bonding mechanisms in cold spraying: the contributions of metallurgical and mechanical components. J Therm Spray Technol 18(3):364–379

Ikeda H et al (1999) Strain rate induced amorphization in metallic nanowires. Phys Rev Lett 82(14):2900–2903
Irissou E, Arsenault B (2007) Corrosion study of cold sprayed aluminum coatings onto Al 7075 alloy. Coating (January 2007):549–554
Irissou E et al (2007) Investigation of Al-Al 2O 3 cold spray coating formation and properties. J Therm Spray Technol:661–668
Israelachvili JN (1974) The nature of van der Waals forces. Contemp Phys 15(2):159–178
Ji G-C et al (2013) Characterization of cold-sprayed multimodal WC-12Co coating. Surf Coat Technol 235:536–543
Jodoin B (2002) Cold spray nozzle Mach number limitation. J Therm Spray Technol 11(December):496–507
Jodoin B, Raletz F, Vardelle M (2006) Cold spray modeling and validation using an optical diagnostic method. Surf Coat Technol 200(14–15):4424–4432
Johnson GR, Cook WH (1983) A constitutive model and data for metals subjected to large strains, high strain rates and high temperatures. Proceedings of the 7th International Symposium on Ballistics 547:541–547
Johnson GR, Holmquist TJ (1994) An improved computational constitutive model for brittle materials. AIP Conf Proc J Appl Phys 309(74):1639–1752
Kapoor R, Nemat-Nasser S (1998) Determination of temperature rise during high strain rate deformation. Mech Mater 27(1):1–12
Karimi A, Martin JL (1986) Cavitation erosion of materials. Int Mater Rev 31(1):1–26
Kim K, Watanabe M, Kuroda S (2009) Jetting-out phenomenon associated with bonding of warm-sprayed titanium particles onto steel substrate. J Therm Spray Technol 18(4):490–499
Kim K, Watanabe M, Kuroda S (2010) Bonding mechanisms of thermally softened metallic powder particles and substrates impacted at high velocity. Surf Coat Technol 204(14):2175–2180
King PC, Jahedi M (2010) Relationship between particle size and deformation in the cold spray process. Appl Surf Sci 256(6):1735–1738
King PC, Zahiri SH, Jahedi M (2008) Focused ion beam micro-dissection of cold-sprayed particles. Acta Mater 56(19):5617–5626
King PC et al (2010) An experimental and finite element study of cold spray copper impact onto two aluminum substrates. J Therm Spray Technol 19(3):620–634
King PC et al (2013) Embedment of copper particles into polymers by cold spray. Surf Coat Technol 216:60–67
King PC et al (2014) Interface melding in cold spray titanium particle impact. Surf Coat Technol 239:191–199
Klinkov SV, Kosarev VF (2006) Measurements of cold spray deposition efficiency. J Therm Spray Technol 15(3):364–371
Kromer R et al (2016) Laser surface texturing to enhance adhesion bond strength of spray coatings – cold spraying, wire-arc spraying, and atmospheric plasma spraying. Surf Coat Technol. 2017. https://doi.org/10.1016/j.surfcoat.2017.05.007
Kwon EH et al (2005) Particle behavior in supersonic flow during the cold spray process. Met Mater Int 11(5):377–381
Lee HY et al (2005) Correlation between Al2O3 particles and interface of Al–Al2O3 coatings by cold spray. Appl Surf Sci 252(5):1891–1898
Legoux JG, Irissou E, Moreau C (2007) Effect of substrate temperature on the formation mechanism of cold-sprayed aluminum, zinc and tin coatings. J Therm Spray Technol 16(5–6):619–626
Li W-Y, Gao W (2009) Some aspects on 3D numerical modeling of high velocity impact of particles in cold spraying by explicit finite element analysis. Appl Surf Sci 255:7878–7892
Li C-J, Li W-Y, Wang Y-Y (2005) Formation of metastable phases in cold-sprayed soft metallic deposit. Surf Coat Technol 198(1–3):469–473
Li C-J, Li W-Y, Liao H (2006) Examination of the critical velocity for deposition of particles in cold spraying. J Therm Spray Technol 15(2):212–222

Li W-Y, Liao H et al (2007a) Numerical simulation of deformation behavior of Al particles impacting on Al substrate and effect of surface oxide films on interfacial bonding in cold spraying. Appl Surf Sci 253(11):5084–5091
Li W-Y, Zhang C et al (2007b) Study on impact fusion at particle interfaces and its effect on coating microstructure in cold spraying. Appl Surf Sci 254(2):517–526
Li W-Y et al (2008) Effect of standoff distance on coating deposition characteristics in cold spraying. Mater Des 29(2):297–304
Li WY, Yin S, Wang XF (2010) Numerical investigations of the effect of oblique impact on particle deformation in cold spraying by the SPH method. Appl Surf Sci 256(2010):3725–3734
Luo X-T et al (2014) High velocity impact induced microstructure evolution during deposition of cold spray coatings: a review. Surf Coat Technol 254:11–20
MacDonald D et al (2016) Effect of nozzle material on downstream lateral injection cold spray performance. J Therm Spray Technol 25(6):1149–1157
Mäkinen H, Lagerbom J, PV (2007) Adhesion of cold sprayed coatings: effect of powder, substrate, and heat treatment. In: Prodceedings of the 2007 Thermal Spray Conference "Thermal Spray 2007: global coating solutions", ITSC 2007. ASM International, Materials Park USA
Marrocco T et al (2006) Production of titanium deposits by cold-gas dynamic spray: numerical modeling and experimental characterization. J Therm Spray Technol 15(2):263–272
McDonald AG et al (2013) Gas-substrate heat exchange during cold-gas dynamic spraying. J Therm Spray Technol 22(2–3):391–397
Mohamed HA, Washburn J (1975) Mechanism of solid state pressure welding. Weld J 54:302–310s
Ning XJ et al (2008) Cold spraying of Al-Sn binary alloy: coating characteristics and particle bonding features. Surf Coat Technol 202(9):1681–1687
Ozdemir OC et al (2016) Estimating the effect of helium and nitrogen mixing on deposition efficiency in cold spray. J Therm Spray Technol 25(4):660–671
Papyrin A (2001) Cold spray technology. Adv Mater Proc 159(9):49–52
Pattison J et al (2008) Standoff distance and bow shock phenomena in the cold spray process. Surf Coat Technol 202(8):1443–1454
Preston DL et al (2003) Model of plastic deformation for extreme loading conditions. J Appl Phys 931(10):1498–1528
Price MC, Kearsley AT, Burchell MJ (2013) Validation of the Preston–Tonks–Wallace strength model at strain rates approaching ∼1011 s−1 for Al-1100, tantalum and copper using hypervelocity impact crater morphologies. Int J Impact Eng 52:1–10
Rafaja D et al (2009) Microstructural characterisation of titanium coatings deposited using cold gas spraying on Al 2 O 3 substrates. Surf Coat Technol 203:3206–3213
Rahmati S, Ghaei A (2014) The use of particle/substrate material models in simulation of cold-gas dynamic-spray process. J Therm Spray Technol 23(3):530–540
Raletz F, Vardelle M, Ezo'o G (2006) Critical particle velocity under cold spray conditions. Surf Coat Technol 201(5):1942–1947
Rollot Y, Régnier S, Guinot J-C (1999) Simulation of micro-manipulations: adhesion forces and specific dynamic models. Int J Adhes Adhes 19(1):35–48
Samson T et al (2015) Effect of pulsed waterjet surface preparation on the adhesion strength of cold gas dynamic sprayed aluminum coatings. J Therm Spray Technol 24(August):984–993
Schmidt T, Gaertner F, Kreye H (2006a) New developments in cold spray based on higher gas and particle temperatures. J Therm Spray Technol 15(December):488–494
Schmidt T et al (2006b) Development of a generalized parameter window for cold spray deposition. Acta Mater 54(3):729–742
Schmidt T et al (2009) From particle acceleration to impact and bonding in cold spraying. J Therm Spray Technol 18(5–6):794–808
Schmidt K et al (2017) Ti surface modification by cold spraying with TiO2 microparticles. Surf Coat Technol 309:749–758
Semenov AP (1961) The phenomenon of seizure and its investigation. Wear 4(1):1–9

Sharma MM, Eden TJ, Golesich BT (2014) Effect of surface preparation on the microstructure, adhesion, and tensile properties of cold-sprayed aluminum coatings on AA2024 substrates. J Therm Spray Technol 24(3):410–422
Stoltenhoff T, Kreye H, Richter HJ (2002) An analysis of the cold spray process and its coatings. J Therm Spray Technol 11(4):542–550
Van Steenkiste T, Smith JR (2004) Evaluation of coatings produced via kinetic and cold spray processes. J Therm Spray Technol 13(2):274–282
Vijay MM et al (2013) US patent-method and apparatus for prepping surfaces with a high-frequency forced pulsed waterjet. 8,550,873 B2
Villafuerte J (ed) (2015) Modern cold spray. Springer International Publishing, Windsor
Vlcek J et al (2005) A systematic approach to material eligibility for the cold-spray process. J Therm Spray Technol 14(1):125–133
Wang Q et al (2010) The influence of ceramic particles on bond strength of cold spray composite coatings on AZ91 alloy substrate. Surf Coat Technol 205:50–56
Wang Q et al (2014) High resolution microstructure characterization of the interface between cold sprayed Al coating and Mg alloy substrate. Appl Surf Sci 289:366–369
Wank A et al (2006) High-resolution microstructural investigations of interfaces between light metal alloy substrates and cold gas-sprayed coatings. J Therm Spray Technol 15(2):280–283
Watanabe Y et al (2014) Influence of substrate temperature on adhesion strength of cold-sprayed coatings. J Therm Spray Technol 24(1–2):86–91
Wigren J (1988) Technical note: grit blasting as surface preparation before plasma spraying. Surf Coat Technol 34(1):101–108
Wong W et al (2011) Influence of helium and nitrogen gases on the properties of cold gas dynamic sprayed pure titanium coatings. J Therm Spray Technol 20(1–2):213–226
Wu J et al (2006) The bond strength of Al–Si coating on mild steel by kinetic spraying deposition. Appl Surf Sci 252(22):7809–7814
Xie Y, Planche MP et al (2016a) Effect of substrate preheating on adhesive strength of SS 316L cold spray coatings. J Therm Spray Technol 25(1–2):123–130
Xie Y, Yin S et al (2016b) New insights into the coating/substrate interfacial bonding mechanism in cold spray. Scr Mater 125:1–4
Xiong Y et al (2008) Dynamic amorphization and recrystallization of metals in kinetic spray process. Appl Phys Lett 92(19):194101
Xiong Y et al (2011) Dependence of bonding mechanisms of cold sprayed coatings on strain-rate-induced non-equilibrium phase transformation. J Therm Spray Technol 20(4):860–865
Yamada M et al (2010) Cold spraying of TiO2 photocatalyst coating with nitrogen process gas. J Therm Spray Technol 19(6):1218–1223
Yin S et al (2011) Examination on substrate preheating process in cold gas dynamic spraying. J Therm Spray Technol 20(4):852–859
Yin S et al (2012) Deformation behavior of the oxide film on the surface of cold sprayed powder particle. Appl Surf Sci 259:294–300
Yin S et al (2013) Deposition behavior of thermally softened copper particles in cold spraying. Acta Mater 61(14):5105–5118
Yin S et al (2015) Effect of substrate temperature on interfacial bonding for cold spray of Ni onto Cu. J Mater Sci 50(22):7448–7457
Zhou XL et al (2011) Preparation of metallic coatings on polymer matrix composites by cold spray. Surf Coat Technol 206(1):132–136
Zou Y et al (2009) Dynamic recrystallization in the particle/particle interfacial region of cold-sprayed nickel coating: electron backscatter diffraction characterization. Scr Mater 61:899–902

Chapter 16
Residual Stresses in Cold Spray Coatings

Vladimir Luzin, Kevin Spencer, Mingxing Zhang, Neil Matthews, Joel Davis, and Michael Saleh

16.1 Introduction

16.1.1 Stress in Cold-Sprayed Coatings

Cold spray is a relatively novel and rapidly developing technology for material deposition. In contrast to thermal spray technologies that deposit molten materials, it is believed that metallurgical bonding in cold spray is achieved in the solid state through the impact of feedstock material particles, accelerated to high speeds, 500–1000 m/s (Papyrin et al. 2007), towards a substrate, and with an accompanying large plastic deformation on impact. The link between spray conditions and coating properties is not fully elucidated. This is partly due to the complexity of the cold spray process, which involves different physical phenomena occurring at different structural scales. High strain rate deformation of the particles (up to 10^9 s^{-1}), and the resultant plastic shock wave, leads to the formation of micro-scale features such as adiabatic shear instabilities (~1 μm) and to the formation of ultrafine grains (~100 nm). On the mesoscale (10–100 μm), specific features are associated with splat morphology, voids, defects, inter-splat boundaries, etc. When the coating is formed, typically 0.5–5 mm thickness, gradients of stress and mechanical properties are observed through the whole thickness of the macroscopic scale.

V. Luzin (✉) • J. Davis • M. Saleh
Australian Nuclear Science and Technology Organisation,
Lucas Heights, NSW 2234, Australia
e-mail: vladimir.luzin@ansto.gov.au; joel.davis@ansto.gov.au; Michael.saleh@ansto.gov.au

K. Spencer • M. Zhang
School of Mechanical and Mining Engineering, The University of Queensland, St Lucia,
QLD 4072, Australia
e-mail: krspencer@gmail.com; mingxing.zhang@uq.edu.au

N. Matthews
Rosebank Engineering Pty Ltd, 836 Mountain Highway, Bayswater, VIC 3153, Australia
e-mail: neil.matthews@rosebank-eng.com.au

P. Cavaliere (ed.), *Cold-Spray Coatings*,
https://doi.org/10.1007/978-3-319-67183-3_16

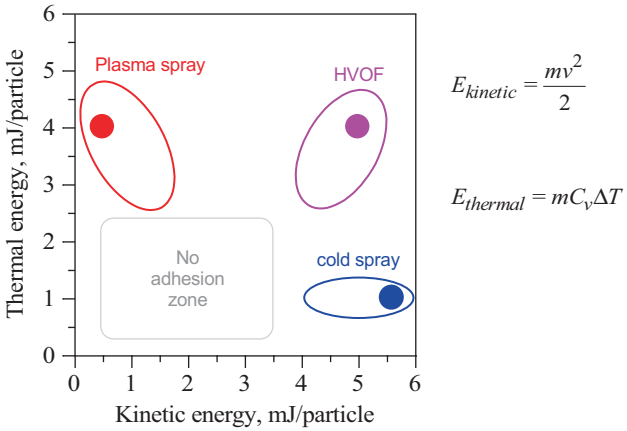

Fig. 16.1 Kinetic energy vs. thermal energy diagram for the three spraying techniques calculated for a 20-μm-size aluminium particle and typical spraying conditions

Cold spray is a highly energetic process as outlined in Fig. 16.1, and the deposited material undergoes some severe processes through microstructural modifications and transformations. These are driven by the large plastic deformations and the elevated temperatures experienced by the deposited particles. The deposition process almost always results into significant residual stresses.

The residual stress in coatings manufactured by the cold spray, which is usually compressive mostly due to kinetic impact of sprayed particles, is often considered from a structural integrity point of view since many physical properties, such as fatigue life or wear resistance, are intrinsically linked to the residual stress state. Therefore, the residual stress analysis became an important part of structural integrity assessment, especially when undesirable stresses (usually large tensile stress) are to be mitigated or, more commonly, when the spraying process is to be optimized to exploit the beneficial features of the residual stresses (usually moderate compressive stress). As such, it is imperative to consider residual stress as a factor in the overall mechanical performance and lifetime assessment of cold-sprayed samples or parts produced by cold spray. The residual stresses, resultant from the cold spray, exhibit interdependency on many spraying parameters, e.g. composition, temperature, particle velocity and particle size. The technological challenge is to tailor the residual stress together with other properties accordingly to the intended application through variations of the spraying parameters and deposition conditions.

However, apart from the technological and functional importance, experimental evaluation of residual stresses in coated systems can answer some deeper scientific questions. Since residual stress formation is intimately linked to the fundamental mechanisms of the cold spray deposition process, the deposition mechanisms can be studied through stress analysis, together with and in relation to other properties.

Despite some contemporary attempts to use cold spray (or thermal spray) to produce 3D objects in the manner of additive manufacturing techniques, the majority of spraying is done on very simple geometry – planar deposits and flat coatings.

Since technological coating thicknesses range from 0.1 mm (e.g. thermal barrier coatings or WC coatings) to several millimetres for surface restoration applications, the experimental technique used to study residual stresses usually require high spatial resolution.

16.1.2 Techniques for Stress Measurements in Coatings

In order to characterize the stress distribution in coating-substrate systems and to resolve the stress in the through-thickness direction, several traditional stress measurement techniques have been used. Methods such as residual curvature measurement for thin films were first carried out by Stoney (1909). Subsequent studies have utilized in situ curvature measurement on thick coatings (Matejicek and Sampath 2003), hole drilling techniques (Santana et al. 2008), X-ray diffraction combined with layer removal method (Santana et al. 2008) and synchrotron radiation (Genzel 2004) to measure stress in coatings or under the treated surfaces.

The general principles used in neutron diffraction stress measurements are well established, and the readers are referred to the works of Hutchings and Krawitz (1992) and Hutchings et al. (2005) for a more comprehensive review of the technique. The applicability of this technique and its suitability to the analysis of coatings, as well as to other many components, rely on the high penetration of neutrons. The half-attenuation depth of neutrons is ~6 mm in steel, ~60 mm in copper and ~60 mm in aluminium, while for X-rays, this value is ~100 μm at best. This high penetration depth of neutrons allows for through-thickness stress scanning in coated samples in totally non-destructive manner. Unlike X-ray-based methods, neutrons are very insensitive to sample surface finishes and do not require any special sample preparations.

Despite successes in the use of neutron diffraction techniques at the turn of the century (Matejicek et al. 1997; Matejicek et al. 1999), the use of neutron diffraction in last two decades has been restrained with respect to analysis of cold or thermally sprayed coatings. This has mostly been due to instrumental limitations: medium spatial resolution (gauge volume size) of ~1 mm, which still poses an issue on some neutron stress scanners, somewhat restricted access to neutron facilities and possibly the lengthy measurement times required for reliable statistics to be gathered. The latter point has consequently led to severe limitations on sample throughput, a key point in optimizing varying coating-substrate configurations. Historically the medium (limited to ~1 mm) spatial resolution led to the so-called partial illumination effect, an experimental artefact resulting from the uneven scattering density within a gauge volume. This usually takes place in near-surface regions and requires analytical or experimental mitigation (Pirling 2011; Suzuki et al. 2013).

However, with the new generation of specialized neutron residual stress diffractometers, which operate at constant wavelengths, such as SALSA (ILL, France), STRESS-SPEC (TUM, Germany) and KOWARI (ANSTO, Australia), stress measurements with high spatial resolution have become more readily available. The

neutron fluxes of these instruments allow a reduction in the spatial resolution, down from 1.0 to 0.1–0.2 mm (Luzin et al. 2017), while maintaining a practical measurement time, usually 5–30 min per point depending on material, sample dimensions, accuracy requirements, etc. With the higher spatial resolutions, the partial illumination problem is conveniently and effectively negated if the gauge volume remains at least 0.1–0.2 mm away from the surface/interface. The short measurement time allows for multiple samples to be studied efficiently, usually six to ten samples within a few days of a typical neutron experimental beam time allocation. The experimental uncertainties associated with neutron stress measurements can be as small as 5 MPa, though actual uncertainties are strongly dependent on elemental composition of the coating-substrate material and on the volume fraction, when investigating multiphase coatings.

In considering the advantages and benefits of the neutron diffraction technique, the acute shortage of suitable instruments around the world poses the most serious limitation on widespread adoption of the technique. The neutron diffraction scanners available for such experiments are largely confined to the very short list of facilities mentioned above. Moreover, time-of-flight instruments based on spallation sources, such as ISIS (UK), SNS (USA) and J-PARC (Japan), are not typically suited to high spatial resolution measurements due to their design constraints.

16.2 Analytical and Experimental Foundation of the Neutron Stress Measurements in Coatings

Coatings produced by cold spray, or by any other spraying technique for that matter, have certain experimental and analytical advantages when flat geometry is utilized, e.g. square coupons. Flat geometry allows for certain assumptions to be made and allows for more affective stress analysis of cold-sprayed samples based on the following considerations:

1. For flat sample geometry, the stress state can be simplified and can be described accurately using an assumption of zero plane stress state with the normal-to-surface stress component equal to zero ($\sigma_N = 0$). The zero plane stress condition is accurate on the outer surfaces, while it is still very accurately fulfilled through the interior regions in the through-thickness direction. Irrespective of the sample's composition, this assumption holds true with good accuracy for typical coating and substrates, in the order of several millimetres in thickness, under condition that the lateral dimensions are greater than the thickness dimension when the edge effects (stress relief on the outer edges) can be neglected. As a rule of thumb, for samples with a lateral dimension to thickness ratio of 10:1, the edge effects do not affect the uniform-in-plane stress state in the central part of the samples, where the plane stress condition is fulfilled with great accuracy.
2. Coating properties are usually uniform in the in-plane directions, assuming being away from edges; therefore, the stress state is fully characterized by the through-thickness distributions of the in-plane stress components, and the stress

can be treated as a one-dimensional function. Therefore, measurements can be done along one line through the sample's thickness greatly minimizing the amount of experimental work, in comparison with more 2D and 3D stress distribution fields that generally require 2D and 3D scanning.

3. The stress state in coatings is also usually equal-biaxial. This is valid in most cases as the process of coating deposition is usually transversely (in-plane) isotropic, assuming the particle stream impacts perpendicular to the surface. Thus, under this assumption only the in-plane stress component needs to be determined, and it fully describes the stress state. Experimentally, this reduces measurements to only two directions, one in-plane and one normal-to-surface (Fig. 16.2), though the equal biaxiality assumption can be experimentally checked by measuring the other in-plane direction, orthogonal to the first one. An example of such confirmational experiments is shown in Fig. 16.3. The three-directional experiment is essential if the assumed transversely isotropic symmetry is absent, e.g. the spraying direction is not perpendicular to the surface but under an oblique angle to the surface.
4. Another advantage is that d_0-problem – finding a proper local stress-free d-spacing or d_0 – can be treated efficiently at once by measuring the d-spacing in two directions, in-plane $d_{\parallel}$ and normal $d_{\perp}$, so that Hooke's equations (diffraction case) can be resolved for one in-plane stress component (henceforth referred to as stress) and the $d_0$value are resolved concurrently as the two unknowns:

$$\sigma_{\parallel} = \frac{1}{\%\%S_2}\frac{d_{\parallel} - d_{\perp}}{d_0} \quad \text{and} \quad d_0 = \frac{1}{\%\%S_2}\left\{\left(\%\%S_2 + 2S_1\right)d_{\perp} - 2S_1 d_{\parallel}\right\} \tag{16.1}$$

where $S_1 = S_1(hkl)$ and $½S_2 = ½S_2(hkl)$ are the diffraction elastic constants of the chosen diffraction reflection (hkl).

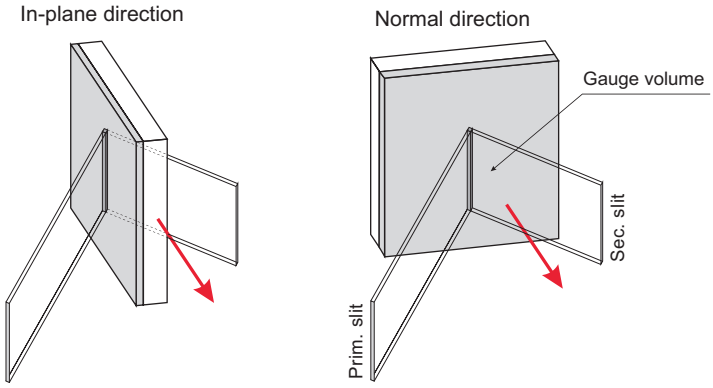

Fig. 16.2 Scattering geometry with two sample orientations for measurements of the two principal directions. The gauge volume is formed by intersection of the incident neutron beam coming through the primary slit and going out through the secondary slit

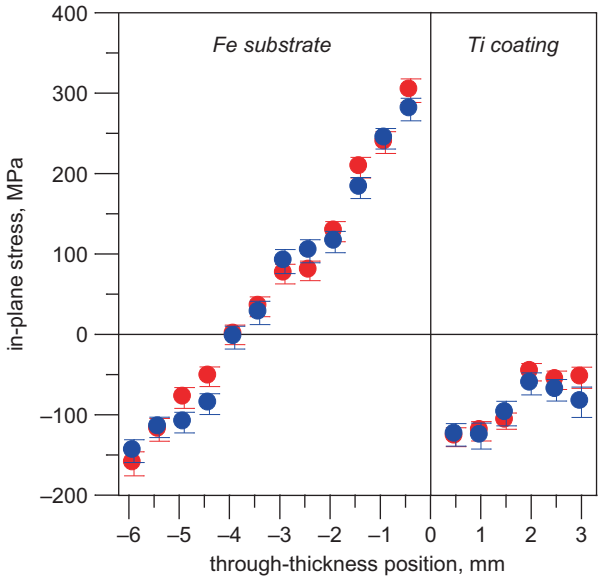

Fig. 16.3 Examples of residual stress equal biaxiality check for a cold-sprayed Ti/Fe sample when two orthogonal stress components (*red* and *blue*) were determined independently. The stress state is biaxial within experimental uncertainties

5. Another notable theoretical consideration relates to the treatment of the in-plane stress component. There is no theoretical framework that necessitates the in-plane stress to be a continuous function across the substrate-coating interface. Conversely, for the normal stress component, these continuity requirements are well explicated, but since these equate to a zero stress component, it is a trivial result. Therefore, through-thickness stress profiles in substrate-coating systems can and usually do exhibit a marked discontinuity at the interface. This is evident in all the experimental and the theoretical profiles reported below.
6. Some favourable experimental implications arise from the simplicity of the considered flat geometry and the simple stress state. In this case the experimental gauge volume can be extended in the in-plane direction (practically to 20–25 mm in the in-plane dimension); thus, even with a small slit size of 0.2 mm, the overall gauge volume remains considerable, 1 mm^3 (0.2 × 0.2 × 25 mm^3); see also Fig. 16.2 for illustration. This allows for rapid stress measurements (by neutron standards) with typical measurement time of ~10 min. As discussed above, 0.1–0.2 mm spatial resolution is congruent to most typical practical applications with the ability to resolve the stress distribution within a few millimetres.
7. From the experimental point of view, using a smaller gauge volume size of ~0.2 mm in the through-thickness direction can essentially eliminate the necessity of dealing with the partial illumination problems. This allows to maintain a fully immersed gauge volume, while still being close enough to the surface/interface. Therefore, measurements with no partial illumination interference can be made as close to the surface as 0.1–0.2 mm. The 180°-flip

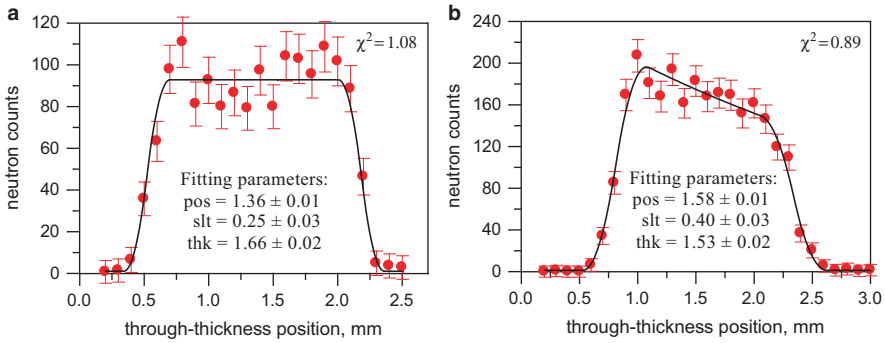

Fig. 16.4 Examples of the integrated intensity profiles obtained in the transmission (**a**, *left*) and reflection (**b**, *right*) geometries by scanning through plate of 1.6 mm thickness (thk) using 0.2 mm slits (slt). Profile fitting (*black lines*) results in the positioning (pos) accuracy of 0.01 mm. Experimental (nominal) gauge volume was 0.2 × 0.2 × 16 mm^3

strategy, which is sometimes used to deal with partial illumination experimentally, might still be useful in addressing similar experimental effects related to gradients of texture or composition; non-uniformity of scatterer; porosity in the sample; and the presence of unknown internal defects, voids and boundaries.

8. High spatial resolution, 0.1–0.2 mm, however, dictates higher positioning accuracy requirements, especially for the shallowest points that can suffer from some partial illumination effects. Ideally, this accuracy should be 0.01–0.02 mm (or ~10% from the spatial resolution) to eliminate such possibility. This accuracy is practically achievable through the use of the surface intensity scans that can resolve such positional accuracy, provided there are no complications arising from large grain sizes, presence of texture gradients or large defects. The use of mechanical, optical or laser scanning positioning systems cannot easily guarantee the required accuracy. A typical example is given in Fig. 16.4 to demonstrate the intensity scan procedure.
9. In order to achieve high spatial resolution experimentally, slits/apertures made of highly neutron-absorbing materials (Cd, Gd, B) are usually used. They are employed as the neutron optical systems of choice, since the neutron radial collimators, an alternative to slits, cannot provide any practical solution for gauge volume sizes less than 0.5 mm. Measurements with slits do not exhibit any disadvantages in comparison with the radial collimators, such as neutron beam divergence, in case of coatings. A high spatial resolution experiment usually assumes a small sample thickness of 1–5 mm. This also conveniently allows small slit-to-sample distances of the same order, therefore minimizing the neutron beam divergence. Theoretically, the divergence takes place, and it can result in a larger gauge size when compared with the nominal gauge size, but this effect is rather small: for a typical 5 mm slit-to-sample distance, the gauge volume size enlargement is ~0.01 mm for the primary beam and ~0.02 mm for the secondary beam (as in case of KOWARI, see below).

10. Since stress distribution in coatings is a one-dimensional elasticity problem, it can be easily interpreted and modelled without the use of finite element models (FEM), which are usually required for general three-dimensional elasticity problems. The layer deposition model developed by Tsui and Clyne (1997a) allows for an empirical description of the one-dimensional stress distribution in the coating-substrate system. The model has only two fitting parameters: one is the deposition stress σ_d, which is characteristic of the spray process and can be tensile (quenching) or compressive (peening). The deposition stress is obviously controlled by the deposition process' physical parameters (particle temperature and velocity) and the particle's material properties. The second parameter is the thermal mismatch $\Delta\varepsilon_{th}$ that accounts for the discrepancy in the thermal expansion coefficient between the substrate and coating materials, $\Delta\varepsilon_{th} = \Delta\alpha\Delta T$, when the temperature of the coating-substrate system drops by ΔT at the end spraying process. Quantitative analysis of the experimental stress profiles in terms of the model allows separation of σ_d and $\Delta\varepsilon_{th}$ and their contribution into the final stress state. Further simplifying the main idea of the analysis, these two terms can be separated through the accurate measurement of the two slopes in the stress profiles across coating and substrate.

    The model was successfully applied to a range of deposition techniques such as plasma spray, high-velocity oxygen-fuel (HVOF) and cold spray (Fig. 16.5). The stress profiles in Fig. 16.5 show the deposition stress parameter that extracted experimentally, while the thermal mismatch stress is essentially zero as there are no discernible differences in the thermal expansion coefficient in the Al/Al systems. It should be noted that for the cold-sprayed samples, the deposition stress is compressive, −22 MPa. Conversely for the plasma spray sample, the deposition stress is tensile, +10 MPa, while for the HVOF sample, the value lies between these two. This observation is a manifestation of the dominant stress-inducing mechanism of the three techniques: peening in the cold spray, quenching in the plasma spray and combination of both in the HVOF. While the layer deposition model deals with the case of free-standing substrate, which is allowed to bend and deform during the deposition process, often other constrained conditions are also considered in accordance with the sample fixation method (Brenner and Senderoff 1949).
11. Analysis of the experimental stress profile in terms of the deposition stress and thermal mismatch, and its decomposition into the two contributions, is essential for the interpretation of the measured stress profiles and, specifically, for the purpose of comparing stresses from different coatings. The resultant stress profiles encompass not only the deposition process parameters, σ_d and $\Delta\varepsilon_{th}$, but also the dependences on coating and substrate thicknesses and material properties. In Fig. 16.6a several simulated stress profiles are shown to illustrate changes as a function of the coating's thickness. While the profiles exhibit measurable differences due to thickness variation, when these profiles are back calculated in terms of deposition stress, all profiles will result in the same deposition stress parameters σ_d (and $\Delta\varepsilon_{th}$ for that matter). The same effect can be observed for changes in substrate material (elastic properties) as shown in Fig. 16.6b.

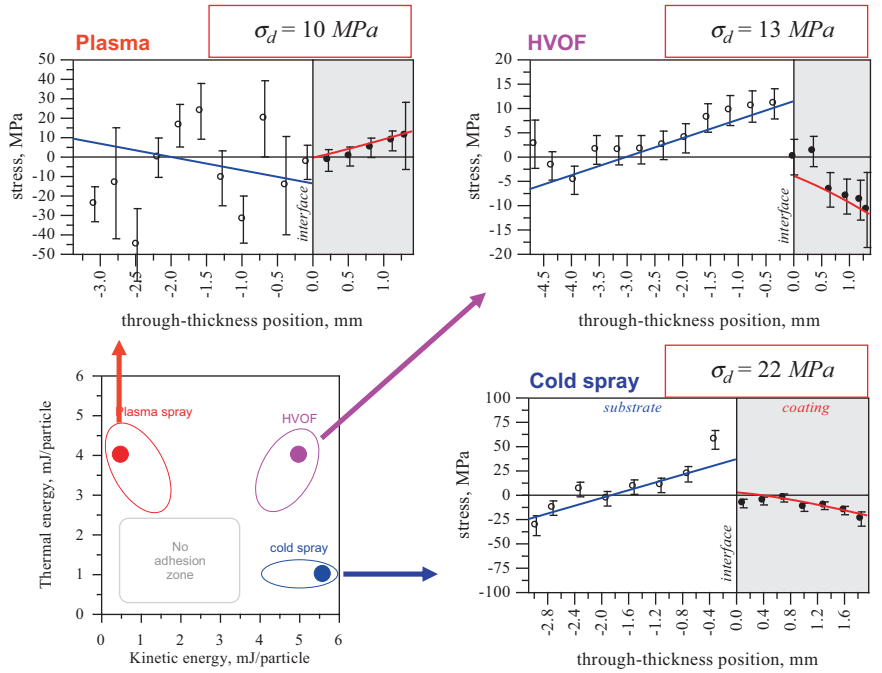

Fig. 16.5 Results of the stress analysis using Tsui and Clyne model for Al/Al-coated samples (substrates are at the *left*, coatings are at the *right*) sprayed by three different techniques. Details can be found in Luzin et al. (2008) (experimental data in the substrate of "plasma" sample is unreliable due to grain size problem resulting in huge statistical oscillations)

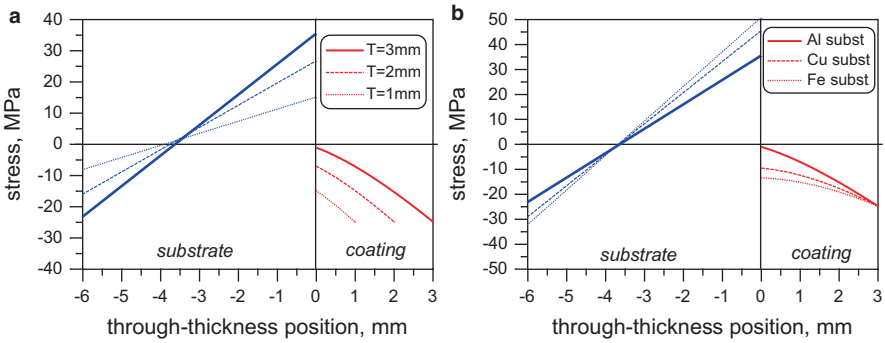

Fig. 16.6 (**a**, *left*) Three stress distributions resulting from the same deposition stress (−25 MPa) but for three different coating thicknesses (3, 2 and 1 mm). (**b**, *right*) Three stress distributions calculated with the same thickness (3 mm), the same deposition stress (−25 MPa) but different substrate material (*Al*, *Cu* and *Fe*). Coating material is Al with Young's modulus of 47 MPa. There is no thermal mismatch term for simplicity

Therefore by performing the above analysis and separating the different contributions, all geometrical factors are eliminated. While the thicknesses of coatings might differ or substrate properties may change, this analysis provides a reliable tool to compare stress in various coatings. Moreover, it can be used for prediction or recalculation of stress profiles in systems of various combinations.

12. The layer deposition model only predicts stresses occurring during the deposition of the coating atop the substrate. However, the experimental stress distributions might display some pre-spraying (initial) stresses, which can exist in the substrates, in addition to the stresses induced by the spraying process. These residual stresses in substrates are usually inherited from the production processes, e.g. rolling, quenching or pre-spraying substrate preparation, e.g. grit/sand blasting. Several strategies are used to address this issue: (i) substrates can be stress relieved prior to coating through annealing. This strategy may not always be available or appropriate for certain cases, e.g. annealing samples after grit blasting might not be deemed acceptable due to the potential for surface oxidation. (ii) A more practical way is to measure stress distribution in the substrates directly and subsequently subtract it from the coated sample profile. The resultant stress distribution can then be treated within the frame of the layer deposition model. This is illustrated in Fig. 16.7a based on the data from the cold-sprayed Al/Al sample (Choi et al. 2007). The expected stress profile in the substrate is a linear function since the substrate can experience only bending, assuming that no material modification occurs during coating. (iii) Alternatively, the initial stress can be an integral part of the extended modelling. This approach is also illustrated in Fig. 16.7b for the same Al/Al system. However, this approach is only practicable in a few simple cases such as peening stress or plastic bending stress, as these are relatively simple and can be easily parametrized with a few empirical constants. In the case of Fig. 16.7b, the peening stress is described by the width and intensity parameters of an eigenstrain function (Korsunsky 2005).
13. For experimental resolution of 0.2 mm, the stress profiling is practical for relatively thick coatings of few millimetres down to 0.4–0.5 mm (Luzin et al. 2017). However, there is a clear limit for this approach. When the coating thickness is reduced and becomes commensurate with the finest attainable resolution of 0.2 mm, the stress profiling through the coating is no longer practically possible. At the best, only the average through-thickness stress value can be obtained experimentally. In this case the stress decomposition cannot be done unambiguously as illustrated by Fig. 16.8.

    The two simulated stress profiles have identical stress distributions in the substrate, identical average through-thickness stresses, but they are representative of two different mechanisms of stress generation. In Fig. 16.8a the stress is attributed to the thermal mismatch (with a deposition stress equal to zero), while for the second case, Fig. 16.8b, the profile is fully determined by the deposition stress (with a thermal mismatch equal to zero). This ambiguity can be resolved by fixing one of the parameters, usually the thermal mismatch term, as it can be conveniently measured using thermocouples in laboratory conditions.

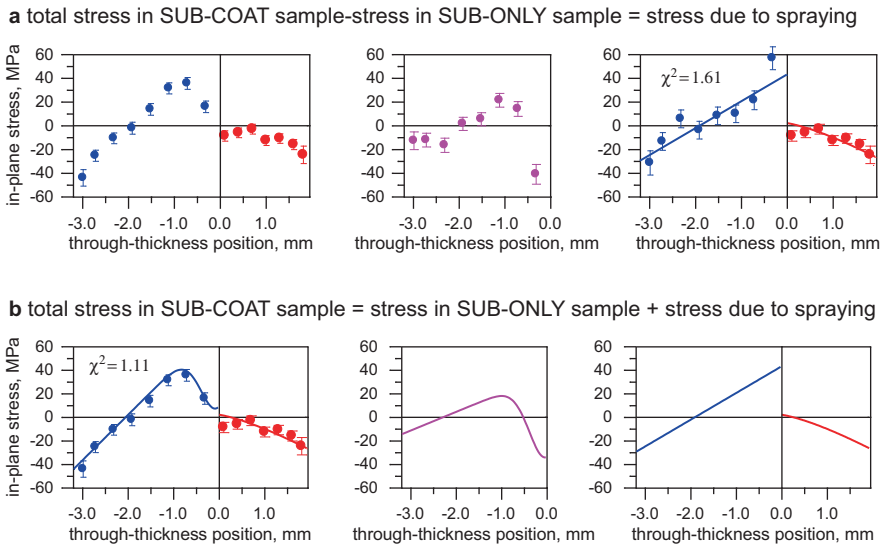

Fig. 16.7 Two ways of dealing with an initial stress distribution in substrate through (**a**, *top*) subtraction of the experimental profile and fitting the result or (**b**, *bottom*) fitting the as-measured profile with inclusion of the initial stress as a part of the model description

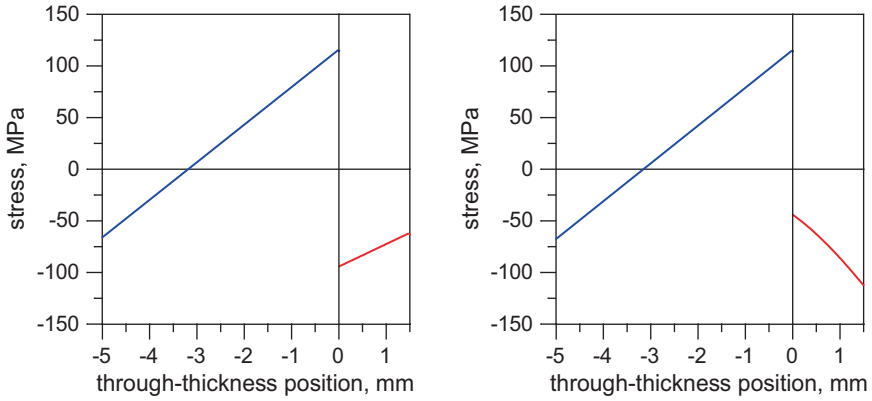

Fig. 16.8 Two stress distributions which correspond to two different mechanisms, thermal mismatch (**a**, *left*) and peening (**b**, *right*), correspondingly

14. Although only single-phase coatings are considered in the manuscript, there is an opportunity with neutron stress scanning to measure two-phase (multiphase) materials in a similar way. The measurement protocol involves measuring each phase separately and the separation of the micro- and macro-stress as described by (Luzin et al. 2010).

15. Although the study of the spray and deposition processes on flat coated samples (flat geometry) may seem like an oversimplification, considering the complex shapes of various industrial components, there are ways to transfer these stress characterizations to more complex geometries. One way is through an analytical approach where the stress parametrization through deposition/thermal mismatch can be applied to other geometries; an example of cylindrical geometries is shown in Tsui and Clyne (1997b). Another way is to use the same parametrization in combination with FEM modelling to compute the local stress at a scale at which sample is locally flat.

16.3 Experimental

In this work we present a systematic study of different materials sprayed using different conditions and cold spray techniques for flat coating geometries. They were studied using neutron residual stress measurement technique as well as several other analytical techniques, to accompany the residual stress analysis. The aim of the study is to establish fundamental understanding of the residual stress formations and also to provide insights on the mechanism of cold spray coating formation in general.

16.3.1 Samples and Spraying Procedures

In this study only pure metals were selected in three groups, FCC, BCC and HCP metals. A rather limited list of materials was composed, based on their availability, industrial relevance, safety issues and suitability to neutron experiment, with four representatives of FCC metals (Al, Cu, Ni, γ-Fe), three HCP metals (Ti, Zn, Co) and one BCC metal (α-Fe).

Samples for the study were sprayed using two cold spray systems:

(i) A Kinetic Metallization (KM) system, manufactured by Inovati (USA) – a low pressure, sonic CS variant
(ii) A CGT Kinetiks 4000, manufactured by Cold Gas Technologies (Germany) – a high pressure, supersonic CS variant

These two systems will be referred throughout the manuscript as KM and CGT.

Both systems operate under choked flow conditions. In the case of the KM system, the gas speed exiting the convergent barrel nozzle is ~Mach 1, and the resultant gas speed depends on the gas used (He or N_2) and can be calculated using isentropic ideal gas relations at Mach 1 (Dykhuizen and Smith 1998). Higher (sonic) velocities can be reached by using He rather than N_2, because He gas has a lower molecular weight and higher specific heat ratio than N_2.

The CGT system uses a convergent-divergent nozzle and high gas driving pressure to produce supersonic conditions, a Mach number ~ 2–2.5, at the nozzle exit. Even though only N2 gas was used with this system, the exit particle and exit velocities were somewhat higher than the KM system using He gas, for the same particle size.

The data on gas temperature T and pressure P (immediately upstream of the nozzle throat) and the estimated exit particle V_p (Dykhuizen and Smith 1998) and gas exit velocity V_g are given in Table 16.1 for the KM process and Table 16.2 for CGT.

The Cu substrates were squares 30 × 30 mm^2 in size and 2.6–2.8 mm thickness. They were cleaned with 1200 grit SiC paper and rinsed with ethanol immediately before spraying. Commercially pure spherical powders produced by gas atomization were used as the feedstock material. The powders used in spraying were as fine as possible to obtain dense coatings and had a particle size in the range 4–16 μm (Tables 16.1 and 16.2).

Coatings were sprayed to a typical thickness of 1–2 mm to provide enough material for characterization.

Table 16.1 KM processing parameters

Sample	Size (μm)	Gas	P (MPa)	T (°C)	V_g (m/s)	V_p (m/s)
Al/Cu	15	He	0.62	140	1035	585
Cu/Cu	6	He	0.62	200	1105	645
Ni/Cu	7	He	0.62	275	1195	630
Zn/Cu	8	He	0.62	65	935	535
Ti/Cu	16	He	0.62	365	1285	557
Fe/Cu	10	He	0.62	370	1295	580
SS/Cu	8	He	0.62	280	1200	625
Co/Cu	4	He	0.62	380	1305	870

Table 16.2 CGT processing parameters

Sample	Size (μm)	Gas	P (MPa)	T (°C)	V_g (m/s)
Ti/Cu	16	N_2	3.9	615	640
Fe/Cu	10	N_2	3.9	615	630
SS/Cu	8	N_2	3.9	520	630
Co/Cu	4	N_2	3.9	600	620

16.3.2 Coating Characterization Methods

1. The microstructure was characterized by employing scanning electron diffraction and EBSD to reveal microstructural features at the micro-scale level (e.g. small-angle boundaries and subgrain structure). The metallographic sections transverse to the spray direction were polished and chemically etched to reveal the particle boundaries. The analysis of average plastic strain of the particles in the coating was estimated by examining deformed particle shapes. It was assumed that on impact (i.e. uniaxial compression), the initially spherical particles were deformed into elliptical shapes (oblate spheroids in 3D). The analysis of aspect ratios $l_{\parallel}l_{\parallel}/l_{\perp}$ of multiple particles (~50 measurements for each sample) allowed for statistical evaluation of the average equivalent plastic strain,

$$\bar{\varepsilon} = \frac{2}{3}\ln\left(l_{\parallel}/l_{\perp}\right).$$

2. Coating density was measured using Archimedes method: rectangular bar specimens were cut from the coatings by electric discharge machining (EDM) with accuracy greater than ±0.01 mm in the linear dimension. Since the bar thickness was the smallest dimension, the uniformity of the bar thickness was a critical parameter in the accuracy of the density determination. The density measured using this technique was estimated to be accurate to at least ±1% for the most thin specimens or better, down to 0.4%, when bar specimen thickness was several millimetres. Although only one specimen representative of the coating was used in the density evaluation procedure, in one case (Al, KM) several samples were tested to check reliability of the procedure with the results being in agreement within error bars.
3. The Young's modulus was determined using the impulse excitation technique (Heritage et al. 1988) on the same set of the rectangular bars sectioned from the coating. Yet again, the critical parameter determining the accuracy of the Young's modulus was through-thickness uniformity of the test specimens, and in a very similar way, the relative accuracy of the Young's modulus measurement was 1% at worst, while 0.5% was more typical.
4. Neutron diffraction texture analysis was carried out using the neutron diffractometer KOWARI (OPAL, ANSTO) (Kirstein et al. 2009). Several pole figures were measured on a 5° × 5° grid to calculate the orientation distribution function. For FCC materials the set of the measured pole figures included (111), (200) and (220), while for the HCP material, the set was (002), (100), (101) and (110). The full pole figures were measured, despite cylindrical symmetry of pole figures, to provide better statistics when averaged over azimuthal angle. Samples for texture measurements were cuboids, with typical size of 5–6 mm, which allowed for a reduction in neutron absorption effects while retaining a sample volume that lends itself to improved neutron counting and grain statistics and, therefore, more reliable results.
5. The residual stress measurements were performed on the neutron diffractometer (stress scanner) KOWARI (Kirstein et al. 2009). A typical 0.2–0.5 mm gauge vol-

ume size was chosen in order to resolve the through-thickness stress distribution. To achieve the best possible through-thickness spatial resolution, the diffraction experiment was done in 90° geometry, and to achieve this, the wavelength of the instrument was varied according to the coating materials and the diffraction reflection used in the measurements. The typical wavelength was in the range of 1.5–1.8 Å; the reflection for FCC materials was (311), (211) for BCC and (112) for HCP. The neutron measurements were done through the whole thickness of the samples, both coating and substrate, to have full stress description of the coating-substrate elastic system. Since scattering properties of different materials vary significantly, the measurement time to measure one location (point) in the samples was also significantly different between samples. Adjustment of measurement time ensured strain measurement accuracy of ~50 μ strains.

Measurements were done accordingly to the protocol described in Sect. 16.2. At each through-thickness location, the diffraction peak position was measured along the two principle directions, in-plane and normal to calculate in-plane stresses assuming a state of balanced biaxial plane stress. In order to evaluate only stresses which originate from the cold spray process, the initially existing stresses in substrates were excluded by performing neutron stress measurements on the "substrate-only" sample and subtracting the obtained stress distribution out of the "coating-substrate" stress profiles.

6. Electron backscattering diffraction (EBSD) analysis was carried out on a transverse cross-section of a cold-sprayed Al6061 CGT coating sample, studied previously (Spencer et al. 2012). It was sprayed using 45 μm powder, N_2 as a carrier gas at a driving pressure of 3.9 MPa and a gas temperature 400 °C. The EBSD map was post-processed using the HKL Channel 5 software. EBSD patterns were collected and analysed in an area 40 × 30 μm^2 around a triple-junction boundary of three particle splats, using a step size of 0.15 μm.
7. Two complementary simulation approaches were used to study the cold spray process with high temporal (ns range) and spatial (μm range) resolution. The first method was a Lagrangian solid element (LE) method which has been successfully used in previous studies of particle impact (see, e.g. (Schmidt et al. 2009; Gu and Kamnis 2009; Grujicic et al. 2004)). This method allows for analysis of the first stage of the particle impact but often results in errors as the simulation progresses due to large element distortions and severe reduction of the computational time steps. The second method is the smooth particle hydrodynamic (SPH) formulation model realized in the hydrocode LS-DYNA. Because it is an element-free Lagrangian formulation, the singularity problem is effectively overcome, and the method allows modelling of the latter stages of deformation, as well as extending modelling to a multiparticle simulation. Simulations of the deposition process as well as the occurrence of debris or jetted particles and the peening stress were treated correctly in this formulation. In the current study, it was possible to simulate the deposition of 400 individual particles of Al6061 with particle size of 15 μm, staggered in four layers, each comprising 10 × 10 particles. The particles impacted an Al6061 substrate surface at velocity of 585 m/s. The substrate dimensions were 200 × 200 × 60 μm and were also modelled using SPH elements, using a coarser resolution. A symmetrical SPH formulation (IFORM = 2) was used in

LS-DYNA, with a variable smoothing length option. The Johnson-Cook constitutive material model with a Mie-Grüneisen equation of state was used to describe the deviatoric and hydrostatic stress within the materials. All technical details of the modelling can be found in (Saleh et al. 2014b).

16.4 Results and Discussion

16.4.1 Coatings Microstructure

The microstructure of the sprayed coatings demonstrated good consolidated quality, with no significant bulk defects (Fig. 16.9). The microstructures of different samples were used to evaluate the average equivalent plastic strain that came for all material very close to −0.5 (see, e.g. a grain in the right bottom corner in Fig. 16.9 that lies at the interface).

16.4.2 Coating Densities

The apparent quality of the sprayed coatings observed using microscopy was confirmed by measuring the coating density, shown in Fig. 16.10. The coatings with a lower fractional bulk density were the BCC and HCP materials, which deform less readily than the FCC materials and likely have more boundary and bulk defects as a result. Another obvious observation is that the CGT consistently produces coatings

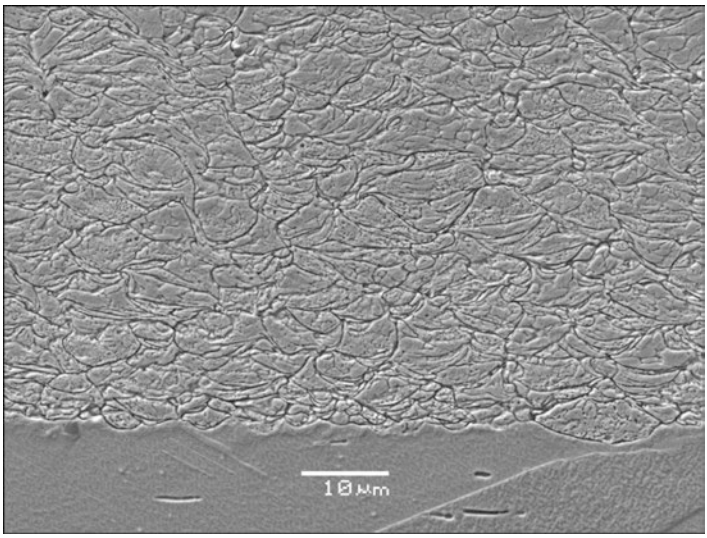

Fig. 16.9 Microstructure of the Cu coating produced by KM

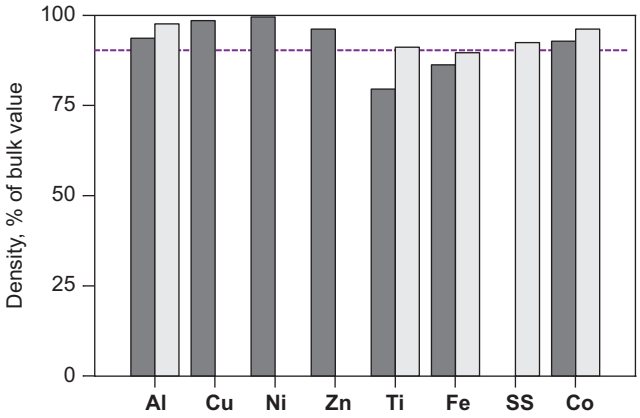

Fig. 16.10 The density of the coatings sprayed by KM (*dark*) and CGT (*light*), expressed as percentage of bulk density. Ninety percent level is marked by a *dotted line*

with a density closer to their bulk equivalents than the KM. The higher velocity in the CGT system and the higher resultant kinetic energy and impact pressure ensure better compaction of the coating materials. The initial deposition temperature may also play a role, but the extent of that influence is difficult to quantify at this stage and requires further study.

16.4.3 Coating Young's Modulus

While density is a measure of the volume porosity (3D defects), the Young's modulus is also sensitive to 2D defects such as cracks and the quality of the particle-particle interfaces. The latter has a stronger impact on the Young's modulus because the volume porosity alone would produce analogous reduction in both the densities and Young's modulus. The fact that Young's modulus can be as low as ~50% of the bulk value (Fe and Ni) or even less (in case of Ti) illustrates the importance of the interparticle bond quality (Fig. 16.11). As with density, the Young's modulus of CGT coatings is larger than for the KM coatings, and this effect is probably more distinct. This suggests that for CGT not only is the particle compaction better but so is the particle cohesion.

16.4.4 Texture Analysis

Examples of the experimental pole figures obtained in the neutron diffraction experiment are shown in Fig. 16.12. Although pole figures are supposed to have a cylindrical symmetry, due to statistical uncertainties, there are variations that are especially visible when textures are not very pronounced. Indeed, the resultant texture is

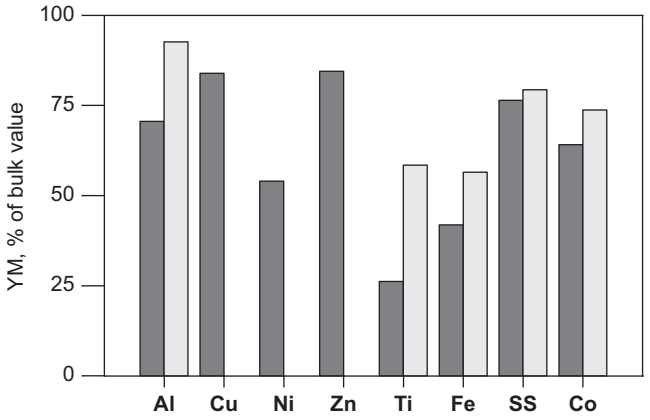

Fig. 16.11 The Young's modulus of the coatings sprayed by KM (*dark*) and CGT (*light*), expressed as percentage of bulk Young's modulus

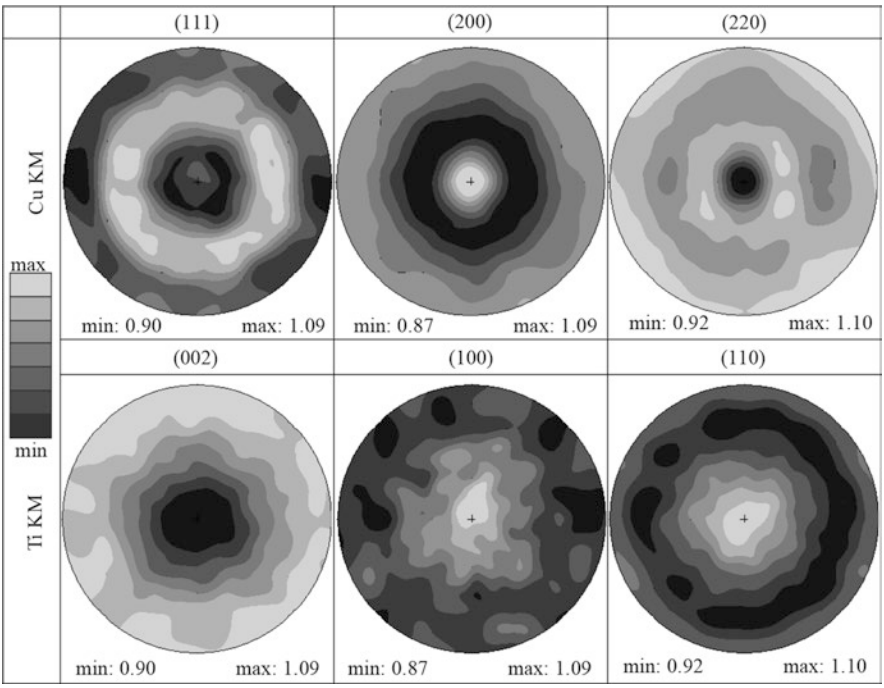

Fig. 16.12 Experimental pole figures for two samples (**a**) *Cu, KM* and (**b**) *Ti, KM* representing two kinds of materials, FCC and HCP (*dark colour* corresponds to maximum)

relatively weak. This is despite the fact that deformation of individual particles is large (~0.5 of equivalent plastic strain) and much stronger texture development is expected. In order to improve the statistics, the pole figure densities obtained by azimuth angle averaging of the measured full pole figures are shown in Fig. 16.13, as

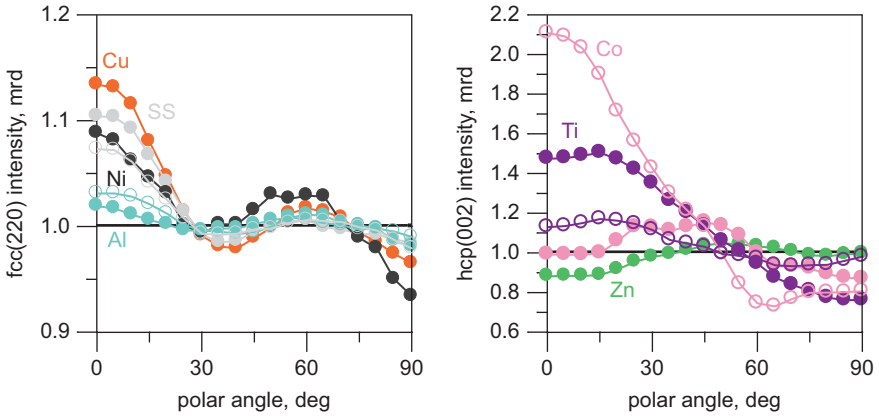

Fig. 16.13 Pole figure densities for different samples produced by KM (*solid symbols*) and CGT (*empty symbols*)

a function of the polar angle only. Pole figures demonstrating the largest min/max ratio were chosen to illustrate texture data, FCC(200) and HCP(002). Examining the fibre components (Matthies et al. 1987; Cho et al. 2004), in case of the Cu sample, the apparent (110) fibre component, which is characteristic of slip on the dominant {111}<110> slip system, has in fact very high intensity (90–100%,). However, the width of this component is very large (65°–70°), resulting in a weak texture. In the case of the Ti and Co CGT-sprayed samples, basal slip on {001}<110> causes the appearance of the (002) fibre component, while for other HCP materials, Zn using the KM technique and Co utilizing the CGT technique, the fibre texture component is of the (10.1) type. In the same way as for FCC metals, the fibre components are broad (width of ~70°), producing a weak texture. The BCC iron samples, for both KM and CGT, do not exhibit any measurable preferred orientation.

16.4.5 Residual Stress Analysis

A typical through-thickness residual stress distribution is shown in Fig. 16.14 for two Ti samples. The accuracy was estimated to be ±10 MPa. In some cases the uncertainties were larger, and in the worst case of Co, the accuracy was ±60 MPa. This was due to the fact that Co has very poor neutron scattering properties: small coherent cross-section (weak diffraction signal), large incoherent cross-section (large background) and high absorption (neutron beam attenuation).

The residual stress profiles were fitted using (Tsui and Clyne 1997a) progressive coating deposition model as described in Sect. 16.2. The quality of the model fit is confirmed by the χ^2 values which were typically close to 1 (e.g. Fig. 16.14). The same routine was applied to all other coating systems presented herein, allowing for separation of all contributions to the overall stress distribution (initial stress, deposition stress, thermal mismatch stress).

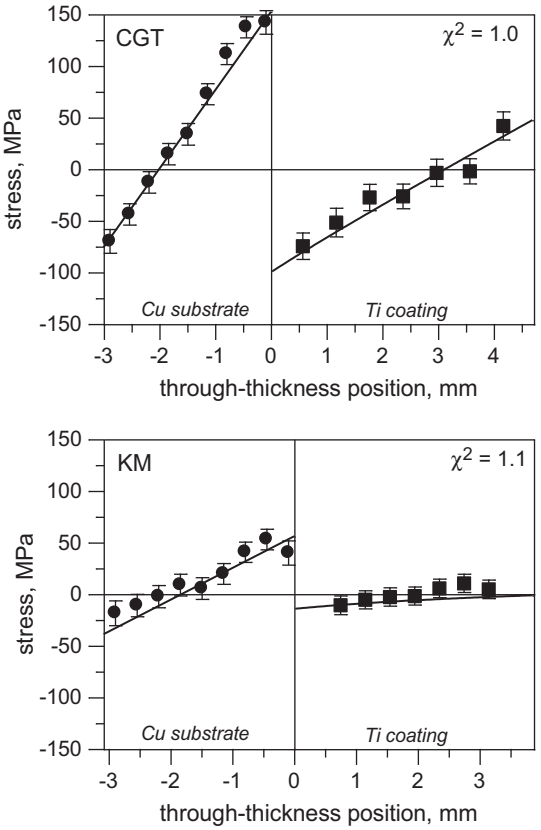

Fig. 16.14 Through-thickness stress distribution in Ti samples sprayed by (**a**) KM and (**b**) CGT

Separation of the contributions allowed the dominant stress formation factor in a given coating-substrate system to be determined. Thus, in the case of the Ti coating shown in Fig. 16.14, the dominant stress factor is the thermal misfit due to the substantial difference in thermal expansion coefficient between Ti and Cu. Along with this statement is the fact that stresses are larger in the CGT sample: the CGT (gas) spraying temperature of 615 °C is much higher than it is in KM, 365 °C, and this generates larger thermal residual stress for the higher temperature process. The contribution from the peening stress is relatively small: when considered alone it can produce stress profiles with a maximum value of only 20 MPa in the Cu substrate close at the interface. Thus, for both Ti coatings, the accumulated residual stress is thermal in origin rather than kinetic (i.e. due to a peening process).

The most important result of the analysis is the values of the deposition stress σ_d for different materials. The deposition stresses for all studied materials and techniques are shown in Fig. 16.15. It is confirmed that cold spray produces compressive deposition stress due to peening observed in earlier works (Luzin et al. 2008; Luzin et al. 2011; Spencer et al. 2012). The magnitude of the peening stress varies clearly with the sprayed material. It is notable that the HCP materials (Zn, Ti, Co) and BCC materials (Fe) did not accumulate a large residual stress, while the FCC

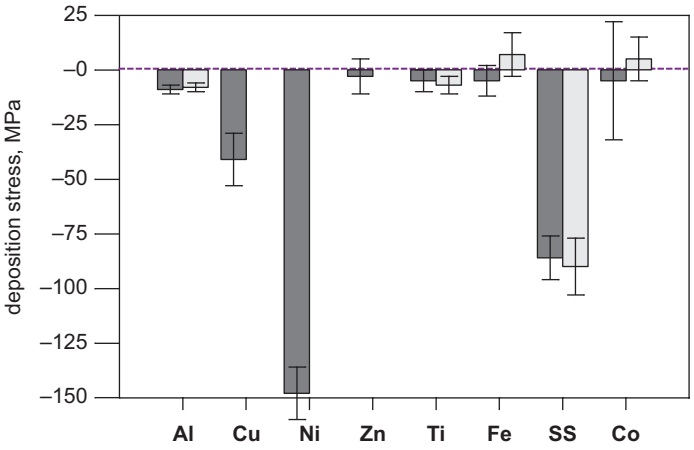

Fig. 16.15 The deposition stress for coatings sprayed by KM (*dark*) and CGT (*light*) techniques

materials (Al, Cu, Ni, stainless steel) tend to exhibit significantly higher level of residual stress. The stress in the FCC materials correlates with the yield stress (YS) of the sprayed material, though the corrections for the temperature dependence and rate dependence must also be considered. The same conclusion has been made based on analysis of cold-sprayed Al alloys (Spencer et al. 2012) and is illustrated in Fig. 16.16. Studying the Al/Al-coated systems eliminates other possibilities like dependence on thermal conductivity, density, Young's modulus, etc. since all elastic and thermal properties were essentially identical for all considered alloys.

16.4.6 EBSD Analyses

A secondary electron image of the EBSD scan region on the surface area of an Al6061 KM sample is shown in Fig. 16.17a, b. The EBSD analysis reveals a complex grain structure that can be visible in Fig. 16.17c. With the measurement resolution of 0.15 μm, the estimated average subgrain size appears to be ~0.5–1 μm. Consistent with previous EBSD analysis done on a cold-sprayed Ni coating (Zou et al. 2009), there is evidence of an ultra-fined grain structure formed by dynamic recrystallization. The approach to estimate the mean grain size through the parameters of the deformation processes, outlined in (Twiss 1997) and used in (Zou et al. 2009) in the case of Ni, was also applied to the present Al6061 cold spray sample. Using an average impact pressure of σ = 800 MPa (Zou et al. 2009), Burgers vector b = 0.286 nm (½ <110>), aluminium shear modulus G = 25.88 GPa and constants n = 0.8 and K = 15 and the relationship between them, $(\sigma/G)(D_R/b)^n = K(\sigma/G)(D_R/b)^n = K$, the estimate of the grain size is D_R ~ 0.7 μm, close to the observed grain size. Away from the particle contact areas, the granular structure appears to be similar in size to the microstructure of the original particles (Fig. 16.17d).

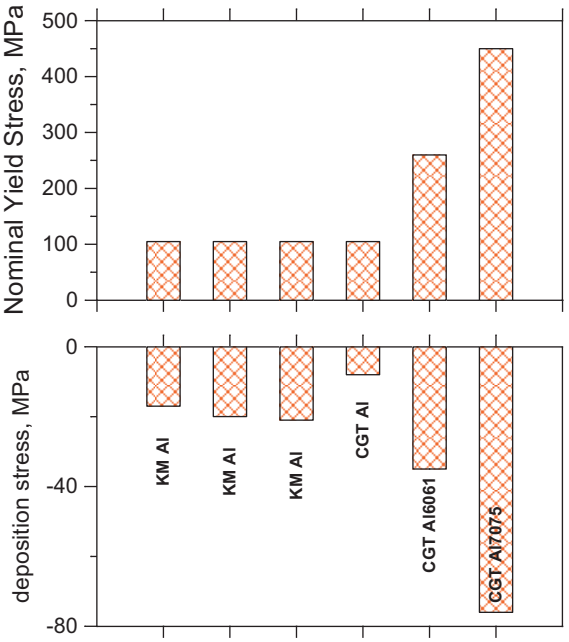

Fig. 16.16 Correlation and proportionality between the deposition stress and YM of the aluminium alloys

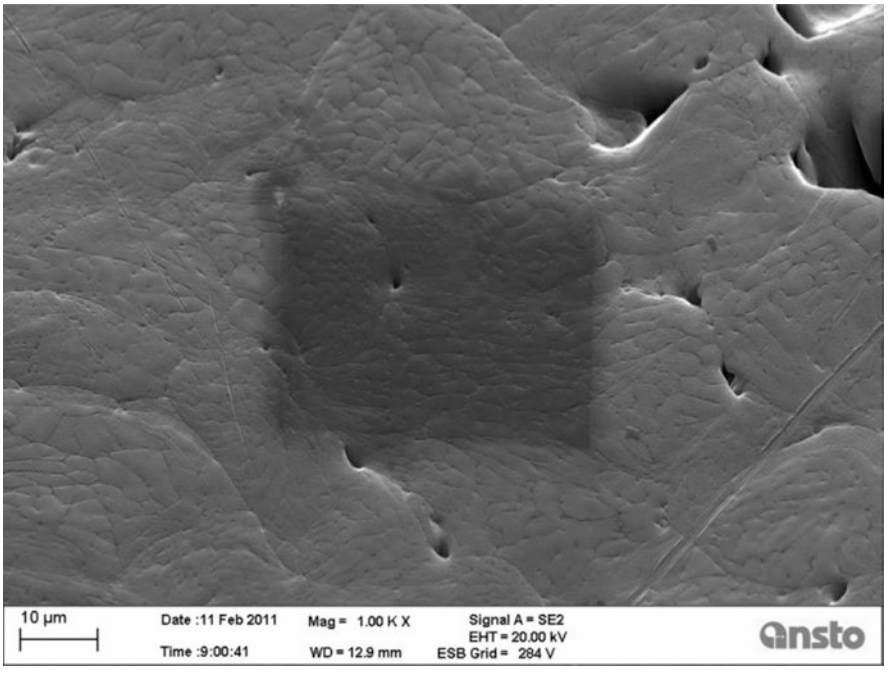

Fig. 16.17 (**a**) SEM image around the area that was analysed by EBSD and the central area, $40 \times 30\ \mu m^2$, has a darker hue due to the exposure to the electron beam; (**b**) SEM image of the area that was analysed by EBSD and (**c**) EBSD map of this area plotted in Euler angle colour scheme and (**d**) comparison with the original grain structure of the powder particle before spray

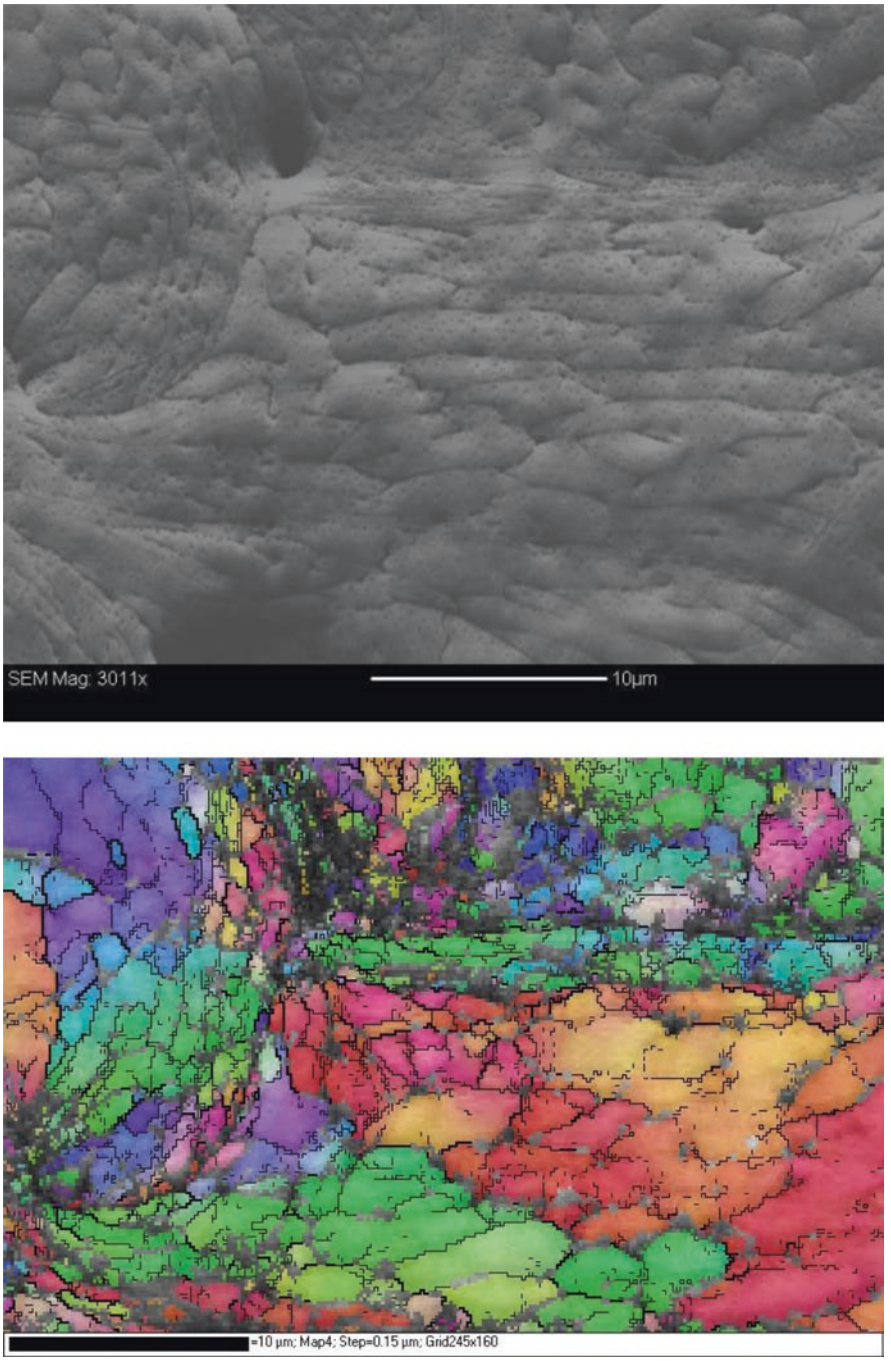

Fig. 16.17 (continued)

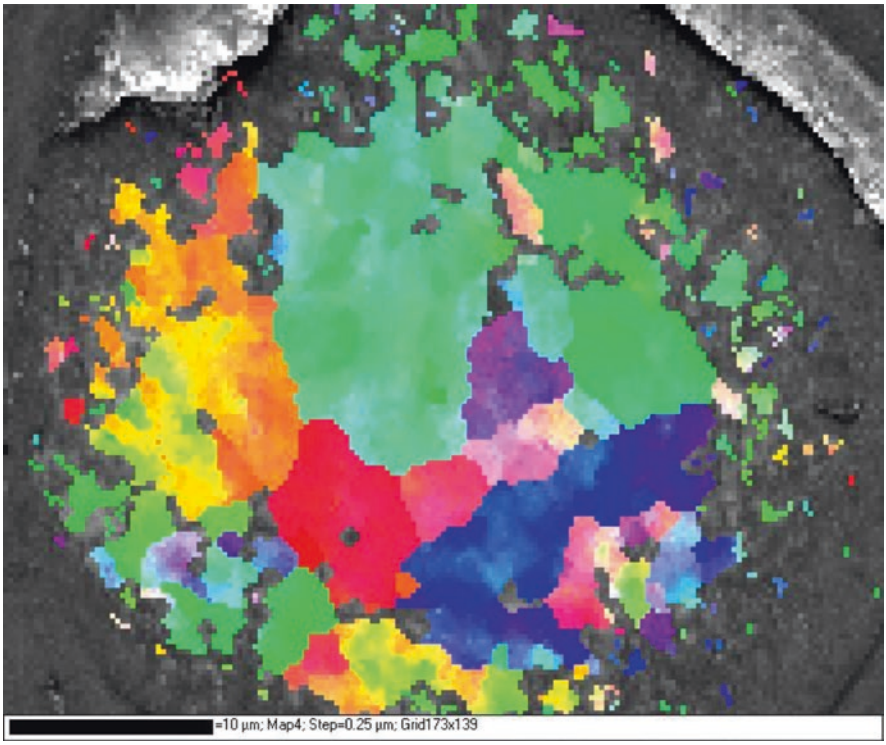

Fig. 16.17 (continued)

16.4.7 Modelling

Both the SPH and the Lagrangian models were able to reproduce the morphology of the deformed particle in a single particle simulation (Fig. 16.18) (Saleh et al. 2014a). This was also observed in earlier studies by (Schmidt et al. 2009; Gu and Kamnis 2009; Grujicic et al. 2004; Assadi et al. 2003). The simulations show that upon impact there is a narrow band at the periphery of the deposited cold spray particles where the temperature increases, and there is strong correlation with the adiabatic shear instability since these regions are characterized by a rapid decrease of the flow stress and a correspondingly rapid rise in plastic strain, as seen in Fig. 16.19. These regions are areas where material jetting is most pronounced and occurs at an angle of 40–45°, measured from the direction of the particle impact (Fig. 16.20). In these regions temperature can approach or exceed the melting point (Fig. 16.19) and therefore create conditions for efficient metallurgical bonding. The localization of both the temperature rise and the large plastic strains in the narrow region around the particle edge also supports the experimental observation of dynamic recrystallization as seen in the EBSD image in Fig. 16.17, with the associated grain refinement in the areas adjacent to the contact boundary.

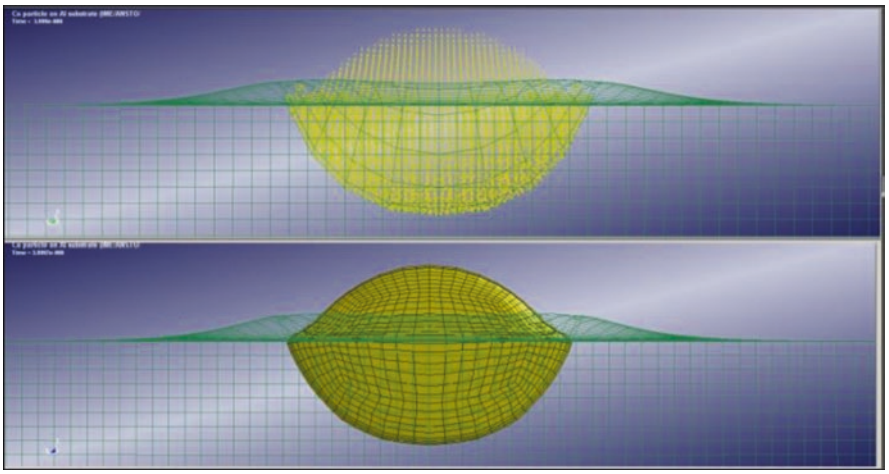

Fig. 16.18 A single particle shape simulation: particle shape by (**a**) SPH and (**b**) Lagrangian methods

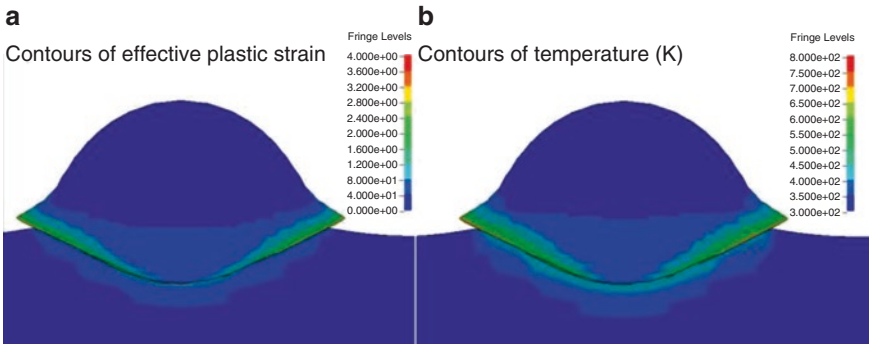

Fig. 16.19 LE single particle shape simulation: localization of (**a**) the effective plastic strain and (**b**) temperature. Original particle size is 15 μm

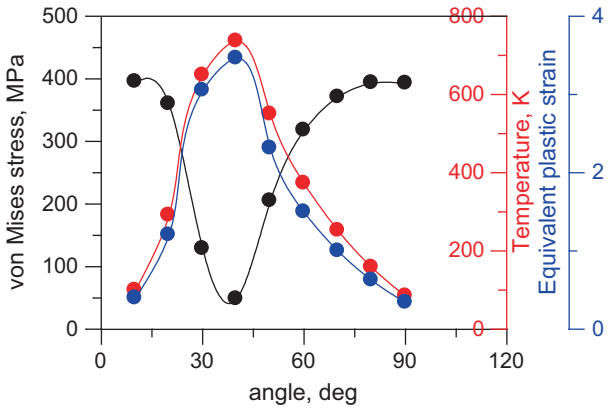

Fig. 16.20 Angular dependence of the localized peak effective plastic strain, stress flow and temperature along the particle contact boundary (in the LE single particle simulation)

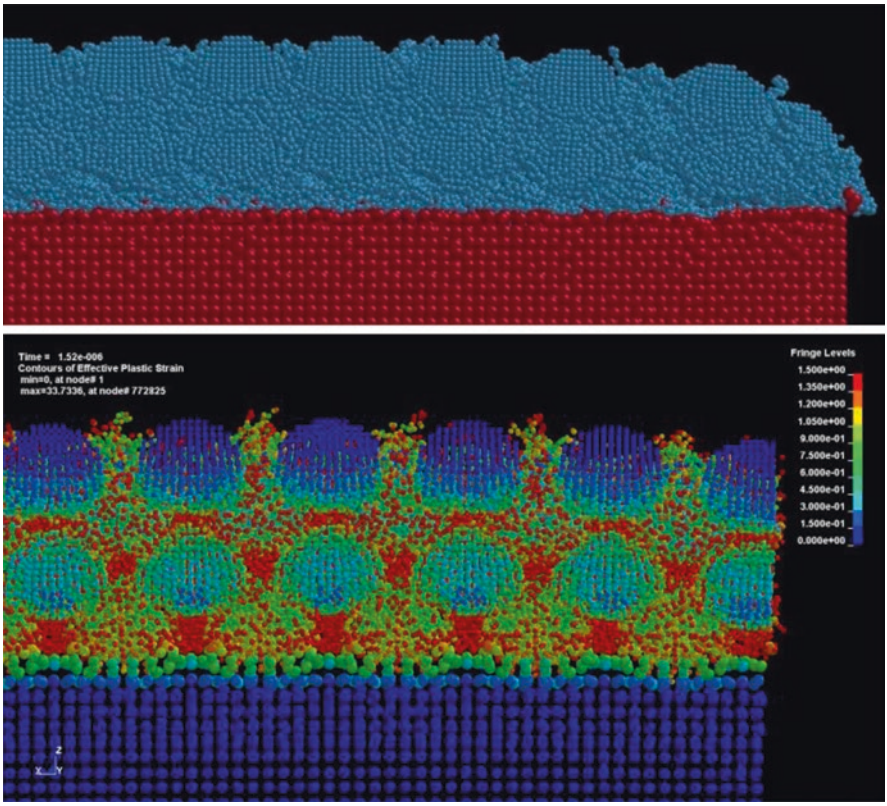

Fig. 16.21 Multiparticle SPH simulation: (**a**) multilayer morphology and (**b**) effective plastic strain map in the cross-section

The results of the multiparticle SPH simulations show the morphology of the cold spray particles is unequivocally affected by the impact of the particle and also by impacts of the particles impacting surface thereafter (Fig. 16.21). The jetting of materials from neighbouring particles allows for lateral linkages through mechanical locking of the semi-molten metals as they cool, but perhaps the more significant effect is the metallurgical bonding in the contact area between particles in the molten conditions. The SPH model was also able to predict two aspects of the stress accumulation during spraying. First, the large compressive stresses induced by the sprayed particles in the substrate due to the shot peening effects. Second, for the coating the model produces an average compressive deposition stress of approximately −10 MPa, which is consistent with the measured value for pure Al in Fig. 16.16 (−17 ± 7 MPa for KM and −8 ± 2 for

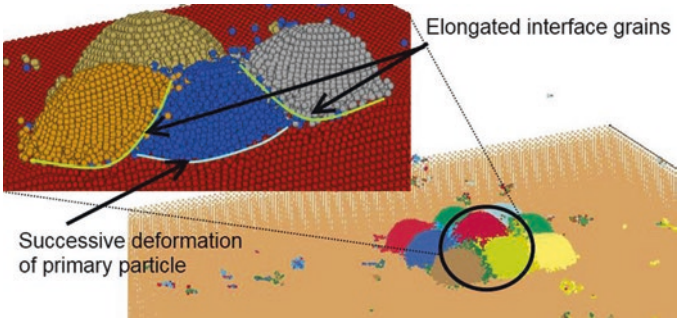

Fig. 16.22 Some details of multiparticle interaction: particle interfaces, ejected material

CGT), but somewhat smaller than for the Al6061 alloy sprayed by KM (−35 ± 6 MPa) (Spencer et al. 2012).

The limited number of particle that can be practically modelled may be responsible since the surface stress relaxation effect is still significant for such a limited thickness of the coating. Another drawback of the model was the almost instantaneous (adiabatic) deposition of all particles rather than the staggered deposition that would allow some heat dissipation, conduction and diffusion; it can be improved in future simulations. Therefore, if these effects are taken into account, this should result in larger compressive stresses. Another result of multiparticle simulation is that model predicts some jetting with material escaping the surface (Fig. 16.22). This results in deposition efficiency less than 100%. There is also some porosity as result of particle-particle collisions and the initially staggered formation, with a resultant computed density being less than bulk. Overall, the reproduction of the particle shape after impact, material jetting and the residual stress profile all suggest that the SPH model can be used to describe multiple particle deposition in cold spray coatings.

16.5 Summary and Conclusions

1. Spraying using CGT, with a higher temperature and velocity, produces coatings with slightly better mechanical properties (Young's modulus, density), owing to the higher compaction and a reduction in the bulk and interfacial defects.
2. Texture analysis using neutron diffraction demonstrates very weak preferred orientation development, suggesting very limited role of deformation by dislocation glide modes. These results suggest that the core of individual particles may not substantially deform and other deformation mechanisms that do not cause lattice rotation are potentially involved, e.g. adiabatic shear banding assisted by local annealing. This is

supported by the EBSD analysis with evidence of the dynamic recrystallization in the particle interface regions as well as the results of simulation.

3. Results of modelling a single particle collision event show that the local temperature may exceed the melting point in the narrow band along particle interfaces. The multiple particle deposition simulation suggests very localized deformation and cohesion with formation of splat-to-splat contacts.
4. The compressive residual stress due to peening effects was confirmed, though for many materials, it is very close to zero. The magnitude of the peening stress is intimately linked to the material's plastic properties. Strong residual stress accumulation is more typical for FCC materials, with their ability to plastically deform and their propensity to form a better splat-to-splat contact. This enables the accumulation of residual stresses whose magnitude, if not proportional, then at least correlates with the yield stress of the materials.
5. The magnitude of the peening stress can also be predicted by the SPH method with multiple particle impact simulation and performing macroscopic averaging over large ensemble of the deposited particles resulting into compressive (peening) overall stress. A significant progress has been achieved in this direction: for the first time, the multiple particle simulation of CS process has been performed using the SPH formulation on a system of 400 individual particles and encompassed more than 1 million individual SPH elements with quantitative metrics used to validate the model's outputs. Experimentally observed peening stress is also predicted by the SPH method and used to validate the model.
6. The detailed 3D maps of the plastic strain and elastic strain fields available through the multiple particle simulation accentuate the highly non-uniform nature of the material on the microscopic level that is underscored by the EBSD analysis. Linking these different scales of physics of the cold spray process is a difficult and problematic task. Relative success can be achieved using empirical modelling approach, when an analytical relationship can be drawn for the residual stress as a function of the yield stress (Spencer et al. 2012; Luzin et al. 2011).
7. Regarding the particle bonding mechanism, our study (experimental and modelling) offers a more or less comprehensive view of the CS process: despite the term "cold", the CS is, in fact, very thermal in nature with splat-to-splat bonding better characterized as a "micro-welding"; when in the very narrow peripheral contact areas of a particle temperatures exceed the melting points, the material is hugely deformed in its plastically soft condition and recrystallized. Therefore, "micro-welding" provides metallurgical bonding, while mechanical interlocking seems to be less important, though it can have a place through jetting. In contrast to the outer periphery of a particle, the central core remains largely undeformed as supported by the weak texture measurements. Deformation in the transitional zone and the formation of preferred orientation are more apparent in the particle-substrate and particle-particle interfaces.
8. Finally, for the empirical studies of the mechanism of coating formation in cold spray, the neutron diffraction stress scanning technique is very useful, while the use of other material characterization techniques greatly extends the degree of understanding of the process.

References

Assadi H, Gärtner F, Stoltenhoff T, Kreye H (2003) Bonding mechanism in cold gas spraying. Acta Mater 51(15):4379–4394

Brenner A, Senderoff S (1949) Calculation of stress in electrodeposits from the curvature of a plated strip. J Res Natl Bur Stand 42:105–123

Cho J-H, Rollett AD, Oh KH (2004) Determination of volume fractions of texture components with standard distributions in Euler space. Metall Mater Trans A 35(13):1075–1086

Choi WB, Li L, Luzin V, Neiser R, Gnäupel-Herold T, Prask HJ, Sampath S, Gouldstone A (2007) Integrated characterization of cold sprayed aluminum coatings. Acta Mater 55(3):857–866

Dykhuizen RC, Smith MF (1998) Gas dynamic principles of cold spray. J Therm Spray Technol 7(2):205–212

Genzel CH (2004) Diffraction stress analysis in thin films and coatings – problems, methods and perspectives. J Neutr Res 12:233–241

Grujicic M, Zhao CL, DeRosset WS, Helfritch D (2004) Adiabatic shear instability based mechanism for particles/substrate bonding in the cold-gas dynamic-spray process. Mater Des 25(8):681–688

Gu S, Kamnis S (2009) Bonding mechanism from the impact of thermally sprayed solid particles. Metall Mater Trans A 40(11):2664–2674

Heritage K, Frisby C, Wolfenden A (1988) Impulse excitation technique for dynamic flexural measurements at moderate temperature. Rev Sci Instrum 59(6):973–974

Hutchings MT, Krawitz AD (eds) (1992) Measurement of residual and applied stress using neutron diffraction. NATO science series E 216. Springer, Netherlands

Hutchings MT, Withers PJ, Holden TM, Lorenttzen T (2005) Introduction to the characterization of residual stress by neutron diffraction. Taylor & Francis Ltd, Boca Raton

Kirstein O, Luzin V, Garbe U (2009) The strain-scanning diffractometer Kowari. Neutron News 20(4):34–36

Korsunsky AM (2005) The modelling of residual stresses due to surface peening using eigenstrain distributions. J Strain Anal Eng 40(8):817–824

Luzin V, Valarezo A, Sampath S (2008) Through-thickness residual stress measurement in metal and ceramic spray coatings by neutron diffraction. Mater Sci Forum 571-572:315–320

Luzin V, Matějíček J, Gnäupel-Herold T (2010) Through-thickness residual stress measurement by neutron diffraction in cu+W plasma spray coatings. Mater Sci Forum 652:50–56

Luzin V, Spencer K, Zhang MX (2011) Residual stress and thermo-mechanical properties of cold spray metal coatings. Acta Mater 59(3):1259–1270

Luzin V, Vackel A, Valarezo A, Sampath S (2017) Neutron through-thickness stress measurements in coatings with high spatial resolution. Mater Sci Forum, in press

Matejicek J, Sampath S, Brand PC, Prask HJ (1997) Residual stress measurement on thermally sprayed coatings. In: Proceedings of the 15th international thermal spray conference, Indianapolis, USA, pp 861–866

Matejicek J, Sampath S, Brand PC, Prask HJ (1999) Quenching, thermal and residual stress in plasma sprayed deposits: NiCrAlY and YSZ coatings. Acta Mater 42(7):607–617

Matejicek J, Sampath S (2003) In situ measurement of residual stresses and elastic moduli in thermal sprayed coatings: part 1: apparatus and analysis. Acta Mater 51(3):863–872

Matthies S, Vinel GW, Helming K (1987) Standard distributions in texture analysis: maps for the case of cubic-orthorhomic symmetry. Akademie-Verlag, Berlin

Papyrin PA, Kosarev PV, Klinkov DS, Alkimov PA, Fomin PV (2007) Cold spray technology. Elsevier, Oxford

Pirling T (2011) Precise analysis of near surface neutron strain imaging measurements. Procedia Eng 10:2147–2152

Saleh M, Luzin V, Spencer K (2014a) Analysis of the residual stress and bonding mechanism in the cold spray technique using experimental and numerical methods. Surf Coat Technol 252:15–28

Saleh M, Luzin V, Spencer K (2014b) Evaluation of the residual stress in the cold spray technique using smooth particle hydrodynamics modelling and neutron diffraction. Mater Sci Forum 777:205–212

Santana YY, Renault PO, Sebastiani M, La Barbera JG, Lesage J, Bemporad E, Le Bourhis E, Puchi-Cabrera ES, Staia MH (2008) Characterization and residual stresses of WC-co thermally sprayed coatings. Surf Coat Technol 202:4560–4565

Schmidt T, Assadi H, Gärtner F, Richter H, Stoltenhoff T, Kreye H, Klassen T (2009) From particle acceleration to impact and bonding in cold spraying. J Therm Spray Technol 18(5):794–808

Spencer K, Luzin V, Matthews N, Zhang MX (2012) Residual stresses in cold spray Al coatings: the effect of alloying and of process parameters. Surf Coat Technol 206(19–20):4249–4255

Stoney GG (1909) The tension of Metalic films deposited by electrolysis. Proc Roy Soc Lond A 82:172–175

Suzuki H, Harjo S, Abe J, Xu P, Aizawa P, Akita K (2013) Effects of gauge volume on pseudo-strain induced in strain measurement using time-of-flight neutron diffraction. Nucl Instrum Meth A 715:28–38

Tsui YC, Clyne TW (1997a) An analytical model for predicting residual stresses in progressively deposited coatings part 1: planar geometry. Thin Solid Films 306(1):23–33

Tsui YC, Clyne TW (1997b) An analytical model for predicting residual stresses in progressively deposited coatings part 1: cylindrical geometry. Thin Solid Films 306(1):34–51

Twiss R (1997) Theory and applicability of a recrystallized grain size paleopiezometer. Pageoph 115(1–2):227–244

Zou Y, Qin W, Irissou E, Legoux J-G, Yue S, Szpunar JA (2009) Dynamic recrystallization in the particle/particle interfacial region of cold-sprayed nickel coating: electron backscatter diffraction characterization. Scripta Mater 61(9):899–902

Chapter 17
Porosity of Ni-Based and Ti-Based Cold-Sprayed Coatings

Alessio Silvello

17.1 Introduction

Cold spray was developed in the former Soviet Union in the 1980s at the Institute of Theoretical and Applied Mechanics of the Siberian Branch of the Russian Academy of Sciences. It is a relatively new spraying method, which has many advantages over other form of thermal spraying, such as minimal heat input and environmentally friendly (Champagne and Helfritch 2016). The process can be separated into two different categories: high pressure can be defined as a process that typically employs a working gas fluid at pressures in excess of approximately 2.5 MPa, while cold spraying at low pressure typically uses a working gas at pressure below 1 MPa. In high-pressure system, the coating material is introduced as a solid powder into a compressed (1–3 MPa) gas stream (air, N_2 or He) that expands through a converging-diverging nozzle. A heater is then used to raise the temperature of the gas and solid particles as they enter the converging section of the nozzle. The increased temperature causes the hot pressurized gas to expand through the converging section of the nozzle, which serves to increase the gas and particle velocities as they are accelerated and forced out the diverging end. Using the supersonic gas jet as a carrier, solid coating particles are accelerated and propelled towards the substrate at very high velocities.

In low-pressure process, air is used for powder transport. The main difference between the spray guns used in the high-pressure and low-pressure process is that in low-pressure process, powders are fed to the gas flow perpendicularly (radial injection) to the diverging part of the nozzle. Additionally, another difference between the low-pressure and high-pressure process is that heating of gas can do only in the spraying gun in low-pressure process, whereas in the high-pressure process, gas is preheated in the separate heating unit and, in addition to that, in the spray gun.

A. Silvello (✉)
Department of Innovation Engineering, University of Salento,
Via Per Arnesano, 73100 Lecce, Italy
e-mail: Alessio.silvello@unisalento.it

P. Cavaliere (ed.), *Cold-Spray Coatings*,
https://doi.org/10.1007/978-3-319-67183-3_17

Upon impact, the particles deform or "splat" and bond to the surface of the substrate. As more and more particles impact the surface, the "splats" build up and form a uniform coating. To obtain a coating with relatively low porosity, the material ductility and the employed processing parameters must be optimized. If not, many pores of various dimensions can be observed in cold spray coatings (Singh et al. 2017). Porosity is strongly dependent on sprayed material and processing parameters. During impact, particles flatten and assume a pancake-like structure characterized by high flattening ratios. The particle's flattening ratio is defined as the ratio between the larger and the smaller particle dimension after splat considering the spherical shape of the sprayed particles (Fig. 17.1). If the plastic deformation is insufficient, particles retain their original spherical shape leading to higher porosity levels. If the particle's flattening and deformation are not sufficient, individual particles are found to not be well bonded to each other which results in low coating moduli (Sundararajan et al. 2013).

Most of the mechanical properties of the deposit become degraded along with the increase of porosity because pores in the coating layer eventually mean unbonded interparticle interfaces. For example, it has been proved by a number of studies that in case of hot corrosion, the corrosion species travel through pores of the coating; hence coating porosity plays a very important role to resist against hot corrosion (Moridi et al. 2014). The porosity acts as a transport conduit for the corrosive solution and delamination and bulk blistering of the coating occurred. The corrosion resistance of the specimen may differ due to this physical property, as the ability of blocking the corrosive environmental species toward the substrate depends upon the presence of porosity or voids in the microstructure of the coating. The lesser the

Fig. 17.1 Example of splatted cold spray particles

porosity value, the better the resistance to corrosion is considered for a coating. The measurement of porosity is important to decide its application in corrosive environment. The high porosity means less load-carrying capacity and low thermal conductivity of the coated components and thus reduced protection of the base material from the corrosive environment of the boilers and incinerators. Thus, lesser porosity means better performance of components in corrosive conditions (Kalsi et al. 2015; Rathod et al. 2014; Wong et al. 2011).

Though, generally, the porosity also affects the hardness values. Due to high impacts of particles in the solid state, the hardness of the coating with low porosity level is found to be higher than that of the substrate and, for example, is suitable for the erosion-corrosion environment. Furthermore, the low porosity of the coating yields higher hardness values than the original feedstock powder. Denser coating indicates larger plastic strain of the spraying particles and thereby severer work-hardening effect.

The unique characteristics of cold spray operation allow it to be applied to temperature-sensitive substrates. The high-velocity, solid-state particles yield depositions with low porosity and minimal or compressive residual stress. Cold spray can thus be applied to applications that do not allow substrate heating or heat-modified coatings and to those applications that require non-porous, well-consolidated deposits.

Finally, crack propagation is also governed by the pore's presence in the coatings. Improved fatigue properties are obtained if low porosity characterizes the cold-sprayed coatings, reducing the incoming of crack initiation especially at the coating-substrate interphases (Cavaliere and Silvello 2016).

In general, an increase in carrying gas pressure (and temperature) leads to an increase in the degree of interparticle bond. In addition, each particle-substrate combination shows a different behaviour related to the critical velocity. As the average impact velocity approaches the critical velocity, there is a greater likelihood of particles not bonding to form a coating, and therefore coatings of increasing porosity and weaker bonding interfaces are expected to form. So, porosity depends not only from critical velocity and carrying gas pressure but also from carrying gas temperature, starting particle dimensions and substrate hardness (Singh et al. 2016; Yin et al. 2014). For example, by developing densely packed spherical-shaped nanostructured feedstock powders with low porosity, the resulting coating has improved properties, including density, microhardness and wear resistance. On the contrary, the increased size and level of porosity in the conventional coatings acted as stress concentration points, which resulted in lower wear resistance and inferior tribological properties.

The low processing temperatures of cold spray minimize or eliminate phase transformations and residual stresses, which is prominent in high-temperature thermal spray processes. To take advantage of the material properties of the feedstock powder, cold spraying was developed because phase transformations, chemical changes, residual stresses and porosity are minimized (if not eliminated) in these coatings due to the low processing temperatures and high velocities (Feng et al. 2013).

Ni-based alloys possess several attractive properties such as wear, erosion-corrosion resistance and good thermal conductivity. Due to these properties, nickel-based coatings are frequently considered for the prevention of erosion-corrosion. For example, Inconel 718 is a Ni-based heat-resistant precipitation hardenable alloy, commonly employed in advanced structural applications. It is strengthened primarily by ordered face-centred cubic (FCC) γ′-Ni3 and ordered body-centred tetragonal (BCT) γ′′-Ni3Nb. Similar to other Ni-based superalloys, Inconel 718 containing substantial amounts of Nb and Ni2Nb is called "Laves phase". This undesired Nb-rich brittle intermetallic phase, which may lower the ductility and higher the porosity and the rupture stress of the material, could be shown during the welding and its high temperature.

Inconel 690 is a high Cr-Ni alloy having excellent resistance to many corrosive aqueous media and high-temperature atmospheres. In addition to its corrosion resistance, it has high strength, good metallurgical stability and favourable fabrication characteristics. The properties of Inconel 690 are useful for various applications involving nitric or nitric/hydrofluoric acid solutions. Examples are tail-gas reheaters used in nitric acid production and heating coils and tanks for nitric/hydrofluoric solutions used in pickling of stainless steels and reprocessing of nuclear fuels. The alloy has a low solubility for carbon, and its microstructure normally contains carbides. The major carbide present in the alloy is M23C6, and the abundance of this phase varies with thermal exposure of the material. MC carbides are transition metal carbides formed during solidification typically from Nb, Ta and C. These carbides can greatly affect the mechanical properties of the material, frequently growing in interdendritic and grain boundary regions. Factors controlling the growth of these carbides are microsegragation levels of the carbide-forming elements, morphology of the γ matrix, local solidification time and temperature.

Another Ni-based superalloy commercial powder is Inconel 625. It exhibits a high corrosion and oxidation resistance and strength and excellent fabricability. For this reason, these alloys are typically used to manufacture engineering components or coatings for cheaper metallic substrates, which should work in extreme conditions including mechanical loads and an aggressive environment at high temperature (Singh et al. 2015). Some of these applications could be found in chemical and petrochemical plants, power generation sector, aircraft engine components, heat exchanger tubing or boilers of waste incinerators. Beyond 650 °C, hardening in Inconel 625 is found to take place by the precipitation of a metastable y"(Ni3Nb) phase, having an ordered FCC structure. This phase eventually transforms to the equilibrium δ-(Ni3Nb) orthorhombic phase. Therefore, cold spray is also attractive because it does not expose the parent or base material to high temperatures, and there is no melting of the powders, thereby avoiding the undesirable effects of oxidation and other associated reactions, such as porosity, normally associated with thermally sprayed coatings (Kaur et al. 2015; Kumar et al. 2015).

Ti and its alloys have been widely used as aircraft parts, medical implant materials and protective coatings due to their high specific strength, fatigue resistance, biocompatibility and corrosion resistance. Since Ti and its alloys are active and easy to get oxidized, the low processing temperature feature makes cold spraying an effective

process to prepare coatings with negligible oxidation from Ti and its alloys. They have the ability of forming a protective oxide layer which is the base of their corrosion resistance. This oxide layer allows to use this material in chemical equipments or prosthetic implants. Based on its phases, Ti alloys can be classified as either α-, β- or α + β alloys. Alpha alloys contain elements such as Al and Sn. These α-stabilizing elements work by either inhibiting change in the phase transformation temperature or by causing it to increase. Alpha alloys are characterized by satisfactory strength, toughness and weldability, but poorer forgeability than β alloys. The absence of a ductile-to-brittle transition, a feature of β alloys, makes α alloys suitable for cryogenic applications. Alpha-beta alloys contain transition elements which tend to decrease the temperature of the α to β phase transition and thus promote development of the BBC (body-centred cubic) β phase. They have compositions that support a mixture of α and β phases and may contain between 10% and 50% β phase at room temperature. The most common α + β alloy is Ti6Al4V. Regarding to Ti6Al4V applications, aerospace industry hoards most of the Ti-based alloy applications due to their high specific strength ratio. These applications go from structural components to jet engines.

In recent years, cold-sprayed coatings based on Ti and its alloys have been intensively investigated, and it was found that these coatings always exhibit porous microstructures and poor interparticle bonding although they are easily deposited (Marrocco et al. 2011). The porosity of the cold-sprayed coatings based on Ti and its alloys can be up to tens of percent. This makes the corrosion resistance and mechanical properties of the cold-sprayed Ti and its alloys much lower than their bulk counterpart.

17.2 Porosity in Ni Alloys

Porosity is strongly dependent on sprayed material and processing parameters. The porosity distribution for three substrates (C steel, aluminium, Inconel 625), for selected processing conditions and for two In625 powders (Cavaliere et al. 2017) with starting dimension −45 + 15 μm and −25 + 5 μm, are shown in Tables 17.1, 17.2, 17.3 and 17.4.

Very low porosity levels are experienced by those coatings sprayed with −45 + 15 μm particle dimension on C steel substrates, with the processing parameters of 800 °C, 4 MPa and 40 mm in temperature, pressure and nozzle-substrate distance. The same low pore dimensions are experienced at 20 mm in distance (Fig. 17.2a). The porosity is generally lower at 800 °C if compared with those coatings sprayed at 850 °C (Fig. 17.2b). Porosity reaches the optimal lower level at 800 °C with respect to the other temperatures, this aspect if underlined for C steel substrate (Fig. 17.3c).

A more energetic impact of the particles on the substrate leads to more plastic deformation, which is part of the coating formation process leading to metallurgical bonding as well as porosity reduction. Several studies showed that the sprayed metallic powder particles impacted on the substrate in a solid state are heavily

Table 17.1 In625 coating, cold sprayed on C steel substrate, porosity as a function of temperature, pressure and standoff distance

In625 powders – 45 + 15 μm C steel substrate			
T (°C)	P (Bar)	SOD (mm)	Porosity (%)
850	40	60	0.86 ± 0.30
850	40	40	2.06 ± 0.50
800	40	60	0.94 ± 0.30
800	40	40	0.24 ± 0.10
800	40	20	0.15 ± 0.10
800	35	40	2.40 ± 0.60
800	35	20	0.18 ± 0.04
750	40	60	5.20 ± 0.10
750	40	20	1.25 ± 0.70
750	35	40	5.10 ± 0.15
750	35	20	0.68 ± 0.18
700	40	40	0.10 ± 0.05
700	40	20	0.49 ± 0.08
700	35	40	0.73 ± 0.10
700	35	20	5.12 ± 0.35

Table 17.2 In625 coating, cold sprayed on Al substrate, porosity as a function of temperature, pressure and standoff distance

In625 powders – 45 + 15 μm Al substrate			
T (°C)	P (Bar)	SOD (mm)	Porosity (%)
850	40	60	0.80 ± 0.20
850	40	40	0.14 ± 0.04
850	40	20	0.38 ± 0.11
800	40	60	0.58 ± 0.11
800	40	40	2.50 ± 0.50
800	35	40	0.49 ± 0.12
800	35	20	0.29 ± 0.01
750	40	60	1.11 ± 0.16
750	40	40	2.70 ± 0.40
750	35	40	1.50 ± 0.50
750	35	20	2.02 ± 0.38
700	40	60	0.62 ± 0.50
700	40	40	1.65 ± 0.90
700	40	20	1.27 ± 0.21
700	35	40	2,00 ± 0.35
700	35	20	2.3 ± 0.25

Table 17.3 In625 coating, cold sprayed on In625 substrate, porosity as a function of temperature, pressure and standoff distance

Ni powders − 45 + 15 μm Inconel 625 substrate			
T (°C)	P (Bar)	SOD (mm)	Porosity (%)
850	40	60	0.95 ± 0.21
850	40	40	0.30 ± 0.09
850	40	20	0.39 ± 0.23
800	40	60	0.13 ± 0.05
800	40	40	2.20 ±0.35
800	40	20	0.10 ± 0.05
800	35	40	0.22 ± 0.07
800	35	20	1,00 ± 0.10
750	40	60	0.21 ± 0.10
750	40	40	1.10 ± 0.07
750	40	20	0.19 ± 0.01
750	35	40	0.49 ± 0.21
750	35	20	0.49 ± 0.11
700	40	60	1.30 ± 0.57
700	40	40	0.40 ± 0.10
700	40	20	0.58 ± 0.07
700	35	40	0.78 ± 0.10
700	35	20	1.60 ± 0.25

Table 17.4 In625 coating, cold sprayed on different substrates, porosity as a function of temperature, pressure and standoff distance

In625 POWDERS − 25 + 5 μm				
Substrate	T (°C)	P (Bar)	SOD (mm)	Porosity (%)
C steel	800	40	40	1.50 ± 0.20
Inconel 625	800	40	40	0.60 ± 0.10
Aluminium	800	40	40	3.80 ± 0.40

deformed in a very short period, typically less than 10 ns, and well bonded to the substrate. The ability of a cold-sprayed particle to undergo plastic deformation and adiabatic shear is a function of material properties, such as yield strength and melting point as well as process conditions, such as deposition temperature, particle velocity, substrate hardness and particle size (Wong et al. 2013). When a particle arrives at the substrate at its critical velocity, adiabatic shear takes place, which then contributes to a formation of a metallurgical bonding. As previously mentioned, the porosity of the coating is directly related to the capability of the particles to flatten during impact, assuming a pancake-like shape with high aspect ratio. Normally, the efficiency of the deposits in terms of porosity reduction is related to high particle

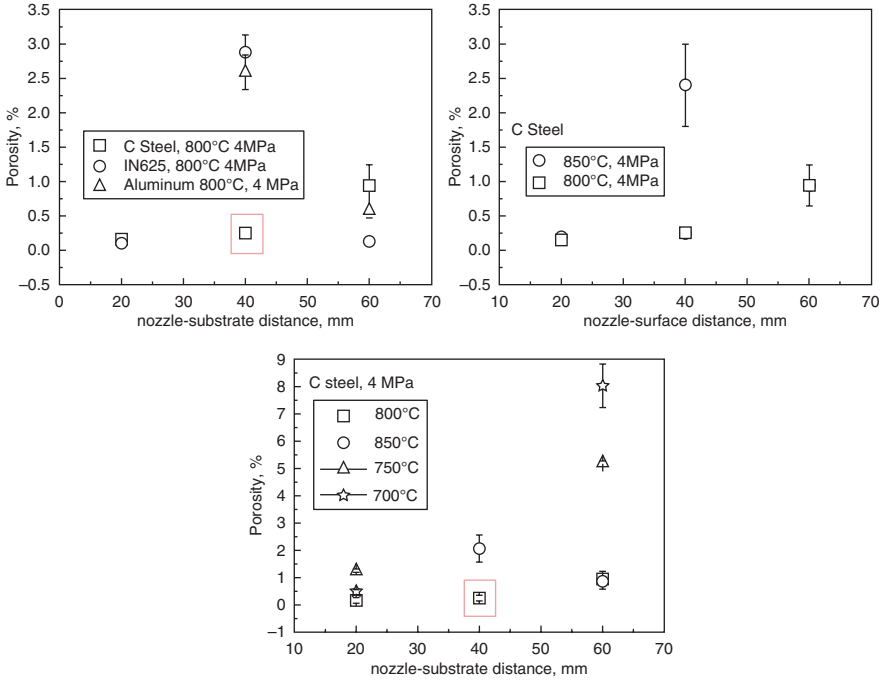

Fig. 17.2 Porosity as a function of the nozzle-substrate distance for the coatings produced at a temperature of 800 °C and a pressure of 4 MPa for C steel, Inconel 625 and aluminium substrates (**a**); porosity as a function of the nozzle-substrate distance for particles sprayed on C steel substrate at 800 and 850 °C (**b**)

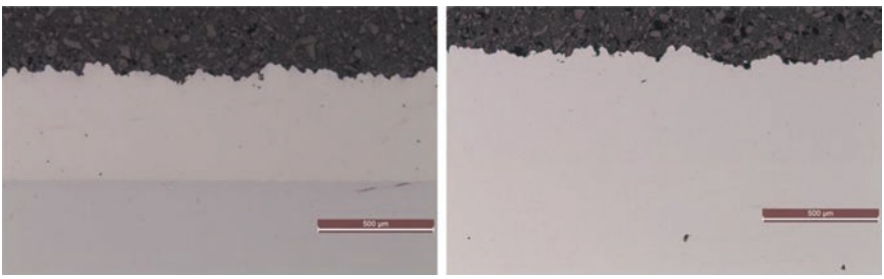

Fig. 17.3 Microstructure of coatings with −45 + 15 μm deposited on C steel (*left*) and Inconel 625 (*right*) substrates with the processing parameters of 800 °C, 4 MPa and 20 mm in temperature, pressure and nozzle-substrate distance

deformation (related to the particle speed and gas pressure). For lower particle speeds, cold-sprayed material porosity is inversely proportional to the gas temperature. In these conditions, the higher the carrying gas temperature, the lower the melting and/or softening, due to deformation that conduces to a decrease in porosity also in the case of high levels of adhesion strength. The highest particle velocities at

impact are reachable through the employment of the highest temperatures. In these conditions, particle deformation increases with an exponential dependence on gas temperature. This leads to a strong decrease in porosity of the studied coatings. In addition, due to the critical conditions of temperature, pressure and velocity, it is believed that plastic deformation feature can take place in the sprayed material (Van Steenkiste and Gorkiewicz 2004). At higher particle velocity, the gas temperature increase leads to a strong drop in the porosity levels. In addition, it is well known that particle velocity can be increased by increasing the gun to substrate distance; in this way it is also possible to improve the deposition efficiency. The spraying distance can also influence the coating porosity because of its influence on the impact velocity. At a distance of 40 and 20 mm, the pores are very few, fine and well distributed without pore concentration at the substrate-coating interface (Fig. 17.3), zone where the pores can act as crack initiation sites that strongly reduce the coating resistance under mechanical loading.

Here the coating behaviour as a function of the starting particle dimensions must be underlined. For example, in the case of Inconel 625 substrate, smaller particles (−25 + 5 μm) sprayed at 800 °C, 4 MPa and 40 mm produce coatings characterized by lower porosity. The common aspect between the different situations is the observation that, in all the cases, pores are concentrated at the coating-substrate interfaces when smaller particles are sprayed (Fig. 17.4).

The particle diameter and spray conditions are found to affect the quality of the deposited layer. In particular, small particle size can result in the formation of high-quality deposited layer, but smaller particles can induce formation of porosity or the other defects, such as in (Ogawa and Seo 2011). Here, particles with dimension less than 4.50 μm have a porosity in the range 3–5%. So that, in order to have a successful coating with low porosity, the particles should have a degree of deformability. They should undergo plastic deformation in order to result in adherent coating.

As a function of substrate material (strongly influencing the critical velocity), flattening ratio shows a linear regression as a function of in-flight velocity (Fig. 17.5). The data are also plotted as a function of the particle velocity/critical velocity ratio (Fig. 17.5b). Such an aspect is consistent with data belonging to cold spray of different materials and presented in literature (Wong et al. 2013; Assadi et al. 2011, 2016).

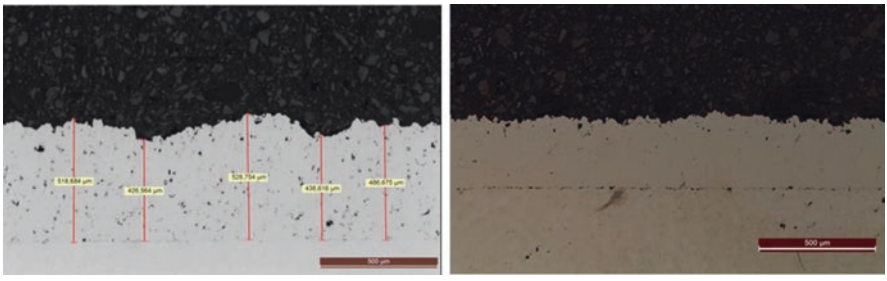

Fig. 17.4 Difference between the coatings sprayed with starting particle dimensions in the ranges −45 + 15 μm (*left*) and −25 + 5 μm (*right*)

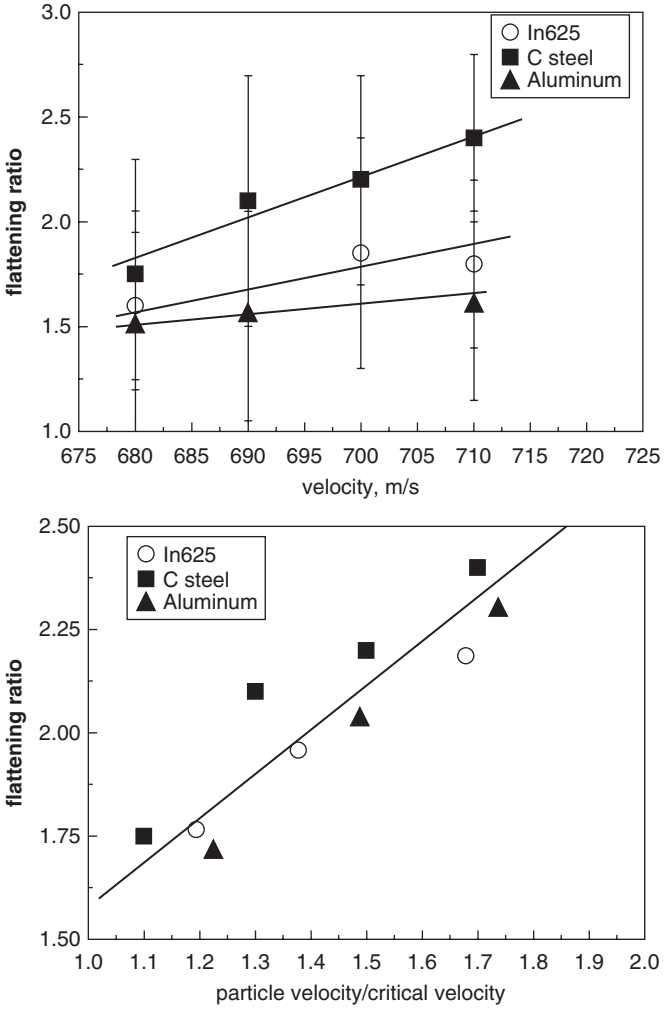

Fig. 17.5 Flattening ratio as a function of in-flight velocity, at 5 mm from the substrate, for In625 sprayed on C steel, In625 and aluminium substrates

Flattening ratio increases as increasing particle velocity (with gas temperature and pressure). It also depends on the critical velocity being related to the substrate hardness. As the substrate/particles hardness decreases, more severe conditions in terms of high pressure and high temperature are required (Gao et al. 2008; Hussain 2013). In general, the yield strength of the material affects the critical velocity necessary to induce adiabatic shear and therefore the ability of the material to deform. In addition, the effect of the substrate hardness on residual stresses is very pronounced (Cavaliere and Silvello 2014). It is clear why, in the same spray conditions, residual stresses are strongly dependent on bulk properties. In the case of softer

bulk, the deformation process strongly changes; a larger amount of deformation is transferred to the bulk with lower deformation levels and consequently lower residual stresses in the coating (Spencer et al. 2012). In the case of higher bulk hardness, a high deformation of particles is recorded leading to an increase in particle flattening. It has been also demonstrated that the surface finishing strongly influences the substrate deposit interface microstructure and consequently the microstructural and mechanical behaviour (Eason et al. 2011); depending on the difference between the hardness of the impacting particles and substrate, the processing parameters can lead to different aspects of the interface: interfacial instability and adiabatic shear instability (Grujicic et al. 2004; Grujicic et al. 2003). The conclusion is that with the same material, the processing conditions can lead to a shift between the behaviours. Also, to investigate about coating properties such as porosity and adhesion strength, a relationship between the nozzle dimensions at that point and the nozzle throat can be used. If A is the nozzle cross-sectional area and A* nozzle cross-sectional area at throat, in the case of helium as carrier gas, we can relate the Mach number of the gas at any location of the nozzle (Fig. 17.6).

A close examination of the coating produced with a nozzle area ratio of 10 reveals particles deformed to a lesser degree with voids and pores surrounding these particles than the coating produced with the larger nozzle area ratio. The reduction of voids and pores in the coating produced with the larger nozzle area ratio is then attributed to the amount of compaction. The measured increase in the particle impact velocity not only enhances the plastic deformation of the particles on impact but also intensifies the continuous compaction of the previously deposited layers of material by the incoming particles.

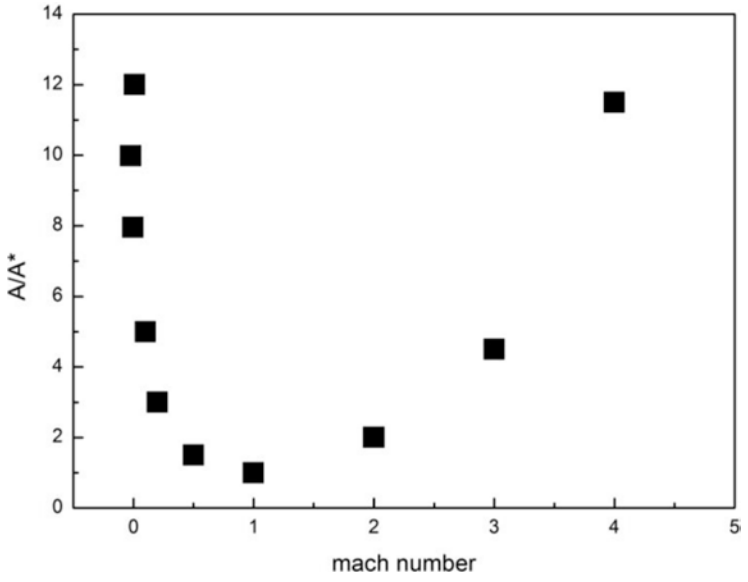

Fig. 17.6 Mach number in different locations of the nozzle

17.3 Porosity in Ti Alloys

Another important process parameter in cold spray process is velocity. As the average impact velocity approaches the critical velocity, there is a greater likelihood of particles not bonding to form a coating, and therefore coatings of increasing porosity and weaker bonding interfaces are expected to form. The cold spray process relies on the correct process variables to ensure that the impact velocity of the particle is greater than the critical velocity. Schmidt and Assadi worked to improve an equation, which predict impact dynamic effects, such as particle bonding or erosion, based on available materials data. Critical particle velocities of Ni and Ti have been experimentally measured to be approximately 630–690 m/s and 680–750 m/s, respectively. Generally, the lower the materials' particle critical velocity, the more suitable the material for deposition. An increase of particle velocities enhances the plastic deformation of the particles on impact and reduces the porosity of the coating by allowing the particles to conform to the existing shape of the coating. In cold spray, the underlayer of the coating usually shows denser microstructure than top layer. The densification of following particles deposited is termed "tamping effect". The tamping effect was firstly observed in cold-sprayed Ti-based coatings. To explain this phenomenon, we have to know that, for example, in a Ti-based coating there are two distinguishable regions: the top porous region and the inner dense region. Apparently, the porosity in the porous region decreases from the coating surface toward the inner and reaches an apparently negligible level at certain thickness. This fact demonstrates that the porosity of the coating layer is gradually reduced by accumulative deformation resulting from all particles over the layer. The following impacting particles force the deposited particles to deform gradually and to fill these voids. Such tamping effect becomes intensive with the increase of particle velocity.

But porosity isn't strongly dependent only on sprayed material and processing parameters. In the case of Inconel 718 sprayed on Inconel 718 substrate, the effects of substrate roughness, standoff distance and spray angle on the deposition behaviour were investigated. It has been found that the deposition behaviour is highly influenced by substrate surface roughness (Fig. 17.7), because single powder particle interaction with substrates of different roughness showed that plastic deformation and interfacial material mixing are higher if powder particles interact with substrates of higher roughness.

So, the results in the Fig. 17.7 showed that the combined effect of substrate preparation and standoff distance has significant effects on coating porosity. The results of the graph shown in Fig. 17.8 indicate that the spray angle and standoff distance have significant relationship with the coating porosity. Porosity values increase by a factor of 3 with decrease in spray angle from 90° to 60°.

The substrate roughness significantly affected the deformation behaviour of particles on impact at the substrate. So that, coating properties were slightly affected by standoff distance in combination with substrate roughness and spray angle.

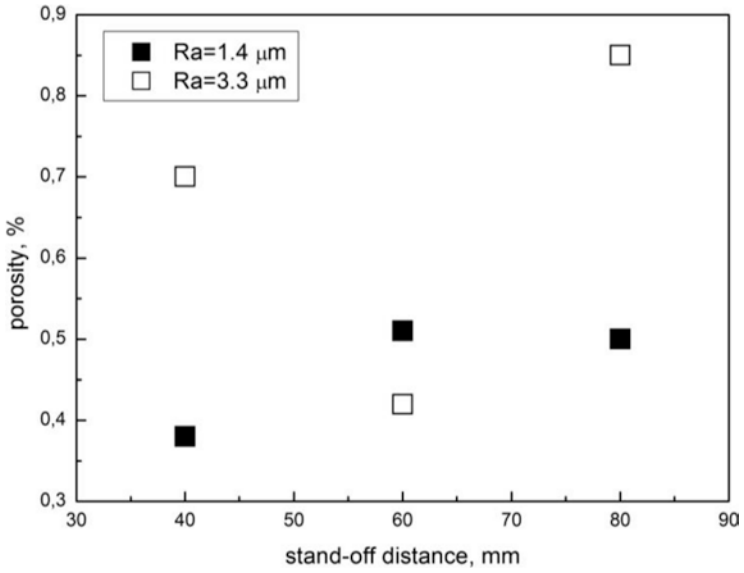

Fig. 17.7 Porosity as a function of standoff distance and surface roughness

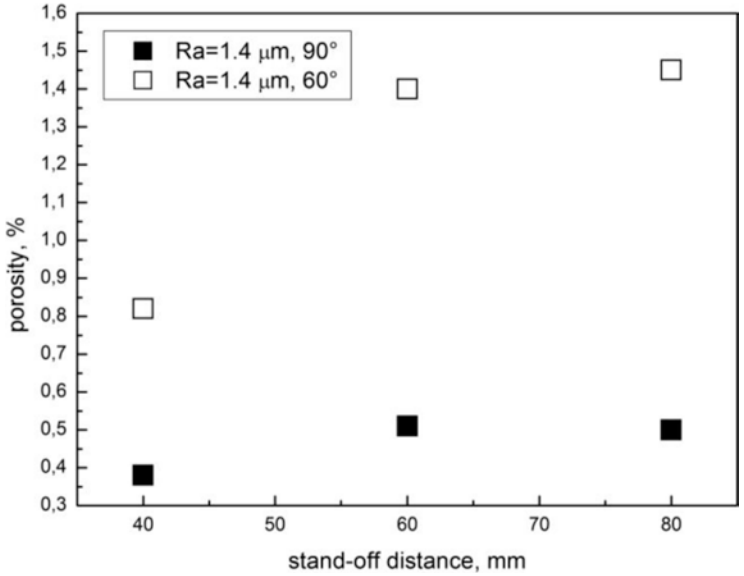

Fig. 17.8 Porosity as a function of standoff distance and spray angle

The type of gas used as the main jet has also had strong effects on the porosity of the coatings. In general, a denser coating structure has been observed when helium has been used as the accelerating gas (comparing to coatings sprayed with nitrogen) because the particle velocity has greatly increased under the same operating conditions. Evidence of this can be found in literature, which reveal the formation of larger pores opened onto surface in titanium coating cold sprayed by using nitrogen as accelerating gas. For example, in the case of Ti, the fact that the powder particles sprayed by cold spray are porous is demonstrated by microscopic investigations. The theory suggests that when such porous Ti particles impact onto the substrate surface, cushioning and crumbling of the powder may result instead of plastic. Depending on the size and distribution of pores in the particles, excess kinetic energy is required in order to compensate for this cushioning and crumbling effect. Thus, depending on the excess particle velocity over the critical velocity, impacting particles either deposit onto the surface or crumble and fall off the surface. As expected, increasing the process gas temperature or changing the gas from nitrogen to helium results in increasing particle impact velocity, which leads to a reduction in the coating porosity. So that, changing the gas from nitrogen to helium and increasing the process gas temperature result in increasing particle impact velocity, which leads to a reduction in the coating porosity. As gas inlet temperature is increased, the amount of porosity in the coating is reduced. Spraying with helium, there is a significant reduction in the porosity of the coating. It also appears that the particle-substrate boundary porosity is reduced. In each case, the qualitative amount of porosity at the particle-substrate boundary is reduced, and consequently the bond seems to have increased. This suggests that gas type and gas inlet temperature are a key factor in improving coating quality from a porosity standpoint and improving the quality of particle-substrate bond. The use of helium as working gas, in the case of Ti alloys, allows not only denser coatings than the one deposited with nitrogen but also gives rise to the higher adhesion strength and higher hardness. So that, the tribological properties showed from coatings deposited with helium as working gas have the lower wear compared to that of the one deposited with nitrogen as working gas. To resume, the improvement of porosity, adhesion strength and hardness of coatings by using helium as carrier gas to cold-sprayed Ti6Al4V on Ti6Al4V substrate allows the improvement of wear and corrosion resistance (Fig. 17.9).

Cold-sprayed substrate porosity, grain refinement and hardness were shown to play a significant role on the wear characteristics of the deposited coatings.

Several studies have been produced regarding the properties of cold-sprayed commercially pure Ti and have shown promise.

Also, in the case of pure Ti cold sprayed onto the Ti substrate (Fig. 17.10), porosity shows minimum levels for high temperature and pressure.

The processing conditions are optimal to reduce melting (Ti has a very high melting point) and to have a non-melting-mediated deformation in order to reach low levels of porosity. Particles of higher impact velocity will deform to a greater extent and therefore help to create a denser deposit with less voids and defects. A lower particle impact velocity translates into a reduction of the particle's kinetic

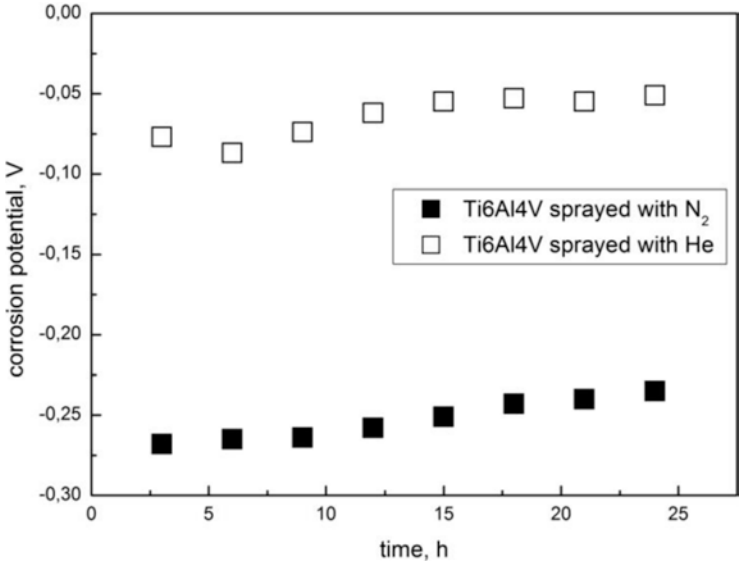

Fig. 17.9 Corrosion potential for the same material sprayed with different carrying gases

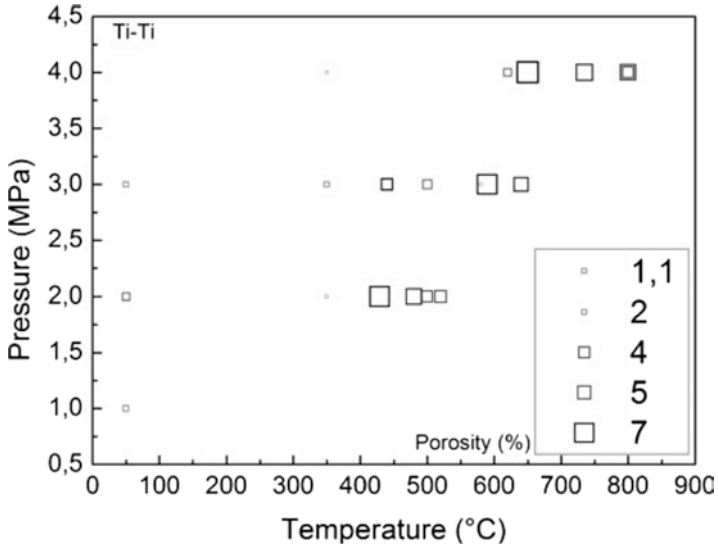

Fig. 17.10 Pure Ti coating porosity as a function of spray temperature and pressure

energy with subsequently reduced deformation and void reduction, resulting in increased porosity.

In the case of pure Ti sprayed on C steel, the minimum levels of porosity (Fig. 17.11) are reached for intermediate values of pressure and temperature, while Ti6Al4V particles sprayed on Ti6Al4V substrate show the best deposition performances in correspondence of high gas pressure and intermediate temperatures.

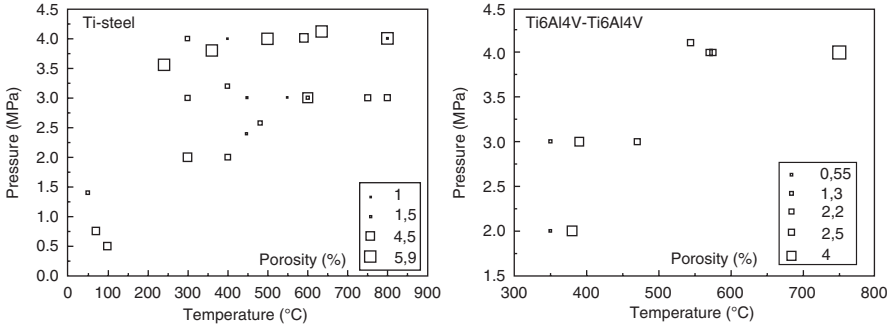

Fig. 17.11 Porosity of pure Ti sprayed on C steel and Ti6Al4V sprayed on Ti6Al4V substrate as a function of temperature and pressure

17.4 Porosity in MMCs

About the shape of particles, the harder spherical powders resulted in lower deposition efficiencies, but the resultant coatings were of higher quality with low porosity and good particle-substrate bonding. To the contrary, the softer powders attained significantly higher mass deposition efficiencies, but the coating quality was poorer, with porosity and poor interface bonding. The ideal powder particles would have a multi-angular morphology, be softer in nature and have a mixed particle size distribution. Generally coatings obtained by deposition of nanocrystalline powder have more porosity in comparison with atomized powder. In the matter of fact, it was determined that coating hardness could indeed be substantially increased via the use of nanocrystalline powder feedstock, but the use of such material also resulted in a substantially higher porosity with decreased density—a product of the increased hardness of the feedstock powder which limited the ability of the powder to deform on impact with the substrate, thus creating a bond between the powder and substrate. A possible way to increase the coating density and yet have improved properties is using a mixture of atomized and cryomilled powders. At low spraying conditions, an irregular, e.g. dendritic powder, may lead to lower porosity, while at higher spraying conditions, spherical powders result in higher strengths. Moreover, particle size and morphology together determine the quality of coatings.

In order to have a successful coating with low porosity, the particles should have a degree of deformability. They should undergo plastic deformation. Therefore, less deformable materials cannot be successfully deposited due to lack of plastic deformation. Producing cold-sprayed coatings of ductile metals mixed with brittle ceramic materials would be a very useful achievement. Particle reinforced MMCs enable physical and mechanical properties to be tailored. Furthermore, hard particles can activate the sprayed surface by removing oxide layers, contamination and impurities. Moreover hard particles create microasperities that favour the bonding of the incoming particles and increase the contact area between the coating and the substrate. So that, in the case of MMC, a beneficial effect due to the increase of

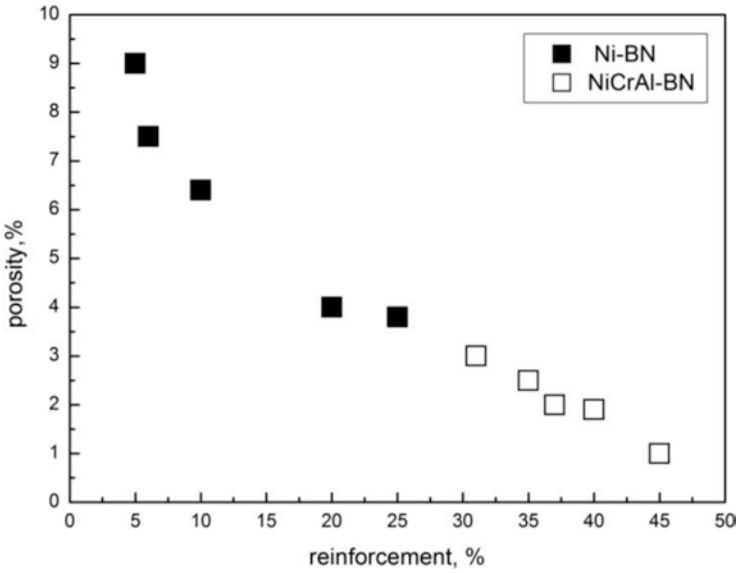

Fig. 17.12 Porosity in MMCs as a function of the reinforcement percentage

reinforcement is observed for the porosity levels. Porosity decreases by increasing reinforcing particles in all the studied conditions (Fig. 17.12) In general, it can be affirmed that, the increase in reinforcement percent increases local plastic deformation (at the same velocity) leading to a decrease in porosity levels.

Particle size and percent in the matrix affect the adiabatic shear instability governing recrystallization. The higher presence of reinforcing particles and smaller dimensions result in a much strain-hardened material due to higher strain rates reached during impact. In cold spray composites, it is believed that porosity is dependent on the capacity of the metallic phase to fill up the gaps with the reinforcing particles (Cavaliere et al. 2014; Cavaliere and Silvello 2015). If the material ductility or the employed processing parameters are not optimized enough, many small pores can be observed in the coatings. A beneficial effect due to the increase of reinforcement is observed for the porosity levels. Porosity decreases by increasing reinforcing particles. Porosity is strongly dependent on sprayed material and processing parameters; during impact particles flatten and assume a pancake-like structure characterized by high flattening ratios. If the plastic deformation is insufficient, particles retain their original spherical shape leading to higher porosity levels in the coatings. In general, it can be affirmed that the increase in reinforcement percent increases local plastic deformation (at the same velocity) leading to a decrease in porosity levels. The results suggest that adding hard particles into initial feedstock can reduce the porosity in the coating. The use of a ceramic metal mixture can enhance the coating quality by reducing porosity of the coating, peening of preexisting layers, removing poorly bonded particles and increasing bond strength of the coating to the substrate. In case of relatively hard matrices, the reinforcement

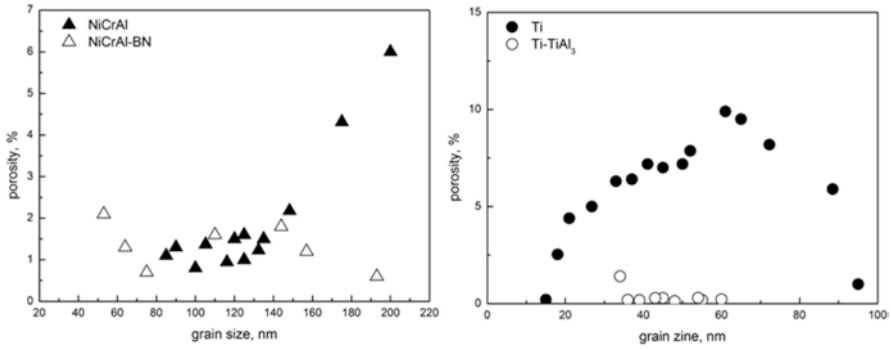

Fig. 17.13 Porosity vs. grain size for Ni-based and Ti-based materials

particles can enhance the plastic deformation and increase the cohesion strength by reducing the porosity. Most often considerable attention was given to increasing the amount of hard particles in the final coating unaware of its possible drawbacks. Optimization principles are crucial consideration for each specific application. Cold-sprayed substrate porosity, with grain refinement and hardness, was shown to play a significant role on the wear characteristics and corrosion resistance of the deposited coatings. Thus, improvements in the coating performance could be achieved by using post-deposition heat treatments, to reduce interconnected porosity. In this sense, laser could be used to perform a local thermal treatment on the top of the coating, reducing surface roughness and sealing open porosity. For example, the reduced porosity and oxide content in cold-sprayed layers should improve the corrosion and oxidation resistance of Ni-based and Ti-based coatings processed by this method. Interconnected porosity could provide a path for aggressive species to attack the substrate. In addition, heterogeneities, like pores, will facilitate corrosion processes. So that, heat treatments homogenize the microstructure removing splat structure and reducing interconnected porosity, which promote an increased oxidation and corrosion resistance. The heat treatments were found to decrease porosity and enhance the bonding between the particles, leading to higher cohesive strength of the deposited materials.

Here it can be demonstrated how ceramic particles addition leads to strong grain refinement thanks to the more severe plastic deformation acting on the matrix during spray. This aspect leads also to a reduction in porosity with further increase in the material strength (Fig. 17.13).

17.5 Conclusion

In the present work, a large number of experimental results for porosity of cold-sprayed Ni-based and Ti-based deposits, obtained in a broad range of processing parameters on metal substrates, are described. The effect of particle size, gas

pressure, temperature and type, particle velocity, substrate hardness, standoff distance and spray angle on coating's porosity were underlined. Such analyses were performed for different particle materials (Ni and Ni alloys, Ti and Ti alloys and MMC) deposited on different substrates. The study allowed us to obtain a very broad experimental space capable of including almost all the possible processing conditions for the actual cold spray technology. To resume, in the case of pure Ni sprayed onto IN718, from 700 °C and 3.5 MPa to 800 °C and 4 MPa for the carrying gas temperature and pressure, an improvement of the coating properties such as of porosity was recorded. The same dense Ni coatings were obtained by using relatively low gas temperature of 400 °C and 450 °C with N_2 as the processing gas. As the gas temperature rose up from 350 °C to 400 °C and 450 °C, the coating porosity decreased from 4.4% to 0.6% and 0.4%, respectively. Furthermore, in the case of a comparison between nano- and micro-Ni-20Cr powders cold sprayed onto a mild steel, the results have shown that the nanostructured coatings have a significantly higher microhardness in comparison with micro-sized, which may be attributed to lower porosity of feedstock powders, due to mechanical milling. Moreover the different porosity levels in the nanoconstructed coatings prevented the increase of elastic modulus and thermal diffusivity over the time when the coatings are subjected to elevated temperatures. For Ni-based superalloys powders sprayed on C steel, the optimal combination of low porosity and high flattening ratio was demonstrated for those coatings sprayed at a temperature of 800 °C, 4 MPa in gas pressure and a standoff distance of 40 mm. The coatings with larger starting particle dimensions showed lower porosity levels with respect to the finer particles. Furthermore, with appropriate heat treatment, porosity can be reduced. This pore reduction can be attributed to the additional metallurgical bonding that could have occurred at high temperatures as a result of sintering effect. For Ni composite powders, such as Ni-BN, a beneficial effect on the porosity was observed with increasing reinforcement percentage, whereas the porosity was lower in unreinforced Ti with respect to the corresponding composite Ti-TiAl3. Hardness differences between the two powders are considered to be the most important influencer on porosity. Adding powders with a difference in hardness can certainly lead to different plastic deformation characteristics. So that, the results showed how relatively small additions of another metallic powder can significantly influence porosity. The higher porosity has a much inferior set of mechanical properties that supports the general acceptance that porosity is detrimental. Hence, in the case of MMC, it was demonstrated that the mechanical properties are dependent from the recrystallization effect of the ceramics phases. Also, the influence of He and N_2 gases on the properties of pure Ti and Ti6Al4V coatings was investigated. In the case of pure Ti, it was concluded that porosity was mostly a function of surface temperature and/or impacting particle temperature. If a much higher inlet gas temperature was used, coatings produced with N_2 were denser than those produced with He. This was due to a greater amount of consolidated region between the particle and to the material jetting as a result of higher surface temperature. The Ti6Al4V coatings deposited with He as working gas had the denser microstructure with a relatively lower porosity level than the one deposited with N_2 working gas because the use of He working gas during the cold

spraying resulted in the more severe deformation of sprayed Ti6Al4V particles. Furthermore, in the case of Ti-based composites, it appears to be a greater amount of porosity at the coating top surface than that found close to the coating-substrate interface. This is due to the way in which cold spray coatings are deposited. Particles that create the initial layers of the coating will be impacted by further impinging particles which would lead to compaction of particles that are already deposited. For particles that are deposited close to the top of the coating surface, there are fewer impinging particles that would lead to compaction of this section of the coating and therefore a more porous structure is expected. During cold spraying, deposited particles near the top surface are inevitably impacted and deformed by the following particles. This leads to a so-called tamping densification effect. Such effect is beneficial to heal up the formed voids and enhance the interparticle bonding. It is noted that both rebounded and deposited particles contribute to the tamping effect. Therefore, increasing the tamping effect of the rebounded particles, e.g. depositing coatings at relatively low particle velocity or blending shot-peening particles into the spray powders, is a potential approach to deposit dense coatings. Also, fully dense Ti parts can be fabricated using cold spray as an additive manufacturing process. This can be accomplished using low-pressure and low-temperature N_2 as the process gas. The key to this result can be attributed to the shaped powder morphology that allows the easy densification and deposition and to a short heat treatment. To finish, porosity reduction is achievable with optimal processing parameters that can be easily obtained by employing high-pressure cold spray equipments.

References

Assadi H, Kreye H, Gartner F, Klassen T (2016) Cold spraying a materials perspective. Acta Mater 116:382–407

Assadi H, Schmidt T, Richter H, Kliemann JO, Binder K, Gärtner F, Klassen T, Kreye H (2011) On parameter selection in cold spraying. J Therm Spray Technol 20(6):1161–1176

Cavaliere P, Perrone A, Silvello A (2014) Mechanical and microstructural behavior of nanocomposites produced via cold spray. Composites B67:326–331

Cavaliere P, Silvello A (2014) Processing parameters affecting cold spay coatings performances. Int J Adv Manuf Technol 71:263–277

Cavaliere P, Silvello A (2015) Mechanical and microstructural behavior of cold-sprayed titanium- and nickel-based coatings. J Therm Spray Technol 24(8):1506–1512

Cavaliere P, Silvello A (2016) Fatigue behavior of cold sprayed metals and alloys: a critical review. Surf Eng 32(9):631–640

Cavaliere P, Silvello A, Cinca N, Canales H, Dosta S, Garcia Cano I, Guilemany JM (2017) Microstructural and fatigue behavior of cold sprayed Ni-based superalloys coatings. Surf Coat Technol doi: https://doi.org/10.1016/j.surfcoat.2017.06.006

Champagne V, Helfritch D (2016) The unique abilities of cold spray deposition. Int Mater Rev 61(7):437–455

Eason PD, Fewkes JA, Kennett SC, Eden TJ, Tello K, Kaufman MJ, Tiryakioglu M (2011) On the characterization of bulk copper produced by cold gas dynamic spray processing in as fabricated and annealed conditions. Mater Sci Eng A528:8174–8178

Feng SQ, Ma B, Wang X-L, Ling G-P (2013) Effects of gas property on quality of NiCoCrAlY coating by cold gas dynamic spraying. Adv Mater Res 815:682–686

Gao P-H, Li C-J, Yang G-J, Li Y-G, Li C-X (2008) Influence of substrate hardness on deposition behavior of single porous WC-12Co particle in cold spraying. Surf Coat Technol 203:384–390

Grujicic M, Saylor JR, Beasley DE, DeRosset WS, Helfritch D (2003) Computational analysis of the interfacial bonding between feed powder particles and the substrate in the cold-gas dynamic spray process. Appl Surf Sci 219:211–327

Grujicic M, Zhao CL, DeRosset WS, Helfritch D (2004) Adiabatic shear instability based mechanism for particle/substrate bonding in the cold-gas dynamic-spray process. Mater Des 25:681–688

Hussain T (2013) Cold spraying of titanium: a review of bonding mechanisms, microstructure and properties. Key Eng Mater 533:53–90

Kalsi SBS, Sidhu TS, Karthikeyan J (2015) Evaluation of NiCoCrAlY coatings deposited on superalloy with novel cold spray process. Surf Eng 31(11):840–845

Kaur N, Kumar M, Sharma SK, Kim DY, Kumar S, Chavan NM, Joshi SV, Singh N (2015) Study of mechanical properties and high temperature oxidation behavior of a novel cold-spray Ni-20Cr coating on boiler steels. Appl Surf Sci 328(15):13–25

Kumar M, Singh H, Singh N, Hong S-M, Choi I-S, Suh J-Y, Chavan NM, Kumar S, Joshi SV (2015) Development of nano-crystalline cold sprayed 20Ni-Cr coatings for high temperature oxidation resistance. Surf Coat Technol 266:122–133

Marrocco T, Hussain T, McCartney DG, Shipway PH (2011) Corrosion performance of laser post-treated cold sprayed titanium coatings. J Therm Spray Technol 20(4):909–917

Rathod WS, Khanna AS, Karthikeyan J, Rathod RC (2014) Effect of N2 and he carrier gases on oxidation behavior of cold sprayed CoNiCrAlY powder to deposit bond coats. T Indian I Metals 67(2):247–262

Moridi A, Hassani-Gangaraj SM, Guagliano M, Dao M (2014) Cold spray coating: review of material systems and future perspectives. Surf Eng 36(6):369–395

Ogawa K, Seo D (2011) In: Benini E (ed) Repair of turbine blades using cold spray technique, Advances in gas turbine technology, ISBN: 978–953–307-611-9, InTech, Available from: http://www.intechopen.com/books/advances-in-gas-turbine-technology/repair-of-turbine-blades-using-coldspray-technique

Singh H, Sidhu TS, Kalsi SS (2015) Microstructure study of cold sprayed 50%Ni-50%Cr coating on Inconel-601. Surf Eng 31(11):825–831

Singh H, Sidhu TS, Kalsi SBS, Karthikeyan J (2016) Evolution of the microstructure by high velocity impacts of particles by cold spray. Surf Coat Technol 31(11):1514–1520

Singh H, Khosla H, Walia GS, Sidhu TS Kalsi SBS, Karthikeyan J (2017) Characteristic study of cold sprayed N06601 superalloy surface. Surf Eng doi: https://doi.org/10.1080/02670844.2017.1312220

Spencer K, Luzin V, Matthews N, Zhang MX (2012) Residual stresses in cold spray Al coatings: the effect of alloying and of process parameters. Surf Coat Technol 206:4249–4255

Sundararajan G, Chavan NM, Kumar S (2013) The elastic modulus of cold spray coatings: influence of inter-splat boundary cracking. J Therm Spray Technol 22(8):1348–1357

Van Steenkiste T, Gorkiewicz DW (2004) Analysis of tantalum coatings produced by the kinetic spray process. J Therm Spray Technol 13:265–273

Wong W, Irissou E, Ryabinin AN, Legoux JG, Yue S (2011) Influence of helium and nitrogen gases on the properties of cold gas dynamic sprayed pure titanium coatings. J Therm Spray Technol 20(1–2):213–226

Wong W, Vo P, Irissou E, Ryabinin AN, Legoux J-G, Yue S (2013) Effect of particle morphology and size distribution on cold-sprayed pure titanium coatings. J Therm Spray Technol 22(7):1140–1153

Yin S, Suo X, Su J, Guo Z, Liao H, Wang X (2014) Effects of substrate hardness and spray angle on the deposition behavior of cold-sprayed ti particles. J Therm Spray Technol 23(1–2):76–83

Chapter 18
Fatigue Properties and Crack Behavior of Cold Spray Coatings

Pasquale Cavaliere and Alessio Silvello

18.1 Introduction

Thin coatings are designed and produced to provide substrate properties improvements in wear, hardness, and corrosion resistance. These coatings can have a positive behavior on fatigue properties, crack initiation and growth, and stress corrosion cracking. The optimal design of coatings requires a suitable characterization of fatigue properties. Those coatings performed for component repairing require crack behavior characterization in order to evaluate the repairing efficiency of the chosen technology. Obviously the fatigue resistance strongly depends on the coating performances in terms of mechanical strength, adhesion strength, residual stresses, and coating defects such as porosity. This aspect becomes crucial for coatings that are mechanically bonded to the substrates where the final properties depend on the particle deformation modes in the solid state. The structural features of the coating are therefore highly dependent on the spray processes and parameters involved during spraying. The improvement of fatigue performances is achieved by decreasing the surface cyclic tensile stress and/or by increasing the surface strength, thereby increasing the resistance to fatigue crack nucleation. To achieve these goals, surface modification processes, which offer simultaneously increase in the surface strength and introduce residual compressive stresses to decrease the surface cyclic tensile stress are needed. To realize the maximum improvement in fatigue performance, surface modifications must be carefully controlled and matched with the particular alloy of interest to ensure that undesirable features (e.g., micro-cracks, incorrect microstructure, etc.) are not introduced during manufacture. In addition, many fatigue failures occur when particular conditions of stress or strain concentrations

P. Cavaliere (✉) • A. Silvello
Department of Innovation Engineering, University of Salento,
Via per Arnesano, 73100 Lecce, Italy
e-mail: pasquale.cavaliere@unisalento.it; alessio.silvello@unisalento.it

P. Cavaliere (ed.), *Cold-Spray Coatings*,
https://doi.org/10.1007/978-3-319-67183-3_18

are neglected. So geometrical stress-strain concentrations at the surface must be fully characterized and taken into account during the design of coated or repaired components. Thus, it is fundamental to focus fatigue properties conditioning that is finalized to restore fatigue resistance once damages have occurred.

Continuous research has been focused on the coating effects on the fatigue behavior of aerospace materials and superalloys. Fatigue life reduction is attributed to the early crack initiation at the coating-substrate interface as a consequence of nonoptimal adhesion due to incorrect process parameters (Ray et al. 2007; Bernstein et al. 1993; Cavaliere and Silvello 2015, 2016, 2017a, b doi: https://doi.org/10.1080/02670844.2017.1287555). In addition, high porosity, tiny cracks, and higher level of surface roughness due to undeformed cold-sprayed particles can have a detrimental effect on fatigue properties. Anyway, many issues should be addressed such as crack initiation and growth due to delamination, as well as crack arrest effects in interaction with load and component and the evolution from microscopic cracks to macroscopic cracks (Bartsch et al. 2008). Obviously such aspects can be correctly analyzed by bending fatigue tests (de Camargo et al. 2007; Freddi et al. 1997; McGrann et al. 1998). To reach the maximum resistance to fatigue crack initiation, the coating should possess superficial hardness to suppress persistent slip bands (PSB) on the surface, interface toughness to suppress cracking and delamination when PSB intersect the interfacial zones, high compressive residual stresses to prevent slip localization, and high adhesion to preserve the mechanical integrity of the substrate-coating system.

For the deeper understanding of the experimental fatigue data, the processes taking place both in substrate and coating during fatigue must be described. The detailed characterization of the fatigue and fracture behavior of coatings and small-scale structures is of paramount importance for the understanding of their in-service duration. These rather complex processes include material property changes, crack initiation, and crack growth. In bulk materials, some of these processes may be observed directly during the fatigue test. Optical crack observation methods, fatigue fuses, brittle paints, or penetration test can be used to detect fatigue crack initiation and describe its growth. Sample stiffness or stress-strain response can be evaluated to assess material property changes. Fatigue degradation of material can be monitored by potential drop methods or magnetic methods, by eddy currents, etc. The aim of the present study is to show the optimal processing parameters in terms of temperature, pressure, nozzle-substrate distance, and starting particle dimensions leading to high density and sound strength of cold spray coatings. The optimized conditions are employed to produce coatings in order to evaluate the crack initiation and growth behavior during fatigue loading and to understand the deformation modes during cyclic loading. This is aimed to improve the on crack propagation in cold-sprayed coatings being a subject very poorly covered by the scientific literature. The precise understanding of crack behavior allows, in fact, to accurately model the mechanical limits and the coating lifetime.

18.2 Experimental

Different cold spray deposits were prepared by employing a commercial cold spray system employing a tungsten carbide de Laval nozzle. The apparatus is equipped with electric gas heater (maximum nominal power of 34 KW) capable of producing and heating up to a nominal temperature of 800 °C. The temperature is varied through the power supply voltage. The powder feeder consists of pressurized vessels where powders are positioned prior to spray. The employed tungsten carbide nozzle, with rectangular cross section, had 2 × 4 mm throat and 2 × 10 mm exit dimensions. All the substrates were grit blasted before spray. The different particle mixtures employed to prepare aluminum-based cold-sprayed coatings for fatigue tests were AA7075 sprayed on AA7075 substrate, AA2024 sprayed on AA7075 substrate, and AA2024 sprayed on AZ91 magnesium alloy substrate. For the crack initiation and growth tests, 30° notched (of 100 μm height is at the center) panels, of 2099 aluminum alloy, measuring 2 mm thick, and 20*20 mm2 area were coated with 7075 and 2198 aluminum alloy particles via cold spray always employing different processing parameters in terms of carrying gas temperature and pressure. In addition, the same panels with 30°, 60°, and 90° notches were cold sprayed with pure Ni and IN625 Ni-based alloy particles. All the substrate and coating materials with the corresponded processing parameters employed during spray are shown in Table 18.1.

The cold spray parameters in the present study were gas temperature and pressure and nozzle-substrate distance; by tuning these parameters, it is possible to vary the particle impact velocity and consequently the mechanical and microstructural behavior of the coatings. A 2-D model of the cold spray nozzle was employed to

Table 18.1 Spray materials, substrates, and processing conditions employed in the present chapter

Particles	Surface	Substrate	Gas temperature (°C)	Pressure (MPa)	Test
AA2024	Flat	AA7075	250–500	1–2.5	Bending fatigue
AA7075	Flat	AA7075	250–500	1–2.5	Bending fatigue
AA2024	Flat	AZ91	250–500	1–2.5	Bending fatigue
AA7075	30° notch	AA2099	450	2.5	Crack propagation
AA2198	30° notch	AA2099	450	2.5	Crack propagation
AA2198	30° notch	AA2099	350	1.5	Crack propagation
Ni	30°, 60°, 90° notch	IN718	700–800	3.5–4	Crack propagation
IN625	30°, 60°, 90° notch	Carbon steel	800	4	Crack propagation
IN625	30°, 60°, 90° notch	IN718	625	4	Crack propagation

analyze the flow field of Ni particles produced by the carrying gas flowing at very high velocities. ANSYS FLUENT commercial software was employed for the simulations. A standard k-ε model was used to take into consideration the turbulence due to the high velocity. The particle velocities and impact temperatures were modeled over the nominal carrying gas temperatures and pressures. The nozzle model was defined fixing that particle-gas flow, temperature, and pressure gradient are zero along the contour. The employed mesh was created automatically using the "quadrilaterals" instrument of the ANSYS software. The coupled implicit density-based solver along with the least square cell-based gradient method was used to simulate the flow field inside the nozzle. The flow, turbulent kinetic energy, and turbulent dissipation rate were modeled using second-order upwind accuracy. The system program solves the Navier-Stokes equations. SST RANS model in ANSYS allows for a more accurate near wall treatment with an automatic switch from a wall function to a low-Reynolds number formulation based on the grid spacing. Therefore, the turbulent model can account with the presence of a wall. The calculations were performed in different conditions of the helium carrier gas temperature and pressure in order to evaluate their effect on the in-flight and on the impact velocities. The data are employed to understand the true conditions of particle impact in order to analyze their effect on the material deformation and on the consequent microstructural and mechanical behavior of the coatings.

The microhardness and the adhesion strength were measured by employing Nano Test MICRO MATERIALTM platform, and for each condition, 19 hardness measurements were taken, and 25 measurements were done for the adhesion strength by automatically setting up the instrument. For the hardness measurements, a Berkovich diamond indenter was employed, the maximum load was fixed at 20 mN with a hold time of 1 s. Adhesion strength was measured employing a spherical indenter. Samples from the notched cold-sprayed panels were cut (By employing a FIB Hitachi, FB-2000A equipment) parallel to the coating-substrate interface in order to perform the adhesion strength measurements. From cold spray coating characterization, it was measured the shear bond strength as a function of the distance from the crack tip.

The coatings' residual stresses were measured through X-ray diffraction by using a Rigaku Ultima + diffractometer; the measurements were done through the employment of the well-known Scherrer equation relating the peaks broadening to the crystallite sizes and through house made software. For selected deposits, transmission electron microscopy observations were performed by employing a JEOL 2011FX TEM to evaluate the grain size and structures. The TEM disks were cut in the direction perpendicular to the spray one. The samples were taken in order to make the interface observation possible. Slices of 300 μm thickness were cut, then they were mechanically polished and then jet polished in methanol +30% HNO3 solution in dry ice at −70°, finally the specimens were polished by ion milling in liquid nitrogen for 1 h.

The porosity was calculated through a statistical analysis performed on Zeiss EVO40 SEM observations, and for each sample, five different images of

$200 \times 200\ \mu m^2$ were analyzed. The porosity data belong to the cross section parallel to the spraying one.

Fatigue tests were performed in bending following the ASTM B-593 standard with load ratio $R = -1$.

Using the ANSYS finite element code, a 3-D finite element model was generated, consisting of isoparametric brick elements. The numerical simulations were carried out using appropriate contact elements of ANSYS to model the interfaces behavior. Cohesive zone models have been thoroughly used for the analysis of structural fracture in the last few years, and they are highly relevant in problems for which the key physical processes involved in the fracture event take place over a very narrow region. The cohesive zone model consists of a constitutive relation between the traction acting on the interface and the corresponding interface separation which represents the displacement jump across the interface. The constitutive relationship between the cohesive stress and the shear separation is experimentally evaluated. The interface surfaces of the materials can be represented by a special set of interface elements or contact elements, and a Cohesive Zone Model (CZM) can be used to characterize the constitutive behavior of the interface. In CZM, fracture is treated as a gradual phenomenon in which separation resisted by cohesive traction takes place across a cohesive zone. The extension of this cohesive zone ahead of the crack tip is modeled using traction-separation law (also known as cohesive law) which relates the cohesive stress to the separation in the process zone. The interface surfaces of the materials can be represented by a special set of interface elements or contact elements, and a CZM model can be used to characterize the constitutive behavior of the interface. Three-dimensional elements CONTA174 and TARGE170 were used to simulate interface separation. They possess the capacity to model the separation of a bonded contact by using the TB command with the CZM (cohesive zone model) label. The bilinear cohesive zone model is available in ANSYS. There are two ways to specify the interface parameters: bilinear interface behavior with tractions and separation distances (TB, CZM command with TBOPT = CBDD) or bilinear material behavior with tractions and critical fracture energies (TB, CZM command with TBOPT = CBDE). Three-phased unit cells with hexagonal symmetry were employed.

Hence, experimental methods are important that permit an assessment of the microstructural crack growth mechanisms and the characterization of the fracture resistance for the entire crack development especially in the case of limited thickness in those cases where focus on long crack propagation is needed. Crack growth tests were performed by employing an Instron 8801 servo hydraulic machine. The specimens were tested in bending with the load direction perpendicular to the coating surface. The tests were performed at room temperature using a sinusoidal waveform at a loading frequency of 20 Hz under constant amplitude loading with load ratio R = 0.1. Crack growth was monitored using a direct current potential drop method.

18.3 Coating Behavior

18.3.1 Coating Process and Microstructure

In cold spray coatings, the in-flight velocity is proportional to the gas temperature and pressure variations (Fig. 18.1), and it increases with the increase of temperature and pressure with a parabolic dependence on the employed processing parameters (Fig. 18.2).

Obviously the dependence is strongly related to the particle dimensions and to the different gas type. For He gas, higher impact velocities growing with a sharper increase are experienced also for smaller particles. Impact velocity strongly influences particles flattening. The higher the impact velocity is the larger is the particle flattening at the impact. This coating material behavior improves coating properties such strength and porosity reduction. The flattening ratio as a function of the ratio impact velocity/critical velocity is shown in Fig. 18.3.

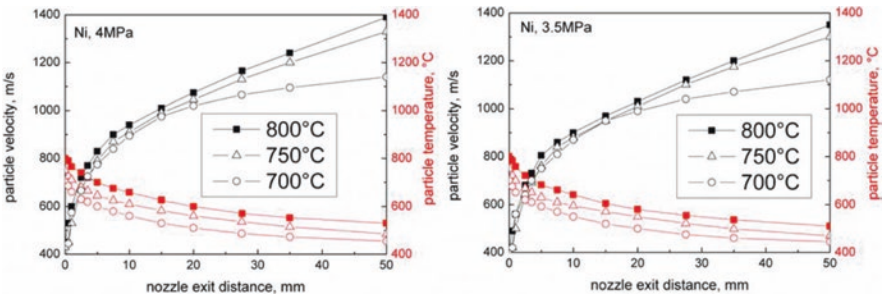

Fig. 18.1 Velocity and temperature profile, along the spray path, as a function of the nozzle exit distance for pure Ni cold sprayed in the range 700–800 °C at 4 and 3.5 MPa, particle dimensions 22,25 μm (Cavaliere et al. 2016)

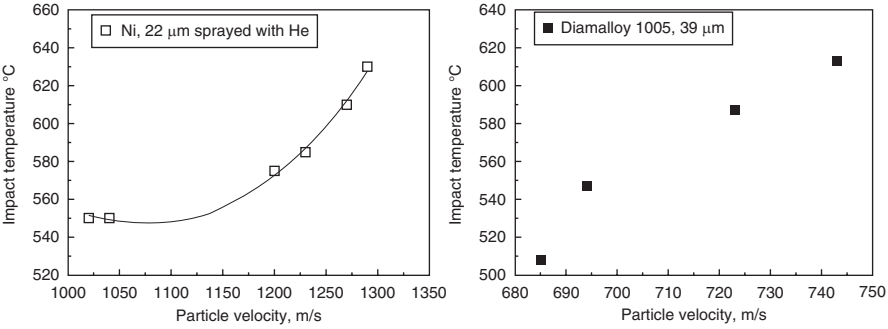

Fig. 18.2 Particle velocity vs. impact temperature for different Ni-based materials, with various dimensions and process conditions

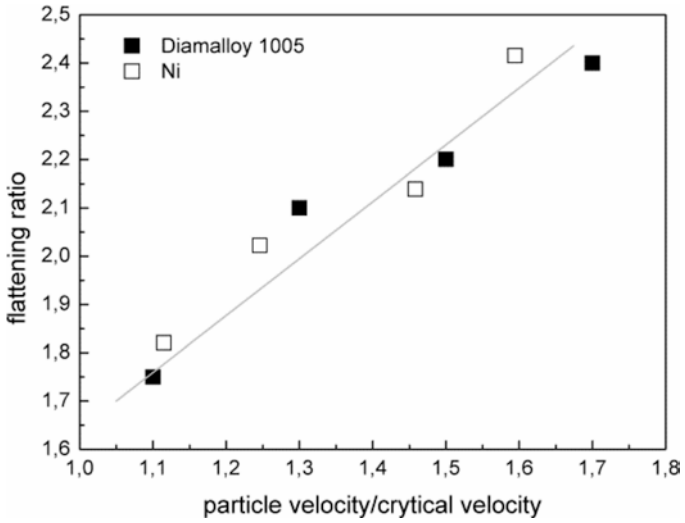

Fig. 18.3 Flattening ratio as a function of particles velocity

Flattening ratio increases as increasing particle velocity (with gas temperature and pressure). It also depends on the critical velocity being related to the substrate hardness. As the substrate/particles hardness decreases, more severe conditions in terms of high pressure and high temperature are required (Hussain 2013; Cetin et al. 2016). In general, the yield strength of the material affects the critical velocity necessary to induce adiabatic shear and therefore the ability of the material to deform. In addition, the effect of the substrate hardness on residual stresses is very pronounced (Cavaliere and Silvello 2016). It is clear why, in the same spray conditions, residual stresses are strongly dependent on bulk properties. In the case of softer bulk, the deformation process strongly changes; a larger amount of deformation is transferred to the bulk with lower deformation levels and consequently lower residual stresses in the coating (Spencer et al. 2012). In the case of higher bulk hardness, a high deformation of particles is recorded leading to an increase in particles flattening. It has been also demonstrated that the surface finishing strongly influences the substrate deposit interface microstructure and consequently the microstructural and mechanical behavior (Eason et al. 2011); depending on the difference between the hardness of the impacting particles and substrate, the processing parameters can lead to different aspects of the interface: interfacial instability and adiabatic shear instability (Grujicic et al. 2003, 2004). The conclusion is that with the same material, the processing conditions can lead to a shift between the behaviors. The main strengthening mechanisms in cold spray coatings are work hardening, dispersion strengthening, and crystal refinement. Now, for a fixed impact velocity, the stress-strain behavior at the substrate contact is scaled in time and space depending on the system size (particle dimension). From this point of view, the factor governing the particle deformation is the energy density governing the strain hardening being

lower for smaller particles. In Assadi et al. (2016), a very interesting table describing the limit of good spray ability for many types of materials is described. The limit for cold-sprayed Ni particles at a temperature of 800 °C and 4 MPa in temperature and pressure, respectively, is indicated as 1.35 (for 30 μm mean particle dimension) and as 1.25 (for 50 μm mean particle dimension), where these values are the rates between the impact and the critical velocities. For these dimensional ranges, major particle dimensions lead to an increase in spray ability; obviously the different gas (He or N_2) strongly influences the particles behavior. This is very consistent with the data reported in the present study referring to Fig. 18.6b. The data are also consistent with those belonging to previous studies (Cavaliere et al. 2016). The same behavior is also confirmed by studies performed on the cold spray of pure Ti particles of different starting dimensions comparable with those of the present paper (Wong et al. 2013).

The higher the impact velocity is the larger is the particle flattening at the impact. This coating material behavior improves coating properties such strength and porosity reduction. Porosity linearly decreases as increasing impact speed and impact temperature. Highest particle velocities are reached by setting the highest carrying gas temperatures, even if impact velocity is higher for He gas (e.g., Fig. 18.4). These conditions produces local melting during the particle deformation, such a behavior is directly related to the increase of temperature. This also corresponds to a strong decrease in the coatings porosity. The higher the impact energy, the higher results the particle plastic deformation leading to substrate-particle metallurgical bonding and porosity reduction (Cavaliere and Silvello 2014).

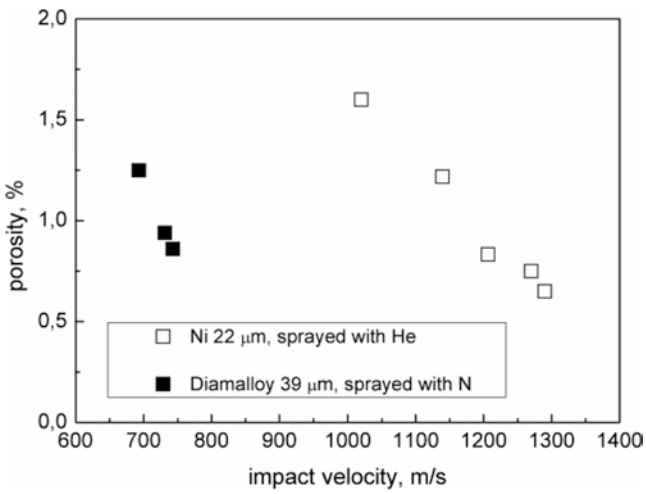

Fig. 18.4 Porosity as a function of process parameters for Ni-based particles

18.3.2 Mechanical Properties

It is believed that the fatigue resistance is strongly increased as the adhesion strength of the coating to the panel is increased; the more the cold-sprayed material adheres to the bulk the more the onset of crack initiation and growth is delayed. The adhesive disbond over the crack region can significantly reduce the stress transfer between the repaired plate and the coating producing a strong drop in repair efficiency. The residual stresses at the interfaces strongly affect the crack behavior. Higher particle velocity results in the improved adhesion strength because of the increase in impact temperature and deformation. Particle-substrate bonding is a combination of different mechanisms. The localized bonding is due to localized impact fusion; in addition, bonding is also due to metal-metal bonding, mechanical locking, and diffusion. Metal-metal locking and mechanical bonding increase with increasing particle velocity, while diffusion bonding is amplified by temperature increase (Wang et al. 2012; Hu et al. 2011). The optimal deformation of the coating material has been identified as the main factor in producing adhesion strength in the coatings (Ghelichi et al. 2014).

A more energetic impact of the particles on the substrate leads to more plastic deformation; this aspect of the coating formation process leads to metallurgical bonding as well as porosity reduction. In this case, the processing conditions are optimal for the reduction of melting and to have a non-melting mediated deformation in order to reach low levels of porosity with very high levels of adhesion strength. The sprayed metallic powder particles impacted onto the substrate in a solid state are heavily deformed in a very short period, typically less than 10 ns, and well bonded to the substrate. Furthermore, the severe and nearly adiabatic plastic deformation generates heating of the impacted region and forms very fine grains with the size of several tens of nanometers within the particles. Adiabatic shear instability produces the high degree of plastic deformation, normally exhibited in the classical jet formation when the particle reaches the substrate. Actually, it seems that a higher particle velocity is necessary to induce much larger plastic deformation. The increase in temperature results in higher particle velocity and consequently higher strain rates during impact. The ability of cold-sprayed particles to undergo plastic deformation and adiabatic shear is a function of material properties, such as yield strength and melting point as well as process conditions, such as deposition temperature, particle velocity, and particle size. When a particle reaches the substrate at its critical velocity, adiabatic shear takes place contributing to the formation of a metallurgical bonding. In general, for each condition of substrate (hardness and roughness), particle pressure, and temperature, it is possible to individuate a critical velocity of the particles. For speeds lower than the critical velocity, bonding is not achieved. The substrate deformation contributes to the formation of an intimate, possibly metallurgical, contact between the materials. In the case of substrate much harder than the cold-sprayed particles, it is possible to obtain good-quality deposits with lower temperatures and particle velocity levels. Here, very high flattening ratios are experienced by those particles impacting on very hard substrates; this

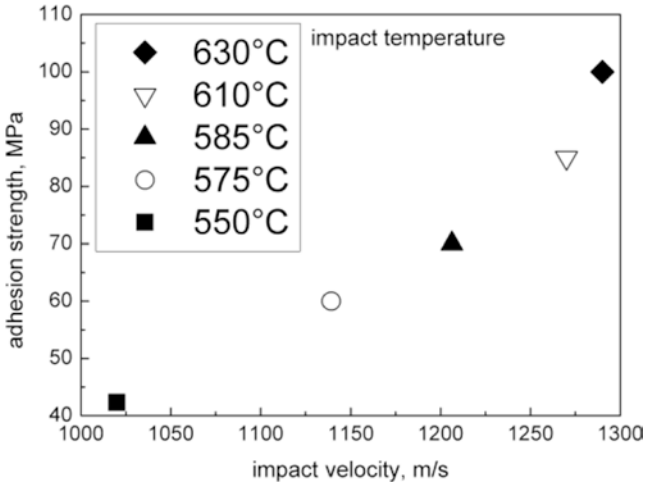

Fig. 18.5 Adhesion strength of cold-sprayed pure Ni as a function of impact velocity and temperature

leads to many mechanical and microstructural improvements such as increase in adhesion strength and hardness, increase in compressive residual stresses, and reduction of porosity. In the case of Ni particles sprayed with He gas, adhesion strength follows a parabolic dependence on the impact speed and impact temperature (Fig. 18.5).

The results are also confirmed for Al, Ti, and Mg alloys largely described in previous papers (Cavaliere and Silvello 2014). The higher particle velocity and gas temperature are, the higher the adhesion strength of the deposits results. As the deposition efficiency decreases, porosity increases and consequently a degradation of all the coating mechanical properties are recorded. In general, the coupling of higher temperatures and pressures (and consequently high velocities) results in high efficiency of the deposits. In Fig. 18.6, they are shown the adhesion strength and deposit porosity as a function of gas pressure and temperature in the case of AA2024 and AA7075 particles sprayed on AA7075 substrate.

Generally, residual stresses are strongly dependent on bulk properties for fixed cold spray processing parameters. For soft bulk, a large amount of deformation is transferred from particles to bulk material; this aspect leads to low residual stresses in the coating. When particle and substrate hardnesses are very similar, the deposition results difficult. If bulk hardness is higher, with respect to the particle one, a high deformation of particles is recorded leading to metallurgical bonding. Residual stresses depend on the strain effect due to the impact and the thermal misfit due to the temperature difference between the particles and the substrate. In the case of softer bulk, the effect of thermal misfit is much lesser pronounced with respect to the strain effect. As additional demonstration, some experiments, performed on preheated substrates, show that over some temperature range, preheating leads to a

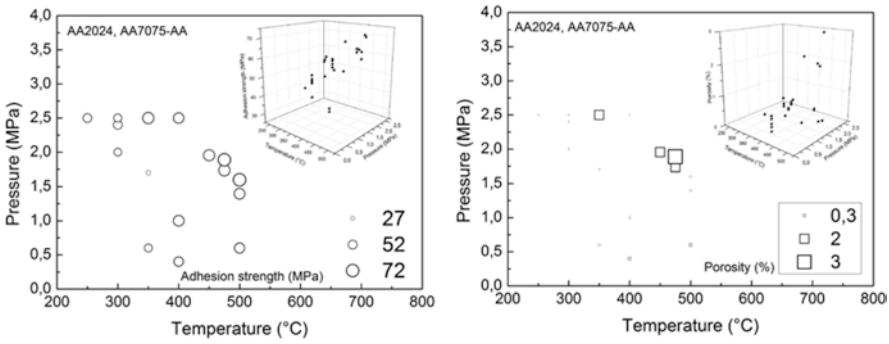

Fig. 18.6 AA2024 and AA7075 sprayed on AA7075 substrate, adhesion strength (**a**) and porosity (**b**)

stronger effect of thermal misfit on residual stresses also in the case of very high pressures employed during spray (Rech et al. 2011). Such aspect was also confirmed by numerical simulations performed in different processing conditions (Yin et al. 2013). In aluminum alloys, a strong dependence of residual stresses from spray temperature and pressure can be underlined. In general, residual stresses in cold-sprayed coated components depend on the strain effect due to the impact and the thermal misfit due to the temperature difference between the particles and the substrate. Literature analyses suggest that, if high-pressure cold spray equipments are employed, high levels of superficial compressive stress state are measured in cold-sprayed samples. Strongly lower compressive residual stresses are revealed by cold-sprayed alloys by using low-pressure machines (Cavaliere and Silvello 2014).

18.3.3 Fatigue

In general, cold spray coating leads to an improvement in fatigue properties of bulk material due to the compressive state of residual stresses. As a matter of fact, the improvement of fatigue resistance with respect to the uncoated material is due to the compressive residual stresses, induced by the process, and to the good adhesion of the coating to the substrate. In addition, the dynamic recrystallization, due the severe plastic deformation of the particles impacting on the surface, produces a nanocrystalline microstructure which acts as a crack initiation delay. The employing of high-pressure cold spray equipment, leading to a coating microstructure characterized by low porosity, optimal splat deformation, high adhesion strength, and high compressive residual stresses state, has a significant increase in fatigue life with respect to the uncoated samples. The optimal microstructural and microstructural properties combination of cold-sprayed coatings is low pores that could act as crack initiation sites, high adhesion strength preventing delamination, and good stress transfer during loading and high superficial compressive residual stresses guaranteeing improved mechanical response. It is demonstrated that optimal metal bonding is improved by

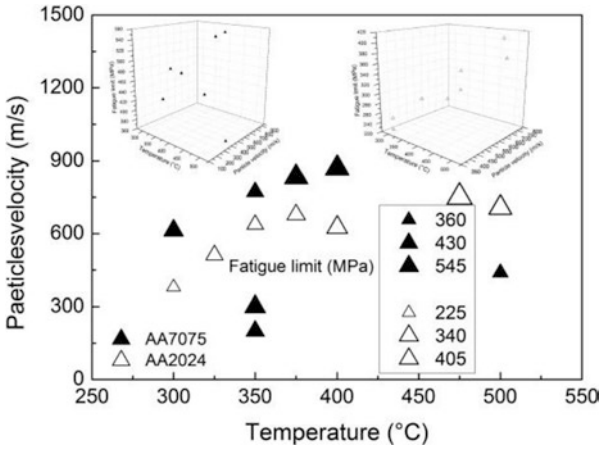

Fig. 18.7 Fatigue properties of AA2024 and AA7075 particles sprayed on AA7075 substrate

increasing particle velocity (high-pressure equipments), while diffusion bonding and recrystallization effect are amplified by temperature increase. In this way, it is possible to increase coating properties by employing higher gas temperatures and intermediate to high gas pressures depending on the particle-substrate characteristics. The high-pressure coating has a beneficial effect of fatigue resistance of all the bulk materials (Fig. 18.7). Such improvement in mechanical properties is attributed to the surface compressive residual stresses state, to the good quality of the coatings in terms of no delamination effects, and to the surface nanocrystallization acting as crack initiation delayer.

In the case of AA7075 particles sprayed on 7075 substrate, the fatigue limit increases for high particle speed in a broad range of temperatures, while for AA2024 particles the fatigue limit shows the best behavior for high gas temperature and high particle speed. After failure, the specimens show good bonding between the coating material and the bulk without presence of delamination of the coatings. Actually, from experimental evidences presented in literature, it is clear how an increase in fatigue life is achievable if sprayed particles are capable of producing a strong modification of the substrate surface like in the case of high-pressure equipments. In other cases, particles are not able to produce such modifications, and no fatigue modifications are experienced by the tested materials. The available results belonging to different authors show that improved fatigue properties are obtained in those coatings characterized by low porosity, high adhesion strength, and high superficial compressive residual stresses. For aluminum-aluminum and aluminum-magnesium coatings, such results are reached by those samples produced with high-pressure cold-sprayed machines. The results belonging to low-pressure cold-sprayed coatings do not show improving in fatigue life also modifying processing parameters or staring particle dimensions up to nanoscales. The employing high-pressure equipments and the using of nonoptimal processing parameters lead to porous coatings with

short fatigue life. Such coupling of conditions can lead also to poor coating-substrate adhesion with consequent observation of crack initiation sites at the coating-substrate interphases with decreasing in fatigue resistance.

18.3.4 Crack Behavior

The analyses of the fracture strength of the coating-substrate system have fundamental significance from a theoretical and technological point of view leading to gain fundamental information for the design and preparation of cold spray coatings. Here, it results crucial the quantification of the stress field around the crack tip (for different geometries) and the deformation mode related to the damage geometry, the applied load, the deformation mode, and the corresponding fracture behavior of the coatings. In general, cold-sprayed coatings exhibit low fatigue life when crack initiates at the interface between the coating and the substrate because of excessive porosity, low adhesion, or low compressive residual stresses leading to premature crack initiation. So crack initiation and growth characterization are fundamental especially in those applications where coatings are performed for sheets repairing. Coating behavior was analyzed firstly through FEM. It is believed that repairing V-notch cracks with cold spray coatings leads to stress intensity reduction and crack initiation locus modification. All the performed simulations were done by previously measuring shear bond strength and yield strength as a function of the crack tip distance by employing nanoindentation and nanoscratch (Cavaliere and Silvello 2017a, b doi: https://doi.org/10.1080/02670844.2017.1287555). Cohesive zone modeling has the advantage that it is based on the fracture energy and can be used to study the crack initiation in different configurations. During the simulations, the stress transfer from the substrate to the coating as well as the stress profile were analyzed and quantified. Obviously the results were compared with the stress concentration on the empty surface at the same deformation levels. Being experimental results, and then taking into account the real conditions of the coating processes, the FE calculations simulate a condition very close to the real one. In the local contact between the substrate and the coating, a small surface characterized by high stresses forms. These stresses rapidly decrease with depth. Cyclic loaded ductile materials are very sensitive to shear stresses. So, in conditions where the interface contact is nonoptimal, the bonding can fail due to shear stresses. The stress distribution becomes more complicated in those cases where geometry plays a crucial role. This is the case of notched substrates where the coating properties can vary with the depth. As a matter of fact, even if the macro deformation is elastic, the contact displacement is a power-low function of the applied load. By repairing the cracks with cold-sprayed coatings, a marked modification of principal stresses is recorded. Figure 18.8a reports the relative values of maximum principal stresses at the same point within the 2099 bulk, obtained by ratioing the results obtained in the absence (σmax2099) and in the presence (σmax2209-7075 or-2198) of 30° V-notch crack

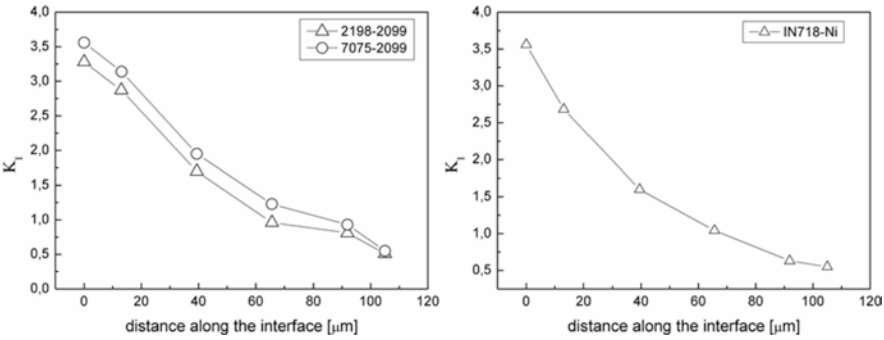

Fig. 18.8 Maximum principal stress ratio between the cracked and the repaired panels

filling. It should be underlined that (i) with an open crack, the stress intensity factor shows its maximum at the crack tip and then it decreases moving along the side toward the sheet surface, and (ii) on the contrary, in the case of a cold-sprayed sealed crack, it exhibits its minimum at the crack tip and then it increases toward the sheet surface.

This is due to the coupling of the increase of the panel strength due to the presence of coating material and to the size and shape of the plastic zone leading to crack growth retardation. The same beneficial effect is recorded for IN718 repaired with Ni particles (Fig. 18.8b). For the same strain level, stress generation is reduced following the apparent behavior of yield stress variation; this is due to the presence of the coating material. When the specimens are bending loaded, the substrate transfers the load across the crack. By increasing the strain level, further cracking takes place and consequently a dense pattern of parallel cracks develop up to a plateau value depending on the notch geometry. Generally, as the adhesion and the substrate stiffness increases, the shorter the distance needed between existing cracks in order to load the coating enough to crack further. The cracks nucleate in a discrete manner very close to the notch and to the maximum bending moment. The crack spacing decreases as the stress concentration decreases. Obviously, the higher the stress transfer is, the less the interface fails. This optimal load transfer continues up to the substrate yielding. Once substrate's yielding occurs, the stress transfer to the coating is reduced and different damage mechanisms can take place. So, the more the yielding of the substrate is delayed the more the crack initiation in the coating occurs. Obviously, the higher compressive residual stresses and interfacial strength are, the more high strains (absolute or cyclic) are needed to induce crack initiation. This is due to the coupling of the increase of the panel strength, thanks to the presence of coating material and to the plastic zone dimension governing the crack growth speed. Stress concentration, in the vicinity of the defects, can be reduced by smoothening the stress flow lines around the notch. The most effective method to mitigate the stress concentration is the addition of materials with good interface properties. Obviously, the efficiency depends on the geometry of the defect. In addition, as increasing the stress concentration by varying the notch geometry, higher

decohesion between the coating and the substrate is revealed. Now, when all the specimens are tested up to the same strain, decohesion is not dominated by straining but it is governed by the tangential traction increase due to the increase in stress concentration. In this way, the crack spacing becomes a measurement of the fracture strength of the coatings. Weaker coatings (due to higher stress concentration) fracture early arriving to decohesion in a very fast way. The application of a reinforcement layer represents an effective method to reduce stress concentration. Appropriate geometry and optimal coating material properties are needed. It is demonstrated that the coating method efficiency is related to the reduction of thermal misfits (cold processing) and similarities among materials. This is the present case where Ni coats a Ni alloy via cold spray. When a coating layer is introduced in the analysis, the interfacial stresses become a crucial point and the affordability of the results depend on the interfacial conditions definition. In addition, if the coating properties are comparable with the substrate's ones, the stress-strain relationships are determined as in a homogeneous body. The precise measurement of mechanical properties at the interface allowed us to demonstrate the accuracy of the proposed method.

By measuring the crack length as a function of the number of loading cycles, it is reported that the resistance of repaired panels is increased of six times in the case of 7075 coatings, while it is increased of more than seven times in the case of repairing with AA2198 cold spray particles. Here, it is demonstrated that the repairing with cold spray can largely contribute to the increase of the global fatigue life of cracked structures. It is believed that the fatigue performances are strongly related to the adhesion strength between the panel and the coating; the more the cold-sprayed material adhere to the bulk the more is delayed the crack initiation and growth. The adhesive disbond over the crack region can significantly reduce the stress transfer between the repaired plate and the coating producing a strong drop in the repair efficiency. In this case also, the residual stresses at the interfaces start to strongly affect the crack behavior. The fatigue properties of the coatings play a crucial role in the reliability of the substrates to which they are deposited. This is obvious for those coatings that are produced for mechanical protection. Now, the resistance to surface crack formation and propagation governs the materials performance and tolerance to mechanical loading that determine the coating durability. Then, it is fundamental to precisely characterize the surface and interface fracture toughness and the deformation modes in different loading conditions. The problem is very complex; in fact, even if a high fracture resistance is required for the coating integrity, high strength is often accompanied with low fracture toughness. This aspect is crucial in cold spray coatings normally characterized by high strength and low ductility all properties leading to a degradation in the fracture behavior of such kind of coatings.

The crack growth rate as a function of the applied ΔK for all the tested panels is shown in Fig. 18.9.

Considering the possibility of increasing the repairing efficiency relating the fatigue performances to the quality of the cold spray deposits, the tested samples were cold sprayed by employing lower temperatures and pressures. In particular, such conditions lead to a strong reduction in the adhesion strength in comparison

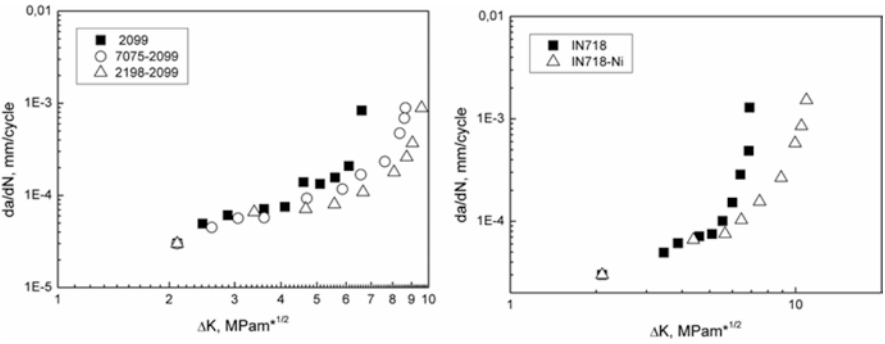

Fig. 18.9 Crack growth rate as a function of the applied ΔK for all the tested panels

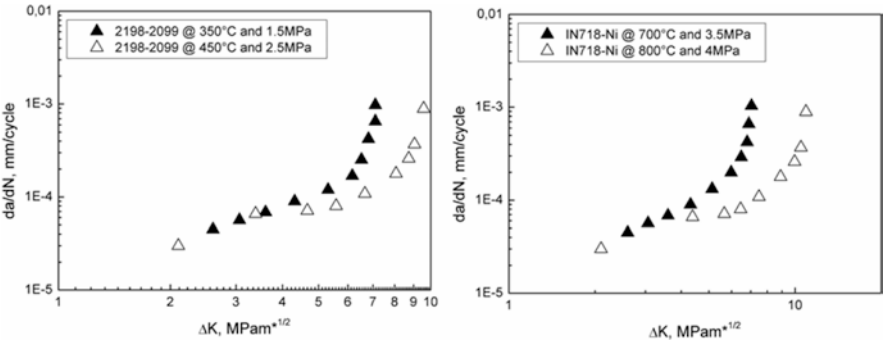

Fig. 18.10 Crack growth rate of cold-sprayed coated panels employing different processing conditions

with the previous employed processing conditions. A decrease in fatigue resistance is underlined by employing processing conditions that produce a decrease in adhesion strength (Fig. 18.10). In particular, a very fast crack growth is revealed with a behavior that in zones II and III becomes very similar to the unrepaired panel.

The fatigue resistance is strongly related to the coating-panel disbond. An efficient crack repairing with cold spray technique should pay strong attention to the deposition conditions leading to optimal microstructural properties of the coatings. In addition, the increased elastic modulus in the case of low porosity cold-sprayed coatings is believed to make such structures sensible to deformation-induced cracking. If high-pressure cold spray equipments are employed, high levels of superficial compressive stress state are measured in cold-sprayed samples. As a matter of fact, the improvement of fatigue resistance with respect to the uncoated material is due to the compressive residual stresses, induced by the process, and to the good adhesion of the coating to the substrate. In addition, the dynamic recrystallization, due the severe plastic deformation of the particles impacting on the surface, produces optimal microstructures which act as crack initiation delay. Residual stresses depend on the strain effect due to the impact and the thermal misfit due to the temperature

difference between the particles and the substrate. In the case of softer bulk, the effect of thermal misfit is much lesser pronounced with respect to the strain effect. As additional demonstration, some experiments, performed on preheated substrates, show that over some temperature range, preheating leads to a stronger effect of thermal misfit on residual stresses also in the case of very high pressures employed during spray. Now, all the cracks initiate at the coating-substrate interface, for this reason the adhesion conditions are fundamental in increasing the fatigue life. It is reported in literature that intercrystalline crack propagation mechanism is dominant in cold spray specimens. Actually, adhesion strength depends on spraying conditions. Particles sprayed with higher gas preheat temperatures are expected to retain some thermal energy and arrive at the substrate at a higher temperature than those with lower gas preheat temperatures. In terms of cold spray coatings, it is important to note that the gas temperature will increase the substrate temperature. Higher particle velocity results in the improvement of adhesion strength because of the increase in impact temperature and deformation. Particle-substrate bonding is a combination of different mechanisms. The localized bonding is due to localized impact fusion; in addition, bonding is also due to metal-metal bonding, mechanical locking, and diffusion. Metal-metal locking and mechanical bonding increase with increasing particle velocity, while diffusion bonding is amplified by temperature increase. In general, the optimal deformation of the coating material is indicated as the main factor leading to strong adhesion strength of the coatings.

Another important aspect related to crack behavior is the different crack geometry filled with similar process parameters (Cavaliere et al. 2017 doi: https://doi.org/10.1016/j.surfcoat.2017.06.006). Such an aspect is shown in Fig. 18.11 for Diamalloy particles sprayed on C steel substrate. Figure 18.11 shows the classical behavior with a slow initial increase of the crack length with the number of cycles. Then a sharp increase in the crack length with the number of loading cycles is experienced. As the number of cycles increases serious deformation concentration occurs in the front of the crack tip. Obviously, such a behavior varies as a function of the notch geometry and of the maximum bending loading. This aspect is well underlined where the crack length increases very sharply in the case of higher load and 60° of notch aperture.

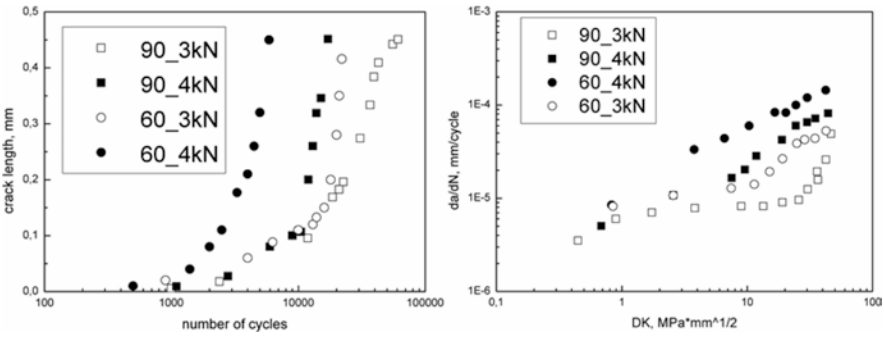

Fig. 18.11 Crack behavior for Diamalloy coated C steel with different V-notch geometries

In the case of coatings, the fracture behavior is very complex being dependent on the substrate properties and on the coating-substrate interface. These properties can, in fact, enhance or inhibit the plastic zone development around the crack tip. This mechanism describes how the coating toughness is related to the crack length. This aspect is amplified in the case of defects (notches) whose dimensions are comparable with those on the coatings. In all the tested samples, crack initiates on the surface of the coating. The surface crack forms on the surface thanks to the machined notch, and then it propagates toward the coating-substrate interface. If the interface strength is high, the cracks propagate in the vertical direction; if the interface strength is low, delamination occurs and the vertical crack is not produced or does not propagate. If a crack induces local delamination during propagation, the fast increase of damage leads to a decrease of the rate of subsequent cracking appearance (Nairn 1997). In the cases of flat specimens (without notches), several surface cracks can appear with a few of these formings along the coating-substrate interface. With the increase in bending loading, the normal strain at the interface increases with a consequent formation of interface cracking. The propagation and coalescence of such cracks can lead to the coating spallation. The mechanism is the following: given the mechanical continuity between the substrate and the coating, high interfacial shear stresses develop during bending. Force is transferred from the substrate to the coating, and it accumulates at the interface as fast as the stress concentration, due to the notch geometry, increases. Once small coating cracks are formed, they grow faster as a function of the stress concentration increases leading to decohesion in the case of low notch angles aperture. The cracks density increase can also lead to cracks coalescence with consequent local delamination. In the case of many superficial cracks, the density is directly proportional to the interface strength (Kim and Nairn 2000). At a maximum load of 3 kN, the crack growth rate is very similar for both the 60° and 90° notched sheets up to 1000 bending cycles, and then the crack growth shows a sharp increase in the case of the 60° notched sample. The difference between the two kinds of notches is more pronounced for a maximum load of 4 kN; here, the crack growth rate is higher in the case of 60° V notch for all the number of loading cycles. For all the notch geometries, the crack growth rate increases as decreasing the notch aperture and increasing the maximum bending load during cyclic tests. For a maximum load of 3 kN, a more pronounced stable crack propagation region can be underlined for both the crack geometries. Cyclic loading leads to stable crack behavior because of the contribution of many sources of energy dissipation such as deflection, pores presence, bridging and micro-cracking. Here the cracks propagate linearly in a stable way starting from the machined notch zone. Although the crack grows, a noticeable amount of deflection with propagation is recorded because of the large plastic deformation ahead of the crack front. As the plastic zone providing higher strain propagation path increases, the enhancement of the crack growth is recorded.

In Ni-based superalloys, the strength and the fatigue resistance are strongly related to the reinforcing phases that precipitate when adequate thermal treatments are performed. IN625 particles were cold sprayed on V-notched IN718 substrates, and solution heat treated at a temperature of 1050 °C for 50 h and then air cooled;

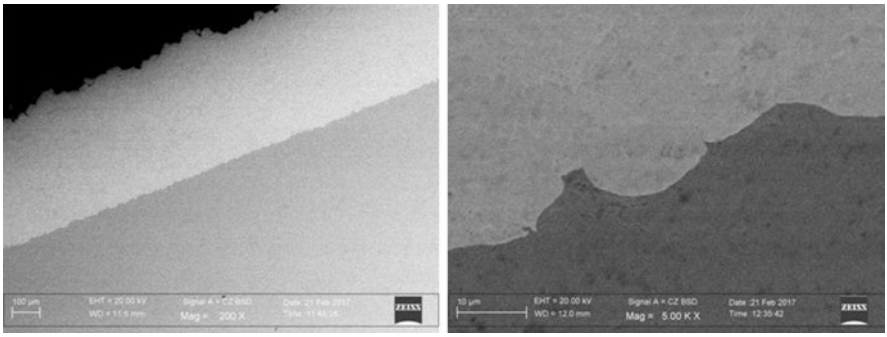

Fig. 18.12 Microstructure of cold-sprayed IN625 coatings produced at 625 °C, 40 bar and 40 mm on IN718 substrate

after solution treatment the material was aged at 650 °C for 600 h. The treatments were performed before fatigue tests in order to compare the results with those belonging to the as sprayed fatigue tested specimens. The coating microstructure before etching shows how the particles splat appears very uniform, and no porosity is revealed at the coating-substrate interface (Fig. 18.12).

The EDS compositional map of the coating sprayed at 625 °C, 40 bar and 40 mm shows that all the alloying elements appear very uniformly distributed (Fig. 18.13).

As a matter of fact, the microstructure of the coatings after solution treatment and ageing is characterized by precipitation of Mo, Nb particles, and carbides (Fig. 18.14).

The compositional maps confirm that the white precipitates contain Mo and Nb; while the black points are the metal carbides. The coating hardness in heat-treated condition is higher with respect to the as sprayed one. The hardness difference by mowing toward the coating is lower for the heat-treated coating. In particular, the hardness reduction at the coating interface is lower in the heat-treated condition (Fig. 18.15).

The crack growth rate as a function of the applied ΔK shows, for both the maximum testing loads and the crack growth, a sharp increase in the case of 60° notches with respect to the 90° ones. The stress concentration is obviously higher in those coatings produced with sharper notch geometry. Actually, the stress intensity factors define the crack tip driving force in linear elastic fracture mechanics. They characterize the crack tip stress field and indicate the propensity for crack extension. The effect of applied tangential displacement (stroke) on the mode I, stress intensity factor, KI for substrate with cracked of the final propagated crack. The difference between the behaviors of samples with different notch geometries becomes more pronounced by increasing the maximum load (Fig. 18.16). Now, if the stress intensity factor, due to loading and crack geometry, is higher than the threshold stress intensity factor, for a given crack length, fatigue damage propagates.

The increased elastic modulus in the case of low porosity cold-sprayed coatings is believed to make such structures sensible to deformation-induced cracking. For

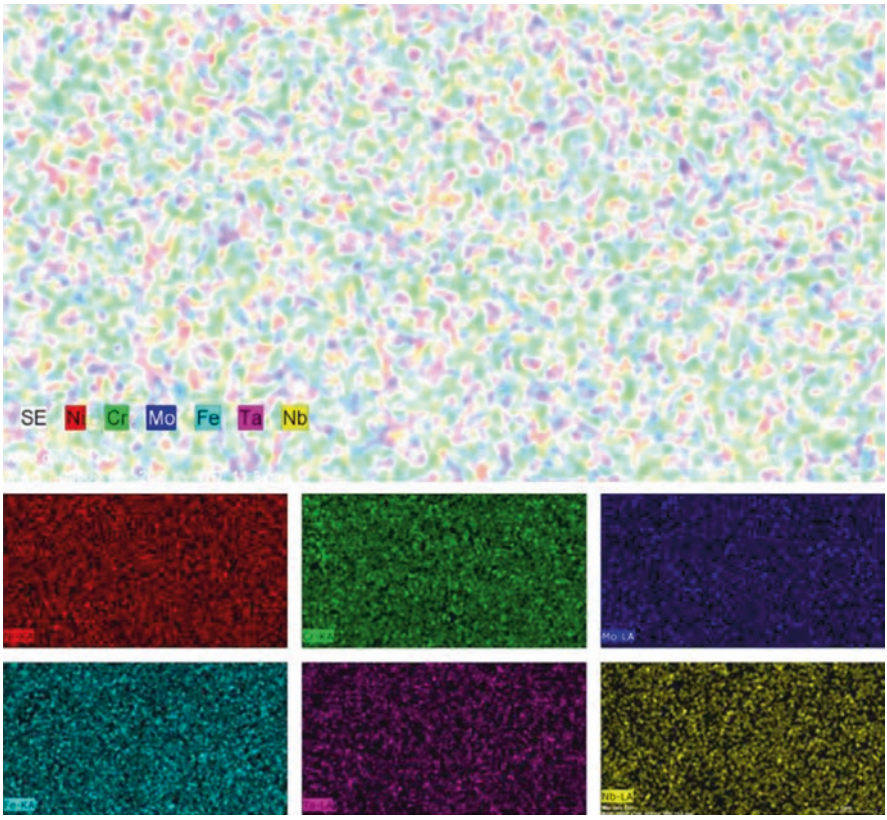

Fig. 18.13 EDS compositional map of the IN625 coating sprayed at 625 °C, 40 bar and 40 mm

the same strain level, stress generation is reduced following the apparent behavior of yield stress variation; this is due to the presence of the coating material. Obviously, the higher the stress transfer is, the less the interface fails. This optimal load transfer continues up to the substrate yielding. Once substrate's yielding occurs, the stress transfer to the coating is reduced and different damage mechanisms can take place. So, the more the yielding of the substrate is delayed the more the crack initiation in the coating occurs. Obviously, the higher compressive residual stresses and interfacial strength are, the more high strains (absolute or cyclic) are needed to induce crack initiation. This is due to the coupling of the increase of the panel strength, thanks to the presence of coating material, and to the plastic zone dimension governing the crack growth speed. Stress concentration, in the vicinity of the defects, can be reduced by smoothening the stress flow lines around the notch. The most effective method to mitigate the stress concentration is the addition of materials with good interface properties. Obviously, the efficiency depends on the geometry of the defect. The application of a reinforcement layer represents an effective method to reduce stress concentration. Appropriate geometry and optimal coating

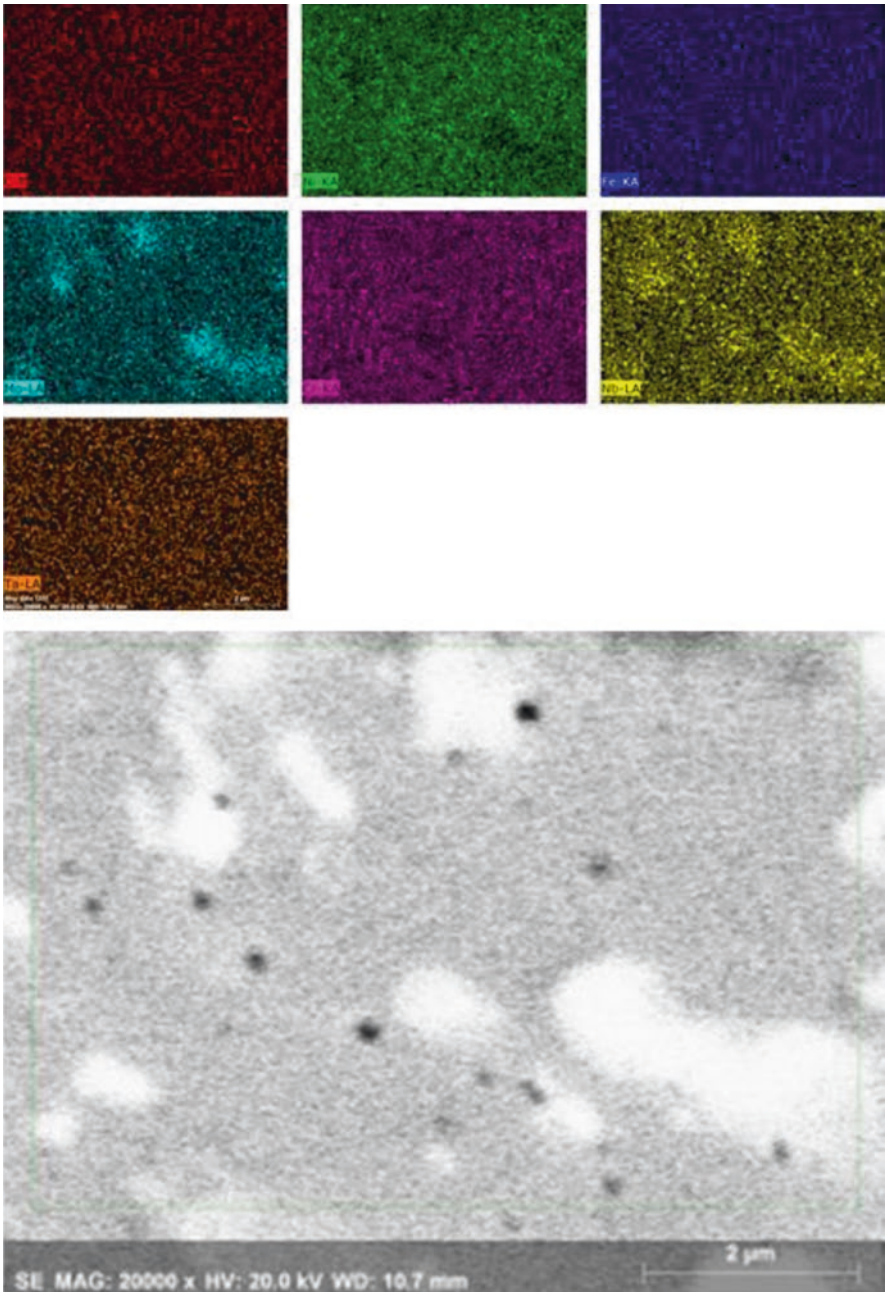

Fig. 18.14 Compositional EDX map of the Mo, Nb precipitates

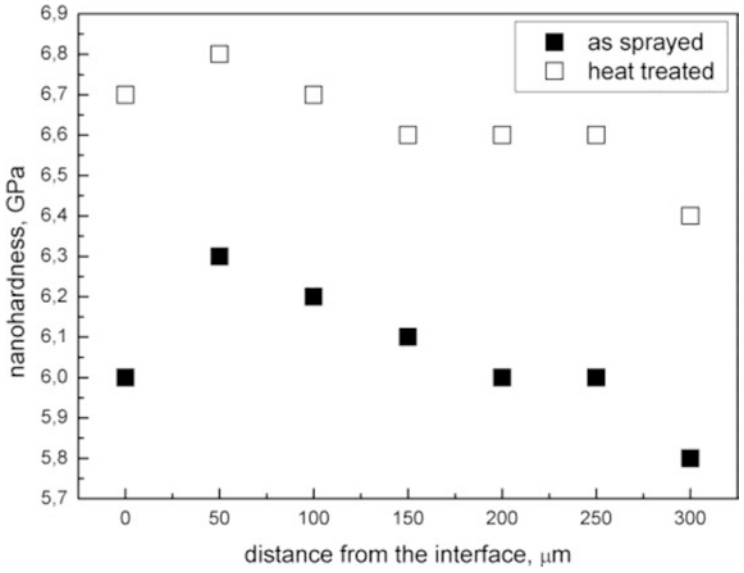

Fig. 18.15 Hardness profiles as a function of the distance from the substrate

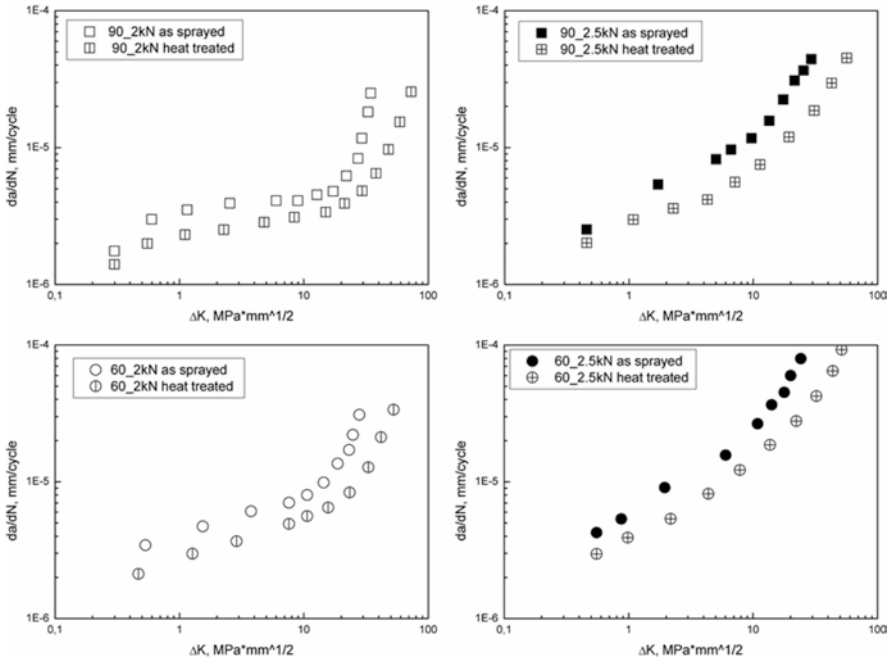

Fig. 18.16 Crack growth rate for all the studied samples in the as sprayed and heat-treated conditions

material properties are needed. It is demonstrated that the coating method efficiency is related to the reduction of thermal misfits (cold processing) and similarities among materials. When a coating layer is introduced in the analysis, the interfacial stresses become a crucial point and the affordability of the results depend on the interfacial conditions definition. In addition, if the coating properties are comparable with the substrate's ones, the stress-strain relationships are determined as in a homogeneous body. The precise measurement of mechanical properties at the interface allowed us to demonstrate the accuracy of the proposed method.

As a matter of fact, the improvement of fatigue resistance with respect to the uncoated material is due to the compressive residual stresses, induced by the process, and to the good adhesion of the coating to the substrate. In addition, the dynamic recrystallization, due the severe plastic deformation of the particles impacting on the surface, produces optimal microstructures which act as crack initiation delay. Residual stresses depend on the strain effect due to the impact and the thermal misfit due to the temperature difference between the particles and the substrate. In the case of soft bulk, the effect of thermal misfit is much lesser pronounced with respect to the strain effect. As additional demonstration, some experiments, performed on preheated substrates, show that over some temperature range, preheating leads to a stronger effect of thermal misfit on residual stresses also in the case of very high pressures employed during spray. Now, all the cracks initiate at the coating-substrate interface; for this reason, the adhesion conditions are fundamental in increasing the fatigue life. It is reported in literature that intercrystalline crack propagation mechanism is dominant in cold spray specimens. Actually, adhesion strength depends on spraying conditions. Particles sprayed with higher gas preheat temperatures are expected to retain some thermal energy and arrive at the substrate at a higher temperature than those with lower gas preheat temperatures. The crack growth rate as a function of the applied ΔK confirms that the crack growth rate increases as decreasing the notch aperture and increasing the maximum bending load during cyclic tests. This aspect is due to the fact that a more weak crack closure is related to the stress increase. For a maximum load of 2 kN a more pronounced stable crack propagation region can be underlined for both the crack geometries. Cyclic loading leads to stable crack behavior because of the contribution of many sources of energy dissipation such as deflection, pores presence, bridging, and micro-cracking. Normally, coatings follow a complex mechanism of fracture due to the specific microstructure. During propagation, crack follows the preexisting network of defects such as transgranular weakness, porosity, intra- and inter-splats defects. In the present case, the main defect form was recognized in the pores presence, so crack growth is governed by the pores presence locally weaking the microstructure and contributing to the crack growth rate increase. Here, the cracks propagate linearly in a stable way starting from the machined notch zone. Although the crack grows, a noticeable amount of deflection with propagation is recorded because of the large plastic deformation ahead of the crack front. As the plastic zone providing higher strain propagation path increases, the enhancement of the crack growth is recorded.

The fatigue resistance is strongly related to the coating-panel disbond. An efficient crack repairing with cold spray technique should pay strong attention to the deposition conditions leading to optimal microstructural properties of the coatings. In addition, the increased elastic modulus, related to low porosity cold-sprayed coatings, is believed to make such structures sensible to deformation-induced cracking. The fatigue behavior of the cold-sprayed repaired sheets increases thanks to optimal compressive residual stresses and to a good adhesion of the coatings to the interfaces. As a matter of fact, high compressive residual stresses, low porosity, and optimal microstructure act as crack initiation and growth delayers. If cracks initiate at the interface between the coating and the substrate interface, the adhesion conditions are fundamental in determining fatigue life. As a demonstration, if nonoptimal process conditions are employed during spray, poor mechanical properties are recorded in the coatings and at the coating-substrate interfaces. This results in a drop in crack resistance as initiation and growth. In general, particle deformation in optimal conditions is recognized as the principal factor contributing to the high adhesion strength of the coatings.

By observing the effect of heat treatment on crack initiation and growth behavior, many results must be underlined. First of all, for the same applied ΔK, crack growth decreases in the case of heat-treated coatings. Normally, such a behavior is attributed to the positive effect of grain boundary strengthening as a consequence of correct heat treatment and to the strengthening effect of precipitates and carbides. Here, the effect of grain boundary cannot be taken into account being the microstructure formed by splatted particle contact. As a consequence, the positive effect on crack growth should be due to the precipitates after heat treatment. This aspect becomes more pronounced at high ΔK where fatigue cracks tends to propagate in a transgranular way. In addition to the precipitates acting as barriers to the crack propagation, it is believed that the presence of large particles acts as dislocation source than improving the homogeneous plastic deformation. In addition, it is suggested that precipitates can reduce the crack tip stress by crack tip blunting so decreasing the crack susceptibility. In Ni-based superalloys, large precipitation volumes increase fatigue resistance at room and high temperature.

18.3.5 Fractography

Cold spray coatings produced with optimal processing conditions show full density or very low porosity. Anyway, being the process at the solid state, particles are not fully welded and the interfacial zones are different from classical grain boundaries. The fracture surfaces aspect is mainly transgranular. The fracture surfaces of the Ni coatings produced at 800 °C and 4 MPa reveals striations that are typical of the cyclic loading. Striations are uniformly distributed on all the surface. Anyway, some zones are characterized by a different behavior. Here, fracture initiates with the typical striations but, at one half of the path, particles decohesion takes place

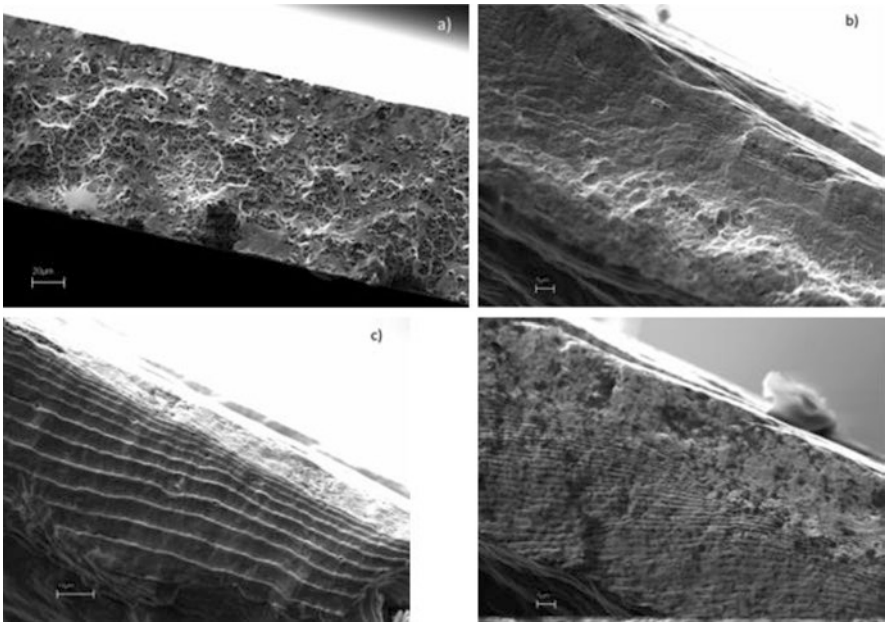

Fig. 18.17 Fracture surfaces of IN625 fatigue tested in different conditions, 60° notch 2.5 MPa (**a**), 60° notch 2 MPa (**b**), 90° notch 2.5 MPa (**c**), and 90° notch 2 MPa (**d**)

becoming the main deformation mechanism. It seems that, by increasing the load concentration, the material loses the ability to dissipate the stress and the deformation becomes inter-particle governed. In these cases, the resistance loss is due to the combination of local microstructural defects and to the achievement of critical load. The fracture surfaces of the IN625 sprayed on IN718 substrate are shown in Fig. 18.17.

The fracture propagates in the mode I in the coating material, no multiple cracks are detected and no additional macroscopic damages can be underlined. In addition, this aspect confirms that the cyclic deformation mode behavior is completely different with respect to the monotonic bending loading. In the latter case, multiple cracking and coating-substrate interface decohesion occurs and, after a given strain, cracks tend to propagate along the interface. This decohesion aspect is demonstrated to be absent in the cyclic loading conditions especially at the lowest maximum load employed during the fatigue tests. The establishment of the relationships between the measured crack initiation and growth and the fracture modes arises from the complex interaction between the fracture and the microstructural of the coatings. Such features govern the deformation behavior during crack growth giving rise to various surface aspects. In the case of the 60° notch, the sample tested at a maximum load of 2.5 MPa shows a brittle inter-particle fracture behavior (Fig. 18.17a). The

only fatigue aspect is revealed by the crack initiation locus on the top of the fracture surface, anyway the fracture surface (in this zone) appears very flat. The crack initiates and its path appears very flat then the damage propagates among the particles interfaces up to failure. A different behavior starts to be experienced by the sample with 60° notch and tested at a maximum load of 2 MPa (Fig. 18.17b). Here, the same mixed-type fracture aspect can be revealed, a brittle behavior in the bottom of the fracture surface and a typical fatigue aspect on the crack initiation locus with the appearance of fatigue striations. Such an aspect becomes much more pronounced in the case of the samples with the 90° notches (Fig. 18.17c, d). Here, fatigue striations are localized on all the fracture surfaces. In particular, the striation distances, as expected, decrease as increasing the maximum load.

18.4 Conclusions

Cold spray coating fatigue properties are related to the deposits microstructure in terms of low porosity, high adhesion strength, grain size, and residual stresses. All those processing parameters leading to very low porosity levels, high adhesion strength, very fine grain size, and high compressive residual stresses induce an improvement in the fatigue life of the cold spray-coated substrates. The variation of gas temperature and particle speed strongly influences the coating microstructure in terms of adhesion strength, porosity, and residual stresses. For the aluminum-aluminum alloy coatings, residual stresses increase as gas pressure increases and temperature decreases; for aluminum-magnesium alloy coatings, a more pronounced dependence on gas pressure was observed in terms of residual stress variation. The high-pressure coating has a beneficial effect of fatigue resistance of all the bulk materials. Such improvement in mechanical properties is attributed to the surface compressive residual stress state, to the good quality of the coatings in terms of no-delamination effects, and to the surface nanocrystallization acting as crack initiation delayer. This aspect is demonstrated by the coatings' cracks initiation and growth behavior. Experiments performed on pre-coating V-notches samples show that in the case of repairing through cold spray, the locus of crack initiation moved toward the surface of the substrate. Crack initiation and growth tests revealed that the repaired panels had up to sixfold crack resistance when optimal processing parameters were used. The repairing procedure resulted very effective also in the case of Ni and Ni-based alloys. Here, the crack initiation and growth tests revealed an increase in eight times of repaired panels resistance in the case of optimal processing conditions settled during spray. A further increase in the fatigue properties can be obtained once thermal treatments are performed after coating.

References

Assadi H, Kreye H, Gartner F, Klassen T (2016) Cold spraying: a materials perspective. Acta Mater 116:382–407

Bartsch M, Baufeld B, Dalkilic S, Chernova L, Heinzelmann M (2008) Fatigue cracks in a thermal barrier coating system on a superalloy in multiaxial thermomechanical testing. Int J Fatigue 30:211–218

Bernstein HL, Grant TS, McClung RC, Allen JM (1993) Prediction of thermal-mechanical fatigue life for gas turbine blades in electric power generation. In: Sehitoglu H (ed) Thermomechanical fatigue behavior of materials, ASTM STP 1186. American Society for Testing and Materials, Philadelphia, pp 212–238

de Camargo JAM, Cornelis HJ, Cioffi VMOH, Costa MYP (2007) Coating residual stress effects on fatigue performance of 7050–T7451 aluminum alloy. Surf Coat Technol 201(24):9448–9455

Cavaliere P, Silvello A (2014) Processing parameters affecting cold spay coatings performances. Int J Adv Manuf Technol 71:263–277

Cavaliere P, Silvello A (2015) Processing conditions affecting residual stresses and fatigue properties of cold spray deposits.Int. J Adv Manuf Technol 81(9):1857–1862

Cavaliere P, Silvello A (2016) Fatigue behavior of cold sprayed metals and alloys: a critical review. Surf Eng 32(9):631–640

Cavaliere P, Silvello A (2017a) Crack repairing in aerospace aluminum alloys panels through cold spray. J Therm Spray Techn 26:661–670

Cavaliere P, Silvello A (2017b) Finite element analyses of pure Ni cold spray particles impact related to coating crack behavior. Surf Eng doi: https://doi.org/10.1080/02670844.2017.1287555

Cavaliere P, Perrone A, Silvello A (2016) Crystallization evolution of cold-sprayed pure Ni coatings. J Therm Spray Technol 25(6):1158–1167

Cavaliere P, Silvello A, Cinca N, Canales H, Dosta S, Garcia Cano I, Guilemany JM (2017) Microstructural and fatigue behavior of cold sprayed Ni-based superalloys coatings. Surf Coat Techno doi: https://doi.org/10.1016/j.surfcoat.2017.06.006

Cetin O, Tazegul O, Kayali ES (2016) Effect of parameters to the coating formation during cold spray process. In: Proceedings of the 2nd World Congress on mechanical, chemical, and material engineering (MCM'16) Budapest, Hungary – August 22–23, 2016. doi: 10.11159/mmme16.140

Eason PD, Fewkes JA, Kennett SC, Eden TJ, Tello K, Kaufman MJ, Tiryakioglu M (2011) On the characterization of bulk copper produced by cold gas dynamic spray processing in as fabricated and annealed conditions. Mater Sci Eng A528:8174–8178

Freddi A, Veschi D, Bandini M, Giovani G (1997) Design of experiments to investigate residual stresses and fatigue life improvement by a surface treatment. Fatigue Fract Engng Mater Struct 20(8):1147–1157

Ghelichi R, Bagherifard S, Mac Donald D, Brochu M, Jahed H, Jodoin B, Guagliano M (2014) Fatigue strength of al alloy cold sprayed with nanocrystalline powders. Int J Fatigue 61:51–57

Grujicic M, Saylor JR, Beasley DE, DeRosset WS, Helfritch D (2003) Computational analysis of the interfacial bonding between feed powder particles and the substrate in the cold-gas dynamic spray process. Appl Surf Sci 219:211–327

Grujicic M, Zhao CL, DeRosset WS, Helfritch D (2004) Adiabatic shear instability based mechanism for particle/substrate bonding in the cold-gas dynamic-spray process. Mater Des 25:681–688

Hu HX, Jiang SL, Tao YS, Xiong TY, Zheng YG (2011) Cavitation erosion and jet impingement erosion mechanism of cold sprayed Ni–Al2O3 coating. Nucl Eng Des 241:4929–4937

Hussain T (2013) Cold spraying of titanium: a review of bonding mechanisms, microstructure and properties. Key Eng Mater 533:53–90

Kim SR, Nairn JA (2000) Fracture mechanics analysis of coating/substrate systems: II. Experiments in bending. Engr Fract Mech 65:595–607

McGrann RTR, Greving DJ, Shadley JR, Rybicki EF, Bodger BE, Somerville DA (1998) The effect of residual stress in HVOF tungsten carbide coatings on the fatigue life in bending of thermal spray coated aluminum. J Therm Spray Technol 7(4):546–552

Nairn JA (1997) Fracture mechanics of composites with residual thermal stresses. J Applied Mech 64:804–810

Ray AK, Dwarakadasa ES, Das DK, Ranganath VR, Goswami B, Sahu JK (2007) Fatigue behavior of a thermal barrier coated superalloy at 800 °C. Mater Sci Eng A448(1):294–298

Rech S, Trentin A, Vezzù S, Legoux JG, Irissou E, Guagliano M (2011) Influence of pre-heated al 6061 substrate temperature on the residual stresses of multipass al coatings deposited by cold spray. J Therm Spray Technol 20(1–2):243–251

Spencer K, Luzin V, Matthews N, Zhang MX (2012) Residual stresses in cold spray al coatings: the effect of alloying and of process parameters. Surf Coat Technol 206:4249–4255

Wang Q, Birbilis N, Zhang M-X (2012) On the formation of a diffusion bond from cold-spray coatings. Met Trans A43(5):1395–1399

Wong W, Vo P, Irissou E, Ryabinin AN, Legoux J-G, Yue S (2013) Effect of particle morphology and size distribution on cold-sprayed pure titanium coatings. J Therm Spray Technol 22(7):1140–1153

Yin S, Sun Y, Wang X, Guo Z, Liao H (2013) Effect of spray angle on temperature distribution within the metallic substrate in cold spraying. J Therm Spray Technol 22(6):983–991

Part VII
Biomedical Coatings

Chapter 19
Cold Spray Coatings for Biomedical Applications

Sergi Dosta, Nuria Cinca, Anna M. Vilardell, Irene G. Cano, and José Maria Guilemany

19.1 Introduction

The use of orthopedic implants is increasing worldwide due to a massive continuous demand on new biomaterials because the population is getting increasingly older, and elderly people have a higher risk of hard tissue failure. Therefore, there is a great interest and challenge in the development of novel technologies to further improve the effective clinical performance of contemporary treatment modalities and devices.

Orthopedic prostheses include both temporary devices, such as bone plates, screws, pins, and intramedullary nails, and permanent devices such as hip, knee, elbow, and ankle implants. These conventional implants are made of metallic biomaterial stainless steel (SS), cobalt-chromium alloy (Co-Cr), or titanium alloys (Ti). Around 70–80% of implants are made of metallic biomaterials, which are especially important for the reconstruction of hard tissue failures. Recent development of novel composite materials with bone-like properties has resulted in increasing popularity of plastic composites at the expense of conventional metallic bone substitutes. Some of biomaterials used in skeletal system applications are shown in Table 19.1 together with medical market numbers.

The design of an orthopedic device includes aspects of the bulk material and coatings. Novel bulk biomaterials or novel formulations of existing biomaterials are being considered to improve their wear characteristics and longevity, as well as interaction with the surrounding biological environment. While innovation on new materials with better mechanical and biological properties is day by day carried out through the collaboration of many scientific disciplines, the improvement on the biofunctionality is also an endeavor. Therefore, the osseointegration by the surface modification of conventional prosthetic materials can still offer many possibilities

S. Dosta • N. Cinca • A.M. Vilardell • I.G. Cano • J.M. Guilemany (✉)
Centre de Projecció Tèrmica (CPT). Dpt. Ciència dels Materials i Enginyeria Metal.lúrgica. Universitat de Barcelona, Martí i Franquès 1, 08028 Barcelona, Spain
e-mail: sdosta@cptub.eu; ncinca@cptub.eu; amartin@cptub.eu; igcano@cptub.eu; jmguilemany@cptub.eu

P. Cavaliere (ed.), *Cold-Spray Coatings*,
https://doi.org/10.1007/978-3-319-67183-3_19

Table 19.1 The human impact and the size of the commercial market for biomaterials and medical devices

Application	Biomaterials used	Number/year – world (or World Market in US$)
Joint replacements (hip, knee, shoulder)	Titanium, stainless steel, polyethylene	2.500.000
Bone fixation plates and screws	Metals, poly(lactic acid) (PLA)	1.500.000
Spine disks and fusion hardware	–	800.000
Bone cement	Poly(methyl methacrylate)	($600 M)
Bone defect repair	Calcium phosphates	–
Artificial tendon or ligament	Polyester fibers	–
Dental implant-tooth fixation	Titanium	($4B)
The biomaterials and healthcare market: Facts and figures (per year)		
Total US healthcare expenditures (1990)	$714 billion	
Total US healthcare expenditures (2009)	$2.5 trillion	
Total US health research and development expenditure (2009)	$139 billion	
Number of medical device companies in the USA	12.000	
Jobs in the US medical device industry (2008)	425.000	
Sales by US medical device industry (2008)	$136 billion	
World medical device market forecast for 2013	$286 billion	

Ratner et al. (2013)

for the improvement of bone reabsorption decreasing the allergenic response. In addition, in many cases, the surgery for prosthesis replacement is extremely aggressive and the cost is high; therefore, whatever solution that can extend the prosthesis life will be very welcome by clinical community.

The surface properties of biomaterials then play a crucial role in determining the success of medical implants and devices. Although a biomaterial has excellent bulk properties for specific application, if the surface properties are not suitable, the implant will fail.

Surface engineering has therefore deeply focused on the impact of the surface chemistry, the topography at the micro- and nanometer level, physicochemical effects, and biological factors such as biochemically mediated cell differentiation, the unavoidable bacterial colonization of the implant, the biologic dimensions, and the histology of surrounding structures. Proper surface modification techniques not only retain the desired bulk attributes of biomedical materials but also improve specific surface properties required by different clinical applications (Liu et al. 2010; Bosco et al. 2012; Bauer et al. 2013). Most of these works deal with titanium and its alloys since they are still considered to be some of the most significant biomaterials,

Table 19.2 Surface description of some of the commercial orthopedic implants

Manufacturer	Surface description
Biomet	Regenerex™: porous Ti alloys RoughCoat™: sintered Co-Cr bead porous coating with and without plasma-sprayed HA
DePuy	Orpington™: porous coating, porous pure Ti alloy coating Porocoat®: porous coating, sintered Co-Cr beads Duofix® HA: plasma-sprayed HA over Porocoat® coating
Smith & Nephew	Stikit: porous three-dimensional asymmetric Ti powder coating RoughCoat™: sintered Co-Cr bead porous coating with and without plasma-sprayed HA
Stryker	PureFix™ HA: plasma-sprayed HA Peri-Apatite™: solution deposited HA coating that uniformly coats three-dimensional porous ingrowth surfaces Plasma-sprayed cpTi with and without PureFix™ HA coating Arc-deposited cpTi with PureFix™ HA coating
Zimmer	Trabecular Metal™: open-cell porous tantalum construct CSTi™, Cancellous-Structured Titanium™ coating with and without plasma-sprayed HA coating Fiber metal: Ti fiber with and without plasma-sprayed HA/TCP coating Co-Cr-beaded ingrowth surfaces
Arcam AB	Trabecular Structures™ : titanium deposition via Electron Beam Melting (EBM)
Astra Tech AB	OsseoSpeed™: grit blasting titania (TiO_2), followed by hydrofluoric acid (HF) treatment
BIOMET 3i implant innovations	NanoTite™: CaP nanoparticle features

due to their resistance to body fluid effects, great tensile strength, flexibility, and high corrosion resistance. However, titanium and its alloys are classified as bioinert materials, and their surfaces need to be modified in order to make them bioactive and promote osseointegration. Through the modification of the topography of titanium and its alloys, the roughness of implant surfaces is increased, thus increasing the surface area of implants compared to larger smooth surfaces. The enlarged surface area enhances cell attachment and increases the biomechanical interlocking between bone tissue and the implant. Surface modifications based on the deposition of coatings retain the mechanical properties of titanium, while the functionality of the implant surface can be upgraded by the application of (bio)chemical compounds that act toward the improvement of bone regeneration. As long as the coating material presents a proper adhesion onto the implant surface, the substrate is responsible for the load-bearing function of the implant, whereas the coating should facilitate optimal integration into the surrounding tissues. Table 19.2 presents some of the characteristics of the current commercial orthopedic implants (Zhang 2011).

Since first clinical reported trials of hydroxyapatite (HA) coatings on femoral stems, HA coatings were extensively used in dental and orthopedic prosthesis. HA coatings are currently being used in total hip and knee replacement implants, ankle and shoulder implants, and screws and pins in bone plates for fixing bone fractures.

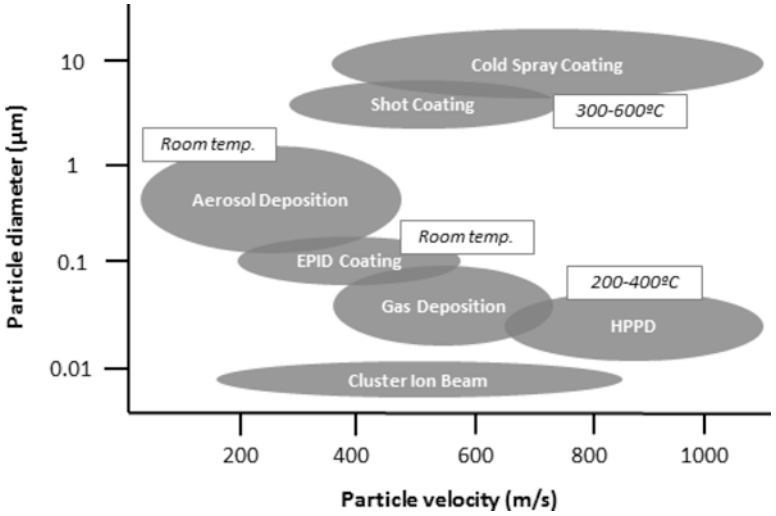

Fig. 19.1 Comparison between AD method and other methods based on collision of solid-state particles (Adapted from Akedo (2008))

After many revision studies, there is still however a controversy about the feasibility of such coatings in front of the porous metallic surfaces (i.e., open porous titanium and tantalum) (Wang et al. 2014; Hailer et al. 2015). Such coatings are usually produced by plasma spraying (PS). Actually, plasma spraying is the commercially accepted method by the Food and Drug Administration (FDA), USA, for producing hydroxyapatite coatings (Amardeep et al. 2013). Nevertheless, the high temperatures and high cooling rates from the PS technique lead to HA decomposition with the formation of a large content of amorphous phases (Sun et al. 2001); vacuum plasma spraying is used to deposit oxygen-sensitive materials such as titanium, but the low-pressure conditions impose a high cost of the technology. Therefore, lower-temperature processes such as the cold spray technology offer many advantages for such applications; Fig. 19.1 plots some of such processes. This book chapter will review the possibilities of the cold spray process for biomedical purposes.

19.2 Biocoatings Via Cold Spray

19.2.1 Metallic Biocoatings

Different biocompatible metals have been sprayed since the cold spraying technology appeared due to their high plasticities and thus the feasibility to produce coatings with good efficiencies. The first metal coatings that were used for biomedical applications were of SS and Ti. In analogy to porous plasma-sprayed titanium

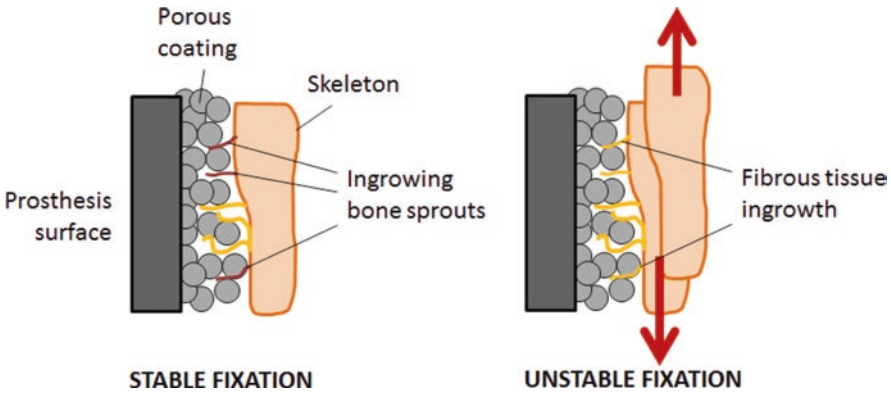

Fig. 19.2 (**a**) Stable implant fixation by bone ingrowth into the pores of the coating. (**b**) Unstable fixation caused by fibrous tissue ingrowth (Adapted from Lozier et al. (2009))

coatings, these have been also produced by CS with the aim to allow bone ingrowth; by growing within the surface voids, strong interlock is established between an endoprosthesis and bone as depicted in Fig. 19.2. Ti and Ti6Al4V coatings have been cold sprayed onto Ti6Al4V substrates (Li et al. 2007; Wong et al. 2009). Porosities up to 22.3 ± 4.7% were achieved before the heat treatment and increased to 29.7 ± 5.1% after the heat treatment, probably by the healing of the incomplete interfaces through the atom diffusion during annealing treatment. It might be also worth noting that the density of the microstructure can be influenced by the tamping effect; this is the successive impact of following particles, therefore leading to more porous structures on the top rather than near the interface with the substrate (Li and Li 2003).

On the other hand, some authors have used materials such as magnesium or aluminum to produce porosity. Sun et al. (Sun et al. 2008) produced porous titanium coatings spraying Mg + Ti powders onto titanium, where the magnesium behaved as space holder and is eliminated by vacuum sintering. Plasma-sprayed porous titanium coatings usually exhibit irregular porosity distribution, and the pores are not well interconnected, while other methods such as sintering titanium beads or fibers have relatively low porosity (<37%) and low cohesive and/or bond strength. By contrast, CS coatings by Mg + Ti resulted in an average porosity of 48.6% and pore sizes in the range of 70–150 μm. Bending modulus and compressive modulus of porous titanium coating were close to the bone and thus may be beneficial to reducing stress shielding. Qiu et al. used aluminum as porogen to form porous titanium coatings (Qiu et al. 2013), which were removed after spraying by alkaline leaching. Considering all tests, the average pore size was between 74 and 91 μm and the pore percentage between 48% and 66%. As a novelty, a new mathematic model has been used to correlate the final porosity in Ti coatings with the process parameters; it includes the use of low-pressure and high-pressure cold spraying, as well as the use of different operating gases (Hamweendo et al. 2014). Figure 19.3 shows the porous morphologies and cross section of both studies with pore sizes of 50–150 μm and

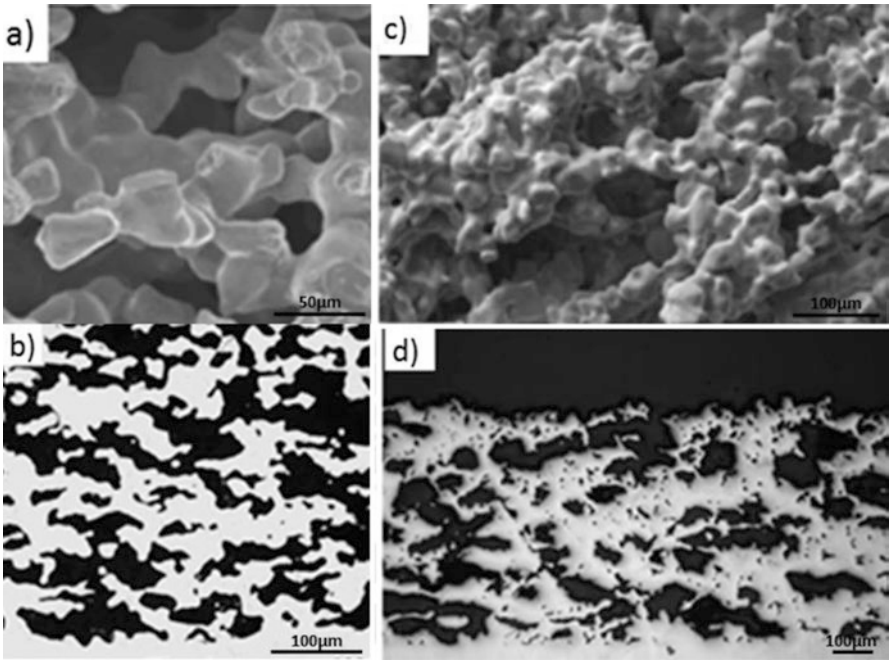

Fig. 19.3 (**a**) Porous Ti coatings; a SEM-free surface image and (**b**) MO cross-sectional image (O'Hare et al. 2010), (**c**) SEM-free surface image, (**d**) SEM cross-sectional image (Gbureck et al. 2003)

70–150 µm, respectively. Another strategy is using coarse particle to produce high roughness and porosity (Guilemany et al. 2014) (Fig. 19.4). The use of such porous coated implants is being in competition however, with the porous components built using 3D additive manufacturing, such as the one being commercialized by Stryker as trititanium (XXX) and by Zimmer (XXX), made of titanium and tantalum, respectively. Some attempts done with tantalum (Ta) by CS also exist, where good interface adhesion, low porosity, and increase of hardness are observed (Van Steenkiste and Gorkiewicz 2004).

Furthermore, the use of materials with a similar young modulus to the human bone may help reducing stress shielding in comparison with Ti alloys. The mechanical properties of the implants are fairly high, and this structural behavior can make some limitations on their direct utilization as implant in load-bearing applications. In this regard, well-adhered, thick, and homogeneous titanium coatings have been also produced onto PEEK biopolymer without its degradation, with the aim to enhance PEEK's biocompatibility for implant applications (Gardon et al. 2013). This responds to the new emerging use of PEEK as a novel alternative within the biomedical field. Also, some attempts were performed by CS SS onto Al5052 alloy substrates (Dikici et al. 2016).

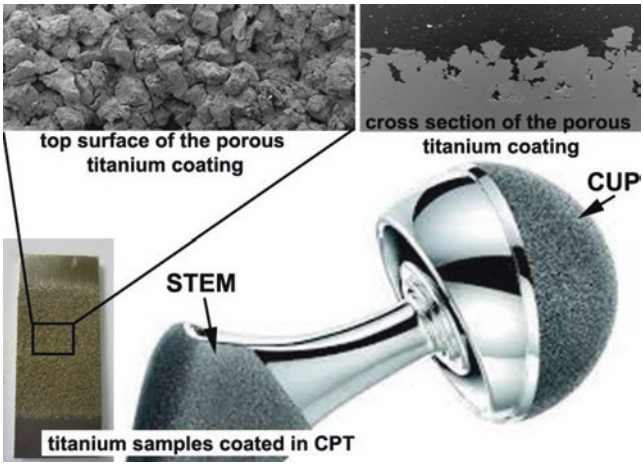

Fig. 19.4 Rough titanium coatings obtained by spraying coarse particles

Table 19.3 CS conditions of metal coatings for biomedical applications

	Feedstock powder	Substrate	Gas	Gas temperature [°C]	Gas pressure [bars]	Standoff distance [mm]	Traverse speed [mm/s]
Li et al. (2007)	Ti Ti6Al4V	Ti6Al4V	Air	520	28	30	–
Sun et al. (2008)	Ti + Mg	Titanium	He	340	10	–	–
Qiu et al. (2013)	CpTi + CpAl CpTi + CpAl + HA	Titanium	He	370	6.9	12.5	1.66
Al-Mangour-a et al. (2013a)	SS 316 + L605alloy	Mild steel	N_2	700	40	80	300

Table 19.3 shows the CS spray conditions of metal coatings used for biocoatings. Spraying onto UHMWPE has also been produced with the aim to avoid having the polyethylene liner and the acetabular cup as two separate components. In such a way, the rough titanium shell and the polymer contacting the femoral head can be achieved within the same component; this was obtained through proper surface activation previous to spraying (Guilemany et al. 2012).

The ability to produce refined grain coatings via CS, due to unchanged microstructure of the feedstock powder material, has been also taken benefit in the biomedical field, specifically in coronary stents. Frattolin et al. developed a newly metallic, nanostructured material for stent application by CS with significantly reduced grain size (Frattolin et al. 2016). Iron and 316 L SS were combined to form

a novel amalgamate with enhanced mechanical strength and a controllable degradation rate, due to the resulting microgalvanic reaction. The investigations conducted indicated that specimens composed of 80% iron and 20% 316 L SS had the most effective combination of mechanical and corrosion properties for biodegradable stent application; Al-Mangour et al. performed mechanical and corrosion properties in stents coated by a mixture of L605 Co-Cr alloy and 316-L SS onto mild steel, where it was observed that the addition of cobalt powders helped to obtain dense coatings (Al-Mangour et al. 2013a, b). A heat treatment improved then the densification and porosity reduction as well as a significant increase of ductility; also, despite in vivo and in vitro tests are still pending, the Co-Cr alloy showed a lower corrosion rate than pure SS, making it suitable for the development of a new class of metallic biomaterials.

Finally, metal coatings have also been produced by CS for bone fracture fixation systems in order to prevent bonding or one or more types of corrosion between the metallic fastener and the metallic bone plate (Loozier et al. 2009). Where the components of an internal fixation device subsequently bond together, the surgeon may have extreme difficultly disengaging one component from the other, such as disengaging a bone screw from within an opening in a bone plate. The bonding may prevent the separation of the components, and therefore, it can result in injuries due to the prevention of the components being removed from the patient. This patented procedure comprises a cold-sprayed metallic coating either within the opening or on the metallic fastener. The cold-sprayed metallic coating comprises a biocompatible metallic material having a third composition that is different than the first and second compositions. Table 19.4 lists a summary of the important properties found in cold-sprayed metallic coatings (Ketola 2014).

19.2.2 Ceramic-Based Biocoatings

Some inorganic coatings are used to promote surface bioactivity, so that there is direct bond to living tissues when implanted. Bioactive fixation forms a bond with higher strength than mechanical fixation. Nevertheless, TiO_2 coatings are currently been investigated by CGS despite its good mechanical properties and biocompatibility. Kliemann et al. studied the formation of TiO_2 particles onto metallic substrates. TiO_2 particles interact as solid spheres with the substrate bonding in a ringlike zone (Kliemann et al. 2011). Particles break into small remnants and remain in the bonding zones. Only if substrate material is brought to the surface and is available to bind other particles, a second layer or parts of it are likely to be attached to the coating on impact. Salim et al. sprayed a novel synthesis of TiO_2 powders for CS which makes it possible the deposition of those particles by CS and the growing up of a layer without the addition of binder, but onto Cu not in biocompatible material (Salim et al. 2011). Nevertheless, investigations are currently running out.

Table 19.4 Main characteristics of CS metallic coatings also with PS

	Author	Coating method	Coating material	Substrate material	Central finding	Additional remarks
Tensile strength	Vo et al. (2013)	CS	Ti6Al4V	Ti6Al4V	Low tensile strength in cold-sprayed condition. Annealing treatment considerably enhances tensile strength	
Fatigue strength	Cizek et al. (2013)	CS	Ti	Ti6Al4V	Reduced fatigue life due to tensile residual stress and increased surface roughness. Annealing treatment enhanced fatigue strength	Fatigue strength reduction might be compensated by using nano-sized powders
	Price et al. (2006)			Ti6Al4V		
	Al-Mangour et al. (2013a, b)		SS 316 L			
Adhesion strength	Sun et al. (2008)	CS	Ti	Ti	Good adhesion strength was displayed by highly porous coatings	Porosity level has relevance in bone ingrowth
	Binder et al. (2011)	CS	Ti	Al	An adequate bonding for biomedical application is easily acquired with titanium particles	
	Price et al. (2006)		Ti	Ti6Al4V		
Corrosion resistance	Trentin et al. (2011)	CS	Ti	CoCr	Cold spray coating acted as a barrier demonstrating protective effect	
	Al-Mangour et al. (2013a, b)		SS316L/CoCr	SS316L/CoCr		
	Koivuluoto (2010)		Ta	pH electrode		

(continued)

Table 19.4 (continued)

	Author	Coating method	Coating material	Substrate material	Central finding	Additional remarks
Porosity	Sun et al. (2008)	CS	Ti	Ti	Favorable pore distribution was obtained using porogen-assisted techniques	
Surface topography	Bae et al. (2010)	CS	Cp-Ti	Steel	Nanocrystalline structure was preserved owing to low thermal input	Favorable cell response is closely related to nanostructured surfaces
Wettability	Shtansky et al. (2012)	CS	Ti	Ti	Hydrophobic behavior was exhibited by coatings composed of coarse particles	Hydrophilic surface upregulates adsorbed proteins and cell adhesions
Antibacterial capacity	Vucko et al. (2012)	CS	Cu	HDPE	Coatings demonstrated antibacterial effect	Antibacterial particles interfere with bacterial cell membrane

19.2.2.1 HA Biocoatings

Previously, the advantages of CS over conventional thermal spray processes have been mainly associated to high temperature-related features. HA coatings have been found to promote fast and enhanced fixation strength, but the long-term stability of the fixation has been reported to still be a challenge in TS techniques; for this main reason, CS is proposed as an alternative to produce HA coatings with high-density and controlled crystallinity. In front of other low-temperature processes such as sol-gel, biomimetic deposition, solution deposition, electrochemical deposition, and atomic layer deposition, HA cold spray technique highlights for its simple and economic process of producing coatings at low temperatures being able to control coating microstructure. Therefore, postdepositional heat treatments are not required to remove organic compounds used in coating preparations (Heimann 2016).

Despite the common sense that HA particle bombardment is like blasting the metal surface of the implant, some approaches have been done in this direction (Ishikawa et al. 1997; O'Hare et al. 2010; Gbureck et al. 2003; O'Neill et al. 2009; O'Sullivan et al. 2010) and even more successful by dealing with a shot-penning route (Byrne et al. 2013). CS of ceramics has been actually compared to other low-temperature powder-based dry manufacturing processes, i.e., aerosol deposition (AD), sometimes known as vacuum cold spray (VCS), and nanoparticle deposition system (NPDS), which appeared in the 1990s and 2000s, respectively. AD is based on the acceleration of submicrometer particles, but low-vacuum conditions are necessary to control the supersonic flow. In NPDS, the source of bonding is attributed to the dissipation of the kinetic energy of the particles. The use of submicrometer feedstock particles seems to be also important, and some plasticity features have been revealed (Chun and Ahn 2011; Chun et al. 2012; Akedo 2006). Dense hydroxyapatite coatings have been deposited on titanium by this method (Hahn et al. 2009; Park et al. 2010). The control of nanoporosity within the coating and the low cost of AD process are big advantages to deposit HA powders, but with very low deposition efficiency. CS is a good alternative for producing HA coatings with the desired micro-nanostructure (Moore et al. 2017).

More recently, Cinca et al. have been able to deposit hydroxyapatite up to high thickness onto Ti6Al4V substrates and have examined the deposition mechanisms as well as pointing out the importance of the feedstock powder structure and surface preparation (Cinca et al. 2016). Mainly, it was found that sintered ceramic HA powders suffer from porous collapse of the structure and almost a complete lack of plastic deformation. However, other modes of inelastic deformation, such as microcracking may provide alternative deformation mechanism. A considerable decrease in crystallite size was observed especially at particle-substrate interfaces. By contrast, the impact of agglomerate nanocrystalline HA powders produces compaction of nanocrystalline grains within the particle. Dense HA coatings are obtained due to the particle consolidation from the tamping effect by the continuous impact of the particles (Vilardell et al. 2016) (Fig. 19.5).

Different numerical and simulation studies have been developed to come upon optimal conditions for cold spraying of spraying HA. Zhang and Zhang (2011)

studied the factors influencing HA particle acceleration using a computational fluid dynamic program FLUENT. The simulation results showed that the HA particle is accelerated by the combination of throat diameter and exit diameter whose expansion ratios lie within the optimal range of 1.5–4. HA particle velocity increases with the increasing of gas pressure notably from 0.2 MPa (150 mm/s) at 0.6 MPa (360 mm/s) and with the decrease of HA particle size until a minimum of 5 μm, where it decelerates steeply, being 5–20 μm size particle suitable for spray with CS. The Taguchi method was used by Singh (2011) to optimize HA conditions in CS; they calculated the percentage contribution of all factors on exit particle velocity of HA powder, being as follows in descending order: Gas Type > Particle Diameter > Gas Inlet Pressure > Particle Temperature > Gas Inlet Temperature. Moreover, they observed the combination of those parameters can alter the result (Singh and Batra 2013), specially gas pressure and gas temperature, as well as particle diameter which has a maximum effect to the particle velocity. Therefore, particle velocity decreases with the increase of gas pressure and particle size, but increases with the increase of gas and particle temperature. Also, the increase of gas pressure and particle temperature consequently increased the particle velocity. In all cases, particle velocity was observed to be maximum with the usage of hydrogen gas followed by helium, nitrogen, and air, respectively. Other authors have investigated the effects of input factors such as standoff distance, surface roughness, substrate heating temperature, and the number of sprays on the mechanical properties of HA onto pure magnesium substrate by using factorial designs (Hasniyati et al. 2016). Those responses were optimized and were able to produce a HA coating of ~40 μm with a high nanohardness (>400 MPa) and elastic modulus (>40GPa). Actually, recent investigations concern biodegradable implants and biocompatible coatings on implant materials, for example, Mg-based alloys for stent applications (Noorakma et al. 2013). However, despite its excellent properties, magnesium-based alloys have not seen tangible applications in biomedical field industry due to their rapidly and localized corrosion behavior. To date, they have been studied within the development of cardiovascular stents, bone fixation material, and porous scaffolds for bone repair. In order to control the degradation rates, they have been coated with HA. Atmospheric plasma studies (APS) have not been applied since its high temperatures could melt the magnesium substrate and decompose HA in other calcium phosphate phases, and the crystallinity of HA might also be lowered due to rapid solidifications. CS has offered solution to both problems (Noorakma et al. 2013). HA coatings onto Mg substrate were tested in simulated body fluids showing good biodegradability and bioactivity. It may be suitable for possible use as biodegradable orthopedic implants such as stents (Noorakma et al. 2013).

Given the lately increasing works on biocompatible polymers for articular prosthesis, pure HA coatings have been produced on PEEK, therefore providing bioactivity to a material that avoids the stress shielding phenomenon normally occurring between a metallic material and the bone and the weak mechanical properties of ceramic substrates (Noh et al. 2012). Coating polymeric biomaterials with calcium phosphate is also one of the most effective methods to enhance biocompatibility. However, calcium phosphate ceramic coatings necessitate a heat treatment at a high

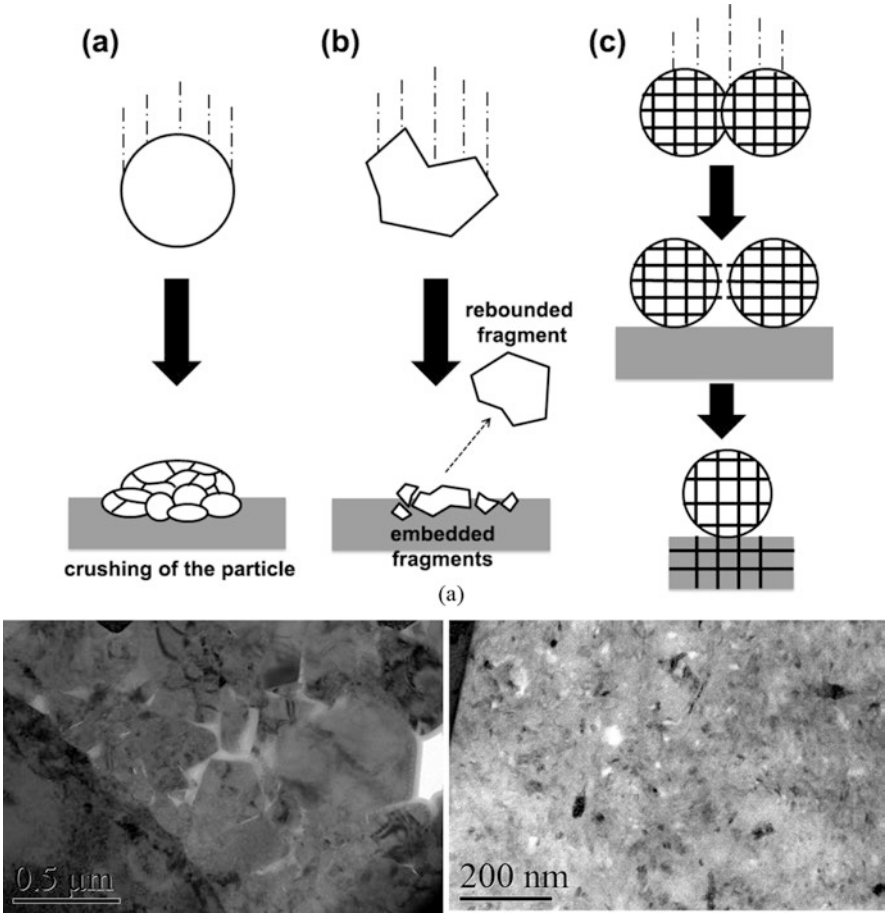

Fig. 19.5 (**a**) Possible deposition mechanisms for brittle materials, (**b**) and (**c**) TEM micrographs of the Ti-HA interface of a sintered and agglomerated nanocrystalline particle deposited by CS, respectively (Cinca et al. 2016; Vilardell et al. 2016)

temperature in order to induce crystallization of the coating layer or necessitate a cost-consuming vacuum deposition method for low-temperature crystallization in order to control/obtain other calcium phosphate phases. In the case of polymeric biomaterials, a heat treatment at a high temperature brings about deformation of polymers, and such deformation eventually deteriorates the performance of polymers, preventing the polymers from being used as biomaterials. Furthermore, a vacuum deposition method at a low temperature may also damage the surfaces of polymers, causing deformation, and requires high production cost to increase productivity, which is not preferable. CS overcomes the limitations of various conventional coating methods and enables coating of the surfaces of polymeric biomaterials while maintaining the intrinsic properties of both the powder and the polymer, with low production cost and high productivity. This patent includes bioactive coatings

Table 19.5 Main characteristics of cold-sprayed HA coatings compared to PS

	Author	Coating method	Coating material	Substrate material	Central finding	Additional remarks
Fatigue strength	Laonapakul et al. (2012a, b)	PS	HA	Ti	Susceptibility to delamination in SBF immersion	Clinically identified problem
	Gledhill (2001)		HA	Ti		
Corrosion resistance	Noorakma et al. (2013)	CS	HA	Mg	Demonstration of degradation of deposited magnesium alloy in simulated body fluid	Cold spray coatings may potentiate controlled magnesium degradation
Anti-inflammatory agents	Taha et al. (2013)	PS	HA	Ti	Drug carriers were successfully immobilized onto coating	

HA; bioglass compounds such as bioglasses containing CaO, SiO_2, and P_2O_5 as main ingredients and crystallized bioglasses; and mixtures thereof (Noh et al. 2012). Lee et al. (2013) also evaluated the bioactivity of HA coatings on PEEK substrates by CS (Hasniyati et al. 2015).

Table 19.5 lists a summary of some properties found in cold-sprayed metallic coatings.

19.2.2.2 HA Composite Biocoatings

Due to the intrinsic brittle nature of ceramics, a direct deposition of a uniform layer with proper adhesion is still a challenge via CS, specially onto the typical metallic prosthesis, i.e., titanium and SS, on account of the inelastic deformation that ends in failure fragmentation. This has already been observed by the few studies reported in the previous section. For a better understanding of this behavior, lots of studies are being carried out on the investigation of failure mechanisms of ceramics at dynamic impacts (Chen et al. 2006; Mukhopadhyay et al. 2010). Significant efforts are thus addressed in the direction of using metal-ceramic and polymer-ceramic composite powders. Some works deal with HA-Ti mixtures (Zhou & Mohanty et al. 2012; Shukla et al. 2001). The results showed that compared to pure Ti coating, cold-sprayed HA/Ti composite coating exhibits higher corrosion current and lower corrosion resistance. However, a post-spray heat treatment can improve the corrosion property of HA/Ti composite coating remarkably. In addition, the mechanical properties such as microhardness and ultimate shear strength of cold-sprayed 20 wt% HAP/Ti composite coating also improved up to three times by a post-spray heat

treatment process. Further, the recrystallization also favored the interfacial bonding and hence improved the mechanical properties (Zhou 2012). Other authors proposed a laser annealing CS (LaCS) hybrid process for the fabrication of near submicron structure coatings of hydroxyapatite (HA) + Ti system (Saphronov and Shishkovsky 2015). LaCS increases the adhesion between the HA and titanium coatings, providing more strength, ductility, and decreasing of HA destruction in the coatings. In comparison with laser annealing detonation spraying, no significant modification of the initial HA composition was observed during the different steps of the coating preparation and spraying. Choudhuri et al. also demonstrated that HA-Ti mixture powders can be cold sprayed achieving a better bond strength (24.45 MPa) than APS (~10–15 MPa) (Choudhuri et al. 2009); two different titanium powders were used in those mixtures: a vacuum atomized commercial pure Ti (Cp-Ti) and a sponge titanium powder both from a particle size ~45 μm. Cp-Ti showed difficulties to build up the coating by encapsulating HA particles, whereas the use of sponge Ti powder was more effective. The maximum incorporation of HA was of 20%; above that percentage, it was found that HA particles got crushed into fragments due to high impacts. In summary, HA/Ti composites show effectiveness on the mechanical properties and biocompatibility. However, sintering parameters should be further investigated to determine better working processing windows for the manufacturing (Arifin et al. 2014). As reported before, aluminum powders have been used as a porogen, in combination with titanium, to achieve porous titanium coatings with higher interconnected macroporosity and larger specific surface area; experimental results indicate desirable open-cell structure with 50–150 μm pore size and 60–65% macroporosity; in order to make these coatings bioactive, HA was added to facilitate bone cell attachment and ingrowth, leading to outstanding in vitro HA mineralization, although long-term studies are required (Qiu et al. 2013). Such authors used two types of HA, a crystalline and an amorphous calcium phosphate nanocrystalline HA (NC-HA), where it could be observed that NC-HA reach a maximum Ca^{2+} mineralization efficiency promoting an early bone fixation.

Other attempts, in that case of cold-sprayed HA composite coatings, include: HA-graphene nanosheet (GN) (Liu et al. 2014a, b), with the aim to avoid the concerns related to its long-term performance, i.e., the intrinsic brittleness and low fracture toughness of HA, and doping HA with silver (Sanpo et al. 2009a, b), with the advantages that silver involve. The addition of graphene has been proved to be very suitable for load-bearing applications, and enhanced significantly fracture toughness and elastic modulus. Also, it exhibits a very reasonable biocompatibility as well; it was even embedded in HA matrix and plastic deformation of certain nano HA particles was revealed. The GN-containing HA coatings markedly enhanced attachment and proliferation of the osteoblast cells, which is most likely attributed to fast adsorption of key serum proteins like fibronectin with elongated stretching conformation on GN. Table 19.6 shows different cases CS conditions for biomedical applications.

Table 19.7 lists a summary of the important properties found in cold-sprayed metallic coatings.

19.3 Clinical Performance

This is a very novel topic and since many few researchers have optimized their coating systems, not many in vitro and in vivo results exist within the literature. In vitro performance can be evaluated by the evaluation of morphological changes of coatings after immersion in SBF. Qiu et al. reported the formation of clusters of fine precipitates for their HA-Ti porous coatings, with similar calcium mineralization efficiencies when using either crystalline HA or amorphous nanocrystalline HA (Qiu et al. 2013). In addition, these authors used the human osteosarcoma-derived SaOS-2 line with the aim to evaluate the cytotoxicity; cell viabilities after 48 h proved that neither of the coatings was cytotoxic. On the other hand, Gardon et al. (2014) studied the differentiation and proliferation of cultured trabecular bone of Ti coatings onto PEEK obtaining a better biological response from Ti than PEEK from 3 days of culture, although optimal properties were shown with nanostructured titanium dioxide. Lee et al. (2013) performed similar studies with cultured human bone marrow mesenchymal stem cells hBMSCs (human bone marrow stromal osteoprogenitor cells) on HA-CS coated PEEK samples. The HA coating facilitated the differentiation and proliferation of cultured hBMSCs and promoted bone fusion with the surrounding iliac bone without the presence of any fibrous layer. Noorakma et al. (2013) deposited an hydroxyapatite layer onto magnesium alloy substrate and demonstrate that in vitro behavior, superior cell adherence with numerous cellular micro extensions on porous Ta samples compared to Ti samples clearly suggests that Ta surfaces are biocompatible and cause no inhibition to bone cell (hFOB) adhesion and growth. Presence of relatively high ECM (extracellular matrix) mineralization on porous Ta samples also indicates that osteoblast cells have started differentiating and ECM remodeling (Balla et al. 2010). In vivo, this porous tantalum biomaterial has desirable characteristics for bone ingrowth; further studies are warranted to ascertain its potential for clinical reconstructive orthopedics (Bobyn et al. 1999).

The addition of graphene to HA coatings significantly enhanced attachment and proliferation of human osteoblast cells, which is most likely attributed to fast adsorption of key serum proteins like fibronectin with elongated stretching conformation on graphene (Mukhopadhyay et al. 2010).

19.4 Antibacterial/Antimicrobial Coatings

Although the use of titanium and its alloys in biomedicine is still important, the infection around the implants remains as a concern. In infection, not only do the patients suffer serious damage, but bacterial infection after implant placement can cause significant complications, thereby increasing medical cost. The paradigm of bacterial attachment and proliferation on surfaces was first recognized in the 1930s. It was established that a bacteria prefer to colonize a solid substrate than living in a planktonic state. The creation of antibacterial surfaces seeks to repel or resist the initial attachments of bacteria by either exhibiting an antibiofouling affect or by

Table 19.6 CS conditions of HA/Ti and HA coatings for biomedical applications

	Feedstock powder	Substrate	Gas	Gas temperature [°C]	Gas pressure [bars]	Standoff distance [mm]	Traverse speed [mm/s]
Qiu et al. (2013)	Cp Ti + Cp Al Cp Ti + Cp Al + HA	Ti	He	370	6.9	12.5	1.66
Noorakma et al. (2013)	HA	AZ51 alloy	Air	500–700	10	40	–
Lee et al. (2013)	HA	PEEK	Air	200/300/400	7/14/20	30	–
Zhou (2012)	Cp Ti + HA	Ti	N_2	700	35	15	–
Choudhuri et al. (2009)	Cp Ti Sponge Ti Sponge Ti + HA	Ti	N_2	400–700	25–38	25	50–400

inactivating any cells coming into contact with the surface. Antibacterial surfaces can be divided in two groups: (i) antibiofouling surfaces that may resist or prevent cellular attachment due to the presence of an unfavorable surface topography or surface chemistry and (ii) bactericidal surfaces that disrupt the cell on contact, causing cell death. The CS process has also emerged as a promising process to functionalize surfaces in such way.

The use of inorganic antimicrobial agents has attracted interest for its improved safety and stability versus organic antimicrobial agents. There has been a great development during recent years in antibacterial coatings, but they are not still clinically much used; however, more developments and investigations are being explored to achieve both excellent tissue integration ability and good antibacterial properties (Zhao et al. 2009). Silver (Ag) has already been highlighted as an antibacterial material. The combination of bioactivity (HA) and antibacterial properties (Ag) has been previously reported, and the results indicated that the antibacterial activity increased with increasing HA-Ag nanopowder concentrations (Zhou and Mohanty 2012). Alternatively, ceramic powder of zinc oxide (ZnO), calcium oxide (CaO), and magnesium oxide (MgO) has found antibacterial activity. Combinations of ZnO/Ti powders with different ratios have been performed to produce composite coated implants (Sanpo et al. 2010); the results show that the viability of cells on ZnO20/Ti80 was higher than on ZnO50/Ti50 and ZnO80/Ti20 samples, thus proving that the cell viability decreased with increasing ZnO concentration in the coating composition. On the other hand, the bactericidal effect of TiO_2 coatings has also been extensively studied; specifically, CS anatase coatings were investigated by Kliemann et al. (2011). A kill rate of 99.99% was obtained after 5 min of exposing the bacteria *Pseudomonas aeruginosa* to UV light with a peak intensity of 360 nm. Certain stagnation of the decay of the bacteria was found, which could be attributed

Table 19.7 Main characteristics of cold-sprayed composite biocoatings

	Author	Coating method	Coating material	Substrate material	Central finding	Additional remarks
Adhesion strength	Melero et al. (2011)	HVOF	TiO_2 + HA	Ti6Al4V	A drop in adhesion strength as a consequence of SBF immersion	
	Qiu et al. (2013)	CS	Ti/HA	TI	Good adhesion strength was displayed by highly porous coatings	Porosity level has relevance in bone ingrowth
	Choudhuri et al. (2009)				An adequate bonding for biomedical application is easily acquired with titanium particles	
Wear resistance	Chen et al. (2010)	CS	Al/CNT	Al	Involvement of carbon nanotubes remarkably reduced the rate of wear	
	Kang et al. (2012)		Al/CNT			
Porosity	Qiu et al. (2013)	CS	Ti/HA	Ti	Favorable pore distribution was obtained using porogen-assisted techniques	
Surface topography	Liu et al. (2014a, b)	CS	HA/graphene	Ti	Nanocrystalline structure was preserved owing to low thermal input	Favorable cell response is closely related to nanostructured surfaces
Antibacterial capacity	Sanpo et al. (2008, 2009a, 2010)	CS	HA-Ag/peek, Zno-Al, ZnO,Ti		Coatings demonstrated antibacterial effect	Antibacterial particles interfere with bacterial cell membrane

to non-coated areas present due to the impossibility of covering all the surface of the substrate by means of anchoring TiO_2 particles. Other coatings that are committed to antibacterial properties, thanks to ZnO, are made of Novaron VZ 600 (a commercially available inorganic antimicrobial powder made from glass, with the functional material being ZnO) onto Ti (Tamai et al. 2009). Those studies were developed to analyze the differences among surfaces using different processing pressures and analysis of the antimicrobial with CS due to the low heat powder resistance. Results have shown that *S. aureus* cells on samples decreased after 24-h culture, even on non-coated plates. Two possibilities were reported: (i) roughness can contribute to antimicrobial ability, and (ii) medium concentration may have been too low for this bacterium.

Moreover, antibacterial coatings not only focus on orthopedic and implant applications but also in touch surfaces where there is certain risk of infection and biomedical tools. For example, metals like copper (Cu) have been employed for this purpose. The specific mechanism by which copper affects cellular structures is not yet proven, but the active agent of cell destruction is generally considered to be the copper ion (Champagne and Helfritch 2013). As the fact that CS deals with high particle velocities leading to extreme work hardening and high dislocation density within the deposit, it causes an increase of ion diffusion through the grain dislocations leading to microbial destruction. Champagne and Helfritch (2013) produced copper surfaces onto aluminum using three thermal spray methods, plasma spray, wire spray, and cold spray, in order to analyze the microbiologic differences and decrease the risk of infection of bacterial contamination on touch surfaces such as a hospital table. CS produced the minimum percentage of MRSA (methicillin-resistant *Staphylococcus aureus*) due to the high number of dislocations within the coating.

On another hand, most of the tools used in the medical and food sectors are made of austenitic stainless steel alloys, and to promote antibacterial properties, some authors have suggested the use of metallic glassy Cu50Ti20Ni30 coatings in the medical and food sectors. Those coatings have high nanohardness and low coefficient friction values and suggest that the inhibition of bacterial biofilm by Cu50Ti20Ni30 may offer viable possibility for controlling biofilm formation (El-Eskandrany and Al-Azmi 2016). Other attempts of antibacterial coatings were performed by mixing with aluminum (Al) powder. The use of aluminum is cause for a number of cosmetic use, repair, corrosion, and protection applications, also for its low density that could be accelerated to very high velocities in CS, and the available commercial variety of composition of Al powders. Table 19.8 summarizes the CS spraying conditions used for the antibacterial coatings referenced within this section.

19.5 Summary

This chapter intended to give an overview of the fundamental and applied research of cold spraying for biomedical applications. All the above coating systems try to satisfy the main requirements for a biocoating, either in biological (biocompatibility and bioactivity), mechanical, or antibacterial terms. Terms like “structural design”

Table 19.8 CS conditions of antibacterial coating

	Feedstock powder	Substrate	Gas	Gas temperature [°C]	Gas pressure [bars]	Standoff distance [mm]	Traverse speed [mm/s]
Sanpo et al. (2009a, b)	HA-Ag (Ag-doped HA) + PEEK	Glass	Air	150–160	11–12	15	50
Sanpo et al. (2010)	ZnO + Ti	Al 6061	He	300–400	13–15	15	60
Tami et al. (2009)	Novaron VZ 600	Ti	N_2	350	30	5	20

and "deposition techniques" are involved in the development of the fabrication process to obtain cost-efficient products making it commercially reproducible and attainable to all types of markets. From this point of view, it is worth taking into consideration the valuable advantages that CS has to offer of non-microstructural changes from feedstock powder, high deposition efficiency, and low-temperature rates and overcoat the wide range of materials that could be applied. Day by day constant work and research demonstrate CS as a new technique to produce coatings.

However, still a big step has to be overcome in order to translate the experimental studies to the real market. More studies in vitro and in vivo from CS technique are required, and the addition of antibacterial components must be performed as a necessity upturn in human health.

Acknowledgments The authors also gratefully acknowledge the helpful comments and suggestions of the reviewers, which have improved the presentation.

References

Akedo J (2006) Aerosol deposition of ceramic thick films at room temperature: densification mechanism of ceramic layers. J Am Ceram Soc 89:1834–1839. https://doi.org/10.1111/j.1551-2916.2006.01030.x

Akedo J (2008) Room temperature impact consolidation (RTIC) of fine ceramic powder by aerosol deposition method and applications to microdevices. J Therm Spray Technol 17:181–198. https://doi.org/10.1007/s11666-008-9163-7

AL-Mangour B, Dallala R, Zhim F et al (2013a) Fatigue behavior of annealed cold-sprayed 316L stainless steel coating for biomedical applications. Mater Lett 91:352–355. https://doi.org/10.1016/j.matlet.2012.10.030

AL-Mangour B, Mongrain R, Irissou E, Yue S (2013b) Improving the strength and corrosion resistance of 316L stainless steel for biomedical applications using cold spray. Surf Coat Technol 216:297–307. https://doi.org/10.1016/j.surfcoat.2012.11.061

Kang AS, Singh G, Chawla V (2013) Some problems associated with thermal sprayed HA coatings: a review. Int J Surf Eng Mater Technol 3(1):10–14

Arifin A, Sulong AB, Muhamad N et al (2014) Material processing of hydroxyapatite and titanium alloy (HA/Ti) composite as implant materials using powder metallurgy: a review. Mater Des 55:165–175. https://doi.org/10.1016/j.matdes.2013.09.045

Bae G, Kang K, Kim J-J, Lee C (2010) Nanostructure formation and its effects on the mechanical properties of kinetic sprayed titanium coating. Mater Sci Eng A 527:6313–6319. https://doi.org/10.1016/j.msea.2010.06.037

Balla VK, Bodhak S, Bose S, Bandyopadhyay A (2010) Porous tantalum structures for bone implants: fabrication, mechanical and in vitro biological properties. Acta Biomater 6:3349–3359

Bauer S, Schmuki P, von der Mark K, Park J (2013) Engineering biocompatible implant surfaces. Prog Mater Sci 58:261–326. https://doi.org/10.1016/j.pmatsci.2012.09.001

Binder K, Gottschalk J, Kollenda M et al (2011) Influence of impact angle and gas temperature on mechanical properties of titanium cold spray deposits. J Therm Spray Technol 20:234–242. https://doi.org/10.1007/s11666-010-9557-1

Bobyn JD, Stackpool GJ, Hacing SA, Tanzer M, Krygier JJ (1999) Characteristics of bone ingrowth and interface mechanics of a new porous tantalum biomaterial. J Bone Joint Surg Br 81:907–914

Bosco R, Van Den Beucken J, Leeuwenburgh S, Jansen J (2012) Surface engineering for bone implants: a trend from passive to active surfaces. Coat 2:95–119. https://doi.org/10.3390/coatings2030095

Byrne GD, O'Neill L, Twomey B, Dowling DP (2013) Comparison between shot peening and abrasive blasting processes as deposition methods for hydroxyapatite coatings onto a titanium alloy. Surf Coat Technol 216:224–231. https://doi.org/10.1016/j.surfcoat.2012.11.048

Champagne V, Helfritch D (2013) A demonstration of the antimicrobial effectiveness of various copper surfaces. J Biol Eng 7:1–7

Chen MW, McCauley JW, Dandekar DP, Bourne NK (2006) Dynamic plasticity and failure of high-purity alumina under shock loading. Nat Mater 5:614–618

Chen Y, Bakshi SR, Agarwal A (2010) Correlation between nanoindentation and nanoscratch properties of carbon nanotube reinforced aluminum composite coatings. Surf Coat Technol 204:2709–2715. https://doi.org/10.1016/j.surfcoat.2010.02.024

Choudhuri A, Mohanty PS, Karthikeyan J (2009) Bio-ceramic composite coatings by cold spray technology. In: Proceedings of the international thermal spray conference, pp 391–396

Chun D-M, Ahn S-H (2011) Deposition mechanism of dry sprayed ceramic particles at room temperature using a nano-particle deposition system. Acta Mater 59:2693–2703. https://doi.org/10.1016/j.actamat.2011.01.007

Chun D-M, Choi J-O, Lee CS, Ahn S-H (2012) Effect of stand-off distance for cold gas spraying of fine ceramic particles (<5μm) under low vacuum and room temperature using nano-particle deposition system (NPDS). Surf Coat Technol 206:2125–2132. https://doi.org/10.1016/j.surfcoat.2011.09.043

Cinca N, Vilardell AM, Dosta S et al (2016) A new alternative for obtaining nanocrystalline bioactive coatings: study of hydroxyapatite deposition mechanisms by cold gas spraying. J Am Ceram Soc 99:1420–1428. https://doi.org/10.1111/jace.14076

Cizek J, Kovarik O, Siegl J et al (2013) Influence of plasma and cold spray deposited Ti layers on high-cycle fatigue properties of Ti6Al4V substrates. Surf Coat Technol 217:23–33. https://doi.org/10.1016/j.surfcoat.2012.11.067

Dikici B, Ozdemir I, Topuz M (2016) Cold spray deposition of SS316L powders on Al5052 substrates and their potential using for Biomedical applications. Int J Chem Mol Nucls Mater Metall Eng 10(4):483–487

El-Eskandrany MS, Al-Azmi A (2016) Potential applications of cold sprayed Cu50Ti20Ni30 metallic glassy alloy powders for antibacterial protective coating in medical and food sectors. J Mech Behav Biomed Mater 56:183–194. https://doi.org/10.1016/j.jmbbm.2015.11.030

Frattolin J, Barua R, Aydin H et al (2016) Development of a novel biodegradable metallic stent based on microgalvanic effect. Ann Biomed Eng 44:404–418. https://doi.org/10.1007/s10439-015-1458-5

Gardon M, Latorre A, Torrell M et al (2013) Cold gas spray titanium coatings onto a biocompatible polymer. Mater Lett 106:97–99. https://doi.org/10.1016/j.matlet.2013.04.115

Gardon M, Melero H, Garcia-Giralt N, Dosta S, Cano IG, Guilemany JM (2014) Enhancing the bioactivity of polymeric implants by means of cold gas spray coatings. J Biomed Mater Res Part B. 102(7):1537–1543

Gbureck U, Masten A, Probst J, Thull R (2003) Tribochemical structuring and coating of implant metal surfaces with titanium oxide and hydroxyapatite layers. Mater Sci Eng C 23:461–465. https://doi.org/10.1016/S0928-4931(02)00322-3

Gledhill H (2001) In vitro fatigue behaviour of vacuum plasma and detonation gun sprayed hydroxyapatite coatings. Biomaterials 22:1233–1240. https://doi.org/10.1016/S0142-9612(00)00273-8

Guilemany JM, Cinca N, Dosta S, Garcia I. (2014) Feasibility of cold gas spraying to produce high roughness high porous titanium coatings for metallic prosthesis. Thermal Spray Centre (CPT). Intellectual properties protection (iPP). Ref.1499 p 21

Guilemany JM, Dosta S, Cinca N, Fernández J, Garcia I. (2012) Feasibility of cold gas spraying to produce metal coatings onto activated polymeric substrates. Thermal Spray Centre (CPT). Intellectual properties protection (iPP). Ref.1240B p 10

Hahn B-D, Park D-S, Choi J-J et al (2009) Dense nanostructured hydroxyapatite coating on titanium by aerosol deposition. J Am Ceram Soc 92:683–687. https://doi.org/10.1111/j.1551-2916.2008.02876.x

Hailer NP, Lazarinis S, Mäkelä KT et al (2015) Hydroxyapatite coating does not improve uncemented stem survival after total hip arthroplasty!: an analysis of 116,069 THAs in the Nordic Arthroplasty Register Association (NARA) database. Acta Orthop 86:18–25. https://doi.org/10.3109/17453674.2014.957088

Hamweendo A., Popoola P. A. I., Botef I. (2014) Mathematical model for predicting process parameters in cold spray of porous Ti coatings. doi: 10.13140/2.1.2846.1123

Hasniyati M, Zuhailawati H, Sivakumar R et al (2015) Cold spray deposition of hydroxyapatite powder onto magnesium substrates for biomaterial applications. Surf Eng 31:867–874. https://doi.org/10.1179/1743294415Y.0000000068

Hasniyati MR, Zuhailawati H, Ramakrishnan S (2016) A statistical prediction of multiple responses using overlaid contour plot on hydroxyapatite coated magnesium via cold spray deposition. Procedia Chem 19:181–188. https://doi.org/10.1016/j.proche.2016.03.091

Heimann RB (2016) The challenge and promise of low-temperature bioceramic coatings: an editorial. Surf Coat Technol 301:1–5. https://doi.org/10.1016/j.surfcoat.2015.12.082

http://www.stryker.com/en-us/products/Orthopaedics/HipReplacement/AcetabularTritaniumAcetabularShell/index.htm

http://www.zimmerbiomet.com/medical-professionals/common/our-science/trabecular-metal-technology.html

Ishikawa K, Miyamoto Y, Nagayama M, Asaoka K (1997) Blast coating method: new method of coating titanium surface with hydroxyapatite at room temperature. J Biomed Mater Res 38:129–134

Kang K, Bae G, Won J, Lee C (2012) Mechanical property enhancement of kinetic sprayed Al coatings reinforced by multi-walled carbon nanotubes. Acta Mater 60:5031–5039. https://doi.org/10.1016/j.actamat.2012.05.034

Ketola J (2014) Cold sprayed coatings in biomedicine, Master's thesis, Tampere University of Technology

Kliemann J-O, Gutzmann H, Gärtner F et al (2011) Formation of cold-sprayed ceramic titanium dioxide layers on metal surfaces. J Therm Spray Technol 20:292–298. https://doi.org/10.1007/s11666-010-9563-3

Koivuluoto H (2010) Microstructural characteristics and corrosion properties of cold-sprayed coatings. Dissertation, Tampere University of Technology

Laonapakul T, Otsuka Y, Nimkerdphol AR, Mutoh Y (2012a) Acoustic emission and fatigue damage induced in plasma-sprayed hydroxyapatite coating layers. J Mech Behav Biomed Mater 8:123–133. https://doi.org/10.1016/j.jmbbm.2011.11.011

Laonapakul T, Rakngarm Nimkerdphol A, Otsuka Y, Mutoh Y (2012b) Failure behavior of plasma-sprayed HAp coating on commercially pure titanium substrate in simulated body fluid (SBF) under bending load. J Mech Behav Biomed Mater 15:153–166. https://doi.org/10.1016/j.jmbbm.2012.05.017

Lee JH, Jang HL, Lee KM, Baek H-R, Jin K, Hong KS et al (2013) In vitro and in vivo evaluation of the bioactivity of hydroxyapatite- coated polyetheretherketone biocomposites created by cold spray technology. Acta Biomater 9:6177–6187

Li C-J, Li W-Y (2003) Deposition characteristics of titanium coating in cold spraying. Surf Coat Technol 167:278–283. https://doi.org/10.1016/S0257-8972(02)00919-2

Li W-Y, Zhang C, Guo X et al (2007) Ti and Ti-6Al-4V coatings by cold spraying and microstructure modification by heat treatment. Adv Eng Mater 9:418–423. https://doi.org/10.1002/adem.200700022j

Liu X, Chu PK, Ding C (2010) Surface nano-functionalization of biomaterials. Mater Sci Eng R Rep 70:275–302. https://doi.org/10.1016/j.mser.2010.06.013

Liu Y, Dang Z, Wang Y et al (2014a) Hydroxyapatite/graphene-nanosheet composite coatings deposited by vacuum cold spraying for biomedical applications: inherited nanostructures and enhanced properties. Carbon 67:250–259. https://doi.org/10.1016/j.carbon.2013.09.088

Liu Y, Huang J, Li H (2014b) Nanostructural characteristics of vacuum cold-sprayed hydroxyapatite/graphene-nanosheet coatings for biomedical applications. J Therm Spray Technol 23:1149–1156. https://doi.org/10.1007/s11666-014-0069-2

Lozier A, Poopola OO, Mason JJ, Forstein M (2009) Bone fracture fixation system, US Papent no US 2009/0198286 A1

Melero H, Fernández J, Dosta S, Guilemany JM (2011) Characterization of novel bioactive hydroxyapatite-TiO2 coatings obtained by high velocity oxy-fuel. In: Proceedings of the thermal spray conference, Hamburg, Germany

Moore B, Asadi E, Lewis G (2017) Deposition methods for microstructured and nanostructured coatings on metallic bone implants: a review. Adv Mater Sci Eng 2017:1–9. https://doi.org/10.1155/2017/5812907

Mukhopadhyay A, Joshi K, Dey A, Chakraborty R, Rav A, Biswas S et al (2010) Shock deformation of coarse grain alumina above Hugoniot elastic limit. J Mater Sci 45:3635–3651. https://doi.org/10.1007/s10853-010-4409-4

Noh JH, Kim DW, An JS, Chang HR, Kim DH, Hong KS, Chin DK (2012) Method for modifying the surface area of a bioinert material. US Patent 0009341 A1, 12 Jan 2012

Noorakma ACW, Zuhailawati H, Aishvarya V, Dhindaw BK (2013) Hydroxyapatite-coated magnesium-based biodegradable alloy: cold spray deposition and simulated body fluid studies. J Mater Eng Perform 22:2997–3004. https://doi.org/10.1007/s11665-013-0589-9

O'Hare P, Meenan BJ, Burke GA et al (2010) Biological responses to hydroxyapatite surfaces deposited via a co-incident microblasting technique. Biomaterials 31:515–522. https://doi.org/10.1016/j.biomaterials.2009.09.067

O'Neill L, O'Sullivan C, O'Hare P et al (2009) Deposition of substituted apatites onto titanium surfaces using a novel blasting process. Surf Coat Technol 204:484–488. https://doi.org/10.1016/j.surfcoat.2009.08.014

O'Sullivan C, O'Hare P, O'Leary ND et al (2010) Deposition of substituted apatites with anticolonizing properties onto titanium surfaces using a novel blasting process. J Biomed Mater Res B Appl Biomater 95B:141–149. https://doi.org/10.1002/jbm.b.31694

Park D-S, Kim I-S, Kim H, et al (2010) Improved biocompatibility of hydroxyapatite thin film prepared by aerosol deposition. J Biomed Mater Res B Appl Biomater n/a-n/a doi: https://doi.org/10.1002/jbm.b.31658

Price TS, Shipway PH, McCartney DG (2006) Effect of cold spray deposition of a titanium coating on fatigue behavior of a titanium alloy. J Therm Spray Technol 15:507–512. https://doi.org/10.1361/105996306X147108

Qiu D, Zhang M, Grøndahl L (2013) A novel composite porous coating approach for bioactive titanium-based orthopedic implants. J Biomed Mater Res 101A:862–872. https://doi.org/10.1002/jbm.a.34372

Ratner BD, Hoffman AS, Schoen FJ, Lemons JE (2013) Introduction – biomaterials science: an evolving, multidisciplinary endeavor. In: Ratner BD, Hoffman AS, Schoen FJ, Lemons JE (eds) Biomaterials science, 3rd edn. Academic Press, San Diego

Salim NT, Yamada M, Nakano H, Fukumoto M (2011) The synthesis of titanium dioxide (TiO2) powder for cold spray process. IOP Conf Series Mater Sci Eng 18:32019. https://doi.org/10.1088/1757-899X/18/3/032019

Sanpo N, Ang SM, Cheang P, Khor KA (2009a) Antibacterial property of cold sprayed chitosan-Cu/Al coating. J Therm Spray Technol 18:600–608. https://doi.org/10.1007/s11666-009-9391-5

Sanpo N, Hailan C, Loke K, Keng KP, Cheang P, Berndt CC, et al. (2010) Biocompatibility and antibacterial property of cold sprayed ZnO/titanium composite coating. In: Mendez-Vilas A (ed). Science and technology against microbial pathogens. Research, development and evaluation. In: proceedings of the international conference on antimicrobial research, World Scientific pp 140–44

Sanpo N, Saraswati, Lu TM, Cheang P (2008) Anti-bacterial property of cold sprayed ZnO-Al coating. In: Proceedings of the 2008 international conference on biomedical engineering and informatics, Sanya, Hainan, China

Sanpo N, Tan M, Cheang P, Khor KA (2009b) Antibacterial property of cold-sprayed HA-Ag/PEEK coating. J Therm Spray Technol 18:10–15

Saphronov V, Shishkovsky I (2015) Laser annealing for gas-dynamical spraying of HA coating upon a titanium surface. Crystals 5:447–457. https://doi.org/10.3390/cryst5040447

Shtansky DV, Batenina IV, Yadroitsev IA et al (2012) A new combined approach to metal-ceramic implants with controllable surface topography, chemistry, blind porosity, and wettability. Surf Coat Technol 208:14–23. https://doi.org/10.1016/j.surfcoat.2012.07.008

Shukla V, Elliott G, Kear B, McCandlish L (2001) Hyperkinetic deposition of nanopowders by supersonic rectangular jet impingement. Script Mater 44:2179–2182

Singh RP (2011) Numerical evaluation, optimization and mathematical validation of cold spraying of hydroxyapatite using taguchi approach. Int J Eng Sci Technol 3:7006–7015

Singh RP, Batra U (2013) Effect of cold spraying parameters and their interaction an hydroxyapatite deposition. J Appl Fluid Mech 6(4):555–561

Sun J, Han Y, Cui K (2008) Innovative fabrication of porous titanium coating on titanium by cold spraying and vacuum sintering. Mater Lett 62:3623–3625. https://doi.org/10.1016/j.matlet.2008.04.011

Sun L, Berndt CC, Gross KA, Kucuk A (2001) Material fundamentals and clinical performance of plasma-sprayed hydroxyapatite coatings: a review. J Biomed Mater Res 58:570–592

Taha M, Chai F, Blanchemain N et al (2013) Validating the poly-cyclodextrins based local drug delivery system on plasma-sprayed hydroxyapatite coated orthopedic implant with toluidine blue O. Mater Sci Eng C 33:2639–2647. https://doi.org/10.1016/j.msec.2013.02.022

Tamai K, Kawate K, Kawahara I, Takakura Y, Sakaki K (2009) Inorganic antimicrobial coating for titanium alloy and its effect on bacteria. J Orthop Sci 14:204–209

Trentin A, Vezzu S, Rech S, Gulizia S and Jahedi M (2011) Biocompatibility of titanium coatings deposites on CoCr by cold spray. In: Proceedings of the international thermal spray conference, Hamburg, Germany

Van Steenkiste T, Gorkiewicz DW (2004) Analysis of tantalum coatings produced by the kinetic spray process. J Therm Spray Technol 13:265–273. https://doi.org/10.1361/10599630419418

Vilardell AM, Cinca N, Cano IG, et al (2016) Dense nanostructured calcium phosphate coating on titanium by cold spray. J Eur Ceram Soc doi: https://doi.org/10.1016/j.jeurceramsoc.2016.11.040

Vo P, Irissou E, Legoux J-G, Yue S (2013) Mechanical and microstructural characterization of cold-sprayed Ti-6Al-4V after heat treatment. J Therm Spray Technol 22:954–964. https://doi.org/10.1007/s11666-013-9945-4

Vucko MJ, King PC, Poole AJ et al (2012) Cold spray metal embedment: an innovative antifouling technology. Biofouling 28:239–248. https://doi.org/10.1080/08927014.2012.670849

Wang J, DiPietro J, Bostrom M et al (2014) Clinical and radiographic outcomes with a hydroxyapatite and porous coated cup design. Adv Orthop Surg 2014:1–5. https://doi.org/10.1155/2014/302969

Wong W., Rezaeian A., Yue S., Wong W., Rezaeian A., Yue S. (2009) Effects of gas temperature, gas pressure, and particle characteristics on cold sprayed pure titanium coatings, International

Thermal Spray Conference (ITSC) 2009 American Society for Metals doi: https://doi.org/10.1361/cp2009itsc0231
Zhang L, Zhang WT (2011) Numerical investigation on particle velocity in cold spraying of hydroxyapatite coating. Adv Mater Res 18:717–722
Zhang S (2011) Biological and Biomedical coatings handbook, vol 2. Taylor & Francis, Boca Raton
Zhao L, Chu PK, Zhang Y, Wu Z (2009) Antibacterial coatings on titanium implants. J Biomedl Mater Res Part B 91B:470–480
Zhou X (2012) Hydroxyapatite/titanium composite coating for biomedical applications. Dissertation, University of Michigan
Zhou X, Mohanty P (2012) Electrochemical behavior of cold sprayed hydroxyapatite/titanium composite in hanks' solution. Electrochim Acta 65:134–140

Index

P. Cavaliere (ed.), *Cold-Spray Coatings*,
https://doi.org/10.1007/978-3-319-67183-3_2